ΕΘΝΙΚΟ ΜΕΤΣΟΒΙΟ ΠΟΛΥΤΕΧΝΕΙΟ

ΣΧΟΛΗ ΠΟΛΙΤΙΚΩΝ ΜΗΧΑΝΙΚΩΝ
ΕΡΓΑΣΤΗΡΙΟ ΣΤΑΤΙΚΗΣ
& ΑΝΤΙΣΕΙΣΜΙΚΩΝ ΕΡΕΥΝΩΝ

NATIONAL TECHNICAL UNIVERSITY
OF ATHENS
SCHOOL OF CIVIL ENGINEERING
INSTITUTE OF STRUCTURAL ANALYSIS
& ANTISEISMIC RESEARCH

# GENERALIZED STRAIGHT AND CURVED BEAM THEORIES WITH ISOGEOMETRIC ANALYSIS

**DOCTORAL THESIS**
for the title of Doctor of Philoshophy in Engineering
submitted in the School of Civil Engineering
(National Technical University of Athens)

**IOANNIS N. TSIPTSIS**
**Diploma in Civil Engineering**
**MSc General Structural Engineering**

**April 2017, Athens, Greece**

**ΕΘΝΙΚΟ ΜΕΤΣΟΒΙΟ ΠΟΛΥΤΕΧΝΕΙΟ**

ΣΧΟΛΗ ΠΟΛΙΤΙΚΩΝ ΜΗΧΑΝΙΚΩΝ
ΕΡΓΑΣΤΗΡΙΟ ΣΤΑΤΙΚΗΣ
& ΑΝΤΙΣΕΙΣΜΙΚΩΝ ΕΡΕΥΝΩΝ

**NATIONAL TECHNICAL UNIVERSITY
OF ATHENS**
SCHOOL OF CIVIL ENGINEERING
INSTITUTE OF STRUCTURAL ANALYSIS
& ANTISEISMIC RESEARCH

**ΕΘΝΙΚΟ ΜΕΤΣΟΒΙΟ ΠΟΛΥΤΕΧΝΕΙΟ**

ΣΧΟΛΗ ΠΟΛΙΤΙΚΩΝ ΜΗΧΑΝΙΚΩΝ
ΕΡΓΑΣΤΗΡΙΟ ΣΤΑΤΙΚΗΣ
& ΑΝΤΙΣΕΙΣΜΙΚΩΝ ΕΡΕΥΝΩΝ

**NATIONAL TECHNICAL UNIVERSITY
OF ATHENS**
SCHOOL OF CIVIL ENGINEERING
INSTITUTE OF STRUCTURAL ANALYSIS
& ANTISEISMIC RESEARCH

# GENERALIZED STRAIGHT AND CURVED BEAM THEORIES WITH ISOGEOMETRIC ANALYSIS

DOCTORAL DISSERTATION
for the title of Doctor of Philosophy in Engineering submitted in
the School of Civil Engineering,
National Technical University of Athens

IOANNIS N. TSIPTSIS
Diploma in Civil Engineering
MSc in General Structural Engineering

**ADVISORY COMMITTEE:**
Sapountzakis J. Evangelos,
Professor NTUA (Supervisor)

Papadrakakis Manolis,
Professor Emeritus NTUA

Koumousis K. Vlasis,
Professor NTUA

**EXAMINATION COMMITTEE:**
Sapountzakis J. Evangelos,
Professor NTUA (Supervisor)

Papadrakakis Manolis,
Professor Emeritus NTUA

Koumousis K. Vlasis,
Professor NTUA

Vayas Ioannis
Professor NTUA

Gantes Charis
Professor NTUA

Psycharis Ioannis
Professor NTUA

Papadopoulos Vissarion
Associate Professor NTUA

# GENERALIZED STRAIGHT AND CURVED BEAM THEORIES WITH ISOGEOMETRIC ANALYSIS

## DOCTORAL DISSERTATION
for the title of Doctor of Philosophy in Engineering submitted in
the School of Civil Engineering,
National Technical University of Athens

### IOANNIS N. TSIPTSIS
Diploma in Civil Engineering
MSc in General Structural Engineering

**ADVISORY COMMITTEE:**
Sapountzakis J. Evangelos,
Professor NTUA (Supervisor)

Papadrakakis Manolis,
Professor Emeritus NTUA

Koumousis K. Vlasis,
Professor NTUA

**EXAMINATION COMMITTEE:**
Sapountzakis J. Evangelos,
Professor NTUA (Supervisor)

Papadrakakis Manolis,
Professor Emeritus NTUA

Koumousis K. Vlasis,
Professor NTUA

Vayas Ioannis
Professor NTUA

Gantes Charis
Professor NTUA

Psycharis Ioannis
Professor NTUA

Papadopoulos Vissarion
Associate Professor NTUA

# Acknowledgments

First and foremost, I would like to express my sincere gratitude to my supervisor, Professor Evangelos Sapountzakis, for his guidance and encouragement throughout the implementation of the present dissertation. His continuous support, motivation and dedicated involvement in every step played a crucial role for the completion of this research effort.

I would also like to express my most sincere gratitude to Professor Vlassis Koumousis and Emeritus Professor Manolis Papadrakakis for serving as members of my doctoral advisory committee. Their beneficial comments, as well as their illuminating lectures have contributed the most to the accomplishment of this effort and are highly appreciated.

My sincere gratitude also goes to Professor Ioannis Vayas, Professor Charis Gantes, Professor Ioannis Psycharis and Associate Professor Vissarion Papadopoulos for serving as members of my doctoral examination committee and for their constructive comments which enriched this dissertation.

Special thanks go to my fellow researchers and friends Vassilis Tsipiras, Andreas Kampitsis, Ioannis Dikaros, Amalia Argyridi and Marina-Myrto Manola for the constructive and inspirational discussions on research matters but mainly for their support all these years. I would also like to thank Mrs. Fani Kouvaki for being always supportive and all my friends for believing in me and encouraging me throughout this effort.

Finally, I would like to express my sincere gratitude and appreciation to my parents Popi and Nikos for their endless love, patience and support. Their continuous encouragement and substantial support has always been a source of courage to me and for that I am deeply grateful.

Ioannis N. Tsiptsis,
Athens, June 2017

"Everything should be made as simple as possible, but not simpler"

A. Einstein

**Περιεχόμενα εκτενούς περίληψης**

# Εκτενής Περίληψη

# Γενικευμένη Θεωρία Ευθύγραμμης και Καμπύλης Δοκού με Ισογεωμετρική Ανάλυση

## I.    Εισαγωγή Εκτενούς Περίληψης

Στη διατριβή αυτή διερευνάται και επιλύεται σειρά προβλημάτων μέσω της ανάπτυξης εξελιγμένων προσομοιωμάτων ευθύγραμμης και καμπύλης δοκού. Πιο συγκεκριμένα, αντιμετωπίζονται τα προβλήματα ανομοιόμορφης στρέψης, γενικευμένης στρέβλωσης λόγω διάτμησης και στρέψης (μέσω των οποίων μελετάται το φαινόμενο της διατμητικής υστέρησης), διαστρέβλωσης (παραμόρφωση των διατομών της δοκού στο επίπεδό τους) καθώς και το πρόβλημα της δυναμικής ανάλυσης ευθύγραμμων και καμπύλων δοκών. Η αντιμετώπιση των προβλημάτων αυτών βασίζεται στη γενικευμένη διατύπωση καινοτόμων θεωριών δοκού (Generalized Beam Theories - GBT), με τις οποίες το πεδίο μετατοπίσεων και οι συνιστώσες των τανυστών παραμόρφωσης και τάσης διατυπώνονται ως γραμμικοί συνδυασμοί γινομένων μονοδιάστατων και διδιάστατων συναρτήσεων.

Η αναλυτική λύση των μονοδιάστατων και διδιάστατων προβλημάτων συνοριακών και αρχικών-συνοριακών τιμών που μορφώνονται εν γένει δεν είναι εφικτή. Ως εκ τούτου, τα προβλήματα αυτά επιλύονται αριθμητικά εφαρμόζοντας τη Μέθοδο Συνοριακών Στοιχείων (Boundary Element Method - BEM), τη Μέθοδο Αναλογικής Εξίσωσης (Analog Equation Method - AEM), η οποία αποτελεί εξέλιξη της BEM, καθώς και τη Μέθοδο Πεπερασμένων Στοιχείων (Finite Element Method - FEM). Όσον αφορά στην επίλυση μονοδιάστατων προβλημάτων, οι αριθμητικές μέθοδοι που χρησιμοποιούνται (AEM και FEM) συνδυάζονται με εργαλεία της Ισογεωμετρικής Ανάλυσης (Isogeometric Analysis - IGA) ώστε να επιτευχθεί μία προσέγγιση με χαμηλότερο υπολογιστικό κόστος καθώς και πιο διαδραστική μεταξύ ανάλυσης και γεωμετρίας που θα επιτυγχάνει πιο αξιόπιστα αποτελέσματα περιορίζοντας το σφάλμα που πηγάζει από την προσέγγιση της γεωμετρίας. Συγκεκριμένα, οι παραμετρικές καμπύλες B-splines και NURBS (Non-Uniform Rational B-Splines) που έχουν υιοθετήσει τα λογισμικά πακέτα μοντελοποίησης με υπολογιστή (Computer-Aided Design - CAD) εφαρμόζονται στην παρούσα διατριβή. Με βάση τις αναπτυχθείσες αναλυτικές και αριθμητικές διαδικασίες συντάσσονται καινοτόμα προγράμματα ηλεκτρονικού υπολογιστή για την ανάλυση τρισδιάστατων ευθύγραμμων και καμπυλόγραμμων ραβδωτών φορέων.

Κάθε κύριο κεφάλαιο της διατριβής αποτελείται από την εισαγωγή, τη διατύπωση του προβλήματος, την αριθμητική επίλυση, αντιπροσωπευτικά αριθμητικά παραδείγματα και τα συμπεράσματα. Στην εισαγωγή κάθε κύριου κεφαλαίου περιέχεται η βιβλιογραφική επισκόπηση του ερευνητικού έργου (*State of the Art*) του αντίστοιχου εξεταζόμενου προβλήματος και παρουσιάζονται τα πρωτότυπα σχετικά στοιχεία της εργασίας. Τέλος, στο τελικό κεφάλαιο παρουσιάζονται τα συμπεράσματα και προτάσεις για μελλοντική έρευνα.

Στα προαναφερθέντα προβλήματα η γενικευμένη στρέβλωση λόγω διάτμησης και στρέψης λαμβάνεται υπόψη μέσω της εισαγωγής στο πεδίο μετατοπίσεων ευθύγραμμης ή καμπύλης δοκού πρόσθετων βαθμών ελευθερίας που συνιστούν ανεξάρτητες παραμέτρους στρέβλωσης. Η επιρροή της διαστρέβλωσης λαμβάνεται υπόψη μέσω της εισαγωγής νέων βαθμών ελευθερίας που συνιστούν παραμέτρους παραμόρφωσης της διατομής, ενώ στην παρούσα ανάλυση η επιρροή του λόγου Poisson λαμβάνεται υπόψη τόσο στην παραμόρφωση της διατομής όσο και στην καθολική ανάλυση της δοκού. Οι ως άνω βαθμοί ελευθερίας εισάγονται στο προτεινόμενο στοιχείο δοκού στα πλαίσια λογισμικού με βάση τη Μέθοδο Άμεσης Στιβαρότητας για την ανάλυση τρισδιάστατων ραβδωτών ευθύγραμμων και καμπύλων φορέων. Όσον αφορά στην ανάλυση καμπύλων δοκών, λαμβάνεται υπόψη η πλήρης αλληλεπίδραση των φαινομένων της στρέψης, της στρέβλωσης και της διαστρέβλωσης σε συνδυασμό με την επιρροή της καμπυλότητας. Τα εργαλεία της Ισογεωμετρικής ανάλυσης χρησιμοποιούνται ως συναρτήσεις για την αναπαράσταση τόσο της γεωμετρίας της δοκού όσο και την παρεμβολή των άγνωστων κινηματικών ποσοτήτων. Βάσει των αναλυτικών και αριθμητικών διαδικασιών που αναπτύσσονται στην εργασία αυτή συντάχθηκε πλήθος προγραμμάτων ηλεκτρονικού υπολογιστή, με τη βοήθεια των οποίων μελετήθηκαν αντιπροσωπευτικά αριθμητικά παραδείγματα ιδιαίτερου θεωρητικού και πρακτικού ενδιαφέροντος, τα οποία καταδεικνύουν την αποτελεσματικότητα και το εύρος εφαρμογής των προτεινόμενων μεθόδων. Η ακρίβεια και αξιοπιστία των ληφθέντων αποτελεσμάτων επιβεβαιώνεται με υπάρχουσες αναλυτικές και αριθμητικές λύσεις, πειραματικά αποτελέσματα, καθώς και με προσομοιώματα στερεών (εξαεδρικών ή τετραεδρικών), κελυφωτών (τετραπλευρικών) και ραβδωτών πεπερασμένων στοιχείων εμπορικών πακέτων λογισμικού. Υπολογίζονται όλα τα εντατικά, παραμορφωσιακά και κινηματικά μεγέθη του κάθε προβλήματος.

Το ερευνητικό έργο που παρουσιάζεται στην παρούσα διδακτορική διατριβή θεωρείται πρωτότυπο και τα κύρια χαρακτηριστικά του συνοψίζονται ως εξής:

1. Το προτεινόμενο μοντέλο είναι κατάλληλο για την πλήρη ανάλυση τρισδιάστατης πρισματικής καμπύλης δοκού τυχούσας διατομής με ένα επίπεδο σταθερής καμπυλότητας λαμβάνοντας υπόψη την επιρροή της στρέβλωσης, της διαστρέβλωσης, του λόγου του Poisson και της καμπυλότητας τόσο στο στατικό όσο και στο δυναμικό πρόβλημα.

2. Η προτεινόμενη δοκός (καμπύλη ή και ευθύγραμμη) υποβάλλεταια στις πλέον γενικές συνθήκες φόρτισης και στήριξης.

3. Η αριθμητική επίλυση των εξελιγμένων θεωριών δοκού και η εφαρμογή τους σε ευθύγραμμες και καμπύλες δοκούς βασίζεται σε εργαλεία της Ισογεωμετρικής ανάλυσης (B-splines, NURBS) προσφέροντας τη δυνατότητα ενσωμάτωσης του σχεδιαστικού μοντέλου στην ανάλυση.

4. Η ανάλυση της διατομής βασίζεται σε ένα επαναληπτικό σχήμα ισορροπίας συνδυασμένο με την ιδιομορφική ανάλυσή της που έχει ως αποτέλεσμα τη μείωση του υπολογιστικού κόστους και της πολυπλοκότητας συγκρίνοντας με την αρχική ιδιομορφική ανάλυση που αναφέρεται στη βιβλιογραφία. Στην παρούσα διαμόρφωση ο χρήστης μπορεί να ορίσει τον αριθμό των ιδιομορφών που χρειάζονται στην ανάλυση για να επιτευχθεί η επιθυμητή ακρίβεια καθώς, επίσης, και την καμπυλότητα της δοκού.

5. Το προτεινόμενο μοντέλο επιτρέπει με ευκολία αλλαγές στη γεωμετρία, στις συνθήκες φόρτισης και στήριξης καθώς και στη διακριτοποίηση που χρησιμοποιείται στην ανάλυση δεδομένου ότι όλες οι διαφοροποιήσεις γίνονται απευθείας στην καμπύλη γεωμετρία της δοκού. Με αυτό τον τρόπο δίνεται η δυνατότητα εύκολων και γρήγορων παραμετρικών αναλύσεων (συγκρίνοντας με

μοντέλα τρισδιάστατων τετραεδρικών ή κελυφωτών στοιχείων) που είναι ιδιαίτερα σημαντική σε πρακτικές εφαρμογές, όπως σε μοντέλα καμπύλων δοκών στη γεφυροποιία.

6. Η χρήση εργαλείων της Ισογεωμετρικής ανάλυσης στην Αναλογική εξίσωση συντελεί στην επίτευξη της επιθυμητής ακρίβειας των αποτελεσμάτων με πολύ μικρότερο υπολογιστικό κόστος (όπως αρχικά συνέβη και με τη μέθοδο πεπερασμένων στοιχείων).

7. Μέσω των προτεινόμενων μοντέλων δοκού επιτυγχάνεται η αξιολόγηση κανονισμών που καθορίζουν τη μέγιστη απόσταση ενδιάμεσων διαφραγμάτων για την αποφυγή της διαστρέβλωσης. Αξίζει να σημειωθεί ότι οι κανονισμοί μπορεί είτε να οδηγήσουν σε επισφαλείς είτε σε αντιοικονομικές λύσεις δεδομένου ότι δε λαμβάνουν υπόψη όλες τις απαιτούμενες παραμέτρους του εκάστοτε προβλήματος.

## II.     Κεφάλαιο 1: Εισαγωγή

Η εισαγωγή της διατριβής (*$1^o$ κεφάλαιο*) είναι αφιερωμένη στο αντικείμενο, στο κίνητρο, στη διάρθρωση και στις πρωτοτυπίες της εργασίας. Παράλληλα, γίνεται σύντομη αναφορά στην ήδη υπάρχουσα ερευνητική εργασία σχετικά με την εισαγωγή των φαινομένων της στρέβλωσης και της διαστρέβλωσης στην ανάλυση των καμπύλων δοκών, καθώς και στην αναγκαιότητα της εισαγωγής των ραβδωτών φορέων και της Ισογεωμετρικής Ανάλυσης στα σύγχρονα μοντέλα ευθύγραμμων και καμπύλων δοκών.

## III.     Κεφάλαιο 2: B-splines δευτέρου βαθμού στην Ανομοιόμορφη στρέψη δοκών

Στο *$2^o$ κεφάλαιο* παρουσιάζεται το πρόβλημα ανομοιόμορφης στρέψης ευθύγραμμων ομογενών δοκών τυχούσας διατομής, υπό τις πλέον γενικές συνοριακές συνθήκες, υποβαλλόμενων σε τυχούσα στρεπτική φόρτιση $m_t = m_t(x)$ (Σχήμα 2.1). Το πρόβλημα της δοκού περιγράφεται από μονοδιάστατο πρόβλημα συνοριακών τιμών και για το σκοπό αυτό χρησιμοποιείται η διαφορική εξίσωση τέταρτης τάξης που επιλύεται ως προς τη στρεπτική γωνία της διατομής:

$$EC_S \frac{d^4\theta_x(x)}{dx^4} - GI_t \frac{d^2\theta_x(x)}{dx^2} = m_t \qquad \text{κατά μήκος} \qquad (2.1a)$$

$$\alpha_1\theta_x(x) + \alpha_2 M_t = \alpha_3 , \qquad \beta_1\frac{d\theta}{dx} + \beta_2 M_b = \beta_3 \quad \text{στα άκρα } x = 0,l \qquad (2.2a,b)$$

Όπου $E$, $G$ είναι τα μέτρα ελαστικότητας και διάτμησης του ισότροπου υλικού της δοκού, $C_S$, $I_t$ είναι οι σταθερές στρέβλωσης (γνωστή ως $I_w$) και στρέψης, $d\theta_x(x)/dx$ είναι ο ρυθμός μεταβολής της στρεπτικής γωνίας της δοκού $\theta_x(x)$ κατά το μήκος της, $M_t$, $M_b$ είναι οι ροπές στρέψης και στρέβλωσης στα άκρα της δοκού και $a_i$, $\beta_i$ είναι συναρτήσεις που μεταβάλλονται κατάλληλα ώστε να μπορεί να προσδιοριστεί κάθε πιθανή συνθήκη στήριξης (π.χ. για πακτωμένο άκρο ισχύει $a_1 = \beta_1 = 1$, $a_2 = a_3 = \beta_2 = \beta_3 = 0$), αντίστοιχα.

(a)



(b)
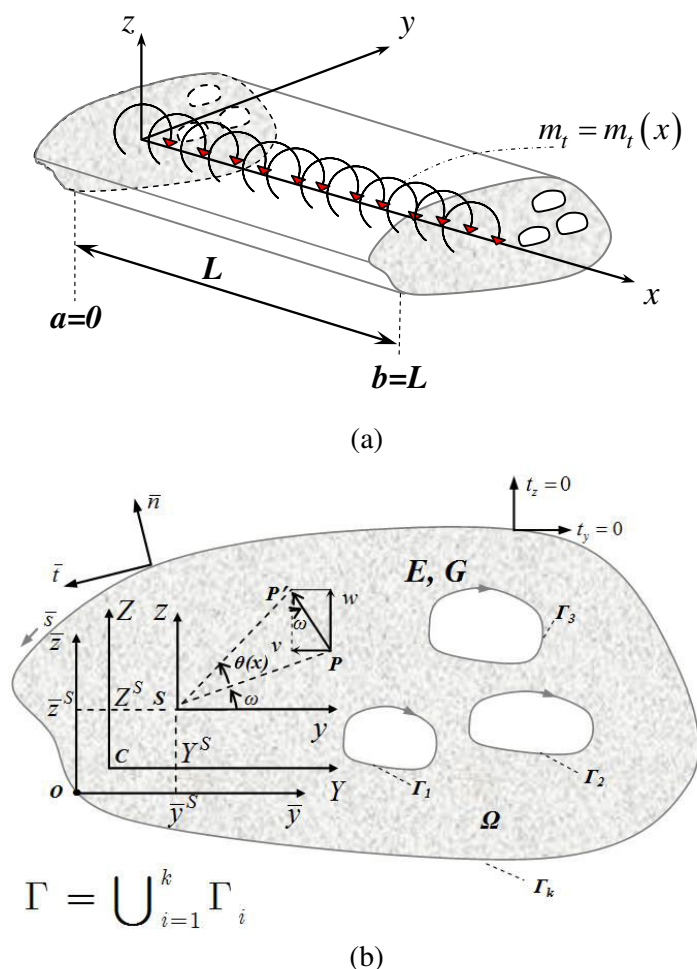
*Σχήμα 2.1. Πρισματική δοκός υποβαλλόμενη σε στρεπτική φόρτιση (a) με τυχούσα διατομή που καταλαμβάνει το διδιάστατο χωρίο Ω (b).*

Η αριθμητική επίλυση του προβλήματος γίνεται με χρήση της Μεθόδου Συνοριακών Στοιχείων (πρόβλημα διατομής) και της Μεθόδου Αναλογικής εξίσωσης-ΑΕΜ (πρόβλημα δοκού: $\dfrac{d^4\theta_x(x)}{dx^4} = q(x)$, όπου $q(x)$ είναι τα ιδεατά φορτία). Το πρόβλημα της διατομής συνίσταται στον υπολογισμό των σταθερών στρέψης και στρέβλωσης (Sapountzakis και Mokos, 2003; Sapountzakis, 2000):

$$C_S = \int_\Omega \varphi_S^{P2} d\Omega \qquad\qquad I_t = \int_\Omega \left( y^2 + z^2 + y\frac{\partial \varphi_S^P}{\partial z} - z\frac{\partial \varphi_S^P}{\partial y} \right) d\Omega \qquad\qquad (2.3a,b)$$

Όπου $\varphi_S^P(y,z)$ είναι η πρωτογενής συνάρτηση στρέβλωσης ως προς το κέντρο διάτμησης της δοκού που υπολογίζεται από κατάλληλα διαμορφωμένο πρόβλημα συνοριακών τιμών.

Τα ιδεατά φορτία που υπολογίζονται μέσω της μεθόδου της Αναλογικής εξίσωσης (Katsikadelis, 2002b) και αποτελούν την τέταρτη παράγωγο του αγνώστου μεγέθους του προβλήματος (στρεπτική γωνία στην προκειμένη), προσεγγίζονται με B-

splines δευτέρου βαθμού που εισάγονται στις ολοκληρωτικές παραστάσεις της προαναφερθείσας αριθμητικής μεθόδου και η επίλυση των οποίων γίνεται είτε αναλυτικά είτε αριθμητικά (Παραρτήματα Α.1 και Α.2). Επομένως, οι μητρωικές εκφράσεις της ΑΕΜ για τη στρεπτική γωνία και τις παραγώγους της γράφονται συναρτήσει των σημείων ελέγχου (control points $P$) που περιγράφουν το B-spline (Παράρτημα Α.2), των μητρώων της ΑΕΜ ([$A$], [$C$]) και των τιμών της στρεπτικής γωνίας και των παραγώγων της στα άκρα της δοκού (διάνυσμα $\{\theta\}$):

$$\{\Theta\} = [A]\{P\} + [C]\{\theta\}$$                                                            (2.4a)

$$\{\Theta'\} = [A']\{P\} + [C']\{\theta\}$$                                                        (2.4b)

$$\{\Theta''\} = [A'']\{P\} + [C'']\{\theta\}$$                                                      (2.4c)

$$\{\Theta'''\} = [A''']\{P\} + [C''']\{\theta\}$$                                                    (2.4d)

Παράλληλα, εφαρμόζεται η μέθοδος της εισαγωγής επιπλέον σημείων ταξιθεσίας (knot insertion) στο διάνυσμα που περιγράφει τη βάση της ισογεωμετρικής καμπύλης των B-splines (knot vector) με σκοπό τη βελτίωση της ακρίβειας της μεθόδου και τη μείωση του υπολογιστικού κόστους (Παράρτημα Α.2).

Μέσω της εν λόγω θεωρίας αναλύονται παραδείγματα ιδιαίτερου πρακτικού ενδιαφέροντος όπου πραγματοποιείται η μελέτη του φαινομένου της αναμοιόμορφης στρέψης για διάφορες διατομές και εξετάζονται τα οφέλη από τη χρήση εργαλείων της Ισογεωμετρικής Ανάλυσης στην παρούσα αριθμητική προσέγγιση καθώς και το πώς επηρεάζεται η ακρίβεια ανάλογα τον τύπο της διατομής για το εν λόγω πρόβλημα. Συγκεκριμένα για λόγους σύγκρισης μελετώνται τέσσερις ίδιες αμφίπακτες δοκοί ενός μέτρου για ομοιόμορφα κατανεμημένη στρεπτική φόρτιση $m_t = 1kNm/m$ αλλά για διαφορετική διατομή (Σχήμα 2.2). Το υλικό των δοκών είναι χάλυβας ($E = 2.1E8kPa$, $v = 0.3$). Οι γεωμετρικές σταθερές των διατομών είναι: (α) $I_t = 6,846cm^4$, $C_S = 12746cm^6$ για την IPE, (β) $I_t = 3,049 \times 10^{-8}m^4$, $C_S = 34,95 \times 10^{-12}m^6$ για την Τ, (γ) $I_t = 8,3903 \times 10^{-8}m^4$, $C_S = 1,1937 \times 10^{-10}m^6$ για την L και (δ) $I_t = 2,010 \times 10^{-8}m^4$ $C_S = 590,10 \times 10^{-12}m^6$ για την UPE.

Στους πίνακες που ακολουθούν δίνονται οι τιμές των στρεπτικών γωνιών και των παραγώγων τους για διάφορες θέσεις κατά μήκος των δοκών με διατομές IPE και Τ (παρόμοια σφάλματα παρατηρούνται για τις UPE και L, αντίστοιχα) υπολογισμένες για την πρωτότυπη ΑΕΜ, την ΑΕΜ με B-splines (AEM-BS) και την αναλυτική λύση (Analytical Solution). Στις περιπτώσεις (β) και (γ) χρειάστηκε να γίνει η εισαγωγή επιπλέον σημείων ταξιθεσίας (CP) για να επιτυχθεί η επιθυμητή ακρίβεια (μέχρι 12 CP). Για την επίτευξη παρόμοιων σφαλμάτων απαιτείται γενικά τετραπλάσιος αριθμός

στοιχείων διακριτοποίησης (NP) για την πρωτότυπη ΑΕΜ. Τέλος, στο Σχήμα 2.3 απεικονίζεται η κατανομή των ιδεατών φορτιών κατά το μήκος της δοκού. Όπως είναι φανερό από τη μορφή των κατανομών, τα ιδεατά φορτία των διατομών IPE και UPE προσεγγίζονται με ακρίβεια από B-splines δευτέρου βαθμού ενώ των διατομών Τ και L φαίνεται να χρειάζονται B-splines ανώτερου βαθμού για να προσεγγιστούν. Αυτό οφείλεται στη σταθερά στρέβλωσης, η οποία είναι πολύ μεγαλύτερη για τις διατομές IPE και UPE.
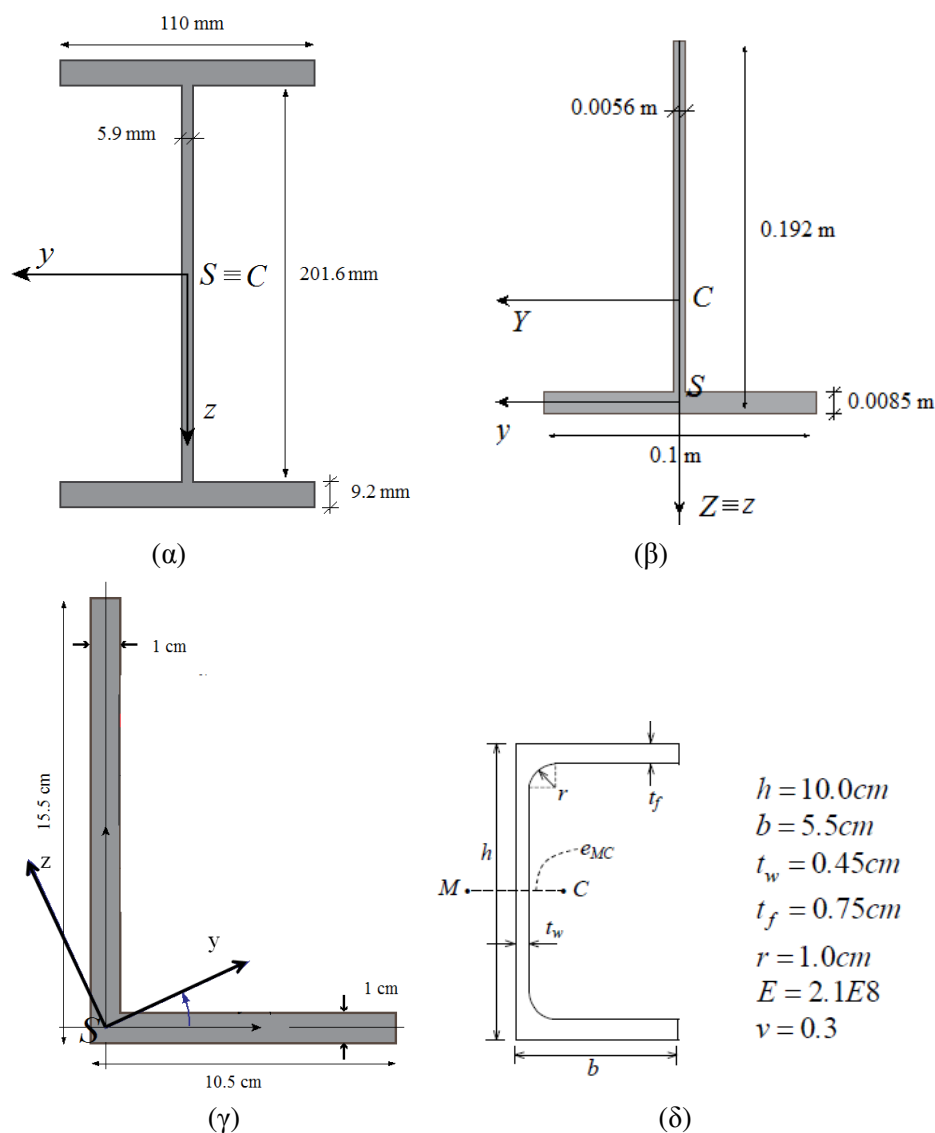


Σχήμα 2.2. Χαλύβδινες διατομές.

Από τις αριθμητικές αναλύσεις των προαναφερόμενων δοκών, προκύπτει ότι για κάποιες διατομές τα B-splines δευτέρου βαθμού μπορούν να δώσουν πολύ ακριβή αποτελέσματα χωρίς την πύκνωση της διακριτοποίησης. Επιπλέον, οι σταθερές της διατομής και κυρίως η σταθερά στρέβλωσης επηρεάζουν αναλογικά τα προκύπτοντα σφάλματα δείχνοντας έτσι ότι η μέθοδος παρουσιάζει σταθερότητα και ακρίβεια. Τέλος, το υπολογιστικό κόστος της ΑΕΜ-BS είναι μικρότερο από την αρχική ΑΕΜ.

| | AEM (3 NP) (1) | AEM-BS (3 CP) (2) | Analytical Solution (3) | Error % (1)-(3) | Error % (2)-(3) |
|---|---|---|---|---|---|
| $\theta_x(1/4)$ | 5,284E-04 | 5,225E-04 | 5,226E-04 | 1,10 | 0,022 |
| $\theta_x(1/2)$ | 9,350E-04 | 9,251E-04 | 9,251E-04 | 1,05 | 0,00 |
| $\theta_x^{'}(1/4)$ | 2,800E-03 | 2,800E-03 | 2,800E-03 | 0,00 | 0,00 |
| $\theta_x^{'}(1/2)$ | 0,000 | 0,000 | 6,210E-08 | 0,00 | 0,00 |
| $\theta_x^{''}(1/4)$ | -3,800E-03 | -3,800E-03 | -3,800E-03 | 0,00 | 0,00 |
| $\theta_x^{''}(1/2)$ | -1,480E-02 | -1,470E-02 | -1,470E-02 | 0,68 | 0,00 |
| $\theta_x^{'''}(1/4)$ | -8,929E-02 | -8,770 E-02 | -8,770 E-02 | 1,81 | 0,00 |
| $\theta_x^{'''}(1/2)$ | 0,000 | 0,000 | -1,800E-06 | 0,00 | 0,00 |
| $\theta_x^{''''}(1/4)$ | 3,659E-01 | 3,657E-01 | 3,657E-01 | 0,05 | 0,00 |
| $\theta_x^{''''}(1/2)$ | 3,433 E-01 | 3,433 E-01 | 3,433 E-01 | 0,00 | 0,00 |

Πίνακας 2.1. Στρεπτικές γωνίες και παράγωγοί τους για τη δοκό με διατομή IPE.

| | AEM-BS (12 CP) (1) | AEM (12 NP) (2) | Analytical Solution (3) | Error % (1)-(3) | Error % (2)-(3) |
|---|---|---|---|---|---|
| $\theta_x(1/8)$ | 1,220E-02 | 1,240E-02 | 1,220E-02 | 0,00 | 1,613 |
| $\theta_x^{'}(1/8)$ | 1,318E-01 | 1,311E-01 | 1,317E-01 | 0,076 | 0,456 |
| $\theta_x^{'}(3/16)$ | 1,206E-01 | 1,154E-01 | 1,204E-01 | 0,166 | 4,153 |
| $\theta_x^{''}(1/8)$ | -2,890E-02 | -5,650E-02 | -2,930E-02 | 1,365 | 48,14 |
| $\theta_x^{''}(3/16)$ | -2,908E-01 | -2,767E-01 | -2,862E-01 | 1,582 | 3,320 |
| $\theta_x^{'''}(1/16)$ | -22,249 | -27,881 | -21,682 | 2,548 | 22,23 |
| $\theta_x^{'''}(1/8)$ | -6,745 | -7,005 | -6,901 | 2,265 | 1,479 |
| $\theta_x^{''''}(1/8)$ | 126,545 | 117,293 | 126,407 | 0,109 | 7,225 |
| $\theta_x^{''''}(3/16)$ | 38,665 | 43,400 | 40,232 | 3,895 | 7,300 |

Πίνακας 2.2. Στρεπτικές γωνίες και παράγωγοί τους για τη δοκό με διατομή T.
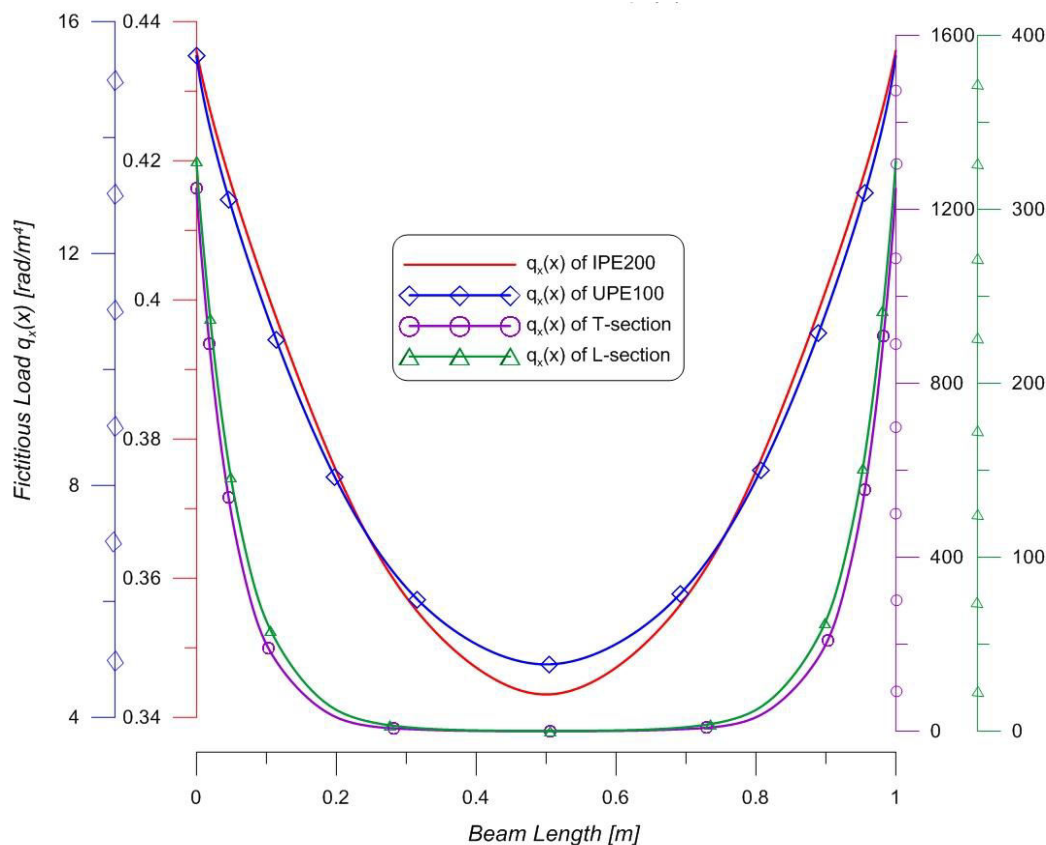
*Σχήμα 2.3. Ακριβείς καμπύλες ιδεατών φορτίων $q(x) = d^4\theta_x(x)/dx^4$ που χρησιμοποιούνται στην ΑΕΜ κατά μήκος των IPE200, UPE100, T-διατομής και L-διατομής δοκών.*

## IV. Κεφάλαιο 3: Στατική και Δυναμική Ανάλυση Γενικευμένης Στρέβλωσης Ευθύγραμμων Δοκών με Ισογεωμετρικές Μεθόδους

Στο $3^o$ κεφάλαιο παρουσιάζεται το πρόβλημα γενικευμένης στρέβλωσης ομογενών δοκών τυχούσας διατομής υπό τις πλέον γενικές συνοριακές συνθήκες, υποβαλλόμενων σε τυχούσα εξωτερική φόρτιση (αξονική: $p_x = p_x(X)$, καμπτική: $p_y = p_y(x)$, $p_z = p_z(x)$, $m_Y = m_Y(x)$, $m_Z = m_Z(x)$, $m_{\varphi_{CY}^P} = m_{\varphi_{CY}^P}(x)$ και $m_{\varphi_{CZ}^P} = m_{\varphi_{CZ}^P}(x)$, στρεπτική: $m_t = m_t(x)$, $m_{\varphi_S^P} = m_{\varphi_S^P}(x)$ και $m_{\varphi_S^S} = m_{\varphi_S^S}(x)$ - Σχήμα 3.1). Η ανάλυση στο κεφάλαιο αυτό επεκτείνεται προκειμένου να καλύψει εκτός από το πρόβλημα στρέψης και το πρόβλημα της κάμψης (λαμβάνονται υπόψη τα φαινόμενα και της στρεπτικής και της καμπτικής διατμητικής υστέρησης). Το οιωνεί στατικό πεδίο μετατοπίσεων καθορίζεται ως εξής:

$$\bar{u}(x,y,z,t) = \bar{u}^P(x,y,z,t) + \bar{u}^S(x,y,z,t) =$$
$$= \underbrace{u(x,t) + \theta_Y(x,t)Z - \theta_Z(x,t)Y + \eta_x(x,t)\phi_S^P(y,z)}_{\pi\rho\omega\tau\omega\gamma\varepsilon\nu\acute{\varepsilon}\varsigma} +$$

$$\underbrace{+\eta_Y(x,t)\phi_{CY}^P(y,z)+\eta_Z(x,t)\phi_{CZ}^P(y,z)+\xi_x(x,t)\phi_S^S(y,z)}_{\delta\varepsilon\upsilon\tau\varepsilon\rho\upsilon\gamma\varepsilon\nu\acute{\varepsilon}\varsigma} \tag{3.1a}$$

$$\bar{v}(x,y,z,t)=v(x,t)-z\theta_x(x,t) \qquad \bar{w}(x,y,z,t)=w(x,t)+y\theta_x(x,t) \tag{3.1b,c}$$
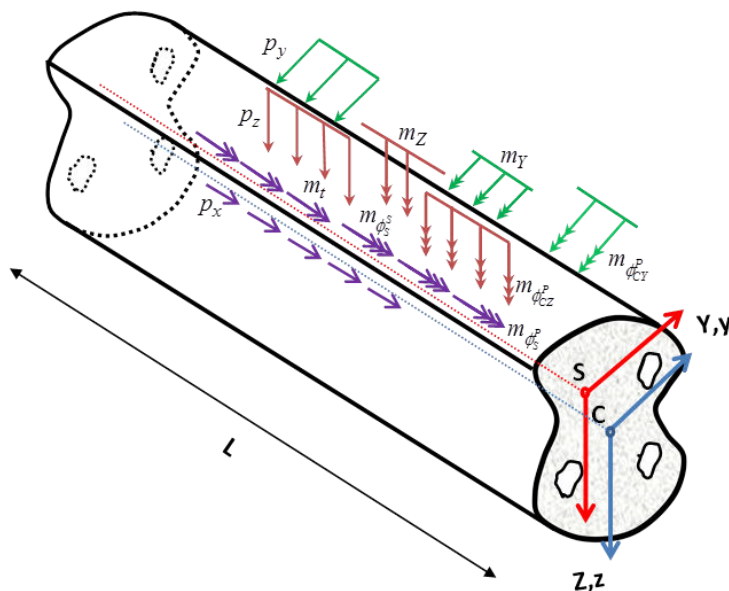


*Σχήμα 3.1. Πρισματική δοκός γενικευμένης φόρτισης και τυχούσας διατομής.*

Όπου $\bar{u}$, $\bar{v}$, $\bar{w}$ είναι η διαμήκης και οι κάθετες μετατοπίσεις της δοκού ως προς το $Sxyz$ σύστημα αξόνων ($S$ είναι το κέντρο διάτμησης); $\bar{u}^P$, $\bar{u}^S$ είναι η πρωτογενής και η δευτερογενής διαμήκης μετατόπιση, αντίστοιχα. $v(x,t)$, $w(x,t)$ είναι οι κάθετες μετατοπίσεις κατά τους άξονες $Y$, $Z$, αντίστοιχα, ενώ $u(x,t)$ είναι η μέση αξονική μετατόπιση της διατομής σε συγκεκριμένη χρονική στιγμή. $\theta_x(x,t)$ είναι η στρεπτική γωνία καθώς $\theta_Z(x,t)$, $\theta_Y(x,t)$ είναι οι γωνίες στροφής κατά τους άξονες $Y$, $Z$, αντίστοιχα, σε συγκεκριμένη χρονική στιγμή. $\eta_x(x,t)$, $\xi_x(x,t)$ είναι οι ανεξάρτητες παράμετροι στρέβλωσης λόγω πρωτογενούς και δευτερογενούς στρέψης, ενώ $\eta_Y(x,t)$, $\eta_Z(x,t)$ είναι οι ανεξάρτητες παράμετροι στρέβλωσης λόγω κάμψης σε συγκεκριμένη χρονική στιγμή; $\varphi_S^P(y,z)$, $\varphi_S^S(y,z)$ είναι η πρωτογενής και δευτερογενής συναρτήσεις στρέβλωσης λόγω στρέψης (συναρτήσεις σχήματος της διατομής) ως προς το κέντρο διάτμησης, ενώ $\varphi_{CY}^P(y,z)$, $\varphi_{CZ}^P(y,z)$ είναι οι πρωτογενείς συναρτήσεις στρέβλωσης λόγω κάμψης ως προς το κέντρο βάρους.

Στο εν λόγω κεφάλαιο εφαρμόζεται επίσης και διαδικασία διόρθωσης του τασικού πεδίου της δοκού (Dikaros και Sapountzakis, 2014) προκειμένου να αυξηθεί η ακρίβεια υπολογισμού κινηματικών και εντατικών μεγεθών, αποφεύγοντας την αύξηση του αριθμού των εμπλεκόμενων βαθμών ελευθερίας. Για τον υπολογισμό των σχετικών

συναρτήσεων στρέβλωσης διατυπώνονται προβλήματα συνοριακών τιμών στο επίπεδο της διατομής με χρήση της εξίσωσης διαμήκους τοπικής ισορροπίας της θεωρίας τρισδιάστατης ελαστικότητας.

Αφού καθοριστούν οι ανεξάρτητες γενικευμένες παραμορφώσεις $\varepsilon_R$ ως $u_{,x}$, $\theta_{Y,x}$, $\theta_{Z,x}$, $\eta_{x,x}$, $\eta_{Y,x}$, $\eta_{Z,x}$, $\xi_{x,x}$, $\gamma_x^P = \theta_{x,x}$, $\gamma_x^S = \eta_x - \theta_{x,x}$, $\gamma_x^T = \xi_x - \eta_x + \theta_{x,x}$, $\gamma_Y^P = v_{,x} - \theta_Z$, $\gamma_Y^S = \eta_Z - v_{,x} + \theta_Z$, $\gamma_Z^P = w_{,x} + \theta_Y$, $\gamma_Z^S = \eta_Y - w_{,x} - \theta_Y$, και οι αντίστοιχες τάσεις $\sigma_R$, χρησιμοποιώντας την έκφραση $\pi_R = \int_L \left( -1/2\varepsilon_R^T C\varepsilon_R + \sigma_R^T\varepsilon_R \right) dx - W$ του διαφορικού λογισμού μπορούν να προσδιοριστούν οι διαφορικές εξισώσεις ισορροπίας της δοκού. $C$ είναι ο τανυστής ελαστικότητας και $W$ είναι το έργο κατανεμημένων φορτίων. Τέλος, προστίθενται οι αδρανειακοί όροι $\int_L \left( 1/2u_{R,tt}^T Mu_{R,tt} \right) dx$ ώστε να καθοριστούν οι εξισώσεις κίνησεις της δοκού ως προς τα κινηματικά μεγέθη. $M$ είναι το τρισδιάστατο μητρώο μάζας και $u_R$ είναι οι γενικευμένες μετατοπίσεις (εξ. 3.1). Επομένως, καθορίζονται οι γενικευμένες εξισώσεις ταλάντωσης της δοκού όπως στη δημοσίευση των Dikaros et al. (2016). Εν συνεχεία, διατυπώνονται δέκα προβλήματα αρχικών-συνοριακών τιμών ως προς τα κινηματικά μεγέθη της δοκού, η επίλυση των οποίων δίδει όλα τα παραμορφωσιακά και εντατικά μεγέθη που είναι απαραίτητα κατά την ανάλυση ραβδωτών φορέων. Στην προκειμένη χρησιμοποιούνται διαφορικές εξισώσεις δευτέρας τάξης. Παράλληλα, διατυπώνονται τα μητρώα δυσκαμψίας και μάζας και επιλύεται το πρόβλημα ιδιοτιμών της δοκού.

Τα ως άνω προβλήματα συνοριακών τιμών προσεγγίζονται αριθμητικά με χρήση της Μεθόδου Συνοριακών Στοιχείων (πρόβλημα διατομής) και της Μεθόδου Αναλογικής εξίσωσης-ΑΕΜ (πρόβλημα δοκού) με B-splines ή με κλασσικά στοιχεία δευτέρου βαθμού. Οσον αφορά το πρόβλημα ελεύθερης ταλάντωσης της δοκού, εκτός από τη μέθοδο της Αναλογικής εξίσωσης, χρησιμοποιείται και η μέθοδος των Πεπερασμένων στοιχείων είτε στην κλασσική της μορφή είτε με NURBS. Μέσω της εν λόγω θεωρίας αναλύονται παραδείγματα ιδιαίτερου θεωρητικού και πρακτικού ενδιαφέροντος όπου πραγματοποιείται η μελέτη του φαινομένου της διατμητικής υστέρησης (λόγω κάμψης και στρέψης) και στη στατική επίλυση και στην ελεύθερη ταλάντωση της δοκού, ενώ η ακρίβεια της προτεινόμενης μεθόδου διαπιστώνεται μέσω συγκρίσεων με υπάρχουσες αναλυτικές και αριθμητικές λύσεις, πειραματικά αποτελέσματα, καθώς και με προσομοιώματα στερεών και κελυφωτών πεπερασμένων στοιχείων.

Συγκεκριμένα, μελετάται μία χαλύβδινη ($E = 2.1E8kPa$, $v = 0.3$) δοκός τριών μέτρων συμπαγούς ορθογωνικής διατομής ($h = 0.5m$, $b = 0.2m$) για διάφορες συνθήκες στήριξης και φόρτισης ($p_z = 250kN/m$ ή $m_t = 100kNm/m$). Οι διαφορές που προκύπτουν στις κατανομές βύθισης του προτεινόμενου μοντέλου δοκού από την κλασσική Euler-Bernoulli δοκό είναι αξιοσημείωτες. Γενικά, όταν χρησιμοποιούνται B-splines οι κατανομές προσεγγίζονται με μεγάλη ακρίβεια με πολύ λιγότερα στοιχεία διακριτοποίησης σε σύγκριση με την αρχική ΑΕΜ. Στη συνέχεια μελετώνται τρεις πρόβολοι με διαφορετικές διατομές (είτε ορθογωνική κλειστή είτε ανοιχτή) και γίνονται συγκρίσεις των κινηματικών μεγεθών, της διρροπής και της ορθής διαμήκους τάσης μεταξύ του προτεινόμενου μοντέλου με B-splines, του μοντέλου της προηγούμενης
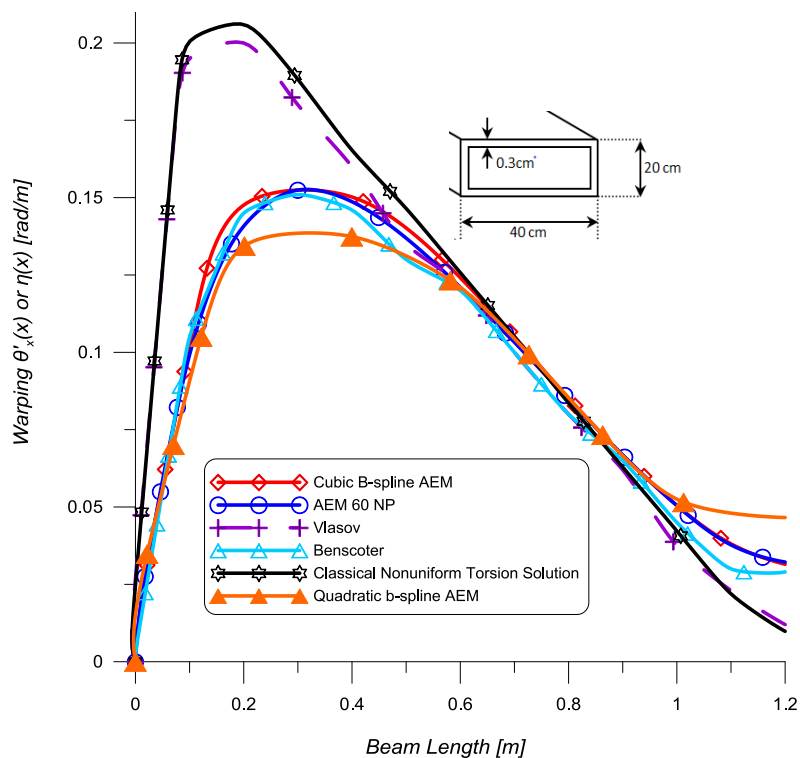
*Σχήμα 3.2. Παράμετρος στρέβλωσης $\eta_x(x)$ κατά μήκος δοκού με κλειστή ορθογωνική διατομή για κατανεμημένη στρεπτική φόρτιση $m_x = 10^6 \, Nm/m$.*

| | $\theta_x(rad)$ at x=L | $\theta_x^{'}(rad/m)$ or $\Psi$ at x=L | $\eta_x(rad/m)$ at x=L | Bimoment $(N/m^2)$ at x=0 |
|---|---|---|---|---|
| Saint-Venant Model | -0.103 | - | - | - |
| Vlasov Model | -0.045 | -0.012 | - | -18.33E-06 |
| FEM- Benscoter Model | -0.045 | -0.011 | - | -18.17E-06 |
| AEM (50 NP) | -0.050 | -0.009 | -0.010 | -16.75E-06 |
| AEM (Quadratic B-spline) | -0.039 | -0.006 | -0.006 | -13.48E-06 |
| AEM (Cubic B-spline) | -0.061 | -0.013 | -0.014 | -18.29E-06 |
| AEM (Quartic B-spline) | -0.046 | -0.008 | -0.008 | -15.50E-06 |
| Classical Nonuniform Torsion Solution-CNT (AEM-BS) | -0.043 | -0.011 | - | -19.13E-06 |

*Πίνακας 3.1. Δοκός ανοικτής διατομής για κατανεμημένη στρεπτική φόρτιση.*

ενότητας (κλασσική θεωρία ανομοιόμορφης στρέψης- CNT), του Vlasov μοντέλου, του μοντέλου Saint-Venant και του μοντέλου Benscoter (Shakourzadeh et al., 1995). Ενδεικτικά αποτελέσματα παρουσιάζονται στο Σχήμα 3.2 και στον Πίνακα 3.1. Τέλος μελετάται πρόβολος δέκα μέτρων κιβοτοειδούς διατομής. Γενικά, B-splines τρίτου βαθμού μπορούν να δώσουν αποτελέσματα με υψηλή ακρίβεια με αρκετά μικρότερο κόστος από την αρχική ΑΕΜ. Η θεωρία δοκού της προηγούμενης ενότητας (CNT) δεν καταφέρνει να εκτιμήσει με ακρίβεια την ορθή τάση και τη διρροπή λόγω της θεώρησης ότι $\theta_x^{'} = \eta_x$. Το ίδιο συμβαίνει και με τη θεωρία Vlasov. Το μοντέλο Benscoter δίνει ακριβή αποτελέσματα στην περίπτωση στρεπτικών φορτίων.

Για τη μελέτη της προτεινόμενης μεθόδου όσον αφορά το δυναμικό πρόβλημα, αρχικα μελετάται η αξονική ελεύθερη ταλάντωση δοκού (σαν ειδική περίπτωση του γενικευμένου προβλήματος) με μοναδιαία χαρακτηριστικά για λόγους σύγκρισης (Hughes et al., 2009) και καταρτίζεται κανονικοποιημένο φάσμα ιδιοσυχνοτήτων (Σχήμα 3.3α). Παρόμοιο φάσμα δημιουργείται και για την περίπτωση ελέυθερης στρεπτικής ταλάντωσης (σαν ειδική περίπτωση του γενικευμένου προβλήματος). Η μέθοδος με NURBS δίνει τα ακριβέστερα αποτελέσματα ενώ η ΑΕΜ παρουσιάζει πολύ μικρότερο άλμα (σφάλμα ή «θόρυβο») σε σχέση με την FEM δίνοντας αρκετά πιο ομαλά φάσματα. Οι υπολογιστικοί χρόνοι για τις διάφορες αριθμητικές μεθόδους αυξάνονται εκθετικά (Σχήμα 3.3β) με την αύξηση των βαθμών ελευθερίας του προβλήματος (1 βαθμός στην πρώτη περίπτωση, 2 στη δέυτερη και 10 στο γενικευμένο πρόβλημα). Γενικά η ΑΕΜ παρουσιάζει μικρότερους χρόνος από τις άλλες μεθόδους. Τέλος, από τα διάγραμματα σύγκλισης που δημιουργούνται για τις πρώτες ιδιοσυχνότητες του γενικευμένου προβλήματος προβόλου δέκα μέτρων με κιβωτοειδή διατομή είναι φανερή η αύξηση (κλίση) καθώς αυξάνεται ο βαθμός των NURBS που ενσωματώνονται στην ΑΕΜ.
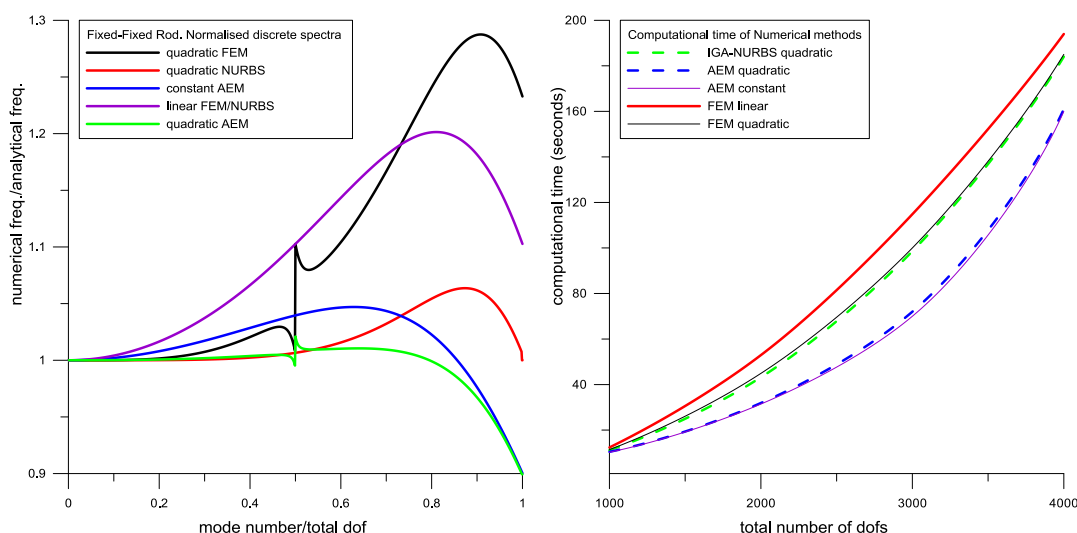


(α)                                        (β)

*Σχήμα 3.3. (α) Κανονικοποιημένο φάσμα ιδιοσυχνοτήτων αξονικής ταλάντωσης αμφίπακτης δοκού για FEM, IGA και ΑΕΜ. (β) Υπολογιστικός χρόνος αριθμητικών μεθόδων για αυξανόμενους βαθμούς ελευθερίας.*

## V.    Κεφάλαιο 4: Στατική και Δυναμική Ανάλυση Γενικευμένης Στρέβλωσης Καμπύλων Δοκών με Ισογεωμετρικές Μεθόδους

Στο *4ο* κεφάλαιο παρουσιάζεται το πρόβλημα γενικευμένης στρέβλωσης ομογενών καμπύλων δοκών τυχούσας διατομής υπό τις πλέον γενικές συνοριακές συνθήκες, υποβαλλόμενων σε τυχούσα εξωτερική φόρτιση (αξονική, καμπτική, στρεπτική- Σχήμα 4.1).
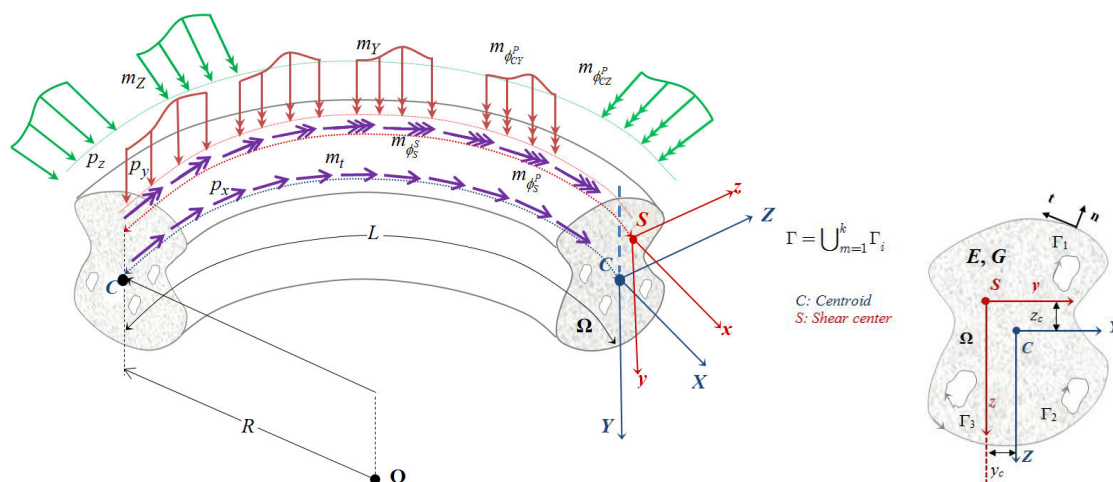


*Σχήμα 4.1. Πρισματική καμπύλη δοκός τυχούσας διατομής που καταλαμβάνει το χωρίο Ω υπό γενικευμένη φόρτιση.*

Η ανάλυση στο κεφάλαιο αυτό επεκτείνεται προκειμένου να ληφθεί υπόψη το φαινόμενο της διατμητικής υστέρησης (λόγω διάτμησης και στρέψης) στην επίλυση καμπυλόγραμμων ραβδωτών φορέων με ένα επίπεδο καμπυλότητας καθώς και η αλληλεπίδραση των αξονικών, καμπτικών και στρεπτικών παραμορφώσεων λόγω αυτής της καμπυλότητας. Οι γενικευμένες παραμορφώσεις $\varepsilon_R$ είναι: $u_{,x}$, $\theta_{Y,x}$, $\theta_{Z,x}$,

$\eta_{x,x}$,    $\eta_{Y,x}$,    $\eta_{Z,x}$,    $\xi_{x,x}$,    $\gamma_x^P = \theta_{x,x} + \dfrac{\theta_Z}{R}$,    $\gamma_x^S = \eta_x - \gamma_x^P = \eta_x - \theta_{x,x} - \dfrac{\theta_Z}{R}$,

$\gamma_x^T = \xi_x - \gamma_x^S = \xi_x - \eta_x + \theta_{x,x} + \dfrac{\theta_Z}{R}$,    $\gamma_Y^P = v_{,x} - \theta_Z$,    $\gamma_Y^S = \eta_Z - v_{,x} + \theta_Z$,

$\gamma_Z^P = w_{,x} + \theta_Y - \dfrac{u}{R}$    και    $\gamma_Z^S = \eta_Y - w_{,x} - \theta_Y + \dfrac{u}{R}$. Βάσει των μεγεθών που αυτές εμπεριέχουν διατυπώνονται οι παραμορφώσεις και τάσεις της καμπύλης δοκού (με

$\dfrac{R}{R+Z} \approx 1 - \dfrac{Z}{R} + \left(\dfrac{Z}{R}\right)^2 = e(R)$ ) που για συντομία δίνονται σε μητρωική μορφή ως εξής:

$$[Aux1] = \begin{bmatrix} 1 & 0 & 0 & 0 & Z & -Y & \phi_S^P & \phi_{CY}^P & \phi_{CZ}^P & \phi_S^S \\ 0 & 1 & 0 & -z & 0 & 0 & 0 & 0 & 0 & 0 \\ 0 & 0 & 1 & y & 0 & 0 & 0 & 0 & 0 & 0 \end{bmatrix} e(R) \qquad (4.1a)$$

$$[Aux2] = \begin{bmatrix} 0 & -\dfrac{1}{R}e(R) & 0 & \dfrac{z}{R}e(R) & 0 & 0 & 0 & 0 & 0 & 0 \\[1em] \dfrac{1}{R}e(R) & 0 & \dfrac{Z}{R}e(R) & -1-\dfrac{Y}{R}e(R) & 0 & 0 & \begin{array}{c}\dfrac{\phi_S^P}{R}e(R)\\ +\phi_{S,y}^P\end{array} & \begin{array}{c}\dfrac{\phi_{CY}^P}{R}e(R)\\ +\phi_{CY,y}^P\end{array} & \begin{array}{c}\dfrac{\phi_{CZ}^P}{R}e(R)\\ +\phi_{CZ,y}^P\end{array} & \begin{array}{c}\dfrac{\phi_S^P}{R}e(R)\\ +\phi_{S,y}^P\end{array} \\[1em] 0 & 0 & 0 & 0 & 1 & 0 & \phi_{S,z}^P & \phi_{CY,z}^P & \phi_{CZ,z}^P & \phi_{S,z}^P \end{bmatrix}$$

<div align="right">(4.1b)</div>

$$\varepsilon = [Aux1]u_{,x} + [Aux2]u \tag{4.1c}$$

$$\sigma = [C][Aux1]u_{,x} + [C][Aux2]u \tag{4.1d}$$

Όπως και στο προηγούμενο κεφάλαιο, εφαρμόζεται επίσης η διαδικασία διόρθωσης του τασικού πεδίου της δοκού με παρόμοιο τρόπο. Για τον υπολογισμό των σχετικών συναρτήσεων στρέβλωσης διατυπώνονται προβλήματα συνοριακών τιμών στο επίπεδο της διατομής με χρήση της εξίσωσης διαμήκους τοπικής ισορροπίας της θεωρίας τρισδιάστατης ελαστικότητας.

Εν συνεχεία, διατυπώνονται δέκα προβλήματα αρχικών-συνοριακών τιμών ως προς τα κινηματικά μεγέθη της δοκού, η επίλυση των οποίων δίδει όλα τα παραμορφωσιακά και εντατικά μεγέθη που είναι απαραίτητα κατά την ανάλυση καμπύλων ραβδωτών φορέων. Στην προκειμένη χρησιμοποιούνται διαφορικές εξισώσεις δευτέρας τάξης για την περιγραφή της στατικής και δυναμικής συμπεριφοράς της καμπύλης δοκού. Παράλληλα, διατυπώνονται τα μητρώα δυσκαμψίας

$$(\delta U = \int_0^L \int_\Omega \left( \delta u_{,x}^T [Aux1]^T + \delta u^T [Aux2]^T \right) \left( [C][Aux1]u_{,x} + [C][Aux2]u \right) \frac{1}{e(R)} d\Omega dx ) \quad \text{και}$$

μάζας $\quad ( \delta W_{\text{mass}} = \int_0^L \int_\Omega \rho \left( \delta u^T [Aux1]^T [Aux1]u_{,tt} \right) \frac{1}{e(R)} d\Omega dx \Rightarrow \delta U = \int_0^L \left( \delta u^T [m_t] u_{,tt} \right) dx )$

και επιλύεται το πρόβλημα ιδιοτιμών της δοκού.

Τα ως άνω προβλήματα συνοριακών τιμών επιλύονται αριθμητικά με χρήση της Μεθόδου Συνοριακών Στοιχείων (πρόβλημα διατομής) και της Μεθόδου Αναλογικής εξίσωσης (πρόβλημα δοκού) με B-splines ή με κλασσικά στοιχεία δευτέρου βαθμού. Εκτός από τη μέθοδο της Αναλογικής εξίσωσης, για το κατά μήκος πρόβλημα της δοκού χρησιμοποιείται και η μέθοδος των Πεπερασμένων στοιχείων είτε στην κλασσική της μορφή είτε σε συνδυασμό με NURBS (αρχικό πολύγωνο ελέγχου

$(x_i, y_i, z_i, w_i)$: $(-R, 0, 0, 1)$, $(-R\cos\left(\dfrac{\phi}{2}\right), R\sin\left(\dfrac{\phi}{2}\right), 0, \cos\left(\dfrac{\phi}{2}\right))$, $(-R\cos(\phi), R\sin(\phi),$

0, 1). Για τη χρονική ολοκλήρωση του προβλήματος χρησιμοποιείται η μέθοδος Newmark. Μέσω της εν λόγω θεωρίας αναλύονται παραδείγματα ιδιαίτερου θεωρητικού και πρακτικού ενδιαφέροντος όπου πραγματοποιείται η μελέτη του φαινομένου της διατμητικής υστέρησης (λόγω κάμψης και στρέψης) στη στατική και δυναμική επίλυση της καμπύλης δοκού, ενώ η ακρίβεια της προτεινόμενης μεθόδου διαπιστώνεται μέσω συγκρίσεων με υπάρχουσες αναλυτικές και αριθμητικές λύσεις, καθώς και με προσομοιώματα στερεών και κελυφωτών πεπερασμένων στοιχείων.

Συγκεκριμένα, μελετάται πρόβολος με διπλά συμμετρική ανοικτή διατομή υπό συγκεντρωμένο κατακόρυφο ή στρεπτικό φορτίο στο άκρο και τα αποτελέσματα από

την ανάλυση του προτεινόμενου μοντέλου είναι παρόμοια με αυτά τρισδιάστατων μοντέλων με πεπερασμένα στοιχεία είτε για μετακινήσεις είτε για τάσεις. Η ίδια δοκός αλλά από διαφορετικό υλικό μελετάται σε ελεύθερη ταλάντωση ($E = 4E7\,N/cm^2$, $G = 2E7\,N/cm^2$, $\rho = 0.025 N\,sec^2/m^4$, $L = 300cm$ και $R = 190.58cm$). Στον Πίνακα 4.1 δίνονται οι πρώτες πέντε ιδιοσυχνότητες για διάφορες αριθμητικές μεθόδους και μοντέλα. Η ανάλυση με NURBS δίνει αποτελέσματα κοντά στο μοντέλο με τρισδιάστατα πεπερασμένα στοιχεία (FEMsolid) με σφάλματα μικρότερα από 5% και για πολύ λίγα στοιχεία. Το Timoshenko καμπύλο στοιχείο δοκού δίνει λανθασμένες τιμές για τις δύο τελευταίες ιδιοσυχνότητες (που κυριαρχεί η στρέψη) δεδομένου ότι δε λαμβάνει υπόψη τη στρέβλωση. Στον Πίνακα 4.2 δίνονται οι πέντε πρώτες ιδιοσυχνότητες για μονοσυμμετρική ανοικτή διατομή ($E = 4E7\,N/cm^2$, $G = 2E7\,N/cm^2$, $\rho = 0.785 N\,sec^2/m^4$, $L = 100cm$ και $R = 63.66cm$). Σε αυτή την περίπτωση παρόλο που το προτεινόμενο μοντέλο δίνει ακριβή αποτελέσματα, το αντίστοιχο Timoshenko παρουσιάζει σημαντικά σφάλματα σχεδόν για όλες τις ιδιομορφές επειδή τα φαινόμενα στρέβλωσης γίνονται εντονότερα. Τέλος, στο Σχήμα 4.2α υπολογίζεται η κάθετη στο επίπεδο της καμπυλότητας μετατόπιση του ελεύθερου άκρου της τελευταίας δοκού για φορτίο $P_Z = -5000\,N$ (κεντρικό στο άκρο) που αυξάνεται στα πρώτα 0.05 δευτερόλεπτα και στη συνέχεια μένει σταθερό. Παρατηρείται ικανοποιητική σύγκλιση μεταξύ των αποτελεσμάτων των μεθόδων.

| A/A | B-splines AEM | FEMsolid (13000) | FEM Timoshenko beam | 5 cubic NURBS | 10cubic NURBS |
|---|---|---|---|---|---|
| 1 | 0.0881 | 0.1028 | 0.0944 | 0.0950 | 0.1120 |
| 2 | 0.4551 | 0.5205 | 0.6214 | 0.5230 | 0.5260 |
| 3 | 0.8790 | 0.9868 | 0.9871 | 1.0502 | 1.1042 |
| 4 | 1.5998 | 1.7888 | 4.5459 | 1.7552 | 1.8002 |
| 5 | 3.2555 | 3.6631 | 4.7959 | 3.4500 | 3.6723 |

Πίνακας 4.1. Ιδιοσυχνότητες καμπύλου προβόλου με διπλά συμμετρική ανοικτή διατομή.

| A/A | FEMsolid (4000) | FEM Curved beam | 5 cubic NURBS | Τύπος Ιδιομορφής |
|---|---|---|---|---|
| 1 | 0.2824 | 0.1788 | 0.2942 | $1^\eta$ ιδιομορφή κατακόρυφης μετατόπισης |
| 2 | 1.3623 | 1.1794 | 1.4211 | $1^\eta$ ιδιομορφή πλευρικής μετατόπισης |
| 3 | 2.2615 | 4.1602 | 2.2205 | $2^\eta$ ιδιομορφή κατακόρυφης μετατόπισης |
| 4 | 5.7508 | 6.4632 | 5.9612 | $1^\eta$ στρεπτική ιδιομορφή |
| 5 | 6.3241 | 31.211 | 6.3709 | $2^\eta$ στρεπτική ιδιομορφή |

Πίνακας 4.2. Ιδιοσυχνότητες καμπύλου προβόλου με μονοσυμμετρική ανοικτή διατομή.

Στο σχήμα 4.2β δίνεται η μετατόπιση του ελεύθερου άκρου προβόλου με ασύμμετρη διατομή για κεντρικά επιβαλλόμενο στο άκρο συγκεντρωμένο φορτίο με σκοπό να καταδειχθεί η μείωση της ακρίβειας του μοντέλου δοκού Timoshenko (μπλε) σε σχέση με το προτεινόμενο μοντέλο (κόκκινο) και το FEMsolid μοντέλο (μαύρο).

<center>(α)                  (β)</center>
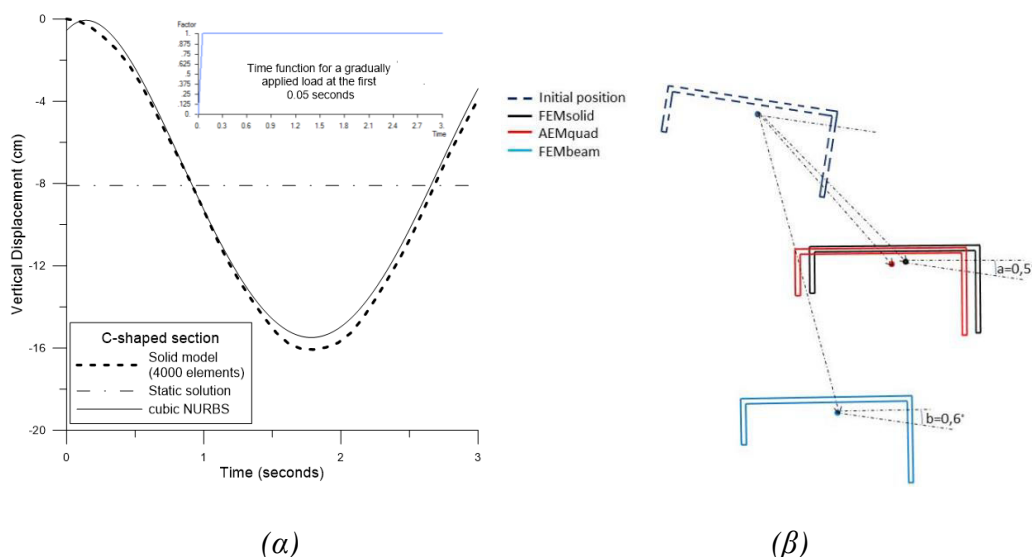
*Σχήμα 4.2. (α)Κάθετη μετατόπιση του ελεύθερου άκρου καμπύλου προβόλου με μονοσυμμετρική διατομή για φορτίο που ασκείται με το χρόνο. (β)Κάθετη μετατόπιση του άκρου προβόλου ασύμμετρης διατομής για στατικό φορτίο.*

Στη συνέχεια μελετάται πρόβολος ( $E = 4E7\,kN/m^2$ , $G = 2E7\,kN/m^2$ , $L = 10\,m$ , $R = 6.366\,m$ ) με μονοσυμμετρική κιβωτοειδή διατομή ( $t/d = 0.02$ και $d/L = 0.1$ όπου t=πάχος και d=ύψος). Στο Σχήμα 4.3 δίνονται οι κατανομές της καμπτικής ροπής, της συνολικής στρεπτικής ροπής και της συνολικής διρροπής (λόγω πρωτογενούς και δευτερογενούς στρέβλωσης) κατά το μήκος της δοκού για έκκεντρο φορτίο $P_Z = 1000\,kN$ . Όσον αφορά την καμπτική ροπή (αριστερά), δίνονται τα αποτελέσματα
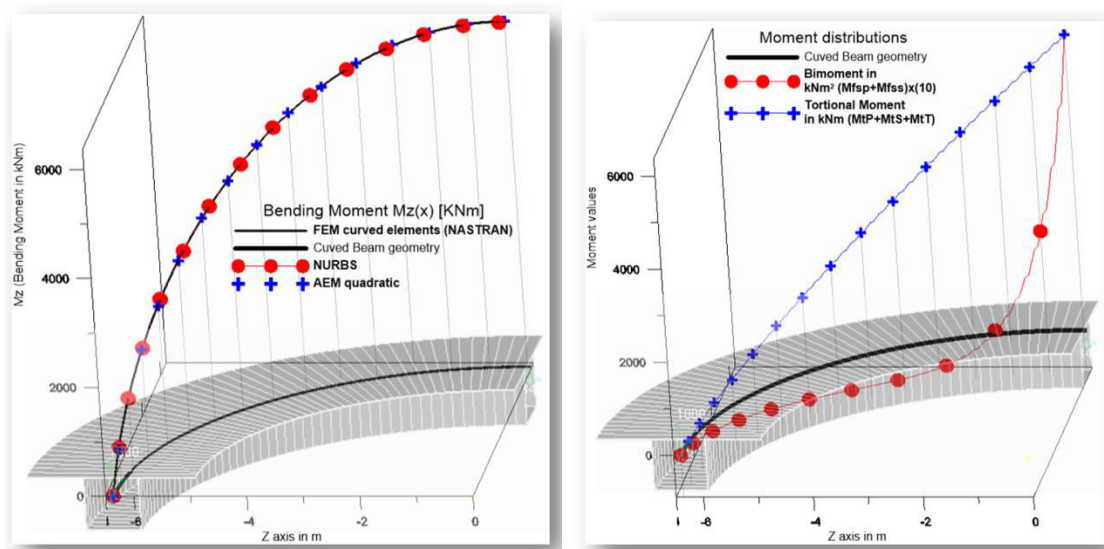


*Σχήμα 4.3. Κατανομή καμπτικής ροπής (αριστερά), στρεπτικής ροπής και διρροπής (δεξιά) κατά μήκος της καμπύλης δοκού χωρίς μετά-επεξεργασία των αποτελεσμάτων για τη μέθοδο με NURBS (ή με περαιτέρω επεξεργασία για τα FEM και ΑΕΜ στοιχεία δοκού χωρίς NURBS).*

για το προτεινόμενο μοντέλο με NURBS, ΑΕΜ χωρίς NURBS (με κλασσικά στοιχεία

δευτέρου βαθμού) και για το Timoshenko στοιχείο δοκού χωρίς NURBS. Τα δύο τελευταία έχουν υποστεί επεξεργασία για να αποτυπωθούν πάνω στην καμπύλη γεωμετρία. Τέλος, στα δεξιά του ίδιου σχήματος αποτυπώνεται η συνολική διρροπή Χ10 και η συνολική στρεπτική ροπή. Στο άκρο η διρροπή είναι το 10% περίπου της στρεπτικής ροπής δεδομένου ότι η πρωτογενής στρεπτική σταθερά της διατομής είναι πολύ μεγαλύτερη από τη σταθερά πρωτογενούς στρέβλωσης.

Παρόμοια με την προηγούμενη περίπτωση δίνονται στο Σχήμα 4.4 (αριστερά) οι κατανομές της κάθετης στο επίπεδο της καμπυλότητας μετατόπισης για το προτεινόμενο μοντέλο με και χωρίς NURBS καθώς και το FEMsolid. Η διατομή είναι μονοσυμμετρική κιβωτοειδής ( $E = 3E7\,kN/m^2$, $G = 1.5E7\,kN/m^2$, $L = 40\,m$, $R = 25.465\,m$, $t/d = 0.086$, $d/L = 0.086$ και $P_Z = 10000\,kN$ ). Τα αποτελέσματα με NURBS δίνουν σωστά την κατανομή των μετατοπίσεων χωρίς περαιτέρω επεξεργασία των αποτελεσμάτων ενώ οι μέθοδοι χωρίς NURBS χρειάζονται επεξεργασία για να αποτυπώσουν σωστά τις καμπύλες παρόλο που δίνουν σωστή μέγιστη μετατόπιση. Στο
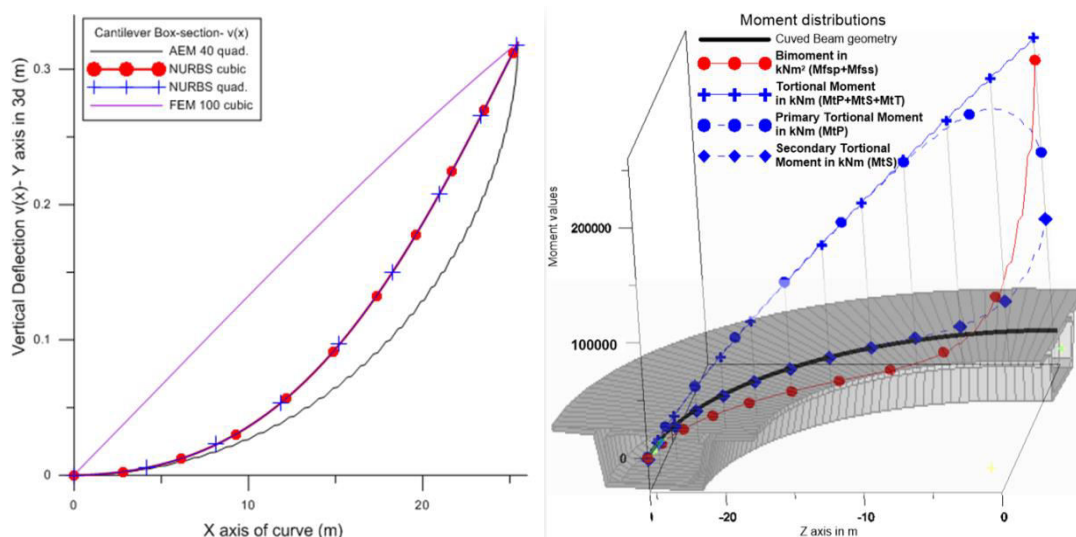


*Σχήμα 4.4. Κατανομή κάθετης μετατόπισης (αριστερά), στρεπτικών ροπών (συνολικής, πρωτογενούς και δευτερογενούς) και διρροπής (δεξιά) κατά μήκος της καμπύλης δοκού χωρίς μετά-επεξεργασία των αποτελεσμάτων για τη μέθοδο με NURBS (ή με περαιτέρω επεξεργασία για τα FEM και AEM στοιχεία δοκού χωρίς NURBS).*

ίδιο σχήμα (δεξιά) δίνονται οι κατανομές της διρροπής και των στρεπτικών ροπών (συνολικής, πρωτογενούς και δευτερογενούς). Είναι φανερό ότι η συνολική διρροπή έχει παρόμοιο μέγεθος με τη στρεπτική ροπή διότι η σταθερά πρωτογενούς στρέβλωσης της διατομής είναι μεγαλύτερη από την πρωτογενή στρεπτική σταθερά της.

Τέλος, μελετάται μία αμφίπακτη καμπύλη δοκός με μονοσυμμετρική κιβοτοειδή διατομή ( $E = 3.25E7\,kN/m^2$, $\nu = 0.1667$, $L = 33\,m$, $R = 100\,m$, $\rho = 2.5t/m^3$, $t/d = 0.1$ και $d/L = 0.065$) για δυναμικό φορτίο μεταβαλλόμενο σύμφωνα με την ημιτονοειδή συνάρτηση $P_Z = 100\cos(2\pi t)\,kN$ στο μέσο του μήκους. Στο Σχήμα 4.4 δίνεται η δυναμική απόκριση διαφορετικών μοντέλων και μεθόδων ως προς τη μετατόπιση στο μέσο του μήκους. Το προτεινόμενο μοντέλο είναι κοντά με το

FEMsolid με ένα διάφραγμα (η τοποθέτηση του διαφράγματος εξηγείται στο $6^O$ κεφάλαιο) δεδομένου ότι δε λαμβάνει υπόψη τη διαστρέβλωση της διατομής. Παράλληλα δεν παρατηρούνται ταλαντώσεις στην αρχή, όπως στο Solid45 (ANSYS) μοντέλο γιατί δε λαμβάνεται υπόψη η απόσβεση χωρίς όμως να μειώνεται η ακρίβεια.
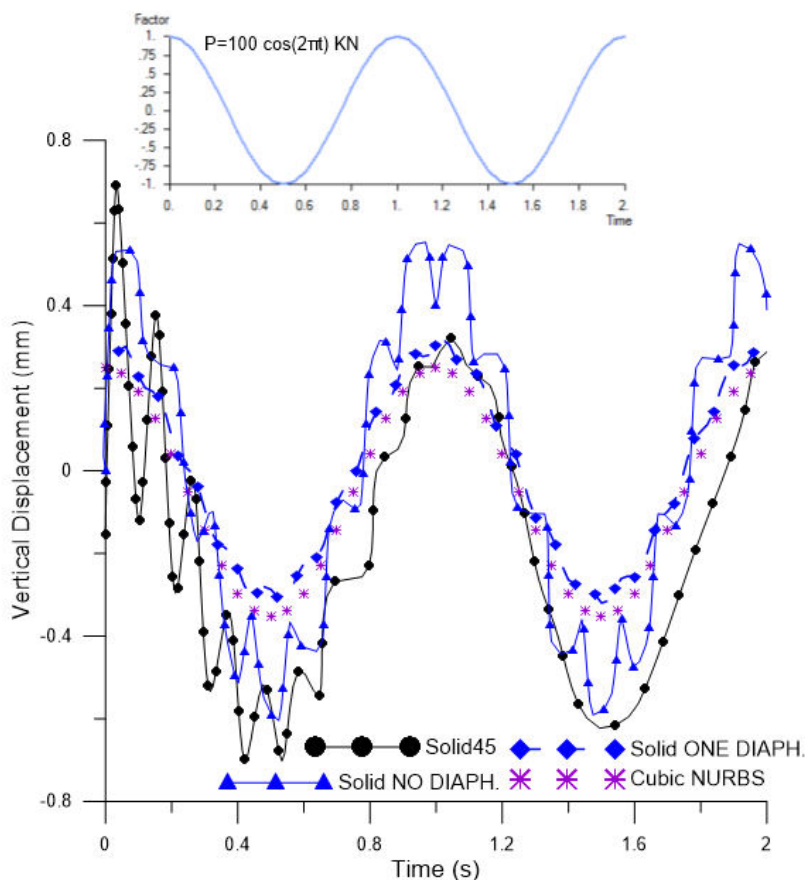


Σχήμα 4.5. Δυναμική απόκριση ως προς την κάθετη μετατόπιση για αμφίπακτη δοκό μονοσυμμετρικής κιβωτοειδούς διατομής υπό ημιτονοειδές μεταβαλλόμενο φορτίο .

# VI.  Κεφάλαιο 5: Ανάλυση Γενικευμένης Διαστρέβλωσης Ευθύγραμμων και Καμπύλων Δοκών με Ισογεωμετρικές Μεθόδους

Στο $5^o$ κεφάλαιο παρουσιάζεται το πρόβλημα της γενικευμένης στρέβλωσης και διαστρέβλωσης σύμμικτων ευθύγραμμων και καμπύλων δοκών τυχούσας διατομής υπό τις πλέον γενικές συνοριακές συνθήκες, υποβαλλόμενων σε τυχούσα εξωτερική φόρτιση. Στο παρόν κεφάλαιο η παραμορφωσιμότητα της διατομής λαμβάνεται υπόψη μέσω διατύπωσης κατάλληλου επαναληπτικού συστήματος εξισώσεων ισορροπίας το οποίο προκύπτει με τη βοήθεια των εξισώσεων τοπικής ισορροπίας της τρισδιάστατης θεωρίας ελαστικότητας σε συνδυασμό με την ιδιομορφική ανάλυση της διατομής. Η αλληλεπίδραση μεταξύ στρέψης, στρέβλωσης και διαστρέβλωσης λαμβάνονται υπόψη στη διατύπωση του προβλήματος συνοριακών τιμών της διατομής σε συνδυασμό με την επίδραση της καμπυλότητας στην περίπτωση καμπύλης δοκού.

Το πεδίο των μετατοπίσεων διαμορφώνεται ως το άθροισμα της κίνησης στερεού σώματος (Saint Venant-SV) και της επιρροής των στηρίξεων (Residual-R) ως εξής:

$$\bar{u}\left(x,y,z\right)=\bar{u}^{SV}\left(x,y,z\right)+\bar{u}^{R}\left(x,y,z\right)=\underbrace{u\left(x\right)+\theta_{Y}\left(x\right)Z-\theta_{Z}\left(x\right)Y}_{\kappa\iota\nu\eta\sigma\eta\;\sigma\tau\epsilon\rho\epsilon\sigmaύ\;\sigmaώ\mu\alpha\tauο\varsigma}+\underbrace{\sum_{i=1}^{m}\alpha_{i}(x)W_{i}(y,z)}_{\sigma\tau\rho\acute{\epsilon}\beta\lambda\omega\sigma\eta}$$

$$\text{(5.1a)}$$

$$\bar{v}\left(x,y,z\right)=\bar{v}^{SV}\left(x,y,z\right)+\bar{v}^{R}\left(x,y,z\right)=\underbrace{v\left(x\right)-z\theta_{x}\left(x\right)}_{\substack{\kappa\iota\nu\eta\sigma\eta\;\sigma\tau\epsilon\rho\epsilon\sigmaύ\\\sigmaώ\mu\alpha\tauο\varsigma}}+\underbrace{\sum_{i=1}^{m}\alpha_{i}(x)_{,x}DY_{i}(y,z)}_{\delta\iota\alpha\sigma\tau\rho\acute{\epsilon}\beta\lambda\omega\sigma\eta\;\kappa\alpha\tauά\;Y}\qquad\text{(5.1b)}$$

$$\bar{w}\left(x,y,z\right)=\bar{w}^{SV}\left(x,y,z\right)+\bar{w}^{R}\left(x,y,z\right)=\underbrace{w\left(x\right)+y\theta_{x}\left(x\right)}_{\substack{\kappa\iota\nu\eta\sigma\eta\;\sigma\tau\epsilon\rho\epsilon\sigmaύ\\\sigmaώ\mu\alpha\tauο\varsigma}}+\underbrace{\sum_{i=1}^{m}\alpha_{i}(x)_{,x}DZ_{i}(y,z)}_{\delta\iota\alpha\sigma\tau\rho\acute{\epsilon}\beta\lambda\omega\sigma\eta\;\kappa\alpha\tauά\;Z}\qquad\text{(5.1c)}$$

Όπου $\bar{u}$, $\bar{v}$, $\bar{w}$ είναι η αξονική, η κάθετη και η ακτινική μετατόπιση τυχαίου σημείου της δοκού ως προς το $Sxyz$, αντίστοιχα. $W(y,z)$ είναι οι συναρτήσεις στρέβλωσης, $DY(y,z)$ και $DZ(y,z)$ είναι οι συναρτήσεις διαστρέβλωσης της διατομής (σε ένα διάνυσμα $D(y,z)$) ενώ $\alpha(x)$ είναι μία συνάρτηση που περιγράφει τη μείωση της έντασής τους κατά το μήκος της δοκού ($\alpha(x)=e^{-cx}$). Τα υπόλοιπα είναι αντίστοιχα με τις προηγούμενες ενότητες. Οι κινήσεις στερεού σώματος περιγράφονται με λεπτομέρεια στη δημοσίευση των Kang και Yoo (1994), με $\sin\theta_{x}\approx\theta_{x},\cos\theta_{x}\approx1$ και τους όρους ανώτερης τάξης να αγνοούνται σε αυτή τη μελέτη.

Αφού οριστούν οι παραμορφώσεις και οι τάσεις εξαιτίας της επίδρασης των στηρίξεων και εφαρμόζοντας τις εξισώσεις τοπικής ισορροπίας της τρισδιάστατης ελαστικότητας παράλληλα με τη σχέση $v_{m}=\lambda_{m}/\left[2\left(\lambda_{m}+\mu_{m}\right)\right]$ (σύμβολα για το λόγο Poisson και τις Lame παραμέτρους), διαμορφώνεται το πρόβλημα συνοριακών τιμών της διατομής ως εξής:

$$\left(\nabla^{2}W\right)_{m}=c^{2}\left[-\frac{2}{1-v_{m}^{e}}\left(W\right)_{m}-\frac{1+v_{m}^{e}}{1-v_{m}^{e}}\left(\nabla D\right)_{m}\right]\qquad\text{(5.2a)}$$

$$\left(\nabla^{2}DY\right)_{m}+\frac{1+v_{m}^{e}}{1-v_{m}^{e}}\left[\left(\nabla D\right)_{m,y}+\left(W_{,y}\right)_{m}\right]=c^{2}\left[-\left(DY\right)_{m}\right]\qquad\text{(5.2b)}$$

$$\left(\nabla^{2}DZ\right)_{m}+\frac{1+v_{m}^{e}}{1-v_{m}^{e}}\left[\left(\nabla D\right)_{m,z}+\left(W_{,z}\right)_{m}\right]=c^{2}\left[-\left(DZ\right)_{m}\right]\qquad\text{(5.2c)}$$

μαζί με τις αντίστοιχες συνοριακές συνθήκες που παραλείπονται εδώ χάρην συντομίας. Όπου $v_{m}^{e}=v_{m}/\left(1-v_{m}\right)$ είναι ο ενεργός λόγος Poisson και $g_{m}=\mu_{m}/\mu_{ref}$, $g_{m}^{*}=\lambda_{m}/\mu_{ref}$ είναι ελαστικές σταθερές ως προς το $\mu_{ref}$ που είναι το μέτρο διάτμησης του υλικού αναφοράς. Χρησιμοποιώντας κατάλληλη διακριτοποίηση, το παραπάνω συζευγμένο πρόβλημα διαμορφώνεται σε ένα πρόβλημα ιδιοτιμών $AF=c^{2}BF$ με $c$ να

είναι οι ιδιοτιμές και $F = \begin{bmatrix} W & DY & DZ \end{bmatrix}^T$ τα ιδιοδιανύσματα. Το επαναληπτικό σχήμα ισορροπίας, που περιγράφεται στις δημοσιεύσεις των Ferradi et al. (2013) και Dikaros και Sapountzakis (2014), χρησιμοποιείται έως ότου να επιτευχθεί ένας ικανοποιητικός αριθμός ιδιομορφών που θα περιγράφει με ακρίβεια τις συναρτήσεις στρέβλωσης με τις αντίστοιχες συναρτήσεις διαστρέβλωσης. Για την αρχικοποίηση αυτής της διαδικασίας χρησιμοποιούνται οι κινήσεις στερεού σώματος ως αρχικές ιδιομορφές και στη συνέχεια για την αποκατάσταση της ισορροπίας προσδιορίζονται οι δευτερεύουσες ιδιομορφές στρέβλωσης και διαστρέβλωσης. Έτσι συνεχίζεται η διαδικασία μέχρι να υπάρχει σύγκλιση προς το ακριβές σχήμα των συναρτήσεων της διατομής. Σε κάθε βήμα εκτελείται κανονικοποίηση των εκάστοτε ιδιομορφών.

Αφού προσδιοριστούν οι συναρτήσεις σχήματος, οι μετατοπίσεις λαμβάνοντας μέχρι και δευτερογενείς ιδιομορφές μπορούν να γραφούν αναλυτικά ως εξής:

$$\bar{u}(x,y,z,t) = \bar{u}^P(x,y,z,t) + \bar{u}^S(x,y,z,t) =$$

$$\underbrace{u(x) + \theta_Y(x)Z - \theta_Z(x)Y + \eta_x(x)\phi_S^P(y,z)}_{\pi\rho\omega\tau o\gamma\varepsilon\nu\varepsilon\dot{\iota}\varsigma} \qquad (5.3a)$$

$$+ \underbrace{\eta_Y(x)\phi_{CY}^P(y,z) + \eta_Z(x)\phi_{CZ}^P(y,z) + \xi_x(x)\phi_S^S(y,z)}_{\delta\varepsilon\upsilon\tau\varepsilon\rho o\gamma\varepsilon\nu\varepsilon\dot{\iota}\varsigma}$$

$$\bar{v}(x,y,z,t) = v(x) - z\theta_x(x)$$

$$+ \underbrace{\zeta_x(x)v_S^P(y,z) + \zeta_Y(x)v_{CY}^P(y,z) + \zeta_Z(x)v_{CZ}^P(y,z)}_{\pi\rho\omega\tau o\gamma\varepsilon\nu\varepsilon\dot{\iota}\varsigma} \qquad (5.3b)$$

$$+ \underbrace{\chi_x(x)v_S^S(y,z) + \chi_Y(x)v_{CY}^S(y,z) + \chi_Z(x)v_{CZ}^S(y,z)}_{\delta\varepsilon\upsilon\tau\varepsilon\rho o\gamma\varepsilon\nu\varepsilon\dot{\iota}\varsigma}$$

$$\bar{w}(x,y,z,t) = w(x) + y\theta_x(x)$$

$$+ \underbrace{\zeta_x(x)w_S^P(y,z) + \zeta_Y(x)w_{CY}^P(y,z) + \zeta_Z(x)w_{CZ}^P(y,z)}_{\pi\rho\omega\tau o\gamma\varepsilon\nu\varepsilon\dot{\iota}\varsigma} \qquad (5.3c)$$

$$+ \underbrace{\chi_x(x)w_S^S(y,z) + \chi_Y(x)w_{CY}^S(y,z) + \chi_Z(x)w_{CZ}^S(y,z)}_{\delta\varepsilon\upsilon\tau\varepsilon\rho o\gamma\varepsilon\nu\varepsilon\dot{\iota}\varsigma}$$

Παράλληλα, δίνεται η δυνατότητα στο χρήστη να λάβει υπόψη παραπάνω αριθμό ιδιομορφών στέβλωσης και διαστρέβλωσης ώστε να επιτευχθεί η επιθυμητή ακρίβεια του προβλήματος. Στη συνέχεια, εισάγονται νέοι βαθμοί ελευθερίας για την καθολική ανάλυση της καμπύλης δοκού, οι οποίοι συνιστούν ανεξάρτητες παραμέτρους των προαναφερθέντων φαινομένων ανώτερης τάξης ($\zeta_x(x)$, $\chi_x(x)$ $\zeta_Y(x)$, $\zeta_Z(x)$, $\chi_Y(x)$, $\chi_Z(x)$ για τη διαστρέβλωση λόγω πρωτογενούς και δευτερογενούς στρέψης και κάμψης). Έτσι, διατυπώνονται είτε δεκαέξι είτε είκοσι δύο προβλήματα συνοριακών τιμών (με δυνατότητα και περισσότερων ανάλογα τον αριθμό φαινομένων ανώτερης τάξης που λαμβάνονται υπόψη) ως προς τα κινηματικά μεγέθη της δοκού, η επίλυση των οποίων δίδει όλα τα παραμορφωσιακά και εντατικά μεγέθη που είναι απαραίτητα κατά την ανάλυση ραβδωτών φορέων. Στο εν λόγω κεφάλαιο λαμβάνεται

επίσης υπόψη και η επιρροή του λόγου Poisson τόσο στην παραμόρφωση της διατομής όσο και στην καθολική ανάλυση της δοκού. Οι παραμορφώσεις της καμπύλης δοκού διαμορφώνονται ως εξής:

$$\varepsilon_{xx} = \left(\overline{u}_{,x} - \frac{\overline{v}}{R}\right)\cdot\left(\frac{R}{R-Y}\right), \quad \varepsilon_{yy} = \overline{v}_{,y}, \quad \varepsilon_{zz} = \overline{w}_{,z} \tag{5.4a}$$

$$\gamma_{xy} = \left(\overline{v}_{,x} + \frac{\overline{u}}{R}\right)\cdot\left(\frac{R}{R-Y}\right) + \overline{u}_{,y}, \quad \gamma_{xz} = \overline{w}_{,x}\cdot\left(\frac{R}{R-Y}\right) + \overline{u}_{,z}, \quad \gamma_{yz} = \overline{w}_{,y} + \overline{v}_{,z} \tag{5.4b}$$

όπου $\dfrac{R}{R-Y}$ τίθεται ως $e(R)$ και είναι για να λάβει υπόψη την επιρροή της καμπυλότητας. Έτσι γράφοντας σε μητρωική μορφή παραμορφώσεις-τάσεις και εφαρμόζοντας την αρχή δυνατών έργων διατυπώνονται τα μητρώα δυσκαμψίας:

$$[Aux1] = \begin{bmatrix} 1 & 0 & 0 & 0 & Z & -Y & \phi_S^P & \phi_{CY}^P & \phi_{CZ}^P & \phi_S^S & 0 & 0 & 0 & 0 & 0 & 0 \\ 0 & 0 & 0 & 0 & 0 & 0 & 0 & 0 & 0 & 0 & 0 & 0 & 0 & 0 & 0 & 0 \\ 0 & 0 & 0 & 0 & 0 & 0 & 0 & 0 & 0 & 0 & 0 & 0 & 0 & 0 & 0 & 0 \\ 0 & 1 & 0 & -z & 0 & 0 & 0 & 0 & 0 & 0 & v_S^P & v_{CY}^P & v_{CZ}^P & v_S^S & v_{CY}^S & v_{CZ}^S \\ 0 & 0 & 1 & y & 0 & 0 & 0 & 0 & 0 & 0 & w_S^P & w_{CY}^P & w_{CZ}^P & w_S^S & w_{CY}^S & w_{CZ}^S \\ 0 & 0 & 0 & 0 & 0 & 0 & 0 & 0 & 0 & 0 & 0 & 0 & 0 & 0 & 0 & 0 \end{bmatrix} e(R) \tag{5.5a}$$

$$[Aux2] = \begin{bmatrix} 0 & -\frac{1}{R}e(R) & 0 & \frac{z}{R}e(R) & 0 & 0 & 0 & 0 & 0 & 0 \\ 0 & 0 & 0 & 0 & 0 & 0 & 0 & 0 & 0 & 0 \\ 0 & 0 & 0 & 0 & 0 & 0 & 0 & 0 & 0 & 0 \\ \frac{1}{R}e(R) & 0 & 0 & 0 & \frac{Z}{R}e(R) & -1-\frac{Y}{R}e(R) & \frac{\phi_S^P}{R}e(R)+\phi_{S,y}^P & \frac{\phi_{CY}^P}{R}e(R)+\phi_{CY,y}^P & \frac{\phi_{CZ}^P}{R}e(R)+\phi_{CZ,y}^P & \frac{\phi_S^S}{R}e(R)+\phi_{S,y}^S \cdots \\ 0 & 0 & 0 & 0 & 1 & 0 & \phi_{S,z}^P & \phi_{CY,z}^P & \phi_{CZ,z}^P & \phi_{S,z}^S \\ 0 & 0 & 0 & 0 & 0 & 0 & 0 & 0 & 0 & 0 \end{bmatrix}$$

$$\cdots \begin{bmatrix} \frac{v_S^P}{R}e(R) & \frac{v_{CY}^P}{R}e(R) & \frac{v_{CZ}^P}{R}e(R) & \frac{v_S^S}{R}e(R) & \frac{v_{CY}^S}{R}e(R) & \frac{v_{CZ}^S}{R}e(R) \\ v_{S,y}^P & v_{CY,y}^P & v_{CZ,y}^P & v_{S,y}^S & v_{CY,y}^S & v_{CZ,y}^S \\ w_{S,z}^P & w_{CY,z}^P & w_{CZ,z}^P & w_{S,z}^S & w_{CY,z}^S & w_{CZ,z}^S \\ 0 & 0 & 0 & 0 & 0 & 0 \\ 0 & 0 & 0 & 0 & 0 & 0 \\ w_{S,y}^P+v_{S,z}^P & w_{CY,y}^P+v_{CY,z}^P & w_{CZ,y}^P+v_{CZ,z}^P & w_{S,y}^S+v_{S,z}^S & w_{CY,y}^S+v_{CY,z}^S & w_{CZ,y}^S+v_{CZ,z}^S \end{bmatrix}$$

$$\tag{5.5b}$$

$$\varepsilon = [Aux1]u_{,x} + [Aux2]u \tag{5.5c}$$

$$\sigma = [C][Aux1]u_{,x} + [C][Aux2]u \tag{5.5d}$$

$$\delta U = \int_0^L \int_\Omega \left( \delta u_{,x}^T [Aux1]^T + \delta u^T [Aux2]^T \right) \left( [C][Aux1]u_{,x} + [C][Aux2]u \right) \frac{1}{e(R)} d\Omega dx \Rightarrow$$

$$\Rightarrow \delta U = \int_0^L \left( \delta u_{,x}^T k_{22} u_{,x} + \delta u^T k_{12} u_{,x} + \delta u_{,x}^T k_{21} u + \delta u^T k_{11} u \right) dx \Rightarrow \text{κατά παράγοντες}$$

$$\Rightarrow \delta U = \int_0^L \left( \delta u^T \left\{ -k_{22} u_{,xx} + [k_{12} - k_{21}] u_{,x} + k_{11} u \right\} \right) dx + \left[ \delta u^T \left\{ k_{22} u_{,x} + k_{21} u \right\} \right]_0^L$$

$$\tag{5.5e}$$

$$[k_l] = \begin{bmatrix} k_{11} & k_{12} \\ k_{21} & k_{22} \end{bmatrix} \tag{5.5f}$$

Όπου $k_{11}$, $k_{12}$, $k_{21}$ και $k_{22}$ (16X16 ή 22X22 κτλ) περιέχουν τις γεωμετρικές σταθερές της διατομής λαμβάνοντας υπόψη τη στρέβλωση, τη διαστρέβλωση και το λόγο Poisson είτε σε ευθύγραμμο είτε σε καμπύλο δοκάρι:

$$k_{11} = \int_{\Omega_m} [Aux1]^T [C][Aux1] \frac{1}{e(R)} d\Omega, \qquad k_{12} = \int_{\Omega_m} [Aux1]^T [C][Aux2] \frac{1}{e(R)} d\Omega$$

$$k_{21} = \int_{\Omega_m} [Aux2]^T [C][Aux1] \frac{1}{e(R)} d\Omega, \qquad k_{22} = \int_{\Omega_m} [Aux2]^T [C][Aux2] \frac{1}{e(R)} d\Omega \tag{5.6}$$

Το έργο των εξωτερικών φορτίων υπολογίζεται ως εξής:

$$[Aux] = \begin{bmatrix} 1 & 0 & 0 & 0 & Z & -Y & \phi_S^P & \phi_{CY}^P & \phi_{CZ}^P & \phi_S^S & 0 & 0 & 0 & 0 & 0 & 0 \\ 0 & 1 & 0 & -z & 0 & 0 & 0 & 0 & 0 & 0 & v_S^P & v_{CY}^P & v_{CZ}^P & v_S^S & v_{CY}^S & v_{CZ}^S \\ 0 & 0 & 1 & y & 0 & 0 & 0 & 0 & 0 & 0 & w_S^P & w_{CY}^P & w_{CZ}^P & w_S^S & w_{CY}^S & w_{CZ}^S \end{bmatrix} \tag{5.7a}$$

$$\delta W = \underbrace{\int_0^L \left( \delta u^T [Aux]^T t \right) dx}_{\delta u^T p} + \left[ \int_\Omega \left( \delta u^T [Aux]^T t \right) d\Omega \right]_0^L \tag{5.7b}$$

Όπου t τα διανύσματα κατεύθυνσης της παράπλευρης επιφάνειας και p τα εξωτερικά φορτία της δοκού.

Λαμβάνοντας υπόψη και τους αδρανειακούς όρους, υπολογίζεται το μητρώο μάζας:

$$\delta W_{\text{mass}} = \int_0^L \int_\Omega \rho \left( \delta u^T [Aux]^T [Aux] u_{,tt} \right) \frac{1}{e(R)} d\Omega dx \Rightarrow \delta W_{\text{mass}} = \int_0^L \left( \delta u^T [m_l] u_{,tt} \right) dx \tag{5.7}$$

Έτσι διαμορφώνονται οι εξισώσεις κίνησης της ευθύγραμμης ή της καμπύλης δοκού μαζί με τις συνοριακές και αρχικές συνθήκες.

Τα ως άνω προβλήματα συνοριακών τιμών επιλύονται αριθμητικά με τη χρήση της Μεθόδου Συνοριακών Στοιχείων (πρόβλημα διατομής) και της Μεθόδου Αναλογικής εξίσωσης (πρόβλημα δοκού) είτε στην αρχική της μορφή είτε με B-splines και NURBS. Εκτός από τη μέθοδο της Αναλογικής εξίσωσης, για το κατά μήκος πρόβλημα της δοκού χρησιμοποιείται και η μέθοδος των Πεπερασμένων στοιχείων σε συνδυασμό με NURBS. Μέσω της εν λόγω θεωρίας αναλύονται παραδείγματα ιδιαίτερου θεωρητικού και πρακτικού ενδιαφέροντος όπου πραγματοποιείται η μελέτη του φαινομένου της διαστρέβλωσης λόγω κάμψης και στρέψης, ενώ η ακρίβεια της προτεινόμενης μεθόδου διαπιστώνεται μέσω συγκρίσεων με προσομοιώματα στερεών και κελυφωτών πεπερασμένων στοιχείων εμπορικού λογισμικού.

Αρχικά μελετάται μία ευθύγραμμη δοκός με συμπαγή ορθογωνική διατομή για διαφορετικά υλικά ώστε να επικυρωθεί η μέθοδος και να εξεταστεί η επιρροή του λόγου Poisson. Στη συνέχεια μελετάται ένας καμπύλος πρόβολος με διπλά συμμετρική διατομή ( $R = 0.636m$, $L = 1m$, $t/d = 0.048$, $d/L = 0.035$ ) για έκκεντρο φορτίο 5 kN στο άκρο. Στο Σχήμα 5.1 δίνεται η κατανομή της συνολικής μετατόπισης και στο Σχήμα 5.2 της ορθής τάσης κατά τον διαμήκη άξονα για το προτεινόμενο μοντέλο με B-splines και το τρισδιάστατο μοντέλο FEMsolid. Τα αποτελέσματα είναι παρόμοια.
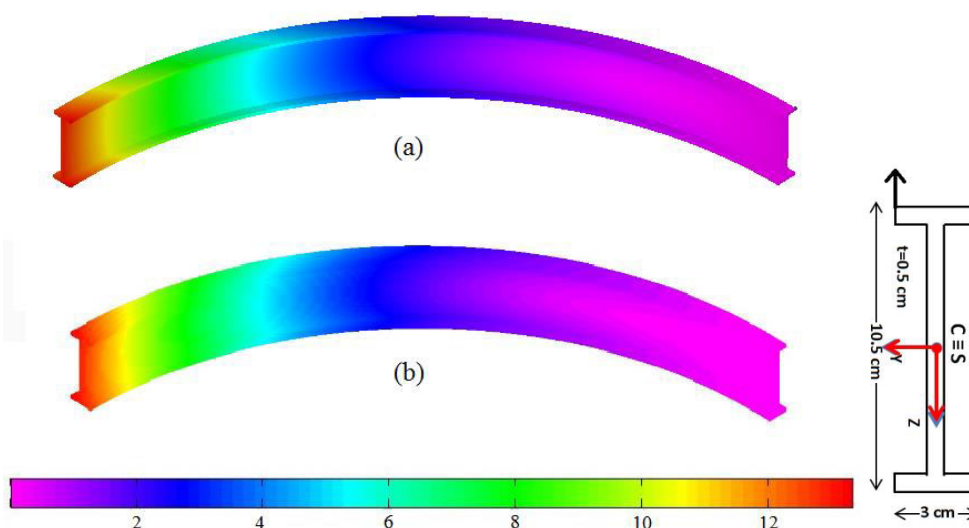


*Σχήμα 5.1. Συνολική μετατόπιση για (a) 3D solid FEM μοντέλο με 7875 τετραπλευρικά στοιχεία και (b) προτεινόμενο (AEM με 10 κυβικά B-splines ή 100 σταθερά στοιχεία) για την I-σχήματος διατομή.*

Παράλληλα στο Σχήμα 5.3 δίνονται οι κατανομές των κινηματικών μεγεθών που αφορούν στην πρωτογενή στρέψη, στρέβλωση και διαστρέβλωση για λόγους σύγκρισης και για να καταδειχθεί η εκθετική μείωση για τα δύο τελευταία μεγέθη. Όπως είναι φανερό, η διαστρέβλωση είναι ασήμαντη για τη συγκεκριμένη διατομή σε σύγκριση με τη στρέβλωση. Αυτό είναι αναμενόμενο γιατί πρόκειται για ανοικτή διατομή. Παράλληλα το μέγεθος της στρέβλωσης είναι σημαντικό σε μεγάλη έκταση κατά το μήκος. Τα παραπάνω διαπιστώνονται από τα αντίστοιχα μεγέθη των ροπών στον Πίνακα 5.1. Η ροπή λόγω πρωτογενούς διαστρέβλωσης από στρέψη είναι ασήμαντη σε σχέση με τη διρροπή λόγω πρωτογενούς στρέβλωσης από στρέψη. Το ίδιο ισχύει και για τη δευτερογενή διρροπή λόγω στρέβλωσης από στρέψη (αυτό σημαίνει ότι το πεδίο

μετατοπίσεων που περιγράφηκε προηγουμένως είναι αρκετό για να επιτευχθεί η επιθυμητή ακρίβεια).
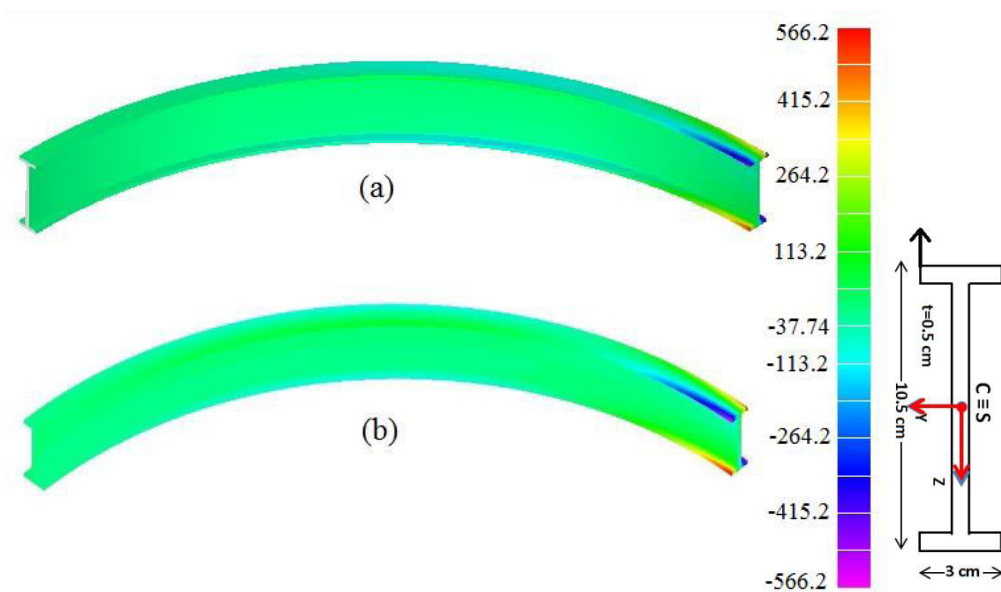


*Σχήμα 5.2. Ορθή τάση $\sigma_{xx}$ για (a) 3D solid FEM μοντέλο με 7875 τετραπλευρικά στοιχεία και (b) προτεινόμενο (AEM με 10 κυβικά B-splines ή 100 σταθερά στοιχεία) για την I-σχήματος διατομή.*
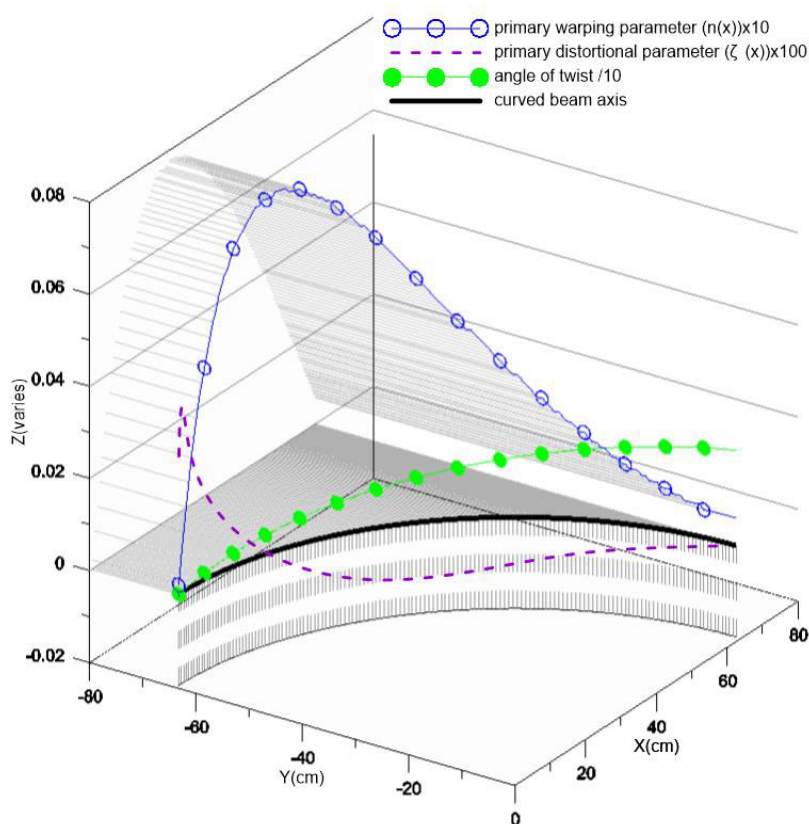


*Σχήμα 5.3. Κινηματικά μεγέθη $\eta_x(x)$, $\zeta_x(x)$ και $\theta_x(x)$ της καμπύλης δοκού I-σχήματος για το προτεινόμενο μοντέλο με NURBS $3^{ου}$ βαθμού.*

| | AEM 10 cubic B-splines | FEM Solid 7875 |
|---|---|---|
| $w(m)$ at $x=L$ | -12.8713 | -12.5466 |
| $\theta_x(rad)$ at $x=L$ | 0.2083 | 0.19702 |
| $\theta_Y(rad)$ at $x=L$ | 0.3274 | 0.3158 |
| $\tau_{xz}^{\max}(\frac{kN}{m^2})$ at $x=1/4L$ | 120.25 | 111.02 |
| $\tau_{xy}^{\max}(\frac{kN}{m^2})$ at $x=1/4L$ | 115.23 | 109.80 |
| $M_Y(kNm)$ at $x=0$ | 330.81 | 325.05 |
| $M_t(kNm)$ at $x=0$ | 323.01 | 318.31 |
| $M_{\phi_S^P}(kNm^2)$ at $x=0$ | 3401.49 | - |
| $M_{\phi_S^S}(kNm^2)$ at $x=0$ | 36.46 | - |
| $M_{Dx}^P(kNm^2)$ at $x=0$ | 16.25 | - |

Πίνακας 5.1. Μετακινήσεις, μέγιστες τάσεις και ροπές για την καμπύλη δοκό *I-*σχήματος για το προτεινόμενο μοντέλο και το αντίστοιχο FEMsolid.

Στη συνέχεια μελετάται πρόβολος κοίλης ορθογωνικής διατομής 5.0X3.5 *m* με πάχος τοιχωμάτων 0.30 *m* ( $E=3E7\,kN/m^2$ , $G=1.5E7\,kN/m^2$ , $v=0$ , $t/d=0.085$ , $d/L=0.087$ ), μήκος τόξου 40 *m* και $R=25.465m$ . Στο Σχήμα 5.4 δίνεται η κατανομή της μέγιστης μετατόπισης για το προτεινόμενο μοντέλο και το FEMsolid μοντέλο. Στο Σχήμα 5.5 δίνονται οι ορθές τάσεις κατά Χ (Α) και Ζ (Β) για τα ίδια μοντέλα. Τα αποτελέσματα είναι παρόμοια με τις μέγιστες τιμές σχεδόν να συμπίπτουν. Στον Πίνακα 5.2 παρουσιάζονται και οι μέγιστες τιμές των διατμητικών τάσεων που είναι σε συμφωνία για τα δύο μοντέλα. Εδώ αξίζει να σημειωθεί ότι εν αντιθέσει με την προηγούμενη ανοικτή διατομή, η διαρροή λόγω πρωτογενούς διαστρέβλωσης από στρέψη είναι δεκαπλάσια της αντίστοιχης ροπής λόγω στρέβλωσης. Οι αντίστοιχες δευτερογενείς διρροπές είναι αρκετά μικρότερες. Αυτό σημαίνει ότι το πεδίο μετατοπίσεων που λαμβάνει μέχρι και δευτερογενείς ιδιομορφές της διατομής είναι αρκετό για να επιτευχθεί η επιθυμητή ακρίβεια. Τέλος, στον Πίνακα 5.3 γίνεται μια παραμετρική μελέτη της επιρροής της καμπυλότητας στο μέγεθος της καμπτικής, στρεπτικής και λόγω διαστρέβλωσης από πρωτογενή στρέψη ροπής. Γι' αυτό το σκοπό καταρτίζονται οι μεταξύ τους λόγοι. Καθώς λοιπόν αυξάνεται η καμπυλότητα και κατά συνέπεια η στρεπτική ροπή, παρατηρείται αύξηση του λόγου της ροπής διαστρέβλωσης

προς την καμπτική ροπή. Αύτος ο λόγος επομένως αποτελεί ένα δείκτη της επιρροής της διαστρέβλωσης στη συμπεριφορά της καμπύλης δοκού. Παράλληλα, ο λόγος της ροπής διαστρέβλωσης προς τη στρεπτική ροπή κυμαίνεται διαφορετικά με την αύξηση της καμπυλότητας. Αρχικά αυξάνεται απότομα για μικρή καμπυλότητα και στη συνέχεια μειώνεται ελάχιστα για κάθε μία αύξηση της καμπυλότητας. Αυτό δείχνει την αστάθεια που δημιουργεί η απόκλιση του διαμήκη άξονα από την ευθεία ακόμα και αν είναι μικρή.
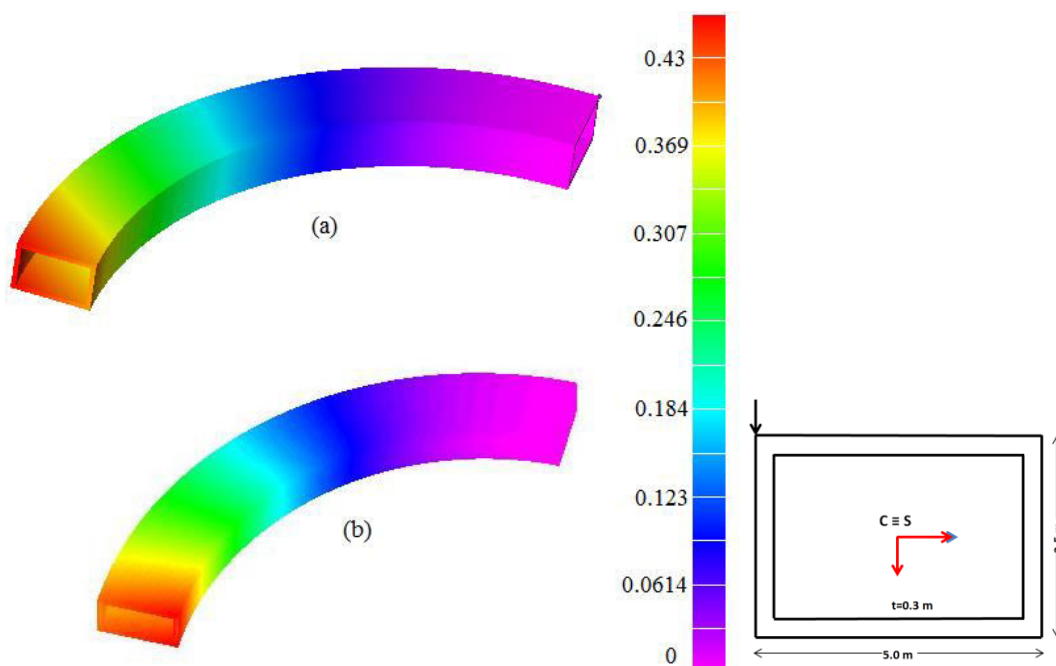


*Σχήμα 5.4. Συνολική μετατόπιση για (a) 3D solid FEM μοντέλο με 2880 τετραπλευρικά στοιχεία και (b) προτεινόμενο (AEM με 10 κυβικά B-splines ή 80 σταθερά στοιχεία) για την κιβωτοειδή διατομή.*
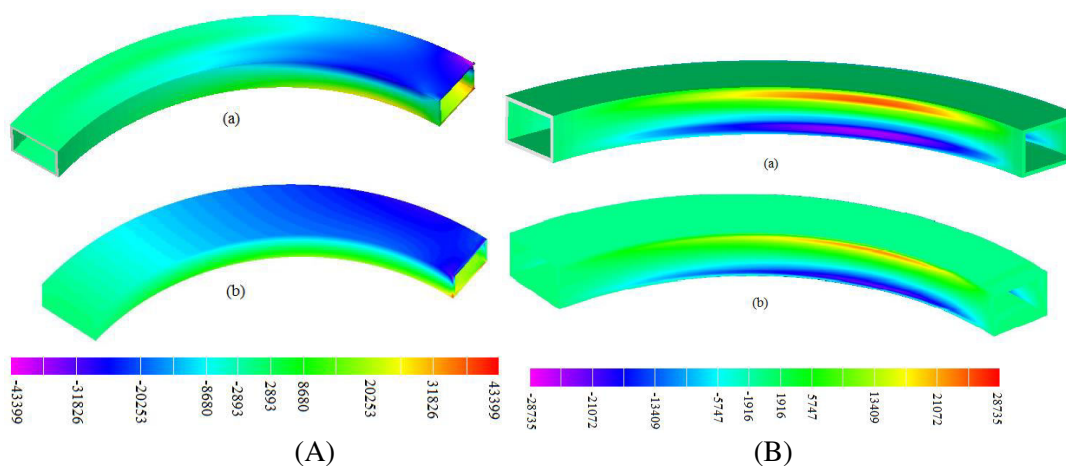


*Σχήμα 5.5. Ορθές τάσεις $\sigma_{xx}$ (A) και $\sigma_{zz}$ (B) για (a) 3D solid FEM μοντέλο με 2880 τετραπλευρικά στοιχεία και (b) προτεινόμενο (AEM με 10 κυβικά B-splines ή 80 σταθερά στοιχεία) για την κιβωτοειδή διατομή.*

| Ορθογωνική κιβωτοειδής διατομή | | AEM 10 cubic B-splines | FEM Solid 2880/ FEM plate 960 |
|---|---|---|---|
| | $w(m)\ at\ x=L$ | 0.4266 | 0.4316 |
| | $\theta_x(rad)\ at\ x=L$ | 0.0100 | 0.0112 |
| | $\theta_Y(rad)\ at\ x=L$ | -0.0131 | -0.0137 |
| $P_z = 5000kN$ eccentric Lateral Loading | $\tau_{xz}^{max}(\frac{kN}{m^2})\ at\ x=0$ | 21532 | 20539 (solid model) |
| | $\tau_{xy}^{max}(\frac{kN}{m^2})\ at\ x=0$ | 12602 | 11502 (solid model) |
| | $M_Y(kNm)\ at\ x=0$ | -139691 | -139824 |
| | $M_t(kNm)\ at\ x=0$ | 127100 | 127324 |
| | $M_{\phi_S^P}(kNm^2)\ at\ x=0$ | -6930.56 | - |
| | $M_{\phi_S^S}(kNm^2)\ at\ x=0$ | -1838.93 | - |
| | $M_{Dx}^P(kNm^2)\ at\ x=0$ | 610306 | - |
| | $M_{Dx}^S(kNm^2)\ at\ x=0$ | -1999.04 | |

Πίνακας 5.2. Μετακινήσεις, μέγιστες τάσεις και ροπές για την κιβωτοειδή καμπύλη δοκό για το προτεινόμενο μοντέλο και το αντίστοιχο FEMsolid.

| Ορθογωνική κιβωτοειδής διατομή | | $\dfrac{M_{Dx}^P}{M_Y}$ at x=0 | $\dfrac{M_{Dx}^P}{M_t}$ at x=0 | $\dfrac{M_Y}{M_t}$ at x=0 |
|---|---|---|---|---|
| | R=∞ | 0.178 | 2.844 | 15.952 |
| | R=76.394m | 1.141 | 5.579 | 4.891 |
| $P_z$ eccentric Lateral Loading | R=50.930m | 1.835 | 5.276 | 2.875 |
| | R=38.197m | 2.581 | 5.101 | 1.976 |
| | R=25.465m | 4.365 | 4.807 | 1.101 |

Πίνακας 5.3. Λόγοι ροπών για διαφορετικές καμπυλότητες της δοκού κιβωτοειδούς διατομής.

Στη συνέχεια μελετάται παρόμοιος πρόβολος με τον προηγούμενο με την ανοικτή διατομή αλλά για μονοσυμμετρική διατομή αυτή τη φορά ($t/d = 0.049$, $d/L = 0.055$). Στη συγκεκριμένη περίπτωση καταδεικνύεται ο ρόλος του επιπέδου φόρτισης στην ανάπτυξη των φαινομένων ανωτέρας τάξης. Συγκεκριμένα, όταν το φορτίο ασκείται παράλληλα με τον άξονα συμμετρίας δεν αναπτύσσονται μεγάλες τιμές ροπών και τάσεων ανώτερης τάξης σε σύγκριση με την αντίθετη περίπτωση είτε για κεντρικά επιβαλλόμενο φορτίο είτε έκκεντρα. Παράλληλα, στην περίπτωση που αναπτύσσονται μεγάλες στρεβλώσεις, η χρήση ενός πεδίου μετατοπίσεων και με τριτογενείς συναρτήσεις στρέβλωσης αυξάνει την ακρίβεια κατά ένα μικρό ποσοστό. Αύτο το ποσοστό θα ήταν ακόμα μεγαλύτερο αν η διατομή ήταν ακόμα πιο λεπτότοιχη.

Η επόμενη καμπύλη δοκός που μελετάται είναι με κιβωτοειδή διατομή ($E = 3E7\,kN/m^2$, $G = 1.5E7\,kN/m^2$, $v = 0$, $t/d = 0.086$, $d/L = 0.086$, $L = 40\,m$, $R = 25.465\,m$) υπό κεντρικό φορτίο $P_Z = 10000\,kN$ στο ελεύθερο άκρο. Στο Σχήμα 5.6 δίνονται οι κατανομές των κινηματικών μεγεθών που αφορούν στην πρωτογενή στρέψη, στρέβλωση και διαστρέβλωση για λόγους σύγκρισης με τα αντίστοιχα μεγέθη της ανοικτής διατομής και για να καταδειχθεί η εκθετική μείωση για τα δύο τελευταία μεγέθη. Εδώ οι παράμετροι στρέβλωσης και διαστρέβλωσης έχουν παρόμοιες κατανομές παρά το διαφορετικό μέγεθος και η παράμετρος στρέβλωσης δεν εκτείνεται τόσο σε ένταση κατά το μήκος όσο προηγουμένως (ανοικτή διατομή).
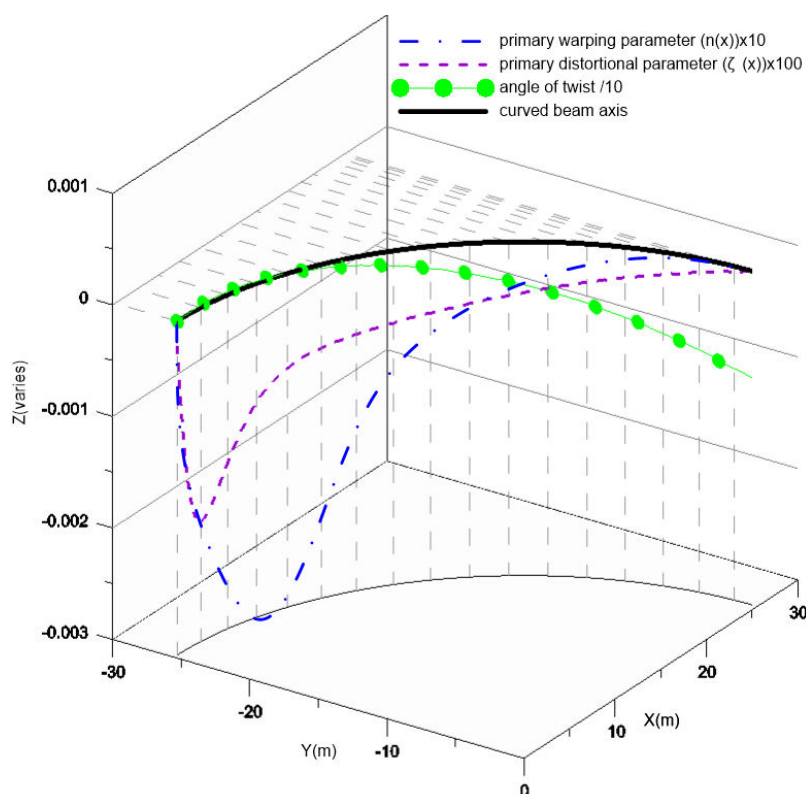


*Σχήμα 5.6. Κινηματικά μεγέθη $\eta_x(x)$, $\zeta_x(x)$ και $\theta_x(x)$ της καμπύλης δοκού κιβωτοειδούς σχήματος για το προτεινόμενο μοντέλο με NURBS $3^{ου}$ βαθμού.*

Στον Πίνακα 5.4 γίνεται σύγκριση του προτεινόμενου μοντέλου, το οποίο είναι σε συμφωνία με το FEMsolid, με το μοντέλο της προηγούμενης ενότητας χωρίς την

| | AEM 10 cubic B-splines | FEM Solid 2714 | AEM 50 quad. GWCB | Timoshenko FEM beam |
|---|---|---|---|---|
| $w(m)$ $at$ $x=L$ | 0.3744 | 0.3547 | 0.3202 | 0.3238 |
| $\theta_x(rad)$ $at$ $x=L$ | 0.0092 | 0.0087 | 0.0067 | 0.0067 |
| $\theta_Y(rad)$ $at$ $x=L$ | -0.0120 | -0.0115 | -0.0104 | -0.0106 |
| $\sigma_{xx}^{\max}(\frac{kN}{m^2})$ $at$ $x=0$ | 40254 | 38230 | 27633 | 28782 |
| $\tau_{xy}^{\max}(\frac{kN}{m^2})$ $at$ $x=0$ | 24135 | 23085 | 16940 | 3714 |
| $M_Y(kNm)$ $at$ $x=0$ | -254316 | -254647 | -254820 | -254648 |
| $M_t(kNm)$ $at$ $x=0$ | -253683 | -254647 | -254700 | -254648 |
| $M_{\phi_S^P}(kNm^2)$ $at$ $x=0$ | -342533 | - | -244940 | 0 |
| $M_{\phi_S^S}(kNm^2)$ $at$ $x=0$ | 36612 | - | 30717 | 0 |
| $M_{Dx}^P(kNm^2)$ $at$ $x=0$ | -366072 | - | - | - |
| $M_{Dx}^S(kNm^2)$ $at$ $x=0$ | 4127 | - | - | - |

Πίνακας 5.4. Μετακινήσεις, μέγιστες τάσεις και ροπές για την κιβωτοειδή καμπύλη δοκό για διάφορα μοντέλα.

διαστρέβλωση και το Timoshenko καμπύλο στοιχείο δοκού. Αξίζει να σημειωθεί ότι η ροπή λόγω πρωτογενούς στρέβλωσης είναι μεγαλύτερη για το παρόν προτεινόμενο μοντέλο σε σχέση με αυτή που υπολογίζεται από το μοντέλο της προηγούμενης ενότητας. Παράλληλα, το Timoshenko στοιχείο δοκού υποεκτιμά σημαντικά τις τάσεις (ιδιαίτερα τη διατμητική) καθώς δε λαμβάνει υπόψη ούτε στρέβλωση ούτε διαστρέβλωση. Τέλος, είναι φανερό ότι η διαστρέβλωση είναι παρόμοια σε μέγεθος με την αντίστοιχη στρέβλωση λόγω στρέψης και μάλιστα λίγο μεγαλύτερη για τη συγκεκριμένη διατομή.

    Η τελευταία δοκός που μελετάται είναι ένας πρόβολος κιβωτοειδούς διατομής ($E = 3.25E7\,kN/m^2$, $G = 1.39E7\,kN/m^2$, $R = 100\,m$, $\nu = 0.1667$, $t/d = 0.1$, $d/L = 0.065$) με μήκος τόξου 33 m υπό κατακόρυφο κεντρικό φορτίο 5000 kN. Η ίδια διατομή μελετάται και σαν σύμμικτη με διαφορετικό υλικό μόνο στο άνω τοίχωμά της ($E = 4E7\,kN/m^2$, $G = 2E7\,kN/m^2$, $\nu = 0$). Στον Πίνακα 5.5 είναι φανερό πως μειώνεται η επιρροή της διαστρέβλωσης και στις τάσεις και στις ροπές στην περίπτωση

που το άνω τοίχωμα (μαζί με τα πτερύγια) της διατομής κατασκευαστεί από υλικό μεγαλύτερης δυσκαμψίας. Το αποτέλεσμα δεν είναι το ίδιο αν βάλουμε σε άλλα τοιχώματα πιο ισχυρό υλικό γιατί για τη συγκεκριμένη φόρτιση (που είναι και συχνή στη γεφυροποιία) το άνω τοίχωμα ανθίσταται περισσότερο μέσω κάμψης ενώ τα πτερύγια που λειτουργούν σαν πρόβολοι και παρουσιάζουν μεγάλες μετατοπίσεις θα γίνουν πιο άκαμπτα. Συγκριτικά με την προηγούμενη κιβωτοειδή διατομή, αξίζει να σημειωθεί ότι στην προκειμένη περίπτωση οι λόγοι των ροπών δείχνουν ότι η συγκεκριμένη δοκός ανθίσταται περισσότερο μέσω καμπτικών μηχανισμών και ότι η διαστρέβλωση λόγω στρέψης που αναπτύσσεται είναι μικρότερη σε ποσοστό κατά το ήμισυ σε σχέση με πριν. Επίσης, όσον αφορά το αντίστοιχο ευθύγραμμο δοκάρι, αξίζει να σημειωθεί ότι η διαστρέβλωση που αναπτύσσεται οφείλεται στην κάμψη και όχι στη στρέψη. Το ίδιο ισχύει και για τη στρέβλωση.
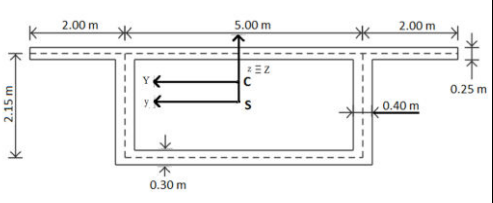
| | | R=100 AEM 10 cubic b-splines | R=100 FEM Solid 6600 | R=∞ AEM 100 constant | R=100 AEM 10 cubic b-splines **σύμμικτη** |
|---|---|---|---|---|---|
| | $w(m)$ at $x=L$ | 0.4001 | 0.3899 | 0.3914 | 0.2616 |
| | $\theta_x(rad)$ at $x=L$ | 0.0039 | 0.0038 | 0 | 0.0019 |
| | $\theta_Y(rad)$ at $x=L$ | -0.0170 | -0.0169 | 0.0174 | -0.0116 |
| | $\sigma_{xx}^{\max}(\frac{kN}{m^2})$ at $x=0$ | 52456 | 51825 | 52122 | 21151 |
| | $\tau_{xy}^{\max}(\frac{kN}{m^2})$ at $x=0$ | 8425 | 7721 | 3992 | 3791 |
| $P_z$ Lateral Loading | $M_Y(kNm)$ at $x=0$ | -161723 | -162023 | -162115 | -161642 |
| | $M_t(kNm)$ at $x=0$ | 26929 | 26969 | 0 | 26916 |
| | $M_{\phi_S^P}(kNm^2)$ at $x=0$ | 18463 | - | 0 | 9152 |
| | $M_{\phi_{CY}^P}(kNm^2)$ at $x=0$ | -3408 | - | -3357.5 | -11338 |
| | $M_{\phi_S^S}(kNm^2)$ at $x=0$ | -6198 | - | 0 | -3130 |
| | $M_{Dx,y}^P(kNm^2)$ at $x=0$ | 62817 (x) 1571 (y) | - | 0 (x) 1144.57 (y) | 20418 (x) 245 (y) |
| | $M_{Dx,y}^S(kNm^2)$ at $x=0$ | -952.89 (x) -1403 (y) | - | 0(x) -1072 (y) | 1691.09 (x) -262 (y) |

Πίνακας 5.5. Μετακινήσεις, μέγιστες τάσεις και ροπές για την κιβωτοειδή καμπύλη δοκό για διάφορα μοντέλα.

Στον Πίνακα 5.6 παρουσιάζονται οι ιδιοσυχνότητες για την προαναφερόμενη ομογενή διατομή με $\rho = 2.5 kN\,sec^2/m^4$. Οι τιμές που προκύπτουν από την εφαρμογή του προτεινόμενου μοντέλου για την αμφίπακτη δοκό είναι γενικά πιο κοντά στις τιμές του FEMsolid χωρίς διάφραγμα ενώ για αρκετές τιμές τα δύο solid μοντέλα δίνουν παρόμοιες τιμές. Γενικά κυριαρχούν οι ιδιομορφές λόγω μετακινήσεων (εκτός στρεπτικής) ως ποσοστό της συνολικής απόκρισης που δίνεται από τις 8 πρώτες ιδιομορφές. Αξίζει να σημειωθεί ότι οι αντίστοιχες τιμές του προβόλου είναι κατά πολύ μειωμένες. Αυτό συμβαίνει επειδή στον πρόβολο (λόγω της επιρροής των συνθηκών στήριξης) τα φαινόμενα στρέβλωσης και διαστρέβλωσης είναι πολύ εντονότερα.

| A/A | FEMsolid 6600 NO Diaph. (πρόβολος) | FEMsolid 6600 NO Diaph. (αμφίπακτη) | FEMsolid 6600 1 Diaph. (αμφίπακτη) | 10 cubic NURBS (αμφίπακτη) | Τύπος ιδιομορφής |
|-----|------|------|------|------|------|
| 1 | 1.725 | 9.328 | 9.414 | 9.470 | $1^{η}$ ιδιομορφή κατακόρυφης μετατόπισης |
| 2 | 4.065 | 17.099 | 19.230 | 16.887 | $1^{η}$ ιδιομορφή πλευρικής μετατόπισης |
| 3 | 9.084 | 20.495 | 21.160 | 21.154 | $1^{η}$ ιδιομορφή στρέψης |
| 4 | 10.183 | 21.174 | 22.126 | 21.949 | $2^{η}$ ιδιομορφή κατακόρυφης μετατόπισης |
| 5 | 19.191 | 27.898 | 35.428 | 26.003 | $2^{η}$ ιδιομορφή πλευρικής μετατόπισης |
| 6 | 22.321 | 31.948 | 36.230 | 32.789 | $3^{η}$ ιδιομορφή κατακόρυφης μετατόπισης |
| 7 | 21.649 | 43.247 | 42.768 | 44.500 | $2^{η}$ ιδιομορφή στρέψης |
| 8 | 29.165 | 47.490 | 47.013 | 49.602 | $3^{η}$ ιδιομορφή στρέψης |

Πίνακας 5.6. Ιδιοσυχνότητες καμπύλης δοκού κιβωτοειδούς διατομής (αμφίπακτη ή πρόβολος).

## VII. Κεφάλαιο 6: Εφαρμογή Κανονισμών για Ενδιάμεσα Διαφράγματα και Αξιολόγηση των διατάξεών τους

Στο *6ο κεφάλαιο* τα μοντέλα που αναπτύχθηκαν στα κεφάλαια 4 και 5 χρησιμοποιούνται σε συνδυασμό με τη Μέθοδο Άμεσης Στιβαρότητας για τη διαμόρφωση των τοπικών και καθολικών μητρώων δυσκαμψίας ευθύγραμμης ή καμπύλης δοκού. Επιπρόσθετα, παρουσιάζονται οι πιο συχνά χρησιμοποιούμενες διατάξεις κανονισμών που καθορίζουν τον αριθμό και τη μέγιστη απόσταση τοποθέτησης ενδιάμεσων διαφραγμάτων για την αποφυγή του φαινομένου της διαστρέβλωσης των διατομών.

Σύμφωνα με τον κανονισμό AASHTO (American Association of State Highway and Transportation Officials- 1993) οι διατάξεις για καμπύλες γέφυρες αυτοκινητόδρομων καθορίζουν τη μέγιστη απόσταση ενδιάμεσων διαφραγμάτων $L_D$ ως

$$L_D \leq L\left(\frac{R}{200L - 7500}\right)^{1/2} \leq 25\,ft \tag{6.1}$$

έτσι ώστε η ορθή τάση διαστρέβλωσης λόγω πρωτογενούς στρέψης να είναι στο 10% της ορθής τάσης λόγω κάμψης και η ορθή τάση για την κάθετη κάμψη να είναι 137.3 Mpa ή και λιγότερο.

Παράλληλα, ο κανονισμός HEPCJ (Hanshin Expressway Public Corporation of Japan- 1988) που παρέχει τις διατάξεις για το σχεδιασμό καμπύλων γεφυρών, προσδιορίζει την προαναφερόμενη μέγιστη απόσταση $L_D$ σε σχέση με την αντίστοιχη απόσταση για ευθύγραμμη δοκό $L_{DS}$ πολλαπλασιασμένη με ένα μειωτικό συντελεστή $\kappa(\phi, L)$ ως εξής

$$L_D = L_{DS}\kappa(\phi, L) \tag{6.2}$$

όπου

$$L_{DS} = \begin{cases} 6m & for \quad L < 60m \\ (0.14L - 2.4)m & for \quad 60m \leq L \leq 160m \\ 20m & for \quad L > 160m \end{cases} \tag{6.3}$$

$$\kappa(\phi, L) = \begin{cases} 1 & for \quad L < 60m \\ 1 - \dfrac{\sqrt{\phi}(L-60)}{100\sqrt{2}} & for \quad 60m \leq L \leq 200m \end{cases} \tag{6.4}$$

με $\phi$ να είναι η γωνία του τόξου που σχηματίζει η καμπύλη δοκός. Οι διατάξεις αυτές στοχεύουν να περιορίσουν το αντίστοιχο ποσοστό που προαναφέρθηκε στο 5% και την τιμή πλευρικής ορθής τάσης στα 4.90 Mpa ή και λιγότερο.

Στη συνέχεια αυτές οι διατάξεις εφαρμόζονται σε μοντέλα δοκών από ραβδωτά (κεφάλαια 4 και 5), στερεά και κελυφωτά στοιχεία με σκοπό τη σύγκριση των αποτελεσμάτων σε ευθύγραμμες και καμπύλες δοκούς καθώς και την αξιολόγηση των διατάξεων αυτών. Τα παραδείγματα που αναλύονται είναι κυρίως πρακτικού ενδιαφέροντος και αφορούν κιβωτοειδείς διατομές όπου τα φαινόμενα της διαστρέβλωσης έχουν ιδιαίτερη σημασία και η χρήση διαφραγμάτων καθίσταται αναγκαία. Τα αποτελέσματα και οι παραμετρικές συγκρίσεις που διενεργούνται καταδεικνύουν τη σημασία της θεώρησης του σχήματος, του λόγου των διαστάσεων της διατομής, του μήκους, της καμπυλότητας και των συνθηκών στήριξης ευθύγραμμης ή καμπύλης δοκού ως παραμέτρους στη μελέτη προσδιορισμού του αριθμού και της απόστασης των διαφραγμάτων κατά μήκος της δοκού καθώς δε λαμβάνονται όλες υπόψη από τις διατάξεις των κανονισμών.

Συγκεκριμένα, μελετάται η ορθογωνική κιβωτοειδής διατομή της πρηγούμενης ενότητας. Σύμφωνα με τον AASHTO πρέπει να χρησιμοποιηθούν 6 ενδιάμεσα διαφράγματα στην περίπτωση καμπύλης δοκού ενώ σύμφωνα με τον HEPCJ είτε για ευθύγραμμη είτε για καμπύλη δοκό πρέπει να χρησιμοποιηθούν 7. Ωστόσο εφαρμόζοντας το προτεινόμενο μοντέλο και συγκρίνοντας μετατοπίσεις και τάσεις για περιπτώσεις με λιγότερα διαφράγματα προκύπτει ότι στην περίπτωση ευθύγραμμης δοκού 1 με 2 διαφράγματα είναι αρκετά για να περιορίσουν τη διαστρέβλωση. Στην περίπτωση της καμπύλης δοκού δεν ισχύει το ίδιο. Καθώς αυξάνεται ο αριθμός των διαφραγμάτων δεν παρατηρείται διαφορά στις τάσεις μετά την τοποθέτηση 4 διαφραγμάτων. Οπότε δεν χρειάζονται 7 αλλά 4 σε αυτή την περίπτωση. Παρόμοια συμπεράσματα προκύπτουν στην περίπτωση θεώρησης των ιδιοσυχνοτήτων για $\rho = 2.5kN\,sec^2/m^4$ της ευθύγραμμης ή της καμπύλης δοκού (Πίνακας 6.1). Είναι φανερό ότι σχεδόν όλες οι ιδιοσυχνότητες είναι παρόμοιες είτε για 4 είτε για 7 διαφράγματα ενώ στην περίπτωση του 1 (προτεινόμενο μοντέλο) ή κανενός διαφράγματος οι ιδιοσυχνότητες διαφέρουν, ειδικά για τις ιδιομορφές με υπερβολική διαστρέβλωση.Αυτό σημαίνει ότι χρειάζονται σίγουρα περισσότερα του 1 διαφράγματα όπως ήταν αναμενόμενο. Όσον αφορά το ευθύγραμμο μοντέλο η σειρά των ιδιομορφών αλλάζει καθώς και η σπουδαιότητα της στρέβλωσης σε αυτές.

| A/A | FEMsolid 2880 NO Diaph. | FEMsolid 2880 7 (4) Diaphs. | FEMsolid 2880 NO Diaph. (straight) | 10 cubic B-splines in AEM (1 Diaph.) | Τύπος Ιδιομορφής |
|---|---|---|---|---|---|
| 1 | 1.605 | 1.726 (1.707) | 1.630 | 1.611 | $1^η$ ιδιομορφή κατακόρυφης μετατόπισης (ασήμαντη στρέβλωση) |
| 2 | 2.221 | 2.261 (2.238) | 2.168 | 2.155 | $1^η$ ιδιομορφή πλευρικής μετατόπισης (ασήμαντη στρέβλωση) |
| 3 | 7.038 | 7.329 (7.242) | 9.167 | 7.063 | $2^η$ ιδιομορφή κατακόρυφης μετατόπισης (σημαντική στρέβλωση) |
| 4 | 9.440 | 9.626 (9.530) | 12.099 | 9.296 | $2^η$ ιδιομορφή πλευρικής μετατόπισης (σημαντική στρέβλωση) |
| 5 | 14.455 | 16.108 (15.875) | 12.791 | 14.795 | $1^η$ ιδιομορφή στρέψης (σημαντική στρέβλωση) |
| 6 | 19.131 | 22.770 (22.087) | 21.591 | 20.552 | $3^η$ ιδιομορφή κατακόρυφης μετατόπισης (υπερβολική στρέβλωση) |
| 7 | 23.306 | 32.479 (32.000) | 29.194 | 22.961 | $3^η$ ιδιομορφή πλευρικής μετατόπισης (υπερβολική στρέβλωση) |
| 8 | 23.478 | 41.895 (36.422) | 22.848 | 25.312 | $2^η$ ιδιομορφή στρέψης (υπερβολική στρέβλωση) |

Πίνακας 6.1. Ιδιοσυχνότητες καμπύλης ή ευθύγραμμης δοκού με ορθογωνική κιβωτοειδή διατομή.

Στη συνέχεια μελετάται καμπύλη δοκός πολύ λεπτότοιχης κιβωτοειδούς διατομής ($E = 4E7\,kN/m^2$, $G = 2E7\,kN/m^2$, $L = 10\,m$, $\rho = 7.85kN\,sec^2/m^4$, $R = 6.366\,m$, $t/d = 0.02$, $d/L =$ 0) υπό έκκεντρο κατακόρυφο φορτίο $P_Z = 1000\,kN$ στο ελεύθερο άκρο. Σύμφωνα με τους κανονισμούς απαιτούνται 2 διαφράγματα είτε στην καμπύλη δοκό είτε στην ευθύγραμμη. Στη δεύτερη περίπτωση από συγκρίσεις του προτεινόμενου μοντελού με το FEMsolid με δύο διαφράγματα προέκυψε ότι τα 2 πληρούν τους περιορισμούς. Ωστόσο στην περίπτωση της καμπύλης δοκού οι κανονισμοί οδηγούν σε επισφαλή αποτελέσματα ειδικά στην προκειμένη περίπτωση πολύ λεπτότοιχης διατομής και μεγάλης καμπυλότητας της δοκού. Στο Σχήμα 6.1 είναι φανερό ότι με 13 διαφράγματα περιορίζεται η ένταση της διαστρέβλωσης κατά το μήκος της δοκού σε σχέση με την περίπτωση 1 διαφράγματος.
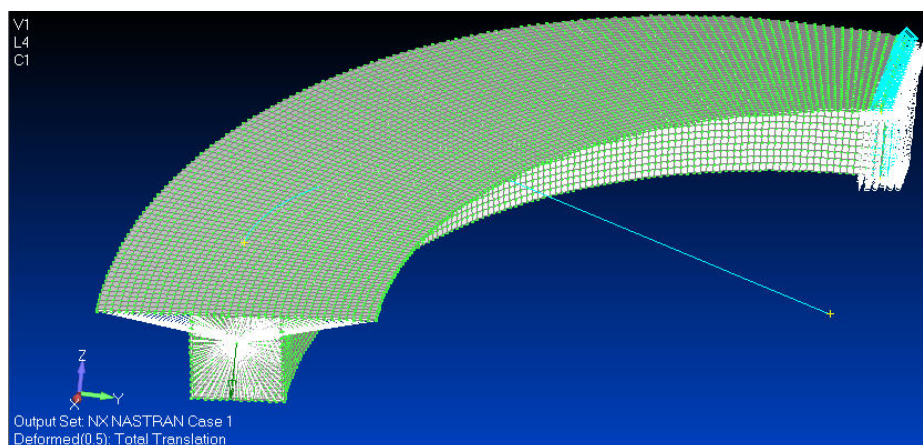


(α)
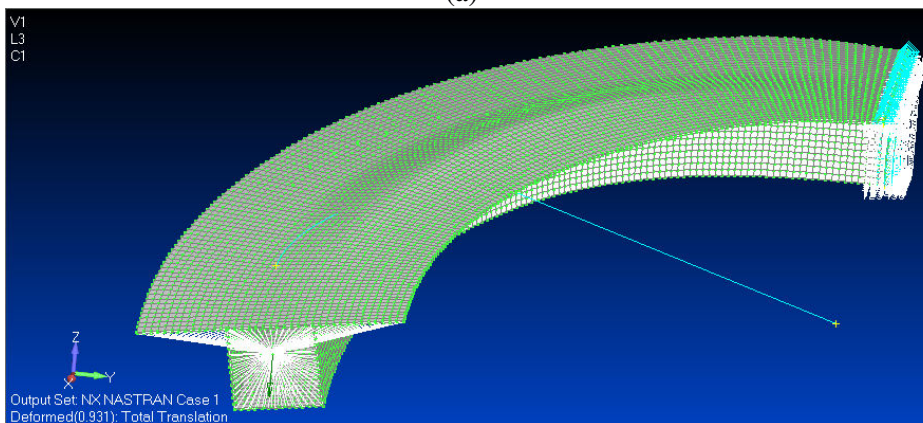


(β)

*Σχήμα 6.1. Παραμορφωμένος φορέας μοντέλων στο FEMAP με 10976 τετραπλευρικά τρισδιάστατα στοιχεία για (α) 13 ή (β) 1 διαφράγματα.*

Παράλληλα στον Πίνακα 6.2 δίνονται τα κινηματικά μεγέθη για διάφορα μοντέλα με διαφορετικές διατάξεις διαφραγμάτων. Είναι φανερό ότι πιο κοντά στο μοντέλο που αναπτύχθηκε σε προηγούμενη ενότητα και δε λαμβάνει υπόψη τη διαστρέβλωση είναι τα FEM μοντέλα με 13 διαφράγματα. Τα μοντέλα με 2 διαφράγματα (σύμφωνα με τους κανονισμούς) δίνουν μεγαλύτερες μετακινήσεις. Επιπλέον, από τον Πίνακα 6.3 είναι φανερό ότι οι ιδιοσυχνότητες του μοντέλου με 13 διαφράγματα και ιδιαίτερα οι ανώτερες, όπου η διαστρέβλωση γίνεται πιο έντονη, είναι πιο κοντά στο προτεινόμενο μοντέλο χωρις διαφράγματα (προηγούμενη ενότητα). Από τα παραπάνω προκύπτει ότι

σε αυτή την περίπτωση οι κανονισμοί οδηγούν σε μία επισφαλή λυση γιατί πρέπει να ληφθούν υπόψη και άλλες παράμετροι του προβλήματος.

| | | $v(m)$ at $x=L$ | $\theta_x(rad)$ at $x=L$ | $\theta_Z(rad)$ at $x=L$ |
|---|---|---|---|---|
| $P_Z$ Lateral Loading | 4 cubic NURBS (Ch. 4-NO dist.) | 0.4879 | -0.0202 | -0.0742 |
| | FEMplate 13 Diaph. | 0.4701 | -0.0231 | -0.0691 |
| | FEMplate 2 Diaph. | 0.5516 | -0.0290 | -0.0812 |
| | FEMplate 1 Diaph. | 0.9748 | -0.0951 | -0.1470 |
| | FEMsolid 13 Diaph. | 0.4647 | -0.0229 | -0.0685 |
| | FEMsolid 2 Diaph. | 0.5346 | -0.0279 | -0.0790 |
| | 8 cubic NURBS (Ch. 5-1 Diaph.) | 0.7844 | -0.0650 | -0.1110 |
| | FEMsolid 1 Diaph. | 0.8215 | -0.0726 | -0.1235 |

Πίνακας 6.2. Κινηματικά μεγέθη για διάφορα μοντέλα με ή χωρίς διαφράγματα για καμπύλη δοκό με λεπτότοιχη κιβωτοειδή διατομή.

| Mode Number | FEMsolid 1 Diaph. | FEMsolid 2 Diaph. | FEMsolid 13 Diaph. | 10cubic NURBS (Ch.4-NO dist.) |
|---|---|---|---|---|
| 1 | 0.1172 | 0.1416 | 0.1548 | 0.1317 |
| 2 | 0.2556 | 0.2615 | 0.2704 | 0.2191 |
| 7 | 0.3262 | 0.3644 | 1.0436 | 1.1042 |
| 8 | 0.3562 | 0.3799 | 1.4233 | 1.2311 |
| 9 | 0.4022 | 0.4761 | 1.5021 | 1.3345 |

Πίνακας 6.3. Ιδιοσυχνότητες για το μοντέλο δοκού του Σχήματος 6.1.

Τα παραπάνω επιβεβαιώνονται πιο συνοπτικά στον Πίνακα 6.4 όπου καταρτίζονται οι αποκλίσεις του μοντέλου που αναπτύχθηκε χωρίς διαστρέβλωση από το μοντέλο με δύο διαφράγματα βάση των κανονισμών για διαφορετικές ακτίνες καμπυλότητας. Η παραμετρική ανάλυση καθίσταται ιδιαίτερα εύκολη με τη χρήση της Ισογεωμετρικής ανάλυσης στο ραβδωτό μοντέλο. Αξίζει να σημειωθεί ότι καθώς αυξάνεται η ακτίνα καμπυλότητας οι αποκλίσεις μεγαλώνουν και αυτό δείχνει ότι τα 2 διαφράγματα δεν αρκούν πλέον για να περιορίσουν τη διαστρέβλωση που γίνεται εντονότερη με την αύξηση της καμπυλότητας.

Στη συνέχεια μελετάται καμπύλη δοκός με κιβωτοειδή διατομή τραπεζοειδούς σχήματος ( $E=3E7\,kN/m^2$ ,     $G=1.5E7\,kN/m^2$ ,     $L=40\,m$ ,     $R=25.465\,m$ ,

$t/d = 0.086$,     $d/L = 0.0$ʹ) για κεντρικό κατακόρυφο φορτίο $P_Z = 10000\,kN$ στο ελεύθερο άκρο. Στον Πίνακα 6.4 δίνονται τα κινηματικά μεγέθη για διάφορα μοντέλα με διαφορετικό αριθμό διαφραγμάτων. Σύμφωνα με τους κανονισμούς χρειάζεται να
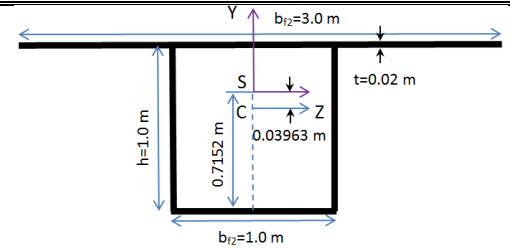
| | | $v(\%)$ at $x=L$ | $\theta_x(\%)$ at $x=L$ | $\theta_Z(\%)$ at $x=L$ |
|---|---|---|---|---|
| $P_Z$ Lateral Loading | R=∞ | 0.00 | 0.64 | 0.00 |
| | R=28.65m | 1.09 | 1.41 | 1.06 |
| | R=12.73m | 3.03 | 3.40 | 1.91 |
| | R=6.37m | 8.73 | 27.60 | 6.08 |

Πίνακας 6.4. Απόκλιση προτεινόμενου μοντέλου χωρίς διαστρέβλωση από το μοντέλο με 2 διαφράγματα (βάση των κανονισμών) για διαφορετικά R.

| | | at $v(m)$ $x=L$ | $\theta_x(rad)$ at $x=L$ | $\theta_Z(rad)$ at $x=L$ |
|---|---|---|---|---|
| $P_Z$ Lateral Loading | 4 cubic NURBS (Ch. 4-NO dist.) | 0.3197 | -0.007029 | -0.0104 |
| | FEMsolid 1 Diaph. | 0.3547 | -0.00867 | -0.0115 |
| | FEMsolid 7 Diaph. | 0.2914 | -0.00756 | -0.0090 |
| | FEMsolid 16 Diaph. | 0.2746 | -0.00778 | -0.0081 |
| | FEMsolid 2 Diaph. | 0.3256 | -0.00782 | -0.0103 |
| | FEMsolid 4 Diaph. | 0.3021 | -0.00753 | -0.0094 |

Πίνακας 6.5. Κινηματικά μεγέθη για διάφορα μοντέλα με ή χωρίς διαφράγματα για καμπύλη δοκό με κιβωτοειδή διατομή.

χρησιμοποιηθούν 6 ή 7 διαφράγματα για την αποφυγή της διαστρέβλωσης. Από τα αποτελέσματα στον πίνακα ωστόσο φαίνεται ότι τα μοντέλα με 2 και 4 διαφράγματα είναι κοντά στο προτεινόμενο καμπύλο στοιχείο προηγούμενης ενότητας που δε λαμβάνει υπόψη τη διαστρέβλωση. Παράλληλα μεταξύ των μοντέλων με 4 και 7 διαφράγματα υπάρχει μικρή διαφορά. Το ίδιο συμπέρασμα προέκυψε και από τον

υπολογισμό των τάσεων $\sigma_{zz}$ και $\sigma_{yy}$. Στην περίπτωση των 2 διαφραγμάτων οι τάσεις είναι γενικά πιο κοντά σε μέγεθος με αυτές του μοντέλου με 4 διαφράγματα από ότι με αυτές του μοντέλου με 1. Όλα αυτά καθιστούν τα 6 ή 7 διαφράγματα που απαιτούν οι κανονισμοί αντιοικονομική λύση και μη αναγκαία για τη συγκεκριμένη διατομή και δοκό. Θεωρώντας τις ιδιοσυχνότητες της δοκού (Πίνακας 6.6), είναι φανερό ότι το μοντέλο με 16 διαφράγματα επιφέρει μικρές διαφοροποιήσεις και κυρίως για τις ιδιομορφές 8, 9 και 10 που είναι αρκετά κοντά στο προτεινόμενο μοντέλο χωρίς διαστρέβλωση. Όσον αφορά τις υπόλοιπες ιδιοσυχνότητες οι τιμές είναι γενικά παρόμοιες.

| A/A | FEMsolid 1 Diaph. | FEMsolid 16 Diaph. | cubic NURBS (Ch. 4-NO dist.) |
|-----|-------------------|--------------------|-----------------------------|
| 1 | 0.0488 | 0.0541 | 0.0412 |
| 2 | 0.1408 | 0.1457 | 0.1203 |
| 3 | 0.1905 | 0.2208 | 0.2501 |
| 4 | 0.3002 | 0.3885 | 0.3200 |
| 5 | 0.4643 | 0.5033 | 0.4452 |
| 6 | 0.5309 | 0.6481 | 0.6465 |
| 7 | 0.6299 | 0.8718 | 0.7046 |
| 8 | 0.6797 | 1.0252 | 0.9412 |
| 9 | 0.7125 | 1.1320 | 1.1889 |
| 10 | 0.7361 | 1.4439 | 1.3252 |

Πίνακας 6.6. Ιδιοσυχνότητες για μοντέλο καμπύλης δοκού με κιβωτοειδή διατομή τραπεζοειδούς σχήματος.

Τελός, μελετάται καμπύλη δοκός είτε ως πρόβολος είτε ως αμφίπακτη με κιβωτοειδή διατομή ($E = 3.25E7\,kN/m^2$, $G = 1.39E7\,kN/m^2$, $R = 100\,m$, $v = 0.1667$, $t/d = 0.1$, $d/L = 0.065$) και με μήκος τόξου 33 m. Ασκείται έκκεντρο κατακόρυφο φορτίο $P_Z = 3000\,kN$. Σύμφωνα με τους κανονισμούς χρειάζονται είτε 5 (AASHTO) είτε 6 (HEPCJ) διαφράγματα για τον περιορισμό της διαστρέβλωσης. Στα Σχήματα 6.2 και 6.3 δίνονται οι αποκλίσεις στα κινηματικά μεγέθη και τις μέγιστες τάσεις (ορθή και διατμητική) του προτεινόμενου μοντέλου με διάφορα διαφράγματα από το FEMsolid μοντέλο χωρίς διαφράγματα. Όσον αφορά στο μοντέλο προβόλου είναι αρχικά φανερό ότι οι αποκλίσεις για τις μέγιστες τάσεις δε μεταβάλλονται για παραπάνω από 4 διαφράγματα. Παράλληλα όσον αφορά στα κινηματικά μεγέθη, παρατηρείται μια απότομη αύξηση της απόκλισης στην περίπτωση του 1 διαφράγματος και στη συνέχεια γενικά μικρότερες μεταβολές. Σχετικά με την απόκλιση της στρεπτικής γωνίας, ναι μεν αυξάνεται αλλά το μέγεθος αυτό καθεαυτό της γωνίας είναι μικρό σε σχέση με τα άλλα κινηματικά μεγέθη. Στην προκειμένη περίπτωση φαίνεται ότι οι κανονισμοί προβλέπουν έναν αριθμό διαφραγμάτων που προς τη μεριά της ασφάλειας μπορεί να θεωρηθεί αναγκαίος και δεν οδηγεί σε αντιοικονομική λύση. Όσον αφορά όμως στο μοντέλο της αμφίπακτης δοκού, οι μέγιστες τάσεις μεταβάλλονται ελάχιστα με την αύξηση των διαφραγμάτων, ειδικά μετά τα 3 διαφράγματα. Οι μετακινήσεις αυξάνονται συνεχώς με την αύξηση των διαφραγμάτων λόγω της διαφοροποίησης στις στηρίξεις αλλά το μέγεθός τους είναι πολύ μικρότερο σε σχέση με την προηγούμενη περίπτωση στήριξης. Εδώ φαίνεται οι κανονισμοί να οδηγούν σε αντιοικονομική λύση δεδομένου ότι από τις τελικές συγκρίσεις των τάσεων 1-2 διαφράγματα αρκούν για να περιορίσουν τη διαστρέβλωση. Αυτό συμβαίνει γιατί οι

κανονισμοί δεν λαμβάνουν υπόψη τις συνθήκες της δοκού και αντιμετωπίζουν πρόβολο και αμφίπακτη με τον ίδιο τρόπο.
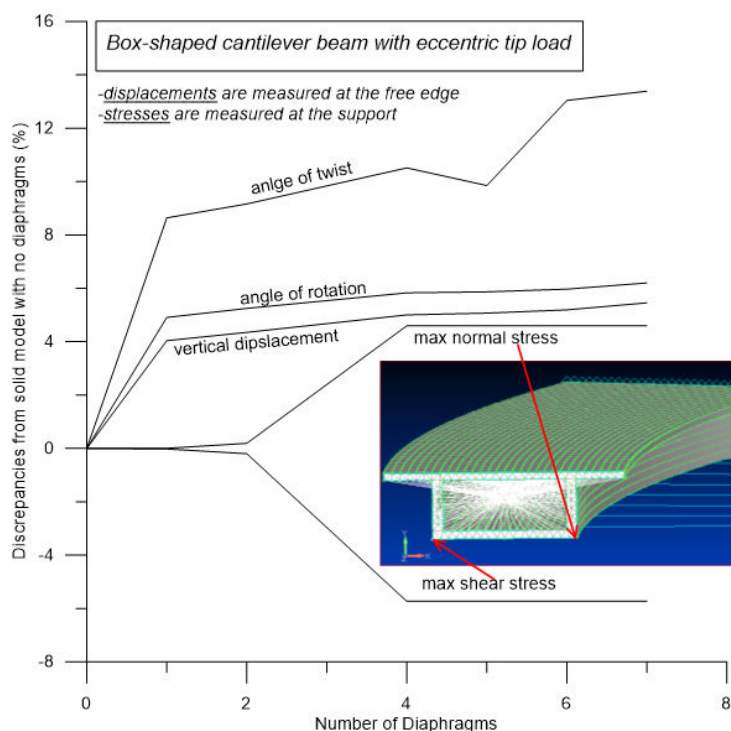


*Σχήμα 6.2. Διαφορές από το μοντέλο με τρισδιάστατα πεπερασμένα στοιχεία χωρίς διαφράγματα για πρόβολο.*
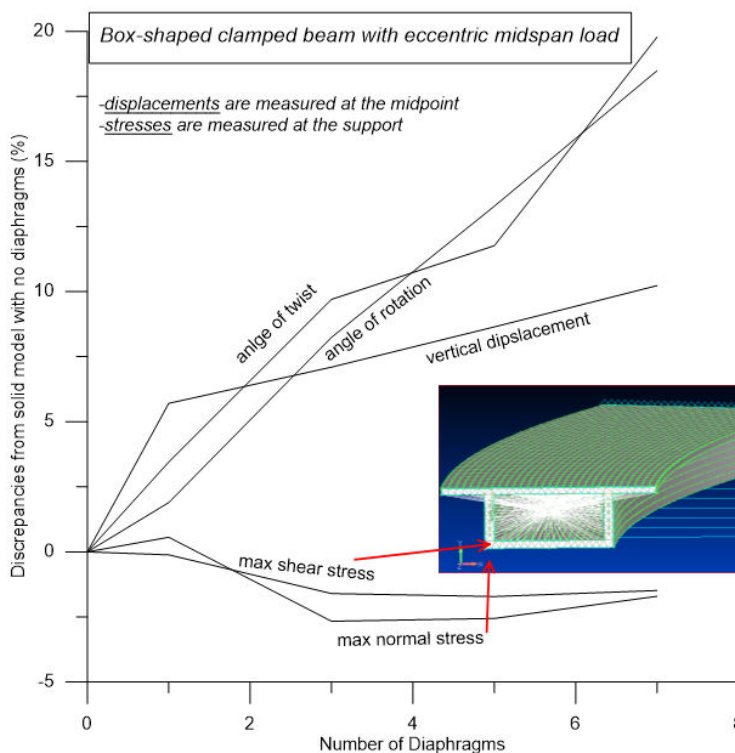


*Σχήμα 6.3. Διαφορές από το μοντέλο με τρισδιάστατα πεπερασμένα στοιχεία χωρίς διαφράγματα για αμφίπακτη.*

# VIII.     Κεφάλαιο 7: Συμπεράσματα

Τέλος στο *7ο κεφάλαιο* συνοψίζονται τα συμπεράσματα που προέκυψαν από την παρούσα ερευνητική συμβολή και παρουσιάζονται κατευθύνσεις για μελλοντική έρευνα.

Συγκεκριμένα, λαμβάνοντας υπόψη ότι οι βασικές καινοτομίες της παρούσας διατριβής συνίστανται στην ενσωμάτωση των εργαλείων της Ισογεωμετρικής ανάλυσης- IGA (B-splines και NURBS) τόσο στην ΑΕΜ όσο και στην ανάλυση ενός νέου στοιχείου καμπύλης δοκού FEM που λαμβάνει υπόψη τη γενικευμένη στρέβλωση και διαστρέβλωση, μπορούν να εξαχθούν συνοπτικά τα παρακάτω συμπεράσματα:

1. Η χρήση των B-splines και NURBS επιτυγχάνει ακριβή αποτελέσματα με μικρότερο υπολογιστικό κόστος τόσο στο στατικό όσο και στο δυναμικό πρόβλημα ευθύγραμμης ή καμπύλης δοκού χωρίς ανάγκη για ιδιαίτερη μετέπειτα επεξεργασία των αποτελεσμάτων. Παράλληλα, βελτιώνονται οι ρυθμοί σύγκλισης που έχει ιδιαίτερη σημασία στην περίπτωση που η θεωρία της δοκού γενικεύεται και εντάσσονται πολλοί βαθμοί ελευθερίας.

2. Στα προβλήματα που μελετώνται στην παρούσα διατριβή διαπιστώνεται ότι B-splines ή NURBS $3^{ου}$ βαθμού μπορούν να δώσουν πολύ ακριβή αποτελέσματα με ή και χωρίς επιπλέον σημεία ταξιθεσίας. Ωστόσο, επειδή ο βαθμός των καμπύλων αυτών και κατά συνέπεια η ακρίβεια της μεθόδου μπορεί να επηρεάζονται από συγκεκριμένες σταθερές της διατομής σε καποιες περιπτώσεις συνίσταται η αύξηση του βαθμού.

3. Η CNT αποτυγχάνει να προβλέψει με την επιθυμητή ακρίβεια τις τάσεις και τις ροπές λόγω πρωτογενούς στρέβλωσης. Τα αποτελέσματα που δίνει είναι παρόμοια με αυτά της θεωρίας Vlasov. Παρόμοια συμπεράσματα ισχύουν για τη θεωρία Saint Venant σε σχέση με τη στρέψη και τη θεωρία Euler-Bernoulli σε σχέση με την κάμψη.

4. Το Timoshenko στοιχείο δοκού (που κυρίως χρησιμοποείται σε εμπορικά προγράμματα) δεν προβλέπει με ακρίβεια τιμές ιδιοσυχνοτήτων λεπτότοιχων ανοιχτών ή κλειστών διατομών ακομά και διπλά συμμετρικών. Παράλληλα, στην περίπτωση κιβωτοειδών διατομών οι τάσεις υποεκτιμώνται.

5. Η αύξηση της καμπυλότητας συντελεί στην αύξηση του μεγέθους των φαινομένων στρέβλωσης και διαστρέβλωσης και κατά συνέπεια επιδρά και στο στατικό και το δυναμικό πρόβλημα.

6. Τα φαινόμενα στρέβλωσης στις ανοικτές διατομές και διαστρέβλωσης στις κλειστές οδηγούν στη μείωση των ιδιοσυχνοτήτων και ιδιαίτερα των ανώτερων στην πρώτη περίπτωση.

7. Οι παραμετρικές αναλύσεις σε καμπύλες δοκούς εκτελούνται με μεγαλύτερη ευκολία λόγω της χρήσης εργαλείων που απεικονίζουν απευθείας τη γεωμετρία.

8. Οι κανονισμοί για την πρόβλεψη της μέγιστης απόστασης ενδιάμεσων διαφραγμάτων μπορεί να οδηγήσουν είτε σε επισφαλείς είτε σε αντιοικονομικές λύσεις γιατί δε λαμβάνουν υπόψη όλες τις παραμέτρους του προβλήματος.

# Table of Contents

# Table of contents

## 5. Generalised distortional analysis of straight and curved beams by Isogeometric Methods

## 6. Application of Diaphragms' guidelines and Assessment

# Chapter 1

# Chapter 1

# Introduction

## 1.1  Motivation of doctoral thesis

### Warping and distortion in curved structural members

It is well known, that in case of a beam under torsional loading where the longitudinal displacements that create warping are restrained due to boundary conditions (e.g. restrained warping due to frontal diaphragm or forked support), the arising torsional moment is nonuniform and normal stresses arise. These are proportional to warping and therefore vary along the length of the beam under consideration. In this case the arising problem is that of the "nonuniform torsion". This problem has been extensively examined in the literature. In an analogy with Timoshenko beam theory, when shear deformation is of importance, the so-called Secondary Torsional Shear Deformation Effect (STSDE) has to be taken into account as well. Moreover, the additional secondary torsional warping due to STSDE can cause similar effects with shear lag in flexure, i.e. a modification of the initial normal stress distribution. Thus, the influence of shear lag phenomenon due to both flexure and torsion, which is not constant along the beam length, should also be considered.

In the majority of works made in recent years, the effects of nonuniform shear warping distribution or, in other words, shear lag phenomenon in flexure, have not been extensively considered in the dynamic problems of beams by the inclusion of the corresponding inertia effects. The same case holds for the problem of torsion. Even though nonuniform torsion has been examined in the literature, the STSDE and the corresponding inertia effects, in analogy to the shear lag in flexure, has not yet been investigated in torsional vibration analysis of beams. Thus, the analyses of beam models with warping effects in the dynamic problem could be used in a broad range of structural applications, such as automobile, aircraft frames, decks of bridges (under traffic and earthquake loading), high-rise buildings (under blast and wind loading), as well as optics, electromagnetics and acoustics, where high frequencies are more important.

Comparing to straight beam formulations, the behavior exhibited by curved beams is far more complex regarding twist deformations. It is well known, that in case of a horizontally curved beam under transverse loading not only vertical displacement but twist deformation with respect to its longitudinal axis arises as well and this cannot be captured by traditional Euler-Bernoulli or Timoshenko beam elements. Even though the formulation remains simple, it fails to capture higher order phenomena such as "shear lag", which are associated with a significant modification of normal stress distribution due to nonuniform shear warping. Similar considerations with the ones made for flexure could be also adopted for the torsional problem, which is also should

be encountered in the analysis of curved-in-plan beams. Regarding curved beam formulations, a series of straight-line segments is generally used in practice in order to approximate the curved geometry. This approximation causes an additional problem that is the transmission of warping, which in general is not taken into account in the analysis of complex structures. For example, an analysis of the cross section of a bridge should be performed in the transverse direction in order to account for warping. Thin-walled straight or curved structures having open or closed cross-section, which are widely used in bridge engineering due to their large bending and torsional rigidities as well as their low self-weight, suffer from these effects. Hence a realistic estimation of stress state employing conventional beam elements becomes difficult, since generally commercial programs consider six degrees of freedom (DOFs) at each node of a member of a spatial frame, ignoring in this way all the warping effects due to corresponding warping restraint. Therefore, it can be concluded that in order to accurately estimate and assess the actual stress state of a spatial framed structure more rigorous analyses need to be performed. The early curved beam models that have been formulated are either restricted to the analysis of only the beam behavior in the plane of curvature or do not take into account secondary shear deformation effect caused by nonuniform warping, while other efforts consider only doubly symmetric cross sections. In general, even in recent or past years, although the planar problem has been extensively studied, comparatively little work has been done concerning the general three dimensional, non-planar, or coupled lateral-torsional responses of curved beams.

When compared to the effort involved in static analysis, there has not been much effort put into the dynamic analysis of curved box girder bridges. The geometric complexities and the spatial coupling effect between bending and torsion make the analysis of curved bridges difficult. Bridge design codes usually provide guidance for the dynamic analysis of straight bridges (dynamic amplification factor, natural frequencies, modelling of vehicles, placement of diaphragms etc.). These design recommendations have been used by some designers for curved bridges, even though some researches carried out revealed that need to be reviewed. When bridges are curved, different kinds of loads can cause lateral bending and torsional modes of vibration in addition to the common longitudinal or flexural modes of vibration and so there are still many possible as well as crucial problems to be investigated regarding the dynamic response, for example, forced vibration due to moving loads and earthquake, vehicle-bridge coupling vibration, and wind-induced vibration.

In-plane deformations, such as distortion, occurring when thin-walled sections undergo bending and torsional deformations can considerably weaken the flexural and torsional stiffness of thin-walled beams. Regarding horizontally curved beams subjected to vertical or radial loads, they inherently exhibit a more complex behavior comparing to straight formulations due to the fact that the effects of primary and secondary torsion are always coupled to those of bending and cross section distortion either for centered or eccentric loads. Even though distortion is larger in magnitude near the beam's ends, it does not remain local (exponentially decays away from the support) and thus it should be considered over the entire domain of the beam to account for its stiffness-weakening effect. In practice distortion is prevented through the

placement of diaphragms in the cross section plane. Regarding the distortional analysis related to the intermediate diaphragms, which is more important for box girders, the number of studies is quite limited. The study related to the distortional analysis of box girders was initiated by Dabrowski (1968) who first formulated the distortional phenomenon of box members with a symmetric cross section. Later and more recently, other research efforts were undertaken regarding the distortional analysis of the structures to give design guidelines on the intermediate diaphragms. However, in most of these studies, the placement of diaphragms was not related whether to dynamic property analysis or dynamic response analysis. In addition to these, elastic constraints cannot be accommodated and due to other assumptions made these proposals lack of generality. Finally, guide specifications for horizontally curved highway bridges do not take into account the boundary conditions and the cross section directly for the specification of the maximum spacing of the intermediate diaphragms through their approximating formulae.

### Importance of beam models

In engineering practice the analysis of beam structural members, which have a longitudinal dimension significantly larger than the cross sectional ones, is frequently encountered. However, refined models either straight or curved with shell or solid elements are widely used in structures, such as for example the deck of a bridge with a thin-walled cross section, for stress or strain analysis. The analysis of such members employing the so-called "Higher-Order Beam Theories" is of increased interest due to their important advantages over more elaborate approaches based on shell or solid finite elements, which are mainly incorporated in commercial software. More specifically

• A Beam formulation reduces significantly modeling effort (solid models require cumbersome post- and pre-processing even in relatively simple cases). The design of box-shaped thin-walled cross sections, the placement of supports, diaphragms and loads, the additional calculations needed in order to derive cross sections' rotations and further manipulations to extract stress values at specific points of solid elements can be very time consuming.

• It permits isolation of structural phenomena and results interpretation contrary to the reduced oversight of the 3-D Finite Element (FEM) models (quantities such as rotation, warping parameter, distortional effects, stress resultants etc. are also evaluated in contrast to solid model which yields only translations and stress components).

• It allows straightforward model handling (support modeling and external loading are easily applied).

• Midline of shell and plate models becomes difficult to be designed for different thicknesses of the same cross section, while midline models exhibit difficulty in capturing warping accurately.

• The investigation of various shell/plate or solid models in order to conduct convergence studies and control membrane and shear locking phenomena becomes time-consuming and multiple models need to be created.

• It avoids difficulties in discretizing a complex structure, while the resulting increased number of DOFs of the 3-D models leads to severe or unrealistic computational time.

• It avoids difficulties in discretizing a structure including thin-walled members (shear-, membrane-locking phenomena).

• It facilitates parametric analyses (solid modeling often requires construction of multiple models).

• It does not require shape functions for the kinematical components; hence the minimum number of elements can be employed, while the accuracy of function derivatives is not compromised.

• Beam models allow the use of different numerical tools (i.e. Isogeometric analysis- IGA, boundary element methods- BEM etc.) for the 2-D cross sectional and the 1-D longitudinal analysis which could be more effective in one case or the other and, thus, leading to an optimum approximating computational procedure.

### Evolution of beam theories and state of the art

Over the past decades, classical beam theories based on specific assumptions fail to describe accurately the structural behavior of beam elements, especially in more complex formulations such as in curved geometries. Among these theories, that of Saint-Venant (SV) still plays a crucial role due to the fact that the analysis reduces to the evaluation of warping and distortional functions over the cross sectional domain. However, this solution is exact for the uniform warping of a beam (warping/distortional deformations are not restrained). Towards improving SV theory, several researchers investigated the so-called SV's principle (stated by Love, 1944) as well as the SV's end-effects in order to derive a more general formulation of beams' kinematics. In most of these studies, the solution is obtained as the sum of the SV'S solution and the residual displacements corresponding to the end-effects. Vlasov (1961) presented the Thin Tube Theory (TTT) and treated different cross section types as special cases of this general theory. Dabrowski (1968) elaborated Vlasov's theory and introduced distortional behavior of box girders with a symmetric cross section. His model introduces the distortion angle as the single degree of freedom which measures the magnitude of the cross-sectional distortion. Schardt (1989, 1994) developed an advanced formulation known as Generalized Beam Theory (GBT) which is a generalization of the classical Vlasov beam theory in order to incorporate flexural and torsional distortional effects. A distinguishing feature of GBT stems from the general character of its cross sectional analysis which enables the determination of cross-section deformation modes as well as their categorization to global, distortional or local ones. Further developments of GBT avoid some of its cumbersome procedures through eigenvalue cross sectional analysis. These approaches are employed nowadays by several researchers. Towards solving the problem for arbitrarily shaped homogeneous or composite cross sections, El Fatmi and Ghazouani (2011) presented a higher order composite beam theory (denoted HOCBT) that starts from the exact expression of SV's solution and introduces in- and out-of-plane independent warping parameters for symmetric orthotropic cross sections with the ability to extended it for arbitrary ones.

However, in-plane warpings are only due to the flexural and axial deformation modes and, thus, it could be stated that this research effort studies Poisson ratio effects rather than distortional effects. Ferradi and Cespedes (2014) presented the formulation of a 3D beam element solving an eigenvalue problem for the distortional behavior of the cross section (in-plane problem) and computing warping functions separately by using an iterative equilibrium scheme. However, to the authors' knowledge, there are no research efforts that introduce a unified distortional and warping eigenvalue analysis of arbitrarily shaped cross sections to the analysis of curved beams.

### Introduction to Isogeometric Analysis

During the last decades the significant development of both software and hardware has made possible various novel approaches to architectural form and design. Rapid advances in CAD (Computer-Aided Design) technology have enabled architects and engineers to overcome traditional design limits and transform any imaginable shape into a persuasive building. The major stages of this new design trend (Free Form Design – FFD) involve parametric modeling, interactive structural analysis and shape optimization, which can be performed through a variety of computational tools available to the design teams.

When it comes to engineering projects consisting of conventional structural elements such as columns, beams and slabs, the behavior of which is easily understood and assessed, the engineer is capable of giving direct feedback to the architect by using well established methods and rules. However, these traditional practices cannot be always applied on complex geometrical configurations. It is often difficult to understand and interpret in advance the structural behavior of such three dimensional layouts. Consequently, this difficulty gives rise to an iterative and time consuming process of geometric design, modeling and simulation, analysis and checking, which often limits the efficiency of structural design and does not necessarily lead to reliable results. This raised the need for better interoperability between software packages used by architectural and structural teams, as well as improved reliability of structural analysis and design tools. Recent attempts towards exploiting the potential of parametric design in combination with finite element analysis (FEA) software led to the development of tools for free-form geometric design based on mechanical principles ("physically-based modelling"), where material and mechanical properties are ascribed to surfaces so that the geometry may be freely deformed by the designer to the desired configuration. This mechanical approach to geometrical modelling leads to acceleration of the process and to the possibility of performing more iterations of a structural solution in order to yield the optimum result.

The connection of the geometric model to the structural one through conventional Finite Element representations sets restrictions on the level of interaction between the stages of structural analysis and design, on the computational time and in some cases on the accuracy of the results. These deficiencies were initially reported during the analysis and design of various mechanical, naval and aeronautical applications, where the creation of an appropriate "simulation-specific" geometry is important, and set the base of a new perspective which requires focusing on a single geometric model, which

can be utilized directly as an analysis model. Consequently, a change from classical FEA to an analysis procedure based on CAD representations is required. This concept is referred to as Isogeometric Analysis and it was introduced by Hughes et al. (2009). According to this novel approach, the structure is discretized exploiting its intrinsic computer-aided geometric definition. Thus, a more interactive approach between geometry and analysis is possible and more accurate results are obtained by diminishing the geometry approximation error.

Nevertheless, even though Isogeometric analysis has been successfully applied in shell problems and could provide solutions to structural engineering problems arising from the use of free-form shell surfaces, limited work seems to exist concerning Isogeometric analysis of three dimensional curvilinear beams. The majority of contemporary free-form projects, apart from complex surfaces, comprise curvilinear grids or stiffener nets. These beam members are an important ingredient for the structural integrity of such constructions. Finite beam elements are an effective and convenient means of analysis of such structures, combining ease of application and interpretation of results with low computational cost. Moreover, up-to-date regulations are based on quantities such as stress resultants, which are readily determined only through beam elements. However, in most cases of FFD process, it is difficult to incorporate the inherent curvature of the beams into the structural model (since usually straight beam FE are used) and cumbersome procedures need to be applied in order to refine the element mesh and capture satisfactorily the curved geometry with straight elements. These procedures inhibit an interactive structural analysis to be performed in an automated manner. Hence, it can be concluded that beam elements should be combined with Isogeometric analysis in order to serve as a useful tool in modern analysis projects.

## 1.2   Objectives and novelties of doctoral thesis

Having established the motivation and the state of the art behind the subject of the present doctoral thesis, the prime objective can be founded, which is to formulate curved beam models enhanced with the capability to take into account shear deformation, generalized warping (shear lag effect) as well as cross sectional distortion. By employing these models it is intended to highlight all the above structural phenomena and their importance in beams' analysis. Another major objective is to incorporate the Isogeometric Analysis in the numerical methods traditionally employed in order to increase the level of accuracy with less computational effort. For this purpose, the main idea of the Isogeometric approach has been applied. This consists of describing the geometry of the problem by B-splines or Non-Uniform Rational B-splines (NURBS) interpolation exactly and using the same interpolating basis to represent the kinematical components of the proposed curved beam model.

The accuracy and reliability of the obtained results have been verified through comparisons with results obtained by the implementation of the Finite Element Method (FEM) employing beam, solid (quadrilateral or triangular) or plate elements in commercial software package, as well as with available analytical solutions and experimental data. In addition to these, design guidelines for specifying the maximum

spacing of intermediate diaphragms have been applied to the aforementioned solid models and compared to the proposed one.

In the present doctoral thesis the Boundary Element Method (BEM) is employed for the solution of two-dimensional problems on the cross sectional domain, while the Analog Equation Method (AEM), which is considered an advancement to classical BEM, and Finite Element Method (FEM) are employed for the solution of one-dimensional problems along the beam length. Isogeometric tools have been integrated in both of the previous numerical approached and their advantages have been highlighted.

The research work presented herein is considered original and its essential features and novel aspects are summarized as follows:

i. The proposed formulation is capable of the complete analysis of spatial curved beams of arbitrary closed or open cross section with one plane of constant curvature (either small or great) considering flexural-torsional shear lag effects and transverse loading to the plane of curvature (as is usually the case in practice). The necessity to include nonuniform warping and STSD effects in the dynamic analysis of curved bridge decks is demonstrated.

ii. The developed beam formulation is capable of the static and dynamic analysis of spatial straight or curved beams of arbitrary closed or open and thin- or thick-cross section considering distortional effects and Poisson ratio. The necessity to include them in the analysis of beams is demonstrated.

iii. The straight or curved beam is subjected to arbitrary external loading including warping and distortional moments and is supported by the most general boundary conditions including elastic support or restraint.

iv. The numerical solution of advanced beam theories and its application to the analysis of straight or horizontally curved beams is based on B-splines and NURBS (Isogeometric Analysis) offering the advantage of integrated computer aided design (CAD) in the analysis.

v. The cross sectional analysis is based on an iterative equilibrium scheme which results in a numerical procedure with less computational effort and complexity comparing to traditional eigenvalue analysis reported in the literature for similar problems. Particularly, modes attributed to different structural phenomena can be separated directly and make the supervision of the results easier. In addition to this, the data post-processing and the iterative procedure become faster due to the fact that warping and distortional functions are calculated separately.

vi. The accuracy level of the numerical method proposed can be decided by the user by setting the desirable number of the modes taken into account and, thus, increasing the number of higher modes added in the final solution.

vii. The developed beam formulation reduces significantly modelling effort due to the fact that there is no need for pre-processing in order to define geometry, which is an important issue even in simple curved beams. Moreover, it allows straightforward model handling (boundary conditions, external loading are easily modelled) compared with three-dimensional solid curved beam models.

viii.   The use of NURBS in AEM results in drastically improved accuracy in spectral calculations over the original AEM, as it is the case also with traditional FEM, while AEM gives highly accurate results either original or combined with IGA tools comparing to corresponding FEM formulations.

ix.   The assessment of the design guidelines which specify the maximum spacing of intermediate diaphragms through comparisons of the proposed curved model to the corresponding solid or plate ones and some parametric studies is a first step towards suggesting further provisions and limitations on the application of these regulations.

## 1.3   Outline of doctoral thesis

The present doctoral thesis is organized in seven chapters and two appendices. Each one of the chapters 2 to 6 consists of an introduction containing the necessary literature review of the corresponding problem, the statement of the problem, the numerical solution, a number of representative numerical examples and finally some concluding remarks. In the final chapter, the main conclusions drawn within the present doctoral thesis are summarized, while suggestions and goals for future research are proposed. The appendices include additional information necessary to understand the basic characteristics and some technical aspects of the numerical techniques employed in the present doctoral thesis.

In Chapter 2, the Analog Equation Method (AEM), a boundary element based method, is employed for the nonuniform torsional problem of bars of arbitrary constant cross section, considering a quadratic B-spline approximation for the fictitious loads of a substitute problem. The fictitious loads are established using a BEM-based technique and the solution of the original problem is obtained from the integral representation of the solution of the substitute problem. The bar is subjected to arbitrarily distributed twisting moments along its length, while its edges are subjected to the most general torsional (twisting and warping) boundary conditions. The problem is numerically solved introducing a quadratic B-spline function for the fictitious load in the integral representations of the aforementioned technique. Numerical results are worked out to illustrate the method, designate its efficiency, accuracy and computational cost, as well as verify its integrity comparing with the results of analytical solutions. In addition to this, refinement procedures have been employed in some of the numerical examples in order to investigate their efficiency in increasing accuracy. Knot insertion, which is one of these, is proved to be very beneficial in refining the B-spline curve and increasing the accuracy.

In Chapter 3, the Analog Equation Method (AEM), a boundary element based method, is employed for the analysis of a homogenous beam element of arbitrary cross section (thin- or thick- walled) taking into account nonuniform warping and shear deformation effects (shear lag due to both flexure and torsion), considering B-splines for the approximation of the fictitious loads. The Isogeometric tools, either integrated in FEM or AEM, are employed for the vibration analysis of this element, too. The beam is subjected to the combined action of arbitrarily distributed or concentrated axial and transverse loading, as well as to bending, twisting and warping moments. Its edges

are subjected to the most general boundary conditions, including also elastic support. Nonuniform warping distributions are taken into account by employing four independent warping parameters multiplying a shear warping function in each direction and two torsional warping functions, which are obtained by solving corresponding boundary value problems, formulated exploiting the longitudinal local equilibrium equation. By employing a distributed mass model system accounting for longitudinal, transverse, rotatory, torsional and warping inertia, ten boundary value problems with respect to the variable along the beam time-dependent one dimensional kinematical components are formulated. The numerical solution or the spectrum analysis of the aforementioned problems is performed through IGA, FEM and AEM, leading to a system of second-order differential equations, which are quasi-static and solved for the static and free vibration case, formulating a generalized eigenvalue problem.

In Chapter 4, the static and dynamic generalized warping problem of horizontally curved beams of arbitrary cross section, loading and boundary conditions is presented. The proposed beam element possesses ten degrees of freedom (DOFs) per node in order to account for out-of-plane nonuniform warping due to both flexure and torsion (shear lag due to both flexure and torsion). This element can be employed in the analysis of curved bridge decks of open or closed (box-shaped) cross section. Great curvature can be considered in order to formulate the expressions of normal and shear strains. Thus, the sectorial properties related to the thickness-curvature effect, which need to be considered in cases of large subtended angle and small radius, are included in this study. The numerical solution of the problem is obtained by Isogeometric tools, either integrated in FEM or AEM. When pure AEM is considered, constant or quadratic elements are employed in order to represent the fictitious loading. The curved structure (e.g. bridge deck) is subjected to the combined action of arbitrarily distributed or concentrated axial and transverse loading, as well as to bending, twisting and warping moments. Its edges are subjected to the most general loading and boundary conditions, including also elastic support, as in the previous chapter. Finally, by employing a distributed mass model system, ten boundary value problems are formulated similarly to the previous chapter. Free vibration characteristics and responses of the stress resultants and displacements to static and moving loading have been studied. The warping functions and the geometric constants including the additional ones due to warping are evaluated employing a pure BEM approach. The results obtained from the beam element are compared to those obtained from finite 3D solutions and other research efforts. Numerical examples are presented to illustrate the efficiency and the accuracy of this formulation.

In Chapter 5, the static and vibration analysis of straight or horizontally curved beams of arbitrary cross section, loading and boundary conditions including generalized cross sectional warping and distortional effects due to both flexure and torsion is presented. The aim of this Chapter is to propose a new formulation by enriching the beam's kinematics both with out-of- and in-plane deformation modes and, thus, take into account both cross section's warping and distortion in the final 1D analysis of curved members, towards developing GBT further for curved geometries while employing independent warping parameters, which are commonly used in Higher

Order Beam Theories (HOBT). A coupled two-dimensional boundary value problem is formulated, with or without considering Poisson ratio for the 2D cross section's domain together with the corresponding boundary conditions. Applying a proper discretization scheme for the cross section, the above mentioned problem will lead to the formulation of an eigenvalue problem which the eigenvalues and the corresponding eigenvectors, for a desired number of modes, can be extracted from. The obtained set of modes contains axial, flexural and torsional modes in order of significance without distinction between them. To avoid the additional effort needed in order to recognize the most significant modes, an iterative local equilibrium scheme is adopted until the error due to residual terms becomes minimal. Together with the warping functions calculated first, the corresponding distortional ones are also obtained and recursively modify the warping functions due to their coupling. With all these additional modes, the beams' kinematics is enriched and capable of describing accurately the displacement and stress distribution in the beam. The functions derived are evaluated employing two dimensional BEM. A set of boundary value problems are formulated with respect to the unknown kinematical components (displacements, rotations and independent parameters), the number of which is defined by the user depending on the accuracy of the results. This linear system is solved using Isogeometric tools, either integrated in in FEM or AEM. The results obtained from the beam element are compared to those obtained from finite 3D solutions and other research efforts. Numerical examples are presented to illustrate the efficiency and the accuracy of this formulation as well as to provide rules of thumb regarding the consideration of distortion and the number of modes needed.

In Chapter 6, the beam formulations presented in Chapters 4 and 5 are employed together with design guidelines which specify the maximum spacing of intermediate diaphragms in order to prevent from excessive distortional effects in cross section's plane. These provisions are combined to FEM solid or plate/shell models and through the comparisons of the results, the solutions provided by the guidelines are assessed with respect to strength of the models against distortion. For this purpose, various box-shaped cross sections and diaphragmatic arrangements have been examined for both the static and dynamic case.

In Chapter 7, the main conclusions drawn in this doctoral thesis are summarized and the key features and novelties of the developed formulations are highlighted. Moreover, directions for further research are suggested.

The present doctoral thesis contains also two appendices. In Appendix A.1, the main concept of the Analog Equation Method is presented regarding the solution ordinary differential equations of $2^{nd}$ and $4^{th}$ order. Finally, in Appendix A.2, the structure of B-splines and NURBS is described together with the procedure followed in order to integrate them in FEM and AEM numerical approximations.

In closing, it is worth here mentioning that the outcome of the conducted research activity presented in this doctoral thesis has been published in international journals and international conferences. These publications are cited at each corresponding chapter.

# Chapter 2

# Chapter 2

# Quadratic B-splines for the Nonuniform Torsional Problem of Bars

## 2.1  Introduction

It is well known, that in case of a beam under torsional loading where the longitudinal displacements that create warping are restrained due to boundary conditions (e.g. restrained warping due to frontal diaphragm or forked support), the arising torsional moment is nonuniform and normal stresses arise. These are proportional to warping and therefore vary along the length of the bar. In this case the arising problem is that of the *nonuniform torsion* and it has been solved by various numerical methods (Eisenberger, 1995; Sapountzakis, 2000; Mokos, 2007). Apart from research efforts in which bars are idealized with computationally demanding three dimensional or shell elements, several researchers proposed specialized beam elements to analyze bars under nonuniform torsion. Due to the mathematical complexity of the problem, the existing analytical solutions are limited to symmetric cross-sections of simple geometry, loading and boundary conditions (Friemann, 1993; Ramm and Hofmann, 1995). Moreover, the finite element method (Gruttmann et al., 1998), the differential quadrature element method (Chen, 1998) and a modified Fourier series method (Kim and Su, 1997) have also been used for the analysis of the nonuniform torsional problem, in the case the geometry of the cross section, its boundary conditions or its loading are not simple.

In general, Boundary Element Methods (BEM) (Katsikadelis, 2002a) have been only sparsely used for problems of torsion and warping. These implement integral equations and are the most contemporary numerical methods for solving boundary value problems. A BEM approach uses in-line elements for discretization, instead of area elements used in Finite Element Methods or Finite Different Methods leading to a small number of elements required to achieve high accuracy. Remodeling to reflect design changes becomes simpler. However, BEM, such as other numerical methods, is not free of drawbacks. Particularly, application of BEM requires the so-called fundamental solution. A promising technique that overcomes these drawbacks is the Analog Equation Method, developed by Katsikadelis (2002b, 1994).

AEM constitutes a numerical method for solving linear and nonlinear boundary value problems (elliptical, parabolic and hyperbolic) with linear or nonlinear boundary conditions. This method is based on BEM while improves it and eliminates its drawbacks. According to AEM, the real problem, which is described by a differential operator not reversed in practice, is transformed to an equal problem which is described by a linear differential operator of the same order with known fundamental solution and

integral representation. In the substitute problem, the geometry of the space under consideration and boundary conditions are preserved, while the non-homogenous terms of the linear operator stand for fictitious loads. Fictitious loads are computed through the numerical implementation of AEM, which leads to a system of linear or nonlinear algebraic equations.

In this chapter, *quadratic B-splines* are integrated in the AEM in order to study their advantages over the traditional AEM and investigate their main features related to the analysis of bars. B-splines have been only sparsely used in finite element analyses (FEM) and boundary element methods (BEM). However, lately integrated computer aided design (CAD) and finite element analyses (FEA) using B-splines gained greater insight with the introduction of NURBS (Non-Uniform Rational B-splines) by Hughes et al. (2009). Thus, an introduction of B-splines in a BE-based numerical technique is a natural starting point for the introduction of *Isogeometric Analysis* in the numerical solution of *advanced beam theories* with BEM either straight (Chapter 3) or *curved* (Chapters 4, 5 and 6). AEM is presented in a general form for one-dimensional boundary value problems described by fourth-order differential equations, such as the nonuniform torsional problem of a homogeneous isotropic bar, which is reduced to solving the fourth-order differential equation with respect to the angle of twist of the cross section. The bar is subjected to an arbitrarily distributed twisting moment while its edges are restrained by the most general linear torsional boundary conditions. The essential features and novel aspects of the present formulation of AEM compared with previous ones are summarized as follows:

i.  The method used is based on quadratic B-splines, that is piecewise quadratic polynomials with C1 continuity (lowest-degree polynomial representing a planar curve), and a collocation discretization methodology with the points of a uniform partition being the collocation points. The most important property of B-splines in general is that both continuity and local controllability can be achieved by their use. Local controllability in simple words is the ability of B-splines to change only a portion of a curve when a single point is moved.

ii. The introduction of the quadratic B-spline to replace the approximation of fictitious loads with constant values and its integration to the expressions of the AEM technique improves accuracy and reduces nodal points required for discretization. Unknown values of the problem are reduced, too.

iii. The dimensions of matrices used for the numerical implementation of AEM become smaller and less algebraic equations are required to compute fictitious loads.

iv. The employed B-spline is a special class of B-splines called uniform quadratic B-spline. As the name implies, parametric quadratic polynomials are used on a uniform knot sequence, which is called the knot vector, composed of successive integers equally spaced (linear elements of the same length used for discretization). Three control points have been used to represent the B-spline which is the minimum number that can be used for a quadratic B-spline (Jüttler,

2013; Piegel and Tiller, 1997; Rogers, 2001). The computation of fictitious loads at collocation points depends now on the calculation of the three control points.

## 2.2 Statement of the problem

Consider a prismatic bar of length l with a cross section of arbitrary shape, occupying the two dimensional multiply connected region $\Omega$ of the $yz$ plane bounded by the K+1 curves $\Gamma_0, \Gamma_1, \Gamma_2, ..., \Gamma_K$ as shown in Fig.1.

When the bar is subjected to the arbitrarily distributed twisting moment $m_t = m_t(x)$ its angle of twist is governed by the following boundary value problem (Sapountzakis and Mokos, 2003; Sapountzakis, 2000)

$$EC_S \frac{d^4\theta_x(x)}{dx^4} - GI_t \frac{d^2\theta_x(x)}{dx^2} = m_t \qquad \text{along the bar} \qquad (2.1a)$$

$$\alpha_1\theta_x(x) + \alpha_2 M_t = \alpha_3 , \qquad \beta_1\frac{d\theta}{dx} + \beta_2 M_b = \beta_3 \quad \text{at the bar ends } x = 0, l \qquad (2.2a,b)$$



(a)

(b)

$$\Gamma = \bigcup_{i=1}^{k} \Gamma_i$$
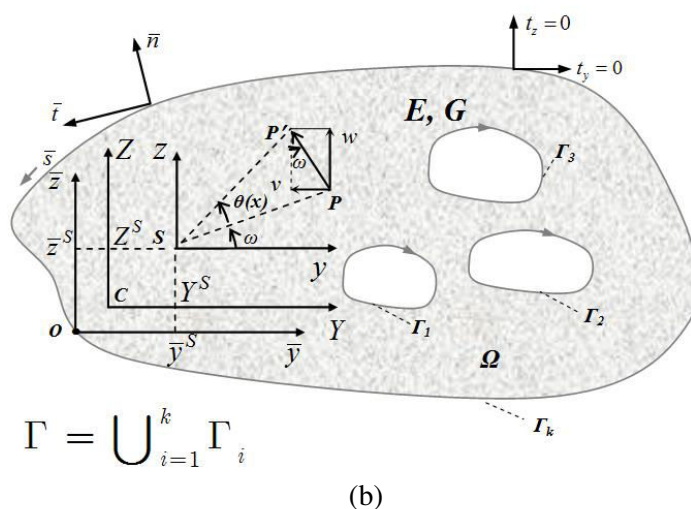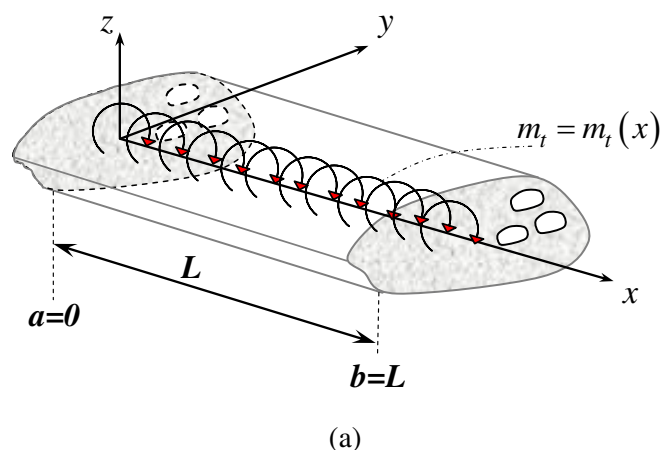
Figure 2.1. Prismatic bar subjected to a twisting moment (a) with a cross section of arbitrary shape occupying the two dimensional region $\Omega$ (b).

where $E$, $G$ are the modulus of elasticity and the shear modulus of the isotropic material of the bar, while $C_S$, $I_t$ are the warping and torsion constants of the bar's cross section, respectively. Moreover, $d\theta_x(x)/dx$ denotes the rate of change of the angle of twist $\theta_x(x)$ and it can be regarded to the torsional curvature, while $M_t$, $M_b$ are the twisting and warping moments due to the torsional curvature at the boundary of the bar, respectively.

The boundary conditions (2.2a,b) are the most general linear torsional boundary conditions for the bar problem, including also the elastic support. It is apparent that all types of the conventional torsional boundary conditions (clamped, simply supported, free or guided edge) can be derived from these equations by specifying appropriately the functions $a_i$ and $\beta_i$ (e.g. for a clamped edge it is $a_1 = \beta_1 = 1$, $a_2 = a_3 = \beta_2 = \beta_3 = 0$).

The solution of the boundary value problem given from eqns. (2.1), (2.2a,b), which represents the nonuniform torsional problem of bars presumes the evaluation of the warping and torsion constants $C_S$, $I_t$, respectively, which are given as (Sapountzakis and Mokos, 2003; Sapountzakis, 2000)

$$C_S = \int_\Omega \varphi_S^{P2} d\Omega \qquad I_t = \int_\Omega \left( y^2 + z^2 + y \frac{\partial \varphi_S^P}{\partial z} - z \frac{\partial \varphi_S^P}{\partial y} \right) d\Omega \qquad (2.3a,b)$$

where $\varphi_S^P(y,z)$ is the primary warping function with respect to the shear center $S$ of the cross section of the bar, which can be established by solving independently the Neumann problem

$$\nabla^2 \varphi_S^P = 0 \text{ in } \Omega \qquad (2.4)$$

$$\frac{\partial \varphi_S^P}{\partial n} = z n_y - y n_z \text{ on } \Gamma \qquad (2.5)$$

where $\nabla^2 = \partial^2 / \partial y^2 + \partial^2 / \partial z^2$ is the Laplace operator; $\partial / \partial n$ denotes the directional derivative normal to the boundary $\Gamma$ and $n_y$, $n_z$ the direction cosines.

## 2.3 Numerical Solution-Integral Representations

The evaluation of the angle of twist $\theta_x(x)$ is accomplished using AEM (Katsikadelis, 2002b). According to this method, for the function $\theta_x(x)$, which is four times continuously differentiable along the bar and three times continuously differentiable at the bar ends, the following relation is valid

$$\frac{d^4\theta_x(x)}{dx^4} = q(x) \tag{2.6}$$

where $q(x)$ is the fictitious load.

The fundamental solution of eqn. (2.6), also known as the fundamental solution of the flexural beam, is a partial solution of the differential equation (A.1.6) given in the Appendix A.1, where instead of $u^*(x,\xi)$ now $\theta_x^*(x,\xi)$ is applied. Employing this fundamental solution, the integral representation of the angle of twist is obtained as in eqn. (A.1.8) and by its differentiation, the expressions for the derivatives of $\theta_x(\xi)$ can be derived as in eqns. (A.1.11).

The introduction of a B-spline in the above mentioned expressions can now be done by substituting $q(x)$ with the polynomial representation of a quadratic B-spline with a uniform knot vector. According to the Appendix A.2, the i$^{th}$ B-spline basis functions of p-degree and the fictitious load curve for a quadratic B-spline are defined. For the sake of convenience (simplify this initial approach of fictitious load using a quadratic B-spline in AEM, make the comparison with the AEM using constant values of fictitious loads easier and the results more obvious) and without any loss of the general character of the method, in the following analysis the length of the bar is considered to be equal to unity.

Now $q(x)$, which is given in eqn. (A.2.4), is substituted in eqn. (A.1.14) and the vector $\{T\}$ can be written as follows

$$\{T\} = \begin{bmatrix} [0] \\ -[F_2] \end{bmatrix} \{P\} \rightarrow \{T\} = [F]\{P\} \tag{2.7}$$

where $\{P\}$ is the 3X1 vector containing the control points ($\{P\} = \begin{bmatrix} P_0 & P_1 & P_2 \end{bmatrix}^T$). Subsequently, applying the integral representations (A.1.8) and (A.1.11) at the collocation points presented in Fig. A.2.1, the following relations are derived, similarly to eqns. (A.1.23)

$$\{\Theta\} = [A]\{P\} + [C]\{\theta\} \tag{2.8a}$$

$$\{\Theta'\} = [A']\{P\} + [C']\{\theta\} \tag{2.8b}$$

$$\{\Theta''\} = [A'']\{P\} + [C'']\{\theta\} \tag{2.8c}$$

$$\{\Theta'''\} = [A''']\{P\} + [C''']\{\theta\} \tag{2.8d}$$

where $(\Theta, \Theta', \Theta'', \Theta''')$ are the vectors containing the values of the angle of twist and its

derivatives $((\theta_x(x), \theta_x'(x), \theta_x''(x), \theta_x'''(x)))$ at collocation points with respect to the control points. The coefficients of the 3X3 square matrices $[A], [A'], [A''], [A''']$ (eqns. (A.1.24)) are also given with respect to the vector of the control points. Afterwards, employing eqns. (A.1.25)-(A.1.28), eqn. (2.1a) yields the following linear system of equations

$$(E[C_S][A_0] - G[I_t][B'']) [P_0 \quad P_1 \quad P_2]^{\mathrm{T}} = \{m_t\} + G[I_t]\{R''\} \tag{2.9}$$

which gives the values of the control points $P_0, P_1$ and $P_2$ instead of the values of $q(x)$ at collocation points as in the original AEM. The diagonal matrix $[A_0]$ contains the values of basis functions $N_{0,1}, N_{1,2}$ and $N_{2,2}$ given in eqns. (A.2.2) for X=$X_{i1}$, $X_{i2}$ and $X_{i3}$ shown in Fig. A.2.1. Matrices $[A], [A'], [A''], [A''']$, $[F]$ and $[B], [B'], [B''], [B''']$ as they have been formed after substitution of B-splines in the relevant integrals are 3X3, 8X3 and 3x3, respectively. The vector of control points substitutes the fictitious load vector of the original AEM. Matrices $[C_S]$ and $[I_t]$ are diagonal with 2X2 dimensions and their values depend on the cross section geometry and primary warping function.

## 2.4   Refinement procedures

These procedures have been described in the Appendix A.2. A new set of control points is derived in eqn. (A.2.7) in order to refine the quadratic B-spline curve of the fictitious load (see Fig. A.2.3). The knot vector examined previously in order to determine the AEM technique by using a B-spline fictitious load is now enriched with the addition of new knots (eqns. (A.2.8)). In order to approximate the curve of fictitious load i.e. in the interval [0, ¼), the basis functions given by the expressions (A.2.9n-A.2.9p) have been substituted in eqn. (A.2.10) and the following expression is obtained

$$q(\xi) = (1-4\xi)^2 P_0 + 6\xi(1-4\xi)P_1 + 8\xi^2 P_2 \quad , if \quad 0 \le \xi < \frac{1}{4} \tag{2.10}$$

The same procedure is followed in order to derive the expression of the B-spline curve for the rest of the intervals with respect to the other control points. It should be noted that the basis functions $((1-4\xi)^2, \; 6\xi(1-4\xi), \; 8\xi^2)$ employed in eqn. (2.10) differ from those extracted from eqn. (A.2.4) $((1-\xi)^2, \; 2\xi(1-\xi), \; \xi^2)$. Therefore, the arising results (and obviously their accuracy compared to the exact solution) are expected to differ when employing the fictitious load given by eqn. (A.2.4) or by eqn. (2.10).

## 2.5   Numerical examples

In order to examine the advantages attained by the use of quadratic B-splines as an approximation of the fictitious loading in the AEM technique (instead of constant values in the original AEM) in terms of accuracy and computational cost, computer

programs have been written and representative examples have been studied. The numerical results have been obtained employing up to 44 nodal points (NP) in the original AEM (AEM) or 12 collocation points (CP) in the B-spline AEM (AEM-BS) and up to 400 boundary elements depending on the cross section type (cross sectional discretization in order to evaluate warping and torsion constants). However it is noted that in most of the treated examples higher accuracy could be also achieved with coarser discretization.

### 2.5.1 Doubly Symmetric I-section

In the first example, a clamped steel ( $E = 2.1E8kPa$, $v = 0.3$ ) bar of length $L=1m$, of a rolled doubly symmetric I-section IPE-200 ( $I_t = 6,846cm^4$, $C_S = 12746cm^6$, $\max \phi_S^P = 47,50cm^2$ according to Kraus and Kindmann, 2009), loaded along its length by a uniformly distributed twisting moment $m_t = 1kNm/m$ has been studied (Fig. 2.2). Three cases are examined, namely i) three discretization elements employing original AEM technique, ii) three collocation points employing AEM-BS and iii) the analytical (exact) solution employing Maple programming (Maplesoft, 2008).



(a)

(b)
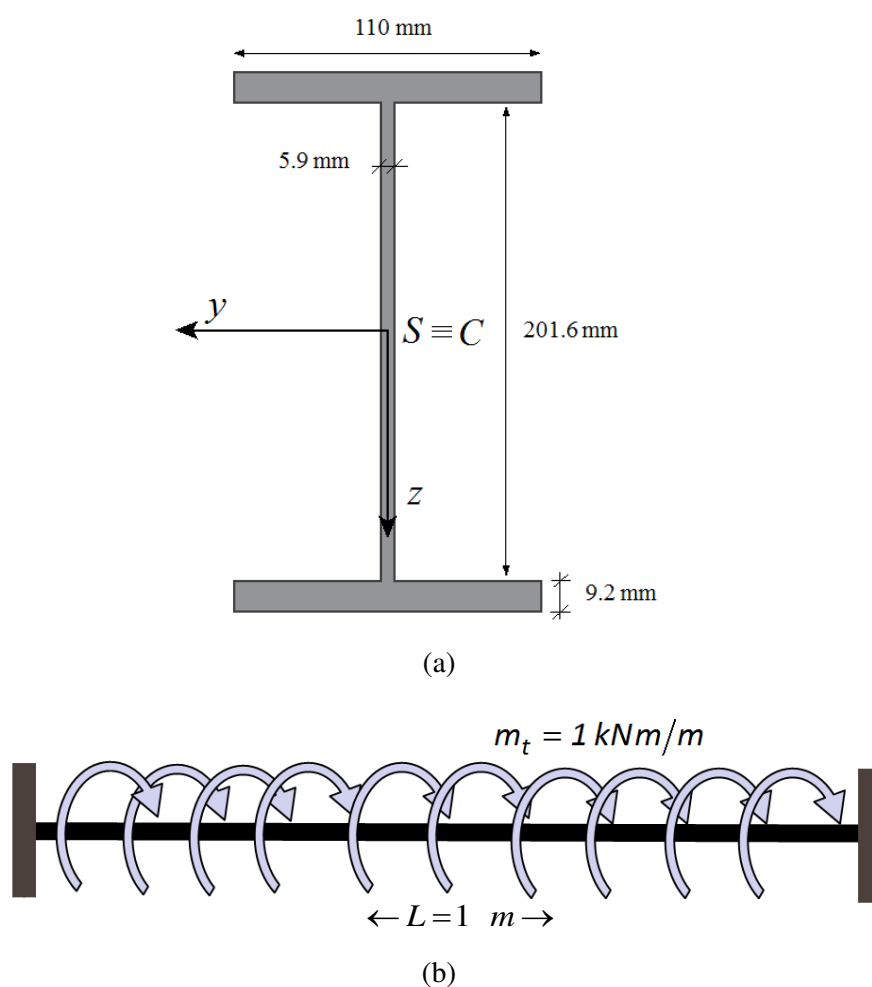
*Figure 2.2. Steel IPE cross section (a) of the clamped bar of example 1(b).*

In Table 2.1 the values of the angle of twist and its derivatives at the three collocation points (Fig. A.2.1) are presented and compared for the three aforementioned cases, noting that the values of the fourth derivative are the values of the fictitious load $q(x)$. From this table, it is observed that the discrepancies between the aforementioned two numerical cases and the analytic one are negligible. Moreover, the computational cost is almost the same for both of the numerical methods and thus, there is no need of any refinement for increased accuracy or decreased computational cost.

|  | AEM (3 NP) (1) | AEM-BS (3 CP) (2) | Analytical Solution (3) | Error % (1)-(3) | Error % (2)-(3) |
|---|---|---|---|---|---|
| $\theta_x(1/4)$ | 5,284E-04 | 5,225E-04 | 5,226E-04 | 1,10 | 0,022 |
| $\theta_x(1/2)$ | 9,350E-04 | 9,251E-04 | 9,251E-04 | 1,05 | 0,00 |
| $\theta_x'(1/4)$ | 2,800E-03 | 2,800E-03 | 2,800E-03 | 0,00 | 0,00 |
| $\theta_x'(1/2)$ | 0,000 | 0,000 | 6,210E-08 | 0,00 | 0,00 |
| $\theta_x''(1/4)$ | -3,800E-03 | -3,800E-03 | -3,800E-03 | 0,00 | 0,00 |
| $\theta_x''(1/2)$ | -1,480E-02 | -1,470E-02 | -1,470E-02 | 0,68 | 0,00 |
| $\theta_x'''(1/4)$ | -8,929E-02 | -8,770 E-02 | -8,770 E-02 | 1,81 | 0,00 |
| $\theta_x'''(1/2)$ | 0,000 | 0,000 | -1,800E-06 | 0,00 | 0,00 |
| $\theta_x''''(1/4)$ | 3,659E-01 | 3,657E-01 | 3,657E-01 | 0,05 | 0,00 |
| $\theta_x''''(1/2)$ | 3,433 E-01 | 3,433 E-01 | 3,433 E-01 | 0,00 | 0,00 |

*Table 2.1. Angle of twist $\theta_x$ (rad) and its derivatives at various positions for the bar element of example 1.*

### 2.5.2 Example 2: Monosymmetric T-section

A clamped steel ($E = 2.1E8kPa$, $v = 0.3$) bar of length $L=1m$, of rolled symmetric T-section ($I_t = 3,049 \times 10^{-8} m^4$, $C_S = 34,95 \times 10^{-12} m^6$ according to Sapountzakis and Dikaros, 2010), loaded along its length by a uniformly distributed twisting moment $m_t = 1kNm/m$ has been studied (Fig. 2.3). Four cases are examined, namely i) three discretization elements employing original AEM technique, ii) three collocation points employing AEM-BS, iii) refinement techniques for AEM-BS and iv) the analytical solution of the fourth order differential equation.

In Fig. 2.4 the angle of twist $\theta_x(x)$ along the bar length and in Table 2.2 $\theta_x(x)$ and its derivatives at the three collocation points (Fig. A.2.1) are presented for the

0.0056 m

0.192 m

$C$

$Y$

$S$

0.0085 m

$y$

0.1 m

$Z \equiv z$

(a)

$m_t = 1\,kNm/m$

$L=1\ m$

(b)
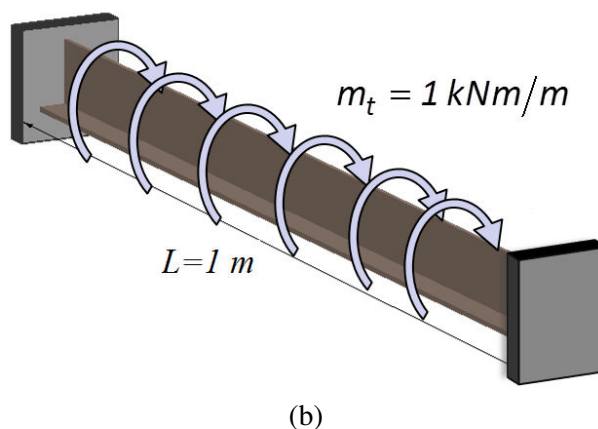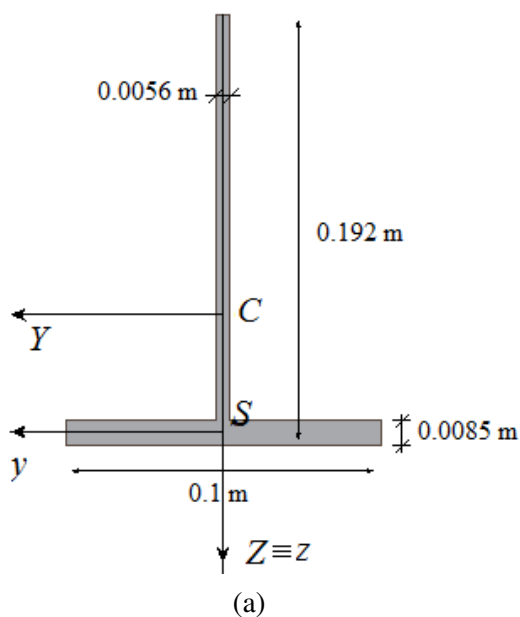
*Figure 2.3. Steel IPE cross section (a) of the clamped bar of example 1(b).*

aforementioned cases i), ii) and iv). From this table and figure, it is obvious that the discrepancies in $\theta_x(x)$, $\theta_x'(x)$ and $\theta_x''(x)$ between the analytical solution and the obtained results employing AEM-BS are quite small compared with the ones obtained employing the original AEM. Moreover, the errors arising from the use of the AEM with three discretization elements are not acceptable since they reach in general the order of 40%. However, for higher order derivatives (third and fourth), the results are inaccurate for both methods. Thus, refinement procedures, described in section 2.4, will be implemented in order to gain more accurate results.

Refinements of the results are attempted by employing eqn. (A.2.7) in order to define new control polygons (by adding successively control points) for the B-spline curve. The new control points are proved to be redundant due to the fact that the quadratic B-spline curve is explicitly defined by three control points. It would be beneficial to add control points through an iterative procedure (as in Chaikin, 1974) when it is aimed to approximate a target B-spline curve, possibly, of a complex shape and with more segments. In our case there is only one segment of the curve spanning the whole bar along its length.
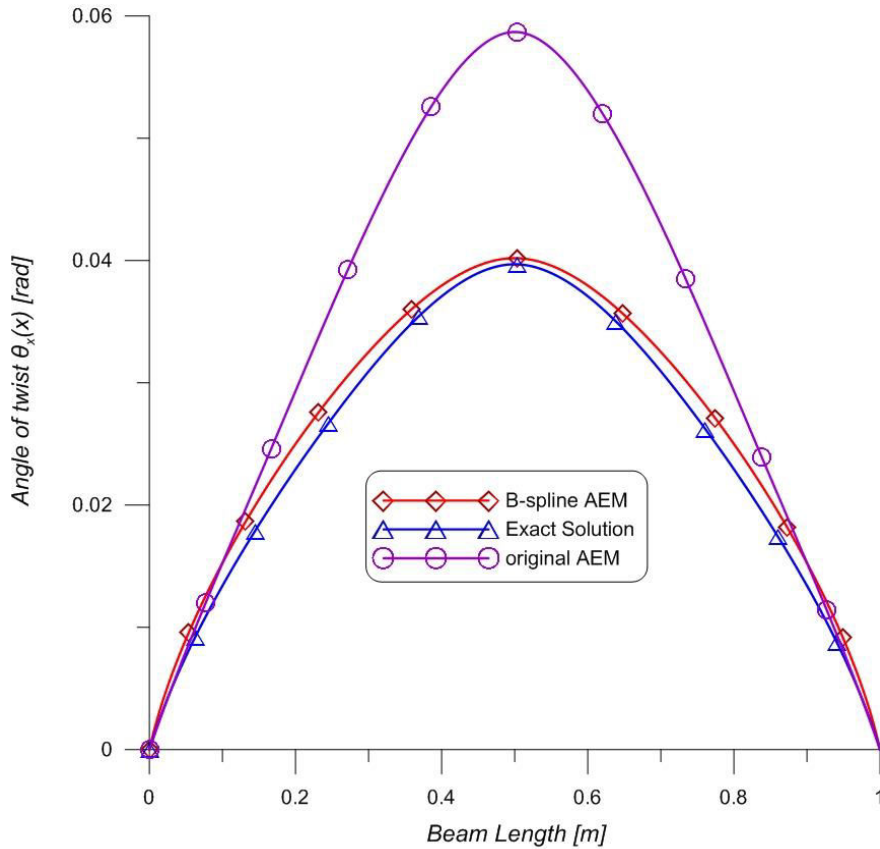
*Figure 2.4. Angles of twist $\theta_x(x)$ of the bar of example 2.*

Thus, in our case, control point insertion should be combined with knot insertion in order to express the same curve using the same degree. This operation of knot insertion is described in Section 2.4 and the basis functions are specified over the [0, ¼) interval of the knot vector. In order to express the segment of the B-spline curve over this interval, three new control points are used. Then, three collocation points are employed in order to compile the results for three different positions along the first quarter of the bar's length. In Table 2.3, the angle of twist $\theta_x(x)$ and its derivatives are presented at the three collocation points (*L/16, L/8* and *3L/16*) in the first quarter of the bar's length for the aforementioned cases i), ii) and iv). From this table, the values derived employing AEM-BS (employing eqn. (2.10)) are almost the same as those of the exact solution and the errors are quite small for higher order derivatives. Only the value of the third derivative at $x = 3L/16$ introduces a relatively large error (around 13%) when employing AEM-BS. Thus, more collocation points could be used to eliminate also this error. Comparing to the values derived by using the original AEM, it is concluded that some of the results are not accurate and the errors can be large, especially for the values of higher order derivatives, for this number of discretization elements. Thus, in Table 2.4 the results obtained when employing 44 discretization elements-nodes for the AEM, 12 collocation points for the AEM-BS and the exact solution are compiled.

|  | AEM (3 NP) (1) | AEM-BS (3 CP) (2) | Analytical Solution (3) | Error % (1)-(3) | Error % (2)-(3) |
|---|---|---|---|---|---|
| $\theta_x(1/4)$ | 3,780E-02 | 2,900E-02 | 2,710E-02 | 28,30 | 6,55 |
| $\theta_x(1/2)$ | 5,870E-02 | 4,020E-02 | 3,970E-02 | 38,22 | 5,71 |
| $\theta_x'(1/4)$ | 1,645E-01 | 1,009E-01 | 9,940E-02 | 39,57 | 1,49 |
| $\theta_x'(1/2)$ | 0,000 | 0,000 | -2,000E-06 | 0,00 | 0,00 |
| $\theta_x''(1/4)$ | -1,881E-01 | -3,227E-01 | -3,679E-01 | 41,74 | 12,29 |
| $\theta_x''(1/2)$ | -4,725E-01 | -4,125E-01 | -4,053E-01 | 14,22 | 1,74 |
| $\theta_x'''(1/4)$ | -2,495 | -1,973 | -6,990E-01 | 71,98 | 64,57 |
| $\theta_x'''(1/2)$ | 0,000 | 0,000 | 6,410E-08 | 0,00 | 0,00 |
| $\theta_x''''(1/4)$ | 19,820 | 27,691 | 12,806 | 35,39 | 53,75 |
| $\theta_x''''(1/2)$ | -22,278 | -2,114 | 2,628E-01 | 98,82 | 87,57 |

*Table 2.2. Angle of twist $\theta_x$ (rad) and its derivatives at various positions of the bar element of example 2.*

To conclude with, it is noted that errors of the same and in general quite small magnitude are obtained when employing in the AEM-BS around the one fourth of the number of nodes used in the original AEM, as collocation points along the length of the bar. This means that the computational cost when employing AEM-BS is much less than that of the original AEM in order to achieve the same or higher level of accuracy.

### 2.5.3 Example 3: Unequal Legged Angle

A clamped steel ($E = 2.1E8kPa$, $v = 0.3$) bar of length $L=1m$, of the unequal legged angle steel cross section ($I_t = 8,3903 \times 10^{-8} m^4$ and $C_S = 1,1937 \times 10^{-10} m^6$, according to Sapountzakis and Dikaros, 2010), loaded along the length by a uniformly distributed twisting moment $m_t = 1kNm/m$ has been studied (Fig. 2.5). Four cases are examined, namely i) three discretization elements employing original AEM technique, ii) three collocation points employing AEM-BS, iii) refinement techniques for AEM-BS and iv) the analytical solution of the fourth order differential equation.

In Table 2.5 the angle of twist and its derivatives at three collocation points (Fig. A.2.1) are presented for the aforementioned cases i), ii) and iv). From this table, it is obvious that the discrepancies in $\theta_x(x)$, $\theta_x'(x)$ and $\theta_x''(x)$ between the analytical solution and the obtained results employing AEM-BS are quite small compared with

| | AEM-BS (12 CP) (1) | AEM (12 NP) (2) | Analytical Solution (3) | Error % (1)-(3) | Error % (2)-(3) |
|---|---|---|---|---|---|
| $\theta_x(1/16)$ | 4,300E-03 | 4,600E-03 | 4,300E-03 | 0,00 | 6,522 |
| $\theta_x(1/8)$ | 1,220E-02 | 1,240E-02 | 1,220E-02 | 0,00 | 1,613 |
| $\theta_x(3/16)$ | 2,020E-02 | 2,040E-02 | 2,020E-02 | 0,00 | 0,980 |
| $\theta_x'(1/16)$ | 1,131E-01 | 1,197E-01 | 1,130E-01 | 0,088 | 5,514 |
| $\theta_x'(1/8)$ | 1,318E-01 | 1,311E-01 | 1,317E-01 | 0,076 | 0,456 |
| $\theta_x'(3/16)$ | 1,206E-01 | 1,154E-01 | 1,204E-01 | 0,166 | 4,153 |
| $\theta_x''(1/16)$ | 7,879E-01 | 7,840E-01 | 7,776E-01 | 1,307 | 0,816 |
| $\theta_x''(1/8)$ | -2,890E-02 | -5,650E-02 | -2,930E-02 | 1,365 | 48,14 |
| $\theta_x''(3/16)$ | -2,908E-01 | -2,767E-01 | -2,862E-01 | 1,582 | 3,320 |
| $\theta_x'''(1/16)$ | -22,249 | -27,881 | -21,682 | 2,548 | 22,23 |
| $\theta_x'''(1/8)$ | -6,745 | -7,005 | -6,901 | 2,265 | 1,479 |
| $\theta_x'''(3/16)$ | -2,522 | -1,033 | -2,196 | 12,930 | 52,97 |
| $\theta_x''''(1/16)$ | 400,623 | 399,301 | 397,164 | 0,863 | 0,535 |
| $\theta_x''''(1/8)$ | 126,545 | 117,293 | 126,407 | 0,109 | 7,225 |
| $\theta_x''''(3/16)$ | 38,665 | 43,400 | 40,232 | 3,895 | 7,300 |

*Table 2.3. Angle of twist $\theta_x$ (rad) and its derivatives for the bar element of example 2, employing knot insertion.*

the ones obtained when employing the original AEM. Moreover, the errors arising from the use of the AEM with three discretization elements are not acceptable since they reach the order of 45%. However, the results are inaccurate for higher order derivatives (third and fourth) for both methods. Thus, the refinement procedure of knot insertion, which is described in section 2.4 and has already been implemented in the previous example of T-section, will be also here employed in order to achieve more accurate results (Table 2.6).

As it is obvious in Table 2.6, the values derived when employing AEM-BS are almost the same as those of the  analytical  solution  and  the errors are quite small for

| | AEM-BS (12 CP) (1) | AEM (44 NP) (2) | Analytical Solution (3) | Error % (1)-(3) | Error % (2)-(3) |
|---|---|---|---|---|---|
| $\theta_x(1/16)$ | 4,300E-03 | 4,300E-03 | 4,300E-03 | 0,00 | 0,00 |
| $\theta_x(1/8)$ | 1,220E-02 | 1,230E-02 | 1,220E-02 | 0,00 | 0,813 |
| $\theta_x(3/16)$ | 2,020E-02 | 2,02E-02 | 2,02E-02 | 0,00 | 0,00 |
| $\theta_x'(1/16)$ | 1,131E-01 | 1,132E-01 | 1,130E-01 | 0,088 | 0,177 |
| $\theta_x'(1/8)$ | 1,318E-01 | 1,317E-01 | 1,317E-01 | 0,076 | 0,00 |
| $\theta_x'(3/16)$ | 1,206E-01 | 1,202E-01 | 1,204E-01 | 0,166 | 0,166 |
| $\theta_x''(1/16)$ | 7,879E-01 | 7,753E-01 | 7,776E-01 | 1,307 | 0,296 |
| $\theta_x''(1/8)$ | -2,890E-02 | -3,120E-02 | -2,930E-02 | 1,365 | 6,090 |
| $\theta_x''(3/16)$ | -2,908E-01 | -2,861E-01 | -2,862E-01 | 1,582 | 0,0350 |
| $\theta_x'''(1/16)$ | -22,249 | -21,916 | -21,682 | 2,548 | 1,066 |
| $\theta_x'''(1/8)$ | -6,745 | -6,926 | -6,901 | 2,265 | 0,362 |
| $\theta_x'''(3/16)$ | -2,522 | -2,169 | -2,196 | 12,960 | 1,252 |
| $\theta_x''''(1/16)$ | 400,623 | 396,388 | 397,164 | 0,863 | 0,195 |
| $\theta_x''''(1/8)$ | 126,545 | 125,800 | 126,407 | 0,109 | 0,480 |
| $\theta_x''''(3/16)$ | 38,665 | 40,262 | 40,232 | 3,895 | 0,0745 |

*Table 2.4. Angle of twist $\theta_x$ (rad) and its derivatives for the bar element of example 2, employing knot insertion and increasing nodal points.*

higher order derivatives, which was not possible before refinement. Only the value of the third derivative at $x = 3L/16$ introduces a relatively large error (around 8%) when employing AEM-BS. Thus, more collocation points could be used to eliminate also this error. Comparing to the values derived when using the original AEM, it is concluded that some of the results are not accurate and the errors can be large, especially for the values of the second order derivative and on, for this number of discretization elements.

In Table 2.7 the results obtained when employing 44 discretization elements-nodes for the AEM, 12 collocation points for the AEM-BS and the exact solution are compiled.
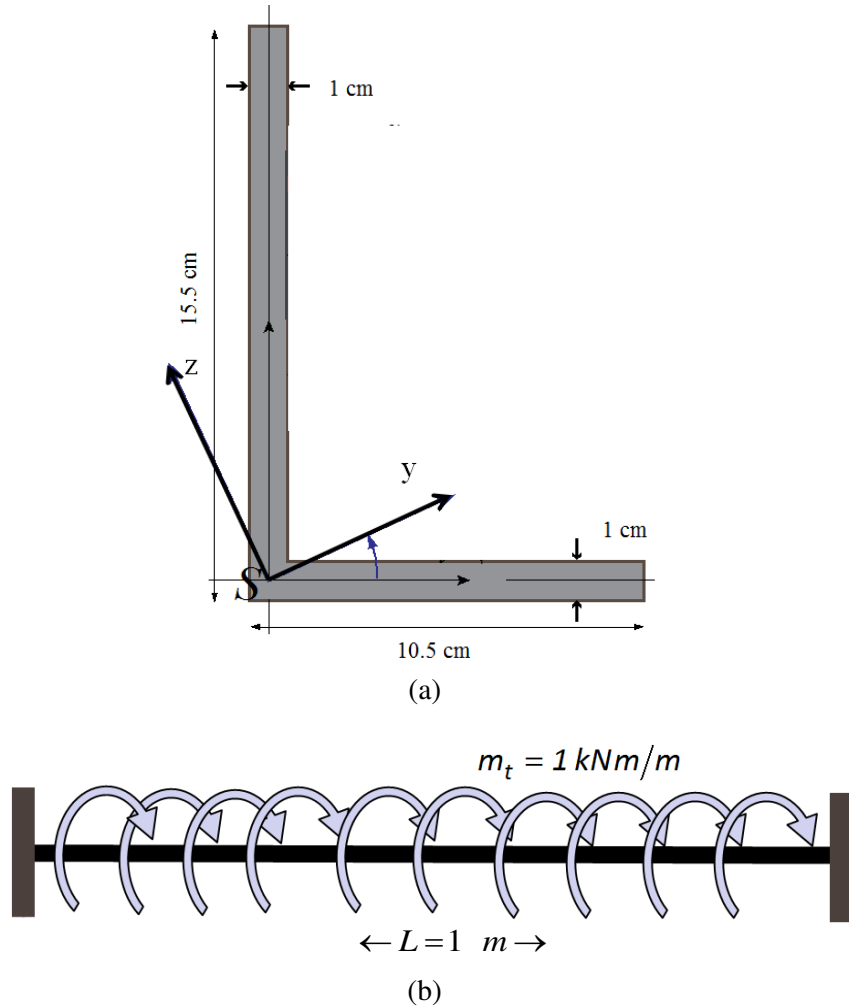
*Figure 2.5. Steel unequal legged angle cross section (a) of the clamped bar (b) studied in example 3.*

To conclude with, it is noted that errors of the same and in general quite small magnitude are obtained when employing in the AEM-BS around the one fourth of the number of nodes used in the original AEM, as collocation points along the length of the bar. This means that the computational cost when employing AEM-BS is much less than that of the original AEM in order to achieve the same or higher level of accuracy.

### 2.5.4 Example 4: UPE-100

A clamped steel ($E = 2.1E8kPa$, $v = 0.3$) bar of length $L=1m$, of the UPE-100 steel cross section ($I_t = 2,010 \times 10^{-8} m^4$ and $C_S = 590,10 \times 10^{-12} m^6$, according to Kraus, 2005), loaded along the length by a uniform twisting moment $m_t = 1kNm/m$ has been studied (Fig. 2.6). Four cases are examined, namely i) three discretization elements employing original AEM technique, ii) three collocation points employing AEM-BS, iii) refinement techniques for AEM-BS and iv) the analytical solution of the fourth order differential equation.

In Table 2.8 the angle of twist and its derivatives at three collocation points (Fig. A.2.1) are presented for the aforementioned cases i), ii) and iv). From this table, it is

| | AEM (3 NP) (1) | AEM-BS (3 CP) (2) | Analytical Solution (3) | Error % (1)-(3) | Error % (2)-(3) |
|---|---|---|---|---|---|
| $\theta_x(1/4)$ | 1,200E-02 | 1,02E-02 | 9,420E-03 | 27,11 | 7,65 |
| $\theta_x(1/2)$ | 2,020E-02 | 1,420E-02 | 1,396E-02 | 30,69 | 1,41 |
| $\theta_x'(1/4)$ | 4,930E-02 | 3,600E-02 | 3,600E-02 | 37,20 | 0,00 |
| $\theta_x'(1/2)$ | 0,00 | 0,00 | 2,000E-07 | 0,00 | 0,00 |
| $\theta_x''(1/4)$ | -6,770E-02 | -1,120E-01 | -1,277E-01 | 46,90 | 12,29 |
| $\theta_x''(1/2)$ | -1,724E-01 | -1,494E-01 | -1,469E-01 | 14,79 | 1,60 |
| $\theta_x'''(1/4)$ | -9,820E-01 | -7,202E-01 | -3,270E-01 | 66,70 | 54,60 |
| $\theta_x'''(1/2)$ | 0,000 | 0,000 | -1,170E-08 | 0,00 | 0,00 |
| $\theta_x''''(1/4)$ | 6,981 | 9,610 | 5,380 | 22,93 | 44,02 |
| $\theta_x''''(1/2)$ | -6,720 | -4,841E-01 | 1,764E-01 | 97,38 | 63,56 |

*Table 2.5. Angle of twist $\theta_x$ (rad) and its derivatives at various positions for the bar element of example 3.*

obvious that the errors arising in the evaluation of $\theta_x(x)$ and its derivatives are in general varying from 0% to around 10%. For the AEM-BS the errors are very small (0-1%) and values are quite close to those derived by the analytical solution of the problem. Moreover, the errors arising from the use of the AEM when employing three discretization elements are not acceptable since they reach the order of 10% while for the AEM-BS the results are very accurate and actually there is no need for any refinement. However, the refinement procedure of knot insertion, which is described in section 2.4 and has already been implemented in previous examples, will be employed in order for the results to be comparable (Table 2.9).

To conclude with, it should be noted that the results obtained by employing the two methods, are both highly accurate for the cross section shown in Fig. 2.6 when refinement procedures are employed. Particularly, the AEM-BS almost coincides with the exact solution and, with the same computational cost, the original AEM gives highly accurate results with small errors, which vary from 0,01% to almost 1%. In order to eliminate errors in the original AEM and achieve the same accuracy as that of the AEM-BS, discretization elements should be increased and, thus, the computational cost will be increased, as was the case in previous examples.

The cross sections of bars studied in this chapter are open-shaped thin-walled cross sections of similar dimensions in order to be able to draw conclusions and make

| | AEM-BS (12 CP) (1) | AEM (12 NP) (2) | Analytical Solution (3) | Error % (1)-(3) | Error % (2)-(3) |
|---|---|---|---|---|---|
| $\theta_x(1/16)$ | 1,400E-03 | 1,500E-03 | 1,400E-03 | 0,00 | 6,667 |
| $\theta_x(1/8)$ | 4,200E-03 | 4,200E-03 | 4,200E-03 | 0,00 | 0,00 |
| $\theta_x(3/16)$ | 7,000E-03 | 7,000E-03 | 7,000E-03 | 0,00 | 0,00 |
| $\theta_x'(1/16)$ | 3,820E-02 | 3,990E-02 | 3,820E-02 | 0,00 | 4,261 |
| $\theta_x'(1/8)$ | 4,590E-02 | 4,570E-02 | 4,590E-02 | 0,00 | 0,436 |
| $\theta_x'(3/16)$ | 4,280E-02 | 4,150E-02 | 4,270E-02 | 0,234 | 2,810 |
| $\theta_x''(1/16)$ | 2,890E-01 | 2,876E-01 | 2,870E-01 | 0,692 | 0,209 |
| $\theta_x''(1/8)$ | 7,900E-03 | 6,000E-04 | 7,800E-03 | 1,266 | 92,31 |
| $\theta_x''(3/16)$ | -9,310E-02 | -8,910E-02 | -9,200E-02 | 1,182 | 3,152 |
| $\theta_x'''(1/16)$ | -7,266 | -8,776 | -7,138 | 1,763 | 18,66 |
| $\theta_x'''(1/8)$ | -2,518 | -2,619 | -2,554 | 1,405 | 2,489 |
| $\theta_x'''(3/16)$ | -9,981E-01 | -4,343E-01 | -9,140E-01 | 8,426 | 52,48 |
| $\theta_x''''(1/16)$ | 118,007 | 117,653 | 117,360 | 0,549 | 0,249 |
| $\theta_x''''(1/8)$ | 42,032 | 40,042 | 41,998 | 0,081 | 4,657 |
| $\theta_x''''(3/16)$ | 14,727 | 15,810 | 15,030 | 2,016 | 4,935 |

*Table 2.6. Angle of twist $\theta_x$ (rad) and its derivatives for the bar element of example 3, employing knot insertion.*

comparisons affected only by the properties of the cross section geometry related to nonuniform torsion ($I_t$ and $C_S$) and not by other secondary effects (i.e. secondary torsional moment deformation effects which are important to closed-shape hollow section bars, according to: Sapountzakis and Mokos, 2003; Mokos, 2007). An interesting aspect to note is that the cross sections having two parallel flanges (i.e. example 1-IPE200 and 4-UPE100) give accurate results, as shown in Tables 2.1 and 2.8, without any need for refinement. Particularly, the results obtained when employing the AEM-BS almost coincide with the results of the exact solution and the errors introduced in the evaluation of the angle of twist and its derivatives are mainly equal to zero for the IPE200 and UPE100 (in general zero for the corresponding with respect to

| | AEM-BS (12 CP) (1) | AEM (44 NP) (2) | Analytical Solution (3) | Error % (1)-(3) | Error % (2)-(3) |
|---|---|---|---|---|---|
| $\theta_x(1/16)$ | 1,400E-03 | 1,400E-03 | 1,400E-03 | 0,00 | 0,00 |
| $\theta_x(1/8)$ | 4,200E-03 | 4,200E-03 | 4,200E-03 | 0,00 | 0,00 |
| $\theta_x(3/16)$ | 7,000E-03 | 7,000E-03 | 7,000E-03 | 0,00 | 0,00 |
| $\theta_x'(1/16)$ | 3,820E-02 | 3,820E-02 | 3,820E-02 | 0,00 | 0,00 |
| $\theta_x'(1/8)$ | 4,590E-02 | 4,590E-02 | 4,590E-02 | 0,00 | 0,00 |
| $\theta_x'(3/16)$ | 4,280E-02 | 4,270E-02 | 4,270E-02 | 0,234 | 0,00 |
| $\theta_x''(1/16)$ | 2,890E-01 | 2,860E-01 | 2,870E-01 | 0,692 | 0,348 |
| $\theta_x''(1/8)$ | 7,900E-03 | 6,500E-03 | 7,800E-01 | 1,266 | 16,667 |
| $\theta_x''(3/16)$ | -9,310E-02 | -9,200E-02 | -9,200E-02 | 1,182 | 0,00 |
| $\theta_x'''(1/16)$ | -7,266 | -7,201 | -7,138 | 1,763 | 0,879 |
| $\theta_x'''(1/8)$ | -2,518 | -2,575 | -2,554 | 1,405 | 0,800 |
| $\theta_x'''(3/16)$ | -9,981E-01 | -9,072E-01 | -9,140E-01 | 8,426 | 0,744 |
| $\theta_x''''(1/16)$ | 118,007 | 117,209 | 117,360 | 0,549 | 0,129 |
| $\theta_x''''(1/8)$ | 42,032 | 41,655 | 41,998 | 0,081 | 0,816 |
| $\theta_x''''(3/16)$ | 14,727 | 15,033 | 15,030 | 2,016 | 0,018 |

*Table 2.7. Angle of twist $\theta_x$ (rad) and its derivatives for the bar element of example 3, employing knot insertion and increasing nodal points.*

height UPE200, which has a torsional constant four times larger than UPE100 and a warping constant two times larger). This happens due to the fact that the AEM is a numerical method with its accuracy based on the approximation of the fictitious load, which is the unknown of the fourth order differential equation considered in the nonuniform problem of torsion (fourth order derivative of the angle of twist). Then, the rest values (angle of twist and the lower order derivatives) are obtained with respect to the values derived for this load, as it is explained in Section 2.2 of this chapter.

As shown in Fig. 2.7, the curves formed to represent the fictitious load given by the analytical solution are closely related to parabolas for the bars with IPE and UPE cross sections. This means that a quadratic B-spline is an accurate approximation of

h=10,0cm
b=5,5cm
tw=0,45cm
tf=0,75cm
r=1,0cm
E=2,1E8
v=0,3

(a)



$m_t = 1\,kNm/m$

$\leftarrow L = 1\ m \rightarrow$
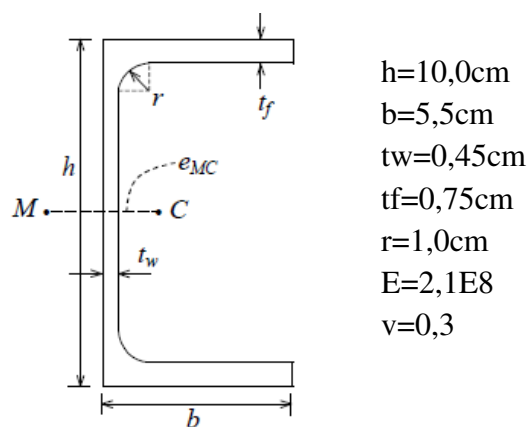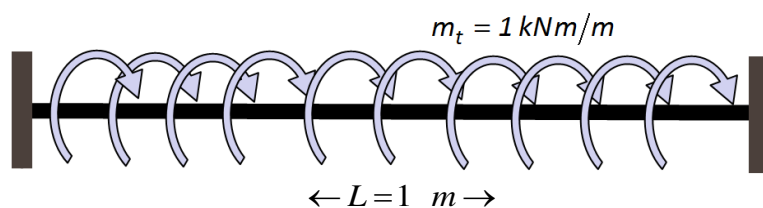
(b)

*Figure 2.6. Steel cross section (a) of the clamped bar (b) studied in example 4.*

|  | AEM-BS (3 CP) (1) | AEM (3 NP) (2) | Analytical Solution (3) | Error % (1)-(3) | Error % (2)-(3) |
|---|---|---|---|---|---|
| $\theta_x(1/4)$ | 9,100E-03 | 9,600E-03 | 9,100E-03 | 0,00 | 5,556 |
| $\theta_x(1/2)$ | 1,580E-03 | 1,670E-02 | 1,580E-03 | 0,00 | 5,952 |
| $\theta_x'(1/4)$ | 4,680E-02 | 5,000E-02 | 4,690E-02 | 0,213 | 6,654 |
| $\theta_x'(1/2)$ | 0,000 | 0,000 | -7,600E-10 | 0,00 | 0,00 |
| $\theta_x''(1/4)$ | -7,590E-02 | -8,320E-02 | -7,670E-02 | 1,043 | 8,505 |
| $\theta_x''(1/2)$ | -2,408E-01 | -2,514E-01 | -2,409E-01 | 0,0415 | 4,177 |
| $\theta_x'''(1/4)$ | -1,409 | -1,549 | -1,403 | 0,419 | 10,435 |
| $\theta_x'''(1/2)$ | 0,000 | 0,000 | 0,00 | 0,00 | 0,00 |
| $\theta_x''''(1/4)$ | 7,075 | 7,129 | 7,065 | 0,134 | 0,900 |
| $\theta_x''''(1/2)$ | 4,915 | 5,051 | 4,913 | 0,045 | 2,800 |

*Table 2.8. Angle of twist $\theta_x$ (rad) and its derivatives at various positions for the bar element of example 4.*

| | AEM-BS (12 CP) (1) | AEM (12 NP) (2) | Analytical Solution (3) | Error % (1)-(3) | Error % (2)-(3) |
|---|---|---|---|---|---|
| $\theta_x(1/16)$ | 9,000E-04 | 9,000E-04 | 9,000E-04 | 0,00 | 0,00 |
| $\theta_x(1/8)$ | 3,200E-03 | 3,200E-03 | 3,200E-03 | 0,00 | 0,00 |
| $\theta_x(3/16)$ | 6,100E-03 | 6,100E-03 | 6,100E-03 | 0,00 | 0,00 |
| $\theta_x'(1/16)$ | 2,770E-02 | 2,770E-02 | 2,770E-02 | 0,00 | 0,00 |
| $\theta_x'(1/8)$ | 4,300E-02 | 4,300E-02 | 4,300E-02 | 0,00 | 0,00 |
| $\theta_x'(3/16)$ | 4,870E-02 | 4,870E-02 | 4,870E-02 | 0,00 | 0,00 |
| $\theta_x''(1/16)$ | 3,361E-01 | 3,359E-01 | 3,361E-01 | 0,00 | 0,06 |
| $\theta_x''(1/8)$ | 1,609E-01 | 1,608E-01 | 1,609E-01 | 0,00 | 0,06 |
| $\theta_x''(3/16)$ | 2,560E-02 | 2,580E-02 | 2,560E-02 | 0,00 | 0,775 |
| $\theta_x'''(1/16)$ | -3,168 | -3,197 | -3,167 | 0,006 | 0,941 |
| $\theta_x'''(1/8)$ | -2,462 | -2,471 | -2,463 | 0,00 | 0,350 |
| $\theta_x'''(3/16)$ | -1,884 | -1,893 | -1,884 | 0,011 | 0,444 |
| $\theta_x''''(1/16)$ | 12,472 | 12,471 | 12,472 | 0,002 | 0,010 |
| $\theta_x''''(1/8)$ | 10,177 | 10,176 | 10,177 | 0,001 | 0,038 |
| $\theta_x''''(3/16)$ | 8,405 | 8,407 | 8,405 | 0,00 | 0,023 |

*Table 2.9. Angle of twist $\theta_x$ (rad) and its derivatives for the bar element of example 4, employing knot insertion.*

this curve, which spans the whole length of the bar preserving its shape. However, in the same figure, it is can be observed that there is a minimum plateau in the curves of fictitious loads of the T-shaped and L-shaped cross section bars between 0,3m and 0,7m along the length of the bar. Thus, the quadratic B-spline is not a very accurate approximation of the fictitious load for these cases of cross section due to the fact that the curve representing the fictitious load is more complex now. This is obvious from the results compiled in Tables 2.2 and 2.5, where the errors introduced, especially for higher order derivatives, are very large.

## 2.6   Concluding Remarks

In this chapter, a BEM based technique, called AEM, is developed for the nonuniform torsion of bars of open-shaped thin-walled cross sections. A quadratic B-spline curve is introduced for the representation of the fictitious load in order to implement an Isogeometric method for the numerical simulation of this particular problem described above. The main conclusions that can be drawn from this investigation are
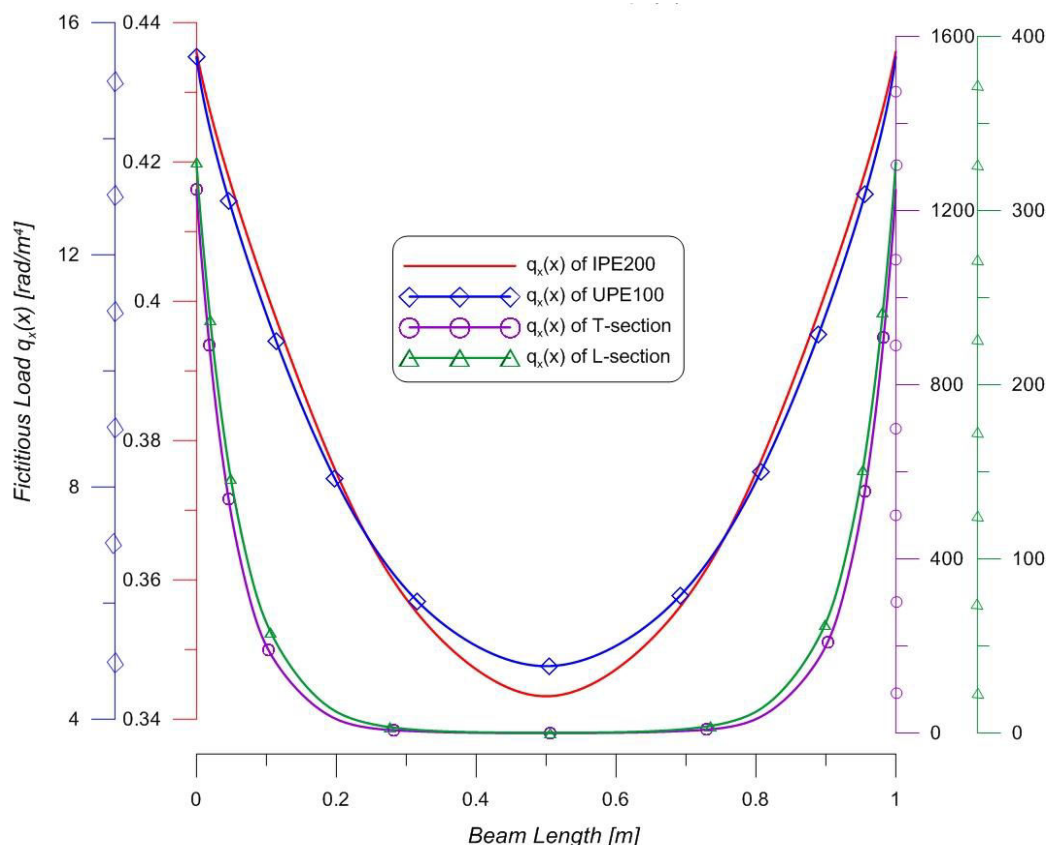


*Figure 2.7.   Exact curves representing the fictitious load   $q(x) = d^4\theta_x(x)/dx^4$*
*considered in AEM along the length of IPE200, UPE100, T-section and L-section bars.*

i.    In some cases, highly accurate and stable results can in general be obtained using a quadratic B-spline curve without the need for any refinement.
ii.   Different section properties affect the errors (especially the warping constant) in a proportionate way giving positive perspectives about the stability and accuracy of the methods described in this chapter.
iii.  The curve used to represent the fictitious load also affects the accuracy of the method and this might cause the necessity of knot insertion or degree elevation for the B-spline curve.

iv. The computational cost is much less using a quadratic B-spline due to the fact that the number of the unknowns is restricted to the number of the control points which depend on the order of the B-spline used.

v. In order to obtain errors closer to the AEM-BS and values closer to those of the analytical solution, quadruple collocation points should be employed as nodes in the original AEM.

# Chapter 3

# Chapter 3

# Generalized static and dynamic warping analysis of Straight Beams by Isogeometric Methods

## 3.1 Introduction

The problem of nonuniform torsion (Chapter 2) has been extensively examined in the literature. In an analogy with Timoshenko beam theory, when shear deformation is of importance, the so-called Secondary Torsional Shear Deformation Effect (STSDE) (Mokos and Sapountzakis, 2011; Tsipiras and Sapountzakis, 2012) has to be taken into account as well. Moreover, the additional secondary torsional warping due to STSDE can cause similar effects with shear lag in flexure (Moffatt and Dowling, 1975; Luo and Li, 2000; Luo, Tang and Li, 2003; Malcolm and Redwood, 1970), i.e. a modification of the initial normal stress distribution. Thus, the influence of shear lag phenomenon due to both flexure and torsion, which is not constant along the beam length, should also be considered. It is noted that due to the complicated nature of torsion, simplified concepts employed in up-to-date regulations, such as "effective width", cannot be applied to take into account this behaviour.

In the majority of works made in recent years, the effects of nonuniform shear warping distribution or, in other words, shear lag phenomenon in flexure, have not been extensively considered in the dynamic problems of beams by the inclusion of the corresponding inertia effects (Dikaros et al., 2016). The same case holds for the problem of torsion (Dikaros et al., 2016; Sapountzakis et al., 2016). Even though nonuniform torsion has been examined in the literature (Sapountzakis and Mokos, 2003; Vlasov, 1963; Zhang and Chen, 1991), the STSDE and the corresponding inertia effects, in analogy to the shear lag in flexure, has not yet been investigated in torsional vibration analysis of beams. Thus, the beam element formulations employed in studies of Dikaros et al. (2016) and Sapountzakis et al. (2016) consider the above mentioned warping effects in the dynamic problem. These beam models could be used in a broad range of structural applications, such as automobile, aircraft frames, decks of bridges (under traffic and earthquake loading), high-rise buildings (under blast and wind loading), as well as optics, electromagnetics and acoustics, where high frequencies are more important.

In order to numerically account for the above mentioned phenomena, Boundary Element Methods (BEM) (Dikaros et al., 2016; Katsikadelis, 2002a; Sapountzakis et al., 2016) have in general been used. The additional geometric constants due to warping and the elementary ones are evaluated employing a pure BEM approach, which uses in-

line elements for discretization of the cross section's boundary, instead of area elements used for cross section's domain in Finite Element Methods (FEM), leading to a small number of elements required achieving high accuracy, while remodeling to reflect design changes becomes simpler. In addition to this, although the FEM computes accurately the field functions, which are the unknowns of the problem, it is ineffective in determining their derivatives. However, BEM, such as other numerical methods, is not free of drawbacks. Particularly, application of BEM requires the so-called fundamental solution, as also mentioned in previous chapter. A promising technique that overcomes these drawbacks is the Analog Equation Method (AEM), developed by Katsikadelis (1994, 2002b). This method is employed in order to derive the stiffness and mass matrices (and, thus, the spectrum of frequencies) formulated according to ten boundary value problems with respect to the displacement and rotation components and the independent warping parameters which describe the beam behavior (Dikaros and Sapountzakis, 2014). A fundamental solution is used for a reduced differential operator (where a fundamental solution exists) and any possible remainder of the differential equation is taken into account as fictitious loading (different for each kinematical component), while preserving the geometry of the space under consideration and the boundary conditions (Fotiu and Irschik, 1989; Fotiu, Irschik and Ziegler, 1987; Irschik and Ziegler, 1998).

The introduction of *Isogeometric Analysis* (IGA) in the AEM technique employed for the *generalized static and dynamic warping analysis* of beams is for the first time demonstrated in the literature. The introduction of B-splines, as an initial research step towards the employment of NURBS, in the AEM technique has only been examined in the work of Sapountzakis and Tsiptsis (2014), presented in chapter 2, for the nonuniform torsional static problem of bars. During past years, in order to increase the accuracy, NURBS basis functions were used in the eigenvalue analysis of elastic rods subjected to longitudinal vibrations and Euler-Bernoulli beams subjected to transverse vibrations (Hughes, 2009). In that study, the properties of smooth NURBS functions are examined and, for a given spectrum of frequencies (given number of degrees of freedom and bandwidth) the improved accuracy in spectral calculations over classical finite elements analysis is demonstrated. Recently, novel Isogeometric tools were used in FEM for the vibration analysis of straight nonlinear Euler–Bernoulli beam (Weeger et al., 2013). In addition to this, NURBS were also used for the representation of the geometry and solution fields of wind turbine blades (Bazilevs et al., 2011). Moreover, Isogeometric collocation methods were employed for the Timoshenko beam problem in order to avoid shear locking (Auricchio et al., 2012; Beirão da Veiga et al., 2012; Echter and Bischoff, 2010). In addition to this, improvement of Isogeometric collocation methods regarding convergence rates has been done by using superconvergent points (Anitescu, Jia, Jessica Zhang and Rabczuka, 2015). In a recent software lab project, an Euler-Bernoulli beam was formulated by using B-Splines and compared to the classical FEM with Hermitian polynomials (Tanyildiz and Özcan, 2010). The results showed clearly that Isogeometric analysis with p-refinement feature is far more effective than classical FEM with Hermitian polynomials for a Bernoulli beam. Except for beams, a NURBS-based Isogeometric approach, where the same

shape functions are used to describe the field variables as the geometry of the domain, is employed for static, free vibration, and buckling analysis of laminated composite Reissner-Mindlin plate structures (Chien et al., 2012). Isogeometric tools have also been used in thin shell analysis with excellent performance (Nguyen-Thanh, Kiendl, Nguyen-Xuan, Wüchner, Bletzinger, Bazilevs and Rabczuk, 2011; Nguyen-Thanh, Valizadeh, Nguyen, Nguyen-Xuan, Zhuang, Areias, Zi, Bazilevs, De Lorenzis and Rabczuk, 2015).

In this chapter, the ten boundary value problems that have been formulated in the work of Dikaros and Sapountzakis (2014) with respect to the displacement and rotation components as well as to the independent warping parameters are solved using the AEM with the aid of Isogeometric Analysis (IGA). B-splines are employed in order to represent the fictitious loading. This is the first research step towards formulating curved beam elements subjected to arbitrary loading and boundary conditions. Additionally, Isogeometric analysis' tools are also applied in the general element formulation for the dynamic nonuniform warping analysis of beams of arbitrary cross section, taking into account shear lag effects due to both flexure and torsion, as presented in Dikaros et al. (2016). Without loss of generality, only free vibrations have been examined due to the fact that the calculation of natural frequencies and the spectrum analysis are of main interest. Nonuniform warping effects are taken into account by using four independent warping parameters which are multiplied to the shear warping function in each direction and to two torsional warping functions (primary and secondary). By employing a distributed mass model system accounting for all of the different inertia, ten second-order differential equations and the corresponding boundary conditions have been formed with respect to the displacement components and the independent warping parameters. These equations describe the problem and are solved as quasi-static (time variable is a parameter) either using the analog equation method (AEM), or the finite element method (FEM) combined with Isogeometric analysis. Isogeometric tools (B-splines and NURBS) are employed for the representation of the basis functions and the fictitious loads of the FEM and AEM formulations, respectively, for the ten different kinematical components. The warping functions, the additional geometric constants due to warping, and the elementary ones are evaluated with a pure BEM approach (Dikaros and Sapountzakis, 2014), i.e., only boundary discretization of the cross section is used. The geometric constants are considered equal to unity in some of the examples for comparison and simplicity reasons. Static problem is actually a special case of the dynamic one and is examined separately.

The new computational tool will overcome the drawbacks of AEM related to *geometry* issues. Particularly, the cumbersome procedures need to be applied in order to refine the element mesh and capture satisfactorily the three dimensional curved geometry with straight beam Finite Elements, which are usually used in practice. This approximation causes an additional problem that is the transmission of warping, which in general is not taken into account in the analysis of complex structures. For example, an analysis of the cross section of a bridge should be performed in the transverse direction in order to account for warping. Thus, the next research step is the

employment of Isogeometric tools (B-splines, NURBS etc.) in the order to capture the exact geometry of the beam elements. This allows for an interactive structural analysis to be performed in an automated manner and without the need for an analysis in the transverse direction. Hence, it can be concluded that beam elements should be combined with Isogeometric analysis in order to serve as a useful tool in modern analysis projects (i.e. curved bridges of closed shape sections).

The essential features and novel aspects of the formulation described in this Chapter compared with the corresponding previous ones are summarized as follows:

i.    The proposed formulation is suitable for the investigation of flexural and torsional shear lag effects in beams of arbitrary closed or open cross sections.

ii.   The method used is based on Isogeometric tools such as B-splines and NURBS. These tools have mainly been employed in finite element analyses (FEM) and only sparsely in boundary element methods (BEM), especially in vibration problems of beams. Thus, an introduction of B-splines and NURBS in a BEM-based numerical technique is a natural starting point for the introduction of Isogeometric Analysis in the numerical solution of advanced beam theories with BEM and its extension to curved beam elements (Chapter 4).

iii.  As also mentioned in the novelties of the previous Chapter and being of more importance here due to the number of equations that describe the problem (ten), the dimensions of matrices used for the numerical implementation of AEM become smaller. This results in easier data management and reduction of computational effort.

iv.   Comparing to previous formulation, results have also been obtained for cubic or quartic B-splines employing four or five control points for the representation of the fictitious load, respectively. Therefore, except for knot insertion, a kind of degree elevation has also been investigated known as the k-refinement procedure.

v.    The use of NURBS in AEM results in drastically improved accuracy in spectral calculations over the original AEM, as it is the case with FEM, while AEM gives highly accurate results either original or combined with IGA tools comparing to corresponding FEM formulations.

vi.   Comparisons with traditional models, which account for nonuniform torsion, have been made in order to indicate the range of their application as well as the obtained level of accuracy.

## 3.2  Statement of the problem

Consider a prismatic beam of length $L$, of arbitrarily shaped cross section, that can surround a finite number of inclusions. The material, occupying the region $\Omega$ of the $yz$ plane (Fig. 3.1) is assumed homogeneous, isotropic and linearly elastic with modulus of elasticity $E$, shear modulus $G$ and Poisson ratio $\nu$. However, the formulation can be easily expanded for composite cross sections.

Let also the boundary of the region $\Omega$ be denoted by $\Gamma$. This boundary curve is piecewise smooth, i.e. it may have a finite number of corners. In Fig. 3.1, $CXYZ$ is the

principal bending coordinate system through the cross section's centroid $C$, while $y_C$ $z_C$, are its coordinates with respect to $Sxyz$ system through the cross section's center of twist $S$. The beam is subjected to the combined action of arbitrarily distributed or concentrated, time-dependent in the dynamic case, axial loading $p_x = p_x(X)$ along $X$ direction, transverse loading $p_y = p_y(x)$ and $p_z = p_z(x)$ along the $y$, $z$ directions, respectively, twisting moments $m_t = m_t(x)$ along $x$ direction, bending moments $m_Y = m_Y(x)$, $m_Z = m_Z(x)$, along $Y$, $Z$ directions, respectively, as well as warping moments $m_{\varphi_S^P} = m_{\varphi_S^P}(x)$, $m_{\varphi_S^S} = m_{\varphi_S^S}(x)$, $m_{\varphi_{CY}^P} = m_{\varphi_{CY}^P}(x)$ and $m_{\varphi_{CZ}^P} = m_{\varphi_{CZ}^P}(x)$ (Fig. 3.1) which are defined in the work of Dikaros and Sapountzakis (2014).



(a)



(b)
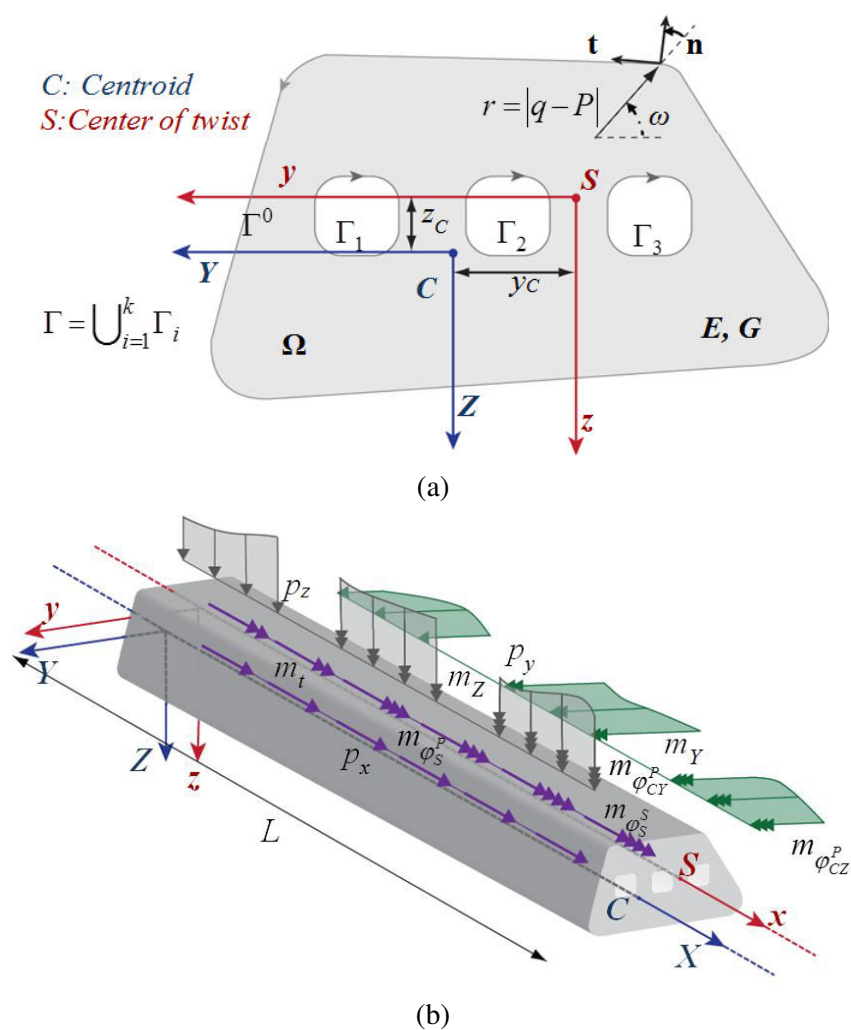
*Figure 3.1.    Prismatic beam under axial-flexural-torsional loading (b) of an arbitrary homogenous cross section occupying the two dimensional region $\Omega$ (a).*

Under the action of the aforementioned general loading and of possible restraints, the beam is leaded to flexural, axial and/or torsional vibrations. In order to take into account the warping rates of change per unit length of the beam at any time instant,

which are responsible for shear lag effects due to both flexure and torsion, four additional time-dependent degrees of freedom (warping parameters), namely $\eta_Y(x,t)$, $\eta_Z(x,t)$, $\eta_x(x,t)$, $\xi_x(x,t)$, are employed as in Dikaros et al. (2016). These additional parameters multiply a shear warping function in each direction ($\varphi_{CY}^P(y,z)$, $\varphi_{CZ}^P(y,z)$) and two torsional warping functions ($\varphi_S^P(y,z)$, $\varphi_S^S(y,z)$), respectively. It is worth here noting that the shear stresses generated by the above displacement considerations exhibit an inconsistency concerning the non-vanishing of tractions on the lateral surface of the beam. This inconsistency may be responsible for non-negligible errors in estimated normal stress values and thus in the present study it is removed by performing a suitable shear stress correction, which is discussed in detail in Dikaros and Sapountzakis (2014).

Within the context of the above considerations, the displacement components of an arbitrary point of the beam at an arbitrary time instant are given as

$$\bar{u}(x,y,z,t) = \bar{u}^P(x,y,z,t) + \bar{u}^S(x,y,z,t) =$$

$$= \underbrace{u(x,t) + \theta_Y(x,t)Z - \theta_Z(x,t)Y + \eta_x(x,t)\phi_S^P(y,z)}_{\text{primary}} +$$

$$+ \underbrace{\eta_Y(x,t)\phi_{CY}^P(y,z) + \eta_Z(x,t)\phi_{CZ}^P(y,z) + \xi_x(x,t)\phi_S^S(y,z)}_{\text{secondary}} \tag{3.1a}$$

$$\bar{v}(x,y,z,t) = v(x,t) - z\theta_x(x,t) \qquad \bar{w}(x,y,z,t) = w(x,t) + y\theta_x(x,t) \tag{3.1b,c}$$

where $\bar{u}$, $\bar{v}$, $\bar{w}$ are the axial and transverse beam displacement components with respect to the $Sxyz$ system of axes; $\bar{u}^P$, $\bar{u}^S$ denote the primary and secondary longitudinal displacements, respectively. Moreover, $v(x,t)$, $w(x,t)$ describe the vertical and lateral deflection of the centre of twist, while $u(x,t)$ denotes the "average" axial displacement of the cross section. $\theta_x(x,t)$ is the (total) angle of twist; $\theta_Z(x,t)$, $\theta_Y(x,t)$ are the angles of rotation due to bending about the centroidal $Y$, $Z$ axes, respectively; $\eta_x(x,t)$, $\xi_x(x,t)$ are the independent warping parameters introduced to describe the nonuniform distribution of primary and secondary torsional warping, while $\eta_Y(x,t)$, $\eta_Z(x,t)$ are the independent warping parameters introduced to describe the nonuniform distribution of primary warping due to shear; $\varphi_S^P(y,z)$, $\varphi_S^S(y,z)$ are the primary and secondary torsional warping functions with respect to the centre of twist,

while $\varphi_{CY}^{P}(y,z)$, $\varphi_{CZ}^{P}(y,z)$ are the primary shear warping functions with respect to the centroid. Finally, it holds that $Z = z - z_C$, $Y = y - y_C$.

Substituting eqns. (3.1) into the well-known three dimensional linear strain-displacement relations, and employing the Hooke's stress-strain law, the non-vanishing components of the Cauchy stress tensor are obtained. The correction of stress components, due to the inconsistency mentioned previously, is performed without increasing the number of global kinematical unknowns, following the analysis presented in Dikaros et al. (2016) as well as in Dikaros and Sapountzakis (2014). To this end, three additional warping functions $\varphi_{CY}^{S}(y,z)$, $\varphi_{CZ}^{S}(y,z)$, $\varphi_{S}^{T}(y,z)$ are introduced in the expressions of stresses.

Defining the independent geometric (derived from displacements) generalized strains $\varepsilon_R$ as $u_{,x}$, $\theta_{Y,x}$, $\theta_{Z,x}$, $\eta_{x,x}$, $\eta_{Y,x}$, $\eta_{Z,x}$, $\xi_{x,x}$, $\gamma_x^P = \theta_{x,x}$, $\gamma_x^S = \eta_x - \theta_{x,x}$, $\gamma_x^T = \xi_x - \eta_x + \theta_{x,x}$, $\gamma_Y^P = v_{,x} - \theta_Z$, $\gamma_Y^S = \eta_Z - v_{,x} + \theta_Z$, $\gamma_Z^P = w_{,x} + \theta_Y$ and $\gamma_Z^S = \eta_Y - w_{,x} - \theta_Y$, deriving the stress resultants $\sigma_R$ after establishing the stress components, substituting the generalized strains and stress resultants in the two field variational principle $\pi_R = \int_L \left( -1/2\varepsilon_R^T C \varepsilon_R + \sigma_R^T \varepsilon_R \right) dx - W$ and following standard arguments in the calculus of variations, results in the governing differential equations of equilibrium of the beam problem. $C$ is the spatial elasticity tensor (containing i.e. cross section rigidities) and $W$ is the external work for distributed or end loads. Finally, in order to derive the differential equations of motion with respect to the kinematical components, the terms of inertia contributions $\int_L \left( 1/2 u_{R,tt}^T M u_{R,tt} \right) dx$ have to be added in the previous and constitutive equations to be employed. $M$ is the spatial mass matrix and $u_R$ are the generalized displacements (kinematical components) previously described. Thus, the generalized vibrational beam behaviour is described by the following differential equations (Dikaros et al., 2016)

$$-E^* A u_{,xx} + \underbrace{\rho A u_{,tt}}_{\text{inertial contribution}} = p_x \tag{3.2a}$$

$$-G\left(A_Y^P + A_Y^S\right)\left(v_{,xx} - \theta_{Z,x}\right) + GA_Y^S \eta_{Z,x} + G\left(D_{\Phi_{CZ}^S \Phi_S^S} - D_{\Phi_{CZ}^S \Phi_S^T}\right)\left(\eta_{x,x} - \theta_{x,xx}\right) +$$
$$+GD_{\Phi_{CZ}^S \Phi_S^T}\xi_{x,x} + \underbrace{\rho A\left(v_{,tt} - z_C \theta_{x,tt}\right)}_{\text{inertial contribution}} = p_y \tag{3.2b}$$

$$-G\left(A_Z^P + A_Z^S\right)\left(w_{,xx} + \theta_{Y,x}\right) + GA_Z^S \eta_{Y,x} + G\left(D_{\Phi_{CY}^S \Phi_S^S} - D_{\Phi_{CY}^S \Phi_S^T}\right)\left(\eta_{x,x} - \theta_{x,xx}\right) +$$
$$+GD_{\Phi_{CY}^S \Phi_S^T}\xi_{x,x} + \underbrace{\rho A\left(w_{,tt} + y_C \theta_{x,tt}\right)}_{\text{inertial contribution}} = p_z \tag{3.2c}$$

$$-E^* I_{ZZ}\theta_{Z,xx} - G\left(A_Y^P + A_Y^S\right)\left(v_{,x} - \theta_Z\right) + GA_Y^S\eta_Z + G\left(D_{\Phi_{CZ}^S\Phi_S^S} - D_{\Phi_{CZ}^S\Phi_S^T}\right)\left(\eta_x - \theta_{x,x}\right) +$$

$$+ GD_{\Phi_{CZ}^S\Phi_S^T}\xi_x + \underbrace{\rho I_{ZZ}\theta_{Z,tt}}_{\text{inertial contribution}} = m_Z \qquad (3.2\text{d})$$

$$-E^* I_{YY}\theta_{Y,xx} + G\left(A_Z^P + A_Z^S\right)\left(w_{,x} + \theta_Y\right) - GA_Z^S\eta_Y - G\left(D_{\Phi_{CY}^S\Phi_S^S} - D_{\Phi_{CY}^S\Phi_S^T}\right)\left(\eta_x - \theta_{x,x}\right) -$$

$$- GD_{\Phi_{CY}^S\Phi_S^T}\xi_x + \underbrace{\rho I_{YY}\theta_{Y,tt}}_{\text{inertial contribution}} = m_Y \qquad (3.2\text{e})$$

$$-G\left(I_t^P + I_t^S + I_t^T\right)\theta_{x,xx} + G\left(I_t^S + I_t^T\right)\eta_{x,x} - GI_t^T\xi_{x,x} +$$

$$+ G\left(D_{\Phi_{CZ}^S\Phi_S^S} - D_{\Phi_{CZ}^S\Phi_S^T}\right)\left(\eta_{Z,x} - v_{,xx} + \theta_{Z,x}\right) + G\left(D_{\Phi_{CY}^S\Phi_S^S} - D_{\Phi_{CY}^S\Phi_S^T}\right)\cdot$$

$$\cdot\left(\eta_{Y,x} - w_{,xx} - \theta_{Y,x}\right) + \underbrace{\rho\left[A\left(-z_C v_{,tt} + y_C w_{,tt}\right) + I_p\theta_{x,tt}\right]}_{\text{inertial contribution}} = m_t \qquad (3.2\text{f})$$

$$-E^*\left(I_{\varphi_{CZ}^P\varphi_S^P}\eta_{x,xx} + I_{\varphi_{CZ}^P\varphi_{CZ}^P}\eta_{Z,xx} + I_{\varphi_{CZ}^P\varphi_S^S}\xi_{x,xx}\right) + GA_Y^S\left(\eta_Z - v_{,x} - \theta_Z\right) +$$

$$+ G\left(D_{\Phi_{CZ}^S\Phi_S^S} - D_{\Phi_{CZ}^S\Phi_S^T}\right)\left(\eta_x - \theta_{x,x}\right) + GD_{\Phi_{CZ}^S\Phi_S^T}\xi_x +$$

$$+ \underbrace{\rho\left(I_{\varphi_{CZ}^P\varphi_S^P}\eta_{x,tt} + I_{\varphi_{CZ}^P\varphi_S^S}\xi_{x,tt} + I_{\varphi_{CZ}^P\varphi_{CZ}^P}\eta_{Z,tt}\right)}_{\text{inertial contribution}} = m_{\varphi_{CZ}^P} \qquad (3.2\text{g})$$

$$-E\left(I_{\varphi_{CY}^P\varphi_S^P}\eta_{x,xx} + I_{\varphi_{CY}^P\varphi_{CY}^P}\eta_{Y,xx} + I_{\varphi_{CY}^P\varphi_S^S}\xi_{x,xx}\right) + GA_Z^S\left(\eta_Y - w_{,x} + \theta_Y\right) +$$

$$+ G\left(D_{\Phi_{CY}^S\Phi_S^S} - D_{\Phi_{CY}^S\Phi_S^T}\right)\left(\eta_x - \theta_{x,x}\right) + GD_{\Phi_{CY}^S\Phi_S^T}\xi_x +$$

$$+ \underbrace{\rho\left(I_{\varphi_{CY}^P\varphi_S^P}\eta_{x,tt} + I_{\varphi_{CY}^P\varphi_S^S}\xi_{x,tt} + I_{\varphi_{CY}^P\varphi_{CY}^P}\eta_{Y,tt}\right)}_{\text{inertial contribution}} = m_{\varphi_{CY}^P} \qquad (3.2\text{h})$$

$$-E^*\left(I_{\varphi_S^P\varphi_S^P}\eta_{x,xx} + I_{\varphi_{CY}^P\varphi_S^P}\eta_{Y,xx} + I_{\varphi_{CZ}^P\varphi_S^P}\eta_{Z,xx}\right) + G\left(I_t^S + I_t^T\right)\left(\eta_x - \theta_{x,x}\right) - GI_t^T\xi_x +$$

$$+ G\left(D_{\Phi_{CZ}^S\Phi_S^S} - D_{\Phi_{CZ}^S\Phi_S^T}\right)\left(\eta_Z - v_{,x} + \theta_Z\right) + G\left(D_{\Phi_{CY}^S\Phi_S^S} - D_{\Phi_{CY}^S\Phi_S^T}\right)\cdot$$

$$\cdot\left(\eta_Y - w_{,x} - \theta_Y\right) + \underbrace{\rho\left(I_{\varphi_S^P\varphi_S^P}\eta_{x,tt} + I_{\varphi_{CY}^P\varphi_S^P}\eta_{Y,tt} + I_{\varphi_{CZ}^P\varphi_S^P}\eta_{Z,tt}\right)}_{\text{inertial contribution}} = m_{\varphi_S^P} \qquad (3.2\text{i})$$

$$-E^*\left(I_{\varphi_{CY}^P\varphi_S^S}\eta_{Y,xx} + I_{\varphi_{CZ}^P\varphi_S^S}\eta_{Z,xx} + I_{\varphi_S^S\varphi_S^S}\xi_{x,xx}\right) + GI_t^T\left(\xi_x - \eta_x + \theta_{x,x}\right) +$$

$$+ GD_{\Phi_{CZ}^S\Phi_S^T}\left(\eta_Z - v_{,x} + \theta_Z\right) + GD_{\Phi_{CY}^S\Phi_S^T}\left(\eta_Y - w_{,x} - \theta_Y\right) +$$

$$+ \underbrace{\rho\left(I_{\varphi_S^S\varphi_S^S}\xi_{x,tt} + I_{\varphi_{CY}^P\varphi_S^S}^\rho\eta_{Y,tt} + I_{\varphi_{CZ}^P\varphi_S^S}^\rho\eta_{Z,tt}\right)}_{\text{inertial contribution}} = m_{\varphi_S^S} \qquad (3.2\text{j})$$

These governing differential equations are subjected to the initial conditions $(x = 0, L)$ given below (eqns. (3.3a)-(3.3t)) together with the corresponding boundary conditions of the problem, which are described by the following eqns. (3.4a)-(3.4j) at the beam ends $x = 0, L$,

$$u(x,0) = u_0(x) \qquad\qquad u_{,t}(x,0) = u_{0,t}(x) \tag{3.3a,b}$$

$$v(x,0) = v_0(x) \qquad\qquad v_{,t}(x,0) = v_{0,t}(x) \tag{3.3c,d}$$

$$w(x,0) = w_0(x) \qquad\qquad w_{,t}(x,0) = w_{0,t}(x) \tag{3.3e,f}$$

$$\theta_Z(x,0) = \theta_{Z0}(x) \qquad\qquad \theta_{Z,t}(x,0) = \theta_{Z0,t}(x) \tag{3.3g,h}$$

$$\theta_Y(x,0) = \theta_{Y0}(x) \qquad\qquad \theta_{Y,t}(x,0) = \theta_{Y0,t}(x) \tag{3.3i,j}$$

$$\theta_x(x,0) = \theta_{x0}(x) \qquad\qquad \theta_{x,t}(x,0) = \theta_{x0,t}(x) \tag{3.3k,l}$$

$$\eta_Z(x,0) = \eta_{Z0}(x) \qquad\qquad \eta_{Z,t}(x,0) = \eta_{Z0,t}(x) \tag{3.3m,n}$$

$$\eta_Y(x,0) = \eta_{Z0}(x) \qquad\qquad \eta_{Y,t}(x,0) = \eta_{Y0,t}(x) \tag{3.3o,p}$$

$$\eta_x(x,0) = \eta_{x0}(x) \qquad\qquad \eta_{x,t}(x,0) = \eta_{x0,t}(x) \tag{3.3q,r}$$

$$\xi_x(x,0) = \xi_{x0}(x) \qquad\qquad \xi_{x,t}(x,0) = \xi_{x0,t}(x) \tag{3.3s,t}$$

$$a_1 u + \alpha_2 N_b = \alpha_3 \tag{3.4a}$$

$$\beta_1 v + \beta_2 V_{by} = \beta_3 \qquad\qquad \gamma_1 w + \gamma_2 V_{bz} = \gamma_3 \tag{3.4b,c}$$

$$\bar{\beta}_1 \theta_Z + \bar{\beta}_2 M_{bZ} = \bar{\beta}_3 \qquad\qquad \bar{\gamma}_1 \theta_Y + \bar{\gamma}_2 M_{bY} = \bar{\gamma}_3 \tag{3.4d,e}$$

$$\tilde{\beta}_1 \eta_Z + \tilde{\beta}_2 M_{b\varphi_{CZ}^P} = \tilde{\beta}_3 \qquad\qquad \tilde{\gamma}_1 \eta_Y + \tilde{\gamma}_2 M_{b\varphi_{CY}^P} = \tilde{\gamma}_3 \tag{3.4f,g}$$

$$\delta_1 \theta_x + \delta_2 M_{bt} = \delta_3 \qquad \bar{\delta}_1 \eta_x + \bar{\delta}_2 M_{b\varphi_S^P} = \bar{\delta}_3 \qquad \tilde{\delta}_1 \xi_x + \tilde{\delta}_2 M_{b\varphi_S^S} = \tilde{\delta}_3 \tag{3.4h,i,j}$$

where the reaction forces $N_b$, $V_{by} = Q_y^P + Q_y^S$, $V_{bz} = Q_z^P + Q_z^S$, $M_{bZ}$, $M_{bY}$, $M_{b\varphi_{CY}^P}$,

$M_{b\varphi_{CZ}^P}$, $M_{bt} = M_t^P + M_t^S + M_t^T$, $M_{b\varphi_S^P}$, $M_{b\varphi_S^S}$ are given by the following relations in

terms of the kinematical components as

$$N_b = E_{\text{ref}} A u_{,x} \qquad\qquad M_{bY} = E_{\text{ref}} I_{YY} \theta_{Y,x} \qquad\qquad M_{bZ} = E_{\text{ref}} I_{ZZ} \theta_{Z,x} \qquad (3.5\text{a,b,c})$$

$$M_{b\varphi_S^P} = E_{\text{ref}} \left( I_{\varphi_S^P \varphi_S^P} \eta_{x,x} + I_{\varphi_{CY}^P \varphi_S^P} \eta_{Y,x} + I_{\varphi_{CZ}^P \varphi_S^P} \eta_{Z,x} \right) \qquad (3.5\text{d})$$

$$M_{b\varphi_S^S} = E_{\text{ref}} \left( I_{\varphi_{CY}^P \varphi_S^S} \eta_{Y,x} + I_{\varphi_{CZ}^P \varphi_S^S} \eta_{Z,x} + I_{\varphi_S^S \varphi_S^S} \xi_{x,x} \right) \qquad (3.5\text{e})$$

$$M_{b\varphi_{CY}^P} = E_{\text{ref}} \left( I_{\varphi_{CY}^P \varphi_S^P} \eta_{x,x} + I_{\varphi_{CY}^P \varphi_{CY}^P} \eta_{Y,x} + I_{\varphi_{CY}^P \varphi_S^S} \xi_{x,x} \right) \qquad (3.5\text{f})$$

$$M_{b\varphi_{CZ}^P} = E_{\text{ref}} \left( I_{\varphi_{CZ}^P \varphi_S^P} \eta_{x,x} + I_{\varphi_{CZ}^P \varphi_{CZ}^P} \eta_{Z,x} + I_{\varphi_{CZ}^P \varphi_S^S} \xi_{x,x} \right) \qquad (3.5\text{g})$$

$$Q_y^P = G_{\text{ref}} D_{\Phi_{CZ}^P \Phi_{CZ}^P} \gamma_Y^P \quad\quad Q_y^S = -G_{\text{ref}} \left( D_{\Phi_{CZ}^S \Phi_{CZ}^S} \gamma_Y^S + D_{\Phi_{CZ}^S \Phi_S^S} \gamma_x^S + D_{\Phi_{CZ}^S \Phi_S^T} \gamma_x^T \right) \qquad (3.5\text{h,i})$$

$$Q_z^P = G_{\text{ref}} D_{\Phi_{CY}^P \Phi_{CY}^P} \gamma_Z^P \quad\quad Q_z^S = -G_{\text{ref}} \left( D_{\Phi_{CY}^S \Phi_{CY}^S} \gamma_Z^S + D_{\Phi_{CY}^S \Phi_S^S} \gamma_x^S + D_{\Phi_{CY}^S \Phi_S^T} \gamma_x^T \right) \qquad (3.5\text{j,k})$$

$$M_t^P = G_{\text{ref}} I_t^P \theta_{x,x} \qquad\qquad M_t^S = -G_{\text{ref}} \left( D_{\Phi_S^S \Phi_S^S} \gamma_x^S + D_{\Phi_{CZ}^S \Phi_S^S} \gamma_Y^S + D_{\Phi_{CY}^S \Phi_S^S} \gamma_Z^S \right) \qquad (3.5\text{l,m})$$

$$M_t^T = G_{\text{ref}} \left( D_{\Phi_S^T \Phi_S^T} \gamma_x^T + D_{\Phi_{CZ}^S \Phi_S^T} \gamma_Y^S + D_{\Phi_{CY}^S \Phi_S^T} \gamma_Z^S \right) \qquad (3.5\text{n})$$

The quantities $GD_{ii}$ ($i = \Phi_{CY}^P, \Phi_{CZ}^P$) multiplying $\gamma_Z^P$ and $\gamma_Y^P$ respectively, correspond to the shear rigidities of Timoshenko beam theory. Thus, the simplified notation $GA_i^P$ ($i = Z, Y$) could be adopted for these quantities. Similarly, $GD_{ii}$ ($i = \Phi_{CY}^S, \Phi_{CZ}^S$) refer to the secondary shear rigidities due to nonuniform shear warping and can be denoted as $GA_i^S$ ($i = Z, Y$). Finally, $GD_{ii}$ ($i = \Phi_S^S, \Phi_S^T$) refer to the secondary (Tsipiras and Sapountzakis, 2012) and tertiary torsional rigidities and can be also denoted as $G_{\text{ref}} I_t^S$, $G_{\text{ref}} I_t^T$, respectively.

The evaluation of the above mentioned rigidities presumes the establishment of the warping functions due to shear $\Phi_{CY}^P$, $\Phi_{CZ}^P$, $\Phi_{CY}^S$, $\Phi_{CZ}^S$ and due to torsion $\varphi_S^P$, $\Phi_S^S$ , $\Phi_S^T$, which is presented in detail in Dikaros and Sapountzakis (2014). The warping

functions in each direction are considered to be independent. This means that when bending is considered, pure axial and torsional are excluded. Local equilibrium equation in the longitudinal direction can be written as follows

$$\sigma_{xx,x} + \tau_{xy,y} + \tau_{xz,z} = 0 \Rightarrow$$
$$\left( E_{ref}\theta_Y Z \right)_{,y} + \left( G_{ref}\gamma_Z^P \Phi_{CY,y}^P \right)_{,y} + \left( G_{ref}\gamma_Z^P \Phi_{CY,z}^P \right)_{,z} = 0$$

(3.6)

recalling eqns. (3.5b), (3.5j) and $-M_{bY,x} + Q_Z^P = m_Y = 0$ eqn. (3.6) can be written as

$$\frac{M_{bY,x}}{I_{YY}} Z + G_{ref}\gamma_Z^P \left( \Phi_{CY,yy}^P + \Phi_{CY,zz}^P \right) = 0 \Rightarrow$$

(3.7)

$$G_{ref}\gamma_Z^P \frac{A_Z^P}{I_{YY}} Z + G_{ref}\gamma_Z^P \nabla^2 \Phi_{CY}^P = 0 \Rightarrow \nabla^2 \Phi_{CY}^P = -\frac{A_Z^P}{I_{YY}} Z \Rightarrow -\frac{I_{YY}}{A_Z^P} \nabla^2 \Phi_{CY}^P = Z$$

where $\bar{\Phi}_{CY}^P = -\frac{I_{YY}}{A_Z^P} \Phi_{CY}^P$. Following this concept, the rest of the warping functions can also be established.

Finally, $\alpha_k$, $\beta_k$, $\bar{\beta}_k$, $\tilde{\beta}_k$ $\gamma_k$, $\bar{\gamma}_k$, $\tilde{\gamma}_k$, $\delta_k$, $\bar{\delta}_k$, $\tilde{\delta}_k$ $(k=1,2,3)$ are functions specified at the boundaries of the beam ($x=0,L$). The boundary conditions (3.4) are the most general boundary conditions for the problem at hand, including also the elastic support. It is apparent that all types of the conventional boundary conditions (clamped, simply supported, free or guided edge) can be derived from these equations by specifying appropriately these functions (e.g. for a clamped edge it is $\alpha_1 = \beta_1 = \bar{\beta}_1 = \tilde{\beta}_1 = \gamma_1 = \bar{\gamma}_1 = \tilde{\gamma}_1 = \delta_1 = \bar{\delta}_1 = \tilde{\delta}_1 = 1$ , $\alpha_2 = \alpha_3 = \beta_2 = \beta_3 = \bar{\beta}_2 = \bar{\beta}_3 = \tilde{\beta}_2$ $= \tilde{\beta}_3 = \gamma_2 = \bar{\gamma}_3 = \tilde{\gamma}_2 = \tilde{\gamma}_3 = \delta_2 = \delta_3 = \bar{\delta}_2 = \bar{\delta}_3 = \tilde{\delta}_2 = \tilde{\delta}_3 = 0$).

## 3.3  Numerical Solution with AEM-Integral Representations

According to the precedent analysis, the axial-flexural-torsional static and dynamic analysis of beams of arbitrary cross section including generalized warping effects reduces in establishing the components $u(x,t)$, $v(x,t)$, $w(x,t)$, $\theta_x(x,t)$, $\theta_Z(x,t)$, $\theta_Y(x,t)$, $\eta_x(x,t)$, $\eta_Y(x,t)$, $\eta_Z(x,t)$ and $\xi_x(x,t)$ having continuous derivatives up to the second order with respect to $x$ at the interval $(0,l)$ and up to the first order at $x=0,L$ and for the dynamic problem up to the second order with respect to $t$, satisfying the initial-boundary value problem described by the coupled governing differential equations along the beam, the initial conditions and the boundary conditions at the beam ends $x=0,L$ given in the previous section.

Eqns. (3.2), (3.3) and (3.4) can be solved using the Analog Equation Method. According to this method, let $u(x,t)$, $v(x,t)$, $w(x,t)$, $\theta_x(x,t)$, $\theta_Z(x,t)$, $\theta_Y(x,t)$,

$\eta_x(x,t)$,  $\eta_Y(x,t)$,  $\eta_Z(x,t)$ and  $\xi_x(x,t)$ be the sought solutions of the aforementioned problem. Setting as $u_1(x,t) = u(x,t)$, $u_2(x,t) = v(x,t)$, $u_3(x,t) = w(x,t)$, $u_4(x,t) = \theta_x(x,t)$, $u_5(x,t) = \theta_Y(x,t)$, $u_6(x,t) = \theta_Z(x,t)$, $u_7(x,t) = \eta_x(x,t)$ $u_8(x,t) = \eta_Y(x,t)$, $u_9(x,t) = \eta_Z(x,t)$ and $u_{10}(x,t) = \xi_x(x,t)$ and differentiating with respect to $x$ these functions two times, respectively, yields

$$\frac{d^2 u_i(x,t)}{dx^2} = q_i(x,t), \quad (i = 1,...,10) \tag{3.8}$$

where $q(x)$ is the fictitious load.

Eqns. (3.8) are quasi-static, i.e. the time variable appears as a parameter and they indicate that the solution of eqns. (3.2), (3.3) and (3.4) can be established by solving eqns. (3.8) under the same boundary conditions, provided that the fictitious load distributions $q_i(x,t)$ ($i = 1,...,10$) are first established (Appendix A.1). These distributions can be determined using AEM. The fundamental solution of eqn. (3.8) is a partial solution of the differential equation (A.1.32) given in the Appendix A.1, where instead of $u^*(x,\xi)$. Employing this fundamental solution, the integral representations of the kinematical components are obtained as in eqn. (A.1.34) and by its differentiation, the expressions for their first derivative can be derived as in eqn. (A.1.36).

The introduction of B-splines or NURBS in the above mentioned expressions can now be done by substituting $q_i(x,t)$ with the polynomial representation of a quadratic B-spline or NURBS with a uniform knot vector $\Xi$ with $\xi_i \in [0,1]$ (Appendix A.2), which is the parameter space similar to the classic FE subdivision. The first and last knot values are repeated depending on the B-spline degree $p$ and their multiplicity is usually $p+1$. In one dimension, basis functions formed are interpolatory at the ends of the parameter space interval (knot vector with multiplicities). However, nonuniform knot vectors and repeated knots can also be used with NURBS. According to Piegel and Tiller (1997), the NURBS basis functions can be expressed in terms of B-splines basis defined in the Appendix A.2 by the Cox-De Boor recursive formula.

Now $q_i(x,t)$, which is given in eqn. (A.2.30), is substituted in eqn. (A.1.39) and the vector $\{T\}$ can be written as follows

$$\{T\} = \begin{bmatrix} [0] \\ -[F_2] \end{bmatrix} \{P\} \rightarrow \{T\} = [F]\{P\} \tag{3.9}$$

where $\{P\}$ is the 3X1 vector containing the control points ($\{P\} = \begin{bmatrix} P_0 & P_1 & P_2 \end{bmatrix}^T$) for a quadratic B-spline. Subsequently, applying the integral representations (A.1.34) and

(A.1.36) at the collocation points presented in Fig. A.2.1, the following relations are derived, similarly to eqns. (A.1.47)

$$\{U_i\} = [A]\{P_i\} + [C]\{u_i\}$$
(3.10a)

$$\{U_i'\} = [A']\{P_i\} + [C']\{u_i\}$$
(3.10b)

where $(U_i, U_i')$ are the vectors containing the values of different kinematical components and their first derivative at internal collocation points with respect to the control points. The coefficients of the 3X3 square matrices $[A], [A']$ (eqns. (A.1.48)) are also given with respect to the vector of the control points for each kinematical component. For the rest of the AEM matrices, eqns. (A.1.49)-(A.1.52) are employed.

Then, the stiffness and mass matrices of the beam element which behavior is described by eqns. (3.2) can be calculated. These equations in matrix form are given as

$$[m_t]\{\ddot{U}_i\} + [k_t]\{\bar{U}_i\} = \{p_t\}$$
(3.11)

$[m_t], [k_t]$ are the generalized mass and stiffness matrices, respectively. $\{p_t\}$ is the load vector which is equal to $\{0\}$ for the free vibration case examined in this chapter. Static problem can be derived as a special case of this relation. Thus, $\{D\}$ vector is equal to $\{0\}$. $\{\ddot{U}_i\}$ is the vector containing the second derivatives of the different kinematical components with respect to time (in static case $\{\ddot{U}_i\} = \{0\}$) while $\{\bar{U}_i\}$ is the generalized unknown vector containing $\{U_i\}$ and $\{U_i'\}$ vectors. Thus, eqn. (3.11) can be re-written as follows

$$[m_t][B]\{\ddot{q}_t\} + [k_t][\bar{B}]\{q_t\} = \{0\}$$
(3.12)

where $\{\ddot{q}_t\}$ and $\{q_t\}$ are the values of the control points when AEM is combined with B-splines or NURBS while $[\bar{B}]$ contains the $[B]$ and $[B']$ matrices. It should be noted here that $\{\ddot{q}_t\}$ and $\{q_t\}$ no longer stand for fictitious loads, as in the original form of AEM, but for control points, the number of which depends on the B-spline's or NURBS's structure.

Regarding the dynamic problem, the interest is in the natural frequencies and modes in which the beam vibrates for the different motions. These are obtained by separation of variables and $u_i(x,t)$ is assumed to have the form

$$u_i(x,t) = u_i(x)e^{i\omega t}$$
(3.13)

where $u_i(x)$ is a function of only the spatial variable $x$, while $i = \sqrt{-1}$, and $\omega$ is the natural frequency. Inserting (13) into (11) (thus, into (12)) and dividing by the common exponential term results in the following typical generalized eigenvalue problem

$$\left( [k_t] - \omega^2 [m_t] \right) u_i = \{0\} \tag{3.14}$$

which can be tackled through any solver.

The same process, as described above, has been followed when substituting  with the polynomial representation of cubic or quartic B-splines and NURBS with uniform knot vectors (Appendix A.2).

The rest of the AEM equations are formulated as previously described for the quadratic B-spline. The diagonal matrix $[A_0]$ is also determined and contains the values of basis functions $N_{i,j}$ $(i = 1...n \;\; and \;\; j = 2...p)$ for the $n$ different collocation points and different $p$-degree B-spline cases. This matrix is employed in order to discretize the second order terms (actually the $q_i(x,t)$) of the governing differential equations (for lower order terms the matrices in eqns. (A.1.51) and (A.1.52) are employed). Then, $[m_t], [k_t]$ are formulated and eqn. (3.14) is solved. The natural frequencies are finally obtained. Matrices $[A, A']$, $[F]$ and $[B, B']$ as they have been formed after the integration of quadratic B-splines in the relevant integrals are 30X30, 40X30 and 30X30, respectively. Similarly the same matrices are 40X40, 40X40 and 40X40, respectively, in the case of cubic B-splines. The vector (4X10)X1 of the control points substitutes the fictitious load vector of the original AEM. In the same way, eqns. (3.2) yield a linear system of equations which gives the values of the control points $P_{0i}$, $P_{1i}, P_{2i}, P_{3i}$ and $P_{4i}$, instead of the values of the quartic $q_i(x)$ at collocation points. The diagonal matrix $[A_0]$ contains now the values of basis functions $N_{0,4}, N_{1,4}, N_{2,4}, N_{3,4}$ and $N_{4,4}$ for the five collocation points. Finally, in case of a quartic B-splines, matrices $[A, A']$, $[F]$ and $[B, B']$ are 50X50, 40X50 and 50X50, respectively. The dimension of the new control point vector is (5X10)X1.

## 3.4 Numerical Solution with FEM and NURBS

Instead of B-splines, NURBS curves in terms of B-spline basis functions can be employed either in FEM or AEM. The description of the numerical procedures is given in the Appendix A.2.

In this chapter, the geometry of the beam is described by a NURBS structure with initial control points given by the following spatial coordinates $(x_i, y_i, z_i, w_i)$: (0, 0, 0, 1), $(\dfrac{L}{2}, 0, 0, 1)$, ($L$, 0, 0, 1), and the straight beam geometry is obtained in this way.

$[m_t], [k_t]$ matrices can finally be obtained following the procedures described in section A.2.4 of the Appendix A.2.

It is important to note here that regarding pre-processing (geometry, materials, cross-sectional constants, definition of the initial NURBS' structure and meshes for the different unknowns), there are no important differences between the AEM and FEM with NURBS integrated. However, during processing more matrices with smaller dimensions (depending on the number of the unknowns) need to be assembled and handled in the iterative loops of the FEM comparing to the AEM in order to derive global stiffness and mass matrices (this is due to the different discretizing procedure of the differential equations). Thus, even though final AEM stiffness and mass matrices are larger in dimensions, computational effort is similar for both FEM and AEM with NURBS. In addition to this, accuracy of the results becomes higher for the AEM due to the fact that the second order derivatives of the unknowns (fictitious loads) are approximated in the AEM technique with NURBS (see in the dynamic examples' section where comparisons are provided). Finally, post-processing becomes easier when employing AEM due to the fact that the derivatives of the unknowns have been calculated during processing.

## 3.5  Numerical examples

On the basis of the numerical procedures presented in the previous sections, computer programs have been written and representative examples have been studied. AEM (either in its original form or with Isogeometric tools integrated), FEM and IGA have been employed and compared with respect to computational effort and accuracy in the evaluation of different quantities either for the static or the dynamic case. It should be noted here that the same hardware and software have been used in order to obtain the numerical results.

Regarding the static problem, the numerical results have been obtained employing up to 400 nodal points (NP) in the original AEM with constant values for the fictitious loads. Then, the results when employing collocation points (CP) in the B-spline AEM (Quadratic, Cubic and Quartic B-spline AEM) and nodal points in the original AEM are compared with the previous ones as well as, with the results obtained by the application of the Finite Element Method  (FEM) employing either beam, shell or solid elements (FEMAP, 2010). In some of the examples, the obtained results have been compared with the corresponding values derived by the Euler-Bernoulli, Vlasov thin-walled and classical nonuniform torsion (CNT) (Sapountzakis and Tsiptsis, 2014) beam theories. In the classical nonuniform torsion theory, described in Chapter 2, AEM is employed in order to solve the fourth-order differential equation with respect to the angle of twist of the cross section. In addition to these, up to 400 boundary elements depending on the cross section type (cross sectional discretization) have been employed in order to evaluate the geometric constants.

Regarding the dynamic problem, natural frequencies and spectrum analysis for the free vibration problem of beams (frequently encountered in structures) including warping effects are examined. Except for constant (AEM), quadratic elements have been also used in the AEM technique (AEM 2nd). The "AEM 2nd", which is mainly used in this work, has been described in Appendix A.1. In addition to this, a

commercial FEM package with solid and shell modelling capabilities (FEMAP, 2010) is employed to compare and verify the results of the proposed method.

### 3.5.1 Static Case

#### Example 1: Beam of Rectangular cross section subjected to uniformly distributed transverse or torsional loading

In the first example, a steel ($E = 2.1E8kPa$, $v = 0.3$) beam of rectangular cross section ($h = 0.5m$, $b = 0.2m$) with its edges subjected to various boundary conditions (fixed-fixed, fixed-free, fixed-pinned) and of length $L = 3m$ has been studied. The beam is loaded along its length by a uniformly distributed either transverse load $p_z = 250kN/m$ or twisting moment $m_t = 100kNm/m$. In Table 3.1 the geometric constants of the beam are presented.

$$A = 1.0000E - 01\, m^2 \qquad I_{\varphi_S^S \varphi_S^S} = 7.9582E - 07\, m^6$$

$$I_{ZZ} = 8.3333E - 05\, m^4 \qquad I_{\varphi_{CY}^P \varphi_S^P} = 0.0000E00\, m^5$$

$$I_{YY} = 8.3333E - 03\, m^4 \qquad I_{\varphi_{CY}^P \varphi_S^S} = 1.5127E - 15\, m^5$$

$$I_{\varphi_{CY}^P \varphi_{CY}^P} = 9.9153E - 05\, m^4 \qquad A_Y^P = 8.3218E - 02\, m^2$$

$$A_Z^S = 7.8539E - 03\, m^2 \qquad I_t^P = 3.1227E - 04\, m^4$$

$$I_t^S = 6.7341E - 03\, m^4 \qquad I_t^T = 9.6591E - 05\, m^4$$

$$D_{\Phi_{CY}^S \Phi_S^S} = 1.3327E - 12\, m^3 \qquad D_{\Phi_{CY}^S \Phi_S^T} = 8.0228E - 12\, m^3$$

$$I_{\varphi_{CZ}^P \varphi_S^S} = 0.0000E00\, m^5 \qquad I_{\varphi_{CZ}^P \varphi_S^P} = 0.0000E00\, m^5$$

$$I_{\varphi_{CZ}^P \varphi_{CZ}^P} = 9.6854E - 07\, m^4 \qquad A_Z^P = 8.3331E - 02\, m^2$$

$$D_{\Phi_{CZ}^S \Phi_S^S} = 0.0000E00\, m^3 \qquad D_{\Phi_{CZ}^S \Phi_S^T} = 1.1313E - 15\, m^3$$

$$I_{\varphi_S^P \varphi_S^P} = 6.6430E - 06\, m^6 \qquad A_Y^S = 8.1575E - 04\, m^2$$

*Table 3.1. Geometric constants of the beam of example 1.*

In Table 3.2 the kinematical components along the beam length with fixed end conditions are presented for i) three elements employing original AEM technique (AEM3), ii) three collocation points employing AEM with quadratic B-spline and iii) 400 elements employing original AEM technique (AEM400). From this table, it is obvious that in general the discrepancies between the AEM400 and the obtained results employing a quadratic B-spline are quite small compared with the ones obtained when employing the AEM3. However, a finer discretization is needed. Additionally, in Figures 3.2, 3.3 and 3.4 the deflection $w(x)$ along the beam length with various boundary conditions is presented for i) 201 discretization elements employing original

| | AEM (400 NP) (1) | AEM-BS (3 CP) (2) | AEM(3 NP) (3) | Error % (1)-(2) | Error % (1)-(3) |
|---|---|---|---|---|---|
| $w'(0.50)$ | -6.645E-05 | -6.644E-05 | -4.220E-05 | 0.01 | 36.49 |
| $w'(1.50)$ | 0.000E-00 | 0.000E-00 | 0.000E-00 | 0.00 | 0.00 |
| $\theta_y(0.50)$ | 2.987E-05 | 2.977E-05 | 1.890E-05 | 0.33 | 36.72 |
| $\theta_y(1.50)$ | 0.000E-00 | 0.000E-00 | 0.000E-00 | 0.00 | 0.00 |
| $\theta_y'(0.50)$ | 1.697E-05 | 1.785E-05 | 1.512E-05 | 5.18 | 10.90 |
| $\theta_y'(1.50)$ | -5.357E-05 | -5.357E-05 | -3.024E-05 | 0.00 | 43.55 |
| $\eta_y(0.50)$ | -3.306E-05 | -3.168E-05 | -2.012E-05 | 4.17 | 39.14 |
| $\eta_y(1.50)$ | 0.000E-00 | 0.000E-00 | 0.000E-00 | 0.00 | 0.00 |
| $\eta_y'(0.50)$ | -1.681E-05 | -1.700E-05 | -1.610E-05 | 1.12 | 4.22 |
| $\eta_y'(1.50)$ | 3.693E-05 | 3.703E-05 | 3.219E-05 | 0.27 | 12.83 |
| $q_w(0.50)$ | 1.843E-05 | 1.445E-05 | 1.743E-05 | 21.59 | 5.43 |
| $q_w(1.50)$ | 9.069E-05 | 9.243E-05 | 6.696E-05 | 1.91 | 26.16 |
| $q_{\theta_y}(0.50)$ | -1.419E-04 | -1.428E-04 | -9.074E-05 | 0.63 | 36.05 |
| $q_{\theta_y}(1.50)$ | 0.000E-00 | 0.000E-00 | 0.000E-00 | 0.00 | 0.00 |
| $q_{\eta_y}(0.50)$ | 1.073E-04 | 1.220E-04 | 9.659E-05 | 12.05 | 9.98 |
| $q_{\eta_y}(1.50)$ | 0.000E-00 | 0.000E-00 | 0.000E-00 | 0.00 | 0.00 |

*Table 3.2. Kinematical components and their derivatives of the rectangular cross section beam of example 1 for uniformly distributed transverse loading and fixed edges.*

AEM technique (AEM 201 Elements), ii) three collocation points employing AEM with quadratic B-spline (AEM Quadratic B-spline), iii) four collocation points employing AEM with cubic B-spline (AEM Cubic B-spline), iv) Euler-Bernoulli solution and v) FEM solution using quadrilateral solid finite elements (810 elements) in FEMAP (2010). From these figures, the validity of the present results can be

confirmed, since their convergence to the ones retrieved from the solid model is remarkable. It can also be observed that the AEM with the quadratic B-spline gives satisfactory results for all different cases of boundary conditions. The results derived from the AEM with the cubic B-spline almost coincide with the ones of the FEM model solution. The deflections derived by the Euler-Bernoulli solution are quite smaller.
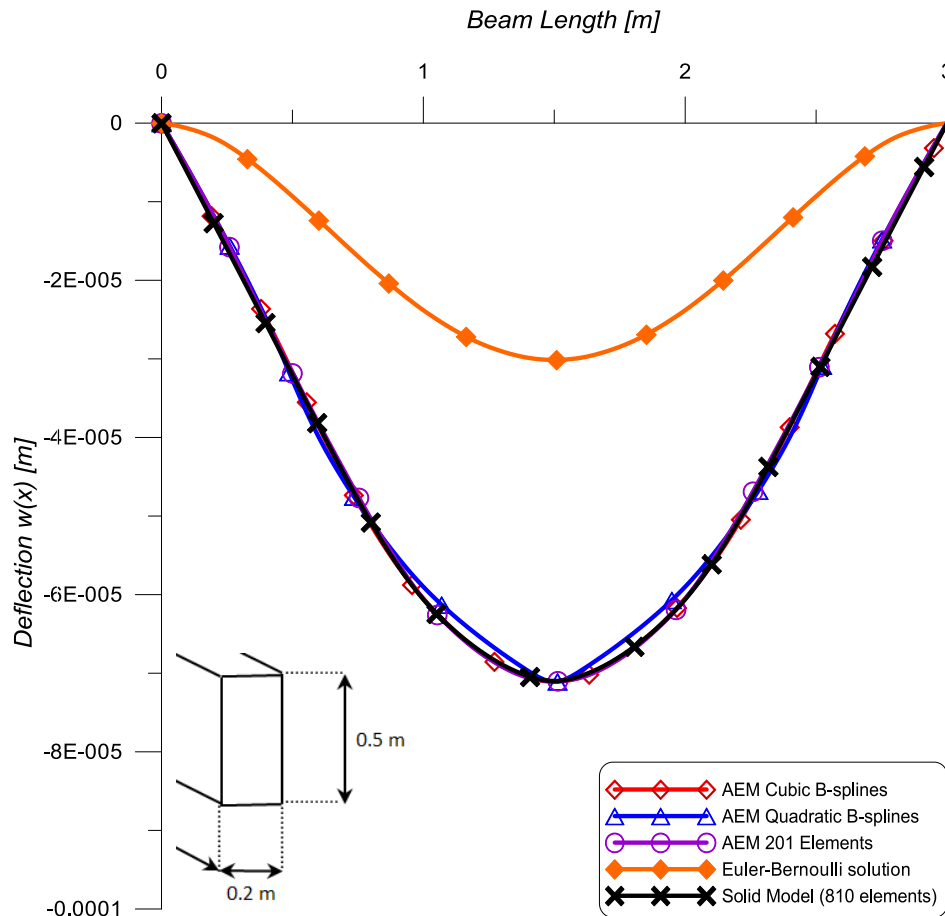


*Figure 3.2. Deflection  $w(x)$  along the length of the clamped beam of example 1 for uniformly distributed transverse loading.*

Finally, the beam is studied for three different boundary conditions with respect to the evaluation of the angle of twist   along its length due to distributed twisting moment. Four cases are examined, namely i) 201 discretization elements employing original AEM technique (AEM 201 Elements), ii) three collocation points employing AEM with quadratic B-spline (AEM Quadratic B-spline), iii) four collocation points employing AEM with cubic B-spline (AEM Cubic B-spline), iv) classical nonuniform torsion solution (CNT) and v) (only for the fixed-pinned case) five collocation points employing AEM with quartic B-spline (AEM Quartic B-spline). In Figures 3.5, 3.6 and 3.7 the angle of twist $\theta_x(x)$ along the beam length is presented for the aforementioned cases. From these figures, it is obvious that the convergence of the CNT results to the ones retrieved from the  AEM  with 201 elements of  the present study is  remarkable.
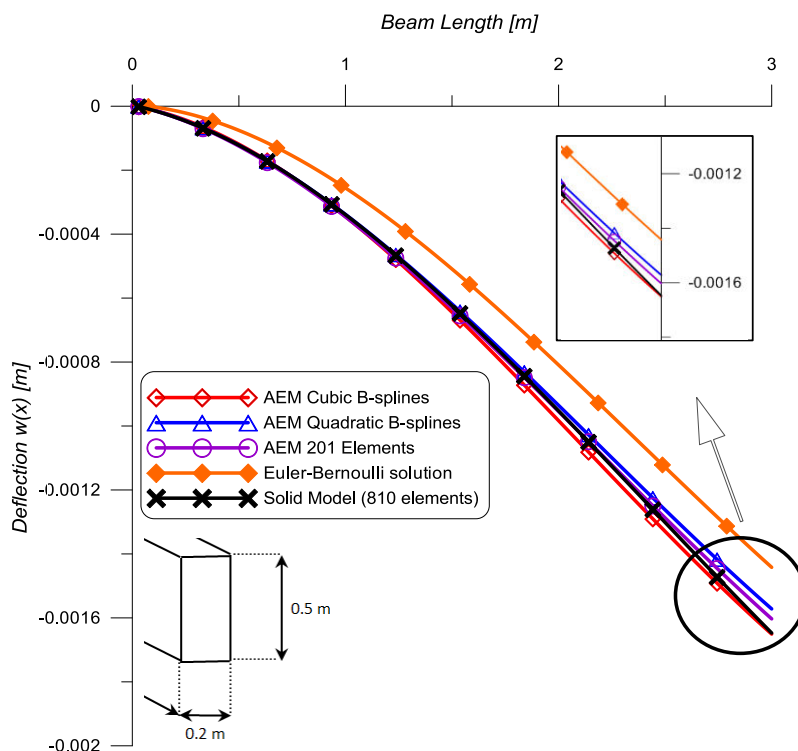
*Figure 3.3. Deflection  $w(x)$  along the length of the cantilever beam of example 1 for uniformly distributed transverse loading.*
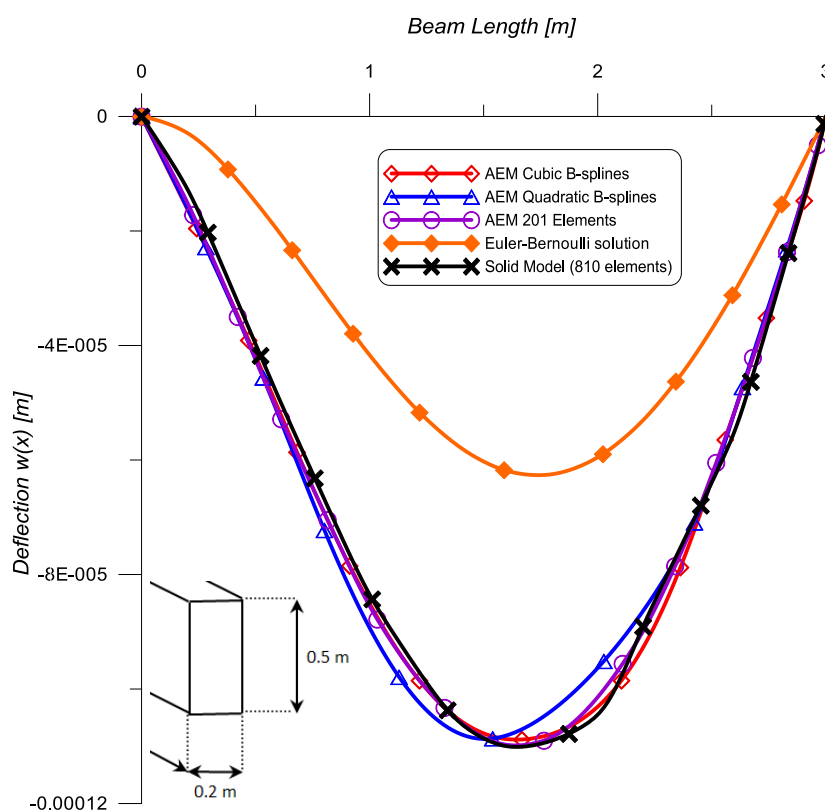


*Figure 3.4.   Deflection  $w(x)$  along the length of the beam of example 1 with one edge pinned for uniformly distributed transverse loading.*

It can also be observed that the AEM with either the quadratic or the cubic B-spline gives satisfactory results for all different cases of boundary conditions. The errors comparing to the original AEM with 201 constant elements are ranging from 1 to 10% for the cases of the two fixed support and the fixed-pinned support. In the last case a quartic B-spline is employed and the results derived from the AEM almost coincide with the ones of the original one. Regarding the cantilever beam, the errors are larger for both the quadratic and the cubic B-spline AEM ranging from 10-20%. An improvement in the results around 5% is achieved by the employment of the cubic B-spline. However, a finer discretization should be adopted and a knot insertion refinement procedure should be implemented.
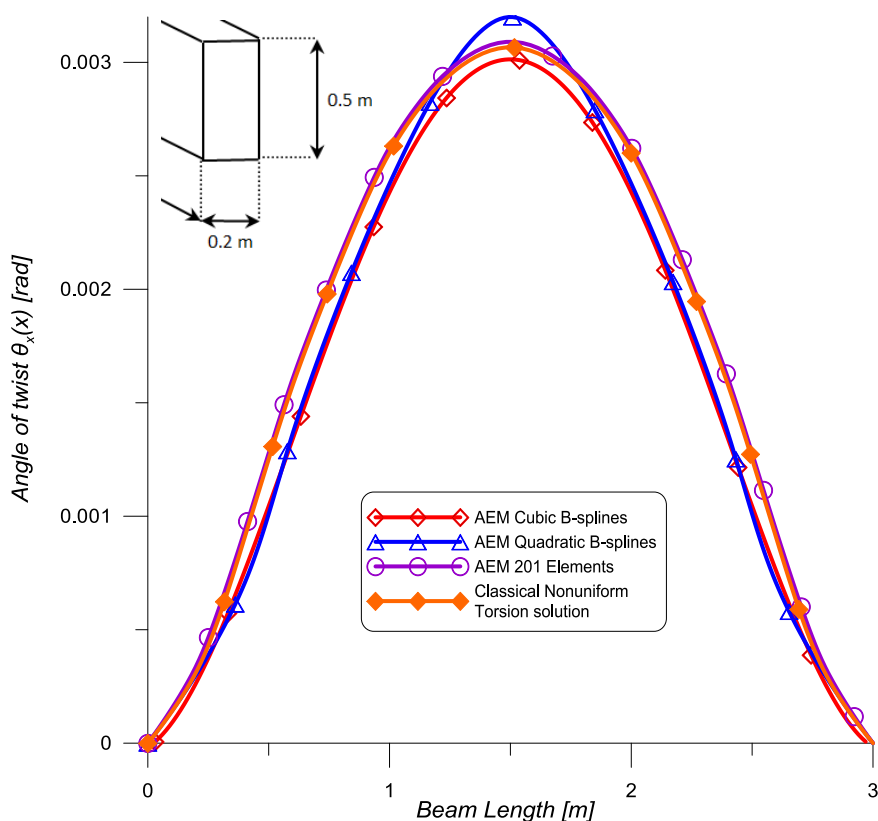


*Figure 3.5.  Angle of twist $\theta_x(x)$ along the length of the clamped beam of example 1 for uniformly distributed twisting moment.*

### Example 2: Cantilever beams of various cross sections

In this example, in order to further investigate the employment of B-splines in the AEM and validate their efficiency, three cantilever beams of different lengths and cross sections are examined (Fig. 3.8). The first beam has a thin-walled rectangular cross section ($E = 2.0E8kPa$ and $G = 0.77E8kPa$) and is subjected to a uniformly distributed twisting moment $m_x = 10^6 Nm/m$. The second one has a channel section ($E = 2.0E8kPa$ and $G = 0.77E8kPa$) and is subjected to a uniformly distributed twisting moment $m_x = -4.07 \ 10^6 Nm/m$, while the third beam has a box shaped cross
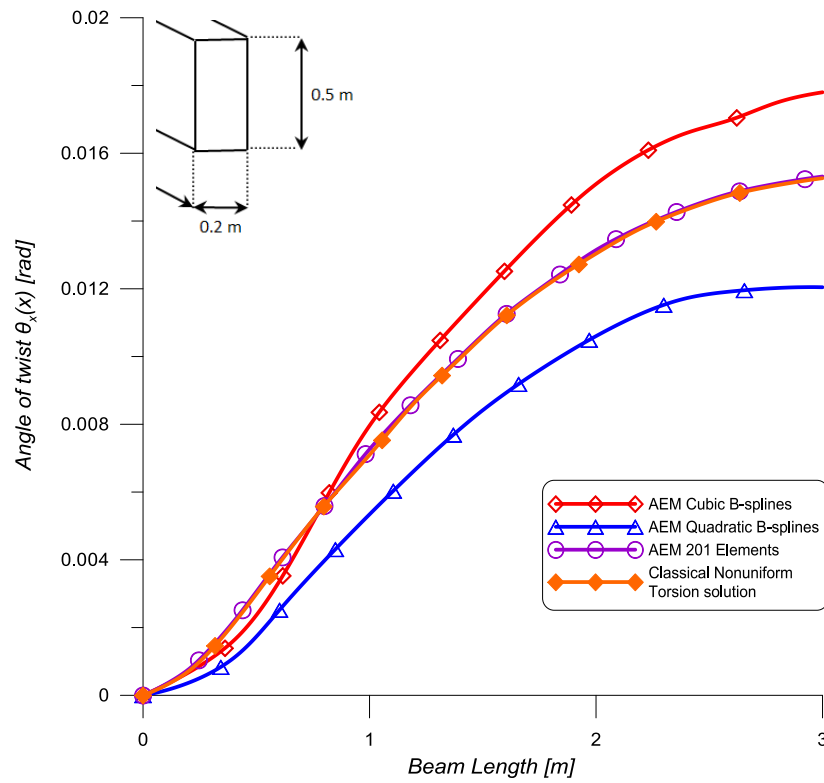
Figure 3.6. Angle of twist $\theta_x(x)$ along the length of the cantilever beam of example 1 for uniformly distributed twisting moment.
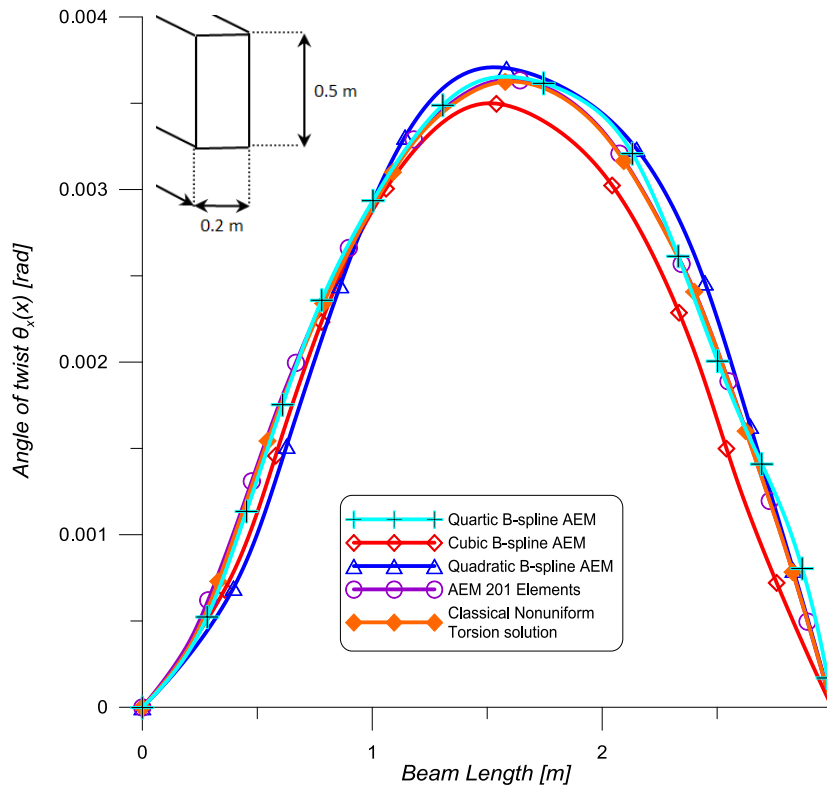


Figure 3.7. Angle of twist $\theta_x(x)$ along the length of the beam of example 1 with one edge pinned for uniformly distributed twisting moment.
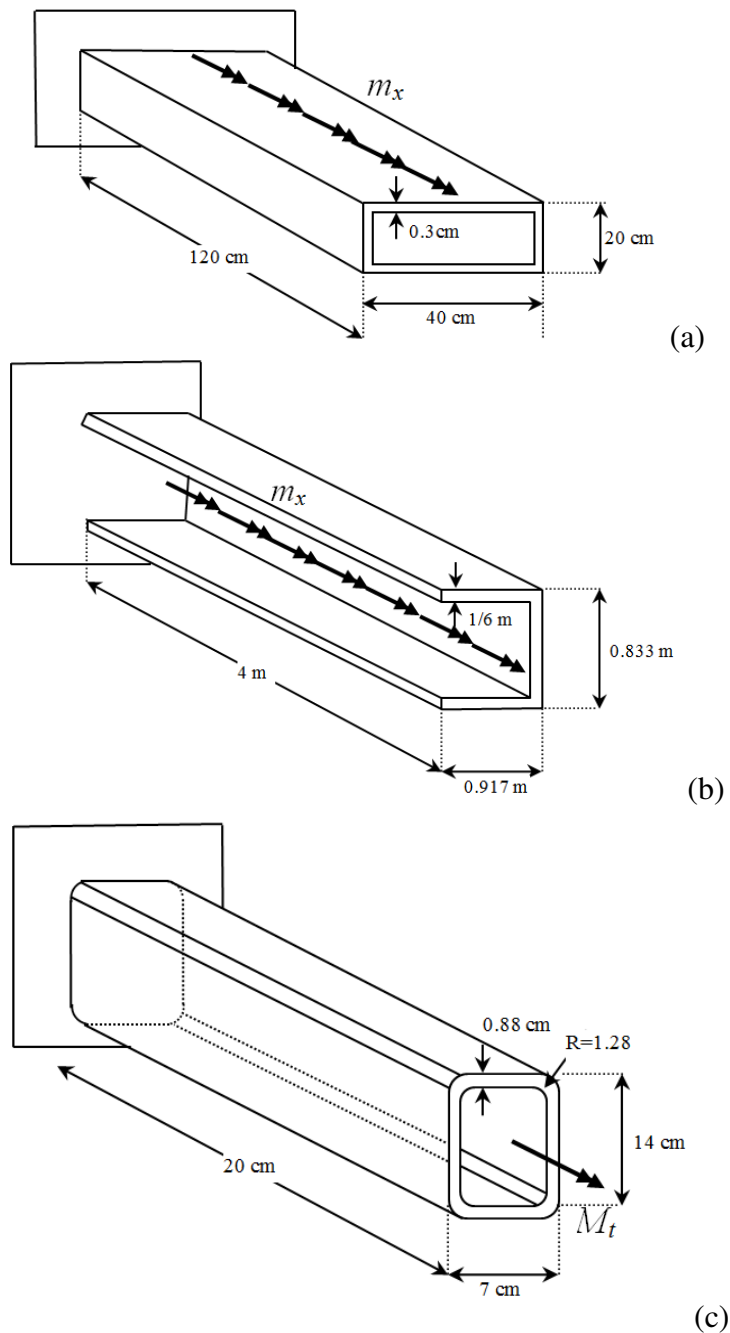
*Figure 3.8. Cantilever beams of example 2.*

section ( $E = 2.0E8kPa$  and  $G = 0.77E8kPa$ ) and is subjected to a concentrated torsional moment $M_t = 100kNm$  at its free end. The geometric constants of these cross sections are shown in Tables 3.3, 3.4 and 3.5, respectively. The above described beams have also been analyzed in the study of Shakourzadeh, Guo and Batoz (1995) and numerical results for comparison reasons have been retrieved. In that paper, a finite element is formulated for the torsional problem of thin-walled beams. The element is based on Benscoter's beam theory (1954), which is validated for open and closed cross sections.

$$A = 3.5640\text{E-}03\,m^2 \qquad I_{\varphi_S^S \varphi_S^S} = 2.21788886\text{E-}09\,m^6$$

$$I_{ZZ} = 7.78650920\text{E-}05\,m^4 \qquad I_{\varphi_{CY}^P \varphi_S^S} = 0.00000000\text{E+}00\,m^5$$

$$I_{YY} = 2.69378920\text{E-}05\,m^4 \qquad I_{\varphi_{CY}^P \varphi_S^S} = 0.00000000\text{E+}00\,m^5$$

$$I_{\varphi_{CY}^P \varphi_{CY}^P} = 1.40119273\text{E-}07\,m^4 \qquad A_Y^P = 7.91148291\text{E-}04\,m^2$$

$$A_Z^S = 1.93975546\text{E-}05\,m^2 \qquad I_t^P = 6.19570799\text{E-}05\,m^4$$

$$I_t^S = 6.16615084\text{E-}06\,m^4 \qquad I_t^T = 3.75179617\text{E-}07\,m^4$$

$$D_{\Phi_{CY}^S \Phi_S^S} = 0.00000000\text{E+}00\,m^3 \qquad D_{\Phi_{CY}^S \Phi_S^T} = 0.00000000\text{E+}00\,m^3$$

$$I_{\varphi_{CZ}^P \varphi_S^S} = 0.00000000\text{E+}00\,m^5 \qquad I_{\varphi_{CZ}^P \varphi_S^P} = 0.00000000\text{E+}00\,m^5$$

$$I_{\varphi_{CZ}^P \varphi_{CZ}^P} = 1.12607239\text{E-}06\,m^4 \qquad A_Z^P = 2.18275518\text{E-}03\,m^2$$

$$D_{\Phi_{CZ}^S \Phi_S^S} = 0.00000000\text{E+}00\,m^3 \qquad D_{\Phi_{CZ}^S \Phi_S^T} = 0.00000000\text{E+}00\,m^3$$

$$I_{\varphi_S^P \varphi_S^P} = 5.22724849\text{E-}08\,m^6 \qquad A_Y^S = 9.55232254\text{E-}05\,m^2$$

$$A = 4.44772210\text{E-}01\,m^2 \qquad I_{\varphi_S^S \varphi_S^S} = 1.07642608\text{E-}02\,m^6$$

$$I_{ZZ} = 4.25321449\text{E-}02\,m^4 \qquad I_{\varphi_{CY}^P \varphi_S^P} = -1.43209111\text{E-}05\,m^5$$

$$I_{YY} = 6.27919392\text{E-}02\,m^4 \qquad I_{\varphi_{CY}^P \varphi_S^S} = -4.03347367\text{E-}05\,m^5$$

$$I_{\varphi_{CY}^P \varphi_{CY}^P} = 1.29358905\text{E-}03\,m^4 \qquad A_Y^P = 1.01777250\text{E-}01\,m^2$$

$$A_Z^S = 1.43432816\text{E-}02\,m^2 \qquad I_t^P = 4.06950264\text{E-}03\,m^4$$

$$I_t^S = 5.30518011\text{E-}02\,m^4 \qquad I_t^T = 6.06074025\text{E-}03\,m^4$$

$$D_{\Phi_{CY}^S \Phi_S^S} = -1.03282342\text{E-}03\,m^3 \qquad D_{\Phi_{CY}^S \Phi_S^T} = -2.61359277\text{E-}04\,m^3$$

$$I_{\varphi_{CZ}^P \varphi_S^S} = -2.45065230\text{E-}05\,m^5 \qquad I_{\varphi_{CZ}^P \varphi_S^P} = 4.66645327\text{E-}03\,m^5$$

$$I_{\varphi_{CZ}^P \varphi_{CZ}^P} = 3.91521766\text{E-}03\,m^4 \qquad A_Z^P = 2.63511886\text{E-}01\,m^2$$

$$D_{\Phi_{CZ}^S \Phi_S^S} = 1.70052343\text{E-}02\,m^3 \qquad D_{\Phi_{CZ}^S \Phi_S^T} = -6.77916688\text{E-}03\,m^3$$

$$I_{\varphi_S^P \varphi_S^P} = 5.94116813\text{E-}03\,m^6 \qquad A_Y^S = 1.43432816\text{E-}02\,m^2$$

*Tables 3.3, 3.4.  Geometric constants of the beams in Figs. 3.8a,b.*

In Figures 3.9, 3.10 and 3.11, the angle of twist $\theta_x(x)$, the warping parameter $\eta_x(x)$ and the bimoment $M_{\phi_s^P}(x)$ along the length of the first beam (Fig. 3.8a) are presented for i) 60 discretization elements employing original AEM technique (AEM 60 NP), ii) three collocation points employing AEM with quadratic B-spline (Quadratic

$$A = 3.38624000\text{E+01}cm^2 \qquad I_{\varphi_S^S \varphi_S^S} = 4.34476587\text{E+01}cm^6$$

$$I_{ZZ} = 2.46538571\text{E+02}cm^4 \qquad I_{\varphi_{CY}^P \varphi_S^P} = 1.34918546\text{E-07}cm^5$$

$$I_{YY} = 7.84377181\text{E+02}cm^4 \qquad I_{\varphi_{CY}^P \varphi_S^S} = 3.82919447\text{E-08}cm^5$$

$$I_{\varphi_{CY}^P \varphi_{CY}^P} = 1.15805537\text{E+01}cm^4 \qquad A_Y^P = 2.21434846\text{E+01}cm^2$$

$$A_Z^S = 1.09904970\text{E+00}cm^2 \qquad I_t^P = 6.43745820\text{E+02}cm^4$$

$$I_t^S = 1.04886357\text{E+02}cm^4 \qquad I_t^T = 1.65791201\text{E+01}cm^4$$

$$D_{\Phi_{CY}^S \Phi_S^S} = 1.64341928\text{E-08}cm^3 \qquad D_{\Phi_{CY}^S \Phi_S^T} = 1.01087738\text{E-08}cm^3$$

$$I_{\varphi_{CZ}^P \varphi_S^S} = -3.91408624\text{E-03}cm^5 \qquad I_{\varphi_{CZ}^P \varphi_S^P} = -7.92012433\text{E-05}cm^5$$

$$I_{\varphi_{CZ}^P \varphi_{CZ}^P} = 3.06429838\text{E+00}cm^4 \qquad A_Z^P = 2.21434846\text{E+01}cm^2$$

$$D_{\Phi_{CZ}^S \Phi_S^S} = -1.70739803\text{E-03}cm^3 \qquad D_{\Phi_{CZ}^S \Phi_S^T} = 9.02887530\text{E-03}cm^3$$

$$I_{\varphi_S^P \varphi_S^P} = 8.61853898\text{E+02}cm^6 \qquad A_Y^S = 1.34697939\text{E+00}cm^2$$

*Table 3.5. Geometric constants of the beam in Fig. 3.8c.*
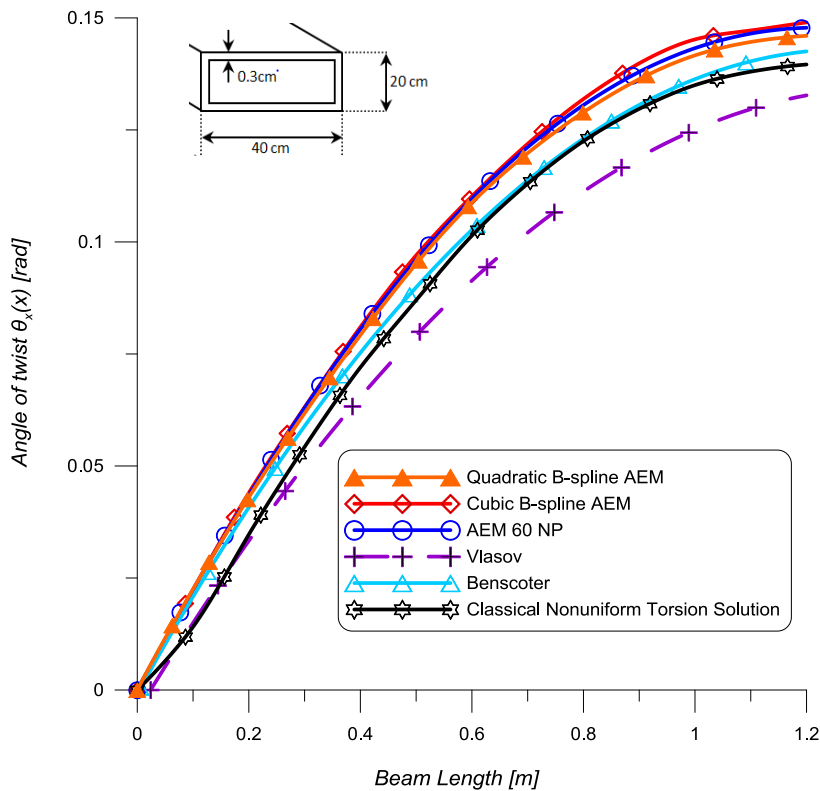


*Figure 3.9. Angle of twist $\theta_x(x)$ along the length of the beam of example 2 shown in Fig. 3.8a.*

B-spline AEM), iii) four collocation points employing AEM with cubic B-spline (Cubic B-spline AEM), iv) Vlasov model solution (Roark and Young, 1975), v) FEM
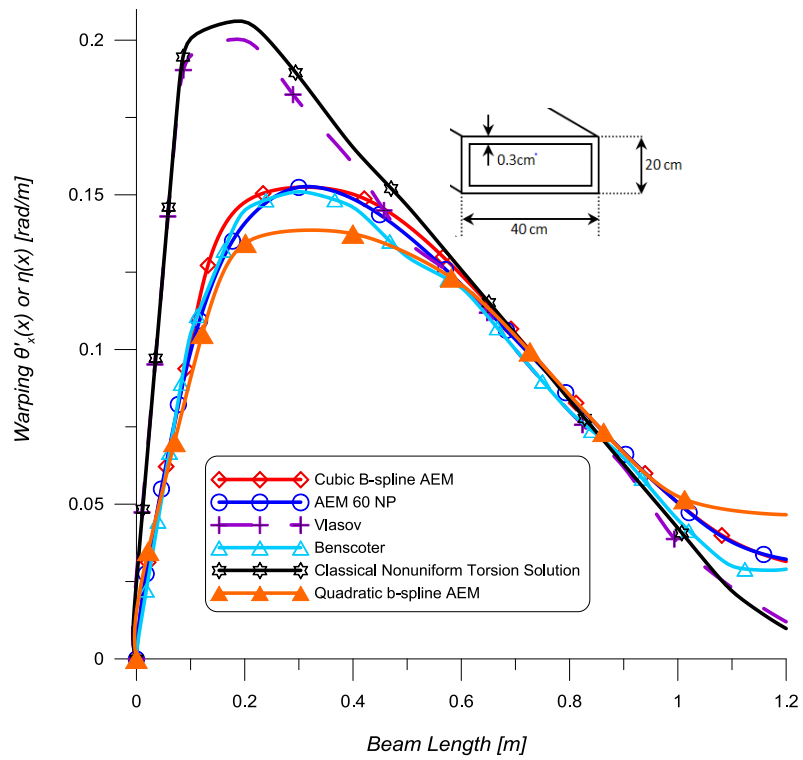
Figure 3.10. Warping $\eta_x(x)$ along the length of the beam of example 2 shown in Fig. 3.8a.
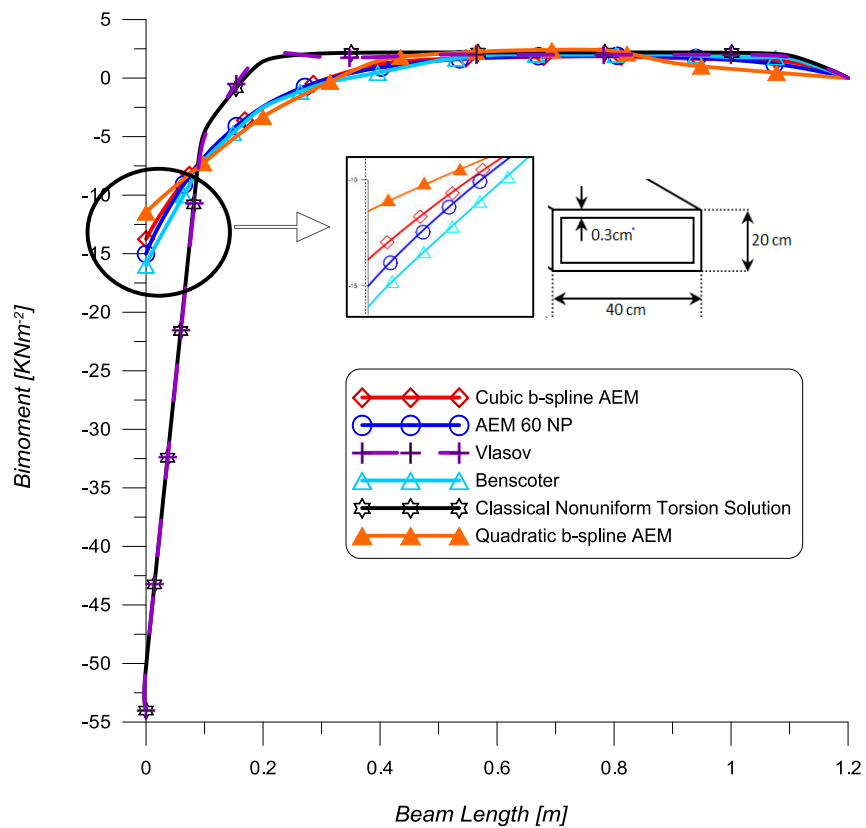


Figure 3.11. Bimoment due to primary warping along the length of the beam of example 2 shown in Fig. 3.8a.

solution (Benscoter model) and vi) classical nonuniform torsion solution (CNT) (analogous to $\theta_x'(x)$).

In Table 3.6, the values of the angle of twist $\theta_x(x)$, the warping parameter $\eta_x(x)$ and the bimoment $M_{\phi_s^P}(x)$ at the free end of the second beam (Fig. 3.8b) are compiled for i) 50 discretization elements employing original AEM technique (AEM 50 NP), ii) three collocation points employing AEM with quadratic B-spline (Quadratic B-spline AEM), iii) four collocation points employing AEM with cubic B-spline (Cubic B-spline AEM), iv) five collocation points employing AEM with quartic B-spline (Quartic B-spline AEM) v) Vlasov model solution (Roark and Young, 1975), vi) Saint-Venant Model (Roark and Young, 1975), vii) FEM solution (Benscoter model) and viii) classical nonuniform torsion solution with quadratic B-spline representation of the fictitious load in the fourth order differential equation (AEM-BS).

In Figures 3.12 and 3.13, the angle of twist $\theta_x(x)$ and the warping parameter $\eta_x(x)$ along the length of the third beam are presented for i) 60 discretization elements employing original AEM technique (AEM 60 NP), ii) four collocation points employing AEM with cubic B-spline (Cubic B-spline AEM), iii) Vlasov model solution (Roark and Young, 1975), iv) FEM solution (Benscoter model), v) classical nonuniform torsion solution (CNT) and vi) Shell model of 154 quadrilateral shell elements as described in the work of Shakourzadeh, Guo and Batoz (1995). Additionally, in Figure 3.14, the axial stress as stated in the work of Shakourzadeh, Guo and Batoz (1995) in eqn. 30 is presented for i) four collocation points employing AEM with cubic B-spline (Cubic B-spline AEM), ii) Vlasov model solution (Roark and Young, 1975), iii) FEM solution (Benscoter model) and iv) Shell model of 154 quadrilateral shell elements as described in the work of Shakourzadeh, Guo and Batoz (1995).

As can be seen in Fig. 3.9, the results obtained by the AEM of the present study, as well as the AEM with quadratic and cubic B-splines, differ from the corresponding values derived by the Benscoter's model solution and CNT solution, which almost coincide. This difference is around 5% and, thus, the influence of the secondary warping can be important for a beam with closed cross section. Regarding Vlasov's model solution, the values of the angles of twist are smaller than the corresponding values given by the AEM with the cubic B-splines by around 15% or more.

From Fig. 3.10, it is obvious that the results of AEM and cubic B-spline AEM are quite close to the Benscoter's model solution with deviations around 5%. Cubic B-splines give more accurate results than quadratic B-splines with respect to the evaluation of the warping parameter. It can also be observed that Vlasov's model and CNT solution give much different results than the other numerical approximations. Regarding the evaluation of the bimoment, similar comments can be made as it is obvious from Fig. 3.11.

According to the results compiled in Table 3.6 for the beam with the channel cross section, it can be observed that the maximum values of the angle of twist obtained

| | $\theta_x\,(rad)$ at x=L | $\theta_x'\,(rad/m)$ or $\Psi$ at x=L | $\eta_x\,(rad/m)$ at x=L | Bimoment $(N/m^2)$ at x=0 |
|---|---|---|---|---|
| Saint-Venant Model | -0.103 | - | - | - |
| Vlasov Model | -0.045 | -0.012 | - | -18.33E-06 |
| FEM- Benscoter Model | -0.045 | -0.011 | - | -18.17E-06 |
| AEM (50 NP) | -0.050 | -0.009 | -0.010 | -16.75E-06 |
| AEM (Quadratic B-spline) | -0.039 | -0.006 | -0.006 | -13.48E-06 |
| AEM (Cubic B-spline) | -0.061 | -0.013 | -0.014 | -18.29E-06 |
| AEM (Quartic B-spline) | -0.046 | -0.008 | -0.008 | -15.50E-06 |
| Classical Nonuniform Torsion Solution (AEM-BS) | -0.043 | -0.011 | - | -19.13E-06 |

*Table 3.6. Comparison between different methods for the beam in Fig. 3.8b.*

by the solutions of the present methods AEM and AEM with quadratic or cubic B-splines differ from the Vlasov's and Benscoter's models by 12% to 35%. However, the results obtained when employing a quartic B-spline are in good agreement with the Benscoter's model regarding the angle of twist and with the original AEM regarding warping parameter and bimoment. It should be noted that the bimoments calculated for the presented methods are only due to the primary torsional warping.

Regarding the box beam shown in Fig. 3.8c, the numerical results are given in Figs. 3.12-3.14 and compared with the results of the shell model. These comparisons show that the numerical values obtained by the presented methods almost coincide with the results of the shell and Benscoter's models. Particularly, the employment of a cubic B-spline in the AEM gives highly accurate results with respect to the axial stress estimation. However, Vlasov's and CNT models lead to important errors.

**Example 3: Cantilever Beam of Monosymmetric box-shaped cross section**

In the last example, a cantilever beam of a monosymmetric box-shaped cross section, as this is shown in Fig. 3.15, ( $E = 4 \times 10^7\ kN/m^2$ , $G = 2 \times 10^7\ kN/m^2$ , $L = 10\,m$ ) under a concentrated load $P_z = 1000\,kN$ eccentrically applied at its tip cross section, is examined. In Table 3.7 the geometric constants of the cross section are presented as computed in the work of Dikaros and Sapountzakis (2014) employing pure BEM. The aforementioned load case has also been analyzed by Ferradi et al. (2013)
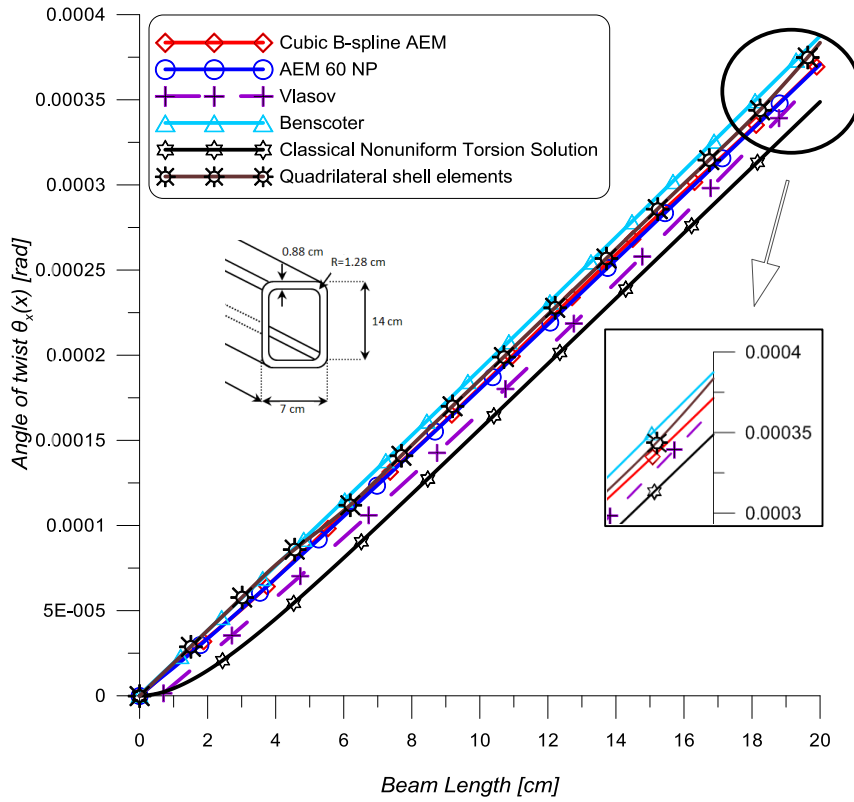
*Figure 3.12. Angle of twist $\theta_x(x)$ along the length of the beam of example 2 shown in Fig. 3.8c.*
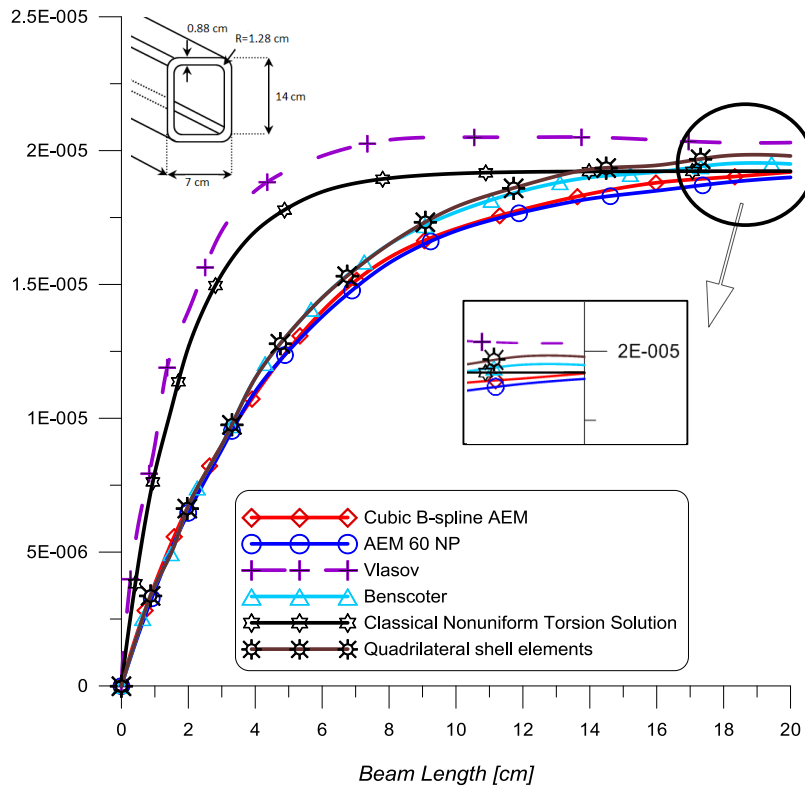


*Figure 3.13. Warping $\eta_x(x)$ along the length of the beam of example 2 shown in Fig. 3.8c.*
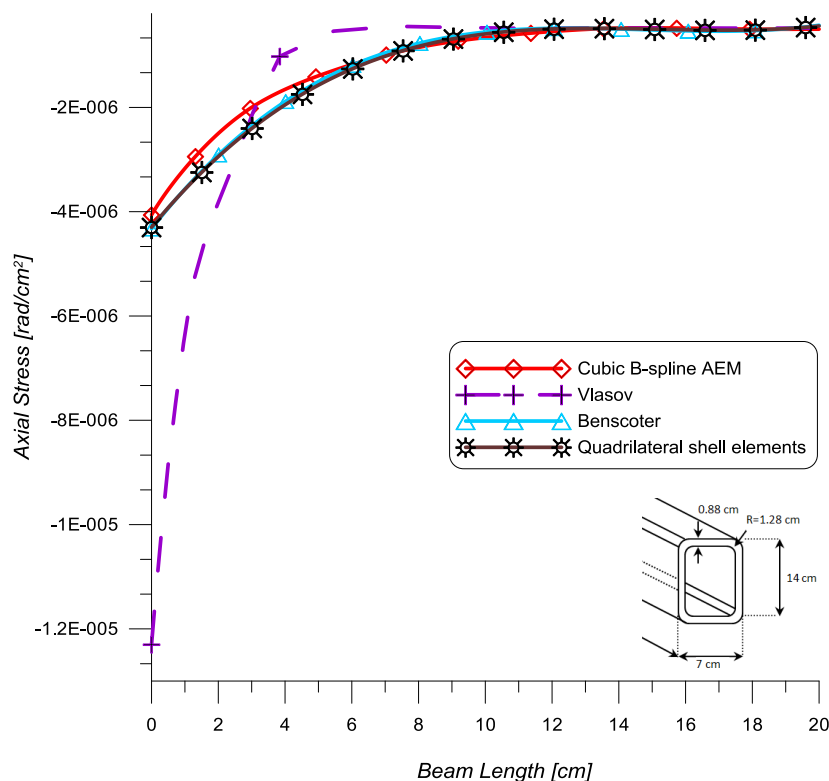
*Figure 3.14. Axial stress due to primary warping along the length of the beam of example 2 shown in Fig. 3.8c.*

and in this study proper adjustments have been made so as to account for different coordinate systems.

In Figs. 3.16-3.18 values of the kinematical components $w(x)$, $\theta_x(x)$ and $\theta_Y(x)$ are, respectively, presented and compared to the ones obtained from the FEM beam model presented in the study of Ferradi et al. (2013). From all of the
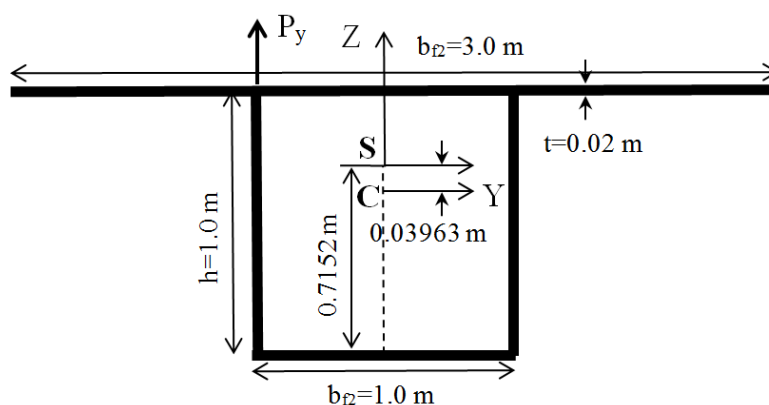


*Figure 3.15. Cross section of example 3.*

aforementioned figures it can be easily observed that the present results and the corresponding ones of the FEM model presented in Ferradi et al. (2013) are in excellent

agreement. Regarding the AEM with the B-splines, it should be noted that the AEM with cubic and quartic B-splines coincide with the original AEM of the present study either with constant or linear elements (Dikaros and Sapountzakis, 2014). It is also obvious that the AEM with the quadratic B-spline gives slightly different results from the ones of the aforementioned models.

$$A = 1.1960E-01\,m^2 \qquad I_{\varphi_S^S \varphi_S^S} = 7.7889E-05\,m^6$$

$$I_{ZZ} = 5.6570E-02\,m^4 \qquad I_{\varphi_{CY}^P \varphi_S^P} = -2.8455E-04\,m^5$$

$$I_{YY} = 1.9962E-02\,m^4 \qquad I_{\varphi_{CY}^P \varphi_S^S} = 1.5685E-04\,m^5$$

$$I_{\varphi_{CY}^P \varphi_{CY}^P} = 9.9893E-04\,m^4 \qquad A_Y^P = 6.3665E-02\,m^2$$

$$A_Z^S = 2.3014E-03\,m^2 \qquad I_t^P = 2.0184E-02\,m^4$$

$$I_t^S = 3.7487E-03\,m^4 \qquad I_t^T = 1.4397E-04\,m^4$$

$$D_{\Phi_{CY}^S \Phi_S^S} = -9.2153E-04\,m^3 \qquad D_{\Phi_{CY}^S \Phi_S^T} = 0.00000000E+00\,m^3$$

$$I_{\varphi_{CZ}^P \varphi_S^S} = 0.00000000E+00\,m^5 \qquad I_{\varphi_{CZ}^P \varphi_S^P} = 0.00000000E+00\,m^5$$

$$I_{\varphi_{CZ}^P \varphi_{CZ}^P} = 7.0222E-04\,m^4 \qquad A_Z^P = 3.2130E-02\,m^2$$

$$D_{\Phi_{CZ}^S \Phi_S^S} = 0.00000000E+00\,m^3 \qquad D_{\Phi_{CY}^S \Phi_S^T} = 3.0309E-04\,m^3$$

$$I_{\varphi_S^P \varphi_S^P} = 9.2289E-04\,m^6 \qquad A_Y^S = 7.2076E-03\,m^2$$

*Table 3.7. Geometric constants of the beam in Fig. 3.15.*

In the same figures, the maximum values are also presented for all of the models studied. An improvement in the results is achieved by the employment of the quartic B-spline. However, the AEM with the cubic B-spline gives highly accurate results with a much smaller computational effort comparing to the original AEM.

In Fig. 3.19 a model of the beam implemented in FEMAP (2010) employing FEM quadrilateral solid elements is shown. In the same figure the total deflection is also recorded. Regarding the aforementioned kinematical components, their values almost coincide with the corresponding ones obtained by the use of the cubic B-spline in the AEM without any need for refinement. It is worth here noting that in order to obtain the distributions of the kinematical components from the solid model, rigid diaphragms were placed in regular distances, permitting the measurement of rotation angles and translations of the reference nodes. The existence of diaphragms also ensured the absence of local distortional phenomena of the cross sectional profiles. In order to compare the computational effort for the different numerical models, the computational times have been recorded. Particularly, the real computational time for the analysis of the solid model in FEMAP (2010) is 5.3 seconds, 0.5 second for the analysis when employing the AEM with cubic B-spline, 2.8 seconds for the AEM with

| | $-w(x)/10(m)$ at $x=L$ |
|---|---|
| Quartic b-spline AEM | -0,04317 |
| Cubic b-spline AEM | -0,04347 |
| Quadratic b-spline AEM | -0,0514 |
| AEM 100 constant elements | -0,04328 |
| AEM 203 linear elements | -0,04329 |
| FEM- Ferradi et. al | -0,04329 |
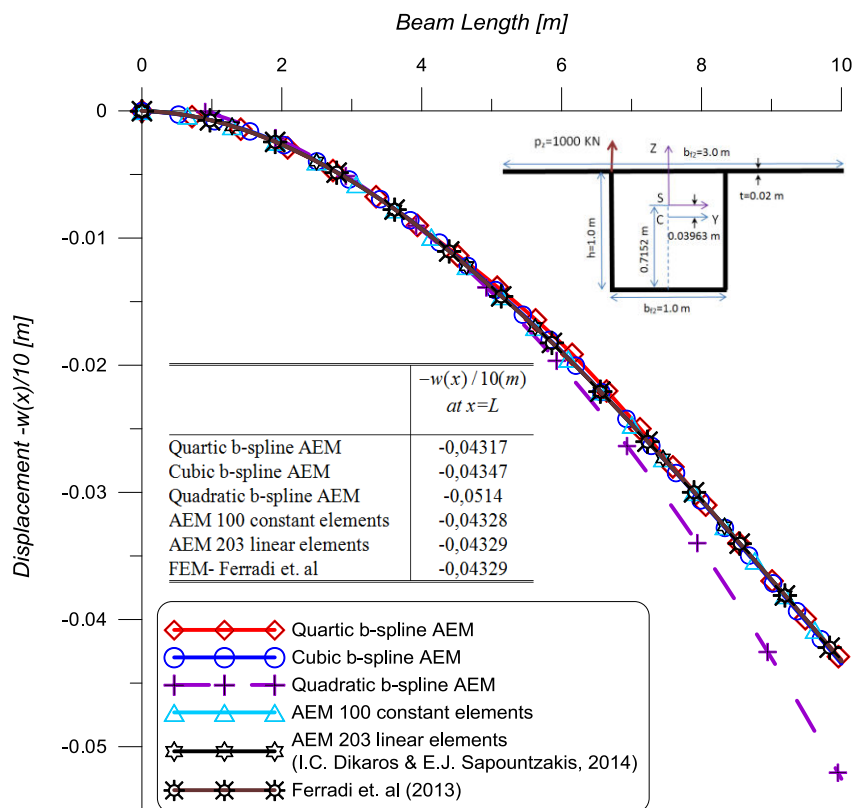
*Figure 3.16. Deflection* $-w(x)/10$ *along the length of the beam of example 3.*



| | $\theta_x(rad)$ at $x=L$ |
|---|---|
| Quartic b-spline AEM | -0,01212 |
| Cubic b-spline AEM | -0,0124 |
| Quadratic b-spline AEM | -0,01197 |
| AEM 100 constant elements | -0,01224 |
| AEM 203 linear elements | -0,01224 |
| FEM- Ferradi et. al | -0,01224 |
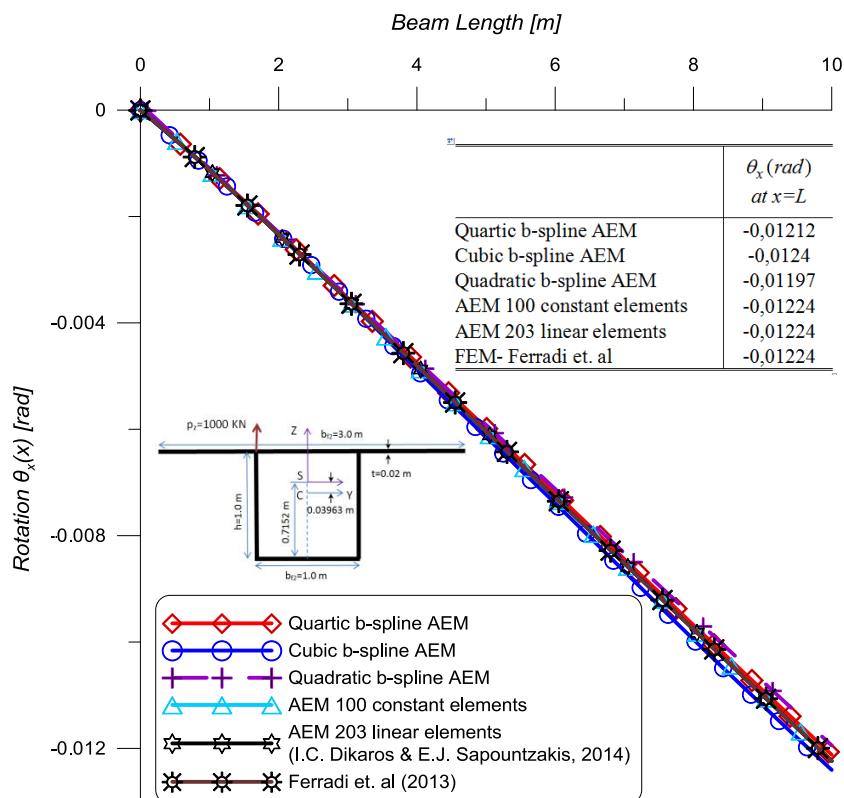
*Figure 3.17. Angle of twist* $\theta_x(x)$ *along the length of the beam of example 3.*
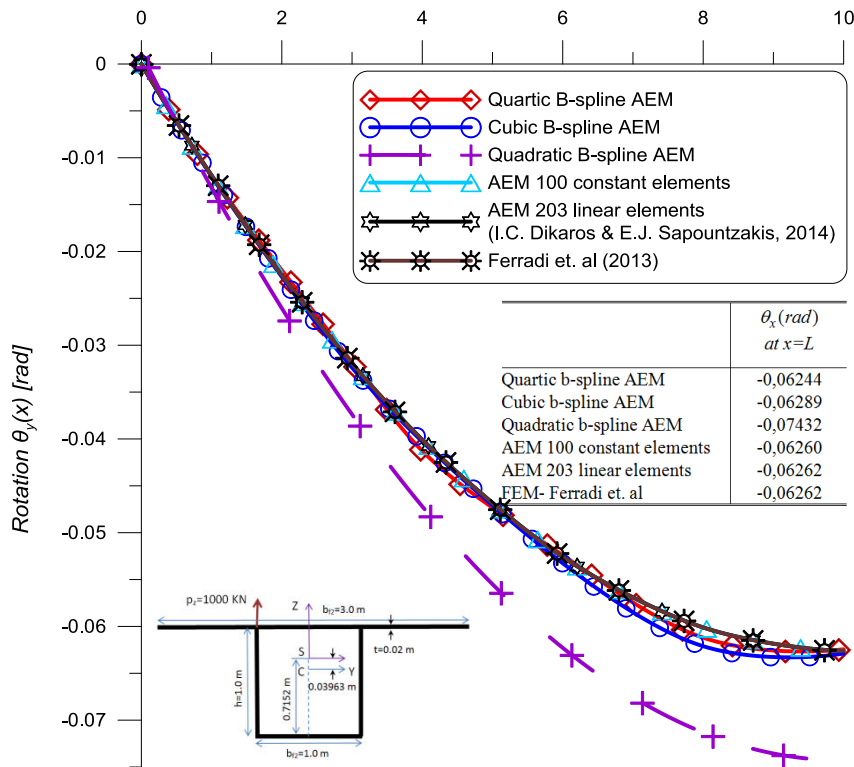
*Figure 3.18. Angle of twist $\theta_Y(x)$ along the length of the beam of example 3.*
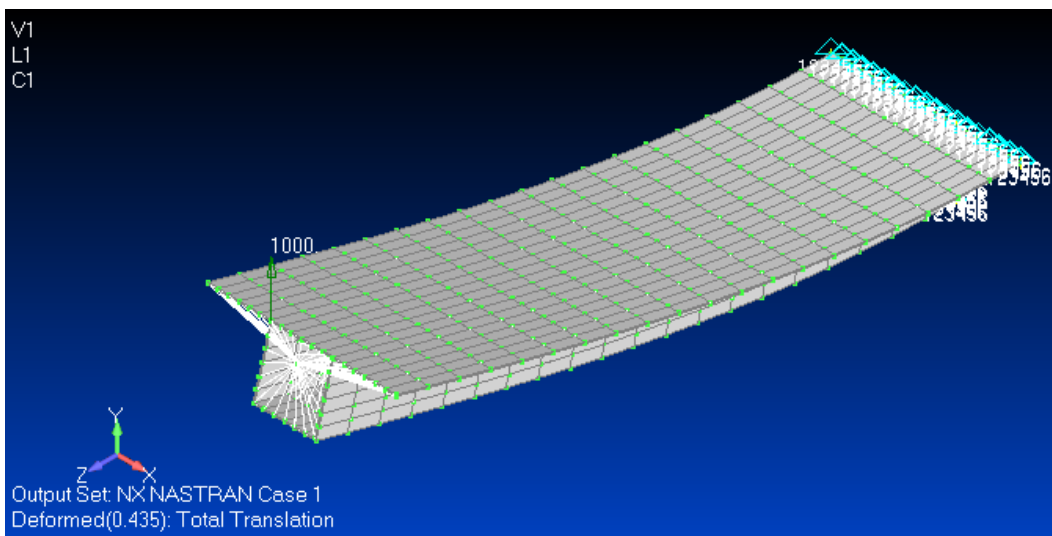


*Figure 3.19. Model in FEMAP (2010) employing 780 quadrilateral solid finite elements. Deflection $w(x)$ is displayed along the length of the beam of example 3.*

200 constant elements and 1 second for the CNT. It should be noted here that all the analyses have been carried out in the same computer, without any effort for optimization, the run times mentioned consist of times for the assembly as well as the solution and the languages used were VBA (Visual Basic for Applications) and Matlab tool. However, other aspects should also been considered in order to estimate the
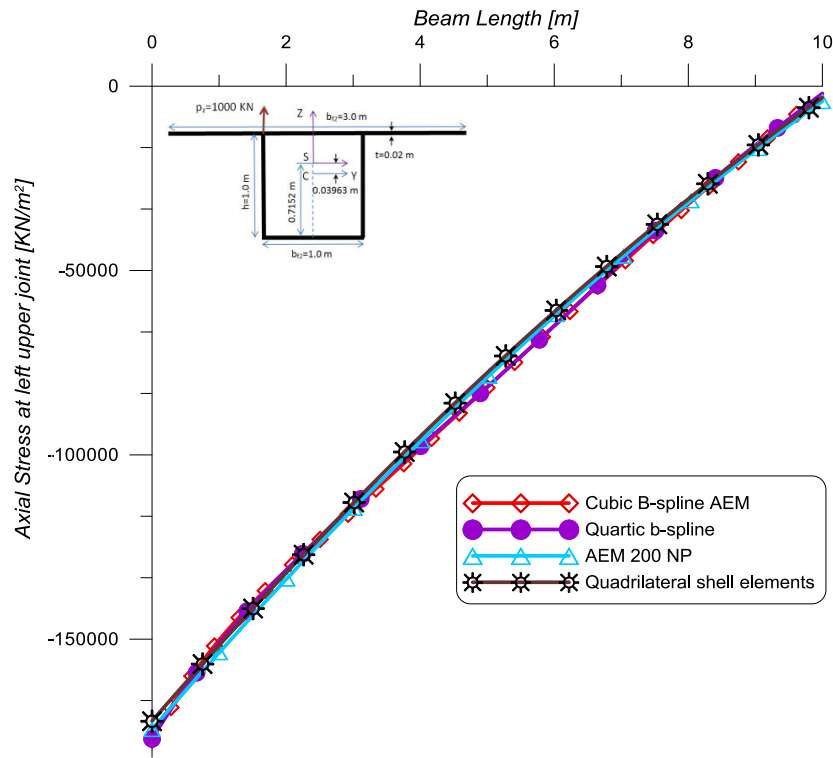
*Figure 3.20. Primary axial stress due to bending about the centroidal axis Y and primary torsional warping at left upper joint of example's 3 beam.*
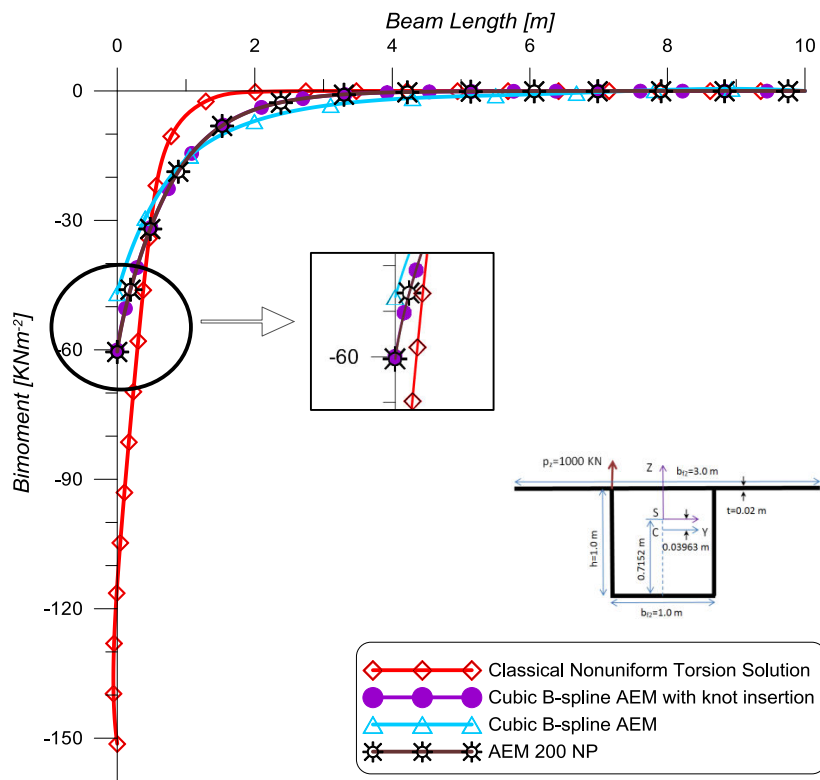


*Figure 3.21. Bimoment due to primary warping along the length of the beam of example 3.*

computational effort needed with respect to the accuracy of the results, as it is mentioned in Chapter 2.

In Fig. 3.20, the values of the axial stress due to bending and primary warping obtained along the length of the beam when employing either original AEM or AEM with B-splines are shown and compared to the ones obtained from the FEM beam model shown in Fig. 3.19. Moreover, in Fig. 3.21, the values of bimoment due to primary warping are displayed when employing original AEM with 200 NP, AEM with cubic B-spline, either having 4 control points along the whole length of the beam or more after knot insertion (Appendix A.2), and CNT with 201 NP. It is obvious that the results obtained by the use of CNT are inaccurate, especially for the first quarter of the length of the beam, due to the fact that the primary warping is not accurately estimated. In addition to this, the results coincide with the original AEM, which has been validated through comparisons with solid models and it is considered accurate, when employing knot insertion for the cubic B-spline. The need for knot insertion becomes imperative due to the fact that the cubic B-spline with 4 control points fails to describe accurately the distribution of bimoment due to primary warping along the length of the beam with arising errors being around 20%. Degree elevation (with quartic B-spline) improves the accuracy of the results by around 10%.

### 3.5.2 Dynamic Case

#### Example 4: Spectra of natural frequencies and Computational times

In the fourth example, two simple special cases of the problem described by eqns. (3.2) have been studied for simplicity and comparison reasons aiming to verify the proposed numerical method (AEM with constant or quadratic elements in its original form) and demonstrate its efficiency comparing to other methods.

The first one is the eigenproblem representing the free longitudinal vibration of a beam fixed at both ends described by elastodynamic eqn. (3.2a), considering $p_x = 0$. The beam is assumed to move only in the longitudinal direction. The characteristics of the beam ($E^* \approx E$, $A$ and $\rho$) are considered equal to 1 as in §5.1.2. of Hughes et al. (2009). Then, eqn. (3.2a) can be written in matrix form according to AEM as follows

$$-\rho[B]\{\ddot{q}\} + E\{q\} = 0, \quad q(x,t) = u_{,xx} \tag{3.15}$$

which is subjected to the initial conditions (3.3a,b) and the corresponding boundary conditions (3.4a) ($x \in (0,l)$) with $a_1 = 1, \alpha_2 = \alpha_3 = 0$. The analytical solution of the free axial vibration problem can be obtained as $\omega_n = n\pi, \ for \ n = 1,...,\infty$. Computer programs have been written in order to solve eqn. (3.15) of AEM and the elastodynamic eqn. (3.2a) either employing classical $C^0$-continuous quadratic FEs or $C^1$-continuous quadratic NURBS functions. The quality of the numerical methods employed is assessed by comparing the ratio of the numerically computed frequencies with the analytical result. FEs and NURBS solutions are identical to those presented by

Hughes et al. (2009). However, in this study AEM (in its original form) results have been added and compared with respect to computational time and effort. The analyses were carried out employing 1000 degrees of freedom (dofs) for all of the numerical methods for comparison reasons.

In Fig. 3.22 the normalized natural frequency results (ratio of the numerical solution to the analytical one) versus the ratio of the mode number $n$ to the total number
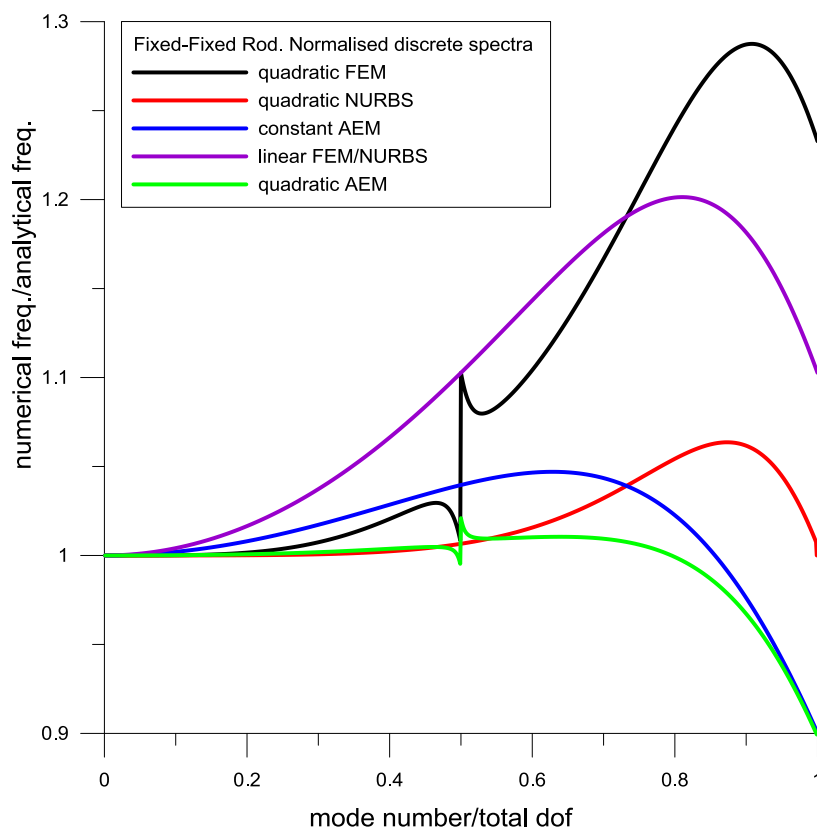


*Figure 3.22. Normalized discrete spectra of natural frequencies employing FEM, IGA and AEM for the free axial vibration of a fixed beam.*

of dofs ($N{\approx}1000$) has been plotted. According to Hughes et al. (2009) and from Fig. 3.22, it is obvious that NURBS functions exhibit a better behavior comparing to FEs and AEM with constant or quadratic elements. In the case of piecewise linear FEs, loss in accuracy of the results exhibits a highly increasing rate over the most of the spectrum. Thus, quadratic FEs need to be employed. In this case, the finite element results depict the so-called acoustical branch for $n/N < 0.5$ and an optical branch for $n/N > 0.5$ (Hughes et al., 2009). This branching is due to the fact that each basis function is associated with each node, as with the piecewise linear basis, and in this case there are two distinct types of functions: those associated with the end-point nodes at element boundaries, and those corresponding to mid-point nodes on element interiors. The same case is for the AEM with quadratic elements but without significantly increasing loss of accuracy, as it is the case in quadratic FEM. However, the influence of branching is much smaller in this case and this is attributed to the AEM

matrices constructed (eqns. (A.1.48) and (A.1.51) of the Appendix A.1) which are the results of sequential integrations by parts employing all discretization elements for each data entry associated with each collocation point (named the pole in BEM). This is the reason why matrices in AEM, which is BEM-based, are fully populated and not diagonal like in FEM. Alternatively, the quadratic NURBS basis functions, and thus differential equations of the algebraic system, are all identical, and no such branching takes place. Finally, AEM with constant elements gives highly accurate results (5% error comparing to NURBS) and no branching takes place. The values of computational time needed in order to calculate the numerical frequencies are compiled in Table 3.8. All of the numerical methods demand a computational time of the same order of magnitude.

| Numerical method (1000 dofs) | Computational time (seconds) |
|---|---|
| Quadratic FEM | 11.42 |
| Quadratic NURBS | 11.18 |
| Linear FEM/NURBS | 12.37 |
| Constant AEM | 10.27 |
| Quadratic AEM | 10.46 |

*Table 3.8. Computational time of free axial vibration analysis for the numerical methods presented in Fig. 3.22 (one kinematical component).*

The second special case of the eqns. (3.2) studied is the eigenproblem of the free torsional vibration considering STSDE and $m_t = m_{\varphi_S^P} = 0$. The beam is subjected only to torsion and warping. The characteristics of the beam ($E^* \approx E$, $A$, $I_t^P$, $I_t^S$, $I_{\varphi_S^P \varphi_S^P}$, $I_p$ and $\rho$) are considered equal to 1 for simplicity. Then, eqns. (3.2f) and (3.2i) can be written as

$$\rho I_P \theta_{x,tt} - G\left(I_t^P + I_t^S\right)\theta_{x,xx} + GI_t^S \eta_{x,x} = 0 \tag{3.16a}$$

$$\rho I_{\varphi_S^P \varphi_S^P} \eta_{x,tt} - EI_{\varphi_S^P \varphi_S^P} \eta_{x,xx} + GI_t^S\left(\eta_x - \theta_{x,x}\right) = 0 \tag{3.16b}$$

while boundary conditions remain the same as stated in eqns. (3.3k, l), (3.3q, r), (3.4f) and (3.4i) with

$$M_{bt} = M_t^P + M_t^S = GI_t^P \theta_{x,x} - GI_t^S\left(\eta_x - \theta_{x,x}\right) \tag{3.17a}$$

$$M_{b\varphi_S^P} = EI_{\varphi_S^P \varphi_S^P} \eta_{x,x} \tag{3.17b}$$

and $\delta_1 = 1, \delta_2 = \delta_3 = 0, \bar{\delta}_1 = 1, \bar{\delta}_2 = \bar{\delta}_3 = 0.$

Finally, eqns. (3.16) can be written in matrix form according to AEM as

$$
\begin{bmatrix} \rho I_P b_{111} & \rho I_P b_{112} \\ \rho I_{\varphi_S^P \varphi_S^P} b_{121} & \rho I_{\varphi_S^P \varphi_S^P} b_{122} \end{bmatrix} \begin{Bmatrix} \ddot{q}_1 \\ \ddot{q}_2 \end{Bmatrix} +
$$

$$
\begin{bmatrix} -G\left(I_t^P + I_t^S\right) + GI_t^S b_{221} & GI_t^S b_{222} \\ GI_t^S b_{121} - GI_t^S b_{211} & -EI_{\varphi_S^P \varphi_S^P} + GI_t^S b_{122} - GI_t^S b_{212} \end{bmatrix} \begin{Bmatrix} q_1 \\ q_2 \end{Bmatrix} \qquad (3.18)
$$

$$
+ \begin{Bmatrix} \rho I_P r_{11} + GI_t^S r_{22} \\ \rho I_{\varphi_S^P \varphi_S^P} r_{12} + GI_t^S r_{12} - GI_t^S r_{21} \end{Bmatrix} = \begin{Bmatrix} 0 \\ 0 \end{Bmatrix}, q_1(x,t) = \theta_{x,xx}, q_2(x,t) = \eta_{x,xx}
$$

where $r_{ij}, i, j = 1,2$ are the values compiled in $\{R\}$ and $\{R'\}$ (eqns. (A.1.52) of the Appendix A.1), which are equal to zero for homogenous boundary conditions, while $b_{ijk}, i, j, k = 1,2$ are the values in $[B]$ and $[B']$ (eqns. (A.1.51) of the Appendix A.1). Thus, the numerical solution employing AEM with constant or quadratic elements can be obtained. Due to the fact that it is quite cumbersome to derive the analytical solution, normalization has been done with respect to the results of AEM with 2000 constant elements (4000 dofs for two kinematical components) which in fact are quite close to the corresponding ones obtained by the analysis of a solid FEM model, as it is also implied in the examples of Dikaros et al. (2016) (88 elements per meter of length used in the AEM give discrepancies less or around 1% comparing to solid FEM models). Comparisons have been made between AEM, FEM and NURBS solutions for different orders and number of elements (i.e. "FEM500 2nd" means 500 quadratic FEs).

In Fig. 3.23, as in Fig. 3.22, the normalized natural frequency results (ratio of the numerical solution to the "approximate" analytical one given by AEM) versus the ratio of the mode number $n$ to the total number of dofs ($N \approx 1000$) has been plotted. The branching mentioned in Fig. 3.22 for quadratic FEM is again obvious in Fig. 3.23 for "FEM500 2nd" with the jump displaced in $n/N \approx 0.85$. This implies higher accuracy comparing to the previous example due to the larger number of dofs (2002 dofs). The same case is for the AEM with quadratic elements and for the same number of dofs but with a much smaller influence of the branching in the accuracy of the results. It should be noted here that quadratic AEM spectrum exhibits two small jumps at $n/N \approx 0.55$ and $n/N \approx 0.80$ due to the fact that there are two kinematical components in this case. Two jumps are also depicted for the case of "FEM300 2nd" where the total number of dofs is 1202. The increasing loss in accuracy is conspicuous. More accurate results are obtained by "NURBS500 2nd", "FEM1000 1st" and "AEM1000". It should be noted here that there is a "knee" at $n/N \approx 0.85$ for the "NURBS500 2nd" and a steep decrease in accuracy after this point. A similar "knee" can be observed in "AEM500" at $n/N \approx 0.80$ but with a smaller decrease in accuracy after this point. Highly accurate results
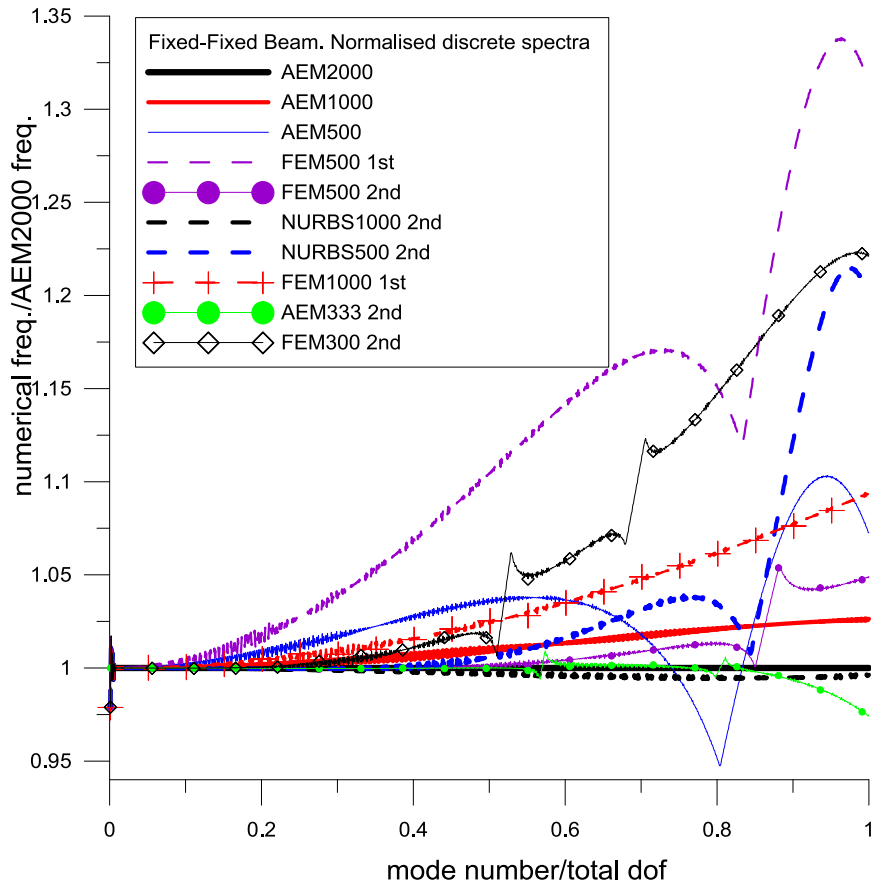
*Figure 3.23. Normalized discrete spectra of natural frequencies employing FEM, IGA and AEM for the free torsional vibration with STSDE of a fixed beam.*

| Numerical method (≈2000 dofs) | Computational time (seconds) |
|---|---|
| FEM500 2nd | 44.91 |
| NURBS1000 2nd | 43.19 |
| FEM1000 1$^{st}$ | 52.94 |
| AEM1000 | 31.45 |
| AEM333 2nd | 31.90 |

*Table 3.9. Computational time of free torsional vibration analysis for the numerical methods presented in Fig. 3.23 (two kinematical components).*

(maximum discrepancy 2.5% at $n/N=1.00$ and less than 0.5% for $0<n/N<0.90$) and smooth spectrum curves have been achieved by "NURBS1000 2nd" and "AEM333 2nd" which employ around 2000 dofs. The values of computational time needed in order to calculate the numerical frequencies are compiled in Table 3.9. All of the numerical methods demand a computational time of the same order of magnitude. However, comparing with the time in the previous case of one kinematical component, the increase is smaller for the AEM technique than that of the other methods examined.

Similar plots of spectra can be derived for free transverse or bending vibrations as well as for the generalized vibration case presented in this chapter. Regarding accuracy and computational effort of the different methods studied, conclusions are similar to the previous cases studied. In Fig. 3.24, computational time of various numerical methods versus dofs for different problems derived from the general one described by eqns. (3.2) has been plotted. It is obvious that the rate of change while number of dofs increases is steeper for FEM with quadratic elements and quadratic NURBS comparing with AEM, either with constant or quadratic elements which computational time is similar for. The same case is for FEM with linear elements but with larger computational time comparing to all other methods. Thus, AEM technique seems to be
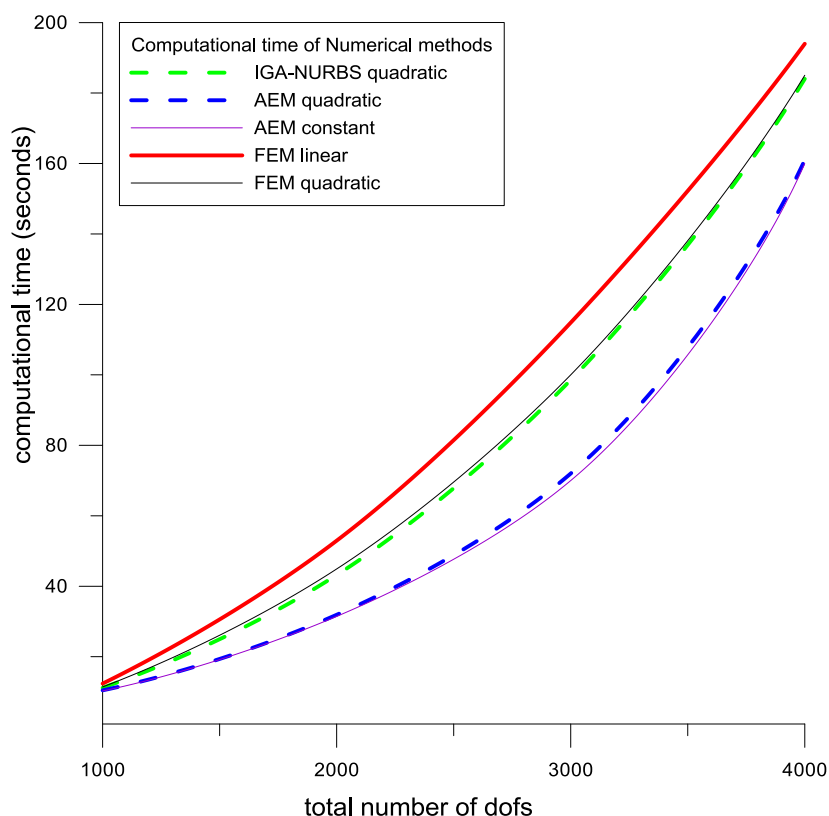


*Figure 3.24. Computational time of different numerical methods for increasing number of dofs.*

computationally more efficient as the number of the unknowns increases comparing to all other methods. Finally, it should be noted here that the number of dofs is selected to be the same for all of the numerical methods employed and large enough in order to adequately describe the whole frequency spectrum that each method produces.

### Example 5: Eigenfrequencies and convergence rates

In the fifth example, the free torsional vibration of two steel ($E = 210GPa$, $G = 80.8GPa$, $\rho = 8.002kN\,sec^2/m^4$) bars of different lengths and cross sections, clamped at both ends have been studied. Particularly, the eigenproblem described by

eqns. (3.16) has been solved and the first four eigenfrequencies have been obtained employing different numerical methods. Fig. 3.25 shows the properties of the models created. B-splines have been employed in AEM for the representation of the fictitious load, as earlier described. Comparisons have been made with the results of FEM solid models (Sapountzakis et al., 2016) and AEM with quadratic elements in order to verify the proposed formulation and demonstrate the improvement of the original AEM when comparing to the AEM with B-splines.
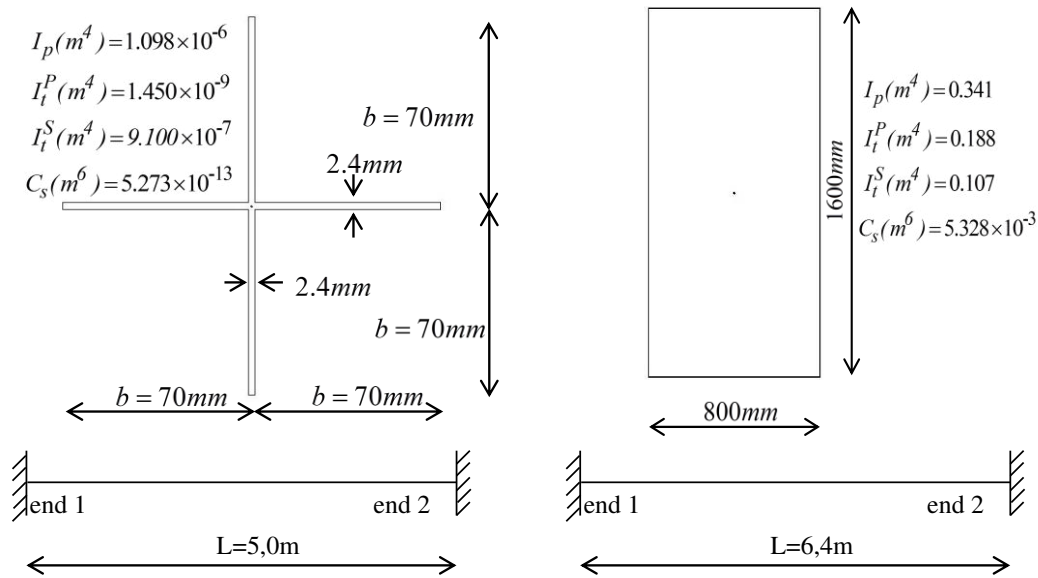


*Figure 3.24. Cross sections of bars of example 5 along with their lengths and boundary conditions*

Results have been compiled in Table 3.10 for the two cross section cases. It is obvious that in general more discretization elements need to be employed for the case of the cruciform cross section especially for higher frequencies. However, AEM with quartic B-splines improves the results for both cross sections with only 10 dofs (actually is the same to one discretization element) and without the need of knot insertion only for the rectangular cross section comparing to FEM solid and AEM with quadratic elements (300x3=900 dofs). Accurate results for the cruciform case (errors less than 5%) can be achieved by inserting 2 more knots (4 dofs more). AEM with cubic B-splines gives accurate results for rectangular cross section while knot insertion needs to be employed in the cruciform section case in order to obtain the first three modes. To obtain accurate values 8 new knots need to be inserted (16 additional dofs). This could be explained considering the fact that a quartic B-spline can simulate better the eigenmode of the cruciform cross section than the cubic one. Moreover, this cross section is very thin-walled (thickness/width $<<0.1$ and height/length $<<0.1$) and extremely suffers from out-of-plane warping (very low warping rigidity, $C_S = I_{\varphi_S^P \varphi_S^P} << I_t = (I_t^P + I_t^S + I_t^T)$). It should be noted here that the rest of the cross sections employed in this example have in general much higher warping rigidities

($C_S = I_{\varphi_S^P \varphi_S^P} \gg I_t$) as well as much higher height to length ratio due to the fact that these are more frequently encountered in structural engineering practice. These limitations could be used as a rule of thumb in choosing the least number of elements and the optimum order of the approximation curve in order to achieve the maximum accuracy when the proposed method is employed. However, if the two ratios mentioned above become much lower than that of the cruciform cross section, it might be necessary to employ more elaborate beam theories or even solid models.

| Mode Number | 3d FEM (278000 3d 6edral quad) | AEM (300 quadratic elements) | AEM Cubic B-splines (20 dofs) | AEM quartic B-splines (10 dofs) |
|---|---|---|---|---|
| | Hz | Errors (%) | | |
| 1 | 11.07 | 4.91 | 9.05 | 9.34 |
| 2 | 22.16 | 4.85 | 8.18 | 11.79 |
| 3 | 33.28 | 4.77 | 9.83 | 4.69 |
| 4 | 44.48 | 4.59 | 31.52 | 16.02 |
| Mode Number | 3d FEM (40960 3d 6edral quad) | AEM (50 quadratic elements) | AEM Cubic B-splines (8 dofs) | AEM quartic B-splines (10 dofs) |
| | Hz | Errors (%) | | |
| 1 | 193.07 | 0.32 | 1.04 | 0.38 |
| 2 | 389.16 | 0.61 | 0.02 | 0.25 |
| 3 | 590.27 | 0.95 | 9.39 | 0.49 |
| 4 | 797.14 | 1.25 | 2.82 | 6.52 |
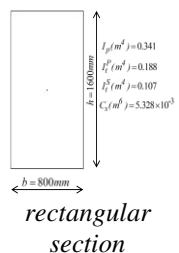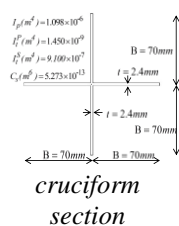
*Table 3.10. Eigenfrequencies and errors for the free torsional vibration problem of the beams shown in Fig.3.24.*

In Fig. 3.25 the numerical errors versus the discretization quadratic elements employed in AEM have been plotted for the cruciform section case. The method converges in a high rate when the elements employed are increased up to 100, which is almost the first one third of the elements used in order to obtain the maximum accuracy (or the minimum error taken less than 5%). AEM with cubic B-splines fails to capture the eigenfrequencies of the third and fourth modes without knot insertion (8 dofs). When knot insertion is employed (20 dofs) only the fourth eigenfrequency cannot be accurately evaluated. The large difference in errors after knot insertion implies high convergence rate for the AEM with cubic B-splines.

Two cases of the free generalized vibration problem (eqns. (3.2)) have been studied in the second example, too. The first case is a steel ($E = 210GPa$,

$G = 80.8GPa$, $\rho = 7.85kN\,sec^2/m^4$) beam of a HEB500 cross section, as shown in Fig. 3.26a and Dikaros et al. (2016), of length $L = 2.5m$ clamped at both ends. The
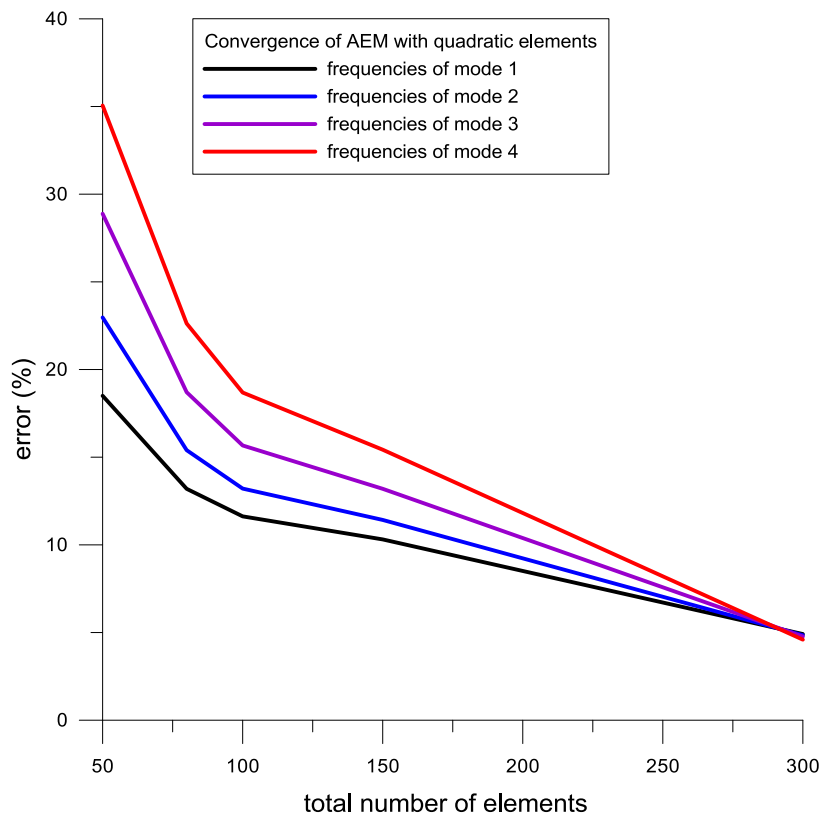


*Figure 3.25. Convergence rate of the AEM with quadratic elements for the cruciform cross section of example 5.*

second one is a steel ($E = 40GPa$, $G = 20GPa$, $\rho = 7.85kN\,sec^2/m^4$) cantilever beam of a box-shaped cross section, as shown in Fig. 3.26b, of length $L = 10m$. Fig. 3.26 shows also the properties of the aforementioned cross sections. B-splines have been employed in AEM for the representation of the fictitious load, as earlier described. Comparisons have been made with the results of FEM solid models and AEM with quadratic elements.

Results have been compiled in Table 3.11 for the two cross sections. Highly accurate results have been obtained when employing either cubic or quartic B-splines in the AEM technique for both cases examined. In addition to this, there is no need for knot insertion. Discrepancies from solid model are in general smaller in the first case of the HEB section keeping the same dofs number.

Finally, the convergence of the proposed formulation is studied with respect to the eigenfrequencies of the box-shaped cross section described above. For this purpose, the log-log scale plots have been created for increasing number of elements and different numerical methods, namely original AEM with quadratic elements ("AEM2nd") and AEM with NURBS, of up to the fifth order, integrated ("AEMNURB2nd", "AEMNURB3rd", "AEMNURB4th" and "AEMNURB5th"). It

can be concluded that the convergence rate is improved when employing NURBS in the AEM technique and the order is increased for few elements.



$A\left(cm^2\right)=239.11$          $I_{ZZ}\left(cm^4\right)=12624.32$

$I_{YY}\left(cm^4\right)=107259.34$    $I_{\varphi_{CZ}^P\varphi_{CZ}^P}\left(cm^4\right)=125.69$

$I_{\varphi_{CY}^P\varphi_{CY}^P}\left(cm^4\right)=193.09$    $A_Z^P\left(cm^2\right)=149.42$

$A_Z^S\left(cm^2\right)=12.11$        $A_Y^P\left(cm^2\right)=71.13$

$A_Y^S\left(cm^2\right)=8.70$         $I_{\varphi_S^P\varphi_S^P}\left(cm^6\right)=6920545.97$

$I_{\varphi_S^S\varphi_S^S}\left(cm^6\right)=82942.84$   $I_p\left(cm^4\right)=119883.67$

$I_t^P\left(cm^4\right)=551.59$        $I_t^S\left(cm^4\right)=82012.61$

$I_t^T\left(cm^4\right)=-4441.85$

$A\left(cm^2\right)=1196$            $I_{ZZ}\left(cm^4\right)=5657000$

$I_{YY}\left(cm^4\right)=1996200$     $I_{\varphi_{CZ}^P\varphi_{CZ}^P}\left(cm^4\right)=70222$

$I_{\varphi_{CY}^P\varphi_{CY}^P}\left(cm^4\right)=99893$   $A_Z^P\left(cm^2\right)=321.30$

$A_Z^S\left(cm^2\right)=23.01$         $A_Y^P\left(cm^2\right)=636.65$

$A_Y^S\left(cm^2\right)=72.08$         $I_{\varphi_S^P\varphi_S^P}\left(cm^6\right)=922890000$

$I_{\varphi_S^S\varphi_S^S}\left(cm^6\right)=77889000$   $I_p\left(cm^4\right)=7671955$

$I_t^P\left(cm^4\right)=2018400$       $I_t^S\left(cm^4\right)=374870$

$I_t^T\left(cm^4\right)=14397$         $I_{\varphi_{CY}^P\varphi_S^S}\left(cm^5\right)=1568500$

Fig. 3.26. Cross sections of bars of example 5 along with their cross section properties.

## 3.6 Concluding Remarks

In this chapter, a BE based technique, called AEM either in its original form or combined with Isogeometric tools is developed and studied for the generalized static and free vibration problem considering warping effects of arbitrarily shaped cross section beams supported by general boundary conditions. Quadratic, cubic and quartic B-spline curves are introduced for the representation of the fictitious load in order to implement an Isogeometric method for the numerical simulation of the static problem described above. Special cases of the general vibration problem have also been examined in order to compare the results of IGA with those of AEM and FEM. The main conclusions that can be drawn from this investigation are:

I.   Regarding the static problem
i.   In most cases, highly accurate and stable results can in general be obtained by using a quadratic B-spline curve without the need for any refinement. However, in some cases a finer discretization is needed. In cases where shear lag effects are

not negligible, a cubic or a quartic B-spline representation of the fictitious load gives more accurate results (i.e. box-shaped cross sections).

| | Mode Number | 3d FEM (24300 3d 6edral quad) | AEM (30 quadratic elements) | AEM Cubic B-splines (8 dofs) | AEM quartic B-splines (10 dofs) |
|---|---|---|---|---|---|
| | | Hz | Errors (%) | | |
| | 1 | 203.11 | 0.02 | 0.80 | 0.03 |
| | 2 | 238.33 | 0.05 | 1.78 | 0.37 |
| HEB500 section | 3 | 415.93 | 0.01 | 0.14 | 0.06 |
| | 4 | 473.25 | 0.02 | 1.52 | 1.84 |
| | Mode Number | 3d FEM (780 3d 6edral quad) | AEM (30 quadratic elements) | AEM Cubic B-splines (8 dofs) | AEM quartic B-splines (10 dofs) |
| | | Hz | Errors (%) | | |
| | 1 | 0.85 | 4.33 | 3.65 | 4.31 |
| Box-shaped section | 2 | 1.32 | 1.10 | 1.20 | 1.10 |
| | 3 | 1.99 | 0.65 | 1.99 | 1.98 |
| | 4 | 3.01 | 2.65 | 3.81 | 3.56 |
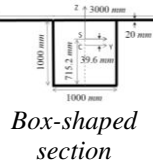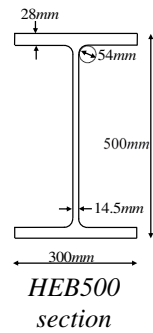
*Table 3.11. Eigenfrequencies and errors for the free generalized vibration problem of the beams with cross sections shown in Fig.3.26.*

ii.   CNT fails to give accurate results in the evaluation of primary warping distribution and axial stresses or bimoments due to primary warping in the case of closed cross sections. Results are quite close to those obtained by employing the Vlasov model. The same case is for the Saint Venant model regarding torsion and the Euler-Bernoulli model regarding bending.

iii.   A FEM element formulation based on Benscoter's beam theory (1954) gives highly accurate results only in the case of torsional loading and it is used to validate and compare with the results obtained by the application of the present method.

iv.   The computational effort is much less using B-splines due to the fact that the number of the unknowns is restricted to the number of the control points which depends on the order of the B-spline used.

v.   A cubic B-spline is proposed in order to improve the accuracy of AEM and simultaneously reduce the computational effort for this particular application due to the fact that its application makes possible to accurately describe the behavior of a beam subjected to the most general loading and boundary conditions by the least computational cost comparing to all other methods mentioned in this paper.
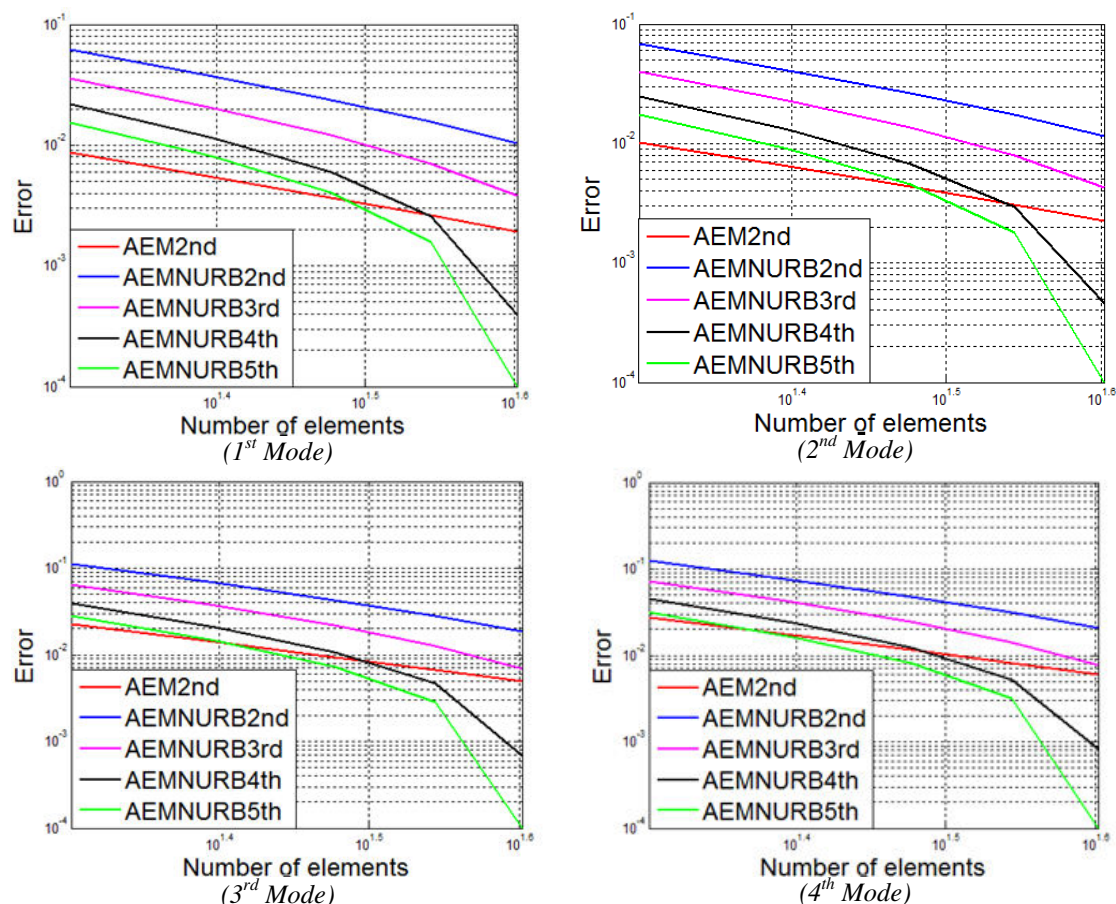
*Fig. 3.27. Comparison of eigenfrequencies' convergence on log-log scale plots for the first four modes of the box-shaped beam of example 5.*

II.   Regarding the dynamic problem

i.   AEM technique with constant elements exhibits no branching in the normalized frequency spectrum, as it is the case in quadratic FEM elements, while it maintains accuracy in the results of high frequencies. Quadratic elements in AEM depict a branch with much smaller impact than FEM, while they improve the accuracy comparing to AEM with constant elements.

ii.   Computational time becomes smaller for the AEM technique as the number of dofs increases comparing both to FEs and NURBS. However, the most accurate results can be obtained for the whole spectrum of frequencies when employing NURBS.

iii.   Convergence rate of AEM with constant or quadratic elements can be improved when B-splines or NURBS are used for the representation of the fictitious loads. This would make it possible to obtain the desired level of accuracy without increasing discretization elements in a disproportionate way.

iv.   In cases of very thin-walled beams, which are susceptible to warping and torsional phenomena, more elements need to be used for the AEM technique with constant or quadratic elements. Quartic and cubic B-splines with or without knot

insertion can help to reduce number of unknowns drastically while keep the accuracy on a high level.

# Chapter 4

# Chapter **4**

# Generalized static and dynamic warping analysis of Curved Beams by Isogeometric Methods

## 4.1  Introduction

Comparing to straight beam formulations, the behavior exhibited by curved beams is far more complex regarding twist deformations. It is well known, that in case of a horizontally curved beam under transverse loading not only vertical displacement but twist deformation with respect to its longitudinal axis arises as well and this cannot be captured by traditional Euler-Bernoulli or Timoshenko beam elements. Both of these theories maintain the assumption that cross sections remain plane after deformation. Even though the formulation remains simple, it fails to capture higher order phenomena such as "shear lag", which are associated with a significant modification of normal stress distribution due to nonuniform shear warping (Dikaros and Sapountzakis, 2014). This phenomenon has been reported long ago (Reissner, 1946; Malcolm and Redwood, 1970; Moffatt and Dowling, 1975;) in many structural members such as beams of box-shaped cross sections, folded structural members or beams of materials weak in shear. In up-to-date regulations, shear lag effect in flexure is considered in the analysis by the "effective breadth" concept (Eurocode 3, Part 1.5, 2004; Eurocode 4, Part 1.1, 2004; Eurocode 3, Part 2, 2004). However, this simplifying approach may fail to capture satisfactorily the actual structural behavior of the member, since the influence of shear lag phenomenon is not constant along the beam length, while apart from the geometrical configuration of the cross section it depends also on the type of loading (Ie and Kosmatka, 1992; Katsikadelis and Sapountzakis, 2002). Similar considerations with the ones made for flexure could be also adopted for the torsional problem, which is also encountered in the analysis of curved-in-plan beams. In the case of torsional loading where the longitudinal displacements that create warping are restrained due to boundary conditions, the arising torsional moment is nonuniform, as mentioned in Chapter 3. The aforementioned prevention of warping leads to the development of normal stresses, which are proportional to warping and therefore vary along the length of the bar (nonuniform torsion). Considering the above, the influence of shear lag phenomenon due to both flexure and torsion, which is not constant along the beam length, should be also considered for curved geometries. These problems have been extensively examined in the literature but mainly for straight beams. Regarding curved beam formulations, a series of straight-line segments is generally used in practice in order to approximate the curved geometry though ignoring warping transmission

between these segments, as mentioned in Chapter 3. Vlasov (1961) presented a solution for curved beams with open arbitrary cross sections. Then, Dabrowski (1965) gave an analysis for closed box-shaped cross sections. Having in mind the above, it is easily concluded that the influence of shear lag phenomenon due to both flexure and torsion, which is not constant along the beam length, should be also considered for curved geometries. The early curved beam models that have been formulated are either restricted to the analysis of only the beam behavior in the plane of curvature (Zhu et al., 2010; Cazzani et al., 2014; Cazzazi et al., 2016) or do not take into account secondary shear deformation effect caused by nonuniform warping (Heins and Spates, 1970; Luo and Li 2000; Luu et al., 2015), while other efforts consider only doubly symmetric cross sections (Koo and Cheung, 1989; Zhu et al., 2016). In general, even in recent or past years, although the planar problem has been extensively studied, comparatively little work has been done concerning the general three dimensional, non-planar, or coupled lateral-torsional responses of curved beams (Yoo, 1979; Rosen and Abromovich, 1984; Koo and Cheung, 1989, Gendy and Saleeb, 1992; Zhu et al, 2010).

The above described effects may become substantial in complex structural forms comprising box-shaped homogeneous or composite cross sections, curved members, short spans or arbitrary loading. Thin-walled straight or curved structures having open or closed cross-section, which are widely used in bridge engineering due to their large bending and torsional rigidities as well as their low self-weight, suffer from these effects. Hence a realistic estimation of stress state employing conventional beam elements becomes difficult, since generally commercial programs consider six degrees of freedom (DOFs) at each node of a member of a spatial frame, ignoring in this way all the warping effects due to corresponding warping restraint (Murín, 1998; Murín, 1999; Murín, and Kutiš, 2002). Therefore, it can be concluded that in order to accurately estimate and assess the actual stress state of a spatial framed structure more rigorous analyses need to be performed. Even though refined models based on shell/plate or solid finite elements provide the means to perform such analyses, the inclusion of nonuniform warping effects in straight or curved beam elements based on so-called "Higher Order Beam Theories" (El Fatmi, and Ghazouani, 2011; Ghazouani, and El Fatmi, 2011; Sapountzakis, and Tsiptsis, 2015) is of increased interest due to their important advantages over more elaborate approaches such as traditional solid and plate models. More specifically

• A Beam formulation reduces significantly modeling effort (solid models require cumbersome post- and pre-processing even in relatively simple cases).

• It permits isolation of structural phenomena and results interpretation contrary to the reduced oversight of the 3-D Finite Element (FEM) models (quantities such as rotation, warping parameter, stress resultants etc. are also evaluated in contrast to solid model which yields only translations and stress components).

• It allows straightforward model handling (support modeling and external loading are easily applied).

• It avoids difficulties in discretizing a complex structure, while the resulting increased number of DOFs of the 3-D models leads to severe or unrealistic computational time.

• It avoids difficulties in discretizing a structure including thin-walled members (shear-, membrane-locking phenomena).

• It facilitates parametric analyses (solid modeling often requires construction of multiple models).

• It does not require shape functions for the kinematical components; hence the minimum number of elements can be employed, while the accuracy of function derivatives is not compromised.

• The use of shell or plate elements cannot give accurate results since warping of the walls of a cross section cannot be taken into account (midline model).

When compared to the effort involved in static analysis, there has not been much effort put into the dynamic analysis of curved box girder bridges (Heins, and Sahin, 1979). The geometric complexities and the spatial coupling effect between bending and torsion make the analysis of curved bridges difficult. Bridge design codes usually provide guidance for the dynamic analysis of straight bridges (dynamic amplification factor, natural frequencies, modelling of vehicles, placement of diaphragms etc.). These design recommendations have been used by some designers for curved bridges, even though some researches carried out (Cantieni, 1983; Ontario Highway Bridge Design Code, 1983; Billing and Green, 1984) revealed that need to be reviewed. When bridges are curved, different kinds of loads can cause lateral bending and torsional modes of vibration in addition to the common longitudinal or flexural modes of vibration and so there are still many possible as well as crucial problems to be investigated regarding the dynamic response, for example, forced vibration due to moving loads and earthquake, vehicle-bridge coupling vibration, and wind-induced vibration (Shi et al., 2009; Huang et al., 2012; Dimitrakopoulos and Zeng, 2015; Jun et al. 2014). Some research efforts analyzed out-of-plane vibrations of beams either with uniform or varying cross section and curvature (Huang et al., 2000; Tüfekçi, and Doğruer, 2006). In other studies, the dynamic responses of thin-walled curved box girder bridges due to truck loading have been investigated. The curved box girder bridges has been numerically modelled using finite elements which take into account the torsional warping, distortion and distortional warping (Huang et al., 1998; Nallasivam et al., 2007). Finally, to the authors' knowledge, the effects on linear and nonlinear vibrational responses of translational and rotational springs at the ends of a beam have mainly been investigated for straight geometry formulations (Wattanasakulpong and Chaikittiratana, 2014). In addition to this, most of the previous models have been formulated for specific type of loading and cross section either considering or not some higher order phenomena.

In this chapter, the static and dynamic generalized warping problem of *horizontally curved beams* of *arbitrary cross section*, loading and boundary conditions is presented. The proposed beam element possesses ten degrees of freedom (DOFs) per node in order to account for out-of-plane nonuniform warping due to both flexure and torsion (shear lag due to both flexure and torsion). This element can be employed in the analysis of curved bridge decks of open or closed (box-shaped) cross section. Except for these effects, curvature influences also the internal forces and deformations of the curved continuous beam, even for dead loading, due to the fact that the curved beam produces coupling between axial force, bending moments and torque, leading to the

development of both angle of twist and displacement in the radial direction. Great curvature can be considered in order to formulate the expressions of normal and shear strains. Thus, the sectorial properties related to the thickness-curvature effect, which need to be considered in cases of large subtended angle and small radius, are included in this study. The numerical solution of the problem is obtained by *Isogeometric tools*, either integrated in the Finite Element Method (FEM) (Hughes et al., 2009) or in a Boundary Element based Method (BEM) called Analog Equation Method (AEM) (Katsikadelis, 1994 and 2002b). When pure AEM is considered, constant or quadratic elements are employed in order to represent the fictitious loading. To the authors' knowledge Isogeometric analysis (IGA) is for the first time employed in the static and dynamic design of curved beams with higher order beam theories, especially combined with a BEM-based method. The developed horizontally curved model takes into account simultaneously in and out of the curvature's plane flexure, extension and torsion and permits the investigation of their coupling. The structure (e.g. bridge deck) is subjected to the combined action of arbitrarily distributed or concentrated axial and transverse loading, as well as to bending, twisting and warping moments. Its edges are subjected to the most general loading and boundary conditions, including also elastic support. The displacements of an arbitrary point of the cross section is obtained as the sum of  the St. Venant solution combined with residual displacements due to end-effects (Pai, 2014) which are responsible for the generation of self-equilibrating stress distributions (Reagan and Pilkey, 2002). These additional displacements are written as a sum of two-dimensional functions (out-of-plane warping functions) multiplied by independent parameters expressing their longitudinal intensity (El Fatmi and Ghazouani, 2011; Ghazouani and El Fatmi, 2011). Particularly, nonuniform warping distributions are taken into account by employing four independent warping parameters multiplying a shear warping function in each direction and two torsional warping functions, which are obtained by solving corresponding boundary value problems, formulated exploiting the longitudinal local equilibrium equation (Sapountzakis and Tsiptsis, 2015). Finally, by employing a distributed mass model system accounting for longitudinal, transverse, rotatory, torsional and warping inertia, ten boundary value problems, described by second-order differential equations, with respect to the variable along the beam, time-dependent and one-dimensional kinematical components are formulated. Free vibration characteristics and responses of the stress resultants and displacements to static and moving loading have been studied. The warping functions and the geometric constants including the additional ones due to warping are evaluated employing a pure BEM approach. It should be noted here that the sectorial properties related to the thickness-curvature effect need to be considered in cases of large subtended angle and small radius due to the fact that the arising differences become considerable (Kim and Kim, 2005).

The essential features and novel aspects of the formulation described in this Chapter compared with previous ones are summarized as follows:

i.   The proposed formulation is capable of the complete analysis of spatial curved beams of arbitrary closed or open cross section with one plane of constant

curvature (either small or great) considering flexural-torsional shear lag effects and transverse loading to the plane of curvature (as is usually the case in practice). The necessity to include nonuniform warping and STSD effects in the dynamic analysis of curved bridge decks is demonstrated.

ii. The developed beam formulation reduces significantly modelling effort due to the fact that there is no need for pre-processing in order to define geometry, which is an important issue even in simple curved beams. Moreover, it allows straightforward model handling (boundary conditions, external loading are easily modelled) compared with three-dimensional solid curved beam models.

iii. It avoids difficulties in discretizing a structure including thin-walled members (shear-locking, membrane-locking phenomena).

iv. A BEM based technique is for the first time used in the generalized analysis of curved beams.

v. The numerical solution of advanced beam theories and its application to the analysis of horizontally curved beams is based on B-splines (for straight beam formulations see: Sapountzakis and Tsiptsis, 2014; Sapountzakis and Tsiptsis, 2017) and NURBS (Isogeometric Analysis) offering the advantage of integrated computer aided design (CAD) in the analysis (Koo et al., 2013). In addition to this, the order of the basis functions can be defined by the user.

Numerical examples are worked out to illustrate the method, designate its efficiency, accuracy and computational cost, as well as verify its integrity comparing with the results of traditional methods used for the analysis of beams. NURBS and B-splines of various degrees have been employed. Knot insertion and degree elevation are proved to be very beneficial in refining the B-spline curve and increasing the accuracy (Hughes et al., 2009).

## 4.2  Statement of the problem

### 4.2.1 Curved beam model and generalized warping

A prismatic curved beam element of arc length $L$ with an arbitrarily shaped cross section of homogenous, isotropic and linearly elastic material with modulus of elasticity $E$ and shear modulus $G$, occupying the region $\Omega$ of the $yz$ plane (Fig. 4.1a) is considered in Fig. 4.1b. The boundary of the region $\Omega$ is denoted by $\Gamma$. This boundary curve is piecewise smooth (i.e. it may have a finite number of corners) and contains a finite number of inclusions. In Fig. 4.1 $CXYZ$ is the principal bending coordinate system through the cross section's centroid $C$ (considered as the flexural system with no lack of accuracy), while $y_C$, $z_C$ are its coordinates with respect to $Sxyz$ reference coordinate system through the cross section's shear center $S$. It holds that $y_C = y - Y$ and $z_C = z - Z$. The initial radius of curvature, which is considered constant in one plane, is denoted by $R$ and can be parallel either to $Z$ or to $Y$ axis depending on the system of axis considered (Fig. 4.1a). The beam element is subjected to the combined action of arbitrarily distributed or concentrated axial loading $p_x = p_x(X)$ along $X$ direction, transverse loading $p_y = p_y(x)$ and $p_z = p_z(x)$ along

the $y$, $z$ directions, respectively, twisting moments $m_x = m_x(x)$ along $x$ direction, bending moments $m_Y = m_Y(x)$, $m_Z = m_Z(x)$ along $Z$, $Y$ directions, respectively, as well as to warping moments (bimoments) $m_{\varphi_x^P} = m_{\varphi_x^P}(x)$, $m_{\varphi_Y^P} = m_{\varphi_Y^P}(x)$, $m_{\varphi_Z^P} = m_{\varphi_Z^P}(x)$ and $m_{\varphi_x^S} = m_{\varphi_x^S}(x)$ (Fig. 4.1b) (Sapountzakis and Tsiptsis, 2015).



(a)



(b)
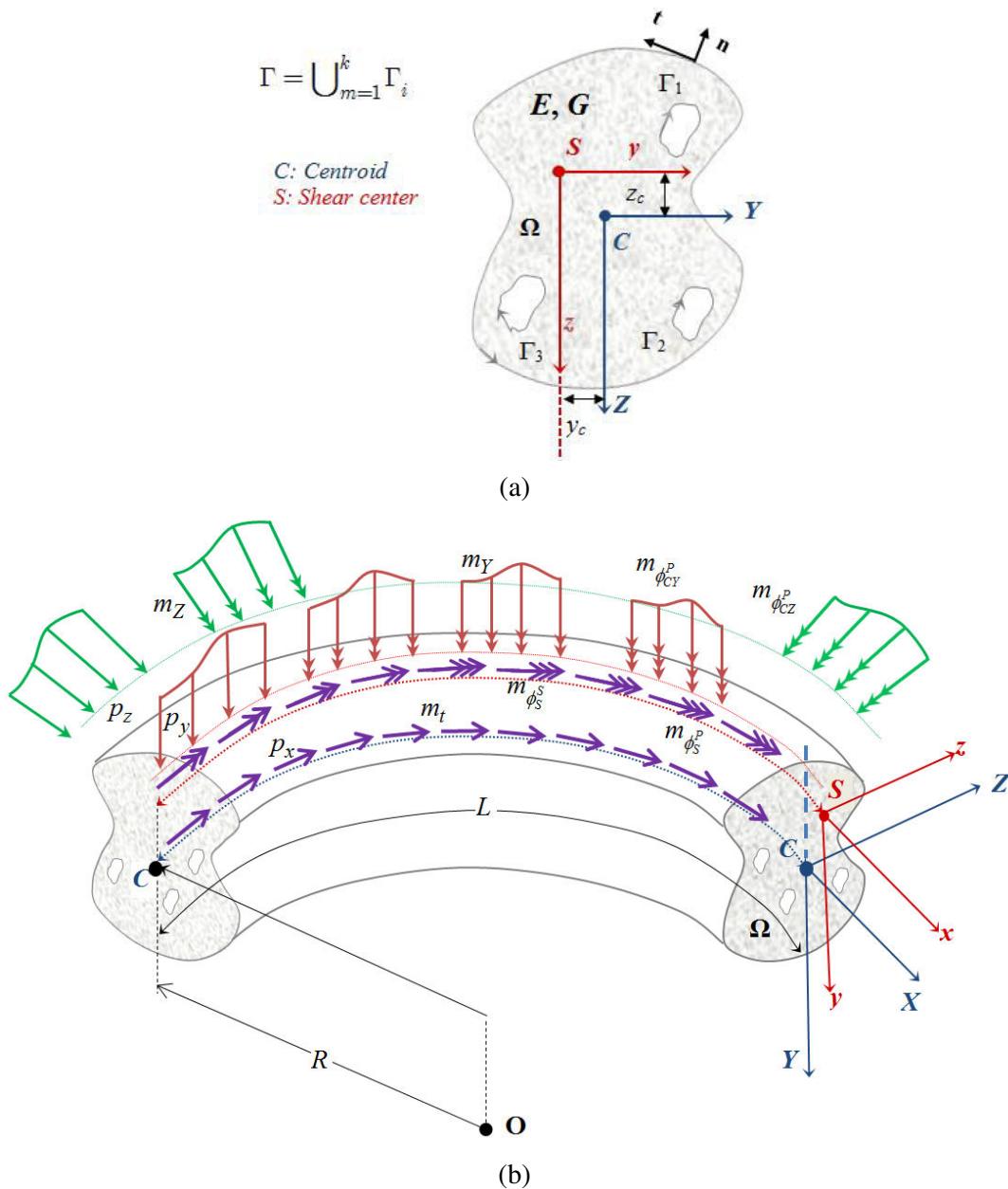
*Figure 4.1. Prismatic curved beam under axial-flexural-torsional loading (b) of an arbitrary homogenous cross section occupying the two dimensional region Ω (a)*

Under the action of the aforementioned arbitrary external loading and of possible restraints, the beam member is leaded to nonuniform flexure and/or nonuniform torsion. It is well-known that the bending moment at a beam cross

section represents the distribution of normal stresses due to bending (primary normal stresses $\sigma_{xx}^P$). It is important to notice here that comparing to straight beam formulation, the normal stress distribution is no more linear and follows a hyperbolic function (Fig. 4.2). Due to the aforementioned bending moment variation along the beam length (nonuniform bending and in a similar way for nonunifrom torsion), shear stresses arise on horizontal sections of an infinitesimal curved beam element (Fig. 4.3), equilibrating the variation of normal stresses due to bending. Cauchy
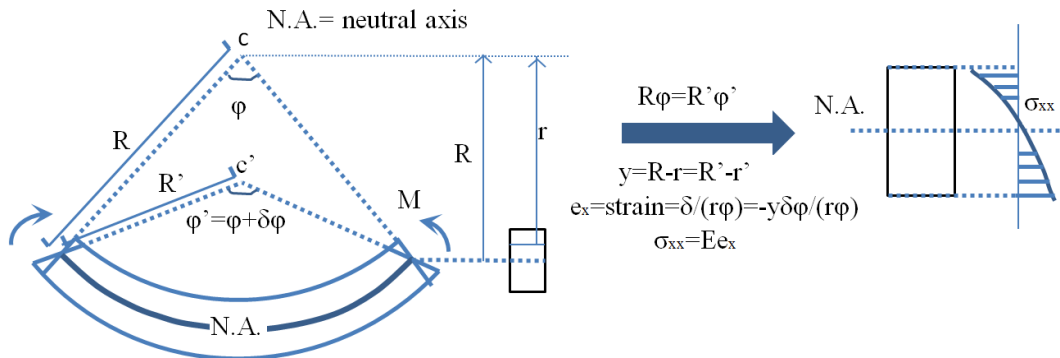


Figure 4.2. Primary stress distribution of infinitesimal curved beam element due to initial curvature.
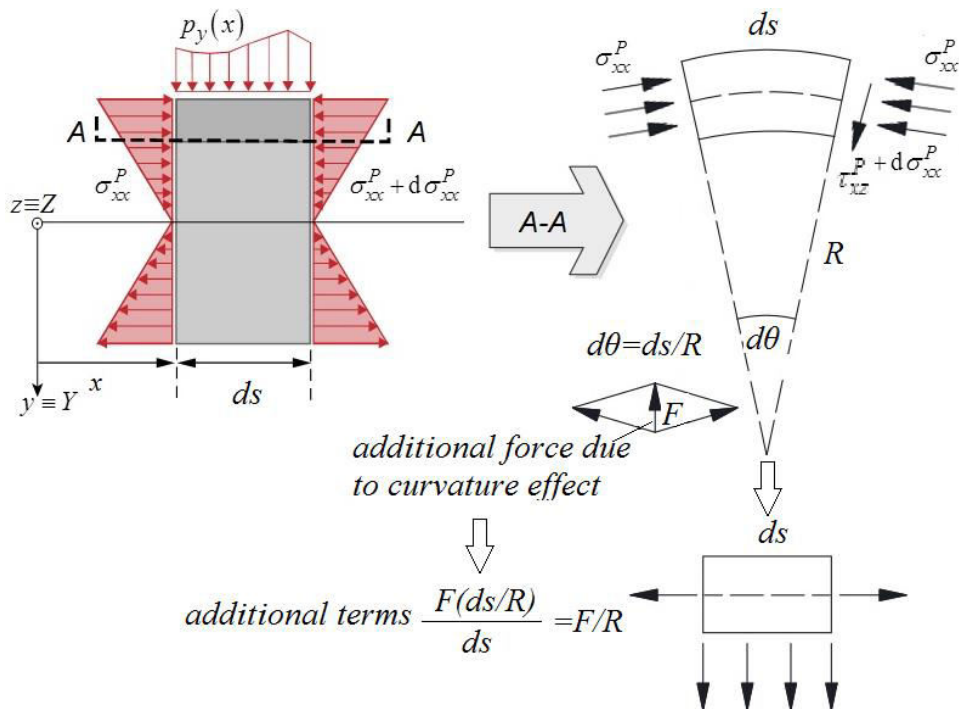


Figure 4.3. Primary stress of infinitesimal curved beam element and additional terms due to curvature effect. "Perturbed" straight beam formulation.

principle dictates that corresponding shear stresses arise on the plane of the cross section as well. If the assumption that plane sections remain plane after deformation (Euler-Bernoulli or Timoshenko beam theories) is maintained, the arising shear stresses

obtain a uniform distribution over the section (Dikaros, and Sapountzakis, 2014). However, this distribution violates local equilibrium since the requirement of vanishing tractions $\tau_{xn}$ on the lateral surface of the beam is not satisfied. Thus, the aforementioned shear stresses exhibit a nonuniform distribution over the cross section's domain so that both local equilibrium and vanishing tractions $\tau_{xn}$ on the lateral surface of the beam are satisfied. These nonuniform shear stresses will be referred to as primary (or St.Venant) shear stresses $(\tau_{xy}^P, \tau_{xz}^P)$ and lead the cross section to warp. Furthermore, due to the nonuniform character of this warping along the beam length a secondary normal stress distribution $\sigma_{xx}^S$ is developed. This normal stress distribution is responsible for the well-known shear lag phenomenon and it is taken into account by employing an independent warping parameter multiplying the warping function, which depends on the cross sectional configuration. The nonuniform distribution of secondary normal stresses $\sigma_{xx}^S$ along the length of the beam results in the development of secondary shear stresses $\tau_{xy}^S$, $\tau_{xz}^S$, which equilibrate the variation of $\sigma_{xx}^S$ at an infinitesimal beam element. However, the secondary shear stress distribution arising from the use of the aforementioned independent warping parameter fails to fulfill the zero-traction condition on the lateral surface of the beam. In order to remove this inconsistency, a shear stress correction is performed modifying the stress field by adding an additional warping function to "correct" $\tau_{xy}^S$, $\tau_{xz}^S$, according to Dikaros and Sapountzakis (2014). The above remarks are also valid for the problem of nonuniform torsion taking into account secondary torsional shear deformation effect – STSDE (Mokos, and Sapountzakis, 2011; Tsipiras, and Sapountzakis, 2012; Dikaros, and Sapountzakis, 2014). In the following analysis, in order to take into account torsional shear lag effects as well, the normal stress distribution due to secondary torsional warping $\varphi_S^S$ is also taken into account (secondary warping normal stress $\sigma_{xx}^S$). This distribution is equilibrated by corresponding tertiary shear stresses $\tau_{xy}^T$, $\tau_{xz}^T$ which, similarly with the case of shear lag analysis in flexure, require a correction. In the present analysis this is achieved by adding an additional torsional warping function.

Within the above described rationale, in order to take into account nonuniform flexural and torsional warping (including shear lag effect due to both flexure and torsion), in the study of the aforementioned element at each node of the element ends, four additional degrees of freedom are added to the well-known six DOFs of the classical three-dimensional frame element. The additional DOFs include four independent parameters, namely $\eta_Y$, $\eta_Z$, $\xi_x$, $\eta_x$, multiplying a shear warping function in each direction and two torsional warping functions, respectively. These DOFs describe the "intensities" of the corresponding cross sectional warpings along the beam length, while these warpings are defined by the corresponding warping function ($\varphi_Y^P$, $\varphi_Z^P$, $\varphi_x^P$, $\varphi_x^S$), depending only on the cross sectional configuration. Thus, the "actual" deformed configurations of the cross section due to primary (in each direction)

shear and primary, secondary torsional warpings are given as $\eta_Y(x,t)\varphi_Y^P(y,z)$, $\eta_Z(x,t)\varphi_Z^P(y,z)$, $\eta_x(x,t)\varphi_x^P(y,z)$ and $\xi_x(x,t)\varphi_x^S(y,z)$ at any time instant and position along the beam longitudinal axis, respectively. Moreover, additional terms are added due to curvature effect (Fig. 4.3) and the curved beam can be treated as a "perturbed" straight beam avoiding a more refined treatment, which would be more beneficial to geometries with large curvatures. Force F in Fig. 4.3 stands in general for any additional vector (even displacement or strain) that will be added as a result of the differential geometry. Finally, the corresponding stress resultants of the aforementioned additional DOFs are the warping moments $M_{\varphi_Y^P}$, $M_{\varphi_Z^P}$, $M_{\varphi_x^P}$, $M_{\varphi_x^S}$ (bimoments) along the beam length, arising from corresponding normal stress distributions. These bimoments due to the aforementioned warpings constitute additional "higher order" stress resultants, which are considered in the nonuniform shear and torsion theories.

Within the context of the above considerations, the displacement components of an arbitrary point of the beam at an arbitrary time instant are given as

$$\bar{u}(x,y,z,t) = \bar{u}^P(x,y,z,t) + \bar{u}^S(x,y,z,t) =$$

$$\underbrace{u(x,t) + \theta_Y(x,t)Z - \theta_Z(x,t)Y}_{rigid\ body\ movement}$$

$$+ \underbrace{\eta_x(x,t)\phi_S^P(y,z) + \eta_Y(x,t)\phi_{CY}^P(y,z) + \eta_Z(x,t)\phi_{CZ}^P(y,z) + \xi_x(x,t)\phi_S^S(y,z)}_{out\text{-}of\text{-}plane\ warping} \qquad (4.1a)$$

$$\bar{v}(x,y,z,t) = \underbrace{v(x,t) - z\theta_x(x,t)}_{rigid\ body\ movement} \qquad \bar{w}(x,y,z,t) = \underbrace{w(x,t) + y\theta_x(x,t)}_{rigid\ body\ movement} \qquad (4.1b,c)$$

where $\bar{u}$, $\bar{v}$, $\bar{w}$ are the axial and transverse beam displacement components with respect to the *Sxyz* system of axes; $\bar{u}^P$, $\bar{u}^S$ denote the primary and secondary longitudinal displacements (given in Chapter 3), respectively. Moreover, $v(x,t)$, $w(x,t)$ describe the vertical and lateral deflection of the centre of twist, while $u(x,t)$ denotes the "average" axial displacement of the cross section. $\theta_x(x,t)$ is the (total) angle of twist; $\theta_Z(x,t)$, $\theta_Y(x,t)$ are the angles of rotation due to bending about the centroidal $Y$, $Z$ axes, respectively; $\eta_x(x,t)$, $\xi_x(x,t)$ are the independent warping parameters introduced to describe the nonuniform distribution of primary and secondary torsional warping, while $\eta_Y(x,t)$, $\eta_Z(x,t)$ are the independent warping parameters introduced to describe the nonuniform distribution of primary warping due to shear.

After establishing the displacement field, the strain-displacement relations will be used for the curved beam element. The general shell theory for cylindrical shells (Sanders, 1963) can also explain the occurrence of additional terms. More specifically, the additional terms due to curvature regarding the axial strain $\varepsilon_{xx}$ are $\dfrac{\overline{w}}{R}$ (which stands for the increase in length due to the radial displacement $w$ according to Timoshenko and Woinowsky-Krieger (1959), when $R$ is parallel to $Z$) and $\dfrac{\theta_x}{R}$ (which is the decrease in the bending curvature with respect to $Z$ axis, when $R$ is parallel to $Z$). Thus, assuming $\dfrac{Z}{R} << 1$ (Gendy and Saleeb, 1992) and approximating $\dfrac{R}{R+Z} \approx 1 - \dfrac{Z}{R} + \left(\dfrac{Z}{R}\right)^2 = e(R)$ for the strain in the tangential direction in cylindrical coordinates, the axial strain-displacement relation is given as

$$
\varepsilon_{xx} = \left(\overline{u}_{,x} + \frac{\overline{w}}{R}\right) \cdot \left(1 - \frac{Z}{R} + \left(\frac{Z}{R}\right)^2\right) = \left[\underbrace{\left(u_{,x} + \frac{w}{R} + \theta_{Y,x}Z - (\theta_{Z,x} - \frac{\theta_x}{R})Y + \eta_{x,x}\phi_S^P\right)}_{\text{primary}} + \right.
$$

$$
\left. \underbrace{\left(\eta_{Y,x}\phi_{CY}^P + \eta_{Z,x}\phi_{CZ}^P + \xi_{x,x}\phi_S^S\right)}_{\text{secondary}} \right] \cdot \left(1 - \frac{Z}{R} + \left(\frac{Z}{R}\right)^2\right) \tag{4.2}
$$

According to the shear components of strain

$$
\gamma_{xy} = \left(\overline{v}_{,x}\right) \cdot \left(1 - \frac{Z}{R} + \left(\frac{Z}{R}\right)^2\right) + \overline{u}_{,y} = \left(v_{,x} - z\theta_{x,x}\right)\left(1 - \frac{Z}{R} + \left(\frac{Z}{R}\right)^2\right) + \overline{u}_{,y} \tag{4.3a}
$$

$$
\gamma_{xz} = \left(\overline{w}_{,x} - \frac{\overline{u}}{R}\right) \cdot \left(1 - \frac{Z}{R} + \left(\frac{Z}{R}\right)^2\right) + \overline{u}_{,z} = \left(w_{,x} + y\theta_{x,x} - \frac{\overline{u}}{R}\right)\left(1 - \frac{Z}{R} + \left(\frac{Z}{R}\right)^2\right) + \overline{u}_{,z} \tag{4.3b}
$$

Defining the independent geometric (derived from displacements) generalized strains $\varepsilon_R$ as $u_{,x}$, $\theta_{Y,x}$, $\theta_{Z,x}$, $\eta_{x,x}$, $\eta_{Y,x}$, $\eta_{Z,x}$, $\xi_{x,x}$, $\gamma_x^P = \theta_{x,x} + \dfrac{\theta_Z}{R}$, $\gamma_x^S = \eta_x - \gamma_x^P = \eta_x - \theta_{x,x} - \dfrac{\theta_Z}{R}$, $\gamma_x^T = \xi_x - \gamma_x^S = \xi_x - \eta_x + \theta_{x,x} + \dfrac{\theta_Z}{R}$, $\gamma_Y^P = v_{,x} - \theta_Z$, $\gamma_Y^S = \eta_Z - v_{,x} + \theta_Z$, $\gamma_Z^P = w_{,x} + \theta_Y - \dfrac{u}{R}$ and $\gamma_Z^S = \eta_Y - w_{,x} - \theta_Y + \dfrac{u}{R}$, and neglecting $\dfrac{Z}{R}$ effect for shear strains (viewed as higher order term by itself), the shear strain-displacement relations are given as

$$\gamma_{xy} = \left\{ \gamma_Z^P \left[ Z_{,y} + \left( \varphi_{CY,y}^P \right)_m \right] + \gamma_Y^P \left[ Y_{,y} + \left( \varphi_{CZ,y}^P \right)_m \right] + \gamma_x^P \left[ -z + \left( \varphi_{S,y}^P \right)_m \right] \right\} +$$
<center>primary</center>

$$+ \left\{ \gamma_Z^S \left( \varphi_{CY,y}^P \right)_m + \gamma_Y^S \left( \varphi_{CZ,y}^P \right)_m + \gamma_x^S \left[ \left( \varphi_{S,y}^P \right)_m + \left( \varphi_{S,y}^S \right)_m \right] \right\} + \left[ \gamma_x^T \left( \varphi_{S,y}^S \right)_m \right] \qquad (4.4a)$$
<center>secondary       tertiary</center>

$$\gamma_{xz} = \left\{ \gamma_Z^P \left[ Z_{,z} + \left( \varphi_{CY,z}^P \right)_m \right] + \gamma_Y^P \left[ Y_{,z} + \left( \varphi_{CZ,z}^P \right)_m \right] + \gamma_x^P \left[ y + \left( \varphi_{S,z}^P \right)_m \right] \right\} +$$
<center>primary</center>

$$+ \left\{ \gamma_Z^S \left( \varphi_{CY,z}^P \right)_m + \gamma_Y^S \left( \varphi_{CZ,z}^P \right)_m + \gamma_x^S \left[ \left( \varphi_{S,z}^P \right)_m + \left( \varphi_{S,z}^S \right)_m \right] \right\} + \left[ \gamma_x^T \left( \varphi_{S,z}^S \right)_m \right] \qquad (4.4b)$$
<center>secondary       tertiary</center>

It is worth here noting that the term $\dfrac{\theta_Z}{R}$ has been added to the primary shear strain due to torsion $\gamma_x^P$ according to the concept presented in Fig. 4.3. Additionally, the primary transverse shear strain $\gamma_Z^P$ due to flexure in *XZ* plane (which is the plane of curvature) can be defined if the equations of general shell theory (Sanders, 1963) are employed and considering that the Kirchhoff hypothesis is not valid ( $w_{,x} \neq \theta_Y$ ). On the contrary, the primary transverse shear strain $\gamma_Y^P$ due to flexure in *XY* plane is not affected by the curvature. The above mentioned expressions of shear strains are also analytically derived according to the refined theory of thick cylindrical shells presented in (Voyiadjis and Karamanlidis, 1990).

Employing the Hooke's stress-strain law, the resulting components of the Cauchy stress tensor can be obtained after substituting the components of the strain tensor given in eqns. (4.2, 4.4) as

$$\sigma_{xx} = E\varepsilon_{xx} = \left[ E\left( u_{,x} + \frac{w}{R} + \theta_{Y,x}Z - (\theta_{Z,x} - \frac{\theta_x}{R})Y + \eta_{x,x}\phi_S^P \right) + \right.$$
<center>primary</center>

$$\left. \underbrace{E\left( \eta_{Y,x}\phi_{CY}^P + \eta_{Z,x}\phi_{CZ}^P + \xi_{x,x}\phi_S^S \right)}_{\text{secondary}} \right] \cdot \left( 1 - \frac{Z}{R} + \left( \frac{Z}{R} \right)^2 \right) \qquad (4.5a)$$

$$\tau_{xy} = G\gamma_{xy} = G\left\{ \gamma_Z^P \left[ Z_{,y} + \left( \varphi_{CY,y}^P \right)_m \right] + \gamma_Y^P \left[ Y_{,y} + \left( \varphi_{CZ,y}^P \right)_m \right] + \gamma_x^P \left[ -z + \left( \varphi_{S,y}^P \right)_m \right] \right\} +$$
<center>primary</center>

$$+G\left\{\gamma_Z^S\left(\varphi_{CY,y}^P\right)_m+\gamma_Y^S\left(\varphi_{CZ,y}^P\right)_m+\gamma_x^S\left[\left(\varphi_{S,y}^P\right)_m+\left(\varphi_{S,y}^S\right)_m\right]\right\}+\left[G\gamma_x^T\left(\varphi_{S,y}^S\right)_m\right] \qquad (4.5b)$$

$$\underbrace{\phantom{+G\left\{\gamma_Z^S\left(\varphi_{CY,y}^P\right)_m+\gamma_Y^S\left(\varphi_{CZ,y}^P\right)_m+\gamma_x^S\left[\left(\varphi_{S,y}^P\right)_m+\left(\varphi_{S,y}^S\right)_m\right]\right\}}}_{\text{secondary}}\quad\underbrace{\phantom{\left[G\gamma_x^T\left(\varphi_{S,y}^S\right)_m\right]}}_{\text{tertiary}}$$

$$\tau_{xz}=G\gamma_{xz}=G\left\{\underbrace{\gamma_Z^P\left[Z_{,z}+\left(\varphi_{CY,z}^P\right)_m\right]+\gamma_Y^P\left[Y_{,z}+\left(\varphi_{CZ,z}^P\right)_m\right]+\gamma_x^P\left[y+\left(\varphi_{S,z}^P\right)_m\right]}_{\text{primary}}\right\}+$$

$$+G\left\{\gamma_Z^S\left(\varphi_{CY,z}^P\right)_m+\gamma_Y^S\left(\varphi_{CZ,z}^P\right)_m+\gamma_x^S\left[\left(\varphi_{S,z}^P\right)_m+\left(\varphi_{S,z}^S\right)_m\right]\right\}+\left[G\gamma_x^T\left(\varphi_{S,z}^S\right)_m\right] \qquad (4.5c)$$

$$\underbrace{\phantom{+G\left\{\gamma_Z^S\left(\varphi_{CY,z}^P\right)_m+\gamma_Y^S\left(\varphi_{CZ,z}^P\right)_m+\gamma_x^S\left[\left(\varphi_{S,z}^P\right)_m+\left(\varphi_{S,z}^S\right)_m\right]\right\}}}_{\text{secondary}}\quad\underbrace{\phantom{\left[G\gamma_x^T\left(\varphi_{S,z}^S\right)_m\right]}}_{\text{tertiary}}$$

where $(\cdot)_{,i}$ denotes differentiation with respect to $i$. However, as stated above, attention should be paid to the fact that the terms $G\gamma_Z^S\phi_{CY,i}^P$, $G\gamma_Y^S\phi_{CZ,i}^P$, $G\gamma_x^T\phi_{S,i}^S$ ($i=y,z$) are not capable of representing an acceptable shear stress distribution, leading to violation of the longitudinal local equilibrium equation and the corresponding zero-traction condition on the lateral surface of the beam. Thus, a correction of stress components is performed without increasing the number of global kinematical unknowns. Three additional warping functions $\varphi_{CY}^S(y,z)$, $\varphi_{CZ}^S(y,z)$, $\varphi_S^T(y,z)$ are introduced in expressions (4.5b, c) and the components of the Cauchy stress tensor in the region $\Omega$ are modified as

$$\tau_{xy}=G\underbrace{\left\{\gamma_Z^P\Phi_{CY,y}^P+\gamma_Y^P\Phi_{CZ,y}^P+\gamma_x^P\left(z+\phi_{S,y}^P\right)\right\}}_{\text{primary}}+$$

$$+\underbrace{G\left(\gamma_Z^S\Phi_{CY,y}^S+\gamma_Y^S\Phi_{CZ,y}^S+\gamma_x^S\Phi_{S,y}^S\right)}_{\text{secondary}}+\underbrace{G\gamma_x^T\Phi_{S,y}^T}_{\text{tertiary}} \qquad (4.6a)$$

$$\tau_{xz}=G\underbrace{\left[\gamma_Z^P\Phi_{CY,z}^P+\gamma_Y^P\Phi_{CZ,z}^P+\gamma_x^P\left(-y+\phi_{S,z}^P\right)\right]}_{\text{primary}}+$$

$$+\underbrace{G\left(\gamma_Z^S\Phi_{CY,z}^S+\gamma_Y^S\Phi_{CZ,z}^S+\gamma_x^S\Phi_{S,z}^S\right)}_{\text{secondary}}+\underbrace{G\gamma_x^T\Phi_{S,z}^T}_{\text{tertiary}} \qquad (4.6b)$$

where, according to Dikaros, and Sapountzakis (2014),

$$\Phi_{CY}^P=Z+\phi_{CY}^P \qquad\qquad \Phi_{CY}^S=\phi_{CY}^P+\phi_{CY}^S \qquad\qquad (4.7a,b)$$

$$\Phi_{CZ}^P=Y+\phi_{CZ}^P \qquad\qquad \Phi_{CZ}^S=\phi_{CZ}^P+\phi_{CZ}^S \qquad\qquad (4.7c,d)$$

$$\Phi_S^S = \phi_S^P + \phi_S^S \qquad\qquad \Phi_S^T = \phi_S^S + \phi_S^T \qquad\qquad\qquad (4.7\text{e,f})$$

In order to establish the differential equations of equilibrium based on the corrected shear stresses (eqns. (4.6)), the principle of virtual work

$$\delta W_{\text{int}} = \delta W_{\text{ext}} \qquad\qquad\qquad (4.8)$$

is employed, where

$$\delta W_{\text{int}} = \int_V \left( \sigma_{xx}\delta\varepsilon_{xx} + \tau_{xy}\delta\gamma_{xy} + \tau_{xz}\delta\gamma_{xz} \right) dV \qquad\qquad\qquad (4.9)$$

$$\delta W_{\text{ext}} = \int_{\text{Lat}} \left( t_x\delta\overline{u} + t_y\delta\overline{v} + t_z\delta\overline{w} \right) dF \qquad\qquad\qquad (4.10)$$

In the above equations, $\delta(\cdot)$ denotes virtual quantities; $t_x$, $t_y$, $t_z$ are the components of the traction vector applied on the lateral surface of the beam including the end cross sections, denoted by $F$ and $V$ is the volume of the beam.
The geometric constants of the beam are obtained by the following definitions

$$A = \int_\Omega d\Omega \qquad S_Y = \int_\Omega Z\, d\Omega \qquad S_Z = \int_\Omega Y\, d\Omega \qquad\qquad (4.11\text{a,b,c})$$

$$I_{YY} = \int_\Omega Z^2\, d\Omega \qquad I_{ZZ} = \int_\Omega Y^2\, d\Omega \qquad I_{YZ} = \int_\Omega YZ\, d\Omega \qquad (4.11\text{d,e,f})$$

$$S_i = \int_\Omega (i)\, d\Omega, \quad i = \phi_S^P, \phi_{CY}^P, \phi_{CZ}^P, \phi_S^S \qquad\qquad (4.11\text{g})$$

$$I_{ij} = \int_\Omega (i)(j)\, d\Omega, \quad i,j = y, z, \phi_S^P, \phi_{CY}^P, \phi_{CZ}^P, \phi_S^S \qquad\qquad (4.11\text{h})$$

$$D_{ij} = \int_\Omega \left[ \nabla(i)\cdot\nabla(j) \right] d\Omega, \quad i,j = y, z, \phi_S^P, \phi_{CY}^P, \phi_{CZ}^P, \phi_S^S \qquad (4.11\text{i})$$

$$I_t^P = \int_\Omega \left( y^2 + z^2 + z\phi_{S,y}^P - y\phi_{S,z}^P \right) d\Omega \qquad\qquad (4.11\text{j})$$

where $\nabla \equiv (\cdot)_{,y}\mathbf{i}_y + (\cdot)_{,z}\mathbf{i}_z$ is the gradient operator and $\mathbf{i}_y$, $\mathbf{i}_z$ the unit vectors along $y$, $z$ axes, respectively. The quantities $I_{\phi_{Ci}^P\phi_{Ci}^P}$ ($i = Y, Z$) correspond to the shear warping constants, while $I_{\phi_S^P\phi_S^P}$, $I_{\phi_S^S\phi_S^S}$ are the primary and secondary torsional warping constants, respectively. It should be noted that $I_{\phi_S^P\phi_S^P}$ constant coincides with the warping constant $C_S$ of nonuniform torsion beam theory. Employing definitions in

eqns. (4.11), having in mind that *CXYZ* is the centroidal principal bending coordinate system, that *S* is the center of twist of the cross section and exploiting the orthogonality conditions of the warping functions, the following relations are obtained

$$S_Y = S_Z = S_{\phi_S^P} = S_{\phi_{CY}^P} = S_{\phi_{CZ}^P} = S_{\phi_S^S} = 0 \tag{4.12a}$$

$$I_{YZ} = I_{Y\phi_{CZ}^P} = I_{Z\phi_{CY}^P} = I_{Y\phi_S^P} = I_{Z\phi_S^P} = I_{Y\phi_S^S} = I_{Z\phi_S^S} = I_{\phi_S^P\phi_S^S} = 0 \tag{4.12b}$$

$$D_{\Phi_{CY}^P\Phi_{CY}^S} = D_{\Phi_{CZ}^P\Phi_{CZ}^S} = D_{\Phi_S^S\Phi_S^T} = 0 \tag{4.12c}$$

The stress resultants of the beam are defined as

$$N = \int_\Omega \sigma_{xx}\, d\Omega \tag{4.13a}$$

$$M_Y = \int_\Omega \sigma_{xx} Z\, d\Omega \qquad M_Z = -\int_\Omega \sigma_{xx} Y\, d\Omega \tag{4.13b,c}$$

$$M_{\phi_S^P} = \int_\Omega \sigma_{xx}\phi_S^P\, d\Omega \qquad M_{\phi_S^S} = \int_\Omega \sigma_{xx}\phi_S^S\, d\Omega \tag{4.13d,e}$$

$$M_{\phi_{CY}^P} = \int_\Omega \sigma_{xx}\phi_{CY}^P\, d\Omega \qquad M_{\phi_{CZ}^P} = \int_\Omega \sigma_{xx}\phi_{CZ}^P\, d\Omega \tag{4.13f,g}$$

$$Q_y^P = \int_\Omega \left(\tau_{xy}\Phi_{CZ,y}^P + \tau_{xz}\Phi_{CZ,z}^P\right)d\Omega \qquad Q_y^S = -\int_\Omega \left(\tau_{xy}\Phi_{CZ,y}^S + \tau_{xz}\Phi_{CZ,z}^S\right)d\Omega \tag{4.13h,i}$$

$$Q_z^P = \int_\Omega \left(\tau_{xy}\Phi_{CY,y}^P + \tau_{xz}\Phi_{CY,z}^P\right)d\Omega \qquad Q_z^S = -\int_\Omega \left(\tau_{xy}\Phi_{CY,y}^S + \tau_{xz}\Phi_{CY,z}^S\right)d\Omega \tag{4.13j,k}$$

$$M_t^P = \int_\Omega \left[\tau_{xy}\left(\phi_{S,y}^P + z\right) + \tau_{xz}\left(\phi_{S,z}^P - y\right)\right]d\Omega \tag{4.13l}$$

$$M_t^S = -\int_\Omega \left(\tau_{xy}\Phi_{S,y}^S + \tau_{xz}\Phi_{S,z}^S\right)d\Omega \qquad M_t^T = \int_\Omega \left(\tau_{xy}\Phi_{S,y}^T + \tau_{xz}\Phi_{S,z}^T\right)d\Omega \tag{4.13m,n}$$

where $M_i$ ( $i = Y, Z$ ) are the bending moments and $M_i$ ( $i = \varphi_S^P, \varphi_S^S, \varphi_{CY}^P, \varphi_{CZ}^P$ ) are the warping moments (bimoments). $Q_i^j$ ( $i = y, z$  $j = P, S$ ) are the primary and secondary parts of total shear forces $Q_i$ ( $i = y, z$ ). It is noted that the secondary shear forces are also referred to as bishear stress resultants since they equilibrate the corresponding warping moments (bimoments). Similarly, $M_t^j$ ( $j = P, S, T$ ) are the primary, secondary and tertiary parts of total twisting moment $M_t$.

Employing eqns. (4.5a), (4.6a,b), (4.11), (4.12) and (4.13), the expressions of the stress resultants in terms of the kinematical components are obtained as

$$N = EA\left(u_{,x} + \frac{w}{R}\right) + \frac{EI_{YY}}{R}\left(\frac{u_{,xx}}{R} + \frac{w_{,x}}{R^2} - 2\theta_{Y,xx}\right) \tag{4.14a}$$

$$M_Y = EI_{YY}\theta_{Y,x} \tag{4.14b}$$

$$M_Z = EI_{ZZ}\left(\theta_{Z,x} - \frac{\theta_x}{R}\right) \tag{4.14c}$$

$$M_{\phi_S^P} = E\left(I_{\phi_S^P \phi_S^P}\eta_{x,x} + I_{\phi_{CY}^P \phi_S^P}\eta_{Y,x} + I_{\phi_{CZ}^P \phi_S^P}\eta_{Z,x}\right) \tag{4.14d}$$

$$M_{\phi_S^S} = E\left(I_{\phi_{CY}^P \phi_S^S}\eta_{Y,x} + I_{\phi_{CZ}^P \phi_S^S}\eta_{Z,x} + I_{\phi_S^S \phi_S^S}\xi_{x,x}\right) \tag{4.14e}$$

$$M_{\phi_{CY}^P} = E\left(I_{\phi_{CY}^P \phi_S^P}\eta_{x,x} + I_{\phi_{CY}^P \phi_{CY}^P}\eta_{Y,x} + I_{\phi_{CY}^P \phi_S^S}\xi_{x,x}\right) \tag{4.14f}$$

$$M_{\phi_{CZ}^P} = E\left(I_{\phi_{CZ}^P \phi_S^P}\eta_{x,x} + I_{\phi_{CZ}^P \phi_{CZ}^P}\eta_{Z,x} + I_{\phi_{CZ}^P \phi_S^S}\xi_{x,x}\right) \tag{4.14g}$$

$$Q_y^P = GD_{\Phi_{CZ}^P \Phi_{CZ}^P}\gamma_Y^P \tag{4.14h}$$

$$Q_y^S = -G\left(D_{\Phi_{CZ}^S \Phi_{CZ}^S}\gamma_Y^S + D_{\Phi_{CZ}^S \Phi_S^S}\gamma_x^S + D_{\Phi_{CZ}^S \Phi_S^T}\gamma_x^T\right) \tag{4.14i}$$

$$Q_z^P = GD_{\Phi_{CY}^P \Phi_{CY}^P}\gamma_Z^P \tag{4.14j}$$

$$Q_z^S = -G\left(D_{\Phi_{CY}^S \Phi_{CY}^S}\gamma_Z^S + D_{\Phi_{CY}^S \Phi_S^S}\gamma_x^S + D_{\Phi_{CY}^S \Phi_S^T}\gamma_x^T\right) \tag{4.14k}$$

$$M_t^P = GI_t^P\gamma_x^P = GI_t^P\left(\theta_{x,x} + \frac{\theta_Z}{R}\right) \tag{4.14l}$$

$$M_t^S = -G\left(D_{\Phi_S^S \Phi_S^S}\gamma_x^S + D_{\Phi_{CZ}^S \Phi_S^S}\gamma_Y^S + D_{\Phi_{CY}^S \Phi_S^S}\gamma_Z^S\right) \tag{4.14m}$$

$$M_t^T = G\left(D_{\Phi_S^T \Phi_S^T}\gamma_x^T + D_{\Phi_{CZ}^S \Phi_S^T}\gamma_Y^S + D_{\Phi_{CY}^S \Phi_S^T}\gamma_Z^S\right) \tag{4.14n}$$

The quantities $GD_{ii}$ $(i = \Phi_{CY}^P, \Phi_{CZ}^P)$ multiplying $\gamma_Y^P$ and $\gamma_Z^P$ respectively, correspond to the shear rigidities of Timoshenko beam theory. Thus, the simplified notation $GA_i^P$ $(i = Y, Z)$ could be adopted for these quantities. Similarly, $GD_{ii}$ $(i = \Phi_{CY}^S, \Phi_{CZ}^S)$ refer to the secondary shear rigidities due to nonuniform shear warping and can be denoted as $GA_i^S$ $(i = Y, Z)$. Finally, $GD_{ii}$ $(i = \Phi_S^S, \Phi_S^T)$ refer to the secondary and tertiary torsional rigidities and can be also denoted as $GI_t^S$, $GI_t^T$, respectively. In what follows, in order to maintain the compatibility with classical notations, the above simplified symbols will be employed.

Using the expressions of the strain components (eqns. (4.2, 4.4)), the definitions of the stresses and applying the principle of virtual work or any other variational principle following standard arguments in the calculus of variations, the governing differential equations for the curved beam in terms of the kinematical components can be derived. Thus, the local stiffness matrix $[k_t]$ of the spatial curved beam can be evaluated after solving the system of the linear equations.

$$-EA\left(u_{,xx} + \frac{w_{,x}}{R}\right) - \frac{EI_{YY}}{R}\left(\frac{u_{,xx}}{R} + \frac{w_{,x}}{R^2} - 2\theta_{Y,xx}\right) - \frac{G}{R}\left(A_Z^P + A_Z^S\right)\left(w_{,x} + \theta_Y - \frac{u}{R}\right) +$$

$$\frac{G}{R}A_Z^S\eta_Y + \frac{G}{R}\left(D_{\Phi_{CY}^S\Phi_S^S} - D_{\Phi_{CY}^S\Phi_S^T}\right)\left(\eta_x - \theta_{x,x} - \frac{\theta_Z}{R}\right) + \frac{G}{R}D_{\Phi_{CY}^S\Phi_S^T}\xi_x = p_x \qquad (4.15a)$$

$$-G\left(A_Y^P + A_Y^S\right)\left(v_{,xx} - \theta_{Z,x}\right) + GA_Y^S\eta_{Z,x} + G\left(D_{\Phi_{CZ}^S\Phi_S^S} - D_{\Phi_{CZ}^S\Phi_S^T}\right)\left(\eta_{x,x} - \theta_{x,xx} - \frac{\theta_{Z,x}}{R}\right) +$$

$$+GD_{\Phi_{CZ}^S\Phi_S^T}\xi_{x,x} = p_y \qquad (4.15b)$$

$$-G\left(A_Z^P + A_Z^S\right)\left(w_{,xx} + \theta_{Y,x} - \frac{u_{,x}}{R}\right) + GA_Z^S\eta_{Y,x} + G\left(D_{\Phi_{CY}^S\Phi_S^S} - D_{\Phi_{CY}^S\Phi_S^T}\right)\cdot$$

$$\cdot\left(\eta_{x,x} - \theta_{x,xx} - \frac{\theta_{Z,x}}{R}\right) + GD_{\Phi_{CY}^S\Phi_S^T}\xi_{x,x} + \frac{EA}{R}\left(u_{,x} + \frac{w}{R}\right) +$$

$$+\frac{EI_{YY}}{R^2}\left(\frac{u_{,x}}{R} + \frac{w}{R^2} - 2\theta_{Y,x}\right) = p_z \qquad (4.15c)$$

$$-EI_{ZZ}\left(\theta_{Z,xx} - \frac{\theta_{x,x}}{R}\right) - G\left(A_Y^P + A_Y^S\right)\left(v_{,x} - \theta_Z\right) + GA_Y^S\eta_Z + G\left(D_{\Phi_{CZ}^S\Phi_S^S} - D_{\Phi_{CZ}^S\Phi_S^T}\right)\cdot$$

$$\cdot\left(\eta_x - \theta_{x,x} - \frac{\theta_Z}{R}\right) + GD_{\Phi_{CZ}^S\Phi_S^T}\xi_x - \frac{G}{R}\left(D_{\Phi_{CZ}^S\Phi_S^S} - D_{\Phi_{CZ}^S\Phi_S^T}\right)\left(\eta_Z - v_{,x} + \theta_Z\right)$$

$$-\frac{G}{R}\left(D_{\Phi_{CY}^S\Phi_S^S}-D_{\Phi_{CY}^S\Phi_S^T}\right)\cdot\left(\eta_Y-w_{,x}-\theta_Y+\frac{u}{R}\right)-\frac{G}{R}\left(I_t^S+I_t^T\right)\left(\eta_x-\theta_{x,x}-\frac{\theta_Z}{R}\right)+$$

$$+\frac{G}{R}I_t^T\xi_x+\frac{G}{R}I_t^P\left(\theta_{x,x}+\frac{\theta_Z}{R}\right)=m_Z \tag{4.15d}$$

$$-EI_{YY}\theta_{Y,xx}+\frac{2EI_{YY}}{R}\left(u_{,xx}+\frac{w_{,x}}{R}\right)+G\left(A_Z^P+A_Z^S\right)\left(w_{,x}+\theta_Y-\frac{u}{R}\right)-GA_Z^S\eta_Y$$

$$-G\left(D_{\Phi_{CY}^S\Phi_S^S}-D_{\Phi_{CY}^S\Phi_S^T}\right)\left(\eta_x-\theta_{x,x}-\frac{\theta_Z}{R}\right)-GD_{\Phi_{CY}^S\Phi_S^T}\xi_x=m_Y \tag{4.15e}$$

$$-E\left(I_{\phi_{CZ}^P\phi_S^P}\eta_{x,xx}+I_{\phi_{CZ}^P\phi_{CZ}^P}\eta_{Z,xx}+I_{\phi_{CZ}^P\phi_S^S}\xi_{x,xx}\right)+GA_Y^S\left(\eta_Z-v_{,x}+\theta_Z\right)+$$

$$+G\left(D_{\Phi_{CZ}^S\Phi_S^S}-D_{\Phi_{CZ}^S\Phi_S^T}\right)\left(\eta_x-\theta_{x,x}-\frac{\theta_Z}{R}\right)+GD_{\Phi_{CZ}^S\Phi_S^T}\xi_x=m_{\phi_{CZ}^P} \tag{4.15f}$$

$$-E\left(I_{\phi_{CY}^P\phi_S^P}\eta_{x,xx}+I_{\phi_{CY}^P\phi_{CY}^P}\eta_{Y,xx}+I_{\phi_{CY}^P\phi_S^S}\xi_{x,xx}\right)+GA_Z^S\left(\eta_Y-w_{,x}-\theta_Y+\frac{u}{R}\right)+$$

$$+G\left(D_{\Phi_{CY}^S\Phi_S^S}-D_{\Phi_{CY}^S\Phi_S^T}\right)\left(\eta_x-\theta_{x,x}-\frac{\theta_Z}{R}\right)+GD_{\Phi_{CY}^S\Phi_S^T}\xi_x=m_{\phi_{CY}^P} \tag{4.15g}$$

$$-GI_t^P\left(\theta_{x,xx}+\frac{\theta_{Z,x}}{R}\right)+G\left(I_t^S+I_t^T\right)\left(\eta_{x,x}-\theta_{x,xx}-\frac{\theta_{Z,x}}{R}\right)-GI_t^T\xi_{x,x}+$$

$$+G\left(D_{\Phi_{CZ}^S\Phi_S^S}-D_{\Phi_{CZ}^S\Phi_S^T}\right)\left(\eta_{Z,x}-v_{,xx}+\theta_{Z,x}\right)+G\left(D_{\Phi_{CY}^S\Phi_S^S}-D_{\Phi_{CY}^S\Phi_S^T}\right)\cdot$$

$$\cdot\left(\eta_{Y,x}-w_{,xx}-\theta_{Y,x}+\frac{u_{,x}}{R}\right)-\frac{E}{R}I_{ZZ}\left(\theta_{Z,x}-\frac{\theta_x}{R}\right)=m_t \tag{4.15h}$$

$$-E\left(I_{\phi_S^P\phi_S^P}\eta_{x,xx}+I_{\phi_{CY}^P\phi_S^P}\eta_{Y,xx}+I_{\phi_{CZ}^P\phi_S^P}\eta_{Z,xx}\right)+G\left(I_t^S+I_t^T\right)\left(\eta_x-\theta_{x,x}-\frac{\theta_Z}{R}\right)-GI_t^T\xi_x+$$

$$+G\left(D_{\Phi_{CZ}^S\Phi_S^S}-D_{\Phi_{CZ}^S\Phi_S^T}\right)\left(\eta_Z-v_{,x}+\theta_Z\right)+G\left(D_{\Phi_{CY}^S\Phi_S^S}-D_{\Phi_{CY}^S\Phi_S^T}\right)\cdot$$

$$\cdot\left(\eta_Y-w_{,x}-\theta_Y+\frac{u}{R}\right)=m_{\phi_S^P} \tag{4.15i}$$

$$-E\left(I_{\phi_{CY}^P\phi_S^S}\eta_{Y,xx}+I_{\phi_{CZ}^P\phi_S^S}\eta_{Z,xx}+I_{\phi_S^S\phi_S^S}\xi_{x,xx}\right)+GI_t^T\left(\xi_x-\eta_x+\theta_{x,x}+\frac{\theta_Z}{R}\right)+$$

$$+GD_{\Phi_{CZ}^S\Phi_S^T}\left(\eta_Z-v_{,x}+\theta_Z\right)+GD_{\Phi_{CY}^S\Phi_S^T}\left(\eta_Y-w_{,x}-\theta_Y+\frac{u}{R}\right)=m_{\phi_S^S} \tag{4.15j}$$

Substituting eqns. (4.14) to eqns. (4.15), the differential equations of equilibrium of the beam are derived as

$$-N_{,x} - \frac{Q_z}{R} = p_x \tag{4.16a}$$

$$-Q_{y,x} = p_y \qquad\qquad -Q_{z,x} + \frac{N}{R} = p_z \tag{4.16b,c}$$

$$-M_{Z,x} - Q_y + \frac{M_t}{R} = m_Z \qquad -M_{Y,x} + Q_z = m_Y \tag{4.16d,e}$$

$$-M_{\phi_{CZ}^P,x} - Q_y^S = m_{\phi_{CZ}^P} \qquad -M_{\phi_{CY}^P,x} - Q_z^S = m_{\phi_{CY}^P} \tag{4.16f,g}$$

$$-M_{t,x} - \frac{M_Z}{R} = m_t \tag{4.16h}$$

$$-M_{\phi_S^P,x} - M_t^S - M_t^T = m_{\phi_S^P} \qquad -M_{\phi_S^S,x} + M_t^T = m_{\phi_S^S} \tag{4.16i,j}$$

where the externally applied loads are related to the components of the traction vector applied on the lateral surface of the beam $t_x$, $t_y$, $t_z$ as

$$p_i(x) = \int_\Gamma t_i \, ds, \quad i = x, y, z \tag{4.17a}$$

$$m_t(x) = \int_\Gamma -t_z y + t_y z \, ds \tag{4.17b}$$

$$m_Y(x) = \int_\Gamma t_x Z \, ds \qquad\qquad m_Z(x) = -\int_\Gamma t_x Y \, ds \tag{4.17c,d}$$

$$m_i(x) = \int_\Gamma t_x(i) \, ds, \quad i = \phi_S^P, \phi_{CY}^P, \phi_{CZ}^P, \phi_S^S \tag{4.17e}$$

The above differential equations (eqns. (4.15)) are subjected to the corresponding boundary conditions of the problem at hand, which are given as in eqns. (3.4) of chapter 3.

If a curved beam as the one already described on a system of axis shown in Fig. 4.4 is now considered, without neglecting the effect $\frac{Z}{R}$ for shear strains and writing the equations in matrix form, the stiffness matrix can be derived as presented in short below:

$$
[Aux1] = \begin{bmatrix} 1 & 0 & 0 & 0 & Z & -Y & \phi_S^P & \phi_{CY}^P & \phi_{CZ}^P & \phi_S^S \\ 0 & 1 & 0 & -z & 0 & 0 & 0 & 0 & 0 & 0 \\ 0 & 0 & 1 & y & 0 & 0 & 0 & 0 & 0 & 0 \end{bmatrix} e(R) \tag{4.18a}
$$

$$
[Aux2] = \begin{bmatrix} 0 & -\dfrac{1}{R}e(R) & 0 & \dfrac{z}{R}e(R) & 0 & 0 & 0 & 0 & 0 & 0 \\[2mm] \dfrac{1}{R}e(R) & 0 & \dfrac{Z}{R}e(R) & -1-\dfrac{Y}{R}e(R) & 0 & 0 & \begin{array}{c}\dfrac{\phi_S^P}{R}e(R)\\ +\phi_{S,y}^P\end{array} & \begin{array}{c}\dfrac{\phi_{CY}^P}{R}e(R)\\ +\phi_{CY,y}^P\end{array} & \begin{array}{c}\dfrac{\phi_{CZ}^P}{R}e(R)\\ +\phi_{CZ,y}^P\end{array} & \begin{array}{c}\dfrac{\phi_S^P}{R}e(R)\\ +\phi_{S,y}^P\end{array} \\[3mm] 0 & 0 & 0 & 0 & 1 & 0 & \phi_{S,z}^P & \phi_{CY,z}^P & \phi_{CZ,z}^P & \phi_{S,z}^P \end{bmatrix}
$$

$$
\tag{4.18b}
$$

$$
\varepsilon = [Aux1]u_{,x} + [Aux2]u \tag{4.18c}
$$

$$
\sigma = [C][Aux1]u_{,x} + [C][Aux2]u \tag{4.18d}
$$
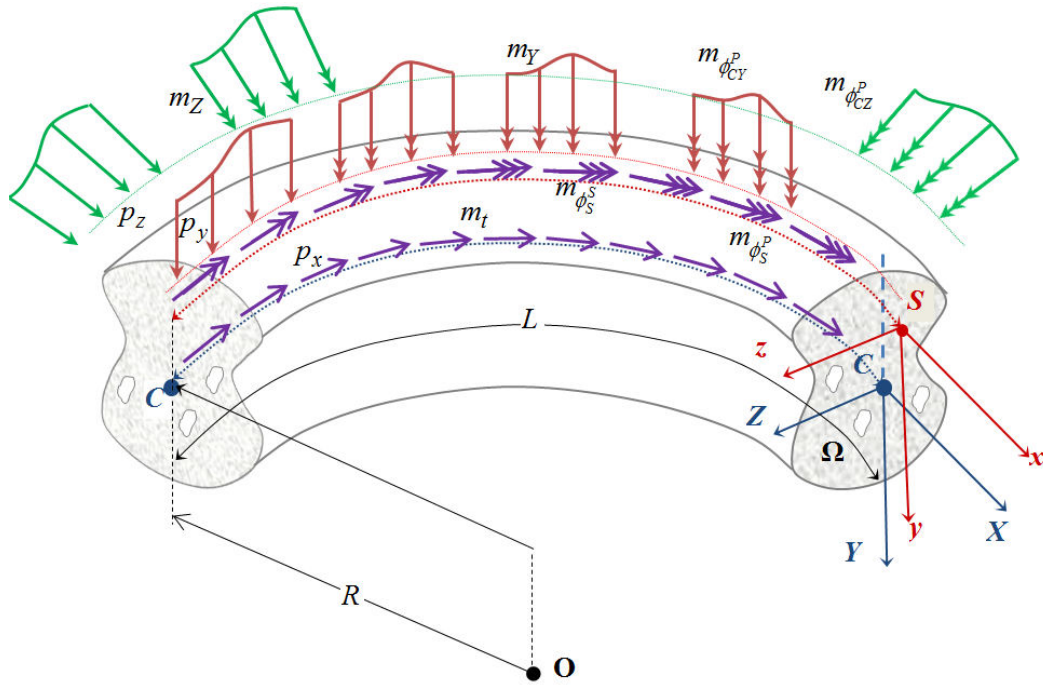


*Figure. 4.4. Prismatic curved beam under axial-flexural-torsional loading of an arbitrary homogenous cross section.*

$$
\delta U = \int_0^L \int_\Omega \left( \delta u_{,x}^T [Aux1]^T + \delta u^T [Aux2]^T \right) \left( [C][Aux1]u_{,x} + [C][Aux2]u \right) \frac{1}{e(R)} d\Omega dx \Rightarrow
$$

$$
\Rightarrow \delta U = \int_0^L \left( \delta u_{,x}^T k_{22} u_{,x} + \delta u^T k_{12} u_{,x} + \delta u_{,x}^T k_{21} u + \delta u^T k_{11} u \right) dx
$$

$$
\Rightarrow \text{by parts integration} \Rightarrow
$$

$$\Rightarrow \delta U = \int_0^L \left( \delta u^T \left\{ -k_{22}u_{,xx} + [k_{12} - k_{21}]u_{,x} + k_{11}u \right\} \right) dx + \left[ \delta u^T \left\{ k_{22}u_{,x} + k_{21}u \right\} \right]_0^L \quad (4.18e)$$

$$[k_l] = \begin{bmatrix} k_{11} & k_{12} \\ k_{21} & k_{22} \end{bmatrix} \quad (4.18f)$$

where $[Aux1]$, $[Aux2]$ are auxiliary matrices to express strains ε in matrix form, $\dfrac{1}{e(R)} d\Omega dx = dV$ is the differential volume of the curved beam for constant radius of curvature, $[C]$ is the elasticity matrix employed to derive stresses σ, $\delta U$ is the virtual strain energy and $k_{11}$, $k_{12}$, $k_{21}$ and $k_{22}$ are 10X10 coefficient matrices containing the geometric properties of the cross section. These are calculated as follows

$$k_{11} = \int_{\Omega_m} [Aux1]^T [C][Aux1] \frac{1}{e(R)} d\Omega, \qquad k_{12} = \int_{\Omega_m} [Aux1]^T [C][Aux2] \frac{1}{e(R)} d\Omega$$

$$k_{21} = \int_{\Omega_m} [Aux2]^T [C][Aux1] \frac{1}{e(R)} d\Omega, \qquad k_{22} = \int_{\Omega_m} [Aux2]^T [C][Aux2] \frac{1}{e(R)} d\Omega$$

$$(4.19)$$

From eqn. (4.18e) after integrating by parts, it holds that

$$NQM = k_{22}u_{,x} + k_{21}u \quad (4.20)$$

where $NQM$ is the vector of the stress resultants at the beam's ends.

## 4.2.2 Curved beam model and Equations of Motion

In order to derive the differential equations of motion with respect to the kinematical components, the terms of inertia contributions $\delta W_{mass} = \int_V \rho \left( \bar{u}_{,tt} \delta \bar{u} + \bar{v}_{,tt} \delta \bar{v} + \bar{w}_{,tt} \delta \bar{w} \right) dV$ have to be added in the previous and constitutive equations should be employed. $\rho$ is the density of the material and $\bar{u}, \bar{v}, \bar{w}$ are the generalized displacements as previously described. Thus, the spatial mass matrix $[m_t]$ can finally be derived. This is given in matrix form as follows

$$\delta W_{mass} = \int_0^L \int_\Omega \rho \left( \delta u^T [Aux1]^T [Aux1] u_{,tt} \right) \frac{1}{e(R)} d\Omega dx \Rightarrow \delta U = \int_0^L \left( \delta u^T [m_t] u_{,tt} \right) dx \quad (4.21)$$

The generalized vibrational beam behavior is described by the differential equations given below. Unlike the stiffness matrix and mass matrix of structure, it is not necessary to construct the global damping matrix from the element damping matrix by assembling technique and thus no damping matrix of element is needed to be derived. Much commercial software employs Rayleigh damping which is a linear

combination of mass matrix and stiffness matrix. For the proposed curved beam formulation damping is neglected.

$$-EA\left(u_{,xx}+\frac{w_{,x}}{R}\right)-\frac{EI_{YY}}{R}\left(\frac{u_{,xx}}{R}+\frac{w_{,x}}{R^2}-2\theta_{Y,xx}\right)-\frac{G}{R}\left(A_Z^P+A_Z^S\right)\left(w_{,x}+\theta_Y-\frac{u}{R}\right)+$$

$$\frac{G}{R}A_Z^S\eta_Y+\frac{G}{R}\left(D_{\Phi_{CY}^S\Phi_S^S}-D_{\Phi_{CY}^S\Phi_S^T}\right)\left(\eta_x-\theta_{x,x}-\frac{\theta_Z}{R}\right)+\frac{G}{R}D_{\Phi_{CY}^S\Phi_S^T}\xi_x$$

$$+\underbrace{\rho A u_{,tt}}_{\text{inertial contribution}}=p_x \qquad\qquad (4.22a)$$

$$-G\left(A_Y^P+A_Y^S\right)\left(v_{,xx}-\theta_{Z,x}\right)+GA_Y^S\eta_{Z,x}+G\left(D_{\Phi_{CZ}^S\Phi_S^S}-D_{\Phi_{CZ}^S\Phi_S^T}\right)\left(\eta_{x,x}-\theta_{x,xx}-\frac{\theta_{Z,x}}{R}\right)+$$

$$+GD_{\Phi_{CZ}^S\Phi_S^T}\xi_{x,x}+\underbrace{\rho A\left(v_{,tt}-z_C\theta_{x,tt}\right)}_{\text{inertial contribution}}=p_y \qquad\qquad (4.22b)$$

$$-G\left(A_Z^P+A_Z^S\right)\left(w_{,xx}+\theta_{Y,x}-\frac{u_{,x}}{R}\right)+GA_Z^S\eta_{Y,x}+G\left(D_{\Phi_{CY}^S\Phi_S^S}-D_{\Phi_{CY}^S\Phi_S^T}\right)\cdot$$

$$\cdot\left(\eta_{x,x}-\theta_{x,xx}-\frac{\theta_{Z,x}}{R}\right)+GD_{\Phi_{CY}^S\Phi_S^T}\xi_{x,x}+\frac{EA}{R}\left(u_{,x}+\frac{w}{R}\right)+$$

$$+\frac{EI_{YY}}{R^2}\left(\frac{u_{,x}}{R}+\frac{w}{R^2}-2\theta_{Y,x}\right)+\underbrace{\rho A\left(w_{,tt}+y_C\theta_{x,tt}\right)}_{\text{inertial contribution}}=p_z \qquad\qquad (4.22c)$$

$$-EI_{ZZ}\left(\theta_{Z,xx}-\frac{\theta_{x,x}}{R}\right)-G\left(A_Y^P+A_Y^S\right)\left(v_{,x}-\theta_Z\right)+GA_Y^S\eta_Z+G\left(D_{\Phi_{CZ}^S\Phi_S^S}-D_{\Phi_{CZ}^S\Phi_S^T}\right)\cdot$$

$$\cdot\left(\eta_x-\theta_{x,x}-\frac{\theta_Z}{R}\right)+GD_{\Phi_{CZ}^S\Phi_S^T}\xi_x-\frac{G}{R}\left(D_{\Phi_{CZ}^S\Phi_S^S}-D_{\Phi_{CZ}^S\Phi_S^T}\right)\left(\eta_Z-v_{,x}+\theta_Z\right)$$

$$-\frac{G}{R}\left(D_{\Phi_{CY}^S\Phi_S^S}-D_{\Phi_{CY}^S\Phi_S^T}\right)\cdot\left(\eta_Y-w_{,x}-\theta_Y+\frac{u}{R}\right)-\frac{G}{R}\left(I_t^S+I_t^T\right)\left(\eta_x-\theta_{x,x}-\frac{\theta_Z}{R}\right)+$$

$$+\frac{G}{R}I_t^T\xi_x+\frac{G}{R}I_t^P\left(\theta_{x,x}+\frac{\theta_Z}{R}\right)+\underbrace{\rho I_{ZZ}\theta_{Z,tt}}_{\text{inertial contribution}}=m_Z \qquad\qquad (4.22d)$$

$$-EI_{YY}\theta_{Y,xx}+\frac{2EI_{YY}}{R}\left(u_{,xx}+\frac{w_{,x}}{R}\right)+G\left(A_Z^P+A_Z^S\right)\left(w_{,x}+\theta_Y-\frac{u}{R}\right)-GA_Z^S\eta_Y$$

$$-G\left(D_{\Phi_{CY}^S\Phi_S^S}-D_{\Phi_{CY}^S\Phi_S^T}\right)\left(\eta_x-\theta_{x,x}-\frac{\theta_Z}{R}\right)-GD_{\Phi_{CY}^S\Phi_S^T}\xi_x$$

$$+\underbrace{\rho I_{YY}\theta_{Y,tt}}_{\text{inertial contribution}}=m_Y \qquad\qquad (4.22e)$$

$$-E\left(I_{\phi^P_{CZ}\phi^P_S}\eta_{x,xx}+I_{\phi^P_{CZ}\phi^P_{CZ}}\eta_{Z,xx}+I_{\phi^P_{CZ}\phi^S_S}\xi_{x,xx}\right)+GA^S_Y\left(\eta_Z-v_{,x}+\theta_Z\right)+$$

$$+G\left(D_{\Phi^S_{CZ}\Phi^S_S}-D_{\Phi^S_{CZ}\Phi^T_S}\right)\left(\eta_x-\theta_{x,x}-\frac{\theta_Z}{R}\right)+GD_{\Phi^S_{CZ}\Phi^T_S}\xi_x$$

$$+\rho\underbrace{\left(I_{\varphi^P_{CZ}\varphi^P_S}\eta_{x,tt}+I_{\varphi^P_{CZ}\varphi^S_S}\xi_{x,tt}+I_{\varphi^P_{CZ}\varphi^P_{CZ}}\eta_{Z,tt}\right)}_{\text{inertial contribution}}=m_{\phi^P_{CZ}} \qquad (4.22\text{f})$$

$$-E\left(I_{\phi^P_{CY}\phi^P_S}\eta_{x,xx}+I_{\phi^P_{CY}\phi^P_{CY}}\eta_{Y,xx}+I_{\phi^P_{CY}\phi^S_S}\xi_{x,xx}\right)+GA^S_Z\left(\eta_Y-w_{,x}-\theta_Y+\frac{u}{R}\right)+$$

$$+G\left(D_{\Phi^S_{CY}\Phi^S_S}-D_{\Phi^S_{CY}\Phi^T_S}\right)\left(\eta_x-\theta_{x,x}-\frac{\theta_Z}{R}\right)+GD_{\Phi^S_{CY}\Phi^T_S}\xi_x$$

$$+\rho\underbrace{\left(I_{\varphi^P_{CY}\varphi^P_S}\eta_{x,tt}+I_{\varphi^P_{CY}\varphi^S_S}\xi_{x,tt}+I_{\varphi^P_{CY}\varphi^P_{CY}}\eta_{Y,tt}\right)}_{\text{inertial contribution}}=m_{\phi^P_{CY}} \qquad (4.22\text{g})$$

$$-GI^P_t\left(\theta_{x,xx}+\frac{\theta_{Z,x}}{R}\right)+G\left(I^S_t+I^T_t\right)\left(\eta_{x,x}-\theta_{x,xx}-\frac{\theta_{Z,x}}{R}\right)-GI^T_t\xi_{x,x}+$$

$$+G\left(D_{\Phi^S_{CZ}\Phi^S_S}-D_{\Phi^S_{CZ}\Phi^T_S}\right)\left(\eta_{Z,x}-v_{,xx}+\theta_{Z,x}\right)+G\left(D_{\Phi^S_{CY}\Phi^S_S}-D_{\Phi^S_{CY}\Phi^T_S}\right)\cdot$$

$$\cdot\left(\eta_{Y,x}-w_{,xx}-\theta_{Y,x}+\frac{u_{,x}}{R}\right)-\frac{E}{R}I_{ZZ}\left(\theta_{Z,x}-\frac{\theta_x}{R}\right)$$

$$+\rho\underbrace{\left[A\left(-z_C v_{,tt}+y_C w_{,tt}\right)+I_p\theta_{x,tt}\right]}_{\text{inertial contribution}}=m_t \qquad (4.22\text{h})$$

$$-E\left(I_{\phi^P_S\phi^P_S}\eta_{x,xx}+I_{\phi^P_{CY}\phi^P_S}\eta_{Y,xx}+I_{\phi^P_{CZ}\phi^P_S}\eta_{Z,xx}\right)+G\left(I^S_t+I^T_t\right)\left(\eta_x-\theta_{x,x}-\frac{\theta_Z}{R}\right)-GI^T_t\xi_x+$$

$$+G\left(D_{\Phi^S_{CZ}\Phi^S_S}-D_{\Phi^S_{CZ}\Phi^T_S}\right)\left(\eta_Z-v_{,x}+\theta_Z\right)+G\left(D_{\Phi^S_{CY}\Phi^S_S}-D_{\Phi^S_{CY}\Phi^T_S}\right)\cdot$$

$$\cdot\left(\eta_Y-w_{,x}-\theta_Y+\frac{u}{R}\right)+\rho\underbrace{\left(I_{\varphi^P_S\varphi^P_S}\eta_{x,tt}+I_{\varphi^P_{CY}\varphi^P_S}\eta_{Y,tt}+I_{\varphi^P_{CZ}\varphi^P_S}\eta_{Z,tt}\right)}_{\text{inertial contribution}}=m_{\phi^P_S} \qquad (4.22\text{i})$$

$$-E\left(I_{\phi^P_{CY}\phi^S_S}\eta_{Y,xx}+I_{\phi^P_{CZ}\phi^S_S}\eta_{Z,xx}+I_{\phi^S_S\phi^S_S}\xi_{x,xx}\right)+GI^T_t\left(\xi_x-\eta_x+\theta_{x,x}+\frac{\theta_Z}{R}\right)+$$

$$+GD_{\Phi^S_{CZ}\Phi^T_S}\left(\eta_Z-v_{,x}+\theta_Z\right)+GD_{\Phi^S_{CY}\Phi^T_S}\left(\eta_Y-w_{,x}-\theta_Y+\frac{u}{R}\right)$$

$$+\rho\underbrace{\left(I_{\varphi^S_S\varphi^S_S}\xi_{x,tt}+I^\rho_{\varphi^P_{CY}\varphi^S_S}\eta_{Y,tt}+I^\rho_{\varphi^P_{CZ}\varphi^S_S}\eta_{Z,tt}\right)}_{\text{inertial contribution}}=m_{\phi^S_S} \qquad (4.22\text{j})$$

Except for the boundary conditions there are also the initial conditions at beam's ends similar to those defined in eqns. (3.3) of Chapter 3.

After establishing the stiffness and mass matrices of the spatial curved beam element the equation of motion in matrix form can be given as follows

$$[m_t]\{\ddot{U}_i\} + [k_t]\{\bar{U}_i\} = \{p_t\} \tag{4.23}$$

where $[m_t]$, $[k_t]$ are the generalized mass and stiffness matrices, respectively. $\{p_t\}$ is the load vector which is equal to $\{0\}$ for the free vibration case. $\{\ddot{U}_i\}$ is the vector containing the second derivatives of the different kinematical components with respect to time while $\{\bar{U}_i\}$ is the generalized unknown vector containing the values of the kinematical components and their first derivatives, which will be evaluated numerically.

The natural frequencies and modes in which the beam vibrates for the different motions can be obtained by separation of variables and $u_i(x,t)$ is assumed to have the form given in eqn. (3.13). Finally, the typical generalized eigenvalue problem described by eqn. (3.14) is formulated and solved.

## 4.3  Numerical Solution with AEM combined to IGA

According to the precedent analysis, the axial-flexural-torsional static and dynamic analysis of curved beams of arbitrary cross section including generalized warping effects reduces in establishing the components $u(x,t)$, $v(x,t)$, $w(x,t)$, $\theta_x(x,t)$, $\theta_Z(x,t)$, $\theta_Y(x,t)$, $\eta_x(x,t)$, $\eta_Y(x,t)$, $\eta_Z(x,t)$ and $\xi_x(x,t)$ having continuous derivatives up to the second order with respect to $x$ at the interval $(0, L)$ and up to the first order at $x = 0, L$ and for the dynamic problem up to the second order with respect to $t$, satisfying the initial-boundary value problem described by the coupled governing differential equations along the beam, the initial conditions and the boundary conditions at the beam ends $x = 0, L$ given in the previous section. The problem is solved using the Analog Equation Method in a similar way as the one described in detail in Chapter 3.

## 4.4  Numerical Solution with FEM and NURBS

Instead of B-splines, NURBS curves in terms of B-spline basis functions can be employed either in FEM or AEM. The description of the numerical procedures is given in the Appendix A.2.

In this chapter, the geometry of the beam is described by a NURBS structure (Appendix A.2) with initial control points given by the following spatial coordinates $(x_i, y_i, z_i, w_i)$: $(-R, 0, 0, 1)$, $(-R\cos\left(\dfrac{\phi}{2}\right), R\sin\left(\dfrac{\phi}{2}\right), 0, \cos\left(\dfrac{\phi}{2}\right))$, $(-R\cos(\phi), R\sin(\phi), 0, 1)$, and the arc which describes the longitudinal axis of the curved beam is obtained

in this way. $w_i$ ($\in \square$) are weights of the control polygon which defines the arc and is $\phi$ the angle formed by the arc at the center of the circle that it is a part of. However, any curve can be represented with the aid of NURBS. The aforementioned polygon will be later refined as new knots will be inserted and degree will be elevated in order to achieve more accurate results. $[m_t], [k_t]$ matrices can finally be obtained following the procedures described in section A.2.4 of the Appendix A.2.

## 4.5 Numerical examples

In order to validate the proposed formulation of the curved beam element described above in static or dynamic analysis and examine the advantages attained by the use of the numerical methods proposed in terms of simplicity, accuracy and computational effort, computer programs have been written and representative examples have been studied. The numerical results have been obtained employing NURBS, beam Finite Elements (FEs) and constant or quadratic elements for the representation of the AEM fictitious loads. Then, the results are compared to those obtained by the application of the Finite Element Method (FEM) employing beam, solid (quadrilateral or triangular) or plate/shell elements. The computer software FEMAP (2010) has been used for this purpose. In addition to these, up to 800 boundary elements depending on the cross section type (cross sectional discretization) have been employed in order to evaluate the geometric constants with BEM. Domain discretization has been performed with BEM in some cases, too. Finally, the Newmark time integration scheme (Bathe, 1996) is employed for the dynamic analysis.

### 4.5.1 Doubly Symmetric Cross Section (I-shaped)

In the first example, a cantilever beam ($E = 7.3E11 kPa$, $G = 2.8E11 kPa$) of a doubly symmetric I-shaped cross section (Fig. 4.5) is examined. It is subjected to either a concentrated radial force $P_z = 10N$ applied at the centroid of its free end or a torsional moment $M_t = 10Nm$ applied at the same position. Its length is 300 cm and
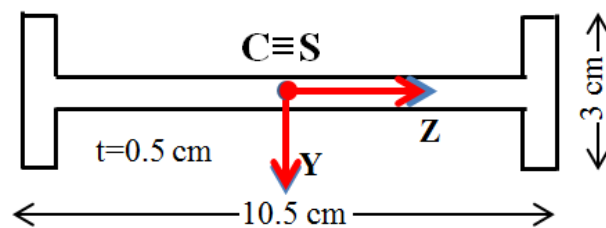


*Figure 4.5. Cross section of example 4.5.1.*

the radius of curvature is 190.58 cm. In Table 4.1 the geometric constants of the beam are presented.

This beam has also been analyzed in the study of Kim et al. (2004) as a thin-walled beam employing a finite element solution. In this latter analysis only a primary warping parameter due to torsion ($\eta_x(x)$) is taken into account, neglecting primary

warping due to shear $(\eta_Y(x), \eta_Z(x))$ and, thus, shear lag effect due to shear. In addition to this, secondary warping parameter due to torsion $(\xi_x(x))$, which accounts for shear lag effect due to torsion, is neglected, too. In Table 4.2 the values of the kinematical components $u(x)$, $w(x)$ and $\theta_Y(x)$ for the radial force at the free edge of the beam are presented for i) 200 constant elements employing the AEM (AEMconst), ii) 200 quadratic elements employing AEM (AEMquad), iii) 13027 quadrilateral solid elements in FEMAP (2010) (FEMsolid) and iv) 4320 shell elements mentioned in Kim et al. (2004) (FEMshell). In the same table the values of the kinematical components $v(x)$, $\theta_x(x)$ and $\theta_Z(x)$ for the torsional moment at the free edge of the first beam are also presented. In addition to this, the values of normal stresses $\sigma_{xx}$ at the upper and lower tips of the cross section are shown at the mid span of the beam for the solid and shell models as well as for the AEMquad. Finally, normal stresses $\sigma_{xx}$ and shear

$$A = 7.75000000\text{E}+00\,cm^2 \qquad I_{\varphi_S^S \varphi_S^S} = 1.27645901\text{E}+00\,cm^6$$

$$I_{ZZ} = 2.34895833\text{E}+00\,cm^4 \qquad I_{\varphi_{CY}^P \varphi_S^P} = 1.79746986\text{E}-10\,cm^5$$

$$I_{YY} = 1.10786458\text{E}+02\,cm^4 \qquad I_{\varphi_{CY}^P \varphi_S^S} = 2.61521456\text{E}-11\,cm^5$$

$$I_{\varphi_{CY}^P \varphi_{CY}^P} = 1.16705460\text{E}-01\,cm^4 \qquad A_Y^P = 4.85212071\text{E}+00\,cm^2$$

$$A_Z^S = 6.21759591\text{E}-01\,cm^2 \qquad I_t^P = 6.55741917\text{E}-01\,cm^4$$

$$I_t^S = 6.64776201\text{E}+01\,cm^4 \qquad I_t^T = -2.57312637\text{E}+01\,cm^4$$

$$D_{\Phi_{CY}^S \Phi_S^S} = 1.09684225\text{E}-09\,cm^3 \qquad D_{\Phi_{CY}^S \Phi_S^T} = 2.21344669\text{E}-09\,cm^3$$

$$I_{\varphi_{CZ}^P \varphi_S^S} = 1.62507369\text{E}-11\,cm^5 \qquad I_{\varphi_{CZ}^P \varphi_S^P} = -8.61873073\text{E}-13\,cm^5$$

$$I_{\varphi_{CZ}^P \varphi_{CZ}^P} = 2.77747414\text{E}-01\,cm^4 \qquad A_Z^P = 2.84724686\text{E}+00\,cm^2$$

$$D_{\Phi_{CZ}^S \Phi_S^S} = 9.68034449\text{E}-12\,cm^3 \qquad D_{\Phi_{CZ}^S \Phi_S^T} = 9.69835763\text{E}-10\,cm^3$$

$$I_{\varphi_S^P \varphi_S^P} = 5.63639219\text{E}+01\,cm^6 \qquad A_Y^S = 1.77955610\text{E}-01\,cm^2$$

*Table 4.1. Geometric constants of the beam of example 4.5.1.*

stresses $\tau_{xy}$ at the upper and lower tips of the cross section are shown at the fixed end of the beam for the solid and the AEMquad models. It is obvious that in both load cases the results of this study for either kinematical components or stresses almost coincide with those of the solid model (discrepancies 3-4%), while shell elements give less accurate results by 2% to almost 6%.

The same beam model has also been examined for the dynamic case of the proposed beam element with the following characteristics: $E = 4E7\,N/cm^2$, $G = 2E7\,N/cm^2$, $\rho = 0.025\,N\,sec^2/m^4$, $L = 300\,cm$ and $R = 190.58\,cm$. In Fig. 4.6 a
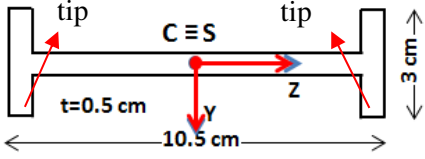
| | | $u(cm)$ at $x=L$ | $w(cm)$ at $x=L$ | $\theta_Y(rad)$ at $x=L$ |
|---|---|---|---|---|
| $P_z$ Radial Loading | AEMconst | -4.3490 | 6.8226 | -0.0454 |
| | AEMquad | -4.3135 | 6.7684 | -0.0450 |
| | FEMsolid | -4.3105 | 6.7715 | -0.0450 |
| | FEMshell | -4.0930 | 6.4290 | -0.0431 |
| | | $v(cm)$ at $x=L$ | $\theta_x(rad)$ at $x=L$ | $\theta_Z(rad)$ at $x=L$ |
| $M_t$ Torsional Moment | AEMconst | 2.3250 | 0.0894 | 0.0445 |
| | AEMquad | 2.3300 | 0.0873 | 0.0435 |
| | FEMsolid | 2.3413 | 0.0879 | 0.0432 |
| | FEMshell | 2.4710 | 0.0897 | 0.0452 |

| | | $\sigma_{xx}$ (N/cm2) at Z=4.75cm | $\sigma_{xx}$ (N/cm2) at Z=-4.75cm |
|---|---|---|---|
| $P_z$ Radial Loading | Values at Mid span | | |
| | AEMquad | -58.47 | 59.68 |
| | FEMsolid | -59.58 | 62.21 |
| | FEMshell | -56.66 | 58.92 |
| $P_z$ Radial Loading | Values at Fixed end | $\sigma_{xx}$ (N/cm2) at Z=4.75cm | $\sigma_{xx}$ (N/cm2) at Z=-4.75cm |
| | AEMquad | -89.68 | 91.89 |
| | FEMsolid | -90.78 | 94.95 |
| $P_z$ Radial Loading | Values at Fixed end | $\tau_{xy}$ (N/cm2) at Z=4.75cm | $\tau_{xy}$ (N/cm2) at Z=-4.75cm |
| | AEMquad | 10.30 | -11.02 |
| | FEMsolid | 10.82 | -11.56 |

Table 4.2. Kinematical components and stresses of the beam of Fig. 4.5 for
various load cases.
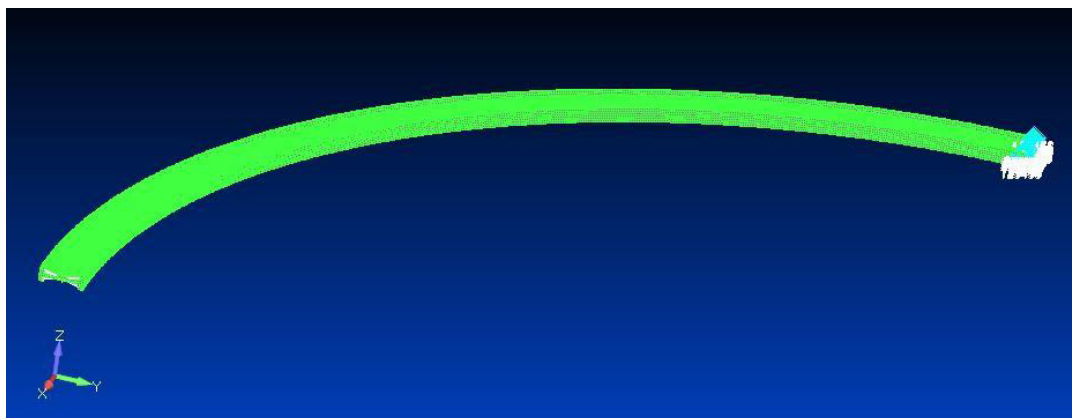
*Figure 4.6. Model in FEMAP employing 13000 quadrilateral solid finite elements for example 4.5.1.*

model of the beam implemented in FEMAP (2010) employing 13000 FEM quadrilateral solid elements is shown.

In Table 4.3 the values of different eigenfrequencies have been compiled for i) the proposed curved beam elements with quartic B-splines in AEM (analytically integrated), ii) 13000 quadrilateral solid elements (FEMAP, 2010), iii) FEM curved beam elements (FEMAP, 2010), iv) the proposed curved beam elements with 5 cubic NURBS in FEM and v) the proposed curved beam elements with 10 cubic NURBS in FEM. Analysis with cubic NURBS gives results quite close to the solid model with errors around 5% for the first five eigenfrequencies. The same case is for the FEM curved beam elements (Timoshenko beam element) with respect to the first three modes while there is a significant loss in accuracy for the rest two. In addition to these, the errors between the two approximations with NURBS are in general less than 5% and this implies high convergence rate of the method employed as well as better accuracy for higher frequencies. Finally, regarding the B-spline solution in the AEM, errors become larger (around 10%) but still valid if the fact that only 5 control points employed with the quartic B-spline is considered.

| Mode Number | B-splines AEM | FEMsolid (13000) | FEM Curved beam | 5 cubic NURBS | 10cubic NURBS |
|---|---|---|---|---|---|
| 1 | 0.0881 | 0.1028 | 0.0944 | 0.0950 | 0.1120 |
| 2 | 0.4551 | 0.5205 | 0.6214 | 0.5230 | 0.5260 |
| 3 | 0.8790 | 0.9868 | 0.9871 | 1.0502 | 1.1042 |
| 4 | 1.5998 | 1.7888 | 4.5459 | 1.7552 | 1.8002 |
| 5 | 3.2555 | 3.6631 | 4.7959 | 3.4500 | 3.6723 |

*Table 4.3. Eigenfrequencies of the beam of Fig. 4.5.*

In Fig. 4.7 the first four modes are presented for the proposed beam formulation with 50 quadratic elements in AEM and for the solid model (Fig. 4.6). The initial geometry is also displayed in the figure. Highly accurate results have been obtained

comparing to the solid model results. It is worth here noting the importance of torsion in the dynamic response of the curved beam due to the open shape of the cross section.



1.   First mode of Vertical displacement                    2.   First mode of Torsion



3.   First mode of Lateral displacement                    4.   Second mode of Torsion
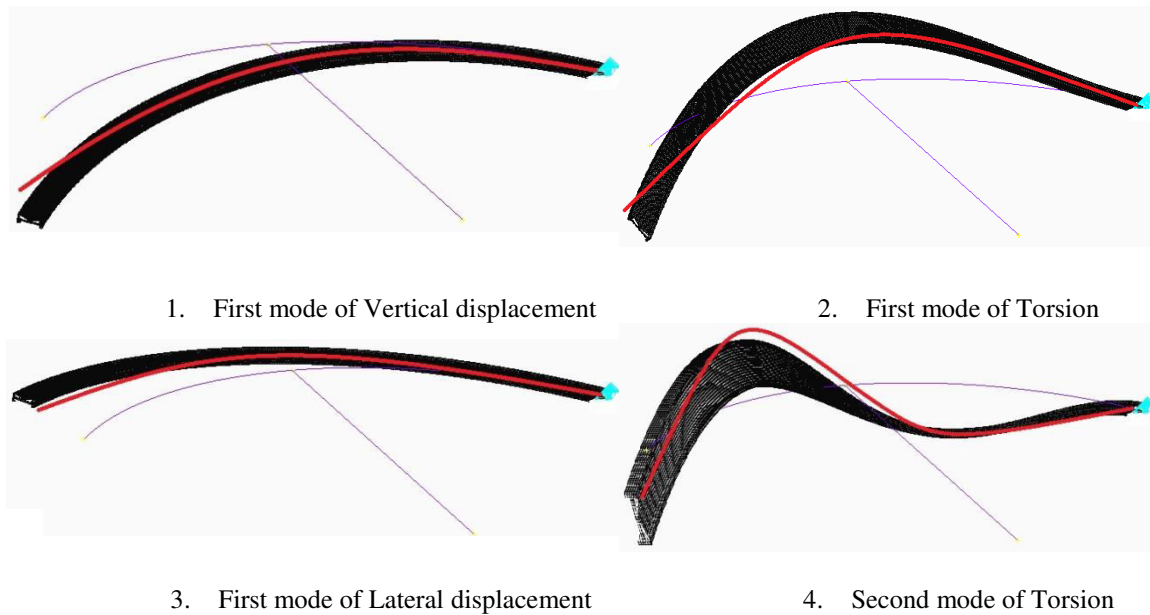
*Figure 4.7. First four eigenvectors for the model of Fig. 4.6 (Proposed formulation with AEM in red line, solid model in black and initial curved geometry in purple line).*

### 4.5.2 C-shaped cross sections either Monosymmetric or Non-symmetric

In the second example, two cantilever beams are examined. The first one has a monosymmetric (Fig. 4.8) cross section ($E = 7.3E11kPa$, $G = 2.8E11kPa$) and is subjected to a concentrated radial $P_z = 10N$ or vertical $P_y = 10N$ force applied at the centroid of its free end. Its length is 100 cm and the radius of curvature is 63.66 cm. The second beam has a non-symmetric (Fig. 4.9) cross section ($E = 2.07E8kPa$, $G = 8.27E7kPa$) and is subjected to a concentrated radial force $P_z = 0.8KN$ applied at the centroid of its free end. Its length is 14.36m and the radius of curvature 9.14m.
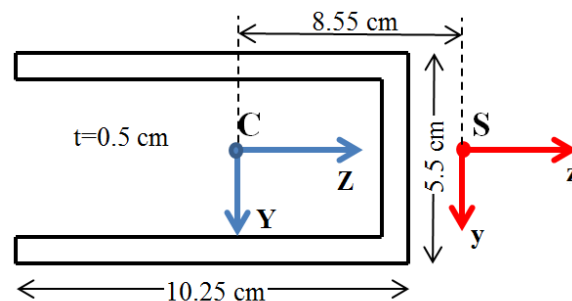


*Figure 4.8. Monosymmetric cross section of example 4.5.2.*

The geometric constants of the aforementioned cross sections are shown in Tables 4.4 and 4.5, respectively. Similarly to the previous I-shaped cross section, the

monosymmetric C-shaped cross section of this example is also examined in Kim et al. (2004) as a thin-walled beam employing a finite element solution.
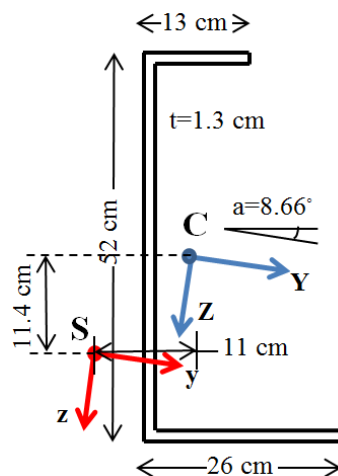


*Figure 4.9. Non-symmetric cross section of example 4.5.2.*

| | |
|---|---|
| $A = 1.250\text{E}+01\,cm^2$ | $I_{\varphi_S^S \varphi_S^S} = 1.30719236\text{E}+03\,cm^6$ |
| $I_{ZZ} = 6.80729167\text{E}+01\,cm^4$ | $I_{\varphi_{CY}^P \varphi_S^P} = 6.26886158\text{E}+01\,cm^5$ |
| $I_{YY} = 1.33635339\text{E}+02\,cm^4$ | $I_{\varphi_{CY}^P \varphi_S^S} = 4.46209563\text{E}-01\,cm^5$ |
| $I_{\varphi_{CY}^P \varphi_{CY}^P} = 6.24400310\text{E}+00\,cm^4$ | $A_Y^P = 8.64548828\text{E}+00\,cm^2$ |
| $A_Z^S = 9.82159616\text{E}-02\,cm^2$ | $I_t^P = 1.03367369\text{E}+00\,cm^4$ |
| $I_t^S = 5.66448858\text{E}+01\,cm^4$ | $I_t^T = 2.56637649\text{E}+00\,cm^4$ |
| $D_{\Phi_{CY}^S \Phi_S^S} = 9.93083855\text{E}-01\,cm^3$ | $D_{\Phi_{CY}^S \Phi_S^T} = -4.32978562\text{E}-01\,cm^3$ |
| $I_{\varphi_{CZ}^P \varphi_S^S} = 4.40225634\text{E}-12\,cm^5$ | $I_{\varphi_{CZ}^P \varphi_S^P} = 9.57456336\text{E}-13\,cm^5$ |
| $I_{\varphi_{CZ}^P \varphi_{CZ}^P} = 1.40971390\text{E}+00\,cm^4$ | $A_Z^P = 1.22335946\text{E}+00\,cm^2$ |
| $D_{\Phi_{CZ}^S \Phi_S^S} = 3.17917698\text{E}-12\,cm^3$ | $D_{\Phi_{CZ}^S \Phi_S^T} = 2.86944080\text{E}-13\,cm^3$ |
| $I_{\varphi_S^P \varphi_S^P} = 6.66168740\text{E}+02\,cm^6$ | $A_Y^S = 6.96056233\text{E}-01\,cm^2$ |

*Table 4.4. Geometric constants of the Monosymmetric cross section of example 4.5.2.*

In Table 4.6 the values of the kinematical components $u(x)$, $w(x)$ and $\theta_Y(x)$ for the radial force at the free edge of the monosymmetric beam are presented for i) 200 constant elements employing AEM (AEMconst), ii) 50 quadratic elements employing AEM (AEMquad), iii) 4033 quadrilateral solid elements in FEMAP (2010) (FEMsolid) and iv) the approximate "analytical" solution mentioned in Kim et al. (2004), considering only primary warping and ignoring shear lag effects. In the same table the

$$A = 1.12903000\text{E-}02\,m^4 \qquad I_{\varphi_S^S \varphi_S^S} = 5.19927646\text{E-}07\,m^6$$

$$I_{ZZ} = 4.58891474\text{E-}05\,m^4 \qquad I_{\varphi_{CY}^P \varphi_S^P} = -4.23401342\text{E-}07\,m^5$$

$$I_{YY} = 4.45437341\text{E-}04\,m^4 \qquad I_{\varphi_{CY}^P \varphi_S^S} = 7.81208062\text{E-}08\,m^5$$

$$I_{\varphi_{CY}^P \varphi_{CY}^P} = 1.18320830\text{E-}05\,m^4 \qquad A_Y^P = 5.67165454\text{E-}03\,m^2$$

$$A_Z^S = 1.97293283\text{E-}04\,m^2 \qquad I_t^P = 6.01029864\text{E-}07\,m^4$$

$$I_t^S = 1.81123894\text{E-}04\,m^4 \qquad I_t^T = 8.20613408\text{E-}06\,m^4$$

$$D_{\Phi_{CY}^S \Phi_S^S} = -5.83081216\text{E-}06\,m^3 \qquad D_{\Phi_{CY}^S \Phi_S^T} = 6.76039764\text{E-}05\,m^3$$

$$I_{\varphi_{CZ}^P \varphi_S^S} = -3.99169511\text{E-}08\,m^5 \qquad I_{\varphi_{CZ}^P \varphi_S^P} = 9.39180437\text{E-}07\,m^5$$

$$I_{\varphi_{CZ}^P \varphi_{CZ}^P} = 3.54561974\text{E-}06\,m^4 \qquad A_Z^P = 2.79916897\text{E-}03\,m^2$$

$$D_{\Phi_{CZ}^S \Phi_S^S} = 1.97293283\text{E-}04\,m^3 \qquad D_{\Phi_{CY}^S \Phi_S^T} = 6.76039764\text{E-}05\,m^3$$

$$I_{\varphi_S^P \varphi_S^P} = 1.12271655\text{E-}06\,m^6 \qquad A_Y^S = 1.97293283\text{E-}04\,m^2$$

*Table 4.5. Geometric constants of the Non-symmetric cross section of example 4.5.2.*



| | | $u(cm)$ at $x=L$ | $w(cm)$ at $x=L$ | $\theta_Y(rad)$ at $x=L$ |
|---|---|---|---|---|
| | AEMconst | -0.1426 | 0.2228 | -0.00418 |
| $P_z$ Radial Loading | AEMquad | -0.1426 | 0.2228 | -0.00417 |
| | FEMsolid | -0.1462 | 0.2168 | -0.00418 |
| | Approximate | -0.1306 | 0.2062 | -0.00411 |
| | | $v(cm)$ at $x=L$ | $\theta_x(rad)$ at $x=L$ | $\theta_Z(rad)$ at $x=L$ |
| | AEMconst | 9.3503 | 0.2128 | 0.2500 |
| $P_y$ Lateral Loading | AEMquad | 9.4134 | 0.2133 | 0.2505 |
| | FEMsolid | 9.9442 | 0.2086 | 0.2348 |
| | Approximate | - | - | - |

*Table 4.6. Kinematical components of the beam of Fig. 4.8 for various load cases.*

values of the kinematical components $v(x)$, $\theta_x(x)$ and $\theta_Z(x)$ for the lateral force at the free edge of the second beam are also presented. From this table, it is obvious that in general the discrepancies between the AEM and the solid model are quite small (variation of errors from 0 to 5%). It is also important to mention that the use of quadratic elements reduces the computational effort of the AEM. However, computational time remains small either for constant or quadratic elements compared with solid model. More specifically, the required computational time calculated for the same hardware was 3 seconds for the AEMquad (50 elements), 17 seconds for the AEMconst (200 elements) and 30 seconds for the FEMsolid (4033 solid elements) model, without considering the time needed for modeling.

In Fig. 4.10 the models in FEMAP (2010) are presented for both load cases. It is worth here noting that the results for the case of the radial force derived from the analytical solution (Kim et al., 2004) show larger discrepancies from the solid model compared to those of the proposed model with the values of the kinematical components being smaller. This is due to the fact that the displacements $\eta_x(x)$, $\eta_Y(x)$, $\eta_Z(x)$ and $\xi_x(x)$ are ignored in the aforementioned solution. These additional degrees of freedom are taken into account in this study and they should be considered especially in the case of the lateral force applied on the vertical axis, which is not the axis of symmetry.

In Table 4.7 the values of the kinematical components $u(x)$, $w(x)$, $\theta_Y(x)$, $v(x)$, $\theta_x(x)$ and $\theta_Z(x)$ for the radial force at the free edge of the non-symmetric beam are presented for i) curved beam elements in FEMAP (2010) (FEMbeam), ii) 150 quadratic elements employing AEM technique (AEMquad) and iii) 5474 quadrilateral solid elements in FEMAP (2010) (FEMsolid). In the same table the value of normal stress at the tip of the cross section is presented at the mid span of the beam for the FEMsolid and the AEMquad models. It is obvious that the AEMquad model (errors 3-12%) gives a better prediction of the beam's behavior regarding the displacements and the normal stress (due to the consideration of secondary effects) than the FEMbeam model (errors 17-55%) either in the plane of the curvature or in the lateral plane. It is worth here noting that for comparison reasons and in order to moderate distortional phenomena two diaphragms have been employed in the solid model, namely one at the mid span and one at the free edge of the beam. Regarding the normal stress, the error between the AEMquad and the FEMsolid models is around 10%.

In Figs. 4.11a and 4.11b the FEMbeam and the FEMsolid models are presented in order to demonstrate the dissimilar deformed shapes, while in Fig. 4.11c the free end positions at deformed state of the aforementioned methods are shown demonstrating the good agreement between AEMquad and FEMsolid models.

The beam model with the monosymmetric cross section has also been examined for the dynamic case of the proposed beam element with the following characteristics:

$E = 4E7 \; N/cm^2$,         $G = 2E7 \; N/cm^2$,         $\rho = 0.785 N \sec^2 / m^4$,         $L = 100cm$ and

$R = 63.66cm$. The same FEMsolid (Fig. 4.10) model previously described has been employed here, too.
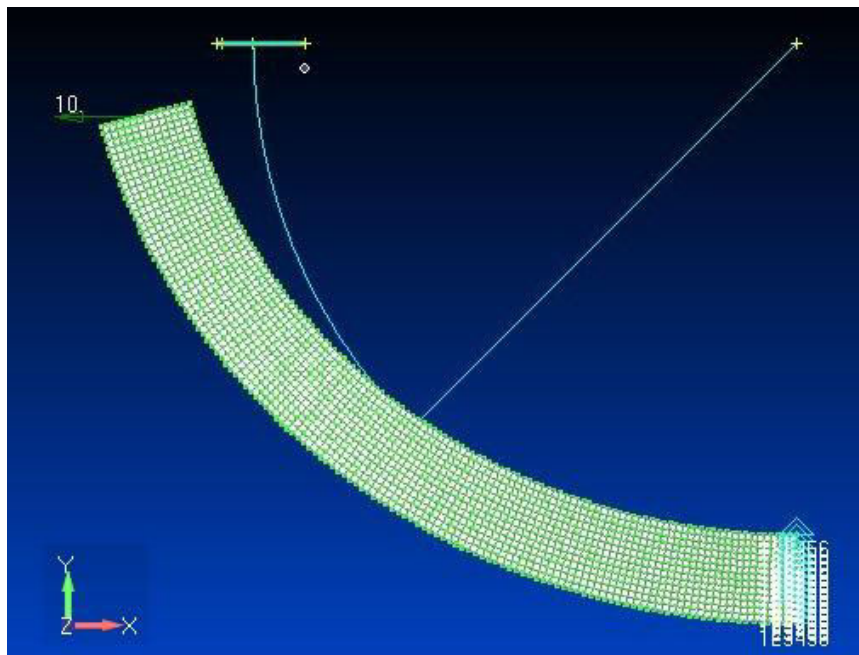


(a)
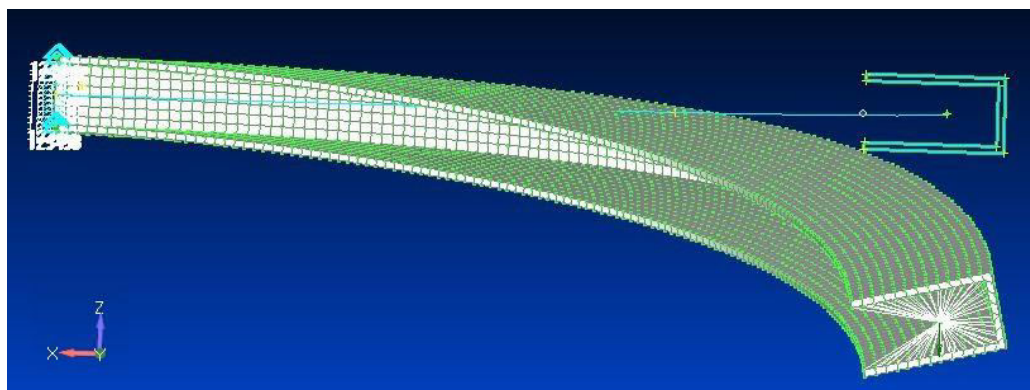


(b)

*Figure 4.10. Deformed shapes of solid models for the beam of Fig. 4.8 (a) for radial force and (b) for lateral force. (Z axis of the model corresponds to Y of this study and X axis of the model to Z of this study).*

In Table 4.8 the values of different eigenfrequencies have been compiled for i) 4033 quadrilateral solid elements (FEMAP, 2010), ii) FEM curved beam elements - FEMbeam (FEMAP, 2010) and iii) the proposed curved beam elements with 5 cubic NURBS in FEM. In addition to this, the description of the predominant modes has been noted. Regarding the results of the proposed formulation, it should be noted that errors are less than 5% comparing to the FEM solid model.

As it is the case in the previous example of the I-shaped cross section, torsional modes again dominate over bending ones (for 2$^{nd}$ mode of vertical displacement torsion is excessive) in the dynamic response of this curved structure due to the open shape of

the cross section which implies low torsional rigidity. It should also be noted here that the accuracy of the FEM curved beam approximation is less than the previous case, which was for doubly symmetric cross section, due to the fact that the neutral axis offsets from the shear center as well as warping are not accounted for.

| | | $u(m)$ at $x=L$ | $w(m)$ at $x=L$ | $\theta_Y(rad)$ at $x=L$ |
|---|---|---|---|---|
|  | FEMbeam | -0.0036 | 0.0057 | -0.0008 |
| | AEMquad | -0.0051 | 0.0086 | -0.0012 |
| | FEMsolid | -0.0060 | 0.0097 | -0.0013 |
| | | $v(m)$ at $x=L$ | $\theta_x(rad)$ at $x=L$ | $\theta_Z(rad)$ at $x=L$ |
| | FEMbeam | 0.0229 | 0.0098 | 0.0062 |
| $P_z$ *Radial Loading applied at C* | AEMquad | 0.0115 | 0.0084 | 0.0043 |
| | FEMsolid | 0.0100 | 0.0081 | 0.0038 |
| | | $\sigma_{xx}$ *(N/cm2) at Z=0.30cm* *(near mid span)* | | |
| | AEMquad | 4916.22 | | |
| | FEMsolid | 5475.41 | | |

*Table 4.7. Kinematical components and normal stress of the beam of Fig. 4.9 for radial concentrated force.*

Finally, considering the curved beam model of Fig. 4.10b and a vertical load $P_Z = -5000\ N$ applied gradually for the first 0.05 seconds at the centroid of the free end, the dynamic response is examined.

In Fig. 4.12 the out of the curvature plane displacement is plotted for a time interval of 3 seconds as well as the static response to show the dynamic amplification at each time. The time function that multiplies the load is also displayed. It is obvious that the proposed model employing cubic NURBS is quite close to the solid model response. The amplification factor of the transient response is equal to 1.98 for a system's period T=0.28 seconds (first mode) at time t=1.8 seconds where the maximum value of vertical displacement occurs as shown in Fig. 4.12.
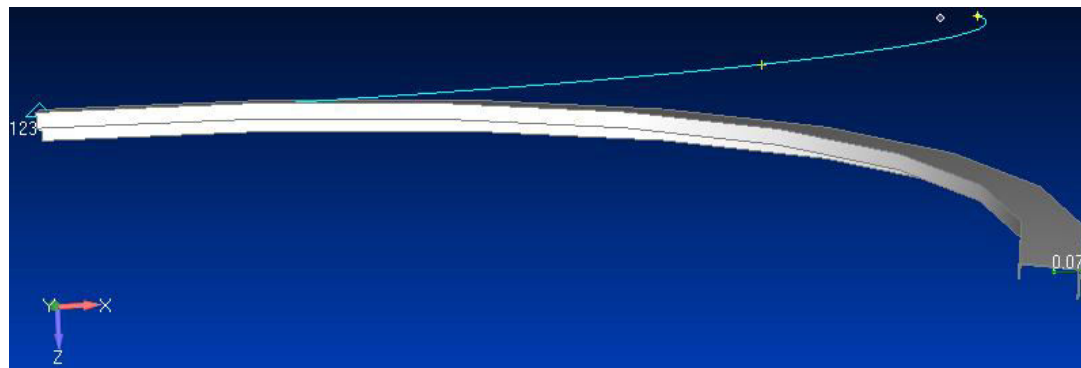
(a)
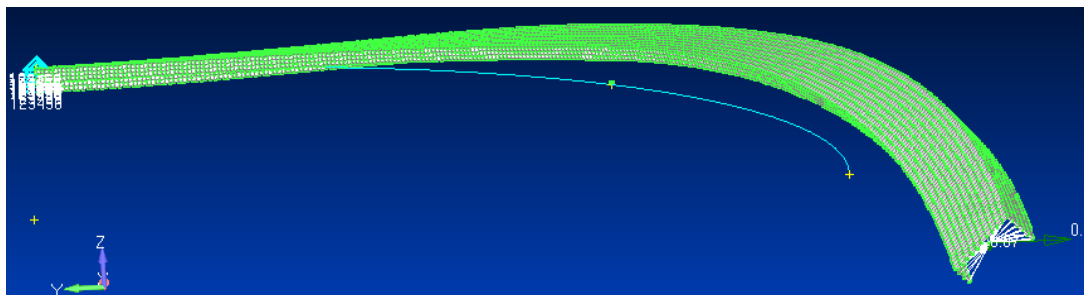


(b)
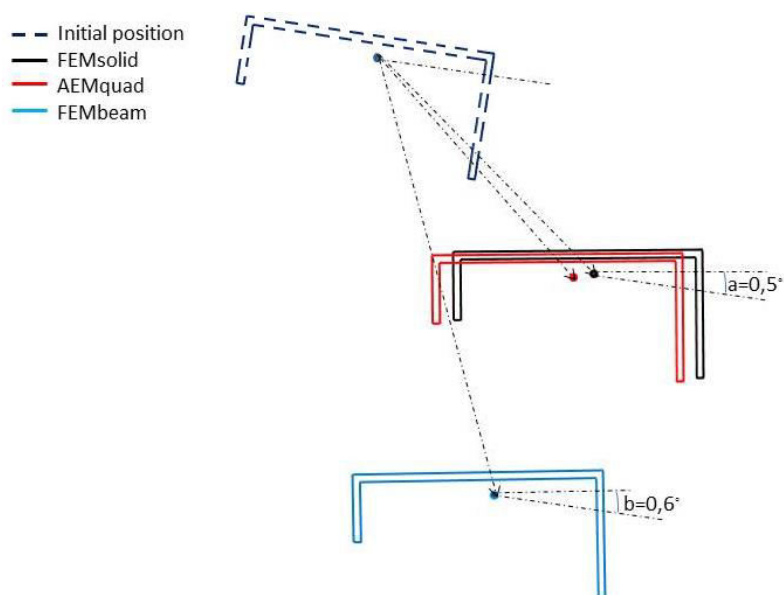


(c)

*Fig.4.11. Deformed shapes of the non-symmetric beam for radial force employing FEM beam elements (a) and FEM solid elements (b) (axes have been taken in a different way compared with the beam formulation of this study). Free end position at deformed state for the various methods (c).*

### 4.5.3 Box-shaped Monosymmetric cross sections

In the third example, three box-shaped cross sections are examined for various beam models with respect to loading, boundary conditions and geometry.

The first beam has the box-shaped cross section shown in Fig. 3.15 of Chapter 3 and exhibits the same geometric constants as those compiled in Table 3.7 of the

| Mode Number | FEMsolid (4000) | FEM Curved beam | 5 cubic NURBS | Type of mode |
|---|---|---|---|---|
| 1 | 0.2824 | 0.1788 | 0.2942 | 1st mode of Vertical displacement |
| 2 | 1.3623 | 1.1794 | 1.4211 | 1st mode of Lateral displacement |
| 3 | 2.2615 | 4.1602 | 2.2205 | 2nd mode of Vertical displacement |
| 4 | 5.7508 | 6.4632 | 5.9612 | 1st mode of Torsion |
| 5 | 6.3241 | 31.211 | 6.3709 | 2nd mode of Torsion |

*Table 4.8. Eigenfrequencies of the beam of Fig. 4.8.*
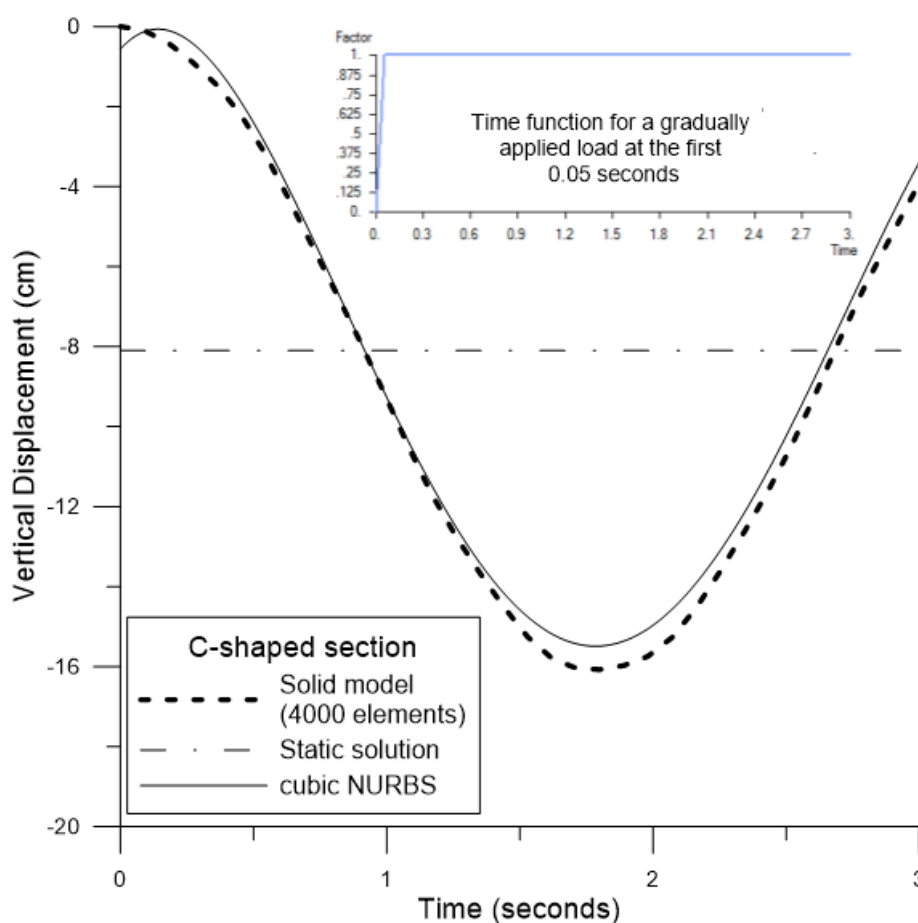


*Figure 4.12. Out-plane displacement at the tip of the curved beam model shown in Fig. 4.10b for gradually applied dynamic loading.*

same Chapter. The curved beam model examined at first has the following characteristics: $E = 4E7\,kN/m^2$, $G = 2E7\,kN/m^2$, $L = 10\,m$, $R = 6.366\,m$. It is subjected to a concentrated load either $P_z = 1000\,kN$ or $P_y = 1000\,kN$ eccentrically applied at its free end. This cross section is thin-walled and it holds that $t/d = 0.02$ and $d/L = 0.1$ ($t$=thickness and $d$=height or width). This implies that significant distortional phenomena will arise.

In Table 4.9 the values of the kinematical components $v(x)$, $\theta_x(x)$ and $\theta_Y(x)$ for the lateral force $P_y$ at the free edge of the beam are presented for i) curved beam elements in FEMAP (2010) (FEMbeam), ii) 100 quadratic elements employing AEM technique (AEMquad), iii) 10976 quadrilateral solid elements in FEMAP (2010) (FEMsolid) (the deformed shape of the solid model for this load case is shown in Fig. 4.13).

In the same table the values of the kinematical components $v(x)$, $\theta_x(x)$, $\theta_Y(x)$, $u(x)$, $w(x)$ and $\theta_Z(x)$ for the radial force $P_z$ at the free edge of beam are also presented. In the first case, the AEMquad gives results closer to the solid model (errors 5-7%) than the FEMbeam model (errors 8-12%). It is worth here noting that diaphragms in the plane of the cross section have been employed along the length of
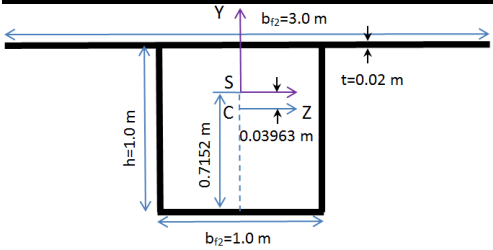
|  |  | $v(m)$ at $x=L$ | $\theta_x(rad)$ at $x=L$ | $\theta_Y(rad)$ at $x=L$ |
|---|---|---|---|---|
| $P_y$ Lateral Loading | FEMbeam | -0.5150 | 0.0276 | 0.0752 |
|  | AEMquad | -0.4961 | 0.0297 | 0.0719 |
|  | FEMsolid | -0.4734 | 0.0315 | 0.0666 |
|  |  | $u(m)$ at $x=L$ | $w(m)$ at $x=L$ | $\theta_Y(rad)$ at $x=L$ |
|  | FEMbeam | 0.0593 | 0.0930 | -0.0173 |
|  | AEMquad | -0.0616 | 0.0945 | -0.0183 |
|  | FEMsolid | -0.0604 | 0.0947 | -0.0183 |
| $P_z$ Radial Loading |  | $v(m)$ at $x=L$ | $\theta_x(rad)$ at $x=L$ | $\theta_Z(rad)$ at $x=L$ |
|  | FEMbeam | 0.0059 | -0.0062 | -0.0013 |
|  | AEMquad | 0.0059 | -0.0060 | -0.0013 |
|  | FEMsolid | 0.0054 | -0.0055 | -0.0014 |

*Table 4.9. Kinematical components of a curved beam with the cross section shown in Fig. 3.15 for various load cases.*

the beam in the solid model in order to reduce the impact of distortion and to obtain comparable results. The optimum number of these diaphragms will be investigated in Chapter 6. In this case case the discrepancies in the results are similar to those of the first load case with the FEMbeam model showing larger errors than the AEMquad for the $u(x)$, $w(x)$ and $\theta_Y(x)$ displacements, which are in the plane of the curvature.
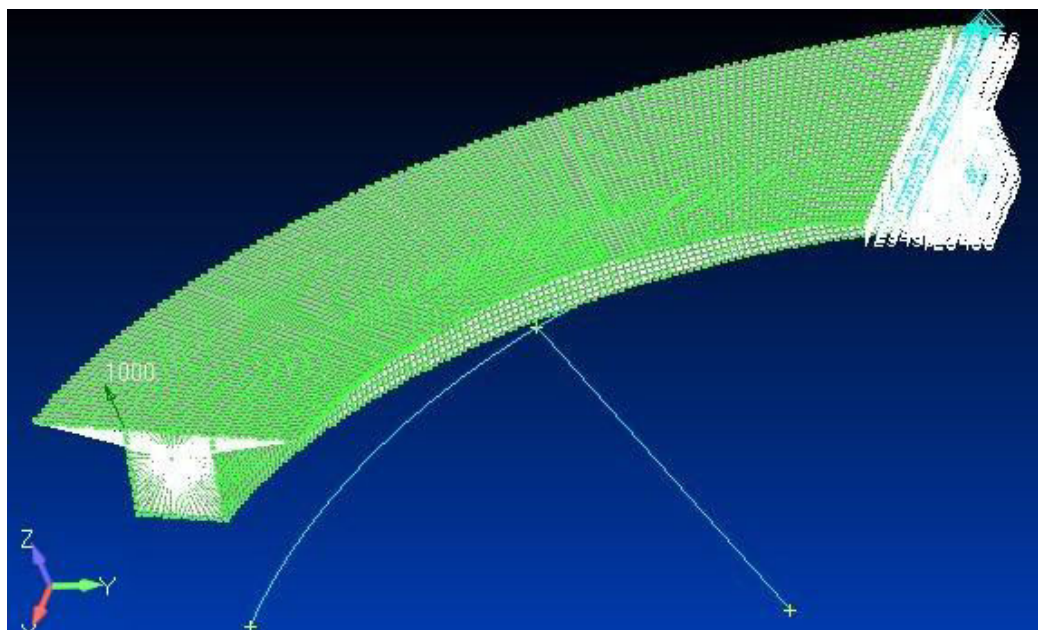


*Figure 4.13. Deformed shape of the solid model of a curved beam with the box-shaped cross section shown in Fig. 3.15 of Chapter 3 for lateral force employing FEM solid elements (axes have been taken in a different way comparing to the beam formulation of this study).*

Some aspects of numerical procedure employed are examined in the following. Particularly, in Fig. 4.14 the distribution of the vertical deflection $v(x)$ for the concentrated load $P_y = 1000\,kN$ in the vertical direction eccentrically applied this time at its free end. Curved beam elements proposed can accurately give the maximum deflection of the beam model under consideration. However, the distribution along the X axis of the arc in plan can satisfactorily be described only by the NURBS approximation of the proposed beam model due to the fact that the same NURBS functions, as for the representation of the kinematical components, have been used to describe the geometry of the curved beam and no post-processing computations need to be done as in FEM beam elements (after solving the problem values have to be compiled as vectors and be analyzed on the curve). The discrepancies arising between the NURBS' model and the solid one are probably due to the number of the diaphragms used in order to derive the values of $v(x)$ and their positions along the length, which make the solid model stiffer than it should be. Another reason might be the shear locking phenomenon.
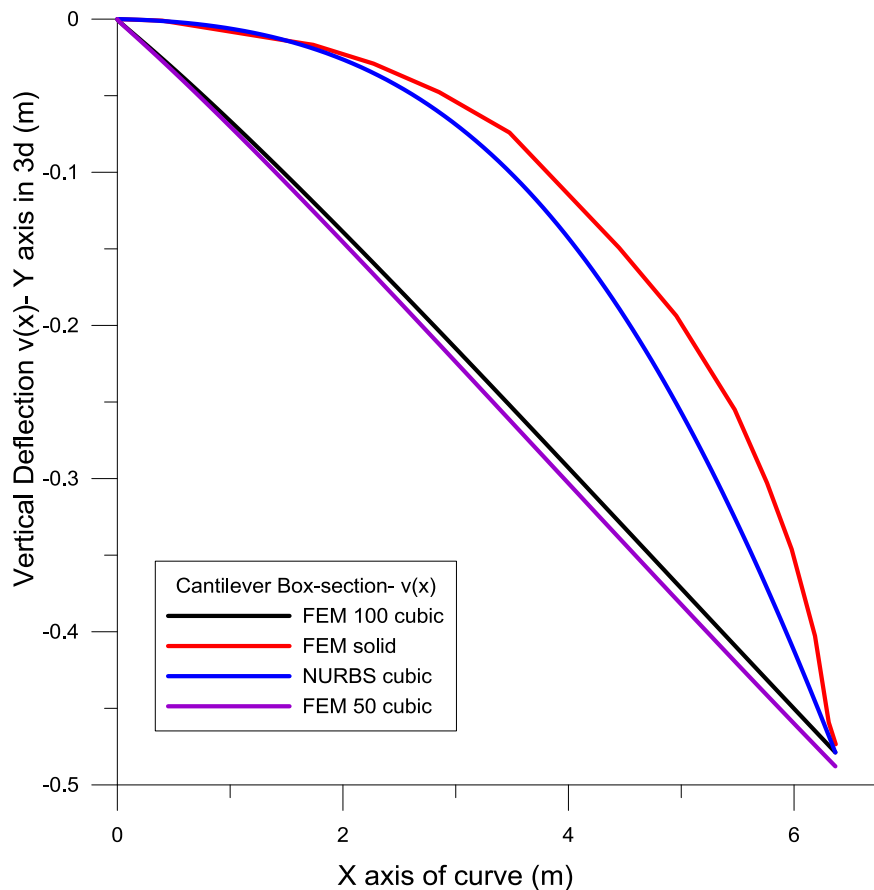
*Figure 4.14.  v(x) distributions derived from the analysis of solid and curved beam models of the cross section shown in Fig. 3.15.*

Additionally, the free vibration problem of the aforementioned curved beam has been studied and the values of different eigenfrequencies have been compiled in Table 4.10 for different models. It is obvious that the analysis employing the proposed curved beam formulation with NURBS approximation is closer to the FEM solid model with 13 diaphragms while the eigenfrequencies of the solid model with 1 diaphragm are quite smaller. However, the diaphragmatic model seems to be stiffer than the proposed model especially for higher eigenfrequencies. It is also worth noting that convergence is obtained with few beam elements when NURBS are employed.

| Mode Number | FEMsolid 1 Diaph. | FEMsolid 13 Diaph. | 4 cubic NURBS | 10cubic NURBS |
|---|---|---|---|---|
| 1 | 0.1172 | 0.1548 | 0.1317 | 0.1317 |
| 2 | 0.2556 | 0.2704 | 0.2191 | 0.2191 |
| 7 | 0.3262 | 1.0436 | 1.1045 | 1.1042 |
| 8 | 0.3562 | 1.4233 | 1.2313 | 1.2311 |
| 9 | 0.4022 | 1.5021 | - | 1.3345 |

*Table 4.10. Eigenfrequencies of the beam of Fig. 4.13.*

In Fig. 4.15 the bending moment distribution is plotted for different methods employing either the proposed beam elements or the ones used in commercial software
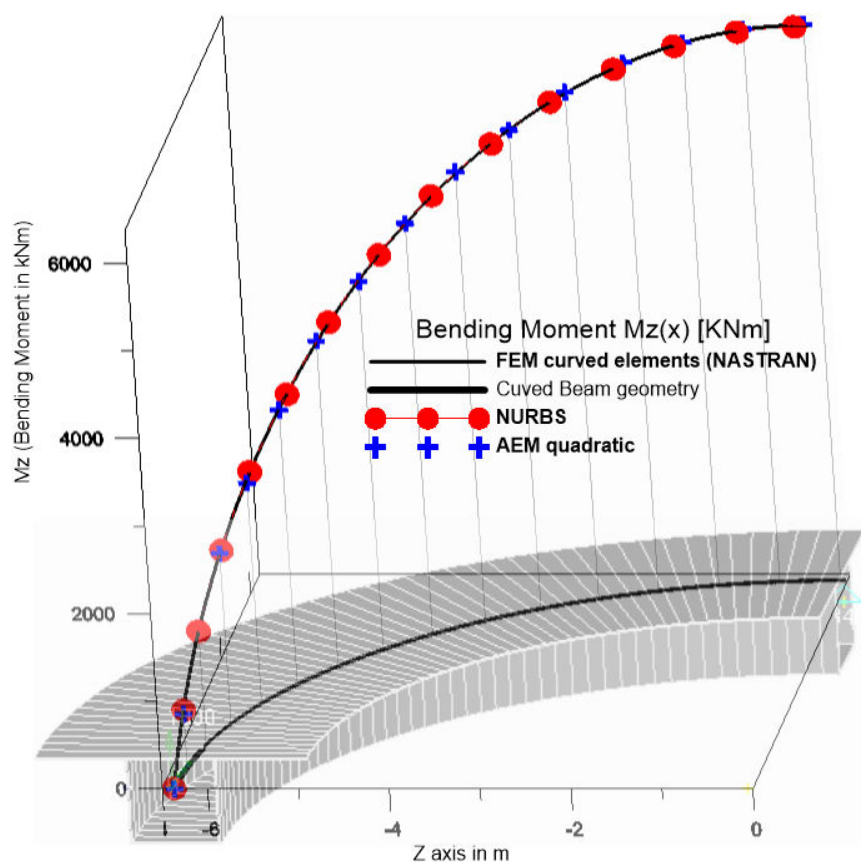


*Figure 4.15.* $M_Z(x)$ *distributions derived from the analysis of curved beam models with a box-shaped cross section (Fig. 3.15) and printed directly along with the curved model.*

(Timoshenko beam elements). The proposed method is validated. It is worth noting here that when employing NURBS there is no need for post processing of data in order to derive stresses and stress resultants as it is the case in FEM. This is due to the fact that the same basis functions are used for the representation of geometry and kinematical components. Thus, the matter is just to derive deformations and their first derivative employing the same NURBS structure for specific locations along the curve of the beam. In addition to this, when employing AEM much more discretization elements need to be used for the same accuracy level.

In Fig. 4.16 the torsional moment and bimoment distributions are plotted employing the analysis of the proposed beam model with NURBS on the curved model directly without any post-processing. Considering commercial FEM beam elements secondary Torsional moments and bimoments are not considered. However, the magnitude of bimoment near the fixed support is around 10% of the total Torsional moment and should be indeed considered in the analysis. In addition to this, secondary Torsional moment varies from 15 (near support) to 0% of the total Torsional moment and should also be considered.
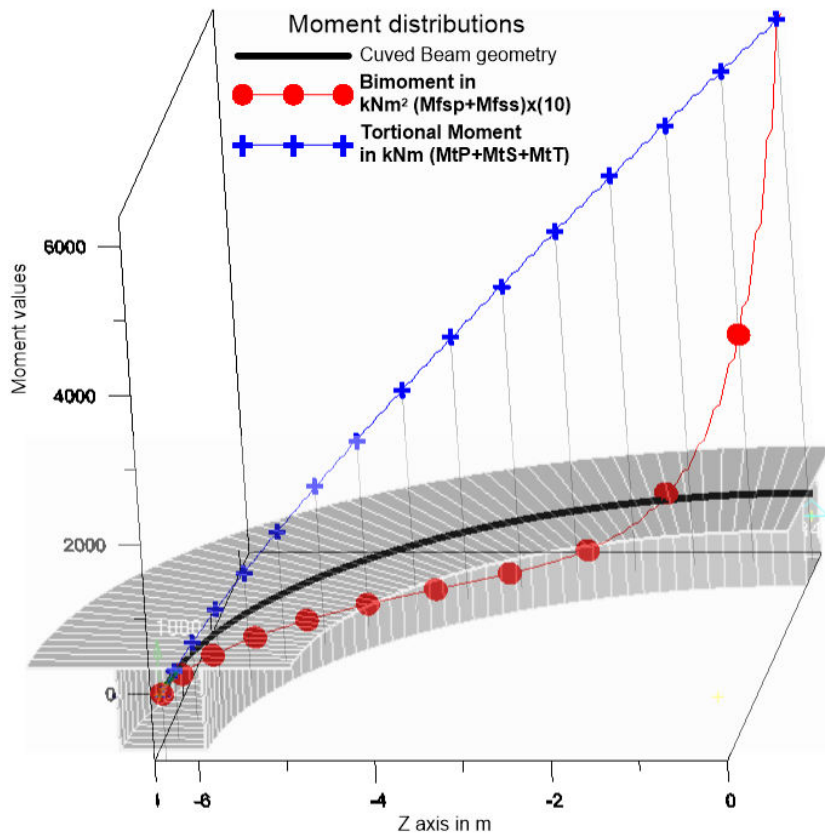
*Figure 4.16. Torsional Moment and Bimoment distributions derived from the analysis of the proposed curved beam model with a box-shaped cross section (Fig. 3.15) and printed directly along with the curved model.*

Finally, in Fig. 4.17 the dynamic response of the curved cantilever beam previously described is plotted in terms of the tip deflection out of the curvature plane. The eigenfrequency of the first mode is 49.08 rad/sec (T=0.0204 seconds). A static load $P_y = 2000 \, kN$ applied at the centroid of the free end has been dynamically applied in three different ways, namely suddenly applied for 0.025 seconds, gradually applied for the first 0.005 seconds and gradually applied for 0.015 seconds. It is obvious that the amplification is less severe for the last case due to the fact that the load rise is more gradual. This is equal to 1.3 while for the case of the suddenly applied load is equal to 1.95. Regarding the other case of gradually applied load but with a shorter rise time, the amplification factor is equal to 1.83. Considering a straight beam of the same length and loading, the amplification factor for the case of transient response is equal to 1.98.

The second beam has a box-shaped cross section shown in Fig. 4.18 and the geometric constants compiled in Table 4.11. The curved beam model examined at first has the following characteristics: $E = 3E7 \, kN/m^2$, $G = 1.5E7 \, kN/m^2$, $L = 40 \, m$, $R = 25.465 \, m$. It is subjected to a concentrated load either $P_y = 600 \, kN$ eccentrically applied as shown in Fig. 4.18. This cross section is thin-walled as the previous cross section considered in this example and it holds that $t / d = 0.086$ and $d / L = 0.086$.
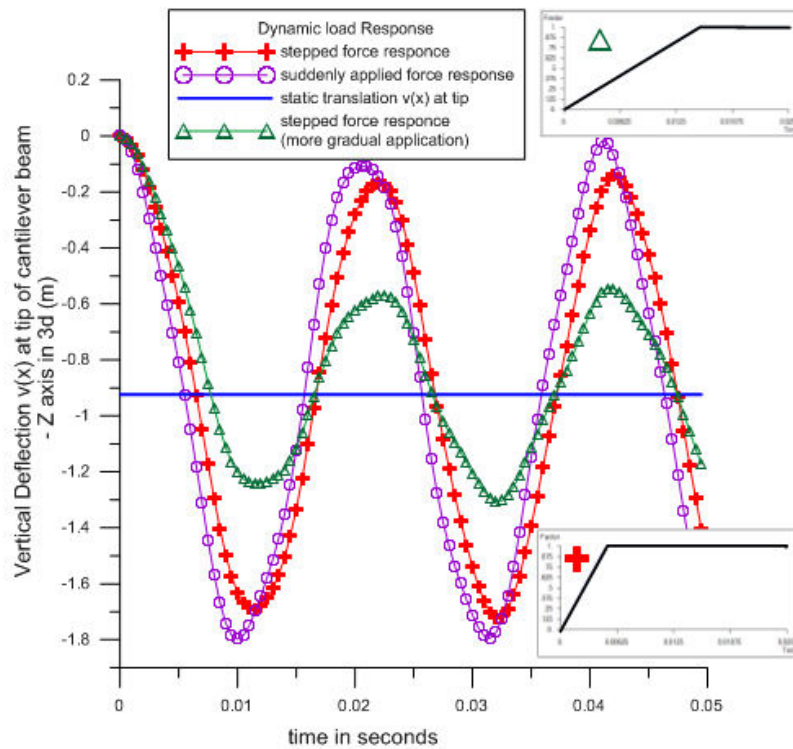
*Figure 4.17. Deflection at the tip of the curved cantilever beam shown in Fig. 4.13 for different cases of dynamic loading.*
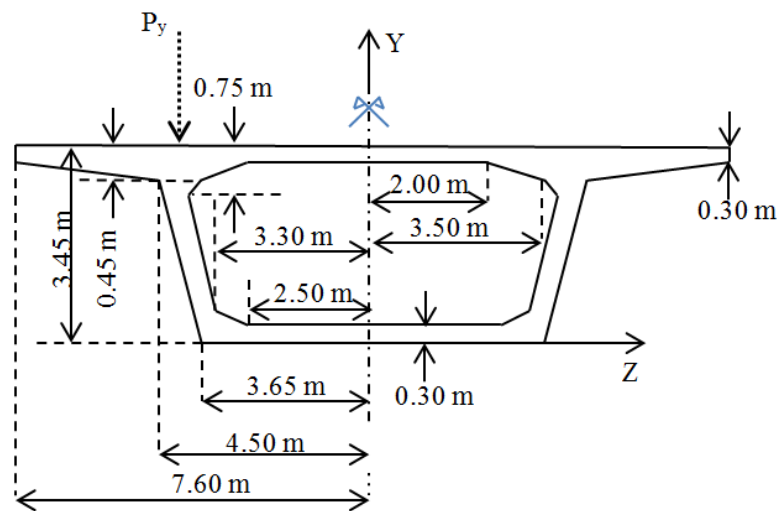


*Figure 4.18. Box-shaped cross section of the beam of example 4.5.3.*

In Table 4.12, the values of the kinematical components $v(x)$, $\theta_x(x)$ and $\theta_Y(x)$ for the lateral force $P_y$ at the midspan of the beam and for fixed end conditions are presented for i) curved beam elements in FEMAP (2010) (FEMbeam), ii) 100 quadratic elements employing AEM technique (AEMquad), iii) 2714 quadrilateral solid elements in FEMAP (2010) (FEMsolid) (the deformed shape of the solid model is given in Fig. 4.19). As it can be easily verified, the AEMquad model gives results in

general closer to the solid one. However, it should be noted that no diaphragms in the plane of the cross section have been employed in the solid model due to the fact that this procedure becomes computationally inefficient regarding the obtained level of accuracy and cumbersome for this particular cross section.

$$A = 1.1280\text{E+}01m^2 \qquad I_{\varphi_S^S \varphi_S^S} = 1.42222320\text{E+}01m^6$$

$$I_{YY} = 1.69887612\text{E+}02m^4 \qquad I_{\varphi_{Cz}^P \varphi_S^P} = -2.81492352\text{E+}00m^5$$

$$I_{ZZ} = 1.90664591\text{E+}01m^4 \qquad I_{\varphi_{Cz}^P \varphi_S^S} = 3.96237278\text{E+}00m^5$$

$$I_{\varphi_{Cz}^P \varphi_{Cz}^P} = 3.35829281\text{E+}00m^4 \qquad A_Z^P = 2.60795231\text{E+}00m^2$$

$$A_Y^S = 7.69037695\text{E-}01m^2 \qquad I_t^P = 4.24643347\text{E+}01m^4$$

$$I_t^S = 2.70455808\text{E+}01m^4 \qquad I_t^T = 1.21016082\text{E+}00m^4$$

$$D_{\Phi_{Cz}^S \Phi_S^S} = 2.62674568\text{E-}01m^3 \qquad D_{\Phi_{Cz}^S \Phi_S^T} = 3.63838338\text{E-}01m^3$$

$$I_{\varphi_{CY}^P \varphi_S^S} = 6.20215034\text{E-}13m^5 \qquad I_{\varphi_{CY}^P \varphi_S^P} = -1.28945357\text{E-}13m^5$$

$$I_{\varphi_{CY}^P \varphi_{CY}^P} = 1.20295288\text{E+}00m^4 \qquad A_Y^P = 6.75899175\text{E+}00m^2$$

$$D_{\Phi_{CY}^S \Phi_S^S} = 1.17081534\text{E-}13m^3 \qquad D_{\Phi_{CY}^S \Phi_S^T} = 2.75075432\text{E-}14m^3$$

$$I_{\varphi_S^P \varphi_S^P} = 6.27435249\text{E+}01m^6 \qquad A_Z^S = 2.97414035\text{E-}01m^2$$

*Table 4.11. Geometric constants of the box-shaped cross section shown in Fig. 4.18.*



| | | $v(m)$ at x=L | $\theta_x(rad)$ at x=L | $\theta_Y(rad)$ at x=L |
|---|---|---|---|---|
| $P_y$ Vertical Loading (eccentrically applied) | FEMbeam | -5.57E-4 | 1.81E-5 | -1.81E-5 |
| | AEMquad | -5.63E-4 | 2.25E-5 | -2.23E-5 |
| | FEMsolid | -5.60E-4 | 2.14E-5 | -2.17E-5 |

*Table 4.12. Kinematical components of a curved beam with the cross section shown in Fig. 4.18 for vertical load and fixed end conditions.*

The same cross section is employed for a beam model of the same length and material with $\rho = 2.5t / m^3$. This is examined either as cantilever (similar to Fig. 4.20) or clamped (Fig. 4.19) for the dynamic case of the proposed beam element.
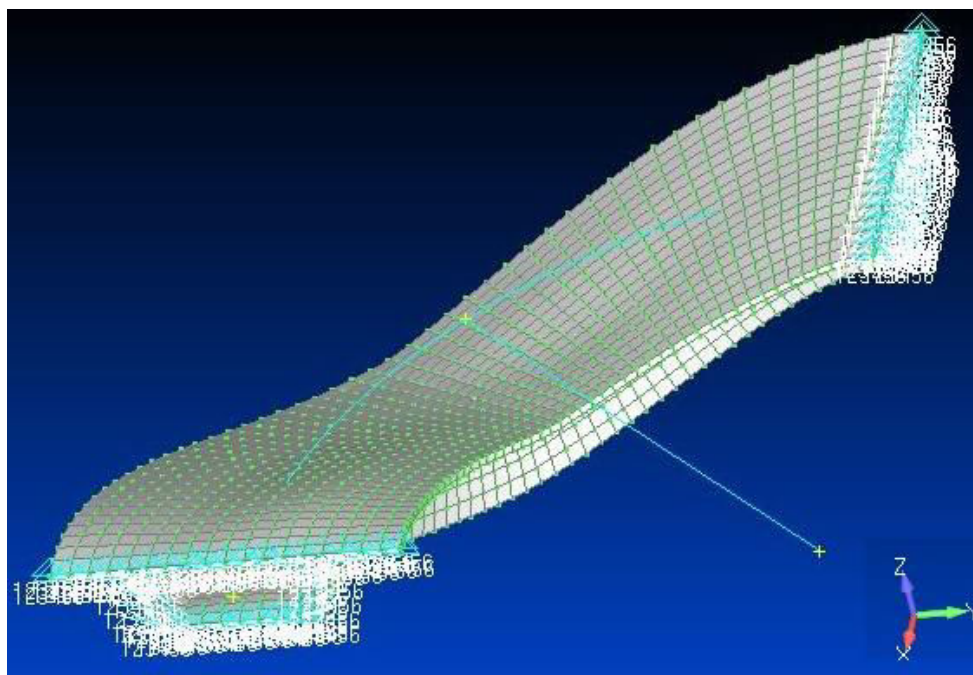
*Figure 4.19. Deformed shape of the solid models of the beam with the cross section shown in Fig. 4.18 for vertical force employing FEM solid elements (axes have been taken in a different way comparing to the beam formulation of this study).*
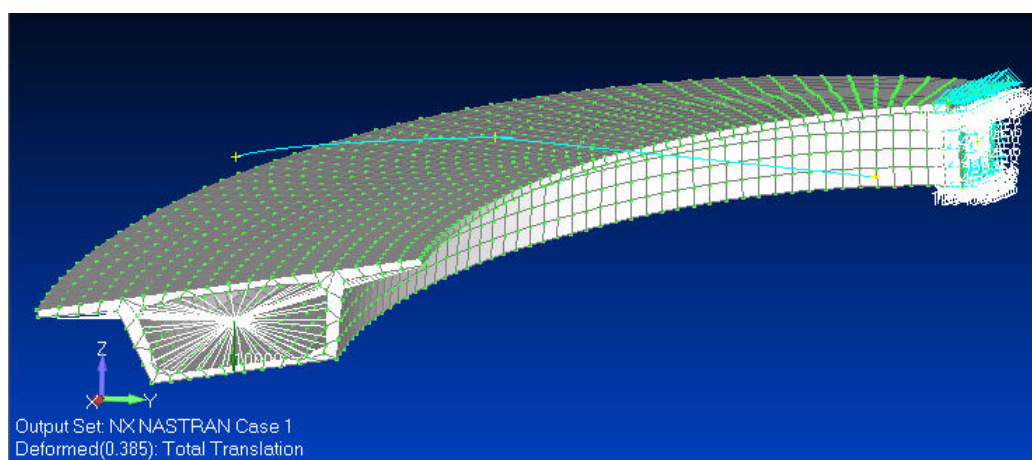


*Figure 4.20. Deformed shape of model in FEMAP employing 2714 quadrilateral solid finite elements for the beam of the box-shaped cross section shown in Fig. 4.18.*

The eigenfrequencies either for cantilever or clamped beam are compiled in Table 4.13 for the proposed formulation and the solid model. Comparing the values between models, it should be noted that errors are similar for both cases of boundary conditions and around 5% in general. However, some errors are 6-8% and this might be attributed to the selection of the right frequencies from the solid model (to those exactly corresponding to the proposed model) which has thousands of nodes to account for.

| Mode Number | Cantilever | | Clamped | |
|---|---|---|---|---|
| | 10cubic NURBS | FEMsolid (2714) | 10 cubic NURBS | FEMsolid (2714) |
| 1 | 0.0489 | 0.0488 | 0.2512 | 0.2306 |
| 2 | 0.1305 | 0.1408 | 0.5020 | 0.5252 |
| 3 | 0.2015 | 0.1905 | 0.7212 | 0.7547 |
| 4 | 0.2992 | 0.3002 | 0.7965 | 0.8111 |
| 5 | 0.4410 | 0.4644 | 0.9421 | 0.9120 |

*Table 4.13. Eigenfrequencies of the beam with cross section shown in Fig. 4.18 either cantilever or clamped.*

Finally, for comparison reasons to the open shape cross sections of previous examples, the predominant eigenvectors are presented in Fig. 4.21. The first three and the fifth modes are given. The fifth is the first mode for torsion while the previous ones are either displacement or bending modes due to the fact that box-shaped cross section exhibit high torsional rigidity.

In order to further validate the proposed formulation the aforementioned box-shaped cross section is employed for the beam model presented in Fig. 4.20. This has the same properties as those previously mentioned and it is subjected to a concentrated load $P_y = 10000\,kN$ concentrically applied.

In Table 4.14 the values of the kinematical components $v(x)$, $\theta_x(x)$ and $\theta_Z(x)$ for the vertical force $P_y$ concentrically applied at the free edge of the beam are presented for i) the proposed curved beam elements with NURBS (cubic), ii) 2714



1.  First mode of Vertical displacement

2.  First mode of Lateral displacement

3.  First mode of Vertical Bending

5.  First mode of Torsion
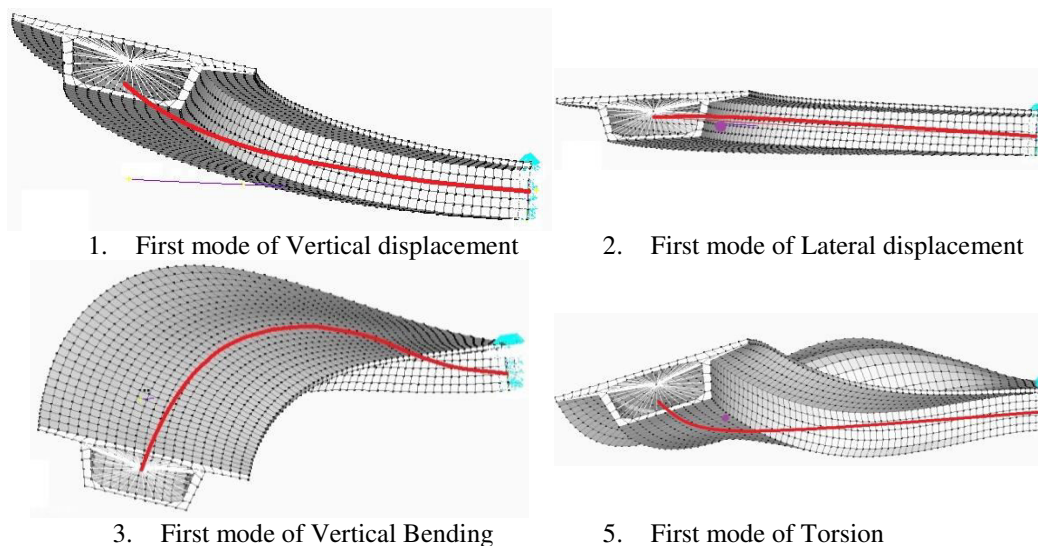
*Figure 4.21. Eigenvectors for the model of Fig. 4.20 (Proposed formulation with AEM in red line, solid model in black and initial curved geometry in purple line or purple point).*

quadrilateral solid elements with 2 diaphragms in FEMAP (2010) (FEMsolid 2 Diaph.) and iii) 40 quadratic elements in the AEM technique (AEM 40 quad.). After trying

different diaphragmatic arrangements, this one showed results closer to the proposed formulation. However, the placement of intermediate diaphragms for this particular case will be discussed in Chapter 6. Both analyses employing the beam formulation proposed give accurate results comparing to FEM solid model with the one diaphragm used in order to apply load concentrically (FEMsolid). However, the analysis with NURBS exhibits less computational cost due to the coarser discretization needed.
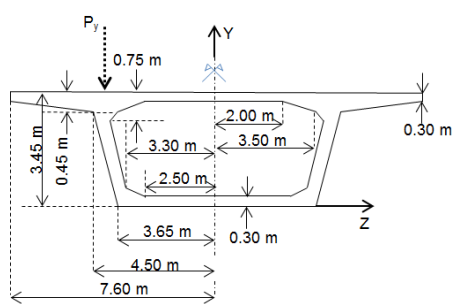
|  | | $v(m)$ at $x=L$ | $\theta_x(rad)$ at $x=L$ | $\theta_Z(rad)$ at $x=L$ |
|---|---|---|---|---|
| $P_y$ Lateral Loading | 4 cubic NURBS | 0.3197 | -0.007029 | -0.0104 |
| | FEMsolid 2 Diaph. | 0.3256 | -0.00782 | -0.0103 |
| | AEM 40 quad. | 0.3197 | -0.07020 | -0.0104 |

*Table 4.14. Kinematical components of the beam of Fig. 4.20 for vertical load.*

Similarly to previous box-shaped cross section, in Fig. 4.22 the distribution of the vertical deflection $v(x)$ along the x axis of the curved in plan geometry for the concentrated load in the vertical direction mentioned previously. As it is the case in the previous example, curved beam elements proposed can accurately give the maximum deflection of the beam model under consideration. It is worth noting here that the approximation of the $v(x)$ distribution when employing quadratic elements in the AEM technique exhibits a stiffer behavior comparing to NURBS approximation.

In Fig. 4.23 the distribution of total, primary and secondary Torsional moments are plotted along the length of the curved beam for the concentrated load in the vertical direction. In addition to this, the bimoment distribution has also been plotted. It is worth noting here that Torsion and Warping are of the same order of magnitude near the support for this specific cross section (this was not the case in the previous box-shaped cross section). Thus, Warping effect will cause important discrepancies between the commercial FEM beam elements and the one proposed in this study. Secondary Torsional moment has a considerable value near support, too.

Considering the curved beam of Fig. 4.19 with fixed end supports and a load $P_y = 20000\,kN$ applied at the centroid of the mid span, the amplification factor of the transient response for is equal to 1.90 for a system's period T=0.127 seconds (first mode) at time t=0.0675 seconds.

The last beam has a box-shaped cross section shown in Fig. 4.24 and the geometric constants compiled in Table 4.15. The curved beam model examined at first
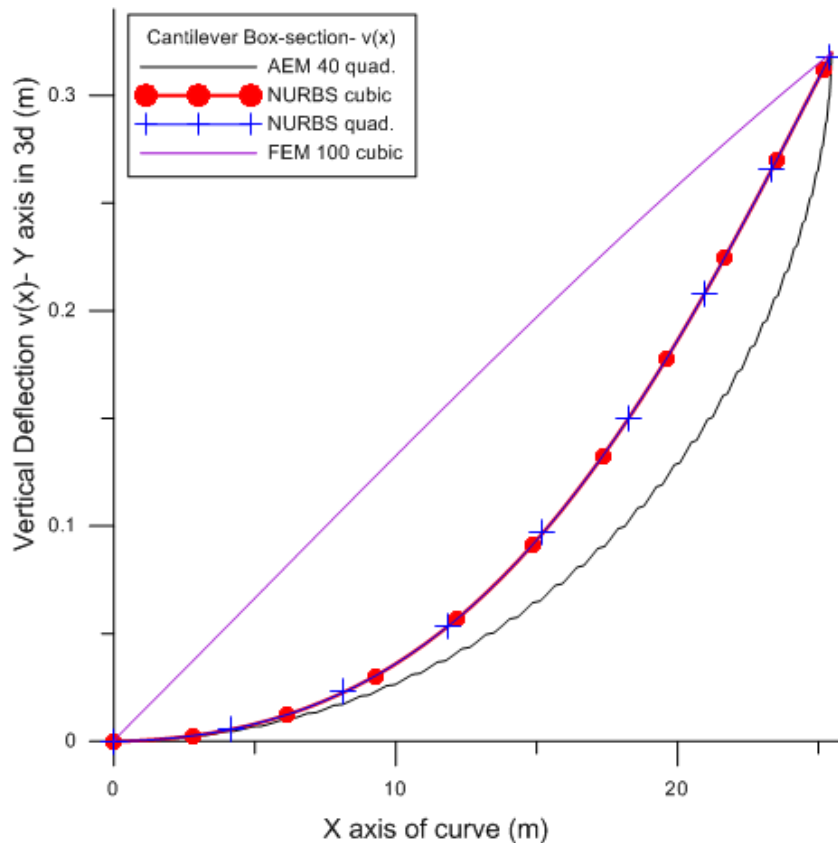
*Figure 4.22. $v(x)$ distributions derived from the analysis of solid and curved beam*

*models of the cross section shown in Fig. 4.18.*

has the following characteristics: $E = 3.25E7 \, kN/m^2$, $\nu = 0.1667$, $L = 33 \, m$, $R = 100 \, m$ and $\rho = 2.5t / m^3$. It is examined as clamped for the dynamic problem. This cross section is also thin-walled and it holds that $t / d = 0.1$ and $d / L = 0.065$.

    In Table 4.16 the eigenfrequencies are compiled for three different cases, namely proposed formulation, solid model with one diaphragm at midspan (FEMAP, 2010) and solid model without diaphragm (ANSYS-SOLID45) (Wang et al., 2016). The reasoning behind the placement of one diaphragm is in detail explained in Chapter 6. It is important to note that damping is considered in the last case. The eigenfrequencies of the proposed curved beam formulation are quite close to both solid models for the first five modes but they are closer to the solid model of ANSYS after the fifth mode. Thus, damping does not seem to significantly affect the results of the proposed beam model.

    Finally, in Fig. 4.25 the dynamic response is obtained for the cases previously mentioned plus the solid model without diaphragm created with FEMAP (2010) for comparison reasons. The models are subjected to a vertical cosine load applied at midspan. It is worth noting that damping is obvious through the oscillations present at the solid model with damping (ANSYS - SOLID45) at the initial phase of its transient response. The rest of the models exhibit in general a steady state response. However, this does not affect significantly the results when comparing the maximum values of
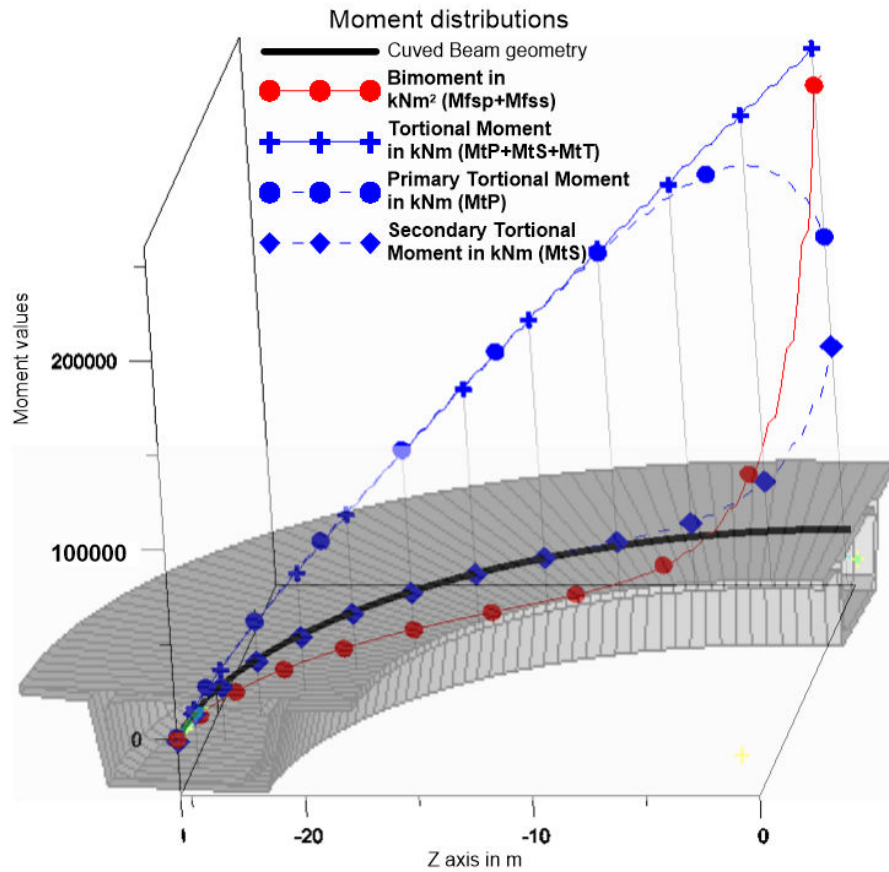
*Figure 4.23. Torsional Moments and Bimoment distributions derived from the analysis of the proposed curved beam model of Fig. 4.20 and printed directly along with the curved model.*
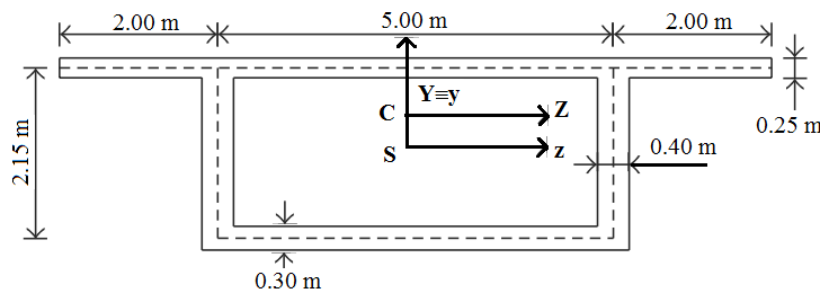


*Figure 4.24. Box-shaped cross section of a beam of example 4.5.3.*

displacement between the solid models without diaphragm. The proposed formulation seems to be closer to the solid model with 1 diaphragm and exhibits a quite smooth behavior following the application of the load due to the absence of damping.

## 4.6  Concluding Remarks

In this chapter, the AEM, a BEM based technique is applied for the static and dynamic analysis of curved homogeneous beams considering nonuniform warping

effects. The presented formulation is based on advanced beam elements taking into account secondary torsional shear deformation effect and shear lag effect due to

| | |
|---|---|
| $A = 5.3700\text{E}+00\,m^2$ | $I_{\varphi_S^S \varphi_S^S} = 1.84556865\text{E}+00\,m^6$ |
| $I_{YY} = 2.851910\text{E}+01\,m^4$ | $I_{\varphi_{CZ}^P \varphi_S^P} = -6.29061071\text{E}-01\,m^5$ |
| $I_{ZZ} = 4.84561718\text{E}+00\,m^4$ | $I_{\varphi_{CZ}^P \varphi_S^S} = 3.17151178\text{E}-01\,m^5$ |
| $I_{\varphi_{CZ}^P \varphi_{CZ}^P} = 3.06077446\text{E}-01\,m^4$ | $A_Z^P = 3.27457767\text{E}+00\,m^2$ |
| $A_Y^S = 1.45066966\text{E}-01\,m^2$ | $I_t^P = 1.02573505\text{E}+01\,m^4$ |
| $I_t^S = 3.95307960\text{E}+00\,m^4$ | $I_t^T = 2.53467905\text{E}-01\,m^4$ |
| $D_{\Phi_{CZ}^S \Phi_S^S} = -2.94263448\text{E}-01\,m^3$ | $D_{\Phi_{CZ}^S \Phi_S^T} = 9.46320932\text{E}-02\,m^3$ |
| $I_{\varphi_{CY}^P \varphi_S^S} = -1.70696790\text{E}-14\,m^5$ | $I_{\varphi_{CY}^P \varphi_S^P} = -1.22749033\text{E}-14\,m^5$ |
| $I_{\varphi_{CY}^P \varphi_{CY}^P} = 3.04551295\text{E}-01\,m^4$ | $A_Y^P = 1.17985944\text{E}+00\,m^2$ |
| $D_{\Phi_{CY}^S \Phi_S^S} = -1.13071027\text{E}-14\,m^3$ | $D_{\Phi_{CY}^S \Phi_S^T} = 2.49995337\text{E}-15\,m^3$ |
| $I_{\varphi_S^P \varphi_S^P} = 4.16066218\text{E}+00\,m^6$ | $A_Z^S = 2.88756060\text{E}-01\,m^2$ |

Table 4.15. Geometric constants of the box-shaped cross section shown in Fig. 4.24.

| Mode Number | FEMsolid 1 Diaph. | Solid45 no Diaph. | cubic NURBS | Type of the predominant modes |
|:---:|:---:|:---:|:---:|:---:|
| 1 | 9.72 (1.73)* | 9.67 (1.22)* | 9.55 | First mode of vertical displacement |
| 2 | 19.21 (0.65) | 19.47 (0.70) | 19.33 | First mode of lateral bending |
| 3 | 21.58 (4.62) | 21.66 (4.97) | 20.58 | First mode of torsion |
| 4 | 22.75 (1.11) | 22.98 (2.10) | 22.49 | Second mode of vertical displacement |
| 5 | 33.59 (13.74) | 36.57 (4.48) | 38.21 | |
| 6 | 37.10 (7.93) | 38.67 (3.55) | 40.04 | |
| 7 | 44.16 (3.50) | 43.74 (2.57) | 42.61 | |
| 8 | 47.68 (11.84) | 51.39 (3.78) | 53.33 | |

Table 4.16. Eigenfrequencies of the clamped beam with cross section shown in Fig. 4.24. *() difference between the corresponding solid model and the proposed beam model (cubic NURBS)

both shear and torsion. The importance of the proposed beam element is highlighted

when considering the advantages of beam models compared with solid ones, as it is mentioned in the introduction. Thus, the main purpose is for the beam formulation to remain simple and with the least number of degrees of freedom needed to describe its
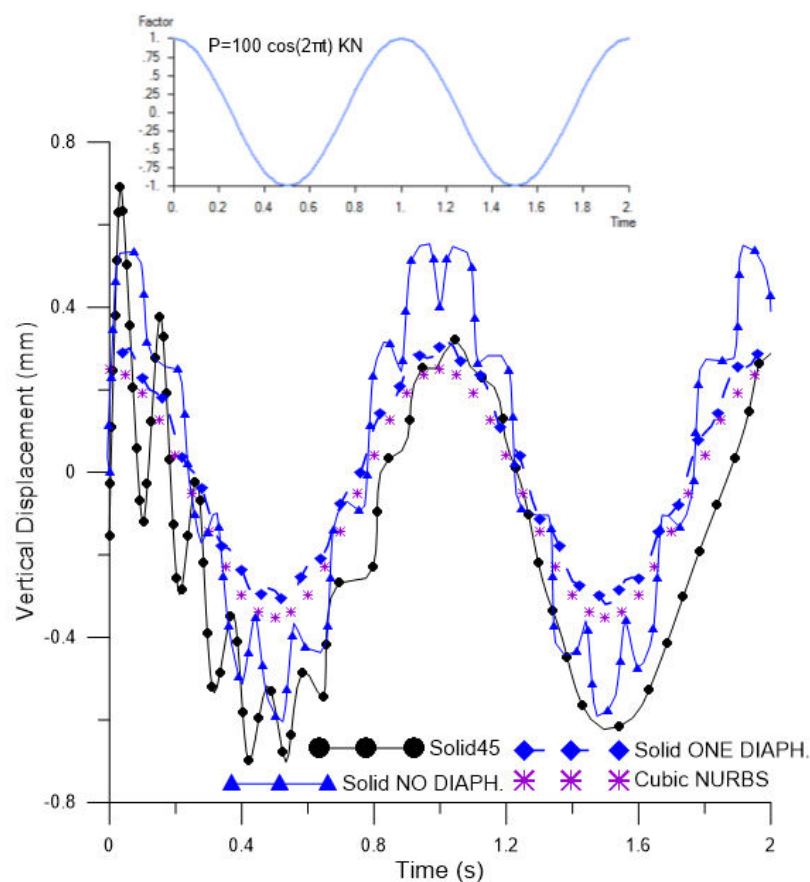


*Figure 4.25. Dynamic response of the clamped beam with the cross section shown in Fig, 4.24 for vertical cosine load.*

behavior accurately (distortional effects and local buckling phenomena increase significantly the dimension of the problem). Quadratic and constant discretization elements have been employed in the AEM technique. In addition to this, Isogeometric tools integrated in FEM and AEM are also applied for the analysis. NURBS structures give another important advantage over solid models, especially with curved geometries, due to the fact that they do not require cumbersome pre- and post-processing while integrate curved geometry in the analysis employing the same shape functions. Moreover, creation of coarse models with quadrilateral solid elements and diaphragms is very time-consuming.

NURBS have been employed in combination with FEM or AEM beam elements and compared to FEM models employing quadrilateral or triangular solid elements or curved beam elements. Some of the results have also been compared to the results of FEM plate/shell models. The main conclusions that can be drawn from this investigation are:

   i.    Highly accurate results can in general be obtained using quadratic elements in the AEM technique.

  ii.    FEM models employing curved beam elements give less accurate results due to the ignorance of generalized warping and STSDE effects, showing quite different deformed shapes than solid and AEMquad models especially in the case of non-symmetric cross section beams. Moreover, AEMquad model gives a good prediction of normal and shear stresses compared to the solid one.

 iii.    AEMquad models give more accurate results than models with shell elements especially in cases where the warping of the walls of a cross section is important (shear lag due to shear and torsion).

 iv.    Highly accurate results can in general be obtained using B-splines in the AEM technique as well as NURBS in FEM beam formulations for the static and dynamic analysis of the proposed beam element. Computational effort, including post-processing of the results, is significantly reduced by the use of NURBS comparing to FEM beam and solid models. Employment of NURBS either in FEM or in AEM results in higher convergence rates and highly accurate results with few elements. In addition to this, NURBS give more accurate values for higher frequencies comparing to traditional FEM beam elements

  v.    FEM curved beam formulations based on Timoshenko beam theory exhibit a significant loss in accuracy for higher frequencies even for doubly symmetric cross sections. Thus, warping effects need to be taken into account in the dynamic analysis.

 vi.    Displacement and bending modes dominate over the torsional ones when considering box-shaped cross sections due to higher torsional rigidities comparing to the open shape cross sections.

 vii.    Amplification factors of the dynamic response of a curved beam either for suddenly or gradually applied force are similar to those of straight beam formulations. The consideration of damping does not alter the response in a significant way for the cases examined.

viii.    The magnitude of bimoment is in general not negligible comparing to the total Torsional moment and both moments can also be of the same order of magnitude as in the example 4.5.3 (cross section of Fig. 4.18). In addition to this, secondary Torsional moments can be significant and should also be considered in the analysis. These higher order additional stress resultants can now be integrated in the analysis' results and plotted in alignment with the curved geometry due to the use of Isogeometric analysis.

# Chapter 5

# Chapter **5**

# Generalized distortional analysis of Straight and Curved beams by Isogeometric Methods

## 5.1  Introduction

In engineering practice the analysis of beam structural members, which have a longitudinal dimension significantly larger than the cross sectional ones, is frequently encountered. However, refined models either straight or curved with shell or solid elements are widely used in structures, such as for example the deck of a bridge with a thin-walled cross section, for stress or strain analysis. The analysis of such members employing the so-called "Higher-Order Beam Theories" (Ferradi et al., 2013; Ferradi, and Cespedes, 2014; El Fatmi, and Ghazouani, 2011) is of increased interest due to their important advantages over more elaborate approaches based on shell or solid finite elements (Sapountzakis and Tsiptsis, 2015), which are mainly incorporated in commercial software. These advantages of beam models or disadvantages of the other approximations have already been mentioned in the introduction of Chapter 4. Particularly, the design of box-shaped thin-walled cross sections, the placement of supports, diaphragms and loads, the additional calculations needed in order to derive cross sections' rotations and further manipulations to extract stress values at specific points of solid elements can also be added to explain more precisely the imperative need for advanced beam elements. In addition to these, midline of shell and plate models becomes difficult to be designed for different thicknesses of the same cross section, while midline models exhibit difficulty in capturing warping accurately. Moreover, the investigation of various shell/plate or solid models in order to conduct convergence studies and control membrane and shear locking phenomena becomes time-consuming and multiple models need to be created. Distortional effects can be isolated and further investigated for each model. Finally, beam models allow the use of different numerical tools (i.e. Isogeometric analysis- IGA, boundary element methods- BEM etc.) for the 2-D cross sectional and the 1-D longitudinal analysis which could be more effective in one case or the other and, thus, leading to an optimum approximating computational procedure.

The evaluation of the cross sectional properties, which are finally incorporated in the one-dimensional beam analysis, is associated with the accuracy of the model regarding the cross sectional behavior. Over the past decades, classical beam theories based on specific assumptions fail to describe accurately the structural behavior of beam elements, especially in more complex formulations such as in curved

geometries. Among these theories, that of Saint-Venant (SV) still plays a crucial role due to the fact that the analysis reduces to the evaluation of warping and distortional functions over the cross sectional domain. However, this solution is exact for the uniform warping of a beam (warping/distortional deformations are not restrained). Towards improving SV theory, several researchers investigated the so-called SV's principle (stated by Love, 1944) as well as the SV's end-effects in order to derive a more general formulation of beams' kinematics. Bauchau (1985) proposed an approach that consists in improving the SV solution by adding a new set of orthonormal eigenwarpings to the uniform ones, derived from energy principles in order to formulate the governing equations. In most of these studies, the solution is obtained as the sum of the SV'S solution and the residual displacements corresponding to the end-effects, as it will be later explained.

In the majority of past research works, thin-walled cross sections have been studied due to their low self-weight comparing to solid ones and, thus, their use in practice. In-plane deformations, such as distortion, occurring when thin-walled sections undergo bending and torsional deformations can considerably weaken the flexural and torsional stiffness of thin-walled beams. Even though distortion is larger in magnitude near the beam's ends, it does not remain local (exponentially decays away from the support) and thus it should be considered over the entire domain of the beam to account for its stiffness-weakening effect. Vlasov (1961) presented the Thin Tube Theory (TTT) and treated different cross section types as special cases of this general theory. Kollbrunner and Basler (1969) and Heilig (1971) were later reformulated TTT for multi-cell boxes with arbitrary cross sections. Kristek (1970) obtained analytical solution for simple practical cases and separated the analysis of transverse distortion from that of torsion with longitudinal warping employing the superposition principle. Wright et al. (1968) studied the distortional warping response of single-cell box girders with longitudinally and transversely stiffened plates employing the beam on elastic foundation (BEF) analogy. Steinle (1970) tackled the torsional distortion problem and introduced distortional stress resultants in the analysis. Kollbrunner and Hajdin (1975) dealt with the extension of the beam theory of prismatic folded structures to include the deformation of the cross section for open and closed cross sections including warping. Other research efforts later expanded TTT considering only box-shaped cross sections (single- or multi-cell) and, thus, being not general (Kermani and Waldron, 1993; Kim and Kim, 1999a; Park et al., 2003; Park et al., 2005b; Razaqpur and Li, 1991; Osadebe and Chidolue, 2012). Schardt (1989, 1994) developed an advanced formulation known as Generalized Beam Theory (GBT) which is a generalization of the classical Vlasov beam theory in order to incorporate flexural and torsional distortional effects. A distinguishing feature of GBT stems from the general character of its cross sectional analysis which enables the determination of cross-section deformation modes as well as their categorization to global, distortional or local ones. Further developments of GBT avoid some of its cumbersome procedures through eigenvalue cross sectional analysis (Ranzi and Luongo, 2011; Jönsson, 1999; Jönsson and Andreassen, 2011; Andreassen and Jönsson, 2012a, 2012b, 2013). These approaches are employed nowadays by several researchers. Camotim, Silvestre and

co-researchers expanded the method to cover a variety of cross sections, orthotropic materials, as well as geometrically nonlinear and inelastic problems (Silvestre and Camotim, 2010; Camotim and Dinis, 2011; Dinis and Camotim, 2011, Gonçalves and Camotim, 2015). Towards solving the problem for arbitrarily shaped homogeneous or composite cross sections, El Fatmi and Ghazouani (2011) presented a higher order composite beam theory (denoted HOCBT) that starts from the exact expression of SV's solution and introduces in- and out-of-plane independent warping parameters for symmetric orthotropic cross sections with the ability to extended it for arbitrary ones. However, in-plane warpings are only due to the flexural and axial deformation modes and, thus, it could be stated that this research effort studies Poisson ratio effects rather than distortional effects. Ferradi and Cespedes (2014) presented the formulation of a 3D beam element solving an eigenvalue problem for the distortional behavior of the cross section (in-plane problem) and computing warping functions separately by using an iterative equilibrium scheme. Genoese, Genoese et al. (2014) developed a beam model with arbitrary cross section taking into account warping and distortion with their evaluation being based on the solution of the 3D elasticity problem for bodies loaded only on the terminal bases and a semi-analytic finite element formulation. Finally, Dikaros and Sapountzakis (2016) presented a general boundary element formulation for the analysis of composite beams of arbitrary cross section taking into account the influence of generalized cross sectional warping and distortion due to both flexure and torsion. In this proposal, distortional and warping functions are evaluated by the same eigenvalue problem and in order of importance.

Regarding horizontally curved beams subjected to vertical or radial loads, they inherently exhibit a more complex behavior comparing to straight formulations due to the fact that the effects of primary and secondary torsion are always coupled to those of bending and cross section distortion either for centered or eccentric loads. Dabrowski (1968) elaborated Vlasov's theory and introduced distortional behavior of box girders with a symmetric cross section. His model introduces the distortion angle as the single degree of freedom which measures the magnitude of the cross-sectional distortion. Bazant and Nimeiri (1974) proposed the skew-ended finite element in order to implement the theory of non-uniform torsion for straight or curved thin-walled cross sections. Oleinik and Heins (1975), and Heins and Oleinik (1976) employing Vlasov's and Dabrowski's theories studied the structural behavior of curved box girders. In-plane deformations were approximated using a differential equation which was solved employing the finite difference method. In addition to this, Martin and Heins (1978) expanded Dabrowski's equation, which predicts the cross-sectional deformations, so that the angular deformations induced at given points along an I-girder curved bridge can be calculated. Zhang and Lyons (1984a, 1984b) employed Dabrowski's theory combined with Finite element method to develop a multi-cell box element for the analysis of curved bridges. Nakai and Yoo (1988) presented an extended study on the analysis and design of curved steel bridges. Razaqpur and Li (1994) extended their previous theory to curved thin-walled box beams. Petrov and Geradin (1998) employing the same concept with El Fatmi and Ghazouani (2011) for straight beams formulated a theory for curved and pre-twisted beams of arbitrary homogeneous cross

sections, covering geometrically nonlinear range as well. Kim and Kim (2002) developed a theory for thin-walled curved beams of rectangular cross section by extending the theory developed earlier for straight beams taking into account warping and distortional deformations. Park et al. (2005a) expanded their previous work (2005b), which was limited to straight box girder bridges, to curved formulations. They developed a curved box beam element which was employed in order to develop design charts for adequate spacing of the intermediate diaphragms of curved bridges. Flexural and torsional displacement functions have been based on those proposed for doubly symmetric cross section by Kang and Yoo (1994) while distortional functions have been derived for a mono-symmetric cross section (Park et al, 2003). Despite the practical interest of their study, their proposal cannot accommodate elastic constraints and due to other assumptions made lacks of generality. In other research efforts, the vibration problems of thin-walled curved box girder bridges due to moving loads have been investigated. The curved box girder bridges have been numerically modelled using finite elements which take into account the torsional warping, distortion and distortional warping (Huang, 2001; Yang et al., 2001; Nallasivam et al., 2007). Other recent research efforts as the following ones mainly constitute design guides with new formulae for specific practical cases rather than a generalized theory for the analysis of curved beams. Particularly, in the study of Zhang et al. (2015), a curved girder is simplified to straight one by using the M/r method and calculation formulae for determining the required diaphragm spacing are obtained by regression analyses. Towards establishing a more general theory, Arici and Granata (2016) employed the Hamiltonian Structural Analysis Method for the analysis of straight and curved thin-walled structures on elastic foundation extending the so-called GBT. To the authors' knowledge, there are no research efforts that introduce a unified distortional and warping eigenvalue analysis of arbitrarily shaped cross sections to the analysis of curved beams.

As far as the free vibration and dynamic response is concerned, it has been noticed in studies of the last decades, mainly for straight beam formulations, that the thin-walled members' behavior can be highly affected by cross section's in-plane (distortion) deformations. There are a number of investigations with various approaches in order to determine the cross sectional deformations which are either restricted to quadrilateral cross sections (Kim and Kim, 1999a,b) or to the evaluation of two distortional modes that are roughly approximated by cubic polynomials (Kim and Kim, 2000). Thin-walled closed piecewise straight beams with angled joints were also studied by Jang and Kim (2009), but arbitrarily shaped sections were not investigated. More recently, Petrolo et al. (2012) as well as Carrera and Varello (2012) developed a beam formulation which can be exploited for the analyses of compact, thin-walled structures and bridge-like cross-sections. However, this approach is only capable of handling problems that involve a limited range of deformation types due to the fact that the displacement field, which is based on, is not formulated in the most general way. In addition to these, Jang et al. (2012) and Bebiano et al. (2013) developed more refined beam models with open- or closed-shaped cross section for the vibration problem. However, their cross sectional analyses are based on beam-

frame and plate models for the discretization of the cross section. However, these approaches depend on the section's shape, the nodal topology and the number of intermediate nodes employed which make the procedure cumbersome while deformation mode selection becomes important for the analysis. Regarding vibration analysis of curved beams including distortional effects, few research efforts have taken into account the complete coupling of torsion, warping, and distortion deformations together with the curvature effect. Zhu et al. (2016) provided a dynamic theory for the spatial vibration analysis of horizontally curved thin-walled rectangular box-shaped beams based on the displacement fields proposed by Kim and Kim (1999a). Thus, to the authors' knowledge, there is no study on the vibration problem of curved beams with arbitrary cross section including in- and out-of-plane deformations.

In modern regulations and design specifications, the importance of torsional and distortional effects in stress or strain analysis of structural members is recognized. Particularly, in sub-sections 6.2.7.1 and 6.2.7.2 of EN 1993-2, Eurocode 3: Design of steel structures - Part 2: Steel bridges, regarding torsion, the designer is obliged to keep the distortional stresses under a specific limiting value or follow some general design rules in case of neglecting distortion. These are presented in clauses (1)-(9) of section 6.2.7, regarding torsion, of EN 1993-1-1, Eurocode 3: Design of steel structures - Part 1-1: General rules and rules for buildings. Nevertheless, no guidelines and specific modelling methodologies offered for the aforementioned effects. It should also be noted that most of the provisions of Eurocode 3 regarding torsion are valid only when distortional deformation can be neglected. The same case is when the stability of uniform members is checked as it is mentioned in clause (1) of section 6.3.3 of EN 1993-1-1. Distortional buckling is encountered in EN 1993-1-3, Eurocode 3 - Design of steel structures - Part 1-3: General rules - Supplementary rules for cold-formed member and sheeting, and EN 1993-1-4, Eurocode 3 - Design of steel structures - Part 1-4: General rules - Supplementary rules for stainless steels. It is taken into account through reduction factors or special arrangements in order to prevent distortion. In addition to these, distortional effect is also suggested be taken into account during the design of unreinforced joints (Section 7.5.2.1(7) of EN 1993-1-8, Eurocode 3: Design of steel structures - Part 1-8: Design of joints) to prevent chord distortional failure and the evaluation of nominal stresses from fatigue actions (Section 4(1) of EN 1993-1-9, Eurocode 3: Design of steel structures - Part 1-9: Fatigue). Regarding design of aluminum structures (Eurocode 9: Design of aluminum structures - Part 1-1: General structural rules and Part 1-3: Structures susceptible to fatigue), some general rules account for distortion and distortional buckling without any specific guidance.

In this study, the static and dynamic analysis of straight or *horizontally curved beams* of *arbitrary cross section*, loading and boundary conditions including generalized cross sectional *warping* and *distortional effects* due to both flexure and torsion is presented. The aim of this Chapter is to propose a new formulation by enriching the beam's kinematics both with out-of- and in-plane deformation modes and, thus, take into account both cross section's warping and distortion in the final 1D analysis of curved members, towards developing GBT further for curved geometries

while employing independent warping parameters, which are commonly used in Higher Order Beam Theories (HOBT). The approximating methods and schemes proposed by Dikaros and Sapountzakis (2014, 2016) are employed and extended in this study. Adopting the concept of end-effects and their exponential decay away from the support (El Fatmi and Ghazouani, 2011), appropriate residual strains are added to those corresponding to rigid body movements. Further, applying Hooke's stress-strain law and employing the equilibrium equations of 3D elasticity, a system of partial differential equations can be derived for each material over the 2D cross section's domain together with the corresponding boundary conditions. Consequently, a coupled two-dimensional boundary value problem is formulated, with or without considering Poisson ratio. Applying a proper discretization scheme for the cross section, the above mentioned problem will lead to the formulation of an eigenvalue problem which the eigenvalues and the corresponding eigenvectors, for a desired number of modes, can be extracted from. The obtained set of modes contains axial, flexural and torsional modes in order of significance without distinction between them. To avoid the additional effort needed in order to recognize the most significant modes, the iterative local equilibrium scheme described in the work of Dikaros and Sapountzakis (2014) is adopted until the error due to residual terms becomes minimal. The above scheme is initialized by employing a pre-assumed vector which corresponds to rigid body movements of the cross section (the so-called central solution). Together with the warping functions calculated first, the corresponding distortional ones are also obtained and recursively modify the warping functions due to their coupling. With all these additional modes, the beams' kinematics is enriched and capable of describing accurately the displacement and stress distribution in the beam. The functions derived are evaluated employing 2D BEM (Katsikadelis, 2002a). The coefficient matrices containing the geometric and mass properties of the cross section can now be calculated, as it will be later explained. Thus, a set of boundary value problems are formulated with respect to the unknown kinematical components (displacements, rotations and independent parameters) for each time instant, the number of which is defined by the user depending on the accuracy of the results. This linear system is solved using *Isogeometric tools*, either integrated in the Finite Element Method (FEM) (Hughes, Cottrell, and Bazilevs, 2009) or in the Analog Equation Method (AEM) (Katsikadelis, 2002b), which is BEM based. Employing the principal of virtual work the new equilibrium equations are derived. Additionally, by employing a distributed mass model system accounting for longitudinal, transverse, rotatory, torsional, warping and distortional inertia, free vibration characteristics and responses of the stress resultants and displacements to static and moving loading can be evaluated. The results obtained from the beam element will be compared to those obtained from finite 3D solutions and other research efforts. Numerical examples are presented to illustrate the efficiency and the accuracy of this formulation as well as to provide rules of thumb regarding the consideration of distortion and the number of modes needed. To the authors' knowledge, the numerical procedures previously mentioned have not been reported in the literature for the analysis of straight or curved beams including distortional effects.

The essential features and novel aspects of the formulation that will be presented in the following compared with previous ones are summarized as follows.

i.   The developed beam formulation is capable of the static and dynamic analysis of spatial straight or curved beams of arbitrary composite cross section with one plane of constant curvature considering warping and distortional effects (in addition to the previous formulations) that are introduced in the same boundary value problem which describes the cross section's deformations.

ii.  The cross sectional analysis is based on an iterative equilibrium scheme which results in a numerical procedure with less computational effort and complexity comparing to traditional eigenvalue analysis reported in the literature for similar problems. Particularly, modes attributed to different structural phenomena can be separated directly and make the supervision of the results easier. In addition to this, the data post-processing and the iterative procedure become faster due to the fact that warping and distortional functions are calculated separately.

iii. The accuracy level of the numerical method proposed can be decided by the user by setting the desirable number of the modes taken into account and, thus, increasing the number of higher modes added in the final solution.

iv.  As also mentioned in Chapter 4, the numerical solution of the straight or curved advanced beam is based on B-splines (Sapountzakis, and Tsiptsis, 2014; Sapountzakis, and Tsiptsis, 2017) and NURBS (Isogeometric Analysis) offering the advantage of integrating computer aided design (CAD) in the analysis.

v.   The straight or curved beam is subjected to arbitrary external loading including warping and distortional moments and is supported by the most general boundary conditions including elastic support or restraint.

vi.  The proposed method employs a BEM approach which requires only boundary discretization for the cross sectional analysis with line or parabolic elements instead of area elements of the FEM solutions, which require the whole cross section to be discretized into triangular or quadrilateral area elements.

## 5.2  Statement of the problem

Let us consider a straight or curved prismatic element (Fig. 4.4 of Chapter 4) of length $L$ with an arbitrarily shaped composite cross section of $m$ homogenous, isotropic and linearly elastic materials with modulus of elasticity $E_m$, shear modulus $G_m$ and and Poisson ratio $v_m$, occupying the region $\Omega_m$ of the $yz$ plane with finite number of inclusions (Fig. 5.1). Let also the boundaries of the regions $\Omega_m$ be denoted by $\Gamma_m$. This boundary curve is piecewise smooth, i.e. it may have a finite number of corners. In Fig. 5.1 $CXYZ$ is the principal bending coordinate system through the cross section's centroid $C$, while $y_C$, $z_C$ are its coordinates with respect to $Sxyz$ reference coordinate system through the cross section's shear center $S$. It holds that $y_C = y - Y$ and $z_C = z - Z$. The initial radius of curvature, denoted by $R$ is

considered constant and it is parallel to $Y$ axis. The displacement vector $\bar{u}(x,y,z)$ of an arbitrary point of the cross section is obtained as the sum of SV solution vector corresponding to the rigid body motion combined with a residual (index R) displacement vector due to end-effects which are responsible for the generation of self-equilibrating stress distributions:

$$\bar{u}(x,y,z)=\bar{u}^{SV}(x,y,z)+\bar{u}^{R}(x,y,z)=\underbrace{u(x)+\theta_Y(x)Z-\theta_Z(x)Y}_{rigid\ body\ movement}+\underbrace{\sum_{i=1}^{m}\alpha_i(x)W_i(y,z)}_{out\text{-}of\text{-}plane\ warping}$$

$$(5.1a)$$

$$\bar{v}(x,y,z)=\bar{v}^{SV}(x,y,z)+\bar{v}^{R}(x,y,z)=\underbrace{v(x)-z\theta_x(x)}_{rigid\ body\ movement}+\underbrace{\sum_{i=1}^{m}\alpha_i(x)_{,x}DY_i(y,z)}_{distortion\ in\ Y\ direction}\quad(5.1b)$$

$$\bar{w}(x,y,z)=\bar{w}^{SV}(x,y,z)+\bar{w}^{R}(x,y,z)=\underbrace{w(x)+y\theta_x(x)}_{rigid\ body\ movement}+\underbrace{\sum_{i=1}^{m}\alpha_i(x)_{,x}DZ_i(y,z)}_{distortion\ in\ Z\ direction}\quad(5.1c)$$

$$\Gamma=\bigcup_{m=1}^{M}\Gamma_{\Omega_m}$$

$$\Gamma_{\Omega_m}=\bigcup_{i=1}^{k}\Gamma_{\Omega_m}^{i}$$

$$\Omega=\bigcup_{m=1}^{M}\Omega_m$$

C: Centroid
S: Shear center
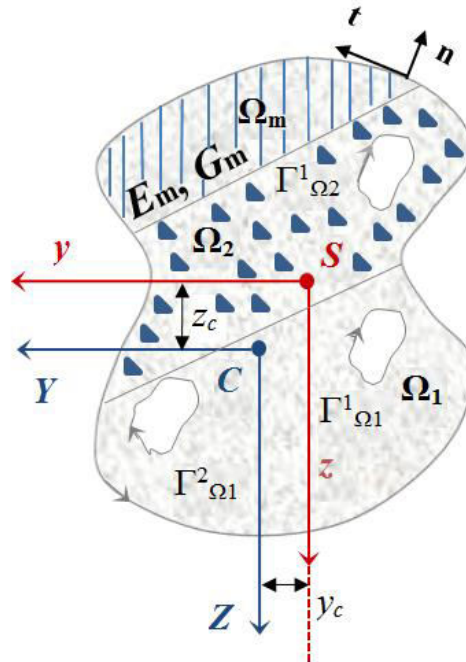


*Figure 5.1. Arbitrary composite cross section of m homogenous materials occupying the two dimensional region $\Omega$.*

where $(\ )_{,j}$ is for differentiation with respect to j, i is the number of higher order cross sectional functions considered, $\bar{u}$, $\bar{v}$, $\bar{w}$ are the axial, transverse and radial beam displacement components with respect to the *Sxyz* system of axes, respectively, $W(y,z)$ is the warping function, $DY(y,z)$ and $DZ(y,z)$ are the distortional functions

of the in-plane deformation mode $D(y,z)$ while $\alpha(x)$ is a function describing the decay of deformation along beam length. Moreover, $v(x)$ and $w(x)$ describe the deflection of the centre of twist $S$, while $u(x)$ denotes the "average" axial displacement of the cross section. $\theta_x(x)$ is the angle of twist due to torsion, while $\theta_Y(x)$ and $\theta_Z(x)$ are the angles of rotation due to bending about the centroidal $Y$, $Z$ axes, respectively. The derivation of rigid body motions is in more detail explained in the work of Kang and Yoo (1994), while $\sin\theta_x \approx \theta_x, \cos\theta_x \approx 1$ assumption is adopted and higher order terms are neglected in this study. Considering the fact that end-effects decay exponentially away from the support, $\alpha(x) = e^{-cx}$ where $c$ is a constant to be specified. However, different expressions of this parameter have also been adopted in other research efforts (i.e. polynomials of various degrees).

After establishing the displacement field, the strain components for $m$th material due to end-effects can be computed as

$$\left(\varepsilon_{xx}\right)_m = \left(\bar{u}^R\left(x,y,z\right)_{,x}\right)_m = \alpha_{,x}\left(W\right)_m \tag{5.2a}$$

$$\left(\varepsilon_{yy}\right)_m = \left(\bar{v}^R\left(x,y,z\right)_{,y}\right)_m = \alpha_{,x}\left(DY_{,y}\right)_m \tag{5.2b}$$

$$\left(\varepsilon_{zz}\right)_m = \left(\bar{w}^R\left(x,y,z\right)_{,z}\right)_m = \alpha_{,x}\left(DZ_{,z}\right)_m \tag{5.2c}$$

$$\left(\gamma_{xy}\right)_m = \left(\gamma_{yx}\right)_m = \left(\bar{v}^R\left(x,y,z\right)_{,x}\right)_m + \left(\bar{u}^R\left(x,y,z\right)_{,y}\right)_m = \alpha_{,xx}\left(DY\right)_m + \alpha\left(W_{,y}\right)_m \tag{5.2d}$$

$$\left(\gamma_{xz}\right)_m = \left(\gamma_{zx}\right)_m = \left(\bar{w}^R\left(x,y,z\right)_{,x}\right)_m + \left(\bar{u}^R\left(x,y,z\right)_{,z}\right)_m = \alpha_{,xx}\left(DZ\right)_m + \alpha\left(W_{,z}\right)_m \tag{5.2e}$$

$$\left(\gamma_{yz}\right)_m = \left(\gamma_{zy}\right)_m = \left(\bar{w}^R\left(x,y,z\right)_{,y}\right)_m + \left(\bar{v}^R\left(x,y,z\right)_{,z}\right)_m = \alpha_{,x}\left[\left(DZ_{,y}\right)_m + \left(DY_{,z}\right)_m\right] \tag{5.2f}$$

Employing the well-known stress-strain constitutive relationship for elastic media and isotropic solid, the stress components of the $m$th material are as follows in matrix form

$$\left(\sigma_{ij}\right)_m = \begin{bmatrix} \lambda tr[\varepsilon] + 2\mu\varepsilon_{xx} & 2\mu\gamma_{xy} & 2\mu\gamma_{xz} \\ 2\mu\gamma_{yx} & \lambda tr[\varepsilon] + 2\mu\varepsilon_{yy} & 2\mu\gamma_{yz} \\ 2\mu\gamma_{zx} & 2\mu\gamma_{zy} & \lambda tr[\varepsilon] + 2\mu\varepsilon_{zz} \end{bmatrix}_m \tag{5.3}$$

where $i, j = x, y, z$, $(tr[\varepsilon])_m = \left( \varepsilon_{xx} + \varepsilon_{yy} + \varepsilon_{zz} \right)_m$ and $\lambda_m, \mu_m$ are the two Láme parameters of the $m$th material. In case poisson ratio $v_m = 0$, $\lambda = 0$ and $E_m = 2\mu$. Employing local equilibrium equations of three-dimensional elasticity considering body forces to be absent, substituting stress components (eq. (5.3)) and the exponential function $\alpha(x)$, the following system of partial differential equations can be derived for the $m$th material as

$$\left[ \mu_m \left( \nabla^2 W \right)_m + c^2 \left( \mu_m + \lambda_m \right) \left( \nabla D \right)_m + c^2 \left( 2\mu_m + \lambda_m \right) \left( W \right)_m \right] e^{-cx} = 0 \qquad (5.4a)$$

$$\left[ c\mu_m \left( \nabla^2 DY \right)_m + c \left( \mu_m + \lambda_m \right) \left( \nabla D \right)_{m,y} - c \left( \mu_m + \lambda_m \right) \left( W_{,y} \right)_m + c^3 \mu_m \left( DY \right)_m \right] e^{-cx} = 0$$
$$(5.4b)$$

$$\left[ c\mu_m \left( \nabla^2 DZ \right)_m + c \left( \mu_m + \lambda_m \right) \left( \nabla D \right)_{m,z} - c \left( \mu_m + \lambda_m \right) \left( W_{,z} \right)_m + c^3 \mu_m \left( DZ \right)_m \right] e^{-cx} = 0$$
$$(5.4c)$$

Thus, the following equations need to be satisfied

$$\left( \nabla^2 W \right)_m = c^2 \left[ -\frac{2\mu_m + \lambda_m}{\mu_m} \left( W \right)_m - \frac{\mu_m + \lambda_m}{\mu_m} \left( \nabla D \right)_m \right] \qquad (5.5a)$$

$$\left( \nabla^2 DY \right)_m + \frac{\mu_m + \lambda_m}{\mu_m} \left[ \left( \nabla D \right)_{m,y} + \left( W_{,y} \right)_m \right] = c^2 \left[ -\left( DY \right)_m \right] \qquad (5.5b)$$

$$\left( \nabla^2 DZ \right)_m + \frac{\mu_m + \lambda_m}{\mu_m} \left[ \left( \nabla D \right)_{m,z} + \left( W_{,z} \right)_m \right] = c^2 \left[ -\left( DZ \right)_m \right]$$
$$(5.5c)$$

Together with the following boundary conditions

$$\begin{cases} \left( \sigma_{xn} \right)_m = \left( \sigma_{xy} \right)_m n_y + \left( \sigma_{xz} \right)_m n_z = 0 & on \quad \left( \Gamma_\Omega \right)_m \\ \left( \sigma_{xn} \right)_m = -\left( \sigma_{xn} \right)_m & on \quad \left( \Gamma_\Omega \right)_m \cup \left( \Gamma_\Omega \right)_n \quad m \neq n \end{cases} \qquad (5.6a)$$

$$\begin{cases} \left( \sigma_{yn} \right)_m = \left( \sigma_{yy} \right)_m n_y + \left( \sigma_{yz} \right)_m n_z = 0 & on \quad \left( \Gamma_\Omega \right)_m \\ \left( \sigma_{yn} \right)_m = -\left( \sigma_{yn} \right)_m & on \quad \left( \Gamma_\Omega \right)_m \cup \left( \Gamma_\Omega \right)_n \quad m \neq n \end{cases} \qquad (5.6b)$$

$$\begin{cases} (\sigma_{zn})_m = (\sigma_{zy})_m n_y + (\sigma_{zz})_m n_z = 0 & on \quad (\Gamma_\Omega)_m \\ (\sigma_{zn})_m = -(\sigma_{zn})_m & on \quad (\Gamma_\Omega)_m \cup (\Gamma_\Omega)_n \quad m \neq n \end{cases}$$ (5.6c)

Employing the relation $v_m = \lambda_m / [2(\lambda_m + \mu_m)]$ and expanding the stresses in the above boundary conditions, the following boundary value problem is formulated

$$\left(\nabla^2 W\right)_m = c^2 \left[ -\frac{2}{1-v_m^e}(W)_m - \frac{1+v_m^e}{1-v_m^e}(\nabla D)_m \right]$$ (5.7a)

$$\begin{cases} (W_{,n})_m = c^2 \left[ -(DY)_m n_y - (DZ)_m n_z \right] & on \ free \ surface \\ g_m(W_{,n})_m + g_n(W_{,n})_n = c^2 (g_m - g_n)\left[ -(DY)_m n_y - (DZ)_m n_z \right] & on \ Interfaces \end{cases}$$ (5.7b)

$$\left(\nabla^2 DY\right)_m + \frac{1+v_m^e}{1-v_m^e}\left[(\nabla D)_{m,y} + (W_{,y})_m\right] = c^2 \left[ -(DY)_m \right]$$ (5.7c)

$$\left(\nabla^2 DZ\right)_m + \frac{1+v_m^e}{1-v_m^e}\left[(\nabla D)_{m,z} + (W_{,z})_m\right] = c^2 \left[ -(DZ)_m \right]$$ (5.7d)

$$\begin{cases} g_m\left\{(DY_{,n})_m + \left[(DY_{,y})_m n_y + (DZ_{,y})_m n_z\right]\right\} + g_m^*\left[(DY_{,y})_m + (DZ_{,z})_m\right]n_y \\ = -g_m^*(W)_m n_y \qquad on \ free \ surface \\ g_m\left\{(DY_{,n})_m + \left[(DY_{,y})_m n_y + (DZ_{,y})_m n_z\right]\right\} + g_m^*\left[(DY_{,y})_m + (DZ_{,z})_m\right]n_y + \\ g_n\left\{(DY_{,n})_n + \left[(DY_{,y})_n n_y + (DZ_{,y})_n n_z\right]\right\} + g_n^*\left[(DY_{,y})_n + (DZ_{,z})_n\right]n_y \\ = -\left(g_m^* - g_n^*\right)(W)_m n_y \qquad on \ Interfaces \end{cases}$$ (5.7e)

$$\begin{cases} g_m\left\{(DZ_{,n})_m + \left[(DY_{,z})_m n_y + (DZ_{,z})_m n_z\right]\right\} + g_m^*\left[(DY_{,y})_m + (DZ_{,z})_m\right]n_z \\ = -g_m^*(W)_m n_z \qquad on \ free \ surface \\ g_m\left\{(DZ_{,n})_m + \left[(DY_{,z})_m n_y + (DZ_{,z})_m n_z\right]\right\} + g_m^*\left[(DY_{,y})_m + (DZ_{,z})_m\right]n_z + \\ g_n\left\{(DZ_{,n})_n + \left[(DY_{,z})_n n_y + (DZ_{,z})_n n_z\right]\right\} + g_n^*\left[(DY_{,y})_n + (DZ_{,z})_n\right]n_z \\ = -\left(g_m^* - g_n^*\right)(W)_m n_z \qquad on \ Interfaces \end{cases}$$ (5.7f)

where $v_m^e = v_m / (1 - v_m)$ is the effective Poisson ratio while $g_m = \mu_m / \mu_{ref}$, $g_m^* = \lambda_m / \mu_{ref}$ are weighted elastic constants with respect to $\mu_{ref}$ which is the shear modulus of reference material. If a plane stress assumption is employed, $v_m^e$ is substituted by $v_m$. When $v_m = 0$ it holds that $g_m = E_m / E_{ref}$ , $g_m^* = 0$, with $E_{ref}$ being the elastic modulus of reference material, and the aforementioned boundary value problem is simplified. Therefore, employing a proper discretization for the cross section, the above coupled boundary value problem (eqs. (5.7)) will lead to the formulation of a generalized eigenvalue problem of the form $AF = c^2 BF$ where $A, B$ are known coefficient matrices, $c$ is the eigenvalue and $F = \begin{bmatrix} W & DY & DZ \end{bmatrix}^T$ is the eigenvector of the problem. The solution of eigenvalue problem yields a set of eigenvalues together with the corresponding eigenvectors which constitute a basis of cross sectional deformation modes suitable for distortional analysis of beams.

As mentioned earlier, the iterative equilibrium scheme described by Ferradi, Cespedes and Arquier (2013) as well as Dikaros and Sapountzakis (2014) is employed here until a sufficient number of modes is obtained to represent accurately the non-uniform warping effects and the corresponding distortional ones. In order to initialize the above stated boundary value problem, the rigid body movements of the cross section are employed. These correspond to SV flexural and torsional warping modes. Afterwards, in order to restore equilibrium the secondary warping modes are determined together with their corresponding distortional ones. Following this concept, the iterative procedure is formulated converging to the exact shape of the warping in a section. Each functional vector $F_{i+1}$ has to fulfil the orthogonality condition with respect to the functions $F_i$ corresponding to the previous set of modes. Knowing that each mode is computed with respect to $c_i^2$, it follows that

$$c_i^2 = \frac{\displaystyle\int_{\Omega_m} F_i^2 d\Omega}{\displaystyle\int_{\Omega_m} F_i F_{i+1} d\Omega} \tag{5.8}$$

After the evaluation of this constant, the normalized $F_{i+1} = c_i^2 F_{i+1}$ can be established and the functions can be obtained.

Within the context of the above considerations and considering up to secondary warping as well as distortional displacements, which are actually the independent parameters, the enriched kinematics of an arbitrary point of the beam for $m$th material at any time instant is given as

$$\bar{u}(x,y,z,t) = \bar{u}^P(x,y,z,t) + \bar{u}^S(x,y,z,t) =$$

$$\underbrace{u(x) + \theta_Y(x)Z - \theta_Z(x)Y + \eta_x(x)\phi_S^P(y,z)}_{\text{primary}} \tag{5.9a}$$

$$+ \underbrace{\eta_Y(x)\phi_{CY}^P(y,z) + \eta_Z(x)\phi_{CZ}^P(y,z) + \xi_x(x)\phi_S^S(y,z)}_{\text{secondary}}$$

$$\bar{v}(x,y,z,t) = v(x) - z\theta_x(x)$$

$$+ \underbrace{\zeta_x(x)v_S^P(y,z) + \zeta_Y(x)v_{CY}^P(y,z) + \zeta_Z(x)v_{CZ}^P(y,z)}_{\text{primary}} \tag{5.9b}$$

$$+ \underbrace{\chi_x(x)v_S^S(y,z) + \chi_Y(x)v_{CY}^S(y,z) + \chi_Z(x)v_{CZ}^S(y,z)}_{\text{secondary}}$$

$$\bar{w}(x,y,z,t) = w(x) + y\theta_x(x)$$

$$+ \underbrace{\zeta_x(x)w_S^P(y,z) + \zeta_Y(x)w_{CY}^P(y,z) + \zeta_Z(x)w_{CZ}^P(y,z)}_{\text{primary}} \tag{5.9c}$$

$$+ \underbrace{\chi_x(x)w_S^S(y,z) + \chi_Y(x)w_{CY}^S(y,z) + \chi_Z(x)w_{CZ}^S(y,z)}_{\text{secondary}}$$

where $\bar{u}^P$, $\bar{u}^S$, denote the primary and secondary longitudinal displacements, respectively. $\eta_x(x)$, $\xi_x(x)$ are the independent warping parameters introduced to describe the nonuniform distribution of primary and secondary torsional warping, while $\eta_Y(x)$, $\eta_Z(x)$ are the independent warping parameters introduced to describe the nonuniform distribution of primary warping due to shear. Similarly, $\zeta_x(x)$, $\chi_x(x)$ are the independent distortional parameters introduced to describe the nonuniform distribution of primary and secondary distortion due to torsion, while $\zeta_Y(x)$, $\zeta_Z(x)$, $\chi_Y(x)$, $\chi_Z(x)$ are the independent distortional parameters introduced to describe the nonuniform distribution of primary and secondary distortion due to flexure. All these parameters are multiplied by the corresponding warping and distortional functions which are components of the $W(y,z)$ and $D(y,z)$ vectors derived by the solution of the coupled boundary value problem stated in eqs. (5.7). In eqs. (5.9), 16 degrees of freedom have been employed in 3D space. These activate 12 cross sectional deformation modes, namely rigid (4), primary (4) and secondary motions (4), including extension.

If tertiary displacements have to be employed for accuracy reasons, the beam's kinematics is enriched further as follows:

$$\bar{u}(x,y,z,t) = \bar{u}^P(x,y,z,t) + \bar{u}^S(x,y,z,t) =$$

$$\underbrace{u(x) + \theta_Y(x)Z - \theta_Z(x)Y + \eta_x(x)\phi_S^P(y,z)}_{\text{primary}}$$

$$+\underbrace{\eta_Y(x)\phi_{CY}^P(y,z) + \eta_Z(x)\phi_{CZ}^P(y,z) + \xi_x(x)\phi_S^S(y,z)}_{\text{secondary}} \qquad (5.10\text{a})$$

$$+\underbrace{\xi_Y(x)\phi_{CY}^S(y,z) + \xi_Z(x)\phi_{CZ}^S(y,z) + \omega_x(x)\phi_S^T(y,z)}_{\text{tertiary}}$$

$$\bar{v}(x,y,z,t) = v(x) - z\theta_x(x)$$

$$+\underbrace{\zeta_x(x)v_S^P(y,z) + \zeta_Y(x)v_{CY}^P(y,z) + \zeta_Z(x)v_{CZ}^P(y,z)}_{\text{primary}} \qquad (5.10\text{b})$$

$$+\underbrace{\psi_x(x)v_S^T(y,z) + \psi_Y(x)v_{CY}^T(y,z) + \psi_Z(x)v_{CZ}^T(y,z)}_{\text{tertiary}} \qquad (5.10\text{b})$$

$$\bar{w}(x,y,z,t) = w(x) + y\theta_x(x)$$

$$+\underbrace{\zeta_x(x)w_S^P(y,z) + \zeta_Y(x)w_{CY}^P(y,z) + \zeta_Z(x)w_{CZ}^P(y,z)}_{\text{primary}}$$

$$+\underbrace{\chi_x(x)w_S^S(y,z) + \chi_Y(x)w_{CY}^S(y,z) + \chi_Z(x)w_{CZ}^S(y,z)}_{\text{secondary}} \qquad (5.10\text{c})$$

$$+\underbrace{\psi_x(x)w_S^T(y,z) + \psi_Y(x)w_{CY}^T(y,z) + \psi_Z(x)w_{CZ}^T(y,z)}_{\text{tertiary}}$$

In this case 22 degrees of freedom have been employed in order to describe the beam's behavior. The additional 6 degrees, namely $\xi_Y(x)$, $\xi_Z(x)$, $\omega_x(x)$, $\psi_x(x)$, $\psi_Y(x)$ and $\psi_Z(x)$, account for 3 tertiary warping and 3 tertiary distortional effects, respectively. These activate 4 additional cross sectional deformation modes including extension. The enrichment of the beam's kinematics can be done automatically by increasing the number of modes, which are an input value for the boundary value problem to be solved. This results in the evaluation of additional cross sectional operators which will be employed in the analysis of the beam model, after establishing the strain components as it will be described in the following.

After establishing the displacement field, the linear strain-displacement relations in the system $(x, y, z)$ can be written as follows

$$\varepsilon_{xx} = \left(\bar{u}_{,x} - \frac{\bar{v}}{R}\right) \cdot \left(\frac{R}{R-Y}\right), \quad \varepsilon_{yy} = \bar{v}_{,y}, \quad \varepsilon_{zz} = \bar{w}_{,z} \qquad (5.11\text{a})$$

$$\gamma_{xy} = \left(\bar{v}_{,x} + \frac{\bar{u}}{R}\right)\cdot\left(\frac{R}{R-Y}\right) + \bar{u}_{,y}, \quad \gamma_{xz} = \bar{w}_{,x}\cdot\left(\frac{R}{R-Y}\right) + \bar{u}_{,z}, \quad \gamma_{yz} = \bar{w}_{,y} + \bar{v}_{,z} \qquad (5.11b)$$

where $\dfrac{R}{R-Y}$ is set as $e(R)$ in the following and introduces the thickness-curvature effect of the curved beam.

    Employing the expressions of the displacement components (eqs. (5.9)), the strains and stresses can be computed. Applying the principle of virtual work or any other variational principle following standard arguments in the calculus of variations, the governing differential equations for the beam in terms of the kinematical components can be derived. Thus, the local stiffness matrix $[k_l]$ of the spatial curved beam can be evaluated after solving a system of linear equations. Finally, the matrix form of stiffness matrix is derived as follows

$$[Aux1] = \begin{bmatrix} 1 & 0 & 0 & 0 & Z & -Y & \phi_S^P & \phi_{CY}^P & \phi_{CZ}^P & \phi_S^S & 0 & 0 & 0 & 0 & 0 & 0 \\ 0 & 0 & 0 & 0 & 0 & 0 & 0 & 0 & 0 & 0 & 0 & 0 & 0 & 0 & 0 & 0 \\ 0 & 0 & 0 & 0 & 0 & 0 & 0 & 0 & 0 & 0 & 0 & 0 & 0 & 0 & 0 & 0 \\ 0 & 1 & 0 & -z & 0 & 0 & 0 & 0 & 0 & 0 & v_S^P & v_{CY}^P & v_{CZ}^P & v_S^S & v_{CY}^S & v_{CZ}^S \\ 0 & 0 & 1 & y & 0 & 0 & 0 & 0 & 0 & 0 & w_S^P & w_{CY}^P & w_{CZ}^P & w_S^S & w_{CY}^S & w_{CZ}^S \\ 0 & 0 & 0 & 0 & 0 & 0 & 0 & 0 & 0 & 0 & 0 & 0 & 0 & 0 & 0 & 0 \end{bmatrix} e(R) \qquad (5.12a)$$

$$[Aux2] = \begin{bmatrix} 0 & -\dfrac{1}{R}e(R) & 0 & \dfrac{z}{R}e(R) & 0 & 0 & 0 & 0 & 0 & 0 \\ 0 & 0 & 0 & 0 & 0 & 0 & 0 & 0 & 0 & 0 \\ 0 & 0 & 0 & 0 & 0 & 0 & 0 & 0 & 0 & 0 \\ \dfrac{1}{R}e(R) & 0 & 0 & 0 & \dfrac{Z}{R}e(R) & -1-\dfrac{Y}{R}e(R) & \dfrac{\phi_S^P}{R}e(R)+\phi_{S,y}^P & \dfrac{\phi_{CY}^P}{R}e(R)+\phi_{CY,y}^P & \dfrac{\phi_{CZ}^P}{R}e(R)+\phi_{CZ,y}^P & \dfrac{\phi_S^S}{R}e(R)+\phi_{S,y}^S \cdots \\ 0 & 0 & 0 & 0 & 1 & 0 & \phi_{S,z}^P & \phi_{CY,z}^P & \phi_{CZ,z}^P & \phi_{S,z}^S \\ 0 & 0 & 0 & 0 & 0 & 0 & 0 & 0 & 0 & 0 \end{bmatrix}$$

$$\cdots \begin{bmatrix} \dfrac{v_S^P}{R}e(R) & \dfrac{v_{CY}^P}{R}e(R) & \dfrac{v_{CZ}^P}{R}e(R) & \dfrac{v_S^S}{R}e(R) & \dfrac{v_{CY}^S}{R}e(R) & \dfrac{v_{CZ}^S}{R}e(R) \\ v_{S,y}^P & v_{CY,y}^P & v_{CZ,y}^P & v_{S,y}^S & v_{CY,y}^S & v_{CZ,y}^S \\ w_{S,z}^P & w_{CY,z}^P & w_{CZ,z}^P & w_{S,z}^S & w_{CY,z}^S & w_{CZ,z}^S \\ 0 & 0 & 0 & 0 & 0 & 0 \\ 0 & 0 & 0 & 0 & 0 & 0 \\ w_{S,y}^P+v_{S,z}^P & w_{CY,y}^P+v_{CY,z}^P & w_{CZ,y}^P+v_{CZ,z}^P & w_{S,y}^S+v_{S,z}^S & w_{CY,y}^S+v_{CY,z}^S & w_{CZ,y}^S+v_{CZ,z}^S \end{bmatrix}$$

$$(5.12b)$$

$$\varepsilon = [Aux1]u_{,x} + [Aux2]u \qquad (5.12c)$$

$$\sigma = [C][Aux1]u_{,x} + [C][Aux2]u \tag{5.12d}$$

$$\delta U = \int_0^L \int_\Omega \left( \delta u_{,x}^T [Aux1]^T + \delta u^T [Aux2]^T \right) \left( [C][Aux1]u_{,x} + [C][Aux2]u \right) \frac{1}{e(R)} d\Omega dx \Rightarrow$$

$$\Rightarrow \delta U = \int_0^L \left( \delta u_{,x}^T k_{22} u_{,x} + \delta u^T k_{12} u_{,x} + \delta u_{,x}^T k_{21} u + \delta u^T k_{11} u \right) dx \Rightarrow \text{by parts integration}$$

$$\Rightarrow \delta U = \int_0^L \left( \delta u^T \left\{ -k_{22} u_{,xx} + [k_{12} - k_{21}]u_{,x} + k_{11} u \right\} \right) dx + \left[ \delta u^T \left\{ k_{22} u_{,x} + k_{21} u \right\} \right]_0^L$$

$$\tag{5.12e}$$

$$[k_l] = \begin{bmatrix} k_{11} & k_{12} \\ k_{21} & k_{22} \end{bmatrix} \tag{5.12f}$$

where [*Aux1*], [*Aux2*] are auxiliary matrices to express strains $\varepsilon$ in matrix form, $\frac{1}{e(R)} d\Omega dx = dV$ is the differential volume of the curved beam for constant radius of curvature, [*C*] is the elasticity matrix employed to derive stresses $\sigma$, $\delta U$ is the virtual strain energy and $k_{11}$, $k_{12}$, $k_{21}$ and $k_{22}$ are 16X16 coefficient matrices containing the geometric properties of the cross section. These are calculated as follows

$$k_{11} = \int_{\Omega_m} [Aux1]^T [C][Aux1] \frac{1}{e(R)} d\Omega, \qquad k_{12} = \int_{\Omega_m} [Aux1]^T [C][Aux2] \frac{1}{e(R)} d\Omega$$

$$k_{21} = \int_{\Omega_m} [Aux2]^T [C][Aux1] \frac{1}{e(R)} d\Omega, \qquad k_{22} = \int_{\Omega_m} [Aux2]^T [C][Aux2] \frac{1}{e(R)} d\Omega$$

$$\tag{5.13}$$

From eq. (5.12e) after integrating by parts, it holds that

$$NQM = k_{22} u_{,x} + k_{21} u \tag{5.14}$$

where *NQM* is the vector of the stress resultants at the beam's ends.

Moreover, the external work can be derived as follows. Employing the auxiliary matrix related to coefficients of the displacements' field

$$[Aux] = \begin{bmatrix} 1 & 0 & 0 & 0 & Z & -Y & \phi_S^P & \phi_{CY}^P & \phi_{CZ}^P & \phi_S^S & 0 & 0 & 0 & 0 & 0 & 0 \\ 0 & 1 & 0 & -z & 0 & 0 & 0 & 0 & 0 & 0 & v_S^P & v_{CY}^P & v_{CZ}^P & v_S^S & v_{CY}^S & v_{CZ}^S \\ 0 & 0 & 1 & y & 0 & 0 & 0 & 0 & 0 & 0 & w_S^P & w_{CY}^P & w_{CZ}^P & w_S^S & w_{CY}^S & w_{CZ}^S \end{bmatrix} \tag{5.15a}$$

and, then, substituting in the expression of virtual work, it holds that

$$\delta W = \int_0^L \left( \delta u^T \left[ Aux \right]^T t \right) dx + \underbrace{\left[ \int_\Omega \left( \delta u^T \left[ Aux \right]^T t \right) d\Omega \right]_0^L}_{\delta u^T p} \qquad (5.15b)$$

where $t$ is the traction vector applied on the lateral surface of the beam including the end cross sections and $p$ is the external load vector of the beam.

Combining eqs. (5.12e) with (5.15b), the expression of the variational total potential energy can be evaluated and, thus, the governing differential equations of the problem can be obtained together with the boundary conditions as

$$-k_{22} u_{,xx} + \left[ k_{12} - k_{21} \right] u_{,x} + k_{11} u = p \qquad (5.16a)$$

$$\alpha_1 u + \alpha_2 NQM = \alpha_3 \qquad (5.16b)$$

where $\alpha_i$ are diagonal matrices and vector containing known coefficients according to the boundary conditions of the beam (i.e. for clamped end $\alpha_1 = 1$ and $\alpha_2 = \alpha_3 = 0$).

Employing the expressions of the displacement components in eqs. (5.10), the cross sectional operators (eqs. (5.13)) and the governing differential equations of the curved beam can be obtained in a similar way when tertiary or higher warping and distortional effects are considered.

In order to derive the differential equations of motion with respect to the kinematical components, the terms of inertia contributions $\delta W_{mass} = \int_V \rho \left( \bar{u}_{,tt} \delta \bar{u} + \bar{v}_{,tt} \delta \bar{v} + \bar{w}_{,tt} \delta \bar{w} \right) dV$ (with $dV = \dfrac{1}{e(R)} d\Omega dx$ ) have to be added in the previous (eqns. 5.12e and 5.15b) and constitutive equations should be employed. $\rho$ is the density of the material and $\bar{u}, \bar{v}, \bar{w}$ are the generalized displacements as previously described. Thus, the local spatial mass coefficient matrix $\left[ m_l \right]$ can finally be derived. This can be extracted in matrix form from the following expression

$$\delta W_{mass} = \int_0^L \int_\Omega \rho \left( \delta u^T \left[ Aux \right]^T \left[ Aux \right] u_{,tt} \right) \frac{1}{e(R)} d\Omega dx \Rightarrow \delta W_{mass} = \int_0^L \left( \delta u^T \left[ m_l \right] u_{,tt} \right) dx \quad (5.17)$$

with [Aux] given in eqn. (5.15a), $u$ representing the total displacement and $\left[ m_l \right]$ being a 16X16 coefficient matrix when displacements of eqns. (5.9) are employed.

Except for the boundary conditions there are also the initial conditions at $x \in (0, L)$ similar to those defined in eqns. (3.3) of Chapter 3. After establishing the stiffness and mass matrices of the spatial curved beam element the equation of motion in matrix form can be given as in eqn. (4.23).

The natural frequencies and modes in which the beam vibrates for the different

motions (including also distortional ones) can be obtained by separation of variables and $u_i(x,t)$ is assumed to have the form given in eqn. (3.13). Finally, the typical generalized eigenvalue problem described by eqn. (3.14) is formulated and solved.

## 5.3  Numerical Solution for the Cross Sectional analysis

The evaluation of the warping and distortional functions is accomplished by solving the problems described by eqns. (5.7). Warping functions $W$ and their derivatives are at first computed by solving eqns. (5.7a,b). Afterwards, these values are inserted as generalized body forces in eqns. (5.7c-f) which are solved as a 2D elasticity problem in order to obtain distortional functions $D$. The solution of the problem is accomplished employing BEM within the context of the method of subdomains and BEM for Navier operator (Katsikadelis 2002a; Beer et al. 2008). Afterwards, the values are normalized through the constant $c_i^2$, as earlier described, and the procedure is repeated for the desired number of modes. Finally, the functions calculated are employed in order to obtain the cross sectional operation factors given in eqns. (5.13) as well as mass operation factors derived by eqn. (5.17). These are used as input values together with the elasticity and function matrices to solve the curved beam model with the methods described below.

## 5.4  Numerical Solution with AEM and NURBS

According to the precedent analysis, the static and vibration analysis of straight or curved beams of arbitrary cross section including generalized warping and distortional effects reduces in establishing the components the kinematical components $u_i$ (either of those in eqns. (5.9) or (5.10)) having continuous derivatives up to the second order with respect to $x$ at the interval $(0,L)$, up to the first order at $x=0,L$, and for the dynamic problem up to the second order with respect to time $t$, satisfying the initial-boundary value problem described by the coupled governing differential equations of equilibrium in eqns. (5.16a) along the beam and the boundary conditions in eqns. (5.16b) at the beam ends, at $x=0,L$ as well as the initial conditions similar to eqns. (3.3). The problem is solved using the Analog Equation Method in a similar way as the one described in detail in Chapter 3.

However, some differences arise here due to the nature of the problem stated. The number of the kinematical components depends on the number of modes employed, as it is obvious from eqns. (5.9) and (5.10).

Eqns. (A.1.34) and (A.1.36) of the Appendix A.1 written for the boundary points constitute a system of four simultaneous integral equations, while the boundary conditions in eqns. (5.16b) are formulated in matrix form giving four more equations. Combining the aforementioned equations, the system (A.1.45) is derived initially for the case described in eqns. (5.9). For this problem, $[E]$ becomes a 64X64 square matrix, $\{u_i\},\{D\},\{T_i\}$ 64X1 vectors, $[E_{11}]$, $[E_{12}]$ 32X32 known coefficient matrices

and $\{D_1\}$ known 32X1 coefficient vector with their dimensions depending on the number of modes employed and all explained in the Appendix A.1.

Particularly in this study, $[E_{11}]$, $[E_{12}]$ are calculated writing eqn. (5.16b) in the following matrix relations

$$[\alpha_{10}+\alpha_{20}k_{21}]u^0+[\alpha_{20}k_{22}]u^0_{,x}=\{\alpha_{30}\} \qquad for \quad x=0$$
$$[\alpha_{1L}+\alpha_{2L}k_{21}]u^L+[\alpha_{2L}k_{22}]u^L_{,x}=\{\alpha_{3L}\} \qquad for \quad x=L$$
(5.17a,b)

and iterating over the number of boundary conditions, which is 16 for each end in this case. $[k_{ij}], i,j=1,2$ are the geometric constant matrices given in eqn. (5.13) and inserted as input in the beam analysis for each discretization element.

Thus, the following system is derived

$$[E]\{u_i\}=\{D\}+[F]\{P_i\}\rightarrow\{u_i\}=[E]^{-1}\{D\}+[E]^{-1}[F]\{P_i\}$$
(5.18)

where $P_i$ are the control points if the fictitious load of AEM is represented by B-splines or NURBS.

After calculating the rest of the AEM matrices as described in the Appendix A.1, the element cross sectional operators are assigned to each discretization element in order to calculate the stiffness matrix of the beam element employing eqn. (5.16a) transformed into matrix form as follows as well as the mass matrix calculated as follows

$$[K]=-[K_{22}]+[K_{12}-K_{21}][B']+[K_{11}][B]$$
(5.19)

$$[M]=\rho[M_l][B]$$
(5.20)

where $[K_{11}],[K_{12}],[K_{21}],[K_{22}]$ and $[M_l]$ are the geometric and mass constant (16XN$_{dof}$) X (16XN$_{dof}$) matrices formulated for all of the discretization elements through an iterative procedure with N$_{dof}$ being their number. The stiffness and mass matrices are formulated either with respect to the values of the fictitious loads in the case of the original AEM or the control points when B-splines are integrated in the AEM.

Additionally, substituting eqns. (A.1.50) of Appendix A.1 into eqn. (5.16a), the load vector applied is written as follows in matrix form

$$\{P\}=\{p\}-([K_{12}-K_{21}]\{R'\}+[K_{11}]\{R\})$$
(5.20)

where $\{p\}$ is a load vector containing the load values along the beam either concentrated or uniformly distributed.

Finally, the global equation system can be formulated and the unknowns can be evaluated. The result is not the displacement vector as in traditional Finite Element (FE) Method (FEM) but it is either the fictitious load, which represents the second derivative of the kinematical components, or the control points. Employing eqns. (A.1.50), the kinematical components and their first derivatives can eventually be obtained. These are employed as input values together with the function matrices in a post-processing procedure in order to derive the total displacements, stresses and stress resultants along the curved geometry.

Instead of B-splines, NURBS curves in terms of B-spline basis functions can be employed either in FEM or AEM. The description of the numerical procedures is given in the Appendix A.2. In this chapter, the geometry of the beam is described as in Chapter 4. After establishing the kinematical components and their derivatives, total displacements can directly be plotted on the curved geometry. Finally, stresses and stress resultants can also be derived without the need for excessive post-processing.

Regarding the vibration analysis, the Newmark time integration scheme (Bathe, 1996), which is widely used in structural dynamics, can be employed, as in the previous chapter. The equation of motion can be expressed at time $t+Dt$ and the step-by-step solution can be computed.

## 5.5   Numerical examples

In order to validate the proposed formulation of the straight or curved beam element described above, investigate the importance of curvature in distortional analysis as well as of distortion in the free vibrational characteristics of a beam and examine the advantages attained by the use of the methods proposed in terms of simplicity, accuracy and computational effort, computer programs have been written and various straight and curved beam models have been studied. The numerical results have been obtained employing NURBS in FEM and constant elements or B-splines for the representation of the AEM fictitious loads. All the algorithms formulated take as input the geometric and mass constant matrices obtained by the cross sectional analysis, which was earlier described.   Then, the results are compared to those obtained by the application of the Finite Element Method (FEM) employing beam, solid (quadrilateral) or plate elements. The computer software FEMAP (2010) has been used for this purpose.

Different FEM models have been created with various discretization elements and with or without Poisson ratio considered. Various cross sections and beam models with different $t/d$ and $d/L$ ratios ($t$, $d$ and $L$ are the thickness, width and length of the straight or curved close- or open-shaped cross section beam model) have been employed in order to estimate the magnitude of distortional effects and the number of modes needed in order to derive accurate results. In addition to these, up to 1000 boundary elements depending on the cross section type (cross sectional discretization) have been employed in order to evaluate the cross sectional operators and functions.

### 5.5.1 Doubly Symmetric cross sections

In this example, in order to validate the proposed formulation and investigate the importance of distortion, Poisson ratio and curvature in the analysis of straight or curved beam models as well as the number of modes needed , the static problems of straight or curved cantilever beams with doubly symmetric cross sections (solid, open or closed) are examined.

The first beam model under consideration has a solid rectangular cross section 20X50 *cm* and a length of 3 *m*. Two different materials are considered with or without Poisson ratio, namely $E = 35000\,kN/m^2$, $\nu = 0.2/0$ and $E = 2.1E8\,kN/m^2$, $\nu = 0.3/0$. For the first material, the beam is subjected to an eccentrically applied load of 1 *kN* at its tip cross section which results in a twisting moment of 0.2 *kNm*.

In Fig. 5.2 the total translation contours are presented for the three dimensional (3D) FEM model (810 quadrilateral solid elements) and the one proposed (AEM with 50 constant elements) considering Poisson ratio. When employing cubic B-splines the same tip displacements are derived with just 8 collocation points (two spline curves) and the computational cost is significantly reduced.
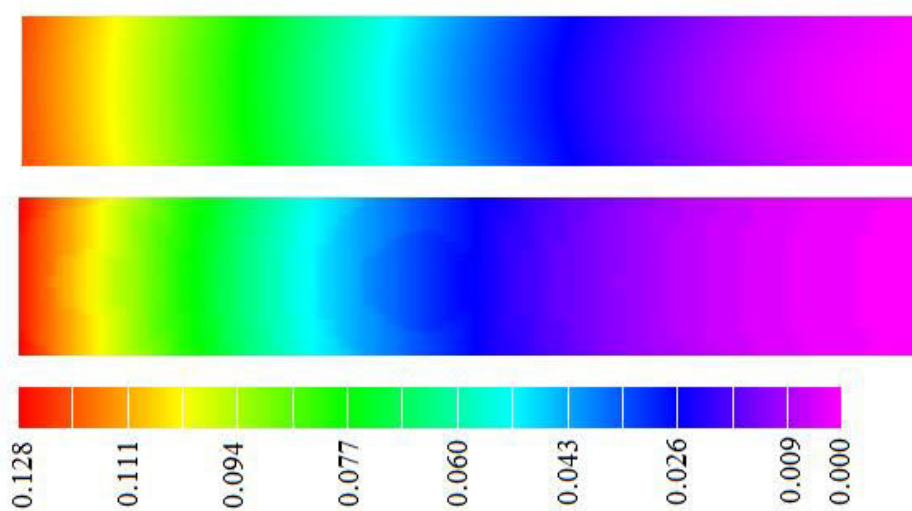


*Figure 5.2. Total translation contours of 3D solid FEM model with 810 quadrilateral elements (above) and the proposed one (AEM with 50 constant elements) for rectangular cross section.*

In Fig. 5.3 the normal stress $\sigma_{xx}$ contours are displayed for the same cases. It is obvious that the two models coincide. The displacement field considered is the one described in eqns. (5.9). It is found that there is no need to consider additional modes. It is also concluded that this particular cross section does not suffer excessively from distortional effects due to the fact that the distortional moments derived from the proposed model are insignificant. Thus, Poisson effects can be isolated and studied. Considering 3D FEM models, it is quite difficult to deduce that distortion is not of importance due to the fact that different structural phenomena cannot be isolated. Different models with various diaphragmatic arrangements have to be considered and

compared in order to come to the same conclusion. Special attention should be paid when too many diaphragms have been used due to shear locking phenomena that make the model falsely stiffer.
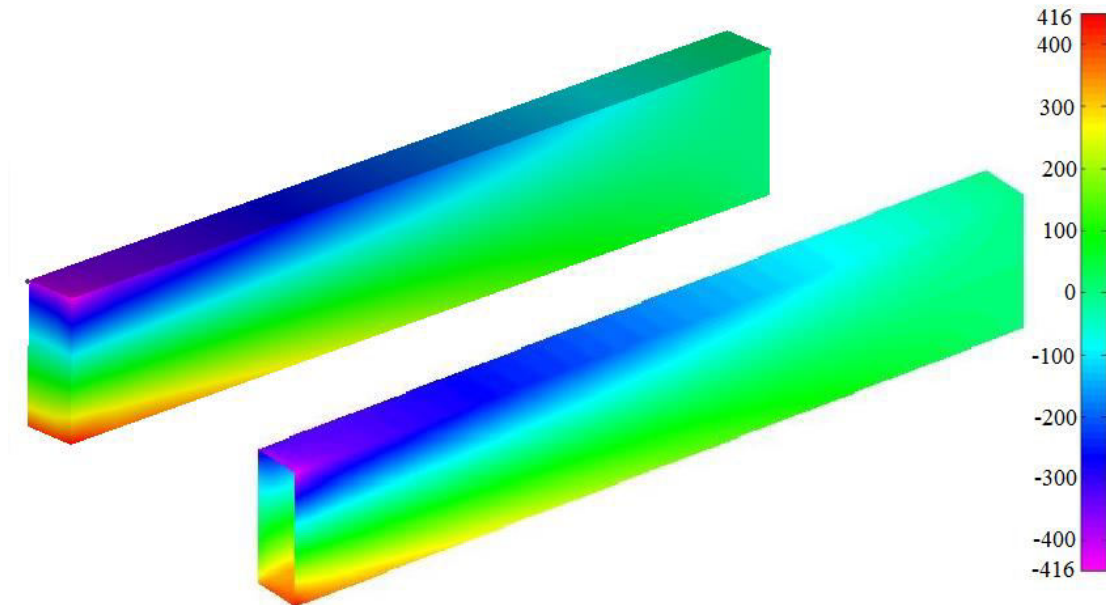


*Figure 5.3. Normal stress $\sigma_{xx}$ contours of 3D solid FEM model with 810 quadrilateral elements (above) and the proposed one (AEM with 50 constant elements) for rectangular cross section.*

In Fig. 5.4 the stress contours derived by the proposed formulation are displayed with or without (indices with 0) considering Poisson ratio. It is depicted visually that $\tau_{xy}$ and $\tau_{xz}$ intensity is less in the case of zero Poisson ratio. It should also be noted that the magnitude of $\varepsilon_{yy}$ and $\varepsilon_{zz}$ (0-2.5 *kN/m²*) normal stresses is almost insignificant in the same case comparing to the one of $v = 0.2$ (85-95 *kN/m²*). Normal stress $\varepsilon_{xx}$ is less by almost 6% in the zero Poisson ratio case (≈380 *kN/m²*) and shear stress $\tau_{yz}$ is insignificant in both cases.

In Fig. 5.5 the stress contours at the support are presented for $E = 2.1E8 \, kN/m^2$ and $v = 0.3 / 0$. Similarly to the previous material case $\tau_{xy}$ and $\tau_{xz}$ stresses are smaller by around 60% as well as $\varepsilon_{yy}$ and $\varepsilon_{zz}$ normal stresses are insignificant in the case of zero Poisson ratio. Normal stress $\varepsilon_{xx}$ is less by almost 9% when Poisson ratio is zero and shear stress $\tau_{yz}$ is insignificant in both cases.

The second beam model under consideration has the I-shaped cross section ($E = 73000 \, kN/m^2$, $G = 28000 \, kN/m^2$, $v = 0.3$, $t/d = 0.048$, $d/L = 0.035$) shown in Fig. 5.6 and a length of 3 *m*. It is subjected to a concentrated force of 10 *kN* at its free end eccentrically applied. The displacement field considered is the one described
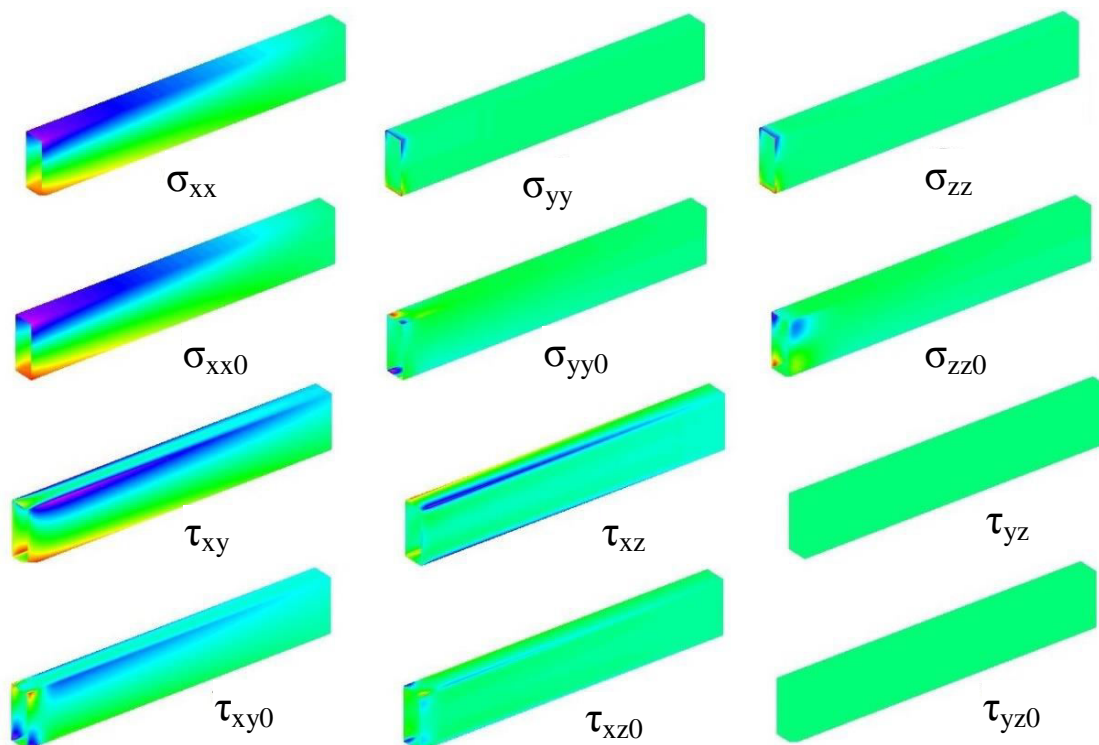
*Figure 5.4. Stress contours derived by the proposed formulation with or without (indices with 0) taking into account Poisson ratio for the rectangular cross section.*
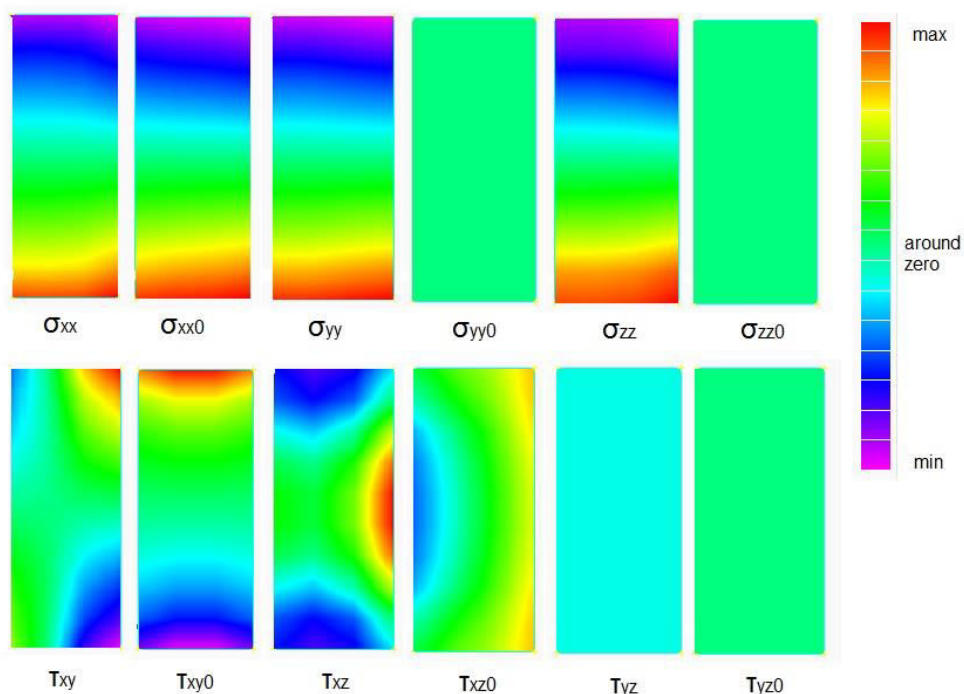


*Figure 5.5. Stress contours for the rectangular cross section cross section at support with or without (indices with 0) taking into account Poisson ratio.*
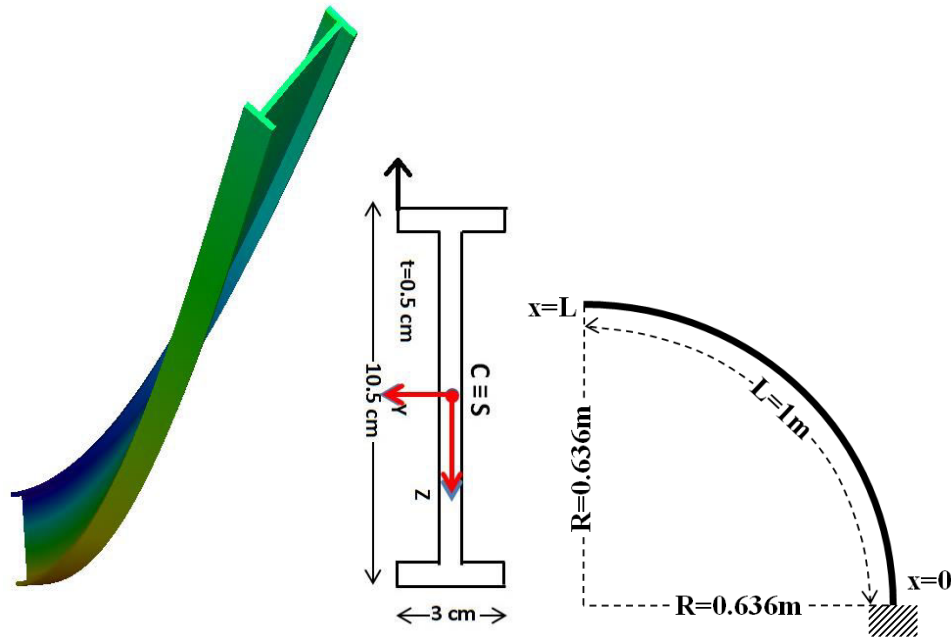
*Figure 5.6. Normal stress $\sigma_{xx}$ contour and deformed view of I-shaped cross section under eccentric loading straight beam and corresponding curved geometry (plan view).*

in eqns. (5.10). In contrast to the previous cross section, $\varepsilon_{yy}$ and $\varepsilon_{zz}$ normal stresses differ from $\varepsilon_{xx}$ by around 40% and are of importance in this case due to the fact that warping and distortional effects arise. However, higher order warping effects are more significant. In addition to this, $\tau_{xy}$ and $\tau_{xz}$ stresses are much larger than the previous case with respect to the magnitude of normal stresses.

The same I-shaped cross section shown in Fig. 5.6 is examined as curved with $R = 0.636m$ and an arc length of 1 $m$ ($d/L = 0.105$), as shown in the same figure. It is subjected to a concentrated force of 5 kN at its free end eccentrically applied. The displacement field considered is the one described in eqns. (5.9).

In Fig. 5.7 the total translation contours are presented for the 3D FEM model (7875 quadrilateral solid elements) and the one proposed (AEM with 10 cubic splines or 100 constant elements).

In Fig. 5.8 the normal stress $\sigma_{xx}$ contours are displayed for the same cases. It is obvious that the models are in coincidence while the use of cubic B-splines significantly reduces the number of discretization elements for the same level of accuracy.

In Fig. 5.9 the distributions along the length of the kinematical components $\eta_x(x)$, $\zeta_x(x)$ and $\theta_x(x)$ are displayed in order to investigate the order of their magnitude along the length and compare them to each other. FEM with NURBS are employed for this purpose. The exponential decay of the primary warping and distortional parameters is illustrated. However, distortion decays faster than warping.
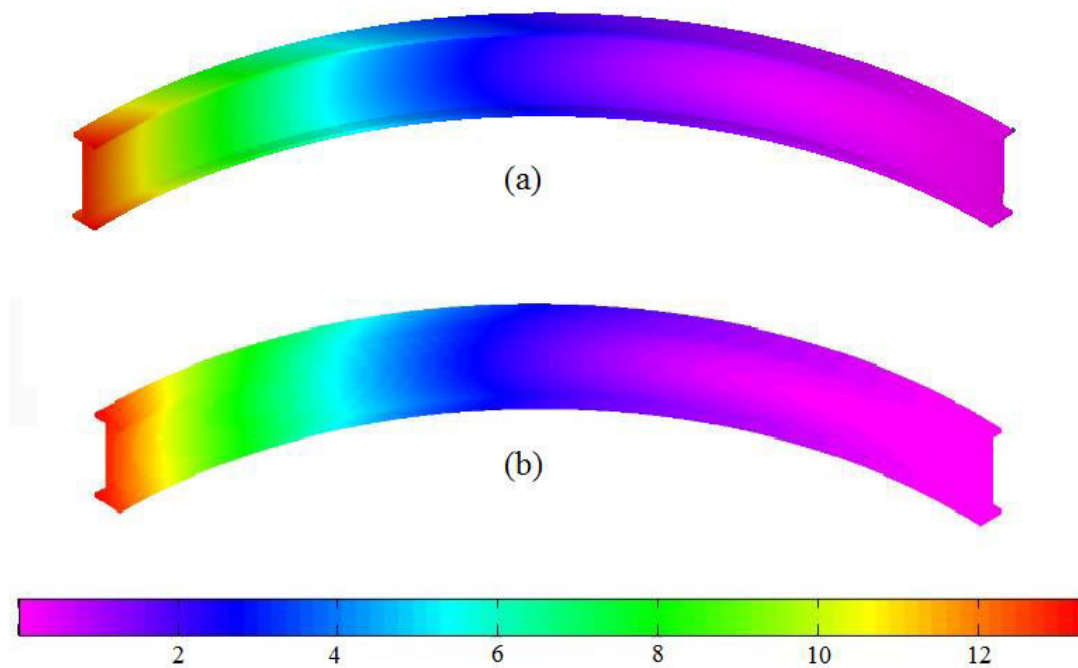
*Figure 5.7. Total translation contours of (a) 3D solid FEM model with 7875 quadrilateral elements and (b) the proposed one (AEM with 10 cubic splines or 100 constant elements) for the I-shaped cross section.*
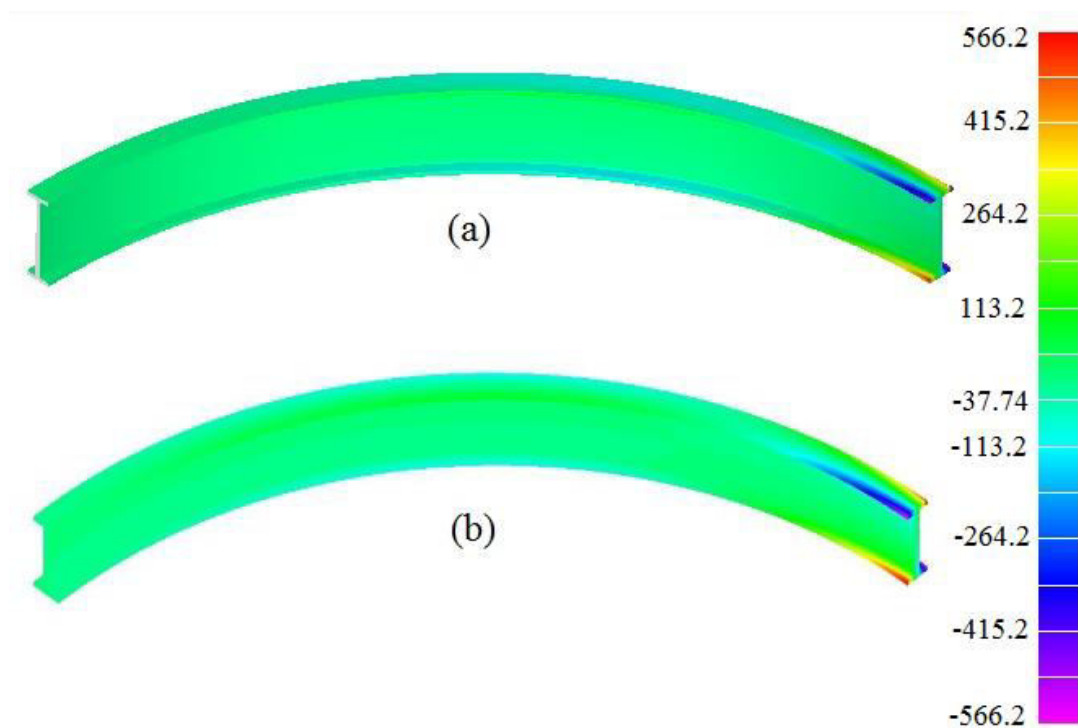


*Figure 5.8. Normal stress $\sigma_{xx}$ contours for (a) 3D solid FEM model with 7875 quadrilateral elements and (b) the one proposed with 10 cubic splines or 100 constant elements in AEM for the I-shaped cross section.*
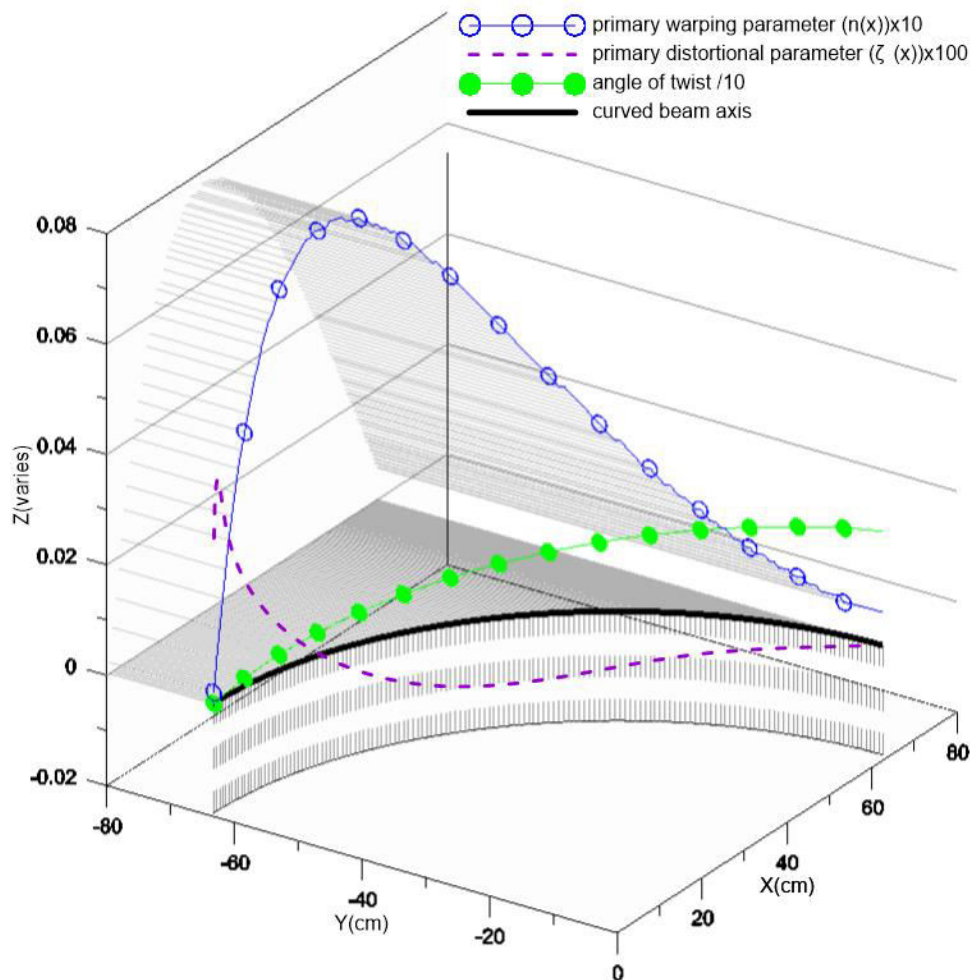
*Figure 5.9. Kinematical components $\eta_x(x)$, $\zeta_x(x)$ and $\theta_x(x)$ of the I-shaped cross section curved beam derived by the proposed formulation with cubic NURBS.*

In Table 5.1 the values of different kinematical components, shear stresses and higher order moments are compiled for the proposed beam formulation and compared to the FEM solid model when it is possible. It should be noted here that primary warping moment is almost ten times larger than twisting and bending moments while the primary distortional moment due to torsion is much lower. These quantities cannot be obtained directly by the FEM solid model. Shear stresses are much lower than normal stress $\sigma_{xx}$. In addition to these, secondary warping and distortional moments are much lower than the primary ones. Thus, there is no need to consider additional higher modes in the analysis.

Fig. 5.10 shows the normalized displacements with respect to FEM solid results at the free end of the beam. The proposed solution using either a cubic (4 collocation points) or a quartic (5 collocation points) give highly accurate results (errors 0-10%). The convergence rate increases further as knots are inserted after the degree elevation (k-refinement). Quadratic B-splines give inaccurate results when the least number of
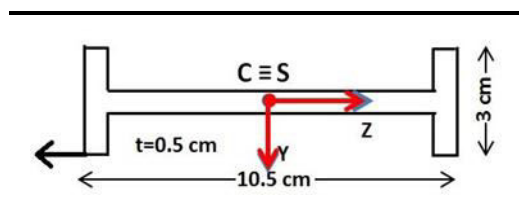
| | AEM<br>10 cubic<br>B-splines | FEM<br>Solid<br>7875 |
|---|---|---|
| $w(m)$ at x=L | -12.8713 | -12.5466 |
| $\theta_x(rad)$ at x=L | 0.2083 | 0.19702 |
| $\theta_Y(rad)$ at x=L | 0.3274 | 0.3158 |
| $\tau_{xz}^{max}(\frac{kN}{m^2})$ at<br>x=1/4L | 120.25 | 111.02 |
| $\tau_{xy}^{max}(\frac{kN}{m^2})$ at<br>x=1/4L | 115.23 | 109.80 |
| $M_Y(kNm)$ at x=0 | 330.81 | 325.05 |
| $M_t(kNm)$ at x=0 | 323.01 | 318.31 |
| $M_{\phi_S^P}(kNm^2)$ at x=0 | 3401.49 | - |
| $M_{\phi_S^S}(kNm^2)$ at x=0 | 36.46 | - |
| $M_{Dx}^P(kNm^2)$ at x=0 | 16.25 | - |

*Table 5.1. Kinematical components, Shear stresses and Stress resultants of the I
-shaped cross section curved beam.*

collocation points is employed. When employing knot insertion for the cubic B-spline (24 collocation points) the results almost coincide to FEM solid solution. Finally, considering the same cross section but with an arc length of 3 m, similar conclusions have been drawn.

The third cantilever beam model studied has a rectangular box-shaped cross section 5.0X3.5 *m* with plate thickness 0.30 *m* ($E = 3E7\,kN/m^2$, $G = 1.5E7\,kN/m^2$, $v = 0$, $t/d = 0.085$, $d/L = 0.087$) and length 40 *m*. Its cross section and curved geometry are shown in Fig. 5.11. In Table 5.2 the values of the kinematical components $w(x)$, $\theta_x(x)$ and $\theta_Y(x)$ at $x = L$ for a vertical force $P_Z = 5000kN$ eccentrically applied at the free edge of the beam are presented for i) proposed curved beam elements with 5 NURBS (cubic) and 1 diaphragm at the free end, ii) 100 constant elements in the AEM technique, iii) 960 plate elements in FEMAP with 1 diaphragm at the free end (FEMplate960), iv) 2880 quadrilateral solid elements with
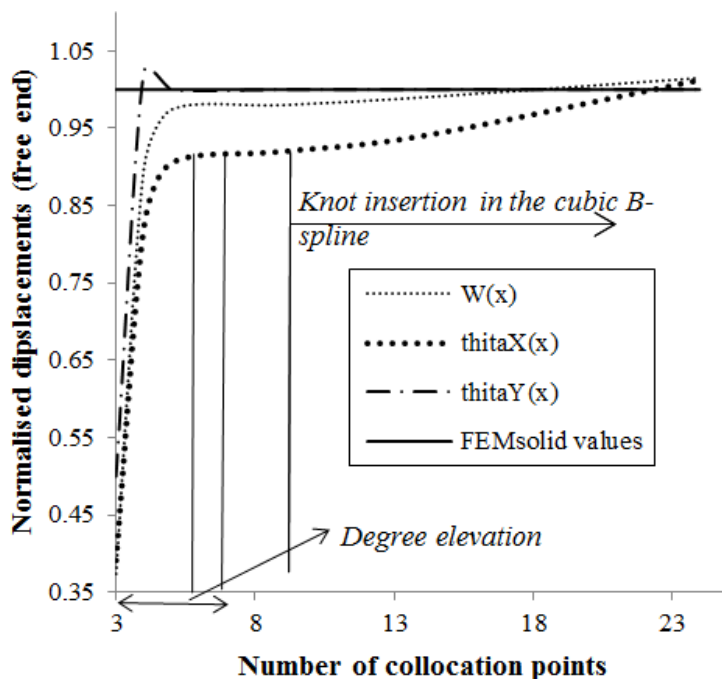
*Figure 5.10. Convergence of normalized displacements at the free end of the I-shaped cross section curved beam.*
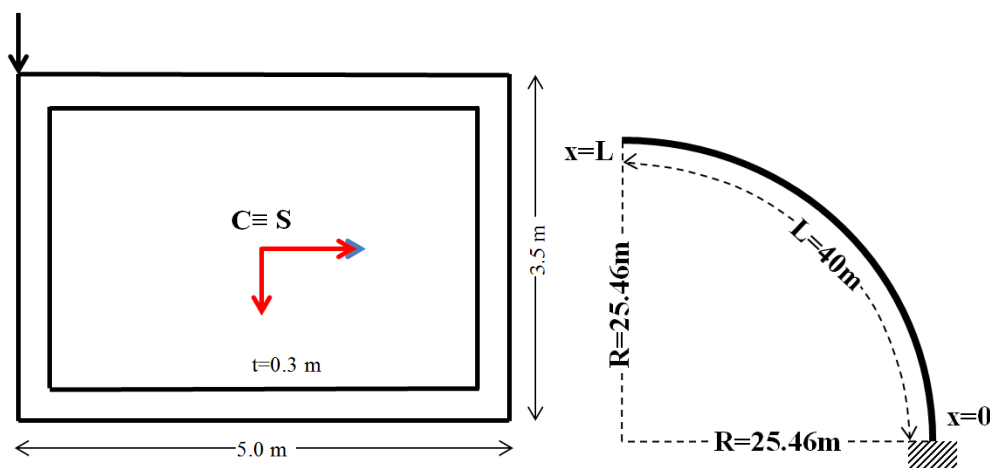


*Figure 5.11.Rectangular box-shaped cross section, applied vertical load at the free end and corresponding curved geometry (plan view).*

1 diaphragm in FEMAP (FEMsolid2880), v) 5760 quadrilateral solid elements with 1 diaphragm in FEMAP (FEMsolid5760) and vi) 2880 quadrilateral solid elements without any diaphragm in FEMAP (FEMsolid2880). All of the results are in coincidence. It should be noted here the great reduction in discretization elements when employing NURBS comparing to all other solutions.

In Fig. 5.12 the normal stress contours are displayed for the 3D solid FEM model (2880 elements) and the proposed formulation with cubic B-splines in the AEM. It is obvious that the two models coincide. After evaluating the stress resultants, it should be noted that primary distortional moment due to torsion is highly important while
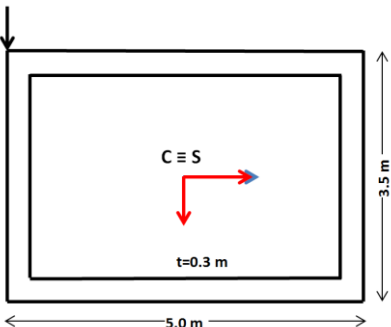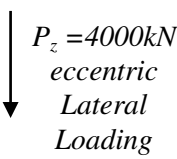
| | | $w(m)$ at $x=L$ | $\theta_x(rad)$ at $x=L$ | $\theta_Y(rad)$ at $x=L$ |
|---|---|---|---|---|
| | 5 cubic NURBS | 0.4042 | 0.0019 | -0.0149 |
| | AEM100 constant | 0.4039 | 0.0019 | -0.0149 |
| $P_z =4000kN$ eccentric Lateral Loading | FEMplate960 1 Diaph. | 0.4094 | 0.0018 | -0.0150 |
| | FEMsolid2880 1 Diaph. | 0.4069 | 0.0018 | -0.0149 |
| | FEMsolid5760 1 Diaph. | 0.4070 | 0.0018 | -0.0149 |
| | FEMsolid2880 NO Diaph. | 0.4168 | varies | -0.0150 |

*Table 5.2. Kinematical components of the doubly symmetric box-shaped cross section straight beam.*
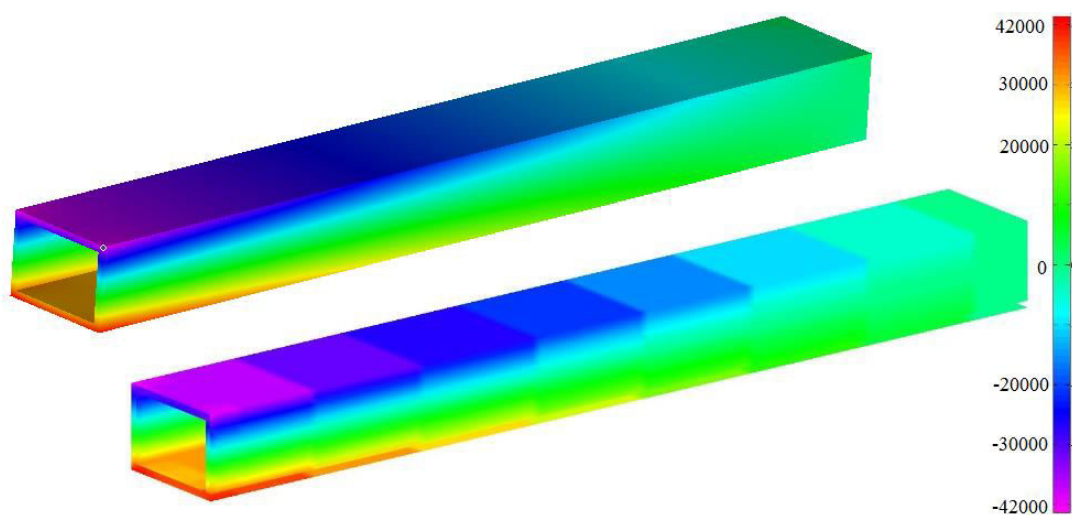


*Figure 5.12. Normal stress $\sigma_{xx}$ contours for 3D solid FEM model with 2880 quadrilateral elements (above) and the one proposed with 10 cubic splines in AEM for the doubly symmetric box-shaped cross section straight beam.*

secondary and tertiary higher order resultants are insignificant. Thus, the displacement field described by eqns. (5.9) exhibits an accurate behavior.

The same box-shaped cross section beam shown in Fig. 5.11 is examined as curved with $R = 25.465m$ and an arc length of 40 $m$. The displacement field considered is the one described in eqns. (5.9). In Table 5.3 the values of different kinematical components, shear stresses and higher order moments are compiled for the proposed beam formulation subjected to a concentrated force of 5000 $kN$ at its free end eccentrically applied (Fig. 5.11). The results are compared to the 3D FEM model

|  |  | AEM 10 cubic B-splines | FEM Solid 2880/ FEM plate 960 |
|---|---|---|---|
|  | $w(m)$ at x=L | 0.4266 | 0.4316 |
|  | $\theta_x(rad)$ at x=L | 0.0100 | 0.0112 |
|  | $\theta_Y(rad)$ at x=L | -0.0131 | -0.0137 |
|  | $\tau_{xz}^{max}(\frac{kN}{m^2})$ at x=0 | 21532 | 20539 (solid model) |
| $P_z =$ 5000kN eccentric Lateral Loading | $\tau_{xy}^{max}(\frac{kN}{m^2})$ at x=0 | 12602 | 11502 (solid model) |
|  | $M_Y(kNm)$ at x=0 | -139691 | -139824 |
|  | $M_t(kNm)$ at x=0 | 127100 | 127324 |
|  | $M_{\phi_S^P}(kNm^2)$ at x=0 | -6930.56 | - |
|  | $M_{\phi_S^S}(kNm^2)$ at x=0 | -1838.93 | - |
|  | $M_{Dx}^P(kNm^2)$ at x=0 | 610306 | - |
|  | $M_{Dx}^S(kNm^2)$ at x=0 | -1999.04 |  |

*Table 5.3. Kinematical components, Shear stresses and Stress resultants of the doubly symmetric box-shaped cross section curved beam.*

(2880 quadrilateral solid elements) or the equivalent plate model (960 plate elements) when it is possible. In contrast to the previous open shaped cross section, primary distortional moment due to torsion is around four times larger than the bending moment while warping moments are insignificant. Secondary distortional moment is

not of importance and, thus, there is no need to consider additional modes in the analysis. In addition to these, shear stresses are larger than the previous case (I-shaped) comparing to the normal stress $\sigma_{xx}$.

In Fig. 5.13 the total translation contours are presented for the FEM solid model and the one proposed (AEM with 10 cubic splines or 80 constant elements). In Fig. 5.14 the normal stresses $\sigma_{xx}$ and $\sigma_{zz}$ contours are displayed for the same cases. It should be noted here that in this case normal stresses $\sigma_{zz}$ and $\sigma_{yy}$ are of more importance comparing to the previous cross section and exhibit large magnitude comparing to normal stress $\sigma_{xx}$.
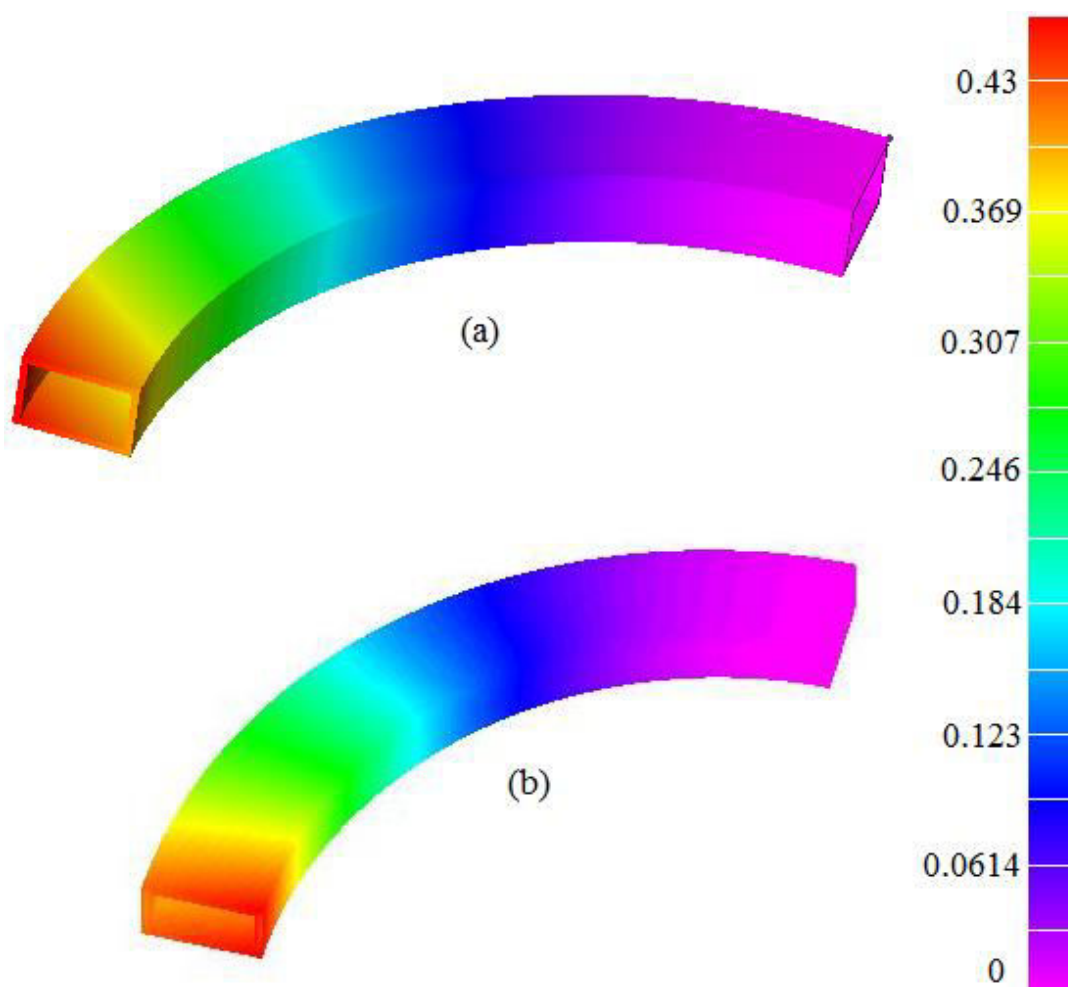


*Figure 5.13. Total translation contours of (a) 3D solid FEM model with 2880 quadrilateral elements and (b) the proposed one (AEM with 10 cubic splines or 80 constant elements) for the doubly symmetric box-shaped cross section curved beam.*
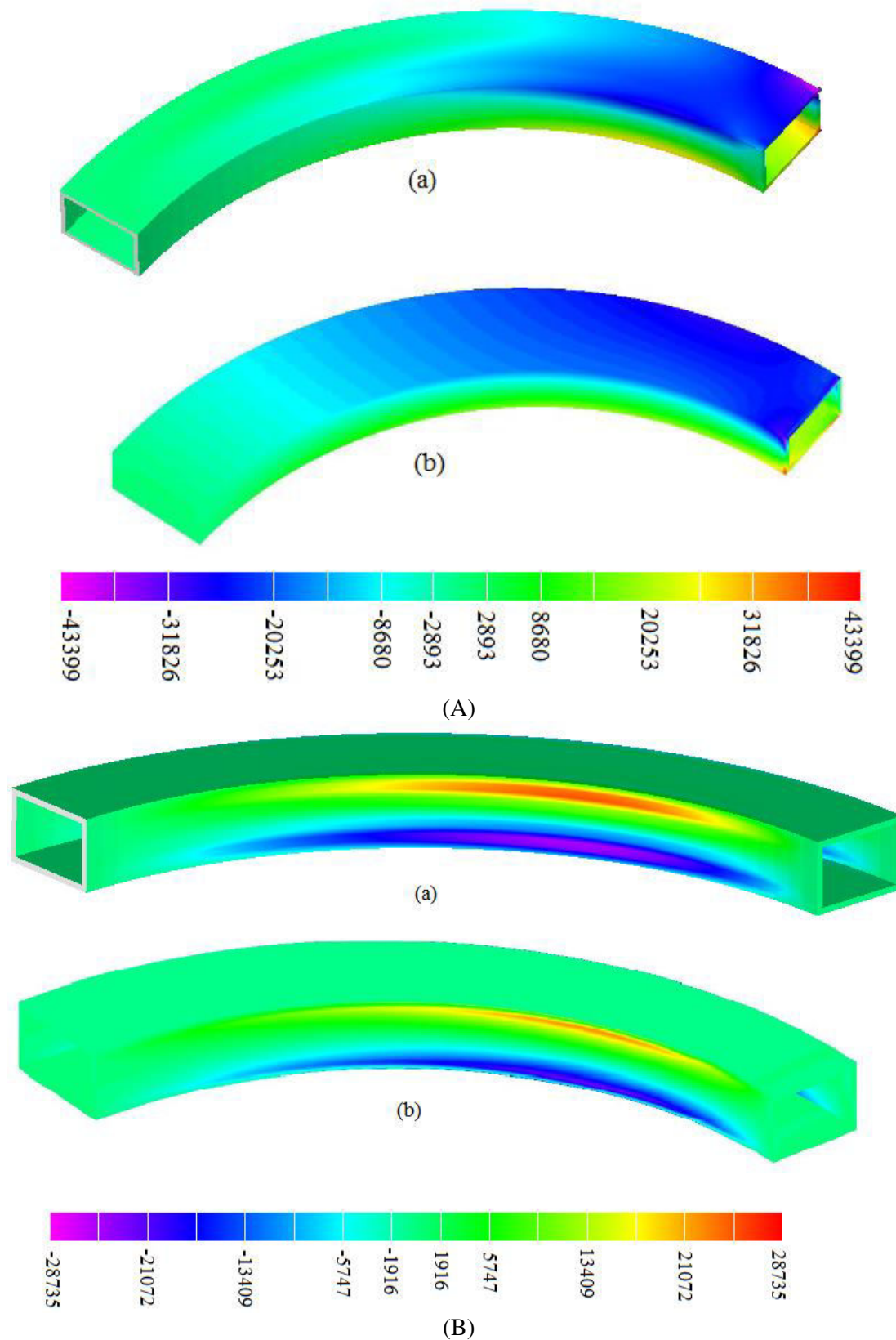
*Figure 5.14. Normal stress $\sigma_{xx}$ (A) and $\sigma_{zz}$ (B) contours (a) for 3D solid FEM model with 2880 quadrilateral elements and (b) the one proposed with 10 cubic splines in AEM or 80 constant elements in AEM for the doubly symmetric box-shaped cross section curved beam.*

Finally, in Table 5.4 three different ratios of moments have been compiled for various curvatures while length remains the same. The corresponding control polygons are shown in Fig. 5.15 together with the various weights, which is the only parameter that has to be changed during the beam's analysis. It is important to notice that as the

| | | $\dfrac{M_{Dx}^{P}}{M_Y}$ at x=0 | $\dfrac{M_{Dx}^{P}}{M_t}$ at x=0 | $\dfrac{M_Y}{M_t}$ at x=0 |
|---|---|---|---|---|
| | R=∞ | 0.178 | 2.844 | 15.952 |
| | R=76.394m | 1.141 | 5.579 | 4.891 |
| $P_z$ eccentric Lateral Loading | R=50.930m | 1.835 | 5.276 | 2.875 |
| | R=38.197m | 2.581 | 5.101 | 1.976 |
| | R=25.465m | 4.365 | 4.807 | 1.101 |

*Table 5.4. Moments' ratios for different radii of curvature obtained by the proposed model for the doubly symmetric box-shaped cross section curved beam.*
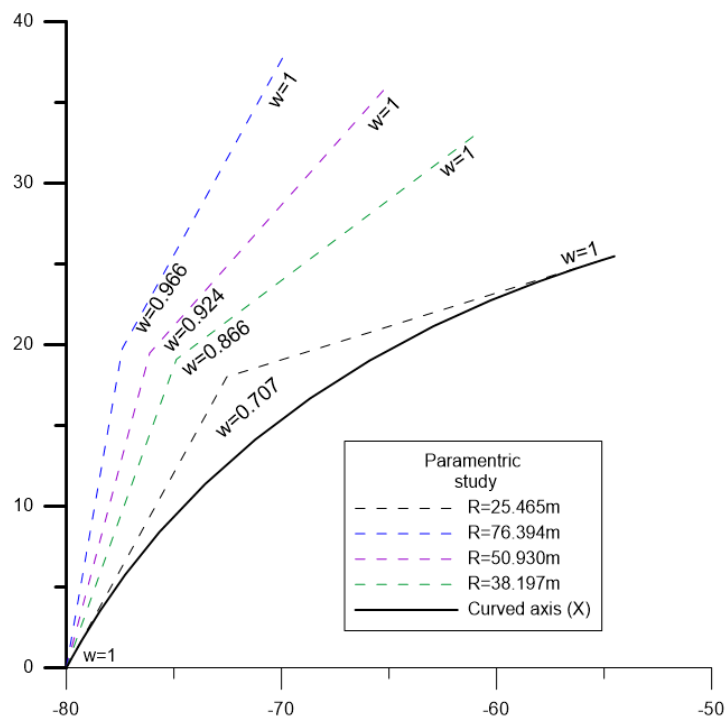


*Figure 5.15. Different curved geometries derived by the corresponding control polygons by changing only one weight while length is the same.*

curvature increases the $\dfrac{M_{Dx}^{P}}{M_{Y}}$ ratio becomes larger and, thus, distortional effects

become more significant. On the other hand, the $\dfrac{M_{Y}}{M_{t}}$ ratio becomes smaller as it was

expected due to the curved geometry and the $\dfrac{M_{Dx}^{P}}{M_{t}}$ ratio, even though it is initially

increased with the increase of curvature, afterwards slightly reduces in magnitude due to the fact that distortion is steadily important comparing to all other quantities. It seems that a critical value of curvature exists at which distortional effects become much larger.

### 5.5.2 Monosymmetric cross sections

In this example, in order to in order to further validate the proposed formulation and investigate the importance of distortion and curved geometry in the analysis of beam models as well as the number of modes needed, the static problems of three curved cantilever beams with monosymmetric cross sections (open or closed) are examined.

A cantilever beam of a monosymmetric C-shaped cross section ($E = 73000\,kN/m^{2}$, $G = 28000\,kN/m^{2}$, $v = 0.3$, $t/d = 0.049$, $d/L = 0.055$) and length of 1 $m$ under a concentrated load $P_{Y} = 100\,kN$ concentrically applied, as this is shown in Fig. 5.16, is examined. The total translation contour and the deformed shape are also presented in Fig. 5.16.
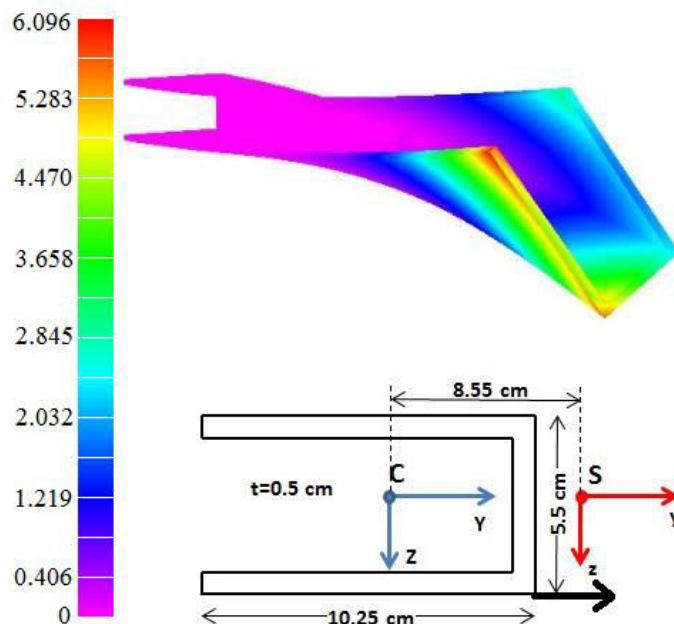


*Figure 5.16. Total translation contours by the proposed solution for the analysis of the C-shaped cross section straight beam and its cross section with the load applied eccentrically (black arrow).*

| | | AEM 5 cubic B-splines | FEM Solid 5100 |
|---|---|---|---|
| | $v(m)\ at\ x=L$ | 3.3922 | 3.4437 |
| | $\theta_x(rad)\ at\ x=L$ | 0.3076 | 0.3015 |
| $P_y = 100kN$ eccentric Lateral Loading | $\theta_Z(rad)\ at\ x=L$ | 0.0508 | 0.0511 |
| | $w(m)\ at\ x=L$ | 2.3705 | 2.4661 |
| | $M_{\phi_S^P}(kNm^2)\ at\ x=0$ | 5459.8 | - |
| | $M_{Dz}^P(kNm^2)\ at\ x=0$ | 1916.7 | - |

*Table 5.5. Kinematical components and Stress resultants for the monosymmetric C-shaped cross section straight beam.*

In Table 5.5 the most significant kinematical components have been compiled for the AEM with cubic B-splines and the FEM solid model along with the values of the primary warping moment due to torsion, which is around 60% of the bending moment, and the primary distortional moment due to bending with respect to Z axis, which is around 20% of the bending moment. It is important to note here that secondary warping and distortion are also significant. Thus, the displacement field suggested to be employed for this case is the one described by eqns. (5.10). However, only tertiary warping is of some importance while tertiary distortion vanishes.

The same C-shaped cross section shown in Fig. 5.16 is examined as curved with $R = 0.636m$ and an arc length of 1 $m$. This beam model is examined for four different load cases, namely concentrically or eccentrically applied radial (parallel to axis of symmetry) and vertical loads, and results are compared to the FEM solid model (4000 quadrilateral solid elements). The proposed formulation is initially accomplished with 10 cubic B-splines in the AEM and the displacement field described by eqns. (5.9).

In Table 5.6 the maximum values of the total displacement, the normal stress $\sigma_{xx}$, the shear stress $\tau_{xy}$, the primary warping moment $M_{\phi_S^P}$, the secondary warping moment $M_{\phi_S^S}$ and the distortional moment $M_{Dx}^P$ due to torsion are compiled for the various load cases. It should be noted here that when the load is applied radially either concentrically or eccentrically the warping and distortional moments are much lower than the case of the vertically applied load which results in significant primary and secondary warping effects. This indicates that additional modes need to be employed.

| AEM 10 cubic B-splines (FEM solid 4000) | | | | |
|---|---|---|---|---|
| $u_{total}^{max}(m)$ at x=L | 0.127 (0.128) | 4.85 (5.45) | 5.01 (5.99) | 0.31 (0.284) |
| $\sigma_{xx}^{max}(\frac{kN}{m^2})$ at x=0 | 17.92 (18.63) | 203.01 (247.1) | 217.31 (260.2) | 20.67 (22.56) |
| $\tau_{xz}^{max}(\frac{kN}{m^2})$ at x=0 | 4.23 (3.75) | 44.75 (38.68) | 48.1 (42.44) | 5.25 (4.81) |
| $M_{\phi_S^P}(kNm^2)$ at x=0 | 0 | 5923.16 | 6591.31 | 229.68 |
| $M_{\phi_S^S}(kNm^2)$ at x=0 | 0 | 1289.18 | 1171.38 | -40.5 |
| $M_{Dx}^P(kNm^2)$ at x=0 | -2.3 | 32.79 | 34.51 | -2.41 |
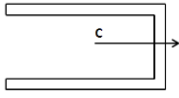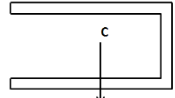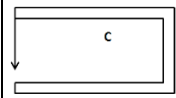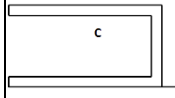
*Table 5.6. Total displacement, stresses and higher order Moments of the C-shaped cross section curved beam for various load cases.*

Thus, in Table 5.7 the values of the same quantities are compiled for the proposed formulation employing either 12 or 16 modes. It is important to note that errors regarding total displacement and stresses are reduced from around 12% (12 modes) to less than 5% (16 modes) comparing to FEM solid model.

Finally, in Table 5.8 the first five eigenfrequencies are compiled for the curved ($R=0.636m$, $\rho=0.785N\,sec^2/m^4$) C-shaped cross section when employing a FEM solid model without diaphragms (NO Diaph.) and the proposed beam formulation with cubic NURBS as well as for the corresponding straight beam element (second column of the Table 5.8) with FEM solid elements without the use of any diaphragms. It is obvious that the values obtained by the proposed beam formulation are in well coincidence with those of the FEM solid solution without any diaphragms. Comparing to the straight beam formulation, the behavior of the beam is different. The first mode exhibits a much lower eigenfrequency for the curved beam model. In general, modes of vertical displacement in curved arrangement are coupled with torsional modes. Particularly, the 4th mode of the straight beam is pure torsional, while all of the vertical modes of the curved beam exhibit torsional displacements, too. It should also be noted

that after the 3$^{rd}$ mode, the eigenfrequencies of the straight beam are lower than those of the curved model, which seems to be stiffer.
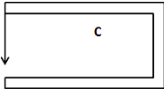
| AEM 10 cubic B-splines | 12 modes | 16 modes |
|---|---|---|
| (FEM solid 4000) | | |
| $u_{total}^{max}(m)$ at x=L | 5.01 (5.99) | 5.87 (5.99) |
| $\sigma_{xx}^{max}(\frac{kN}{m^2})$ at x=0 | 217.31 (260.2) | 252.01 (260.2) |
| $\tau_{xz}^{max}(\frac{kN}{m^2})$ at x=0 | 48.1 (42.44) | 43.8 (42.44) |
| $M_{\phi_S^P}(kNm^2)$ at x=0 | 6591.31 | 7413.57 |
| $M_{\phi_S^S}(kNm^2)$ at x=0 | 1171.38 | 1286.02 |
| $M_{Dx}^P(kNm^2)$ at x=0 | 34.51 | 32.03 |

*Table 5.7. Total displacement, stresses and higher order Moments of the C-shaped cross section curved beam for 12 or 16 modes.*

| Mode Number | FEMsolid NO Diaph. | FEMsolid NO Diaph. (straight) | 10 cubic NURBS | Type of mode |
|---|---|---|---|---|
| 1 | 0.341 | 0.630 | 0.355 | 1$^{st}$ mode of Vertical displacement |
| 2 | 1.843 | 1.749 | 1.849 | 1$^{st}$ mode of Lateral displacement |
| 3 | 2.506 | 2.712 | 2.581 | 2$^{nd}$ mode of Vertical displacement (excessive Torsion) |
| 4 | 7.244 | 3.288 | 6.626 | 1$^{st}$ mode of Torsion |
| 5 | 7.908 | 5.990 | 8.376 | 2$^{nd}$ mode of Torsion |

*Table 5.8. Eigenfrequencies for the monosymmetric C-shaped cross section curved or straight beam.*

The second beam model examined is an initially straight cantilever beam of a trapezoidal box-shaped cross section ($E = 3E7\,kN\!/m^2$, $G = 1.5E7\,kN\!/m^2$, $\nu = 0$, $t/d = 0.086$, $d/L = 0.086$) and length of 40 $m$ under a concentrated load $P_Z = 10000\,kN$ eccentrically applied at its free end, as it is shown in Fig. 5.17. The total translation contour and the deformed shape are also presented in Fig.5.17.
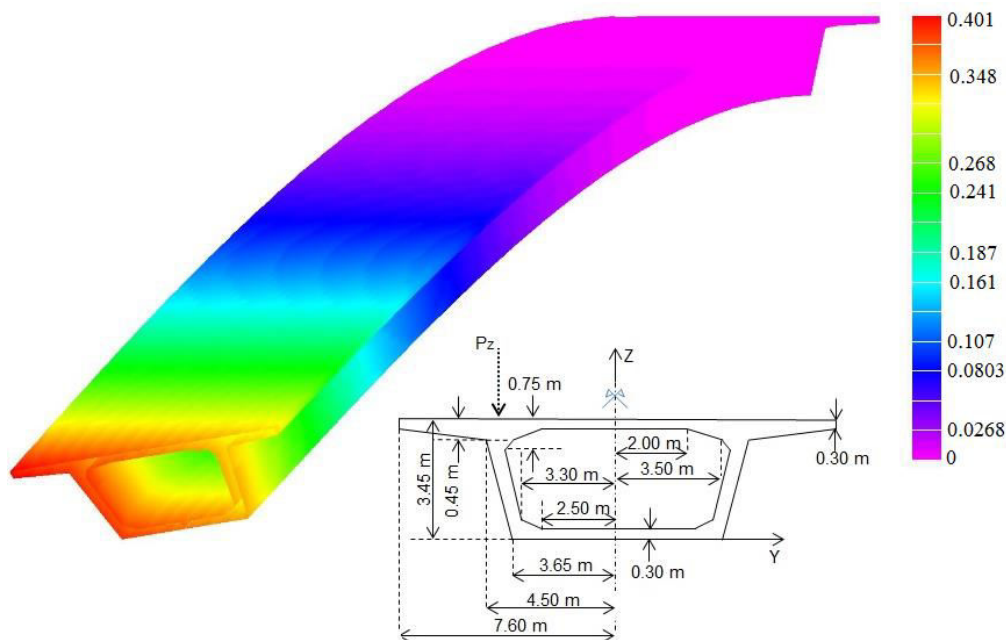


*Figure 5.17. Total translation contours and Deformed shape of the monosymmetric box-shaped trapezoidal cross section straight beam derived by the proposed solution (FEM with NURBS).*

In Table 5.9 the values of the kinematical components $w(x)$, $\theta_x(x)$ and $\theta_Y(x)$ for the vertical force $P_Z$ eccentrically applied at the free edge of the beam are presented for i) proposed beam elements with NURBS (5 cubic), ii) proposed beam elements with NURBS (10 cubic), iii) 1840 quadrilateral solid elements in FEMAP (FEMsolid1840), iv) 2320 quadrilateral solid elements in FEMAP (FEMsolid2320), and v) 4320 quadrilateral solid elements in FEMAP (FEMsolid4320). It seems that high convergence rates can be achieved with few NURBS comparing to FEM solid elements.

In Fig. 5.18 the normal stress $\sigma_{xx}$ contours are displayed for the 3D solid FEM model (2320 elements) and the proposed formulation with constant elements in the AEM. It is obvious that the two models are in well coincidence. After evaluating the stress resultants, it is important to note that bimoments and distortional moments due to torsion are of high importance for this cross section. In addition to this, tertiary distortion is also of some importance. However, the displacement field described by eqns. (5.9) results in quite accurate results (up to secondary higher order phenomena have been considered).
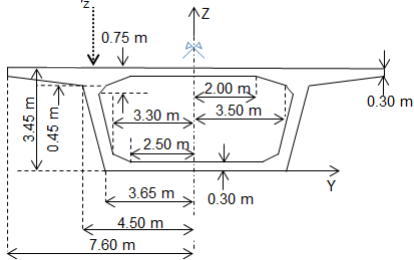
| | | $w(m)$ at $x=L$ | $\theta_x(rad)$ at $x=L$ | $\theta_Y(rad)$ at $x=L$ |
|---|---|---|---|---|
| | 5 cubic NURBS | 0.3790 | 0.0025 | -0.0139 |
| | 10 cubic NURBS | 0.3818 | 0.0025 | -0.0140 |
| $P_y$ =10000kN eccentric Lateral Loading | FEMsolid1840 1 Diaph. | 0.3823 | 0.0024 | -0.0140 |
| | FEMsolid2320 1 Diaph. | 0.3825 | 0.0024 | -0.0140 |
| | FEMsolid4320 1 Diaph. | 0.3827 | 0.0024 | -0.0140 |

Table 5.9. *Kinematical components of the monosymmetric box-shaped trapezoidal cross section straight beam.*
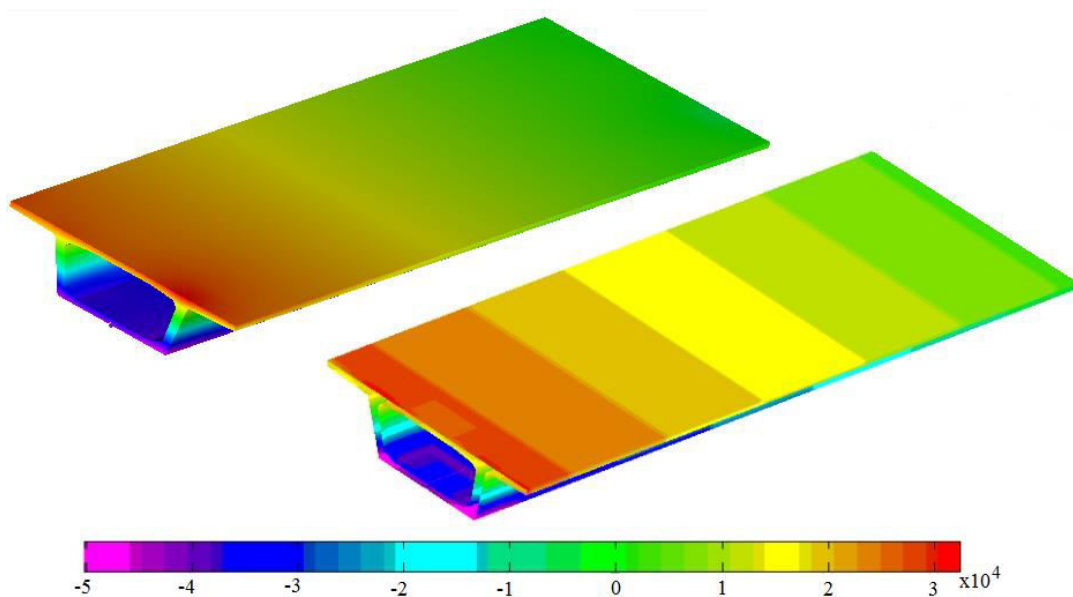


Figure 5.18. *Normal stress $\sigma_{xx}$ contours for 3D solid FEM model with 2320 quadrilateral elements (on the left) and the one proposed with AEM (100 constant elements) for the monosymmetric box-shaped trapezoidal cross section straight beam.*

The same box-shaped cross section shown in Fig. 5.17 is examined as curved with $R = 25.465\,m$ and an arc length of 40 $m$. The second cross section is subjected to a vertical concentrated load $P_Z = 10000\,kN$ concentrically applied at its free end. In

Fig. 5.19 the kinematical components $\eta_x(x)$, $\zeta_x(x)$ and $\theta_x(x)$ are displayed in order to investigate the order of their magnitude and compare them to each other. FEM with NURBS are employed for this purpose. Comparing to the $\eta_x(x)$ and $\zeta_x(x)$ distributions of the I-shaped cross section of the previous example (Fig. 5.9), the corresponding ones in this case exhibit a more similar (to each other) distribution along the length even though they differ in order of magnitude.
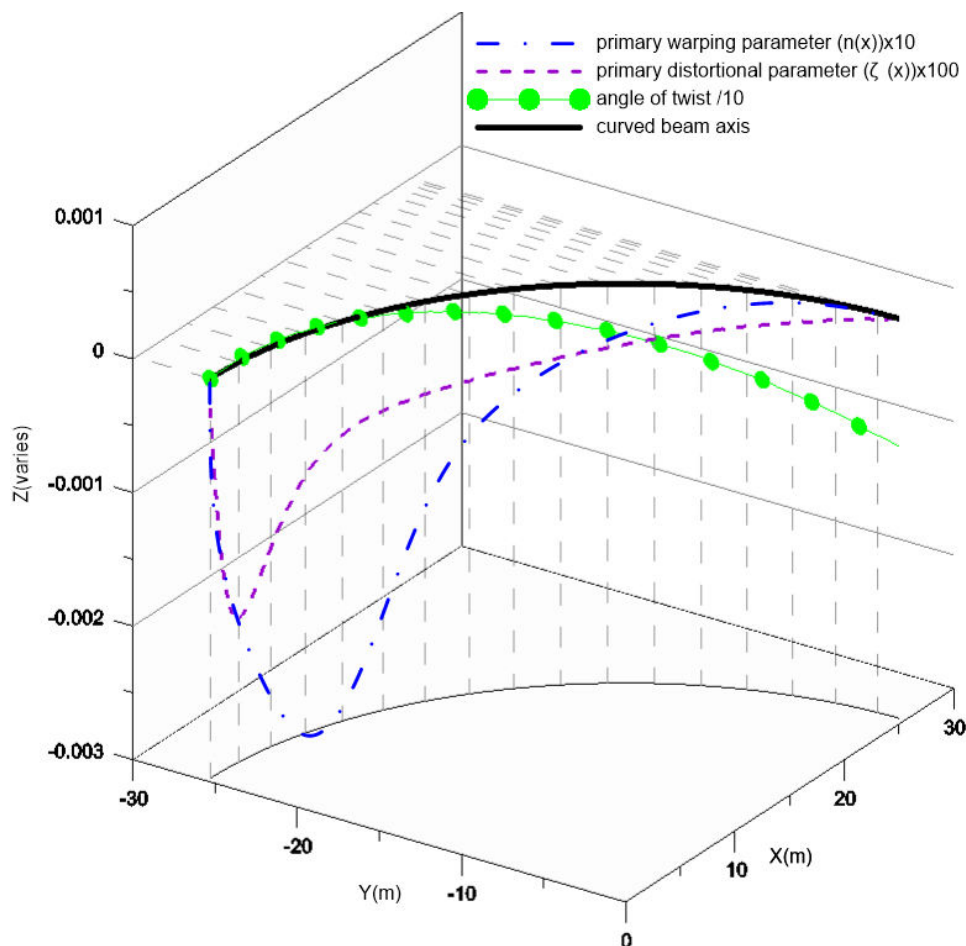


*Figure 5.19. Kinematical components $\eta_x(x)$, $\zeta_x(x)$ and $\theta_x(x)$ of for the monosymmetric box-shaped trapezoidal cross section curved beam with cubic NURBS.*

In Table 5.10 the values of different kinematical components, stresses and higher order moments are compiled for the proposed beam formulation, the 3D FEM model (2714 quadrilateral solid elements) when it is possible, the Generalized Warping Curved Beam (GWCB) formulation (Chapter 4) and the traditional Timoshenko beam element. It is worth noting here that, comparing to the rectangular box-shaped cross section (doubly symmetric), the $\dfrac{M_{Dx}^P}{M_Y}$ ratio is much lower while primary warping and distortional moments are of the same order of magnitude in this case (compare to

Table 5.3 values). The reasons for these are the difference in the cross section shape and the larger overall volume of this beam. Warping moments are much lower when distortion is not considered in the formulation. Shear stress of Timoshenko beam element is significantly less than the other cases.

| | | AEM 10 cubic B-splines | FEM Solid 2714 | AEM 50 quad. GWCB | Timoshenko FEM beam |
|---|---|---|---|---|---|
| | $w(m)$ at $x=L$ | 0.3744 | 0.3547 | 0.3202 | 0.3238 |
| | $\theta_x(rad)$ at $x=L$ | 0.0092 | 0.0087 | 0.0067 | 0.0067 |
| | $\theta_Y(rad)$ at $x=L$ | -0.0120 | -0.0115 | -0.0104 | -0.0106 |
| | $\sigma_{xx}^{max}(\frac{kN}{m^2})$ at $x=0$ | 40254 | 38230 | 27633 | 28782 |
| $P_z =1000kN$ eccentric Lateral Loading | $\tau_{xy}^{max}(\frac{kN}{m^2})$ at $x=0$ | 24135 | 23085 | 16940 | 3714 |
| | $M_Y(kNm)$ at $x=0$ | -254316 | -254647 | -254820 | -254648 |
| | $M_t(kNm)$ at $x=0$ | -253683 | -254647 | -254700 | -254648 |
| | $M_{\phi_S^P}(kNm^2)$ at $x=0$ | -342533 | - | -244940 | 0 |
| | $M_{\phi_S^S}(kNm^2)$ at $x=0$ | 36612 | - | 30717 | 0 |
| | $M_{Dx}^P(kNm^2)$ at $x=0$ | -366072 | - | - | - |
| | $M_{Dx}^S(kNm^2)$ at $x=0$ | 4127 | - | - | - |

*Table 5.10. Kinematical components, Shear stresses and Stress resultants of the monosymmetric box-shaped trapezoidal cross section curved beam.*

As the last case studied in this example, a third box-shaped cross section, as shown in Fig. 4.24, ($E=3.25E7\ kN/m^2$, $G=1.39E7\ kN/m^2$, $R=100\ m$, $v=0.1667$, $t/d=0.1$, $d/L=0.065$) of an arc length of 33 $m$ is subjected to a vertical concentrated load 5000 $kN$ concentrically applied at its free end. This beam is also examined with the same plan view and cross section shape as previously but with a different material for its upper plate (composite cross section), namely $E_1=4\times10^7\ kN/m^2$, $G_1=2\times10^7\ kN/m^2$, $v_1=0$, as shown in Fig. 5.20 (grey color).
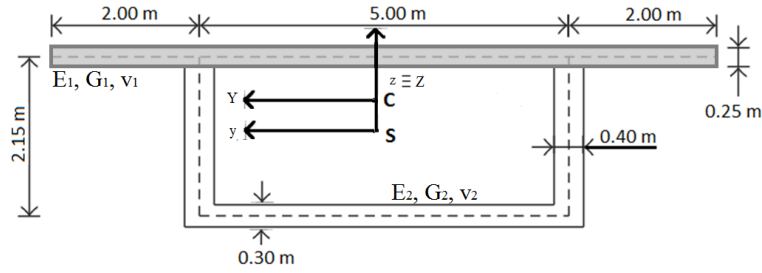
*Figure 5.20. Box-shaped cross section of the composite beam of example 5.5.2.*

In Table 5.11 the values of different kinematical components, stresses and higher order moments are compiled for the proposed beam formulation either curved (R) or

| | | R=100 AEM 10 cubic B-splines | R=100 FEM Solid 6600 | R=∞ AEM 100 constant | R=100 AEM 10 cubic b-splines *composite* |
|---|---|---|---|---|---|
| | $w(m)$ at $x=L$ | 0.4001 | 0.3899 | 0.3914 | 0.2616 |
| | $\theta_x(rad)$ at $x=L$ | 0.0039 | 0.0038 | 0 | 0.0019 |
| | $\theta_Y(rad)$ at $x=L$ | -0.0170 | -0.0169 | -0.0174 | -0.0116 |
| | $\sigma_{xx}^{max}(\frac{kN}{m^2})$ at $x=0$ | 52456 | 51825 | 52122 | 21151 |
| | $\tau_{xy}^{max}(\frac{kN}{m^2})$ at $x=0$ | 8425 | 7721 | 3992 | 3791 |
| $P_z=5000\kappa N$ Lateral Loading | $M_Y(kNm)$ at $x=0$ | -161723 | -162023 | -162115 | -161642 |
| | $M_t(kNm)$ at $x=0$ | 26929 | 26969 | 0 | 26916 |
| | $M_{\phi_S^P}(kNm^2)$ at $x=0$ | 18463 | - | 0 | 9152 |
| | $M_{\phi_{CY}^P}(kNm^2)$ at $x=0$ | -3408 | - | -3357.5 | -11338 |
| | $M_{\phi_S^S}(kNm^2)$ at $x=0$ | -6198 | - | 0 | -3130 |
| | $M_{Dx,y}^P(kNm^2)$ at $x=0$ | 62817 (x) 1571 (y) | - | 0 (x) 1144.57 (y) | 20418 (x) 245 (y) |
| | $M_{Dx,y}^S(kNm^2)$ at $x=0$ | -952.89 (x) -1403 (y) | - | 0(x) -1072 (y) | 1691.09 (x) -262 (y) |

*Table 5.11. Kinematical components, Shear stresses and Stress resultants of the monosymmetric box-shaped cross section straight or curved beam.*

straight ($R=\infty$) and the 3D FEM model (6600 quadrilateral solid elements) when it is possible. Additionally, the corresponding values derived by the analysis of the composite cross section showed in Fig. 5.20 have been compiled for comparison reasons. It should be noted here that the curved beam exhibits larger distortional effects due to torsion comparing to the straight formulation for which warping and distortional effects due to bending are of importance. Curvature alters significantly the contribution of beam's resisting mechanisms and makes it more vulnerable to higher phenomena triggered by the arising torsion. However, comparing to the previous box-shaped cross sections, the ratio $\dfrac{M_{Dx}^{P}}{M_Y}$ is much lower and the beam resists to loading mainly through bending. Considering the corresponding beam element with composite section, it should be noted that its performance is significantly improved through the use of a material with higher stiffness at its upper plate. This becomes obvious through the reduction in stresses and higher order moments due to torsion by more than 50%. However, the primary warping moment due to bending is quite high but still much less than the distortional one (and more desirable than the corresponding quantities due to torsion which causes more brittle failures comparing to bending).

Finally, in Table 5.12 the first eight eigenfrequencies are compiled for the curved

| Mode Number | FEMsolid 6600 NO Diaph. (cantilever) | FEMsolid 6600 NO Diaph. (clamped) | FEMsolid 6600 1 Diaph. (clamped) | 10 cubic NURBS (clamped) | Type of mode |
|---|---|---|---|---|---|
| 1 | 1.725 | 9.328 | 9.414 | 9.470 | 1st mode of Vertical displacement |
| 2 | 4.065 | 17.099 | 19.230 | 16.887 | 1st mode of Lateral displacement |
| 3 | 9.084 | 20.495 | 21.160 | 21.154 | 1st mode of Torsion |
| 4 | 10.183 | 21.174 | 22.126 | 21.949 | 2nd mode of Vertical displacement |
| 5 | 19.191 | 27.898 | 35.428 | 26.003 | 2nd mode of Lateral displacement |
| 6 | 22.321 | 31.948 | 36.230 | 32.789 | 3rd mode of Vertical displacement |
| 7 | 21.649 | 43.247 | 42.768 | 44.500 | 2nd mode of Torsion |
| 8 | 29.165 | 47.490 | 47.013 | 49.602 | 3rd mode of Torsion |

*Table 5.12. Eigenfrequencies for the monosymmetric box-shaped cross section curved beam (clamped or cantilever).*

($R = 100m$, $\rho = 2.5kN\ sec^2/m^4$) monosymmetric box-shaped cross section previously described when employing FEM solid models with 1 or without diaphragms (NO Diaph.) and the proposed beam formulation with cubic NURBS. Both clamped and cantilever beam models have been studied for the FEM solid model without diaphragms (NO Diaph.). It is obvious that the values obtained by the proposed beam formulation are in well coincidence with those of the FEM solid solution without any diaphragms and the accuracy is improved comparing to the corresponding values compiled in Table 4.16 (where distortional effects had not been considered). The placement of the diaphragm at the midpoint of the curved length (forth column of the Table 5.12) results in a slight increase of the eigenfrequencies of the first four modes and a significant increase for the $5^{th}$ and $6^{th}$ modes. In addition to these, comparing to the cantilevered model, the behavior of the beam is much different. All of the eigenfrequencies are decreased while the order of significance is altered for the $6^{th}$ and $7^{th}$ modes. In general distortional effects are of more importance for most of the modes ($3^{rd}$ to $8^{th}$) and torsional modes become more significant comparing to the clamped beam model. It should also be noted here that the procedure of finding the modes of the cantilever beam corresponding to the same ones of the clamped beam is quite cumbersome due to the fact that many local vibrational modes arise in the FEM solid model.

## 5.6 Concluding Remarks

In this chapter, the generalized warping and distortional analysis of straight and curved beams is mainly examined. An iterative equilibrium scheme combined with traditional eigenvalue analysis has been developed in order to derive the cross section's modes that dominate and, thus, permit the isolation of structural phenomena. Various shapes of open or closed cross sections have been considered. Boundary Element Method has been employed for this purpose. Additionally, Isogeometric tools (b-splines and NURBS) integrated in FEM and AEM are applied for the longitudinal analysis of beams allowing for straightforward model handling (i.e. curvature can be easily changed) and reducing significantly computational cost (especially when additional higher order phenomena need to be accounted for). The presented formulation is based on an enriched kinematic field (eqns. (5.9) and (5.10)) taking into account primary, secondary and tertiary higher order phenomena due to both bending and torsion. The importance of the proposed formulation is highlighted when considering the advantages of curved beam models compared to solid and plate ones either for static or free vibrational case. Modelling effort can be significantly reduced (solid models require cumbersome post- and pre-processing even in relatively simple cases) and parametric analyses can be facilitated (construction of multiple solid models is quite cumbersome, especially for complex geometries). Moreover, the FEM beam elements commonly employed in commercial software can be inaccurate. Thus, the main purpose of this beam formulation is to remain simple and with the least number of degrees of freedom needed to describe its behavior accurately. The main conclusions that can be drawn from this investigation are:

i.  Highly accurate results can be obtained using B-splines in the AEM technique as well as NURBS in FE beam formulations for the static analysis of the proposed beam elements. Computational cost and post-processing of the results is significantly reduced by the use of NURBS comparing to FEM plate and solid models. Employment of NURBS in FEM and B-splines in AEM with or without knot insertion results in higher convergence rates, too.

ii.  Poisson effects are in general not negligible even if distortion is not of importance as it is shown for the solid rectangular cross section of the example 5.5.1. In addition to this, it seems that when material constants are larger, Poisson ratio affects the magnitude of stresses more.

iii.  In general, open shaped cross sections suffer more from warping while close ones from distortion. The consideration of up to secondary higher order phenomena (eqns. (5.9)) is generally accurate. However, in some cases of very thin-walled cross sections either open or closed shaped, tertiary phenomena might need to be considered. As a rule of thumb in choosing the least number of modes in order to achieve the maximum accuracy when the proposed method is employed, the limitations $t/d > 0.05$ and $d/L > 0.05$ can be applied.

iv.  Monossymetric and, thus, asymmetric cross sections are more susceptible to higher order phenomena due to this inherent property of their shape, as it can be shown from example 5.5.2 comparing to example 5.5.1.

v.  Increase in curvature causes increase in the distortion due to torsion for thin-walled box-shaped cross sections. Cross sections with cantilever plates at both sides undergo less severe distortional effects due to the fact that bending resisting mechanisms become of importance, too.

vi.  Direction and position of loads can play a significant role in the behavior of curved beams with monossymetric and, thus, asymmetric cross sections due to the fact that the development of higher order warping (in open sections) or distortional (in close shaped) phenomena can be significantly altered.

vii.  The ratios of distortional and warping moments to the bending ones can be indicative of the curved beam's behavior and offers an additional insight into the resisting mechanisms that dominate.

viii.  The distortion of thin-walled box-shaped beams contributes significantly to lowering the natural frequency of torsional and bending vibration modes. Therefore, distortional effects must be considered in order to predict the dynamic behavior of beams accurately.

ix.  Composite cross sections can be easily handled with the proposed BEM approach due to the fact that only boundary discretization is required. Additionally, changes in the arrangement of materials can be easily integrated in the model and significantly improve the resistance of the curved beams against warping and distortion.

x.  Curved geometry alters the dynamic behavior of beam models with open or closed-shaped cross section and not necessarily in the same way.

xi.  The procedure of identifying the type of higher modes becomes quite cumbersome, especially for FEM solid models, thus, making comparisons of the results to other models time-consuming and uncertain.

# Chapter 6

# Chapter 6

# Application of Diaphragms' Guidelines and Assessment

## 6.1  Introduction

Regarding the distortional analysis related to the intermediate diaphragms, which is more important for box girders, the number of researches is quite limited. The study related to the distortional analysis of box girders was initiated by Dabrowski (1968) who first formulated the distortional phenomenon of box members with a symmetric cross section. Later and more recently, other research efforts were undertaken regarding the distortional analysis of the structures to give design guidelines on the intermediate diaphragms. Sakai and Nagai (1981), and Nakai and Murayama (1981) presented several results on the design procedures of the intermediate diaphragms for curved girders and noted that these play a very important role in moderating distortional warping of girders. Yabuki and Arizumi (1989) employing BEF analogy for distortion proposed spacing provisions which can be utilized for steel-plated intermediate diaphragms. More recently, Park et al. (2003 and 2005a) developed a straight and a curved box, respectively, beam finite element having nine degrees of freedom per node in order to propose tentative design charts for adequate maximum spacing of intermediate diaphragms. As mentioned in Chapter 5, their proposal lacks of generality. Yoo et al. (2015) applied the concept of the BEF analogy for the analysis of distortional stresses of horizontally curved box-girders. The proposed procedure is capable of handling simple or continuous single cell box girders (or separated multi-cell box girders) with rigid or deformable interior diaphragms or cross-frames. However, in most of these studies, the placement of diaphragms was not related whether to dynamic property analysis or dynamic response analysis.

Up to the 1980s the design of a bridge structure was based on static analysis, corrected by a dynamic amplification factor (as also mentioned in Chapter 4) which is based on the first natural frequency. An extensive effort was made by Hamed and Frosting (2005) to introduce the effects of warping and distortion of bridge cross-sections. An analytical model is developed in their works where the bridge is idealized as being made of panels which behave as plates in the transversal direction and as Euler–Bernoulli beams in the longitudinal direction (Petrolo et al., 2012). Special attention is paid for distortion by the following bridge design specifications. The Guide Specifications for Horizontally Curved Highway Bridges by the American Association of State Highway and Transportation Officials – AASHTO (1993) specify the maximum spacing of the intermediate diaphragms through an approximate formula as well as the ratio of distortional and bending normal stresses. The Hanshin Expressway

Public Corporation of Japan provides the Guidelines for the Design of Horizontally Curved Girder Bridges – HEPCJ (1988) specifying the maximum spacing of the intermediate diaphragms in curved box girder with respect to that in straight box girders multiplied by a reduction factor. It should be noted here that the boundary conditions and the cross section shape are not taken into account directly for both specifications.

In this chapter, the beam models presented in *Chapters 4* and *5* are mainly employed either in static or dynamic case. The numerical solutions of the problems are similar to previous chapters, too. Additionally, solid or shell/plate *Finite Element models* are employed and the *bridges' design specifications* mentioned above are applied in order to compare the results and *assess* the provisions. The cross sections can be considered not deformable in their plane through the presence of a sufficient number of diaphragms along the straight or curved beam, preventing distortion. The design guidelines related to the intermediate diaphragms have been provided to prevent from excessive distortional warping in the longitudinal direction and transverse bending deformation along the cross section perimeter. Thus, fixed values of the stress ratio of the distortional warping normal stress to the bending normal stress are used. Moreover, having in mind that a rigid diaphragm is usually placed in the sections over each support, both the angle of twist and warping are prevented at these places (bimoment has nonzero values at the support sections).

The assessment of the design guidelines which specify the maximum spacing of intermediate diaphragms through comparisons of the proposed curved models to the corresponding solid or shell/plate ones and some parametric studies is a first step towards suggesting further provisions and limitations on the application of these regulations.

Numerical examples are worked out to evaluate the formulated models, provide comparable results and assess the efficiency of design guidelines with respect to accuracy and cost. For this purpose, various models of straight or curved beams with various arrangements of diaphragms, boundary conditions, geometric properties and loads have been developed.

## 6.2   Statement of the problem-Specifications

The problem of prismatic straight or curved beam models of homogenous or composite arbitrary cross section has already been stated in Chapters 3, 4 and 5. Nonuniform warping and/or distortion distributions can be considered by employing independent parameters, which are the higher degrees of freedom (DOFs), multiplying corresponding warping/distortion modes as this is already described. Thus, the generalized nodal displacement vector in the local coordinate system can be written for both ends of the beam. Its dimension depends on the number of higher cross sectional modes considered. Similarly, higher-order stress resultants arise and these constitute additional generalized forces acting at the nodes of straight or curved beam elements. The standard Direct Stiffness Method (DSM) can be employed in order to formulate the local stiffness matrix of the 3-dimensional beam. Afterwards, the global stiffness and force matrices can be derived by multiplying the local ones with the well-known

rotation matrix of spatial frames. Regarding warping and distortional DOFs, the transformation procedure needs special treatment in case of non-aligned members without any diaphragms. In addition to this, adjacent curved beam elements need special care when there is full warping and distortional continuity. Particularly, approximate modelling techniques at joints need to be adopted and general assumptions to be made (Jang et al., 2008; Jang and Kim, 2010). However, the cases considered in this chapter aim mainly to provide results for comparison with models formulated when the guidelines are applied. Thus, the study of the warping and distortion transmissions between adjacent elements is not within the scope of this chapter.

The placement of diaphragms along the length of the beam-like frame which consists of adjacent aligned beam elements or along the beam model has been done according to the following guidelines. The Guide Specifications for Horizontally Curved Highway Bridges by the American Association of State Highway and Transportation Officials – AASHTO (1993) specify the maximum spacing of the intermediate diaphragms $L_D$ as

$$L_D \leq L\left(\frac{R}{200L - 7500}\right)^{1/2} \leq 25\,ft \tag{6.1}$$

where $L$ and $R$ denote the span length and radius of curvature in feet, respectively. This provision meets the requirement that the distortional normal stress (it is meant due to torsion) is limited within 10% of the bending normal stress and the transverse bending normal stress is limited to 137.3 MPa or lower.

In addition to this, the Hanshin Expressway Public Corporation of Japan provides the Guidelines for the Design of Horizontally Curved Girder Bridges – HEPCJ (1988) specifying the maximum spacing of the intermediate diaphragms in curved box girder with respect to that in straight box girders multiplied by a reduction factor, which is equal to unity for a span length less than 60 m. In those guidelines, design criteria for the spacing of the intermediate diaphragms are specified so that the distortional normal stress (due to torsion) is limited within 5% of the bending normal stress. In addition to this, the transverse bending normal stress due to distortion should be limited to about 4.90 MPa or lower. To account for these restrictions, the guidelines specify the maximum spacing of the intermediate diaphragms in curved box girder bridges as

$$L_D = L_{DS}\kappa(\phi, L) \tag{6.2}$$

where

$$L_{DS} = \begin{cases} 6m & for \quad L < 60m \\ (0.14L - 2.4)m & for \quad 60m \leq L \leq 160m \\ 20m & for \quad L > 160m \end{cases} \tag{6.3}$$

$$\kappa(\phi, L) = \begin{cases} 1 & \text{for} \quad L < 60m \\ 1 - \dfrac{\sqrt{\phi}(L-60)}{100\sqrt{2}} & \text{for} \quad 60m \le L \le 200m \end{cases} \tag{6.4}$$

with $L_{DS}$, $\kappa(\phi, L)$ and $\phi$ being the spacing of the intermediate diaphragms in straight box girder bridges (in m), the reduction factor and the angle formed by the arc at the center of the circle that it is a part of (in rad), respectively.

## 6.3 Numerical Solution

B-splines and NURBS curves in terms of B-spline basis functions can be employed either in FEM or AEM. The description of the numerical procedures is given in the Appendix A.2.

The local stiffness matrices of the elements are computed numerically by applying either the Analog Equation Method (AEM) (Katsikadelis, 1994 and 2002b) or the Finite Element Method (FEM) with Isogeometric tools. Warping and distortion functions as well as geometric constants are evaluated employing a 2-D BEM approach, as described in previous chapters.

## 6.4 Numerical examples

The computer programs that have already been written are employed and compared to FEM solid (quadrilateral or triangular) or plate/shell elements (FEMAP, 2010). Either the static or dynamic problem is examined. Design guidelines for specifying the maximum spacing of intermediate diaphragms have been applied to the aforementioned solid models and compared to the proposed one with or without taking into account distortional effects. Four different examples of thin-walled box-shaped cross sections, which mainly suffer from distortion, with different geometric ratios have been examined. According to thin-walled theory, the upper bounds of these ratios are $t/d < 0.1$ and $d/L < 0.1$, where $t$, $d$ and $L$ are the thickness, width and length of the straight or curved box-shaped cross section, respectively.

### 6.4.1 Box-shaped Doubly Symmetric cross section ($t/d = 0.085$, $d/L = 0.087$)

The first beam has the doubly symmetric box-shaped cross section shown in Fig. 5.11 of Chapter 5. It is examined either as curved beam with an arc length of 40 m or straight one of the same length.

According to the provisions of AASHTO, 6 intermediate diaphragms need to be placed along the curved beam length at equal distances in order to prevent excessive distortion. Additionally, 7 diaphragms have to be employed for the same purpose either in curved or straight beam formulation according to HEPCJ guidelines. Some comments should be made here with respect to the results of the previous chapter. Regarding the values compiled in Table 5.2 for the straight beam formulation, it should be noted that when employing 2 diaphragms the kinematical components at the free end are almost the same with those in the case of 1 diaphragm for all of the methods employed, thus, indicating the absence of excessive distortional phenomena for this

cross section. This is verified when stress values are considered. Significant normal $\sigma_{zz}$ and $\sigma_{yy}$ as well as shear stresses arise only when no diaphragms exist in the model. This implies that only 1 diaphragm needs to be employed in order to prevent distortion instead of the 7 diaphragms required according to HEPCJ. This is also verified when considering the dynamic case ($\rho = 2.5kN\,sec^2/m^4$) with a transient vertical load $P_Z = 5000kN$ applied eccentrically for 3 seconds at the free end. In Fig. 6.1, the response of the beam for the vertical displacement is displayed for three cases, namely models with 2, 4 and without diaphragms, showing that no important differences arise. However, in the case of the same cross section with curved configuration (Table 5.3 and Fig. 5.13), kinematical components are significantly decreased when employing 7 diaphragms. In addition to this, in the case of the 2-diaphragmatic arrangement, $\sigma_{yy}$ remains significant comparing to the model with 6 or 7 diaphragms (quadruple in magnitude). When employing 4 diaphragms, the values of stresses are closer to the arrangement with 7 diaphragms and much lower than the cases of 1 or 2 diaphragms. Therefore, it seems to be more cost-effective to use fewer diaphragms than those required by the provisions with respect to safety.

In Table 6.1 the first eight eigenfrequencies are compiled for the curved ($R = 25.465m$, $\rho = 2.5kN\,sec^2/m^4$) rectangular box-shaped cross section when employing FEM solid models with 7 or without diaphragms (NO Diaph.) and the proposed beam formulation with cubic B-splines in AEM as well as for the corresponding straight beam element (forth column of the Table 6.1) with FEM solid elements without the use of any diaphragms. It is obvious that the values obtained by the proposed beam formulation are in well coincidence with those of the FEM solid solution without any diaphragms. The placement of diaphragms results in a slight increase of the eigenfrequencies of the first four modes and a significant increase for the rest four modes due to the fact that distortion becomes more important as indicated from the description of the modes (last column of the Table 6.1). In addition to these, comparing to the straight beam formulation, the behavior of the beam is different. The first two modes exhibit similar eigenfrequencies for both the curved and straight model. Regarding the rest of the modes, significant discrepancies can be noticed either in the values of the eigenfrequencies or in the order of modes' significance. Particularly, it seems that torsional modes (5th and 7th for the straight beam) are more of importance in the straight beam model comparing to bending modes due to the lower value of the 5th eigenfrequency and the altered order of significance between the 7th and 8th modes. To conclude with, fewer diaphragms can be employed in terms of safety (suggested value is 4) due to the fact that in common practice (as in bridge deck design) the first 3-5 eigenfrequencies, which are not highly affected when comparing arrangements with 4 and 7 diaphragms, are commonly employed in order to derive design quantities. This is also verified when considering the dynamic case of the same transient load studied for the corresponding straight beam, as mentioned in the previous paragraph. In Fig. 6.2 the response of the beam for the vertical displacement is displayed for the same three
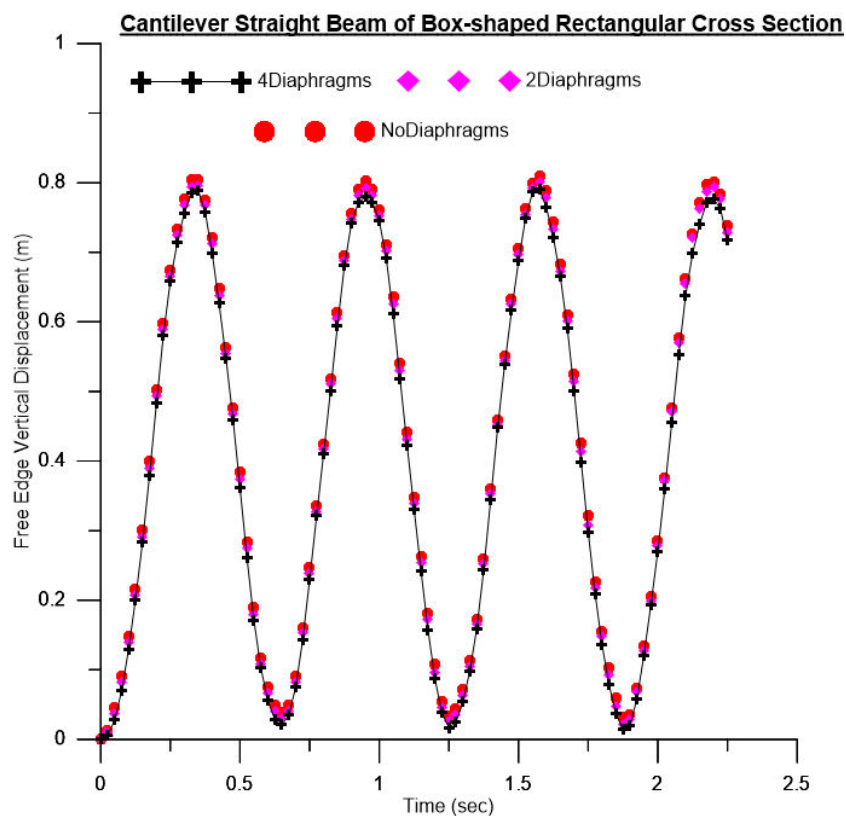
*Figure 6.1. Response of the straight beam with box-shaped cross section for different diaphragmatic arrangements under transient load.*
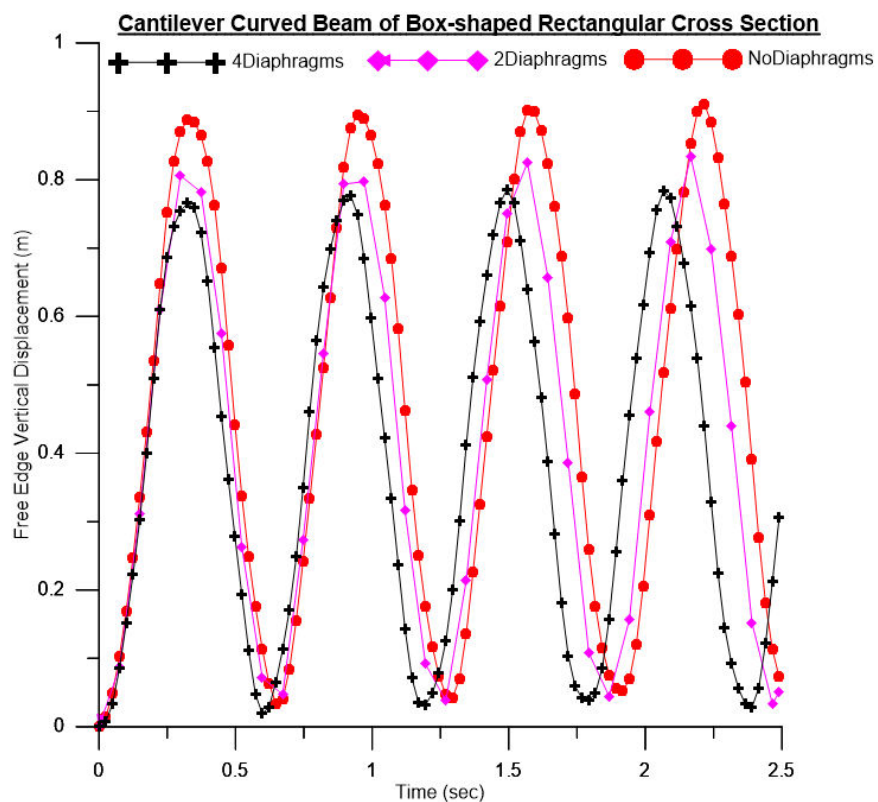


*Figure 6.2. Response of the curved beam with box-shaped cross section for different diaphragmatic arrangements under transient load.*

cases (in order to compare them), showing that the employment of 2 or 4 diaphragms results in the reduction of displacements comparing to the non-diaphragmatic model.

## 6.4.2 Box-shaped Monosymmetric cross section ($t/d = 0.02$, $d/L = 0.1$)

The box-shaped cross section shown in Fig. 3.15 of Chapter 3 with the geometric constants compiled in Table 3.7 of the same chapter is examined here. This cross

| Mode Number | FEMsolid 2880 NO Diaph. | FEMsolid 2880 7 (4) Diaphs. | FEMsolid 2880 NO Diaph. (straight) | 10 cubic B-splines in AEM (1 Diaph.) | Type of mode |
|---|---|---|---|---|---|
| 1 | 1.605 | 1.726 (1.707) | 1.630 | 1.611 | 1st mode of Vertical displacement (insignificant distortion) |
| 2 | 2.221 | 2.261 (2.238) | 2.168 | 2.155 | 1st mode of Lateral displacement (insignificant distortion) |
| 3 | 7.038 | 7.329 (7.242) | 9.167 | 7.063 | 2nd mode of Vertical displacement (significant distortion) |
| 4 | 9.440 | 9.626 (9.530) | 12.099 | 9.296 | 2nd mode of Lateral displacement (significant distortion) |
| 5 | 14.455 | 16.108 (15.875) | 12.791 | 14.795 | 1st mode of Torsion (significant distortion) |
| 6 | 19.131 | 22.770 (22.087) | 21.591 | 20.552 | 3rd mode of Vertical displacement (excessive distortion) |
| 7 | 23.306 | 32.479 (32.000) | 29.194 | 22.961 | 3rd mode of Lateral displacement (excessive distortion) |
| 8 | 23.478 | 41.895 (36.422) | 22.848 | 25.312 | 2nd mode of Torsion (excessive distortion) |

*Table 6.1. Eigenfrequencies for the doubly symmetric box-shaped cross section curved or straight beam.*

section is employed for the beam model described in the example 4.5.3 of Chapter 4
( $E = 4E7\,kN/m^2$ , $G = 2E7\,kN/m^2$ , $L = 10\,m$ , $\rho = 7.85kN\,sec^2/m^4$   $R = 6.366\,m$  or
$R = \infty$  for the straight formulation).

The straight beam under a concentrated load $P_y = 1000\,kN$  in the vertical
direction eccentrically applied at its free end (similarly to the example 3 of Chapter 3)
is examined at first in order to investigate the provisions of the guidelines related to the
spacing of intermediate diaphragms. In Fig. 6.3 a model of the beam implemented in
FEMAP (2010) employing FEM quadrilateral solid elements is shown. In the same
figure the total deflection is also recorded.  It is worth here noting that in order to
obtain the distributions of the kinematical components and stress resultants from the
solid model, rigid diaphragms have to be placed in regular distances (20 in total),
permitting the measurement of rotation angles and translations of the reference nodes.
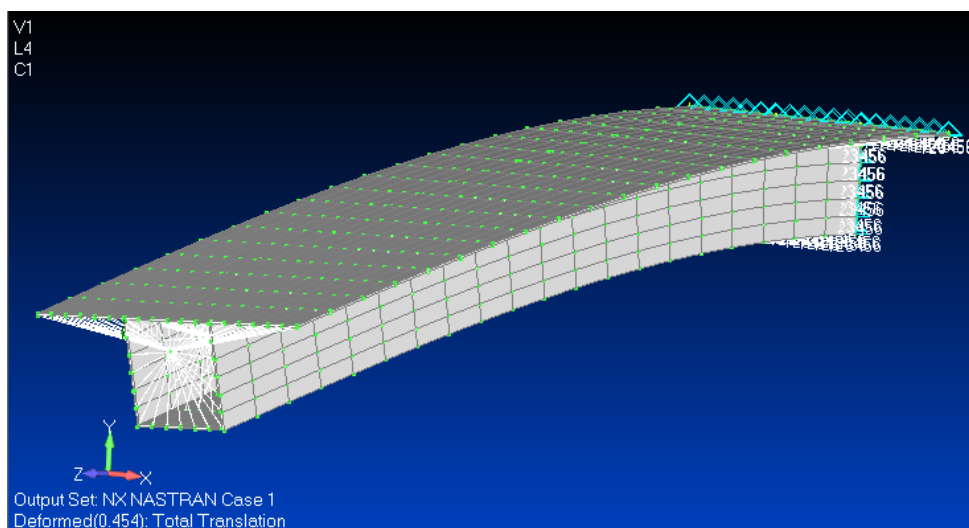


*Figure 6.3. Model in FEMAP employing 780 quadrilateral solid finite elements.
Deflection is displayed along the length of the beam.*

The existence of diaphragms ensured the absence of local distortional phenomena of
the cross sectional profiles. According to the HEPCJ, Fig. 6.4a shows the deformed
shape and total translation of the beam displayed in Fig. 6.3 employing 2 diaphragms
(one at midspan and one at the free edge) while Fig. 6.4b is the same but without the
employment of any diaphragms. Results of models displayed in Figs. 6.3 and 6.4a,
which are similar to each other, almost coincide with the results obtained by the
proposed beam formulation of Chapter 4. However, it is obvious from Fig. 6.4b that the
absence of diaphragms leads to a larger total translation by 18% due to the
development of distortional effects. In addition to this, the same behavior to the model
of Fig. 6.4b is predicted by the proposed formulation of Chapter 5. Thus, HEPCJ
requires a reasonable number of diaphragms for this particular case. This can be
validated when values of stresses are evaluated.

Afterwards, the same beam, as previously described, is considered curved having
the same length and radius of curvature $R = 6.366\,m$  forming an arc of 90° angle in top

view. In Fig. 6.5 two models of the beam implemented in FEMAP (2010) employing FEM quadrilateral solid elements are shown. The difference between the two models is in the use of diaphragms in the cross section plane. In the first one 13 diaphragms have been employed while in the second model only one. The beams are subjected to a vertical concentrated load $P_y = 1000\,kN$ applied at the centroid of their free end cross sections this time. In the same figure the total deflections are also recorded. It is worth here noting that the placement of the rigid diaphragms along the length of the curved beam becomes quite cumbersome due to the complexity of the solid model.
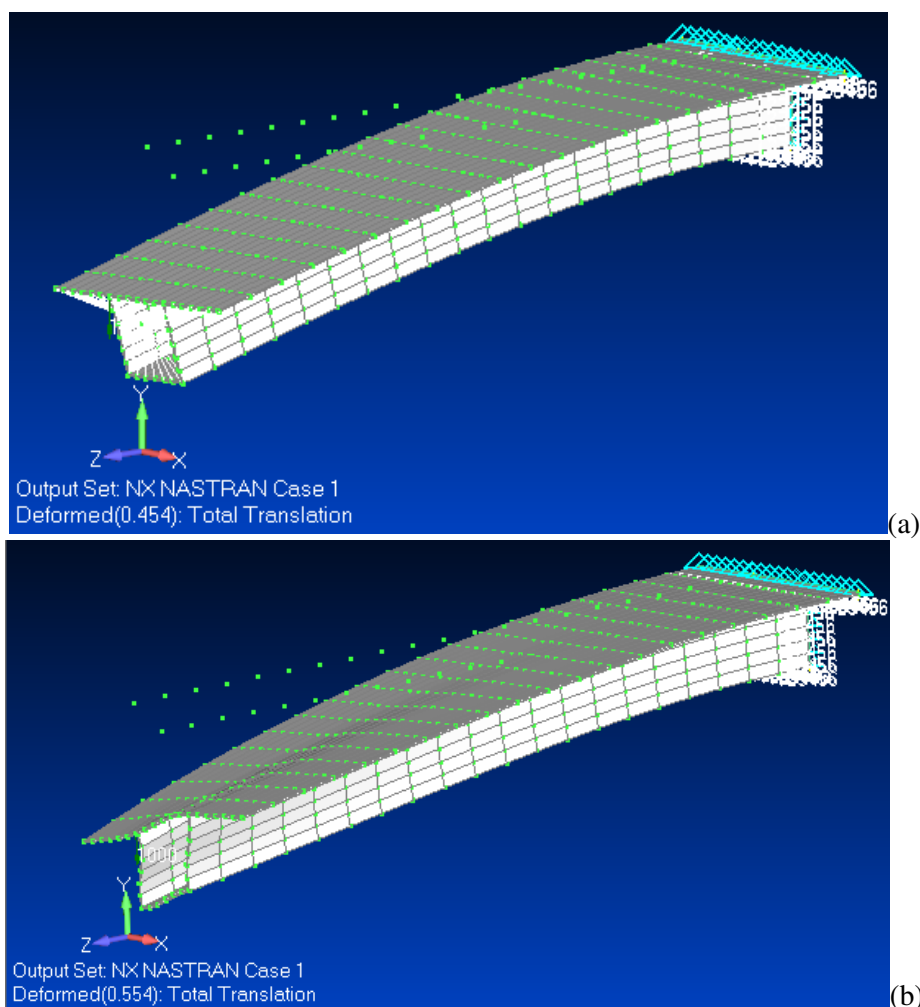


Figure 6.4. Deformed shapes and total vertical translation of the beam with the box-shaped cross section of Fig. 3.15 (a) for 2 diaphragms and (b) without diaphragms.

In addition to this, much more quadrilateral solid elements have been employed comparing to the straight beam formulation (Fig. 6.3) for accuracy reasons. Comparing the deformed shapes of the beams, it is obvious that the existence of diaphragms ensures indeed the absence of local distortional phenomena of the cross sectional profiles along the arc length while the total maximum translation is reduced by 46%. Due to the very thin-walled structure of the cross section, a plate model in FEMAP

(2010) has also been employed for comparison reasons with the solid model and in order to detect any possible locking phenomena present.

In Table 6.2 the values of the kinematical components $v(x)$, $\theta_x(x)$ and $\theta_Z(x)$ for the vertical force $P_y$ concentrically applied at the free edge of the beam are presented for i) proposed curved beam model of Chapter 4 with cubic NURBS (Ch. 4-NO dist.), ii) 1500 quadrilateral plate elements with 13 diaphragms (FEMplate 13 Diaph.), iii) 1500 quadrilateral plate elements with 1 diaphragm (FEMplate 1 Diaph.), iv) 1500 quadrilateral plate elements with 2 diaphragms (FEMplate 2 Diaph.) according to guidelines previously mentioned, v) 10976 quadrilateral solid elements
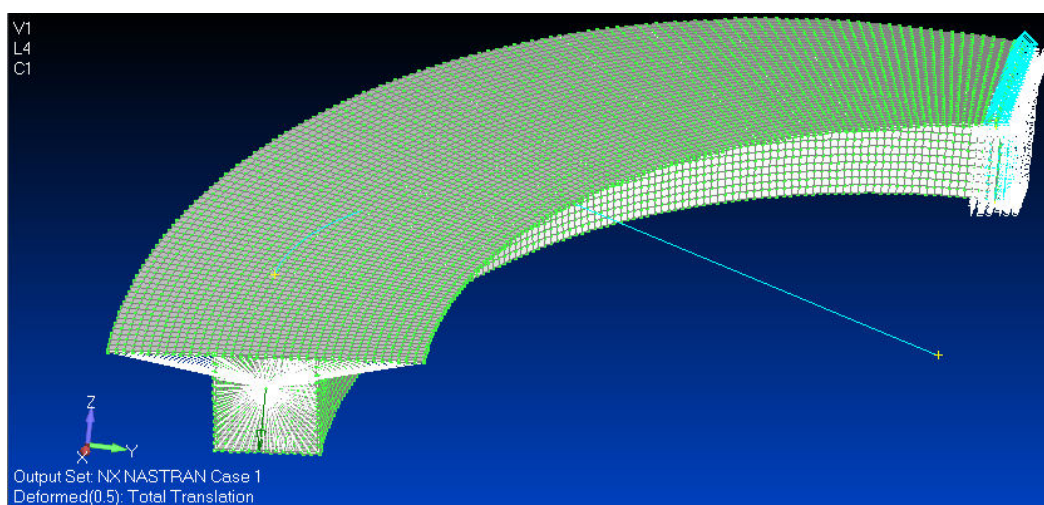


(a)
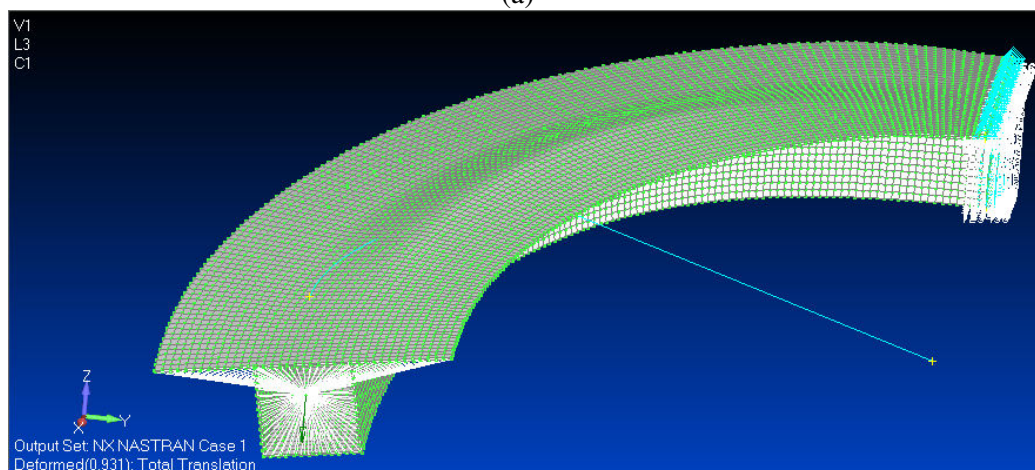


(b)

*Figure 6.5. Deformed shapes of models in FEMAP employing 10976 quadrilateral solid finite elements and (a) 13 diaphragms or (b) one diaphragm.*

with 13 diaphragms in FEMAP (2010) (FEMsolid 13 Diaph.), vi) 10976 quadrilateral solid elements with 2 diaphragms in FEMAP (2010) (FEMsolid 2 Diaph.) according to guidelines previously mentioned, vii) proposed curved beam model of Chapter 5 with cubic NURBS (Ch. 5-1 Diaph.) and viii) 10976 quadrilateral solid elements with one diaphragm in FEMAP (2010) (FEMsolid 1 Diaph.). Analysis with cubic NURBS in the

model of Chapter 4 gives results closer to the solid model with diaphragms, as it is expected, while model of Chapter 5 is closer to solid model with 1 diaphragm due to the arising distortional effects. The results obtained by the analysis of the solid model with diaphragms almost agree with those obtained by the plate model with diaphragms (discrepancies around 1%). However, it is important to notice that the results obtained by the respective models with only 1 diaphragm differ from each other (discrepancies vary from 15 to 23%). The solid model seems to be stiffer than the plate one while the different displacement values are exclusively related to distortional phenomena (mainly attributed to torsion) since the corresponding models with diaphragms (no distortion) show the same level of accuracy. Moreover, regarding the proposed model of Chapter 5 additional higher modes need to be employed in the displacement field due to the very

| | | $v(m)$ at $x=L$ | $\theta_x(rad)$ at $x=L$ | $\theta_Z(rad)$ at $x=L$ |
|---|---|---|---|---|
| $P_y$ Lateral Loading | 4 cubic NURBS (Ch. 4-NO dist.) | 0.4879 | -0.0202 | -0.0742 |
| | FEMplate 13 Diaph. | 0.4701 | -0.0231 | -0.0691 |
| | FEMplate 2 Diaph. | 0.5516 | -0.0290 | -0.0812 |
| | FEMplate 1 Diaph. | 0.9748 | -0.0951 | -0.1470 |
| | FEMsolid 13 Diaph. | 0.4647 | -0.0229 | -0.0685 |
| | FEMsolid 2 Diaph. | 0.5346 | -0.0279 | -0.0790 |
| | 8 cubic NURBS (Ch. 5-1 Diaph.) | 0.7844 | -0.0650 | -0.111 |
| | FEMsolid 1 Diaph. | 0.8215 | -0.0726 | -0.1235 |

*Table 6.2. Kinematical components of a curved beam with the cross section shown in Fig. 3.15 for vertical load and various numerical models.*

thin-walled nature of this cross section. It is worth here noting that if diaphragms are placed in the solid model according to the guidelines (2 diaph. case), the vertical translation is more than the proposed formulation of Chapter 4 (Ch. 4-NO dist.) by 8.7%. Additionally, the angle of twist is increased by 25% and the angle of rotation due to bending by 6%. Discrepancies are slightly larger comparing to the corresponding plate model. This proposed curved beam element is obviously stricter regarding the placement of diaphragms in terms of safety against distortional effects comparing to solid and plate models. This implies the use of more diaphragms comparing to those specified by the guidelines. Additionally, comparing stresses between different solid

models, it is proved that the normal stress due to distortion is more than the specified 10% of the normal stress due to bending for the 2 diaph. model.

A parametric study considering different radii of curvature for the same beam length and cross section has been conducted and different models have been examined. In Table 6.3 the discrepancies between the proposed curved beam formulation of Chapter 4 (Ch. 4-NO dist.) and the model with the diaphragmatic arrangement according to the guidelines have been compiled (FEMsolid 2Diaph.). It is evident that as the curvature of the beam $(1/R)$ becomes greater, the "error" of the specified diaphragmatic model becomes larger in an exponential rate and this rate seems to be greater for torsion. In addition to these, considering the solid model with no diaphragms and comparing to the other models, it seems that distortional effects are of more importance for large curvatures and a more refined treatment should be considered. It should also be noted that that the high ratios of the dimensions to thickness of the cross section's walls is also an important factor, especially for torsion.



| | | $v(\%)$ at $x{=}L$ | $\theta_x(\%)$ at $x{=}L$ | $\theta_Z(\%)$ at $x{=}L$ |
|---|---|---|---|---|
| $P_y$ Lateral Loading | R=∞ | 0.00 | 0.64 | 0.00 |
| | R=28.65m | 1.09 | 1.41 | 1.06 |
| | R=12.73m | 3.03 | 3.40 | 1.91 |
| | R=6.37m | 8.73 | 27.60 | 6.08 |

*Table 6.3. Discrepancies (%) in kinematical components' values for different radii of curvature between the proposed model and those according to guidelines.*

Considering the free vibration problem of the aforementioned curved beam, the Table 4.10 is recalled. In addition to the values compiled in that Table, the eigenfrequencies for the 2-diaphragmatic case have been added for comparison reasons in Table 6.4. Comparing the values of higher models with 1 or 2 diaphragms, it is obvious that are closer to each other than in comparison with the values of the solid model with 13 diaphragms or the proposed formulation of Chapter 4 (Ch. 4-NO dist.).

| Mode Number | FEMsolid 1 Diaph. | FEMsolid 2 Diaph. | FEMsolid 13 Diaph. | 10cubic NURBS (Ch.4-NO dist.) |
|---|---|---|---|---|
| 1 | 0.1172 | 0.1416 | 0.1548 | 0.1317 |
| 2 | 0.2556 | 0.2615 | 0.2704 | 0.2191 |
| 7 | 0.3262 | 0.3644 | 1.0436 | 1.1042 |
| 8 | 0.3562 | 0.3799 | 1.4233 | 1.2311 |
| 9 | 0.4022 | 0.4761 | 1.5021 | 1.3345 |

*Table 6.4. Eigenfrequencies of the beam of Fig. 6.5.*

### 6.4.3 Box-shaped Monosymmetric cross section ($t/d = 0.086$, $d/L = 0.086$)

This beam has the box-shaped cross section shown in Fig. 4.18 and the geometric constants compiled in Table 4.11. Its dimensions to thickness ratios are almost the same with the doubly symmetric box-shaped cross section of example 6.4.1 for comparison reasons. Similarly to that case, either 6 or 7 intermediate diaphragms are required to be employed in order to prevent distortion according to AASHTO or HEPCJ, respectively. The curved beam model examined has the following characteristics: $E = 3E7\,kN/m^2$, $G = 1.5E7\,kN/m^2$, $L = 40\,m$, $R = 25.465\,m$. It is subjected to a concentrated load either $P_y = 10000\,kN$ concentrically applied at its free end.

Additionally to Tables 4.14 and 5.10, in Table 6.5 the values of the kinematical components $v(x)$, $\theta_x(x)$ and $\theta_Z(x)$ for the vertical force $P_y$ concentrically applied at the free edge of the beam are presented for i) proposed curved beam model of Chapter 4 with cubic NURBS (Ch. 4-NO dist.), ii) 2714 quadrilateral solid elements with 1 diaphragm in FEMAP (2010) (FEMsolid), iii) 2714 quadrilateral solid elements with 16 diaphragms in FEMAP (2010) for comparison reasons (FEMsolid 16 Diaph.), iv) 2714 quadrilateral solid elements with 7 diaphragms according to guidelines of HEPCJ (1988) in FEMAP (2010) (FEMsolid 7 Diaph.), v) 2714 quadrilateral solid elements with 2 diaphragms for comparison reasons in FEMAP (2010) (FEMsolid 2 Diaph.) and vi) 2714 quadrilateral solid elements with 4 diaphragms for comparison reasons in FEMAP (2010) (FEMsolid 4 Diaph.).

| | | $v(m)$ at $x=L$ | $\theta_x(rad)$ at $x=L$ | $\theta_Z(rad)$ at $x=L$ |
|---|---|---|---|---|
| | 4 cubic NURBS (Ch. 4-NO dist.) | 0.3197 | -0.007029 | -0.0104 |
| | FEMsolid 1 Diaph. | 0.3547 | -0.00867 | -0.0115 |
| $P_y$ Lateral Loading | FEMsolid 7 Diaph. | 0.2914 | -0.00756 | -0.0090 |
| | FEMsolid 16 Diaph. | 0.2746 | -0.00778 | -0.0081 |
| | FEMsolid 2 Diaph. | 0.3256 | -0.00782 | -0.0103 |
| | FEMsolid 4 Diaph. | 0.3021 | -0.00753 | -0.0094 |

*Table 6.5. Kinematical components of the beam of Fig. 4.20 for vertical load.*

It is worth nothing here that when using 16 diaphragms, the vertical displacement is reduced by 23% while the angle of twist and rotation due to bending are reduced by 10% and 30%, respectively, comparing to the arrangement with 1 diaphragm. The differences in the corresponding values of the models with 2 and 4 diaphragms from those of the model with 1 diaphragm are larger in a disproportionate way when comparing the corresponding values of the same models to those of the model with 7 diaphragms. In addition to this, the proposed formulation gives results closer to the solid model with two diaphragms. Regarding the values of stresses, the discrepancies in shear stresses between models with 2, 4 and 7 diaphragms are not of much importance in comparison with those in normal stresses. However, regarding normal stresses $\sigma_{zz}$ and $\sigma_{yy}$, slightly different values arise for models with 4 and 7 diaphragms. Additionally, the 2-diaphragmatic model exhibits stresses closer to the model with 4 diaphragms than that with 1 diaphragm. These imply that distortional effects are not of the same importance as considered in the guidelines and the use of the numbers of diaphragms specified make the solid model stiffer than it should be in real resulting in uneconomic design practices for a case like this one.

Moreover, the free vibration problem is studied and the ten first eigenfrequencies are evaluated and compiled in Table 6.6 for the solid models and the proposed one in Chapter 4 (Ch. 4- NO dist.) analyzed employing NURBS. The values of the proposed formulation are closer to the solid model with 1 or 16 diaphragms for the first five eigenfrequencies and closer to the solid one with 16 diaphragms for the last three. However, regarding the design quantities, the first eigenfrequencies are of main interest. Thus, it is implied that distortion can be prevented with few number of diaphragms.

| *Mode Number* | FEMsolid 1 Diaph. | FEMsolid 16 Diaph. | cubic NURBS (Ch. 4- NO dist.) |
|---|---|---|---|
| 1 | 0.0488 | 0.0541 | 0.0412 |
| 2 | 0.1408 | 0.1457 | 0.1203 |
| 3 | 0.1905 | 0.2208 | 0.2501 |
| 4 | 0.3002 | 0.3885 | 0.3200 |
| 5 | 0.4643 | 0.5033 | 0.4452 |
| 6 | 0.5309 | 0.6481 | 0.6465 |
| 7 | 0.6299 | 0.8718 | 0.7046 |
| 8 | 0.6797 | 1.0252 | 0.9412 |
| 9 | 0.7125 | 1.1320 | 1.1889 |
| 10 | 0.7361 | 1.4439 | 1.3252 |

*Table 6.6. Eigenfrequencies of the beam of Fig. 4.20.*

### 6.4.4 Box-shaped Monosymmetric cross section ($t/d = 0.1$, $d/L = 0.065$)

The box-shaped cross section shown in Fig. 4.24 with the geometric constants compiled in Table 4.15. The curved beam model considered in Chapters 4 and 5 is examined either as cantilever of clamped for the static problem.

According to guidelines previously mentioned regarding the placement of intermediate diaphragms, either 5 (AASHTO, 1993) or 6 (HEPCJ, 1988) diaphragms should be at least employed in order to fulfill limitations. Considering a cantilever beam, as the less favorable case in terms of boundary conditions, under a concentrated load $P_y = 3000\,kN$ eccentrically applied at its free end, several diaphragmatic arrangements have been performed. The distributions of the main displacements and the maximum stresses arising have been illustrated in Fig. 6.6.
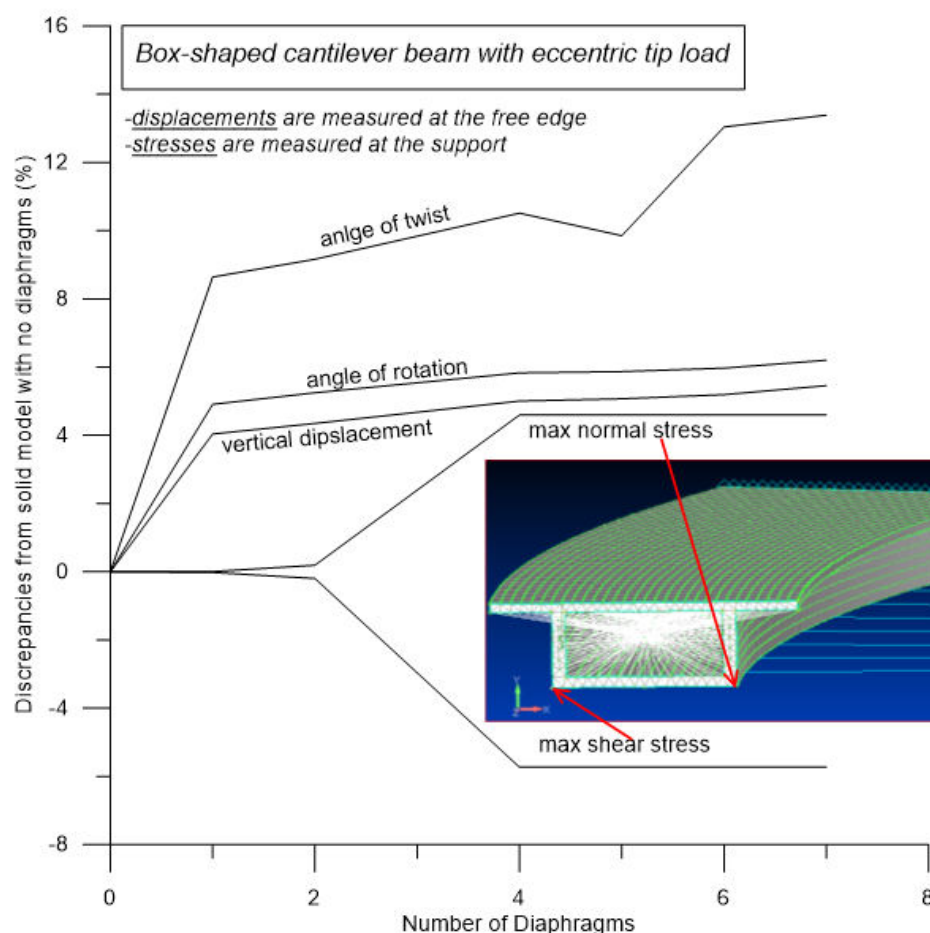


*Figure 6.6. Discrepancies from solid model without diaphragms for a cantilever beam with the cross section shown in Fig. 4.24.*

The proposed formulation in Chapter 4 with NURBS coincides with the FEM model of 6600 triangular solid elements and one rigid diaphragm created with FEMAP (2010) (errors around 0% for displacements and stress resultants). The discrepancies between the proposed formulation and the solid model without any diaphragms are quite small (less than 5%) and only for the angle of twist the difference becomes larger (8.6 %). This implies that the distortion is not of much importance for this cross section and this structural arrangement. Regarding the maximum normal and maximum shear stresses, it seems that after the placement of 4 diaphragms not much difference takes place and even for less than 4 diaphragms the "errors" arising are around 5%. Thus,

guidelines might lead to cost ineffective solutions for this particular curved beam element.

In addition to these, the clamped model of the same beam is considered in Fig. 6.7. Similarly to the previous case of the cantilever beam, the proposed formulation agrees to the solid model with one diaphragm. The discrepancies between the models become larger for displacements as the number of diaphragms increases comparing to the previous case of the cantilever beam. However, stresses, which are of more importance in this case due to the fact that the magnitude of displacements is quite low, are almost unaffected by the placement of diaphragms. Thus, it seems that boundary conditions need to be considered in the specification of diaphragms.
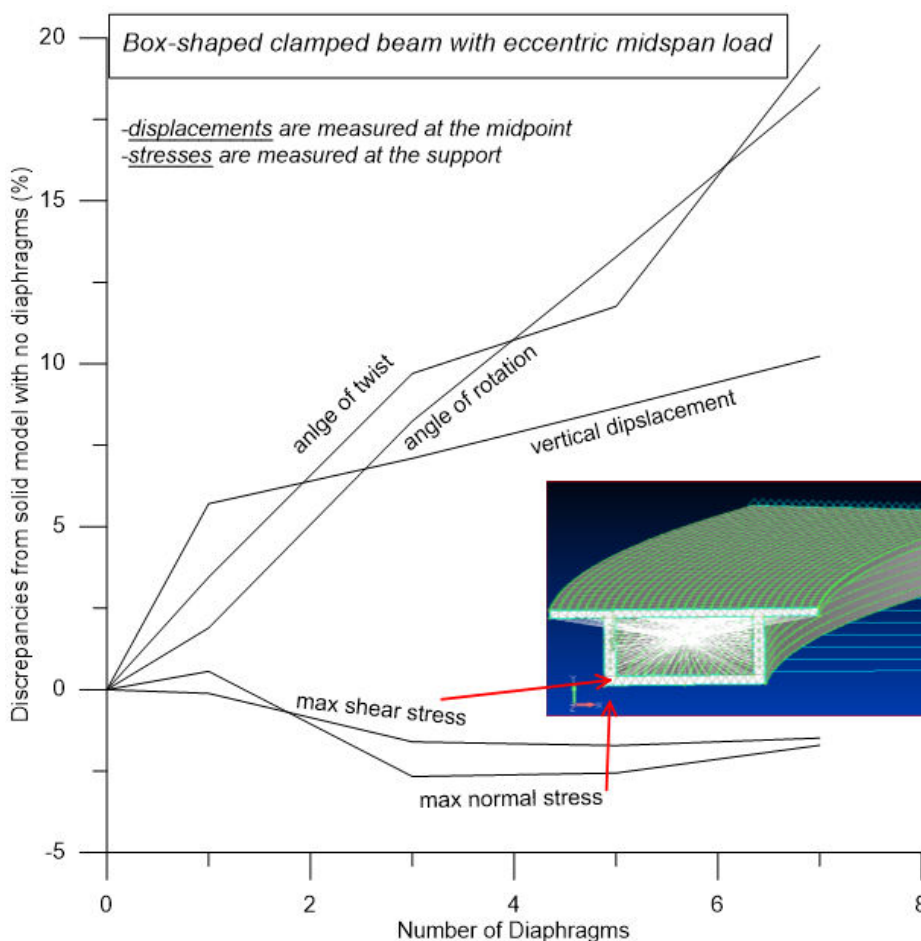


*Figure 6.7. Discrepancies from solid model without diaphragms for a clamped beam with the cross section shown in Fig. 4.24.*

Referring back to Fig. 4.25 of Chapter 4, it should be noted that the placement of the diaphragm in the solid model of FEMAP (2010) causes the reduction of the vertical displacement throughout the application of the dynamic load. The proposed formulation of Chapter 4 which does not considers distortion is closer to this model implying again that much less diaphragms (possibly only 1 instead of 5 or 6) than those specified are adequate to prevent distortional effects.

## 6.5 Concluding Remarks

In this chapter, the proposed formulations of previous chapters are employed for the static and dynamic analysis of straight or curved beams together with FEM solid models in order to further highlight their importance when considering the advantages of beam models compared with solid ones and assess the design guidelines regarding the placement of intermediate diaphragms to prevent distortion. Results have been obtained after placing intermediate diaphragms in the solid models according to guidelines of (AASHTO, 1993) and (HEPCJ, 1988). The main conclusions that can be drawn from this investigation are:

i.  Regarding very thin-walled structures with $t/d < 0.05$ (example 6.4.2), guidelines for spacing of diaphragms to prevent distortional effects seem to lead to more unsafe solutions when curved beams are considered due to the higher magnitude of warping and mainly the distortional one. In such cases the magnitude of the curvature is of importance.

ii.  In structures with higher thickness to width ratios (examples 6.4.1, 6.4.3 and 6.4.4), it seems that the guidelines applied in this study might give uneconomic solutions in order to moderate distortional effects, especially for curved geometries.

iii.  The specification of the maximum spacing of intermediate diaphragms should be encountered as a multi-parameter problem considering cross sectional geometry together with the plan view dimensions and boundary conditions.

iv.  The use of diaphragms seems to moderate the dynamic load impact on the structure.

Finally, material of the beam is also important and its influence on the number of diaphragms needs to be further investigated as structures of different materials are treated differently in practice (i.e. steel or concrete bridge decks).

# Chapter 7

# Chapter **7**

# Concluding Remarks

## 1.1 Conclusions of the conducted research and discussion

In this doctoral thesis, a series of problems concerning the development of advanced curved beam theories have been studied and solved. The main issues addressed are the following:

> ➢ Generalized warping (including shear lag effects due to flexure and torsion) of curved beams,
> ➢ Distortional analysis of curved beams by taking into account Poisson ratio influence,
> ➢ Application of the Isogeometric Analysis to the advanced beam theories proposed and
> ➢ Application of the design guidelines which specify the maximum spacing of intermediate diaphragms and assessment through comparisons of the proposed curved model to the corresponding solid or plate ones.

For the solution of the examined problems, innovative methods have been applied based on Isogeometric tools (B-splines and NURBS) either integrated in FEM or AEM. The main conclusions and aspects of discussion that can be drawn from this doctoral thesis are:

i. Highly accurate results can in general be obtained using B-splines in the AEM technique as well as NURBS in FE beam formulations for the static and dynamic analysis of the proposed beam elements. Computational cost and post-processing of the results is significantly reduced by the use of NURBS comparing to FEM plate and solid models. Employment of NURBS in FEM and B-splines in AEM with or without knot insertion results in higher convergence rates, too.

ii. The curve used to approximate the fictitious load affects the accuracy of the method and this might cause the necessity of knot insertion or degree elevation when employing B-splines or NURBS in the AEM. Different section properties (especially the warping constant) affect the order of the B-splines and NURBS that have to be employed. In order to obtain errors closer to the AEM with Isogeometric tools and values closer to those of the analytical solution, quadruple collocation points should be employed as nodes in the original AEM.

iii. Classical Nonuniform Torsion theory fails to give accurate results in the evaluation of primary warping distribution and axial stresses or bimoments due to primary warping in the case of closed cross sections. Results are quite close to those obtained when employing the Vlasov model. The same case is for the Saint Venant model regarding torsion and the Euler-Bernoulli model regarding bending.

iv.   AEM technique with constant elements exhibits no branching in a normalized frequency spectrum, as it is the case in quadratic FEM elements, while it maintains accuracy in the results of high frequencies. Quadratic elements in AEM depict a branch with much smaller impact than FEM, while they improve the accuracy comparing to AEM with constant elements.

v.    Regarding the generalized dynamic problem of beams, in cases of very thin-walled beams, which are susceptible to warping and torsional phenomena, more elements need to be used for the AEM technique with constant or quadratic elements. Quartic and cubic B-splines with or without knot insertion can help to reduce number of unknowns drastically while keep the accuracy on a high level.

vi.   Regarding generalized curved beam analysis, the magnitude of Bimoment is in general not negligible comparing to the total Torsional Moment and both moments can also be of the same order of magnitude depending on the cross section. In addition to this, secondary Torsional Moments can be significant and should also be considered in the analysis. These higher order additional stress resultants can now be integrated in the analysis' results and plotted in alignment with the curved geometry due to the use of Isogeometric tools.

vii.  FEM curved beam formulations based on Timoshenko beam theory exhibit a significant loss in accuracy for higher frequencies even for doubly symmetric cross sections. Thus, warping effects need to be taken into account in the dynamic analysis.

viii. Displacement and bending modes dominate over the torsional ones when considering box-shaped cross sections due to higher torsional rigidities comparing to the open shape cross sections.

ix.   Regarding very thin-walled structures, guidelines for spacing of diaphragms to prevent distortional effects seem to lead to more unsafe solutions when curved beams are considered due to the high level of warping and mainly the distortional one. In such cases the magnitude of the curvature is of importance. However, in stiffer structures with higher thickness to width ratios, it seems that the guidelines applied might give uneconomic solutions in order to moderate distortional effects. Thus, the specification of the maximum spacing of intermediate diaphragms should be encountered as a multi-parameter problem considering cross sectional geometry together with the plan view dimensions.

x.    Poisson effects are in general not negligible even if distortion is not of importance. In addition to this, it seems that when material constants are larger, Poisson ratio affects the magnitude of stresses more.

xi.   In general, open shaped cross sections suffer more from warping while close ones from distortion. The consideration of up to secondary higher order phenomena is generally accurate. However, in some cases of very thin-walled cross sections either open or closed shaped, tertiary phenomena might need to be considered. As a rule of thumb in choosing the least number of modes in order to achieve the maximum accuracy when the proposed method is employed, some limitations have been provided.

xii.   Increase in curvature causes increase in the distortion due to torsion for thin-walled box-shaped cross sections. Cross sections with cantilever plates at one side undergo less severe distortional effects due to the fact that bending resisting mechanisms are of importance, too.

xiii.  The ratios of distortional and warping Moments to the bending ones can be indicative of the behavior of the curved beam and offer an additional insight into the resisting mechanisms that dominate.

xiv.   Monossymetric cross sections are more susceptible to higher order phenomena due to this inherent property of their shape.

xv.    Composite cross sections of optimal material placement can significantly reduce stresses and, thus, reduce the number of intermediate diaphragms needed to moderate distortional effects.

## 1.2   Suggestions for future research

This doctoral thesis is a contribution to the advanced structural analysis of spatial curved beam elements of arbitrary cross section with the aid of Isogeometric tools. In what follows suggestions that will expand and further improve the presented work are proposed. More specifically

➢ Generalized warping and distortional effects can be incorporated in the geometrically nonlinear analysis of curved beams,

➢ Dynamic distortional analysis of curved beams can be conducted with the aid of Isogeometric tools,

➢ Curvature in two planes can be introduced in order to develop the proposed curved beam element further and broaden its applications,

➢ Placement of diaphragms can be investigated in order to conduct optimization analysis regarding their spacing and positions and

➢ Different constitutive relations for the materials which may compose the cross section of the beam (e.g. orthotropic composites, shape memory alloys) can be explored.

# Appendices

# Appendix A.1

# A.1  The Analog Equation Method for ordinary differential equations

### A.1.1  Basic concepts of the Analog Equation Method

The main concept of the Analog Equation Method can be mathematically represented as follows: Consider the boundary value problem

$$N(u) = g(x), \quad x \in \Omega \qquad \qquad \text{(A.1.1a)}$$

$$B(u) = \overline{g}(x), \quad x \in \Gamma \equiv \partial\Omega \qquad \qquad \text{(A.1.1b)}$$

where $N(\ )$, $B(\ )$ are linear or nonlinear differential operators with constant or variable coefficients, $g(x)$ is a source density or an external loading function of known distribution and $u(x)$ is the sought solution of the problem. Consider $N^*(\ )$ being a linear or nonlinear differential operator of the same order with $N$. By applying this operator to the solution of the problem $u(x)$, we are able to formulate the following equation

$$N^*(u) = q(x), \quad x \in \Omega \qquad \qquad \text{(A.1.2)}$$

where $q(x)$ is an unknown source density function. Equation (A.1.2) is called analog equation of the initial problem and in combination with the boundary conditions (A.1.1b) yields the solution of the original problem, provided that a proper source density function $q(x)$ is first determined. The establishment of this function, which hereinafter will be referred to as fictitious source, density function or fictitious load, is one of the essential features of AEM. The implementation of the method leads to the numerical establishment of fictitious load $q(x)$ in $\Omega$, through the solution of a system of linear or nonlinear algebraic equations. The boundary value problem defined by analog equation (A.1.2) and boundary condition (A.1.1b) is called equivalent or substitute problem. It is noted that the analog equation is defined by a differential operator of the same order with that of the initial problem (A.1.1a) in order for the substitute problem to be subjected to the same number of boundary conditions as well as to ensure the continuity of the solution and its derivatives up to the order of the initial operator $N(\ )$ (Babouskos, 2011). Finally, it is noted that AEM can be easily employed for the solution of boundary value problems with more than one unknown functions $u(x)$ by formulating equation (A.1.2) for each one of the unknowns.

### A.1.2  AEM for ordinary differential equations of the 4$^{th}$ order

Consider the one-dimensional boundary value problem

$$N\left(u(x), \frac{du(x)}{dx}, \frac{d^2u(x)}{dx^2}, \frac{d^3u(x)}{dx^3}, \frac{d^4u(x)}{dx^4}\right) = g(x), \quad x \in (0, L) \tag{A.1.3a}$$

$$\alpha_1 u(x) + \alpha_2 B_1\left(u(x), \frac{du(x)}{dx}, \frac{d^2u(x)}{dx^2}, \frac{d^3u(x)}{dx^3}\right) = \alpha_3, \quad x = 0, L \tag{A.1.3b}$$

$$\beta_1 \frac{du(x)}{dx} + \beta_2 B_2\left(u(x), \frac{du(x)}{dx}, \frac{d^2u(x)}{dx^2}\right) = \beta_3, \quad x = 0, L \tag{A.1.3c}$$

where $N(\ )$ are linear or nonlinear $4^{th}$ order differential operators, $B_1(\ )$, $B_2(\ )$ are linear or nonlinear $3^{rd}$ and $2^{nd}$ order one-dimensional operators, respectively, $\alpha_i, \beta_i$ $(i = 1, 2, 3)$ are functions specified at $x = 0, L$, $g(x)$ is a known source denstity function defined at $(0, L)$ and $u(x)$ is the sought solution of the problem, having continuous derivatives up to the $4^{th}$ order in $(0, L)$ and up to the $3^{rd}$ order at $x = 0, L$. According to the analog equation principle, the substitute problem is also of fourth order, thus the following equation can be formulated, as the simplest analog equation with known fundamental solution

$$\frac{d^4u(x)}{dx^4} = q(x) \quad x \in (0, L) \tag{A.1.4}$$

From a physical point of view, equation (A.1.4) describes the flexural response of a beam according to classical (Euler-Bernoulli) beam theory with stiffness $EI = 1$, under the action of a distributed loading $q(x)$. According to section A.1.1, equation (A.1.4) indicates that the solution of the original problem (A.1.3a) could be obtained as the solution of this equation subjected to the same boundary conditions (A.1.3b,c), provided that the fictitious loading $q(x)$ will be first determined. This can be accomplished as following: The weak form of the analog equation is written as

$$\int_L^0 \left(\frac{d^4u(x)}{dx^4} - q(x)\right) u^*(x, \xi)dx = 0 \Rightarrow \int_L^0 \frac{d^4u(x)}{dx^4} u^*(x, \xi)dx - \int_L^0 q(x)u^*(x, \xi)dx = 0 \tag{A.1.5}$$

where $u^*(x, \xi)$ is a trial function in the sense of Galerkin weighted residuals approach. In order to apply a BEM procedure, the fundamental solution of the one-dimensional Laplace operator is adopted as a trial $u^*(x, \xi)$ function, which is a partial solution of the differential equation

$$\frac{d^4 u^*(x,\xi)}{dx^4} = \delta(x-\xi)$$

(A.1.6)

where $\delta(x-\xi)$ is the Dirac's function in one dimension (Katsikadelis, 2002a). The fundamental solution $u^*(x,\xi)$ is obtained as (Sapountzakis and Katsikadelis 2000)

$$u^*(x,\xi) = \frac{1}{12} l^3 \left(2 + |\rho|^3 - 3|\rho|^2\right)$$

(A.1.7)

with $\rho = r/l$, $r = x-\xi$ being the distance between $\xi$ and $x$, where $x$ is a constant source point while $\xi$ runs through the interval $[0,L]$. By applying sequential integrations by parts in the first integral equation (A.1.5), substituting equations (A.1.4) and (A.1.7) and exploiting the property of the Dirac's function, yields

$$u(\xi) = \int_0^L \Lambda_4(x,\xi)q(x)dx -$$

$$\left[\Lambda_4(x,\xi)\frac{d^3 u(x)}{dx^3} - \Lambda_3(x,\xi)\frac{d^2 u(x)}{dx^2} + \Lambda_2(x,\xi)\frac{du(x)}{dx} - \Lambda_1(x,\xi)u(x)\right]_0^L$$

(A.1.8)

where $\Lambda_i(r)$ $(i=1...4)$ are the kernels (derivatives of $u^*(x,\xi)$), defined as

$$\Lambda_1(x,\xi) = \frac{d^3 u^*(x,\xi)}{dx^3} = \frac{1}{2}\operatorname{sgn}\rho$$

(A.1.9a)

$$\Lambda_2(x,\xi) = \frac{d^2 u^*(x,\xi)}{dx^2} = -\frac{1}{2}l(1-|\rho|)$$

(A.1.9b)

$$\Lambda_3(x,\xi) = \frac{d\, u^*(x,\xi)}{dx} = \frac{1}{4}l^2 |\rho|(|\rho|-2)$$

(A.1.9c)

$$\Lambda_4(x,\xi) = u^*(x,\xi) = \frac{1}{12}l^3 \left(2 + |\rho|^3 - 3|\rho|^2\right)$$

(A.1.9d)

with $\operatorname{sgn}(\ )$ being the signum function, defined as

$$\operatorname{sgn}(r) = \begin{cases} +1, & r > 0 \\ -1, & r < 0 \end{cases}$$

(A.1.10)

for $r = 0$, signum function is not defined.

Relation (A.1.8) constitutes the integral representation of the solution as a function of the fictitious load and boundary quantities. Particularly, if $q(x)$ and all boundary values $\left( u(x), \dfrac{du(x)}{dx}, \dfrac{d^2u(x)}{dx^2}, \dfrac{d^3u(x)}{dx^3} \right)$ at the bar ends $0, L$ are known, $u(\xi)$ can be calculated at any internal point of the bar. Differentiating (A.1.8), the expressions for the derivatives of $u(\xi)$ can be derived

$$\frac{du(\xi)}{d\xi} = -\int_0^L \Lambda_3(x,\xi)q(x)dx -$$

$$\left[ -\Lambda_3(x,\xi)\frac{d^3u(x)}{dx^3} + \Lambda_2(x,\xi)\frac{d^2u(x)}{dx^2} - \Lambda_1(x,\xi)\frac{du(x)}{dx} \right]_0^L \tag{A.1.11a}$$

$$\frac{d^2u(\xi)}{d\xi^2} = \int_0^L \Lambda_2(x,\xi)q(x)dx - \left[ \Lambda_2(x,\xi)\frac{d^3u(x)}{dx^3} - \Lambda_1(x,\xi)\frac{d^2u(x)}{dx^2} \right]_0^L \tag{A.1.11b}$$

$$\frac{d^3u(\xi)}{d^3\xi} = -\int_0^L \Lambda_1(x,\xi)q(x)dx - \left[ -\Lambda_1(x,\xi)\frac{d^3u(x)}{dx^3} \right]_0^L \tag{A.1.11c}$$

where

$$\frac{d\Lambda_1(x,\xi)}{d\xi} = 0 \tag{A.1.12a}$$

$$\frac{d\Lambda_2(x,\xi)}{d\xi} = -\Lambda_1(x,\xi) \tag{A.1.12b}$$

$$\frac{d\Lambda_3(x,\xi)}{d\xi} = -\Lambda_2(x,\xi) \tag{A.1.12c}$$

$$\frac{d\Lambda_4(x,\xi)}{d\xi} = -\Lambda_3(x,\xi) \tag{A.1.12d}$$

Eqns. (A.1.8) and (A.1.11) written for the boundary points $x = 0, L$ constitute a system of four simultaneous integral equations, which are given in matrix form below

$$[E_{21}]\{u_1\} + [E_{22}]\{u_2\} = \{T_2\} \tag{A.1.13}$$

where

$$\{T_2\} = -\begin{Bmatrix} \int_0^L \Lambda_4(x,\xi_0)q(x)dx \\ \int_0^L \Lambda_4(x,\xi_L)q(x)dx \\ \int_0^L \Lambda_3(x,\xi_0)q(x)dx \\ \int_0^L \Lambda_3(x,\xi_L)q(x)dx \end{Bmatrix} = -\begin{Bmatrix} \sum_{j=1}^N q_j F_{1j} \\ \sum_{j=1}^N q_j F_{2j} \\ \sum_{j=1}^N q_j F_{3j} \\ \sum_{j=1}^N q_j F_{4j} \end{Bmatrix} = -\begin{bmatrix} F_{11} & F_{12} & ... & F_{1N} \\ F_{21} & F_{22} & ... & F_{2N} \\ F_{31} & F_{32} & ... & F_{3N} \\ F_{41} & F_{42} & ... & F_{4N} \end{bmatrix}\begin{Bmatrix} q_1 \\ q_2 \\ \vdots \\ q_N \end{Bmatrix} \quad (A.1.14)$$

$$\{u_1\}^T = \left\{ \frac{d^3u(x)}{dx^3}\bigg|_{x=0} \quad \frac{d^2u(x)}{dx^2}\bigg|_{x=0} \quad \frac{du(x)}{dx}\bigg|_{x=0} \quad u(0) \right\} \quad (A.1.15)$$

$$\{u_2\}^T = \left\{ \frac{d^3u(x)}{dx^3}\bigg|_{x=L} \quad \frac{d^2u(x)}{dx^2}\bigg|_{x=L} \quad \frac{du(x)}{dx}\bigg|_{x=L} \quad u(0) \right\} \quad (A.1.16)$$

$$[E_{21}] = \begin{bmatrix} \Lambda_4(0,\xi_0) & -\Lambda_3(0,\xi_0) & \Lambda_2(0,\xi_0) & -(\Lambda_1(0,\xi_0)+1) \\ \Lambda_4(0,\xi_L) & -\Lambda_3(0,\xi_L) & \Lambda_2(0,\xi_L) & -\Lambda_1(0,\xi_L) \\ \Lambda_3(0,\xi_0) & -\Lambda_2(0,\xi_0) & \Lambda_1(0,\xi_0)+1 & 0 \\ \Lambda_3(0,\xi_L) & -\Lambda_2(0,\xi_L) & \Lambda_1(0,\xi_L) & 0 \end{bmatrix} \quad (A.1.17)$$

$$[E_{22}] = \begin{bmatrix} -\Lambda_4(L,\xi_0) & \Lambda_3(L,\xi_0) & -\Lambda_2(L,\xi_0) & \Lambda_1(L,\xi_0) \\ -\Lambda_4(L,\xi_L) & \Lambda_3(L,\xi_L) & -\Lambda_2(L,\xi_L) & \Lambda_1(L,\xi_L)-1 \\ -\Lambda_3(L,\xi_0) & \Lambda_2(L,\xi_0) & -\Lambda_1(L,\xi_0) & 0 \\ -\Lambda_3(L,\xi_L) & \Lambda_2(L,\xi_L) & -(\Lambda_1(L,\xi_L)-1) & 0 \end{bmatrix} \quad (A.1.18)$$

where $N$ is the number of discretization elements. The interval $(0,L)$ is divided into $N$ elements employing the constant element assumption for the fictitious load $q(x)$ which is considered constant in each element and equal to its value at mid-point.

Then, the boundary conditions (A.1.3b,c) are formulated in matrix form as follows

$$[E_{11}]\{u_1\} + [E_{12}]\{u_2\} = \{D_1\} \quad (A.1.19)$$

where $[E_{11}]$, $[E_{12}]$ are 4X4 known coefficient matrices and $\{D_1\}$ is 4X1 known coefficient vector.

Combining eqns. (A.1.13) and (A.1.19), the following is derived

$$\begin{bmatrix} [E_{11}] & [E_{12}] \\ [E_{21}] & [E_{22}] \end{bmatrix} \begin{Bmatrix} \{u_1\} \\ \{u_2\} \end{Bmatrix} = \begin{Bmatrix} \{D_1\} \\ \{0\} \end{Bmatrix} + \begin{Bmatrix} \{0\} \\ \{T_2\} \end{Bmatrix} \rightarrow [E]\{u\} = \{D\} + \{T\}$$
(A.1.20)

where $[E]$ is a square 8X8 matrix, $\{0\}^T = \{0 \quad 0 \quad 0 \quad 0\}$ and $\{u\}, \{D\}, \{T\}$ are 8X1 vectors.

Combining eqn. (A.1.14) and (A.1.20) and the vector $\{T\}$ can be written as follows

$$\{T\} = \begin{bmatrix} [0] \\ -[F_2] \end{bmatrix} \{q\} \rightarrow \{T\} = [F]\{q\}$$
(A.1.21)

where $[0]$ is the 4XN zero matrix and $[F]$ is the 8XN matrix. Substituting eqn. (A.1.21) into eqn. (A.1.20), the following relation is derived

$$[E]\{u\} = \{D\} + [F]\{q\} \rightarrow \{u\} = [E]^{-1}\{D\} + [E]^{-1}[F]\{q\}$$
(A.1.22)

Subsequently, applying the integral representations (A.1.8) and (A.1.11) at the $N$ collocation points, the following relations are derived

$$\{U\} = [A]\{q\} + [C]\{u\}$$
(A.1.23a)

$$\{U'\} = [A']\{q\} + [C']\{u\}$$
(A.1.23b)

$$\{U''\} = [A'']\{q\} + [C'']\{u\}$$
(A.1.23c)

$$\{U'''\} = [A''']\{q\} + [C''']\{u\}$$
(A.1.23d)

where $U, U', U'', U'''$ are the vectors containing the values of the solution and its derivatives ($u(x), u'(x), u''(x), u''(x)$) at collocation points. The coefficients of the $NXN$ square matrices $[A], [A'], [A''], [A''']$ are given by the analytical or the numerical solution of the following integrals

$$A = \int_{\Gamma_j} \Lambda_4(x, \xi_i) q(x) dx$$
(A.1.24a)

$$A' = -\int_{\Gamma_j} \Lambda_3(x, \xi_i) q(x) dx$$
(A.1.24b)

$$A'' = \int_{\Gamma_j} \Lambda_2(x, \xi_i) q(x) dx \tag{A.1.24c}$$

$$A''' = -\int_{\Gamma_j} \Lambda_1(x, \xi_i) q(x) dx \tag{A.1.24d}$$

The $NX8$ $[C], [C'], [C''], [C''']$ matrices are given below

$$[C] = \begin{bmatrix} \Lambda_4(0, \xi_1) & -\Lambda_3(0, \xi_1) & \Lambda_2(0, \xi_1) & -\Lambda_1(0, \xi_1) \\ \vdots & \vdots & \vdots & \vdots \\ \Lambda_4(0, \xi_L) & -\Lambda_3(0, \xi_L) & \Lambda_2(0, \xi_L) & -\Lambda_1(0, \xi_L) \end{bmatrix}$$
$$\begin{bmatrix} & -\Lambda_4(L, \xi_1) & \Lambda_3(L, \xi_1) & -\Lambda_2(L, \xi_1) & \Lambda_1(L, \xi_1) \\ & \vdots & \vdots & \vdots & \vdots \\ & -\Lambda_4(L, \xi_L) & \Lambda_3(L, \xi_L) & -\Lambda_2(L, \xi_L) & \Lambda_1(L, \xi_L) \end{bmatrix} \tag{A.1.25a}$$

$$[C'] = \begin{bmatrix} -\Lambda_3(0, \xi_1) & \Lambda_2(0, \xi_1) & -\Lambda_1(0, \xi_1) & 0 \\ \vdots & \vdots & \vdots & \vdots \\ -\Lambda_3(0, \xi_L) & \Lambda_2(0, \xi_L) & -\Lambda_1(0, \xi_L) & 0 \end{bmatrix}$$
$$\begin{bmatrix} & \Lambda_3(L, \xi_1) & -\Lambda_2(L, \xi_1) & \Lambda_1(L, \xi_1) & 0 \\ & \vdots & \vdots & \vdots & \vdots \\ & \Lambda_3(L, \xi_L) & -\Lambda_2(L, \xi_L) & \Lambda_1(L, \xi_L) & 0 \end{bmatrix} \tag{A.1.25b}$$

$$[C''] = \begin{bmatrix} \Lambda_2(0, \xi_1) & -\Lambda_1(0, \xi_1) & 0 & 0 & -\Lambda_2(L, \xi_1) & \Lambda_1(L, \xi_1) & 0 & 0 \\ \vdots & \vdots & \vdots & 0 & \vdots & \vdots & \vdots & \vdots \\ \Lambda_2(0, \xi_L) & -\Lambda_1(0, \xi_L) & 0 & 0 & -\Lambda_2(L, \xi_L) & \Lambda_1(L, \xi_L) & 0 & 0 \end{bmatrix} \tag{A.1.25c}$$

$$[C'''] = \begin{bmatrix} -\Lambda_1(0, \xi_1) & 0 & 0 & 0 & \Lambda_1(L, \xi_1) & 0 & 0 & 0 \\ \vdots & \vdots & \vdots & 0 & \vdots & \vdots & \vdots & \vdots \\ -\Lambda_1(0, \xi_L) & 0 & 0 & 0 & \Lambda_1(L, \xi_L) & 0 & 0 & 0 \end{bmatrix} \tag{A.1.25d}$$

and their coefficients are calculated with the aid of eqns. (A.1.9).

Substituting eqn. (A.1.22) into eqns. (A.1.23), the following are derived

$$\{U\} = [B]\{q\} + \{R\} \tag{A.1.26a}$$

$$\{U'\} = [B']\{q\} + \{R'\} \tag{A.1.26b}$$

$$\{U''\} = [B'']\{q\} + \{R''\} \tag{A.1.26c}$$

$$\{U'''\} = [B''']\{q\} + \{R'''\} \tag{A.1.26d}$$

where the square matrices $NXN$ can be determined from the following relations

$$[B] = \left[ [A] + [C][E]^{-1}[F] \right] \tag{A.1.27a}$$

$$[B'] = \left[ [A'] + [C'][E]^{-1}[F] \right] \tag{A.1.27b}$$

$$[B''] = \left[ [A''] + [C''][E]^{-1}[F] \right] \tag{A.1.27c}$$

$$[B'''] = \left[ [A'''] + [C'''][E]^{-1}[F] \right] \tag{A.1.27d}$$

and the $NX1$ vectors $\{R\},\{R'\},\{R''\},\{R'''\}$ are given as follows

$$\{R\} = [C][E]^{-1}\{D\} \tag{A.1.28a}$$

$$\{R'\} = [C'][E]^{-1}\{D\} \tag{A.1.28b}$$

$$\{R''\} = [C''][E]^{-1}\{D\} \tag{A.1.28c}$$

$$\{R'''\} = [C'''][E]^{-1}\{D\} \tag{A.1.28d}$$

It should be noted here that in case of homogenous boundary conditions ($\alpha_3 = \beta_3 = 0$) at the ends of the interval, the $\{R\},\{R'\},\{R''\},\{R'''\}$ vectors become equal to zero.

The final step of the AEM is the application of the governing equation of the initial problem (A.1.3a) at the $N$ internal nodal points and subsequently the substitution of the values of the field function $u(x)$ and its derivative at the $N$ internal nodal points according to equations (A.1.23). From the definition of the analog equation (A.1.4) it is apparent that the values of forth derivative of $u(x)$ at the nodal points equals to the corresponding values of the fictitious load vector $q(x)$.

### A.1.3 AEM special case for ordinary differential equations of the 2<sup>nd</sup> order

AEM for 2<sup>nd</sup> order ordinary differential equations is a special case of the previous formulation. Consider the one-dimensional boundary value problem

$$N\left(u(x), \frac{du(x)}{dx}, \frac{d^2u(x)}{dx^2}\right) = g(x), \quad x \in (0, L) \qquad \text{(A.1.29a)}$$

$$\gamma_1 u(x) + \gamma_2 \Gamma_1\left(u(x), \frac{du(x)}{dx}\right) = \gamma_3, \quad x = 0, L \qquad \text{(A.1.29b)}$$

where $N(\ )$ are linear or nonlinear 2$^{nd}$ order differential operators, $\Gamma_1(\ )$ are linear or nonlinear 1$^{st}$ order one-dimensional operators, respectively, $\gamma_i \ (i = 1, 2, 3)$ are functions specified at $x = 0, L$, $g(x)$ is a known source denstity function defined at $(0, L)$ and $u(x)$ is the sought solution of the problem, having continuous derivatives up to the 2$^{nd}$ order in $(0, L)$ and up to the 1$^{st}$ order at $x = 0, L$. According to the analog equation principle, the substitute problem is also of second order, thus the following equation can be formulated, as the simplest analog equation with known fundamental solution

$$\frac{d^2u(x)}{dx^2} = q(x) \quad x \in (0, L) \qquad \text{(A.1.30)}$$

According to section A.1.1, equation (A.1.30) indicates that the solution of the original problem (A.1.29a) could be obtained as the solution of this equation subjected to the same boundary conditions (A.1.29b), provided that the fictitious loading $q(x)$ will be first determined. This can be accomplished as following: The weak form of the analog equation is written as

$$\int_L^0 \left(\frac{d^2u(x)}{dx^2} - q(x)\right) u^*(x, \xi) dx = 0 \Rightarrow \int_L^0 \frac{d^2u(x)}{dx^2} u^*(x, \xi) dx - \int_L^0 q(x) u^*(x, \xi) dx = 0$$

$$\text{(A.1.31)}$$

where $u^*(x, \xi)$ is a trial function in the sense of Galerkin weighted residuals approach. In order to apply a BEM procedure, the fundamental solution of the one-dimensional Laplace operator is adopted as a trial $u^*(x, \xi)$ function, which is a partial solution of the differential equation

$$\frac{d^2u^*(x, \xi)}{dx^2} = \delta(x - \xi) \qquad \text{(A.1.32)}$$

where $\delta(x - \xi)$ is the Dirac's function in one dimension (Katsikadelis, 2002a). The fundamental solution $u^*(x, \xi)$ is obtained as (Sapountzakis and Katsikadelis 2000)

$$u^*(x,\xi) = \frac{1}{2}|r| \tag{A.1.33}$$

With $r = x - \xi$ being the distance between $\xi$ and $x$, where $x$ is a constant source point while $\xi$ runs through the interval $[0, L]$. By applying sequential integrations by parts in the first integral equation (A.1.31), substituting equations (A.1.30) and (A.1.33) and exploiting the property of the Dirac's function, yields

$$u(\xi) = \int_0^L \Lambda_2(x,\xi) q(x) dx - \left[ \Lambda_2(x,\xi) \frac{du(x)}{dx} - \Lambda_1(x,\xi) u(x) \right]_0^L \tag{A.1.34}$$

where $\Lambda_i(r)$ $(i = 1, 2)$ are the kernels (derivatives of $u^*(x,\xi)$), defined as

$$\Lambda_1(x,\xi) = \frac{du^*(x,\xi)}{dx} = \frac{1}{2} \operatorname{sgn} r \tag{A.1.35a}$$

$$\Lambda_2(x,\xi) = u^*(x,\xi) = \frac{1}{2}|r| \tag{A.1.35b}$$

with $\operatorname{sgn}(\ )$ being the signum function, defined as in (A.1.10).

Relation (A.1.34) constitutes the integral representation of the solution as a function of the fictitious load and boundary quantities. Particularly, if $q(x)$ and all boundary values $\left( u(x), \frac{du(x)}{dx} \right)$ at the bar ends $0, L$ are known, $u(\xi)$ can be calculated at any internal point of the bar. Differentiating (A.1.34), the expressions for the derivative of $u(\xi)$ can be derived

$$\frac{du(\xi)}{d\xi} = -\int_0^L \Lambda_1(x,\xi) q(x) dx - \left[ -\Lambda_1(x,\xi) \frac{du(x)}{dx} \right]_0^L \tag{A.1.36}$$

where

$$\frac{d\Lambda_1(x,\xi)}{d\xi} = 0 \tag{A.1.37a}$$

$$\frac{d\Lambda_2(x,\xi)}{d\xi} = -\Lambda_1(x,\xi) \tag{A.1.37b}$$

Eqns. (A.1.34) and (A.1.36) written for the boundary points $x = 0, L$ constitute a system of two simultaneous integral equations, which are given in matrix form below

$$[E_{21}]\{u_1\} + [E_{22}]\{u_2\} = \{T_2\} \tag{A.1.38}$$

where

$$\{T_2\} = -\left\{ \begin{matrix} \int_0^L \Lambda_2(x, \xi_0) q(x) dx \\ \int_0^L \Lambda_2(x, \xi_L) q(x) dx \end{matrix} \right\} = -\left\{ \begin{matrix} \sum_{j=1}^N q_j F_{1j} \\ \sum_{j=1}^N q_j F_{2j} \end{matrix} \right\} = -\begin{bmatrix} F_{11} & F_{12} & \cdots & F_{1N} \\ F_{21} & F_{22} & \cdots & F_{2N} \end{bmatrix} \left\{ \begin{matrix} q_1 \\ q_2 \\ \vdots \\ q_N \end{matrix} \right\} \tag{A.1.39}$$

$$\{u_1\}^T = \left\{ \left. \frac{du(x)}{dx} \right|_{x=0} \quad u(0) \right\} \tag{A.1.40}$$

$$\{u_2\}^T = \left\{ \left. \frac{du(x)}{dx} \right|_{x=L} \quad u(L) \right\} \tag{A.1.41}$$

$$[E_{21}] = \begin{bmatrix} \Lambda_2(0, \xi_0) & -(\Lambda_1(0, \xi_0) + 1) \\ \Lambda_2(0, \xi_L) & -\Lambda_1(0, \xi_L) \end{bmatrix} \tag{A.1.42}$$

$$[E_{22}] = \begin{bmatrix} -\Lambda_2(L, \xi_0) & \Lambda_1(L, \xi_0) \\ -\Lambda_2(L, \xi_L) & (\Lambda_1(L, \xi_L) - 1) \end{bmatrix}$$
(A.1.43)

where $N$ is the number of discretization elements. The interval $(0, L)$ is divided into $N$ elements employing the constant element assumption for the fictitious load $q(x)$ which is considered constant in each element and equal to its value at mid-point (Fig. A.1.1). When $q(x)$ is approximated with quadratic elements (Fig. A.1.2), three collocation points are used for each discretization element.

Then, the boundary conditions (A.1.29b) are formulated in matrix form as follows

$$[E_{11}]\{u_1\} + [E_{12}]\{u_2\} = \{D_1\} \tag{A.1.44}$$

where $[E_{11}]$, $[E_{12}]$ are 2X2 known coefficient matrices and $\{D_1\}$ is 2X1 known coefficient vector.

Combining eqns. (A.1.39) and (A.1.44), the following is derived

$$\begin{bmatrix} [E_{11}] & [E_{12}] \\ [E_{21}] & [E_{22}] \end{bmatrix} \begin{Bmatrix} \{u_1\} \\ \{u_2\} \end{Bmatrix} = \begin{Bmatrix} \{D_1\} \\ \{0\} \end{Bmatrix} + \begin{Bmatrix} \{0\} \\ \{T_2\} \end{Bmatrix} \rightarrow [E]\{u\} = \{D\} + \{T\} \qquad \text{(A.1.45)}$$

where $[E]$ is a square 4X4 matrix, $\{0\}^T = \{0 \quad 0\}$ and $\{u\}, \{D\}, \{T\}$ are 4X1 vectors.

Combining eqn. (A.1.30) and (A.1.45) and the vector $\{T\}$ can be written as follows

$$\{T\} = \begin{bmatrix} [0] \\ -[F_2] \end{bmatrix} \{q\} \rightarrow \{T\} = [F]\{q\} \qquad \text{(A.1.46)}$$

where $[0]$ is the 2XN zero matrix and $[F]$ is the 2XN matrix. Substituting eqn. (A.1.46) into eqn. (A.1.45), the relation (A.1.22) can be similarly be derived.

Subsequently, applying the integral representations (A.1.34) and (A.1.37) at the $N$ collocation points or 3XN in case of quadratic elements, the following relations are derived

$$\{U\} = [A]\{q\} + [C]\{u\} \qquad \text{(A.1.47a)}$$

$$\{U'\} = [A']\{q\} + [C']\{u\} \qquad \text{(A.1.47b)}$$

where $U, U'$ are the vectors containing the values of the solution and its derivatives ( $u(x), u'(x)$ ) at collocation points. The coefficients of the $NXN$ or (3XN)X(3XN), in case of quadratic elements, square matrices $[A], [A']$ are given by the analytical or the numerical solution of the following integrals

$$A = \int_{\Gamma_j} \Lambda_2(x, \xi_i) q(x) dx \qquad \text{(A.1.48a)}$$

$$A' = -\int_{\Gamma_j} \Lambda_1(x, \xi_i) q(x) dx \qquad \text{(A.1.48b)}$$

The $NX4$ $[C], [C'], [C''], [C''']$ matrices are given below

$$[C] = \begin{bmatrix} \Lambda_2(0, \xi_1) & -\Lambda_1(0, \xi_1) & -\Lambda_2(L, \xi_1) & \Lambda_1(L, \xi_1) \\ \vdots & \vdots & \vdots & \vdots \\ \Lambda_2(0, \xi_L) & -\Lambda_1(0, \xi_L) & -\Lambda_2(L, \xi_L) & \Lambda_1(L, \xi_L) \end{bmatrix} \qquad \text{(A.1.49a)}$$

$$\left[C'\right] = \begin{bmatrix} -\Lambda_1(0,\xi_1) & 0 & \Lambda_1(L,\xi_1) & 0 \\ \vdots & 0 & \vdots & 0 \\ -\Lambda_1(0,\xi_L) & 0 & \Lambda_1(L,\xi_L) & 0 \end{bmatrix} \tag{A.1.49b}$$

and their coefficients are calculated with the aid of eqns. (A.1.35).

Substituting eqn. (A.1.45) into eqns. (A.1.47), the following are derived

$$\{U\} = [B]\{q\} + \{R\} \tag{A.1.50a}$$

$$\{U'\} = [B']\{q\} + \{R'\} \tag{A.1.50b}$$

where the square matrices $N$X$N$ or $(3$X$N)$X$(3$X$N)$, in case of quadratic elements, can be determined from the following relations

$$[B] = \left[[A] + [C][E]^{-1}[F]\right] \tag{A.1.51a}$$

$$[B'] = \left[[A'] + [C'][E]^{-1}[F]\right] \tag{A.1.51b}$$

and the $N$X$1$ vectors $\{R\}, \{R'\}$ are given as follows

$$\{R\} = [C][E]^{-1}\{D\} \tag{A.1.52a}$$

$$\{R'\} = [C'][E]^{-1}\{D\} \tag{A.1.52b}$$

It should be noted here that in case of homogenous boundary conditions ($\alpha_3 = \beta_3 = 0$) at the ends of the interval, the $\{R\}, \{R'\}$ vectors become equal to zero.

The final step of the AEM is the application of the governing equation of the initial problem (A.1.29a) at the $N$ or $3$X$N$, in case of quadratic elements, internal nodal points and subsequently the substitution of the values of the field function $u(x)$ and its derivative at the $N$ internal nodal points according to equations (A.1.47). From the definition of the analog equation (A.1.30) it is apparent that the values of forth derivative of $u(x)$ at the nodal points equals to the corresponding values of the fictitious load vector $q(x)$.
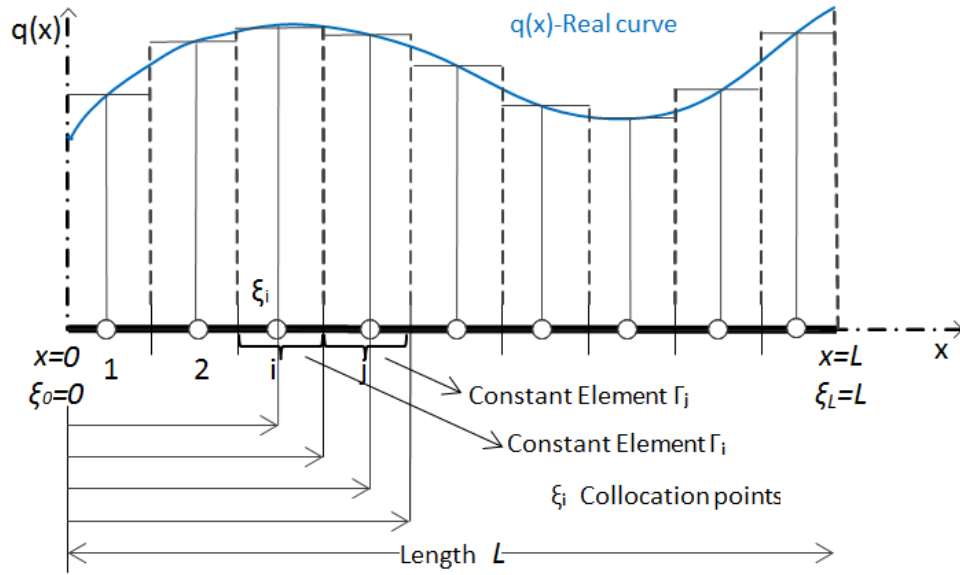
*Fig. A.1.1: Representation of fictitious load q(x) for constant discretization elements and collocation points for a kinematical component.*
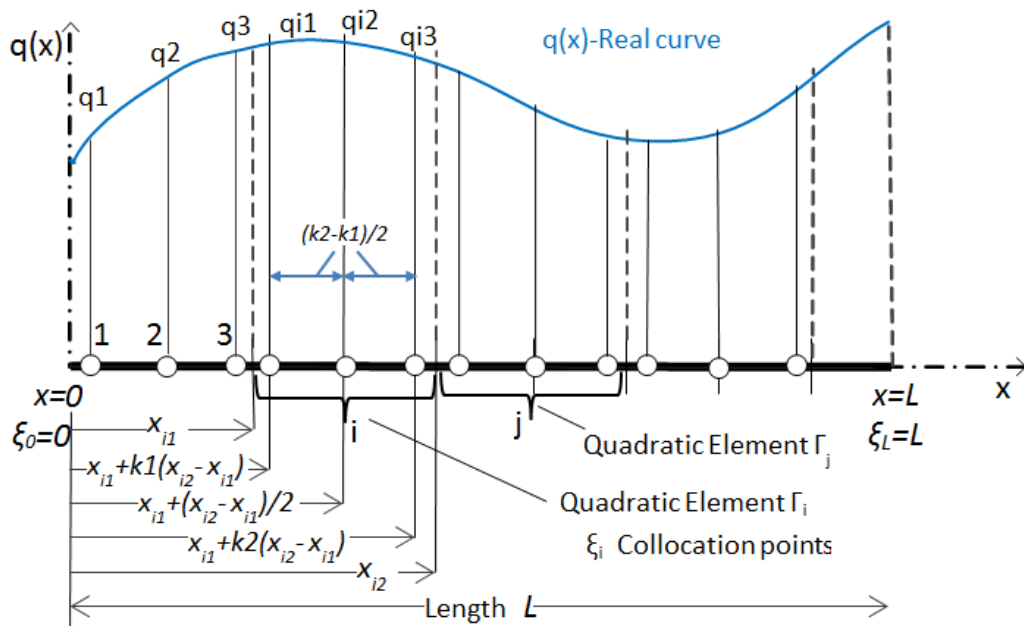


*Fig. A.1.2: Representation of fictitious load q(x) for quadratic discretization elements and collocation points for a kinematical component.*

# Appendix A.2

## A.2  Isogeometric Analysis's tools (B-splines and NURBS)

### A.2.1 Basic concept of the Isogeometric analysis

The term "Isogeometric" refers to the coincidence of the geometric model, which is built in a CAD environment, and the design model (i.e. the FEM or AEM model) used in order to perform the strain-stress analysis. In traditional FEM or AEM analysis, the design and geometric models never coincide due to the fact that even though they are both representations of a true object, they rely on different basis functions. This, in turn, produces concerns related to accuracy in the computations, particularly for curved structures. Additionally, if NURBS are used as basis functions, their smoothness is also inherited by the FEM (Chiozzi, Malagù, Tralli and Cazzani, 2015) or the AEM model. This is particularly important because it allows the circumvention of certain serious difficulties in developing the numerical model (e.g. advanced beams in which, except for bending, shear and torsion, higher order phenomena must be considered making the mesh processing more complicated). Moreover, as the shape functions are approximated better, the error affecting its derivatives becomes smaller. This is important especially in FEM models because stress fields are not the primary solution variables, but need to be computed by differentiating displacements through post-processing techniques. Thus, smoother displacement fields ensure a more accurate approximation of the stresses. This is not an aspect to be considered in the AEM models due to the fact that fictitious loads, which are the highest derivatives of the unknowns, are at first calculated.

### A.2.2  B-splines' basis functions and curves

Description of the model's geometry in commercial CAD packages is based on B-splines and NURBS. Particularly, NURBS basis functions are built on B-splines basis functions, which are piecewise polynomial functions defined by a sequence of coordinates $\Xi = \left\{ \xi_1, \xi_2, ... \xi_{n+p+1} \right\}$, also known as the knot vector, where the knots $\xi_i \in [0,1]$ are points in a parametric domain, in which $p$ and $n$ denote the polynomial order and the total number of basis functions, respectively. The distance between two consecutive knots is named knot span and represents the equivalent of the element domain in traditional finite element. In addition to this, knots represent the collocation points in the AEM. Once the order of the basis functions and the knot vector are known, the ith B-spline basis function of $p$-degree, $N_{i,p}(\xi)$, can be computed by means of the Cox-de Boor recursion formula (Piegel and Tiller, 1997) as

$$N_{i,0(\xi)} = \left\{ \begin{pmatrix} 1 & if \ \xi_i \le \xi < \xi_{i+1} \\ 0 & otherwise \end{pmatrix} \right\}, \quad p = 0 \tag{A.2.1a}$$

$$N_{i,p(\xi)} = \frac{\xi - \xi_i}{\xi_{i+p} - \xi_i} N_{i,p-1}(\xi) + \frac{\xi_{i+p+1} - \xi}{\xi_{i+p+1} - \xi_{i+1}} N_{i+1,p-1}(\xi), \quad p \ge 1 \tag{A.2.1b}$$

These basis functions are piecewise polynomials, which form a basis for the vector space and multiplied by the control points give the representation of the B-spline curve.

Considering the interval $[0,1]$, which contains the bar element with length equal to unity, with $\xi_i \in [0,1]$ and applying eqn. (A.2.1b), the following basis functions are derived for the quadratic B-spline

$$N_{0,2}(\xi) = \frac{\xi-0}{0-0} N_{0,1} + \frac{1-\xi}{1-0} N_{1,1} = \left\{ \begin{pmatrix} (1-\xi)^2 & if\ 0 \leq \xi < 1 \\ 0 & otherwise \end{pmatrix} \right\}$$ (A.2.2a)

$$N_{1,2}(\xi) = \frac{\xi-0}{1-0} N_{1,1} + \frac{1-\xi}{1-0} N_{2,1} = \left\{ \begin{pmatrix} 2\xi(1-\xi) & if\ 0 \leq \xi < 1 \\ 0 & otherwise \end{pmatrix} \right\}$$ (A.2.2b)

$$N_{2,2}(\xi) = \frac{\xi-0}{1-0} N_{2,1} + \frac{1-\xi}{1-1} N_{3,1} = \left\{ \begin{pmatrix} \xi^2 & if\ 0 \leq \xi < 1 \\ 0 & otherwise \end{pmatrix} \right\}$$ (A.2.2c)

where $N_{0,1}, N_{1,1}, N_{2,1}$ and $N_{3,1}$ are calculated from eqns. (A.2.1). Thus, the quadratic B-spline curve is defined by

$$C(\xi) = \sum_{i=0}^{2} N_{i,2}(\xi) P_i$$ (A.2.3)

where $P_i$ are the control points $P_0$, $P_1$ and $P_2$. Substituting eqns. (A.2.2) to eqn. (A.2.3), the expression for the fictitious load $q(x)$ in the AEM is derived as

$$q(x) = P_0 - 2xP_0 + x^2 P_0 + 2xP_1 - 2x^2 P_1 + x^2 P_2$$ (A.2.4)

Three equidistant collocation points have been used, which are presented in the same figure with the control points (Fig. A.2.1).

The same process, as described above, has been followed when substituting with the polynomial representation of cubic or quartic B-splines with uniform knot vectors. Considering the cubic B-spline, the expression of the fictitious load $q(x)$ is derived as

$$q(x) = \frac{(L-x)^3}{L^3} P_0 + \frac{3x(L-x)^2}{L^3} P_1 + \frac{3x^2(L-x)}{L^3} P_2 + \frac{x^3}{L^3} P_3$$ (A.2.5)

where $P_i$ are the control points $P_0$, $P_1$, $P_2$ and $P_3$. If four equidistant collocation points for discretization are employed, the control polygon of the fictitious load curve and the collocation points are presented in Fig. A.2.2 for a kinematical component of the beam theories presented in this PhD thesis.
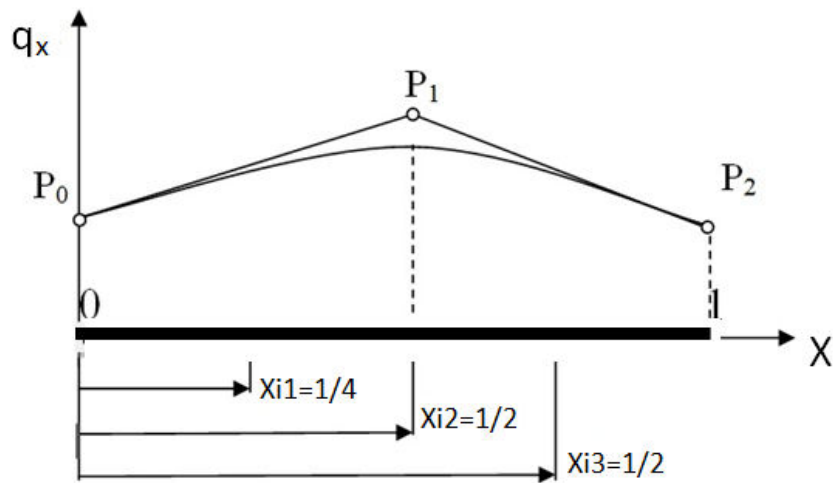
*Fig. A.2.1: Bar element, representation of fictitious load q(x) for quadratic B-spline, control and collocation points.*
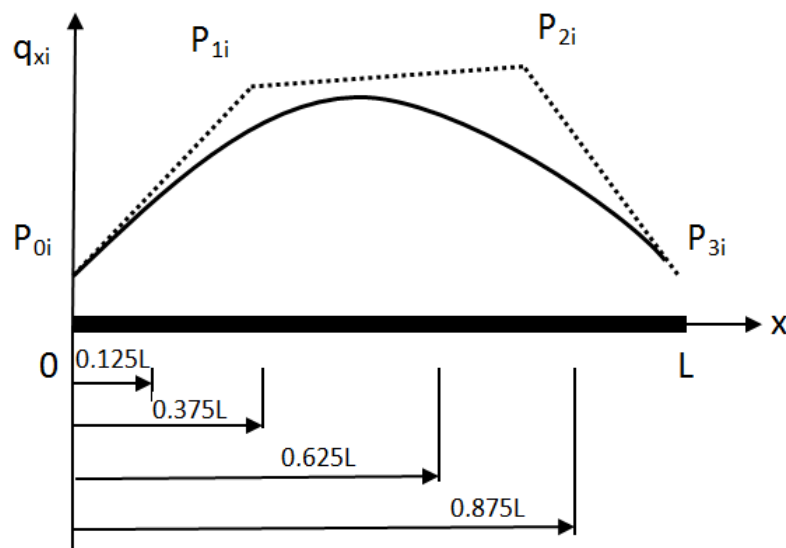


*Fig. A.2.2: Representation of fictitious load q(x) for the cubic B-spline, control and collocation points for the kinematical component i (the control polygon is presented in dashed line).*

Similarly, the expression for the fictitious load $q(x)$ for the quartic B-spline is derived as

$$q(x) = \frac{(L-x)^4}{L^4} P_0 + \frac{4x(L-x)^3}{L^4} P_1 + \frac{6x^2(L-x)^2}{L^4} P_2 + \frac{4x^3(L-x)}{L^4} P_3 + \frac{x^4}{L^4} P_4 \qquad (A.2.6)$$

where $P_i$ are the control points $P_0$, $P_1$, $P_2$, $P_3$ and $P_4$.

## A.2.3 Refinement procedures

The control polygon, which is a set of control points, represents a piecewise linear approximation to the B-spline curve mentioned above. This approximation can

be improved by: (i) generating a refinement of this set of points with the addition of new points, (ii) knot insertion or (iii) degree elevation. The last technique of elevating the degree results in the cubic and quartic B-spline curves mentioned earlier.

To begin with, the refinement of the quadratic B-spline curve is examined according to the works of Kenneth (2000), Chaikin (1974) and Reisenfeld (1975). The initial curve is defined by the control polygon given in Fig. A.2.3a (same as in Fig. A.2.1). Then, employing Chaikin's method, the control points of the refined curve are given in Fig. A.2.3b and can be positioned i.e. at the ¼ and ¾ of the initial lines of the control polygon. So, given a control polygon, a refinement of this set of points can be generated by constructing new points along each edge of the original polygon at a distance of ¼ and ¾ between the endpoints of the edge. This can be represented in matrix form as

$$
\begin{bmatrix} P_0^1 \\ P_1^1 \\ P_2^1 \\ P_3^1 \end{bmatrix} = \frac{1}{4} \begin{bmatrix} 3 & 1 & 0 \\ 1 & 3 & 0 \\ 0 & 3 & 1 \\ 0 & 1 & 3 \end{bmatrix} \begin{bmatrix} P_0 \\ P_1 \\ P_1 \end{bmatrix} = \begin{bmatrix} \frac{3}{4}P_0 + \frac{1}{4}P_1 \\ \frac{3}{4}P_1 + \frac{1}{4}P_0 \\ \frac{3}{4}P_1 + \frac{1}{4}P_2 \\ \frac{3}{4}P_1 + \frac{1}{4}P_1 \end{bmatrix}
\tag{A.2.7}
$$
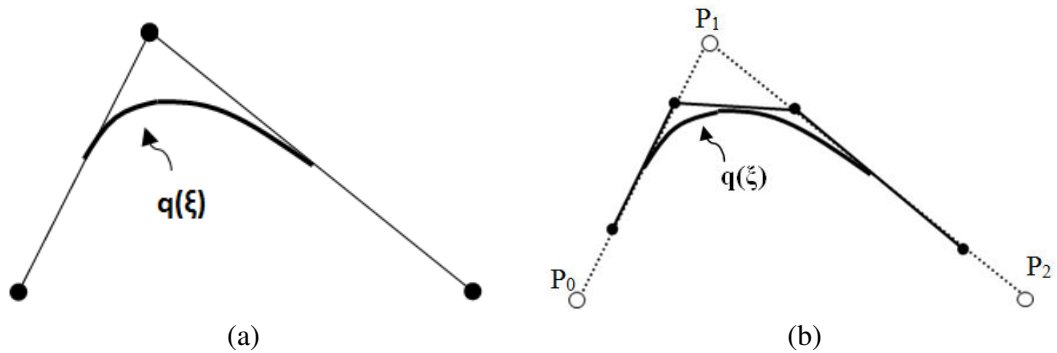


Fig. A.2.3: *Quadratic uniform B-spline curve defined by the control polygon {P0, P1, P2} (a) and refined curve of quadratic B-spline (b).*

This process is then continued until a refinement is reached that accurately represents the curve to a desired resolution. In other words, in the limit, the sequence of control points generated by the refinement procedure converges to a quadratic uniform B-spline curve. In order to express the fictitious load with respect to the new control points, eqn. (A.2.7) is simplified and the control points of the initial polygon are expressed with respect to the new ones ($P_0^1, P_1^1, P_2^1$ and $P_3^1$). The same procedure is repeated for the new set of control points derived, exploiting again eqn. (A.2.7).

In addition to the above mentioned, the improvement of the accuracy of the results can be improved by employing knot insertion. The knot vector earlier described

is now enriched with the addition of new knots. The $N_{i,2}$ $((1-\xi)^2, 2\xi(1-\xi), \xi^2)$ restricted to the interval $\xi_i \in [0,1]$ are the quadratic Bernstein polynomials. For this reason, the B-spline representation, described previously, with a knot vector of the form $\Xi = \{0,0,0,1,1,1\}$ ($p+1$ multiplicity of knots) is a generalization of the Bézier representation. A new knot vector is now specified and a new set of B-spline basis functions is computed. The knot vector determines completely the functions $N_{i,p}(\xi)$.

Thus, considering the knot vector (addition of 3 new knots)

$$U = \{0,0,0,\frac{1}{4},\frac{1}{2},\frac{3}{4},1,1,1\} \quad \text{or}$$

$$U = \{\xi_0 = 0, \xi_1 = 0, \xi_2 = 0, \xi_3 = \frac{1}{4}, \xi_4 = \frac{1}{2}, \xi_5 = \frac{3}{4}, \xi_6 = 1, \xi_7 = 1, \xi_8 = 1\} \tag{A.2.8}$$

the zero-, first- and second- degree basis functions are computed below. Thus, according to eqns. (A.2.1), the following basis functions are derived

$$N_{0,0}(\xi) = N_{1,0}(\xi) = 0 \tag{A.2.9a}$$

$$N_{2,0}(\xi) = \left\{ \begin{pmatrix} 1 & if\ 0 \leq \xi < \frac{1}{4} \\ 0 & otherwise \end{pmatrix} \right\} \tag{A.2.9b}$$

$$N_{3,0}(\xi) = \left\{ \begin{pmatrix} 1 & if\ \frac{1}{4} \leq \xi < \frac{1}{2} \\ 0 & otherwise \end{pmatrix} \right\} \tag{A.2.9c}$$

$$N_{4,0}(\xi) = \left\{ \begin{pmatrix} 1 & if\ \frac{1}{2} \leq \xi < \frac{3}{4} \\ 0 & otherwise \end{pmatrix} \right\} \tag{A.2.9d}$$

$$N_{5,0}(\xi) = \left\{ \begin{pmatrix} 1 & if\ \frac{3}{4} \leq \xi < 1 \\ 0 & otherwise \end{pmatrix} \right\} \tag{A.2.9e}$$

$$N_{6,0}(\xi) = N_{7,0}(\xi) = 0 \tag{A.2.9f}$$

$$N_{0,1}(\xi) = \frac{\xi - 0}{0 - 0} N_{0,0} + \frac{0 - \xi}{0 - 0} N_{1,0} = 0 \tag{A.2.9g}$$

$$N_{1,1}(\xi) = \frac{\xi - 0}{0 - 0} N_{1,0} + \frac{\frac{1}{4} - \xi}{\frac{1}{4} - 0} N_{2,0} = \left\{ \left( \begin{array}{ll} 1 - 4\xi & if \ 0 \le \xi < \frac{1}{4} \\ \\ 0 & otherwise \end{array} \right) \right\} \qquad (A.2.9h)$$

$$N_{2,1}(\xi) = \frac{\xi - 0}{\frac{1}{4} - 0} N_{2,0} + \frac{\frac{1}{2} - \xi}{\frac{1}{2} - \frac{1}{4}} N_{3,0} = \left\{ \left( \begin{array}{ll} 4\xi & if \ 0 \le \xi < \frac{1}{4} \\ \\ 2 - 4\xi & if \ \frac{1}{4} \le \xi < \frac{1}{2} \\ \\ 0 & otherwise \end{array} \right) \right\} \qquad (A.2.9i)$$

$$N_{3,1}(\xi) = \frac{\xi - \frac{1}{4}}{\frac{1}{2} - \frac{1}{4}} N_{3,0} + \frac{\frac{3}{4} - \xi}{\frac{3}{4} - \frac{1}{2}} N_{4,0} = \left\{ \left( \begin{array}{ll} 4\xi - 1 & if \ \frac{1}{4} \le \xi < \frac{1}{2} \\ \\ 3 - 4\xi & if \ \frac{1}{2} \le \xi < \frac{3}{4} \\ \\ 0 & otherwise \end{array} \right) \right\} \qquad (A.2.9j)$$

$$N_{4,1}(\xi) = \frac{\xi - \frac{1}{2}}{\frac{3}{4} - \frac{1}{2}} N_{4,0} + \frac{1 - \xi}{1 - \frac{3}{4}} N_{5,0} = \left\{ \left( \begin{array}{ll} 4\xi - 2 & if \ \frac{1}{2} \le \xi < \frac{3}{4} \\ \\ 4 - 4\xi & if \ \frac{3}{4} \le \xi < 1 \\ \\ 0 & otherwise \end{array} \right) \right\} \qquad (A.2.9k)$$

$$N_{5,1}(\xi) = \frac{\xi - \frac{3}{4}}{1 - \frac{3}{4}} N_{5,0} + \frac{1 - \xi}{1 - 1} N_{6,0} = \left\{ \left( \begin{array}{ll} 4\xi - 3 & if \ \frac{3}{4} \le \xi < 1 \\ \\ 0 & otherwise \end{array} \right) \right\} \qquad (A.2.9l)$$

$$N_{6,1}(\xi) = \frac{\xi - 1}{1 - 1} N_{6,0} + \frac{1 - \xi}{1 - 1} N_{7,0} = 0 \qquad (A.2.9m)$$

$$N_{0,2}(\xi) = \frac{\xi - 0}{0 - 0} N_{0,1} + \frac{\frac{1}{4} - \xi}{\frac{1}{4} - 0} N_{1,0} = \left\{ \left( \begin{array}{ll} (1 - 4\xi)^2 & if \ 0 \le \xi < \frac{1}{4} \\ \\ 0 & otherwise \end{array} \right) \right\} \qquad (A.2.9n)$$

$$N_{1,2}(\xi) = \frac{\xi - 0}{\frac{1}{4} - 0} N_{1,1} + \frac{\frac{1}{4} - \xi}{\frac{1}{2} - 0} N_{2,1} = \left\{ \begin{pmatrix} 4\xi - 16\xi^2 + (\frac{1}{2} - 2\xi)4\xi & if\ 0 \le \xi < \frac{1}{4} \\ (\frac{1}{2} - 2\xi)(2 - 4\xi) & if\ \frac{1}{4} \le \xi < \frac{1}{2} \\ 0 & otherwise \end{pmatrix} \right\} \quad (A.2.9o)$$

$$N_{2,2}(\xi) = \frac{\xi - 0}{\frac{1}{2} - 0} N_{2,1} + \frac{\frac{3}{4} - \xi}{\frac{3}{4} - \frac{1}{4}} N_{3,1} = \left\{ \begin{pmatrix} 8\xi^2 & if\ 0 \le \xi < \frac{1}{4} \\ 2\xi(2 - 4\xi) + (\frac{3}{2} - 2\xi)(4\xi - 1) & if\ \frac{1}{4} \le \xi < \frac{1}{2} \\ (\frac{3}{2} - 2\xi)(3 - 4\xi) & if\ \frac{1}{2} \le \xi < \frac{3}{4} \end{pmatrix} \right\}$$

$$(A.2.9p)$$

$$N_{3,2}(\xi) = \frac{\xi - \frac{1}{4}}{\frac{3}{4} - \frac{1}{4}} N_{3,1} + \frac{1 - \xi}{1 - \frac{1}{2}} N_{4,1} =$$

$$= \left\{ \begin{pmatrix} (2\xi - \frac{1}{2})(4\xi - 1) & if\ \frac{1}{4} \le \xi < \frac{1}{2} \\ (2\xi - \frac{1}{2})(3 - 4\xi) + (2 - 2\xi)(4\xi - 2) & if\ \frac{1}{2} \le \xi < \frac{3}{4} \\ (2 - 2\xi)(4 - 4\xi) & if\ \frac{3}{4} \le \xi < 1 \end{pmatrix} \right\} \quad (A.2.9q)$$

$$N_{4,2}(\xi) = \frac{\xi - \frac{1}{2}}{1 - \frac{1}{2}} N_{4,1} + \frac{1 - \xi}{1 - \frac{3}{4}} N_{5,1} =$$

$$= \left\{ \begin{pmatrix} (2\xi - 1)(4\xi - 2) & if\ \frac{1}{2} \le \xi < \frac{3}{4} \\ (2\xi - 1)(4\xi - 4) + (4 - 4\xi)(4\xi - 3) & if\ \frac{3}{4} \le \xi < 1 \\ 0 & otherwise \end{pmatrix} \right\} \quad (A.2.9r)$$

$$N_{5,2}(\xi) = \frac{\xi - \frac{3}{4}}{1 - \frac{3}{4}} N_{5,1} + \frac{1 - \xi}{1 - 1} N_{6,1} = \left\{ \begin{pmatrix} (4\xi - 3)^2 & if\ \frac{3}{4} \le \xi < 1 \\ 0 & otherwise \end{pmatrix} \right\} \quad (A.2.9s)$$

$$N_{6,2}(\xi) = \frac{\xi-1}{1-1}N_{6,1} + \frac{1-\xi}{1-1}N_{7,1} = 0 \qquad (A.2.9t)$$

and the corresponding quadratic b-spline curve, which is defined by eqn. (A.2.3), is expressed as

$$C(\xi) = \sum_{i=0}^{n} N_{i,2}(\xi)P_i = N_{0,2}P_0 + N_{1,2}P_1 + N_{2,2}P_2 + N_{3,2}P_3 + N_{4,2}P_4 + N_{5,2}P_5 \qquad (A.2.10)$$

Similar procedure can be followed for the knot insertion in cubic and quartic B-splines earlier described.

### A.2.4 FEM and NURBS

In order to discretize ordinary differential equations with FEM, the sought solution of the problem is approximated by means of polynomial interpolating functions of $p$-degree as extensively is described by Onate (2009) and Papadrakakis (2001). Considering beam elements, substituting the displacement approximation for each discretization element ($N$ in total), the equilibrium equations in terms of the nodal displacements of the finite element mesh can be expressed. Paricularly, the main steps of the FEM algorithm are as follows:

1. Selection of the polynomial degree of the basis functions for each displacement and for each discretization element.
2. Determination of the geometric constants and loads of the beam.
3. Definition of the geometry meshes and index matrices for each displacement considered in the beam model.
4. Evaluation of the Gauss Points in the physical space and their Jacobians. This can be performed by using the Gauss quadrature rule. In order to compute Gauss base points and weight factors an algorithm has been employed according to Davis and Rabinowitz (1975).
5. Element and global stiffness and mass matrices' initialization.
6. Evaluation of stiffness and mass matrices in a double loop with respect to the number of elements and the number of gauss points. Derivation of global stiffness and mass matrices by assembling the contributions from the individual elements.
7. Elimination of constrained degrees of freedom (DOF) in the final assembled system employing Lagrange multipliers' method.
8. Global equilibrium equations and solution of the problem.
9. Post-processing in order to evaluate displacements and reaction forces in local and global system at the points where the solution is plotted.

As a next step in discretizing the differential equations of the problem, $p$-degree NURBS interpolating functions can be employed for the representation of the

displacement field. In this case, curve C given in eqn. (A.2.3) has a *p*-degree NURBS representation defined by

$$C_i(\xi) = \sum_{i=1}^{n} R_{i,p}(\xi) P_{ii}$$

(A.2.11)

where $P_{ii}$ are the control points employed for each kinematical component and $R_{i,p}(\xi)$, which are the NURBS basis functions, can be expressed as

$$R_{i,p}(\xi) = \frac{N_{i,p}(\xi) w_i}{\sum_{i=1}^{n} N_{i,p}(\xi) w_i}$$

(A.2.12)

where $N_{i,p}(\xi)$ are given in eqns. (A.2.1) and $w_i$ ($\in \Box$) are weights related to the *i*th control point and increase the capabilities of the B-splines interpolation (Hughes et al., 2009). NURBS share many properties with B-spline basis functions (Piegl and Tiller 1997). Among these, they are all nonnegative, they have a compact support, and build a partition of unity. It should be noted that if all weights are equal, then $R_{i,p}(\xi) = N_{i,p}(\xi)$ and curve *C* is a B-spline curve.

The main idea of the Isogeometric approach is to describe the geometry of the problem by NURBS interpolation exactly and to use the same interpolating basis to represent the generalized displacements. The main steps of the IGA algorithm, when NURBS are integrated in FEM, are similar to those presented for FEM. However, regarding the step 3, there is no need for index matrices and the geometry is defined by an initial control polygon which results in an initial NURBS structure. Afterwards, during pre-processing, one or more meshes are defined for the different kinematical components based on the initial NURBS structure while knot insertion, degree elevation or k-refinement can be employed in order to refine the initial structure directly on these meshes. In addition to these, step 4 is altered here due to the fact that Gauss points and the corresponding Jacobians are evaluated in parametrical and physical space together with the values of the basis functions, their derivatives and the radius of curvature directly on the meshes. Thus, post-processing (step 9) becomes easier and no need for additional loops and calculations of basis functions are demanded.

In case of a curved geometry the following relations need to be employed

$$J = S' = \sqrt{X'^2 + Y'^2}$$

(A.2.13)

$$R = \frac{J}{\left| X'Y'' - X''Y' \right|}$$

(A.2.14)

where $(\ )'$ the derivatives with respect to $\xi$, S the arc length of the beam with one plane of curvature, R the radius of curvature of the beam and X, Y the coordinates on the plane of curvature.

In case of NURBS integration in the AEM, the differences in the algorithm regarding steps 3, 4 and 9 previously mentioned apply here, too. However, two different double loops need to be performed when numerical integration is applied with respect to elements and gauss points in order to evaluate $[A],[A'],[A''],[A''']$ and $[F]$ matrices of the AEM. The rest of the procedure followed in the AEM is the same.

# References

American Association of State Highway and Transportation Officials (1993) *Guide Specifications for Horizontally Curved Highway Bridges*, Washington DC.

Andreassen, M.J. & Jönsson, J. (2012a) Distortional Solutions for Loaded Semi-Discretized Thin-Walled Beams. *Thin-Walled Structures*, 50, 116-127.

Andreassen, M.J. & Jönsson, J. (2012b) Distortional Buckling Modes of Semi-Discretized Thin-Walled Columns. *Thin-Walled Structures*, 51, 53-63.

Andreassen, M.J. & Jönsson, J. (2013) A Distortional Semi-Discretized Thin-Walled Beam Element. *Thin-Walled Structures*, 62, 142-157.

Anitescu, C., Jia, Y., Jessica Zhang, Y. & Rabczuka, T. (2015) An isogeometric collocation method using superconvergent points. *Computational Methods in Applied Mechanics and Engineering*, 284, 1073-1097.

Arici, M. & Granata, M.F. (2016) Unified theory for analysis of curved thin-walled girders with open and closed cross section through HSA method. *Engineering Structures*, 113, 299-314.

Auricchio, F., Beirão da Veiga, L., Kiendl, J., Lovadina, C. & Reali, A. (2012) Locking-free isogeometric collocation methods for spatial Timoshenko rods. *Computer Methods in Applied Mechanics and Engineering*, 263, 113-126.

Babouskos, N. (2011) *Analysis and Optimization of Elastic and Viscoelastic Plates Using the Boundary Element Method*. Athens : National Technical University of Athens. DOI 10.12681/eadd/24943.

Bathe, K. (1996) *Finite Element Procedures*, Prentice Hall, Upper Saddle River, NewJersey.

Bauchau, OA. (1985) A beam theory for anisotropic materials. *Journal of Applied Mechanics*, 52, 416-422.

Bazant, Z.P. & El-Nimeiri, M. (1974) Stiffness method for curved box girders at initial stress. *Journal of the Structural Division*, 100(10), 2071-2090.

Bazilevs, Y., Hsu, M.C., Akkerman, I., Wright, S., Takizawa, K., Henicke, B., Spielman, T. & Tezduyar, T.E. (2011) 3D simulation of wind turbine rotors at full

scale. Part I: Geometry modelling and aerodynamics. *International Journal for Numerical Methods in Fluids*, 65, 207–235.

Bebiano, R., Camotim, D. & Silvestre, N. (2013) Dynamic analysis of thin-walled members using Generalised Beam Theory (GBT). *Thin-Walled Structures*, 72, 188-205.

Beer, G., Smith, I. & Duenser, Ch. (2008) *The Boundary Element Method with Programming – For Engineers and Scientists*. Springer, Wien, New York.

Beirão da Veiga, L., Lovadina, C. & Reali, A. (2012) Avoiding shear locking for the Timoshenko beam problem via isogeometric collocation methods. *Computer Methods in Applied Mechanics and Engineering*, 241-244, 38-51.

Benscoter, S.U. (1954) A theory of Torsion Bending for Multicell Beams. *Journal of Applied Mechanics*, 20, 25-34, 1954.

Billing, J.R. & Green, R. (1984) *Design provisions for dynamic loading of highway bridge.* Transportation Research Report 950. Ontario Ministry of Transportation and Communications, Dowsview, Ontario, Canada, 94-103.

Camotim, D. & Dinis, P.B. (2011) Coupled Instabilities with Distortional Buckling in Cold-Formed Steel Lipped Channel Columns. *Thin-Walled Structures*, 49, 562-575.

Cantieni, R. (1983) *Dynamic load test on highway bridges in Switzerland*, 60 years experience of EMPA. Report no.211. Dubendorf, Switzerland.

Carrera, E. & Varello, A. (2012) Dynamic response of thin-walled structures by variable kinematic one-dimensional models. *Journal of Sound and Vibration*, 331, 5268-5282.

Cazzani, A., Malagú, M. & Turco, E. (2014) Isogeometric analysis of plane-curved beam. *Mathematics and Mechanics of Solids*, Epub ahead of print on April 20, 2014. DOI: 10.1177/1081286514531265.

Cazzani, A., Malagù, M., Turco E. & Stochino, F. (2016). Constitutive models for strongly curved beams in the frame of isogeometric analysis. *Mathematics and Mechanics of Solids*, 21(2), 182–209.

Chaikin, G. (1974) An algorithm for high speed curve generation. *Computer Graphics and Image Processing*, 3, 346–349.

Chen, C. (1998) The warping torsion bar model of the differential quadrature element method. *Computers and Structures*, 66(2-3), 249-257.

Chien, T.H., Nguyen-Xuan, H., Nguyen-Thanh, N., Le, T.H., Nguyen-Thoi, T. & Rabczuk, T. (2012) Static, free vibration, and buckling analysis of laminated composite Reissner–Mindlin plates using NURBS-based isogeometric approach. *International Journal for Numerical Methods in Engineering*, 91, 571-603.

Chiozzi, A., Malagù, M., Tralli, A. & Cazzani, A. (2015) ArchNURBS: NURBS-Based Tool for the Structural Safety Assessment of Masonry Arches in MATLAB. *Journal of Computing in Civil Engineering*, 30(2), 04015010(11). DOI: 10.1061/(ASCE)CP.1943-5487.

Dabrowski, R. (1968) *Curved Thin-walled Girders Theory and Analysis*. Cement and Concrete Association.

Dabrowski, R. (1965) Warping torsion of curved box girders of non-deformable cross-section. *Der Stahlbau*, 34, 135-141.

Davis, P.J. & Rabinowitz, P. (1975) *Methods of Numerical Integration*. New York: Academic Press.

Dikaros, I.C. & Sapountzakis, E.J. (2016) Distorsional Analysis of Beams of Arbitrary Cross Section by BEM. *Proc. of the 11th HSTAM International Congress on Mechanics*, Athens, Greece, 27-30 May.

Dikaros, I.C., Sapountzakis, E.J. & Argyridi, A.K. (2016) Generalized warping effect in the dynamic analysis of beams of arbitrary cross section. *Journal of Sound and Vibration*, 369, 119-146.

Dikaros, I.C. & Sapountzakis, E.J. (2014) Generalized Warping Analysis of Composite Beams of an Arbitrary Cross Section by BEM. I: Theoretical Considerations and Numerical Implementation. *Journal of Engineering Mechanics*, 140(9), 04014062.

Dimitrakopoulos, E.G. & Zeng, Q. (2015) A three-dimensional dynamic analysis scheme for the interaction between trains and curved railway bridges. *Computers and Structures*, 149, 43-60.

Dinis, P.B. & Camotim, D. (2011) Post-Buckling Behaviour and Strength of Cold-Formed Steel Lipped Channel Columns Experiencing Distortional/Global Interaction. *Computers and Structures*, 89, 422-434.

El Fatmi, R. & Ghazouani, N. (2011) Higher Order Composite Beam Theory built on Saint-Venant's Solution. Part-I: Theoretical Developments. *Composite Structures*, 93, 557-566.

Echter, R. & Bischoff, M. (2010) Numerical efficiency, locking and unlocking of NURBS finite elements. *Computer Methods in Applied Mechanics and Engineering*, 199(5-8), 374–382.

Eisenberger, M. (1995) Nonuniform Torsional Analysis of Variable and Open Cross-section Bars. *Thin-Walled Structures*, 21, 93-105.

Eurocode 3 (2004): *Design of Steel Structures- Part 2: General Rules and Rules for Bridges*, European Committee for Standardization, prEN 1994-2.

Eurocode 3 (2004): *Design of Steel Structures- Part 1.5: Plated Structural Elements*, European Committee for Standardization, prEN 1993-1-5.

Eurocode 4 (2004): *Design of Composite Steel and Concrete Structures- Part 1.1: General Rules and Rules for Buildings*, European Committee for Standardization, prEN 1994-1-1.

FEMAP for Windows (2010) Finite element modeling and post-processing software. Help System Index, Version 11.0.1.

Ferradi, M.K. & Cespedes, X. (2014) A New Beam Element with Transversal and Warping Eigenmodes. *Computers and Structures*, 131, 12-33.

Ferradi, M.K., Cespedes, X. & Arquier, M. (2013) A higher Order Beam Finite Element with Warping Eigenmodes. *Engineering Structures*, 46, 748-762.

Fotiu, P., Irschik, H. & Ziegler, F. (1987) Forced vibrations of an elasto-plastic and deteriorating beam, *Acta Mechanica*, 69, 193-203.

Fotiu, P. & Irschik, H. (1989) Modal analysis of vibrating viscoplatic composite beams on multiple supports. *Earthquake Engineering and Structural Dynamics*, 18, 1053-1064.

Friemann, H. (1993) *Schub und Torsion in gerade Staben*. Werner-Verlag, Dusseldorf.

Gendy, A.S., & Saleeb A.F. (1992) On the finite element analysis of the Spatial response of curved beams with arbitrary thin-walled sections. *Computers and Structures*, 44(3), 639-652.

Genoese, A., Genoese, A., Bilotta, A. & Garcea, G. (2014) A Generalized Model for Heterogeneous and Anisotropic Beams Including Section Distortions. *Thin-Walled Structures*, 74, 85-103.

Ghazouani, N. & El Fatmi, R. (2011) Higher Order Composite Beam Theory built on Saint-Venant's Solution. Part-II: Built-in Effects Influence on the Behavior of End-Loaded Cantilever Beams. *Composite Structures*, 93, 567-581.

Gonçalves, R. & Camotim, D. (2015) On distortion of symmetric and periodic open-section thin-walled members. *Thin-Walled Structures*, 94, 314-324

Gruttmann, F., Wagner, W. & Sauer, R. (1998) Zur Berechnung von Wolbfunktion und Torsionskennwerten beliebiger Stabquerschnitte mit der Methode der Finiten Elemente. Bauingenieur, 73(3), 138-143.

Hanshin Expressway Public Corporation (1988) *Guidelines for the Design of Horizontally Curved Girder Bridges*, Japan.

Hamed, E. & Frosting, Y. (2005) Free vibrations of multi-girder and multi-cell box bridges with transverse deformations effects. *Journal of Sound and Vibration*, 279, 699-722.

Heilig, R. (1971) *A Contribution to the Theory of Box Girders of Arbitrary Cross - sectional Shape* (Translated from the German by C. V. Amerongen), Publication No. 145. Cement and Concrete Association (1971).

Heins, C.P. & Oleinik, J.C. (1976) Curved Box Beam Bridge Analysis. *Computers and Structures*, 6, 65-73.

Heins, C.P. & Sahin, M.A. (1979): Natural frequency of curved box girders. *Journal of the Structural Division*, 105(ST12), 2591-600.

Heins, C.P. & Spates, K.R. (1970) Behavior of single horizontally curved girder. *Journal of the Structural Division*, 96, 1511-1524.

Huang, C.S., Tseng, Y.P., Chang, S.H. & Hung, C.L. (2000) Out-of-plane dynamic analysis of beams with arbitrarily varying curvature and cross-section by dynamic stiffness matrix method. *International Journal of Solids and Structures*, 37,495-513.

Huang, D., Wang, T.L. & Shahawy, M. (1998) Vibration of horizontally curved box girder bridges due to vehicles. *Computers and Structures*, 68, 513-528.

Huang, D.Z. (2001) Dynamic analysis of steel curved box girder bridges, *Journal of Bridge Engineering*, 6, 506-513.

Huang, X.M., Huang, X.Y., Zhuo, W. D., Shang-Guan, P. & Li, Y. (2012) Impact effect analysis for a continuous concrete curved bridge due to multi-vehicle loading. *Journal of Shock and Vibration*, 24, 137-142.

Hughes, T., Cottrell, J. & Bazilevs, Y. (2009) *Isogeometric analysis: Toward Integration of CAD and FEA*. Wiley.

Ie, C.A. & Kosmatka, J.B. (1992) On the Analysis of Prismatic Beams Using First-Order Warping Functions. *International Journal of Solids and Structures*, 29(7), 879-891.

Irschik, H. & Ziegler, F. (1998) Dynamics of linear elastic structures with selfstress: A unified treatment for linear and nonlinear problems. *Journal of Applied Mathematics and Mechanics*, 68, 199-205.

Jang, G.-W. & Kim, Y.Y. (2010) Fully Coupled 10-Degree-of-Freedom Beam Theory for Piecewise Straight Thin-Walled Beams with General Quadrilateral Cross Sections. *Journal of Structural Engineering, ASCE*, 136, 1596-1607.

Jang, G.-W. & Kim, Y.Y. (2009) Vibration analysis of piecewise straight thin-walled box beams without using artificial joint springs. *Journal of Sound and Vibration*, 326, 647-670.

Jang, G.-W., Kim, K.J. & Kim, Y.Y. (2008) Higher-order beam analysis of box beams connected at angled joints subject to out-of-plane bending and torsion. *International Journal for Numerical Methods in Engineering*, 75, 1361-1384.

Jang, G.-W., Kim, M.-J. & Kim, Y.Y. (2012) Analysis of Thin-Walled Straight Beams with Generally Shaped Closed Sections Using Numerically Determined Sectional Deformation Functions. *Journal of Structural Engineering*, 138(12), 1427-1435.

Jönsson, J. (1999). Distortional theory of thin-walled beams. *Thin-Walled Structures*, 33(4), 269-303.

Jönsson, J. & Andreassen, M.J. (2011) Distortional Eigenmodes and Homogeneous Solutions for Semi-Discretized Thin-Walled Beams. *Thin-Walled Structures*, 49, 691-707.

Jun, L., Guangwei, R., Jin, P., Xiaobin, L. & Weiguo, W. (2014) Free Vibration Analysis of a Laminated Shallow Curved Beam Based on Trigonometric Shear Deformation Theory. *Mechanics Based Design of Structures and Machines*, 42(1), 111-129. DOI:10.1080/15397734.2013.846224

Jüttler, B. (2013), *Iso-Geometric Methods for Numerical Simulation*. Course notes (Johannes Kepler University, Linz, Austria), part I, International Centre of Mechanical Sciences (CISM), Udine, Italy.

Kang, Y.J. & Yoo, C.H. (1994) Thin-walled curved beams, I: formulation of nonlinear equations. *Journal of Engineering Mechanics*, 120(10), 2072-2101.

Katsikadelis, J.T. (2002a) *Boundary Elements: Theory and Applications*. Elsevier, Amsterdam-London.

Katsikadelis, J.T. (2002b) The Analog Equation Method. A Boundary – only Integral Equation Method for Nonlinear Static and Dynamic Problems in General Bodies. *Theoretical and Applied Mechanics*, 27, 13-38.

Katsikadelis, J.T. (1994) The Analog Equation Method: A Powerful BEM-Based Solution Technique  for Solving Linear and Non-linear Engineering Problems. *Boundary Element Method   XVI*, 167-182.

Katsikadelis, J. T. & Sapountzakis, E. J. (2002) A Realistic Estimation of the Effective Breadth of Ribbed Plates. *International Journal of Solids and Structures*, 39, 897-910.

Kenneth, I.J. (2000) *Quadratic uniform b-spline curve refinement*. On-Line Geometric Modeling Notes, Visualization and Graphics Research group, Department of Computer Science, University of California, Davis.

Kermani, B. & Waldron, P. (1993) Analysis of Continuous Box Girder Bridges Including the Effects of Distortion. *Computers and Structures*, 47(3), 427-440.

Kim, Y. & Su, Y. (1997) A modified Fourier series method for the torsion analysis of bars with multiply connected cross sections. *International Journal of Solids and Structures*, 34(33-34), 4327-4337.

Kim, Y.Y. & Kim, J.H. (1999a) Thin-Walled Closed Box Beam Element for Static and Dynamic Analysis. *International Journal for Numerical Methods in Engineering*, 45, 473-490.

Kim, J.H. & Kim, Y.Y. (1999b) Analysis of thin-walled closed beams with general quadrilateral cross-sections. *Journal of Applied Mechanics*, 66(4), 904-912.

Kim, J.H. & Kim, Y.Y (2000) One-dimensional analysis of thin-walled closed beams having general cross-sections. *International Journal for Numerical Methods in Engineering*, 49(5), 653-668.

Kim, Y.Y. & Kim, Y. (2002) A one-dimensional theory of thin-walled curved rectangular box beams under torsion and out-of-plane bending. *International Journal for Numerical Methods in Engineering*, 53, 1675-1693.

Kim, N. & Kim, M.Y. (2005) Thin-Walled curved beam theory based on centroid-shear centre formulation. *Journal of Mechanical Science and Technology*, 19(2), 589-604.

Kim, N., Yun, H.T. & Kim, M.Y. (2004) Exact static element stiffness matrices of non-symmetric thin-walled curved beams. International Journal for Numerical Methods in Engineering, 61, 274-302.

Kollbrunner, C. F. & Basler, K. (1969) *Torsion in Structures-An Engineering Approach*. Springer, New York.

Kollbrunner, C. & Hajdin, N. (1975). *Dünnwandige Stäbe 2, Stäbe mit deformierbaren Querschnitten, Nicht-elastisches Verhalten dünnwandiger Stäbe*. Springer-Verlag.

Koo, B., Ha, S.H., Kim, H.S. & Cho, S. (2013) Isogeometric Shape Design Optimization of Geometrically Nonlinear Structures. *Mechanics Based Design of Structures and Machines*, 41(3), 337-358. DOI: 10.1080/15397734.2012.750226.

Koo, K.K. & Cheung, Y.K. (1989) Mixed variational formulation for thin-walled beams with shear lag. *Journal of Engineering Mechanics*, 115, 2271-2286.

Kraus, M. & Kindmann, R. (2009) *St. Venant's Torsion Constant of Hot Rolled Steel Profiles and Position of the Shear Centre*. NSCC.

Kraus, M. (2005) *Computerorientierte Berechungsmethoden für beliebige Stabquerscnitte des Stahlbaus*. Von der Fakultät für Bauingenieurwesen der Ruhr-Universität Bochum genehmigte Dissertation zur Erlangung des Grades Doktor-Ingenieur.

Kristek, V. (1970) Tapered Box Girders of Deformable Cross Section. *Journal of the Structural Division*, 96(8), 1761-1793.

Love, A.E.H. (1944) *A Treatise on the Mathematical Theory of Elasticity*. Dover, New York.

Luo, Q.Z. & Li, Q.S. (2000) Shear Lag of Thin-Walled Curved Box Girder Bridges. *Journal of Engineering Mechanics*, 126(10), 1111-1114.

Luo, Q.Z., Tang, J. & Li, Q.S. (2003) Shear Lag Analysis of Beam-Columns. *Engineering Structures*, 25, 1131-1138.

Luu, A. T., Kim, N. I. & Lee, J. (2015) NURBS-based isogeometric vibration analysis of generally laminated deep curved beams with variable curvature. *Composite Structures*, 119, 150-165.

Malcolm, D.J. & Redwood, R.G. (1970) Shear lag in stiffened box-girders. *Journal of the Structural Division*, 96(ST7), 1403-15.

Maplesoft (2008) a division of Waterloo Maple Inc., *Maple User Manual*, Maple 12.0. Sapountzakis, E.J. & Dikaros, I.C. (2010) Nonlinear effects in Elastic Flexural-Torsional Vibrations  of beams of arbitrary cross section. *Recent Patents on Computer Science*, 3, 203-223.

Martin, T.L. & Heins, C.P. (1978) Analysis of distortional stress in curved I girder bridges. *Computers and Structures*, 8, 691-701.

Moffatt, K.R. & Dowling, P.J. (1975) Shear lag in steel box-girder bridges. *Structural Engineering*, 53, 439-48.

Mokos, V.G. (2007) *Contribution to the Generalized Theory of Composite Beams Structures by  the Boundary Element Method*. Thesis for the PhD degree at the NTUA, National Technical University of Athens (in Greek).

Mokos, V.G. & Sapountzakis, E.J. (2011) Secondary Torsional Moment Deformation Effect by BEM. *International Journal of Mechanical Sciences*, 53, 897-909.

Murín, J. (1998) Beam element with varying cross-section satisfying local and global equilibrium conditions. *Journal of Mechanical Engineering*, 49(3), 208-223 [in Slovak].

Murín, J. (1999) 3D beam element with changing cross sectional area. *Journal of Engineering Mechanics*, 1, 25-35 [in Slovak].

Murín, J. & Kutiš, V. (2002) 3D-beam element with continuous variation of the cross-sectional area. *Computers and Structures*, 80, 329-38.

Nakai, H. & Murayama, Y. (1981) Distortional stress analysis and design aid for horizontally curved box girder bridges with diaphragms, *Proc. of the Japan Society of Civil Engineers*, 309, 25-39.

Nakai, H. & Yoo, H. (1988) *Analysis and design of curved steel bridges*. McGraw-Hill, New York.

Nallasivam, K., Dutta, A. & Talukdar, S. (2007) Dynamic analysis of horizontally curved thin-walled box-girder bridge due to moving vehicle. *Shock and Vibration*, 14, 229-248.

Nguyen-Thanh, N., Kiendl, J., Nguyen-Xuan, H., Wüchner, R., Bletzinger, K.U., Bazilevs, Y. & Rabczuk, T. (2011) Rotation free isogeometric thin shell analysis using

PHT-splines. *Computational Methods in Applied Mechanics and Engineering*, 200, 3410-3424.

Nguyen-Thanh, N., Valizadeh, N., Nguyen, M.N., Nguyen-Xuan, H., Zhuang, X., Areias, P., Zi, G., Bazilevs, Y., De Lorenzis, L. & Rabczuk, T. (2015) An extended isogeometric thin shell analysis based on Kirchhoff–Love theory. *Computational Methods in Applied Mechanics and Engineering*, 284, 265-291.

Oleinik, J.C. & Heins, C.P. (1975) Diaphragms for Curved Box Beam Bridges. *Journal of the Structural Division*, 101(10), 2161-2178.

Onate, E. (2009) *Structural Analysis with the Finite Element Method. Linear Statics. Volume 1: Basis and Solids*. Springer (CIMNE).

Ontario Highway Bridge Design Code (OHBDC) (1983) Ministry of Transportation and Communication, Ontario, Canada.

Osadebe, N.N. & Chidolue, C.A. (2012) Torsional-distortional response of thin-walled mono symmetric box girder structures. International Journal of Engineering Research and Applications, 2(3), 814-821.

Pai, P.F. (2014) High-Fidelity Sectional Analysis of Warping Functions, Stiffness Values and Wave Properties of Beams. Engineering Structures, 67, 77-95.

Papadrakakis, M. (2001) *Analysis of Structures with the Finite Element Method*. Papasotiriou Publications (in Greek).

Park, N.H., Choi, Y. & Kang, Y. (2005a) Spacing of intermediate diaphragms in horizontally curved steel box girder bridges. *Finite Elements in Analysis and Design*, 41(9-10), 925-43.

Park, N.H., Choi, S. & Kang Y.J. (2005b) Exact Distortional Behavior and Practical Distortional Analysis of Multicell Box Girders Using an Expanded Method. *Computers and Structures*, 83, 1607-1626.

Park, N.H., Lim, N.H. & Kang Y.J. (2003) A Consideration on Intermediate Diaphragm Spacing in Steel Box Girder Bridges with a Doubly Symmetric Section. *Engineering Structures*, 25, 1665-1674.

Petrolo, M., Zappino, E. & Carrera, E. (2012) Refined free vibration analysis of one-dimensional structures with compact and bridge-like cross-sections. *Thin-Walled Structures*, 56, 49-61.

Petrov, E. & Géradin, M. (1998) Finite Element Theory for Curved and Twisted Beams Based on Exact Solutions for Three-Dimensional Solids, Part 1: Beam Concept and Geometrically Exact Nonlinear Formulation. *Computational Methods in Applied Mechanics and Engineering*, 165, 43-92.

Piegel, L. & Tiller, W. (1997) *The NURBS Book*. Heidelberg: Springer, Berlin.

Ramm, E. & Hofmann T.J. (1995) *Der Ingenieurbau: Grundwissen-Baustatik/Baudynamik*. Ernst und Sohn, Berlin.

Ranzi, G. & Luongo, A. (2011) A New Approach for Thin-Walled Member Analysis in the Framework of GBT. *Thin-Walled Structures*, 49, 1404-1414.

Razaqpur, A.G., & Li, H.G. (1991) A finite element with exact shape functions for shear lag analysis in multi-cell box-girders. *Computers and Structures*, 39(1-2), 155-163.

Razaqpur, A.G. & Li, H.G. (1994) Refined analysis of curved thin-walled multicell box girders. *Computers and Structures*, 53(1), 131-142.

Reisenfeld, R. (1975) On Chaikin's algorithm. *IEEE Computer Graphics and Applications 4*, 3, 304-310.

Reissner, E. (1946) Analysis of shear lag in box beams by the principle of minimum potential energy. *Quarterly of Applied Mathematics*, 41, 268-78.

Roark, R.J. & Young, W.C. (1975) *Formulas for Stress and Strain*. 5th Edition, McGraw-Hill, New York.

Rogers, D.F. (2001) *An Introduction to NURBS with Historical Perspective*. Academic Press, San Diego, CA.

Rosen, A. & Abromovich, H. (1984) Galerkin method as a tool to investigate the planar and non-planar behaviour of curved beams. *Computers and Structures*, 18, 165-174.

Sakai, F. & Nagai, M. (1981) A proposal for intermediate diaphragm design in curved steel box girder bridges. *Proc. of the Japan Society of Civil Engineers*, 305, 11–22.

Sanders, J.L (1963) Nonlinear Theories of Thin Shells. *Quarterly of Applied Mathematics*, 21, 21-36.

Sapountzakis, E.J. & Katsikadelis, J.T. (2000) Analysis of plates reinforced with beams. *Computational Mechanics*, 26, 66-74.

Sapountzakis, E.J. & Mokos, V.G. (2003) Warping Shear Stresses in Nonuniform Torsion by BEM. *Computational Mechanics*, 30(2), 131-142.

Sapountzakis, E.J. & Mokos, V.G. (2003) Warping Shear Stresses in Nonuniform Torsion of Composite Bars by BEM. *Computational Methods in Applied Mechanics and Engineering*, 192, 4337-4353.

Sapountzakis, E.J., Tsipiras, V.J. & Argyridi, A.K. (2016) Torsional Vibration Analysis of Bars Including Secondary Torsional Shear Deformation Effect by the Boundary Element Method. *Journal of Sound and Vibration*, 355, 208-231.

Sapountzakis, E.J. & Tsiptsis, I.N. (2017) B-Splines in the Analog Equation Method for the Generalized Beam Analysis Including Warping Effects. *Computers and Structures*, 180, 60-73.

Sapountzakis, E.J. & Tsiptsis, I.N. (2017) Generalized Vibration Analysis of Beams including Warping Effects by Isogeometric Methods. *Journal of Vibration and Control*. DOI: 10.1177/1077546316685679.

Sapountzakis, E.J. & Tsiptsis, I.N. (2015) Generalized warping analysis of curved beams by BEM. *Engineering Structures*, 100, 535-549.

Sapountzakis, E.J. & Tsiptsis, I.N. (2014) Quadratic B-splines in the analog equation method for the nonuniform torsional problem of bars, *Acta Mechanica*, 225(12), 3511-3534.

Sapountzakis, E.J. (2000) Solution of Nonuniform Torsion of Bars by an Integral Equation Method. *Computers & Structures*, 77, 659-667.

Schardt, R. (1989) *Verallgemeinerte Technische Biegetheorie*. Springer-Verlag.

Schardt, R. (1994) Generalized Beam Theory – An adequate method for coupled stability problems. *Thin-walled Structures*, 19, 161-180.

Shakourzadeh, H., Guo, Y.Q. & Batoz, J.L. (1995) A Torsion Bending Element for thin-walled beams with open and closed cross sections. *Computers and Structures*, 55(6), 1045-1054.

Shi, Y., Xuan, J.M. & Song, Y.F. (2009) Analysis of vehicle-bridge coupling vibration of continuous girder bridge under uneven deck. *Bridge Construction*, 6, 15-22.

Silvestre, N. & Camotim, D. (2010) On the Mechanics of Distortion in Thin-Walled Open Sections. *Thin-Walled Structures*, 48, 469-481.

Steinle, A. (1970) *Torsion and cross-sectional distortion of the single cell box beam*. Beton und Stalbetonbau, 65, 215-222.

Tanyildiz, D.C. & Özcan, A.I. (2010) *An Isogeometric Beam Element using B-Splines*. Software Lab Project, Computation in Engineering, Technical University of Munich.

Timoshenko, S. & Woinowsky-Krieger, S. (1959) *Theory of plates and shells*. McGraw-Hill.

Tsipiras, V.J. & Sapountzakis, E.J. (2012) Secondary Torsional Moment Deformation Effect in Inelastic Nonuniform Torsion of Bars of Doubly Symmetric Cross Section by BEM. *International Journal of Non-linear Mechanics*, 47, 68-84.

Tsiptsis, I. N. & Sapountzakis, E. J. (2017) Isogeometric Analysis for the Dynamic Problem of Curved Structures Including Warping Effects. *Mechanics Based Design of Structures and Machines*, DOI: 10.1080/15397734.2016.1275974.

Tüfekçi, E. & Doğruer, O.Y. (2006) Out-of-plane free vibration of a circular arch with uniform cross-section: Exact solution. *Journal of Sound and Vibration*, 291, 525-538.

Vlasov, V. (1963) *Thin-walled elastic beams*. Jerusalem: Israel Program for Scientific Translations.

Vlasov, V. (1961) *Thin-walled Elastic Beams*, 2nd Edn. National Science Foundation, Washington DC.

Voyiadjis, G. Z. & Karamanlidis, D. (1990) *Advances in the Theory of Plates and Shells*, Elsevier.

Wang, Y., Xu, Y., Luo, Z., Wu, H. & Yan, L. (2016) Spatial Finite Element Analysis for Dynamic Response of Curved Thin-Walled Box Girder Bridges. *Mathematical Problems in Engineering*, Article ID 8460130.

Wattanasakulpong, N. & Chaikittiratana, A. (2014) On the Linear and Nonlinear Vibration Responses of Elastically End Restrained Beams Using DTM. *Mechanics Based Design of Structures and Machines*, 42(2), 135-150. DOI: 10.1080/15397734.2013.847778

Weeger, O., Wever, U. & Simeon, B. (2013) Isogeometric analysis of nonlinear Euler–Bernoulli beam vibrations. *Nonlinear Dynamics*, 72(4), 813-835.

Wright, R.N., Abdel-Samad, S.R. & Robinson, A.R. (1968) BEF Analogy for Analysis of Box Girders. *Journal of the Structural Division*, 94(7), 1719-1743.

Yabuki, T. & Arizumi, Y. (1989) A provision on intermediate diaphragm spacing in curved steel-plated box-bridge-girders, *Structural engineering/earthquake engineering*, JSCE, 6 (2), 207-216.

Yang, Y.B., Wu, C.M. & Yau, J.D. (2001) Dynamic response of a horizontally curved beam subjected to vertical and horizontal moving loads. *Journal of Sound and Vibration*, 242, 519-537.

Yoo, C.H. (1979): Matrix formulation of curved girders. *Journal of Engineering Mechanics*, 105, 971-987.

Yoo, C.H., Kang, J. & Kim. K. (2015) Stresses due to distortion on horizontally curved tub-girders. *Engineering Structures*, 87, 70-85.

Zhang, S.H. & Lyons, L.P.R. (1984a) A thin-walled box beam finite element for curved bridge analysis. *Computers and Structures*, 18(6), 1035-1046.

Zhang, S.H. & Lyons, L.P.R. (1984b) The application of the thin-walled box beam element to multibox bridge analysis. *Computers and Structures*, 18(5), 795-802.

Zhang, Y., Hou,  Z., Li, Y. & Wang, Y. (2015) Torsional behaviour of curved composite beams in construction stage and diaphragm effects. *Journal of Constructional Steel Research*, 108, 1-10.

Zhang, Z. & Chen, S. (1991) A new method for the vibration of thin-walled beams. *Computers and Structures*, 39(6), 597-601.

Zhu, Z., Zhanga, L., Zhenga, D. & Cao, G. (2016) Free vibration of horizontally curved thin-walled beams with rectangular hollow sections considering two compatible displacement fields. *Mechanics Based Design of Structures and Machines*, 44(4), 354-371. DOI: 10.1080/15397734.2015.1075410

Zhu, L., Zhao Y., & Wang G. (2010) Exact solution for in-plane displacement of redundant curved beam. *Structural Engineering and Mechanics*, 34(1), 139-142.